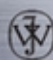


Edited by
Peter Capper

Bulk Crystal Growth

in Electronic, Optical
and Optoelectronic
Materials



 **WILEY**

Wiley Series
in Materials for
Electronic
& Optoelectronic
Applications

Bulk Crystal Growth of Electronic, Optical & Optoelectronic Materials

Wiley Series in Materials for Electronic and Optoelectronic Applications

Series Editors

Dr Peter Capper, *BAE SYSTEMS Infrared Ltd, Southampton, UK*

Professor Safa Kasap, *University of Saskatchewan, Saskatoon, Canada*

Professor Arthur Willoughby, *University of Southampton, Southampton, UK*

Published Titles

Bulk Crystal Growth of Electronic, Optical and Optoelectronic Materials

Edited by P. Capper

Properties of Group-IV, III-V and II-VI Semiconductors, S. Adachi

Forthcoming Titles

Liquid Phase Epitaxy, Edited by P. Capper and M. Mauk

Thin Film Solar Cells: Fabrication, Characterization and Applications,

Edited by J. Poortmans & A. Arkhipov

Optical Properties of Condensed Matter and Applications, Edited by J. Singh

Charge Transport in Disordered Solids with Applications in Electronics,

Edited by S. Baranovski

Dielectric Films for Advanced Microelectronics,

Edited by K. Maex, M. Baklanov and M. Green

Molecular Electronics, M. Petty

Bulk Crystal Growth of Electronic, Optical & Optoelectronic Materials

Edited by

Peter Capper
BAE SYSTEMS Infrared Ltd, Southampton



John Wiley & Sons, Ltd

Copyright © 2005

John Wiley & Sons Ltd, The Atrium, Southern Gate, Chichester,
West Sussex PO19 8SQ, England

Telephone (+44) 1243 779777

Email (for orders and customer service enquiries): cs-books@wiley.co.uk

Visit our Home Page on www.wiley.com

All Rights Reserved. No part of this publication may be reproduced, stored in a retrieval system or transmitted in any form or by any means, electronic, mechanical, photocopying, recording, scanning or otherwise, except under the terms of the Copyright, Designs and Patents Act 1988 or under the terms of a licence issued by the Copyright Licensing Agency Ltd, 90 Tottenham Court Road, London W1T 4LP, UK, without the permission in writing of the Publisher. Requests to the Publisher should be addressed to the Permissions Department, John Wiley & Sons Ltd, The Atrium, Southern Gate, Chichester, West Sussex PO19 8SQ, England, or emailed to permreq@wiley.co.uk, or faxed to (+44) 1243 770620.

Designations used by companies to distinguish their products are often claimed as trademarks. All brand names and product names used in this book are trade names, service marks, trademarks or registered trademarks of their respective owners. The Publisher is not associated with any product or vendor mentioned in this book.

This publication is designed to provide accurate and authoritative information in regard to the subject matter covered. It is sold on the understanding that the Publisher is not engaged in rendering professional services. If professional advice or other expert assistance is required, the services of a competent professional should be sought.

Other Wiley Editorial Offices

John Wiley & Sons Inc., 111 River Street, Hoboken, NJ 07030, USA

Jossey-Bass, 989 Market Street, San Francisco, CA 94103-1741, USA

Wiley-VCH Verlag GmbH, Boschstr. 12, D-69469 Weinheim, Germany

John Wiley & Sons Australia Ltd, 33 Park Road, Milton, Queensland 4064, Australia

John Wiley & Sons (Asia) Pte Ltd, 2 Clementi Loop #02-01, Jin Xing Distripark, Singapore 129809

John Wiley & Sons Canada Ltd, 22 Worcester Road, Etobicoke, Ontario, Canada M9W 1L1

Wiley also publishes its books in a variety of electronic formats. Some content that appears in print may not be available in electronic books.

Library of Congress Cataloging-in-Publication Data

Bulk crystal growth of electronic, optical & optoelectronic materials /
edited by Peter Capper.

p. cm.—(Wiley series in materials for electronic and
optoelectronic applications)

Includes bibliographical references and index.

ISBN 0-470-85142-2 (cloth : alk. paper)

1. Semiconductors—Materials. 2. Optoelectronics—Materials. 3. Crystal
growth. I. Capper, Peter. II. Title. III. Series.

TK7871.B85 2004

621.3815'2—dc22

2004019932

British Library Cataloguing in Publication Data

A catalogue record for this book is available from the British Library

ISBN 0-470-85142-2

Typeset in 10/12pt Times by Laserwords Private Limited, Chennai, India

Printed and bound in Great Britain by Antony Rowe Ltd, Chippenham, Wiltshire

This book is printed on acid-free paper responsibly manufactured from sustainable forestry
in which at least two trees are planted for each one used for paper production.

This book is dedicated to my wife Marian and our young sons Samuel and Thomas for all their forbearance (and loss of football, squash and badminton practice) during the course of the book production.

This page intentionally left blank

Contents

Series Preface	xv
Preface	xvii
Acknowledgements	xxi
List of Contributors	xxiii
Abbreviations	xxvii
1 Silicon	1
<i>Taketoshi Hibiya and Keigo Hoshikawa</i>	
1.1 Introduction	1
1.2 Crystal-growth method and technology	3
1.2.1 High-purity polycrystalline silicon	3
1.2.2 CZ-Si growth apparatus and related furnace parts	6
1.2.3 CZ-Si crystal growth	11
1.2.4 FZ (float-zone) Si crystal growth	13
1.2.5 Wafer processing	16
1.3 Melt process	18
1.3.1 Analysis of heat- and mass-transfer processes	18
1.3.2 Oxygen transportation process and mechanism	24
1.3.3 Control of oxygen concentration by application of cusp magnetic field	27
1.4 Defect and wafer quality	30
1.4.1 Oxygen precipitation and gettering	30
1.4.2 Grown-in defects	33
1.5 Concluding remarks	39
References	40
2 Growth of Gallium Arsenide	43
<i>M.R. Brozel and I.R. Grant</i>	
2.1 Introduction	43
2.2 Doping considerations	45
2.3 Growth techniques	48
2.3.1 Horizontal Bridgman and horizontal gradient freeze techniques	48

2.3.2	Liquid encapsulated Czochralski (LEC) technique	49
2.3.3	Vertical gradient freeze (VGF) technique	53
2.4	Crystalline defects in GaAs	54
2.4.1	Defects in melt-grown, semi-insulating GaAs	54
2.5	Impurity and defect analysis of GaAs (chemical)	59
2.6	Impurity and defect analysis of GaAs (electrical)	61
2.6.1	Introduction to the electrical analysis of defects in GaAs	61
2.7	Impurity and defect analysis of GaAs (optical)	65
2.7.1	Optical analysis of defects in GaAs	65
2.8	Conclusions	67
	Acknowledgments	68
	References	69
3	Computer Modelling of Bulk Crystal Growth	73
	<i>Andrew Yeckel and Jeffrey J. Derby</i>	
3.1	Introduction	74
3.2	Present state of bulk crystal growth modelling	75
3.3	Bulk crystal growth processes	77
3.4	Transport modelling in bulk crystal growth	79
3.4.1	Governing equations	79
3.4.2	Boundary conditions	83
3.4.3	Continuum interface representation	84
3.4.4	Radiation heat-transfer modelling	86
3.4.5	Noninertial reference frames	88
3.4.6	Magnetic fields	88
3.4.7	Turbulence	89
3.5	Computer-aided analysis	89
3.5.1	Discretization	89
3.5.2	Numerical interface representation	90
3.5.3	Deforming grids and ALE methods	92
3.5.4	A simple fixed-grid method	94
3.5.5	Quasi-steady-state models	96
3.6	Modelling examples	98
3.6.1	Float-zone refinement of silicon sheets	98
3.6.2	Bridgman growth of CZT: axisymmetric analysis	102
3.6.3	Bridgman growth of CZT: three-dimensional analysis	104
3.6.4	Morphological stability in solution growth of KTP	106
3.7	Summary and outlook	112
	Acknowledgments	113
	References	113
4	Indium Phosphide Crystal Growth	121
	<i>Ian R. Grant</i>	
4.1	Introduction	121
4.2	Material properties	122
4.3	Hazards	123
4.4	Crystal structure	124

4.5	Synthesis	125
4.6	Single-crystal growth	129
4.7	Defects	132
	4.7.1 Twins	132
	4.7.2 Dislocations	133
4.8	Dislocation reduction	135
4.9	VGF growth	136
4.10	Crystal-growth modelling	139
4.11	Dopants	141
	4.11.1 N-type InP	141
	4.11.2 P-type InP	142
	4.11.3 Semi-insulating InP	142
4.12	Conclusion	145
	Acknowledgements	145
	References	145
5	Bulk Growth of InSb and Related Ternary Alloys	149
	<i>W.F.H. Micklethwaite</i>	
5.1	Introduction—a little history	149
5.2	Why the interest?	150
5.3	Key properties	151
	5.3.1 Crystallography	151
	5.3.2 Growth-critical material parameters	154
	5.3.3 Common growth conditions	154
	5.3.4 Impurities and dopants	154
5.4	Czochralski growth	155
	5.4.1 Challenges	156
	5.4.2 Choice and implications of growth axis	162
	5.4.3 Size evolution and its drivers	163
5.5	Bridgman and VGF growth	164
5.6	Other bulk growth methods	165
5.7	InSb-related pseudobinary (ternary) alloys	165
	5.7.1 (Ga,In)Sb	166
	5.7.2 (In,Tl)Sb	168
	5.7.3 In(As,Sb)	168
	5.7.4 In(Bi,Sb)	168
5.8	Conclusion	169
	References	169
6	GaN Bulk Substrates Grown under Pressure from Solution in Gallium	173
	<i>I. Grzegory, M. Boćkowski and S. Porowski</i>	
6.1	Introduction	173
6.2	Phase diagrams and growth method	175
	6.2.1 Thermodynamic properties of GaN-Ga-N ₂ system	175
	6.2.2 The role of high pressure	178
	6.2.3 Crystallization of GaN from solution	179
	6.2.4 Experimental	182

6.3	Results of spontaneous crystallization in temperature gradient: crystals and physical properties of the crystals	183
6.3.1	Morphology	183
6.3.2	Physical properties of the pressure-grown GaN crystals	185
6.4	Discussion of crystallization in a temperature gradient	188
6.5	Crystallization on the free gallium surface	192
6.6	Directional crystallization on GaN and foreign substrates	194
6.6.1	Seeded growth of GaN from solutions in gallium on GaN substrates	195
6.6.2	Seeded growth of GaN from solutions in gallium on GaN/sapphire substrates	197
6.7	Applications of pressure-grown bulk GaN substrates	201
6.8	Summary and conclusions	203
	References	205
7	Bulk Growth of Cadmium Mercury Telluride (CMT)	209
	<i>P. Capper</i>	
7.1	Introduction	209
7.2	Phase equilibria	210
7.3	Crystal growth	211
7.3.1	SSR	212
7.3.2	THM	217
7.3.3	Bridgman	222
7.4	Conclusions	238
	References	238
8	Bulk Growth of CdZnTe/CdTe Crystals	241
	<i>R. Hirano and H. Kurita</i>	
8.1	Introduction	241
8.2	High-purity Cd and Te	242
8.2.1	Cadmium	242
8.2.2	Tellurium	243
8.3	Crystal growth	243
8.3.1	Polycrystal growth	243
8.3.2	VGF single-crystal growth	244
8.4	Wafer processing	260
8.4.1	Process flow	261
8.4.2	Characteristics	264
8.5	Summary	266
	Acknowledgements	266
	References	266
9	Bulk Crystal Growth of Wide-Bandgap II-VI Materials	269
	<i>M. Isshiki, J.F. Wang</i>	
9.1	Introduction	269
9.2	Physical and chemical properties	270
9.3	Phase diagrams	270

9.4	Crystal-growth methods	270
9.4.1	Growth from vapor phase	272
9.4.2	Growth from liquid phase	276
9.4.3	Crystal growth from solid phase	280
9.5	Crystal growth of wide-bandgap compounds	280
9.5.1	ZnS	280
9.5.2	ZnO	282
9.5.3	ZnSe	284
9.5.4	ZnTe	291
9.6	Conclusions	294
	References	294
10	Sapphire Crystal Growth and Applications	299
	<i>V.A. Tatartchenko</i>	
10.1	Introduction	300
10.2	Sapphire structure	301
10.3	Sapphire crystal growth	302
10.3.1	Verneuil's technique (VT)	302
10.3.2	Floating-zone technique (FZT)	308
10.3.3	Czochralski technique (CzT)	310
10.3.4	Kyropulos technique (KT)	312
10.3.5	Horizontal Bridgman technique (HBT)	313
10.3.6	Heat-exchange method (HEM)	313
10.3.7	Techniques of pulling from shaper (TPS)	314
10.3.8	Flux technique (FT)	318
10.3.9	Hydrothermal technique (HTT)	319
10.3.10	Gas-phase technique (GPT)	319
10.4	Corundum crystal defects	319
10.4.1	Inclusions	319
10.4.2	Dislocations, low-angle grain boundaries, internal stresses	323
10.4.3	Twins	326
10.4.4	Faceting, inhomogeneities of impurity	326
10.4.5	Growth direction	327
10.5	Applications	327
10.5.1	Special windows	327
10.5.2	Domes	328
10.5.3	Substrates	329
10.5.4	Construction material	329
10.6	Brief crystal-growth technique characterization	329
10.6.1	VT	329
10.6.2	FZT	330
10.6.3	CzT	330
10.6.4	KT	330
10.6.5	HBT	330
10.6.6	HEM	330
10.6.7	TPS	330
10.6.8	FT, HTT, GPT	331

10.7 Conclusion	331
References	331
Appendix: sapphire physical properties	334
11 Crystal Growth of Fluorides	339
<i>P.P. Fedorov, V.V. Osiko</i>	
11.1 Introduction	339
11.2 Polymorphism and crystal growth	340
11.3 Solid solutions: decomposition and ordering	342
11.4 Type of compound melting: congruent/incongruent	347
11.5 Phases that are not in equilibrium with melt	347
11.6 Dopant segregation coefficients	348
11.7 Morphological stability	348
11.8 Hydrolysis and melt fluoride growth	350
Acknowledgments	352
References	352
12 Scintillators: Crystal Growth and Scintillator Performance	357
<i>A. Gektin</i>	
12.1 Introduction	357
12.2 Scintillator applications	358
12.2.1 High-energy physics	359
12.2.2 Medical imaging	361
12.3 Scintillation-material efficiency estimation	361
12.4 Halide scintillator growth	364
12.5 Activator distribution in scintillation single crystals	374
12.6 Oxide scintillation crystal growth	376
12.7 Influence of single-crystal perfection on scintillation characteristics	378
12.8 New scintillation crystals	381
12.9 Conclusion	382
List of definitions and abbreviations	383
References	383
13 Growth of Quartz Crystals	387
<i>K. Byrappa</i>	
13.1 Introduction	387
13.2 History of quartz crystal growth	388
13.3 Physical chemistry of the growth of quartz	391
13.4 Solubility	392
13.5 Apparatus	396
13.6 Crystal growth	396
13.7 Growth of high-quality (and dislocation-free) quartz crystals	398
13.7.1 Growth rate	399
13.7.2 Seed effect	400
13.7.3 Nutrient effect	400
13.8 Defects observed in synthetic α -quartz single crystals	401

13.9 Processing of α -quartz for high-frequency devices	402
13.10 Conclusions	404
References	404
14 Crystal Growth of Diamond	407
<i>Hisao Kanda</i>	
14.1 Introduction	407
14.2 Diamond synthesis	408
14.2.1 Phase diagram of carbon	408
14.2.2 Direct transformation	408
14.2.3 Agents for diamond formation	409
14.2.4 Carbon source	411
14.2.5 High-pressure apparatus	412
14.2.6 Diamond growth methods	412
14.3 Properties of diamond single crystals made with high-pressure methods	417
14.3.1 Morphology	417
14.3.2 Surface morphology	419
14.3.3 Inclusions	421
14.3.4 Atomic impurities, color and luminescence	422
14.3.5 Color control	423
14.4 Summary	428
References	428
15 Growth of Silicon Carbide	433
<i>T.S. Sudarshan, D. Cherednichenko, and R. Yakimova</i>	
15.1 Introduction	433
15.2 Historical development	434
15.3 Industrial production of SiC wafers	435
15.3.1 Growth along the conventional c - or [0001] direction	435
15.3.2 Bulk SiC growth along alternate orientations	436
15.3.3 Bulk growth of semi-insulating SiC	436
15.3.4 Bulk-crystal doping	437
15.4 Essentials of the bulk growth process and thermal-stress-generation mechanisms	437
15.4.1 Basics of the bulk growth process	437
15.4.2 Thermal-stress-generation mechanisms	443
15.5 Growth-related defects	444
15.6 Outlook	447
Acknowledgements	447
References	447
16 Photovoltaic Silicon Crystal Growth	451
<i>T.F. Cizzek</i>	
16.1 Introduction	451
16.2 Traditional silicon growth methods applied to PV	452
16.2.1 Czochralski growth	452

16.2.2 FZ growth	455
16.2.3 Comparisons between CZ and FZ growth for PV	456
16.3 Multicrystalline ingot growth methods for PV	459
16.3.1 Casting and directional solidification	459
16.3.2 Semicontinuous electromagnetic casting	461
16.4 Ribbon or sheet growth methods for PV	463
16.4.1 Small-area solid/liquid interface growth methods	463
16.4.2 Large-area solid/liquid interface growth methods	468
16.5 Thin-layer growth on substrates for PV	472
16.6 Comparison of growth methods	473
References	475
17 Bulk Crystal Growth Under Microgravity Conditions	477
<i>Thierry Duffar</i>	
17.1 Introduction	477
17.2 Experimental and technological environment	502
17.2.1 Technical limitations: time, size, power and space management	502
17.2.2 Environmental limitations: the gravity level	504
17.3 Scientific achievements	505
17.3.1 Segregation studies in Bridgman configuration	505
17.3.2 Experiments of crystal growth from a molten zone or molten drop	508
17.3.3 Sample–crucible interactions and structural aspects	510
17.3.4 Growth from solutions	514
17.3.5 Growth from the vapor phase	515
17.4 Conclusion and future directions	516
17.4.1 Summary of major breakthroughs	516
17.4.2 Problems still to be investigated and perspectives	517
References	517
Index	525

Wiley Series in Materials for Electronic and Optoelectronic Applications

This book series is devoted to the rapidly developing class of materials used for electronic and optoelectronic applications. It is designed to provide much-needed information on the fundamental scientific principles of these materials, together with how these are employed in technological applications. The books are aimed at post-graduates students, researchers and technologists, engaged in research, development and the study of materials in electronics and photonics, and industrial scientists developing new materials, devices and circuits for the electronic, optoelectronic and communications industries.

The development of new electronic and optoelectronic materials depends not only on materials engineering at a practical level, but also on a clear understanding of the properties of materials, and the fundamental science behind these properties. It is the properties of a material that eventually determine its usefulness in an application. The series therefore also includes such titles as electrical conduction in solids, optical properties, thermal properties, etc., all with applications and examples of materials in electronics and optoelectronics. The characterization of materials is also covered within the series in as much as it is impossible to develop new materials without the proper characterization of their structure and properties. Structure–property relationships have always been fundamentally and intrinsically important to materials science and engineering.

Materials science is well known for being one of the most interdisciplinary sciences. It is the interdisciplinary aspect of materials science that has led to many exciting discoveries, new materials and new applications. It is not unusual to find scientists with chemical engineering backgrounds working on materials projects with applications in electronics. In selecting titles for the series, we have tried to maintain the interdisciplinary aspect of the field, and hence its excitement to researchers in this field.

Peter Capper
Safa Kasap
Arthur Willoughby

This page intentionally left blank

Preface

Whole industries currently rely on bulk-grown crystals of a variety of materials. These industries range from information technology, based on the ubiquitous silicon, through radiofrequency applications, using gallium arsenide, etc., to telecommunications and lighting, based on III-V compounds, to infrared imaging, based on cadmium mercury telluride, and to high-energy physics and medical imaging using scintillator materials. These materials are used either in the active mode, as for silicon, or in the passive mode where the bulk-grown material is used as a substrate on which to deposit a wide range of binary, ternary, quaternary, etc., compounds by several epitaxial growth processes.

This book is an attempt to summarise the position in a number of these areas where bulk-grown crystals are central to particular industries. The book is aimed at senior under- and post-graduates in physics, chemistry, materials science, electrical engineering and optical engineering disciplines, as well as those employed in the various fields of crystal growth within the relevant industries. It is hoped that the former group will find the book readable both as an introductory text and as a useful guide to the literature. Workers in industry will hopefully find the book useful in bringing them up-to-date information in both their own and other areas of interest. To both groups of readers I trust that the book will prove interesting and a spur to further progress in this key area of technology.

The first chapter deals with the most important semiconductor material, silicon. Silicon-based systems on 'chips' form the basis for the huge information technology industry, which is a fusion of computers and telecommunications. More demanding image-processing requirements in computers require improved throughput and yield of these chips on larger-diameter and high-quality silicon wafers. Currently 300-mm diameter is the industry standard, but R&D work has already taken place on 450-mm crystals (weight ~400 kilograms) as the next logical step in the evolution. A large effort is also underway on theoretical modelling of transport phenomena in these large growth systems to improve our understanding of the growth and defect-production processes. The next chapter discusses the second most studied semiconductor, GaAs, which is used in high-frequency opto- and microelectronic devices in a wide range of applications. Currently, crystals are in production at 150-mm diameter, with 200 mm also recently demonstrated.

Chapter 3 outlines the current situation with regard to transport modelling, including turbulence, of a range of bulk crystal growth processes, including vertical and horizontal Bridgman, vertical gradient freeze, Czochralski, float-zone and travelling heater methods. Examples are given to illustrate the features of this modelling in terms of the growth of silicon sheets, cadmium zinc telluride and potassium titanyl phosphate, as representatives of classes of materials.

The next two chapters deal with the In-based compounds InP and InSb. The former is used as a substrate material for the epitaxial growth of alloys for use in emitters and detectors of IR light at wavelengths matched to optical-fibre transmission, i.e. 1.33 and

1.55 μm . These devices have been used in high-density trunk networks, supporting internet usage and other telecommunications applications, e.g. mobile phones, etc. Currently, crystal diameters are 100 mm with 150-mm diameter material also having been demonstrated. Indium antimonide, InSb, is mainly used in very high performance large mid-IR detectors (up to 1024×1024 pixels) but it also has some applications as magnetic sensors, X-ray monochromators, IR filters and optical immersion lenses. It has the highest room-temperature mobility of any semiconductor and hence has uses such as high-speed transistors. Crystals of 100-mm diameter are now in production and there is a demand for larger sizes, still driven by the need for larger IR focal plane arrays of detectors.

Chapter 6 discusses current work on bulk-grown GaN, a material system that has received much attention recently. Together with additions of Al and In this material is used for short-wavelength optoelectronics and for high-power, high-temperature electronic devices. Currently, high-brightness blue and green LEDs and low-power blue LDs are commercially available. Progress in the field is limited by a lack of large high-quality substrates for the epitaxial growth of multilayer quantum structures. Quasi-bulk GaN can be grown by epitaxy on sapphire, GaAs, etc., but the preferred compound is clearly GaN itself. Currently size is limited (~ 14 mm) but 50-mm growth is being actively researched.

The next three chapters deal with a range of II-VI compounds. Chapter 7 deals with the pre-eminent infrared material, cadmium mercury telluride, CMT. This is the third most-studied semiconductor after Si and GaAs. Despite the current dominance of various epitaxial processes to produce large areas of this material for current focal plane arrays of diodes for thermal-imaging applications, bulk-grown material is still in use for the simpler first-generation IR detectors based on the photoconductive principle. Size is generally limited to 20-mm diameter material, although 40-mm diameter material has been produced, but this is not a major concern as devices tend to be rather small. Chapter 8 describes the production of CdZnTe for use as a substrate material for the epitaxial growth of CMT. Currently production sizes are 100 mm but demonstrations of 125-mm growth have recently been made. This material is also much in demand now for X-ray and gamma-ray detection in a wide range of applications. Chapter 9 covers the field of wide bandgap II-VIs, mainly Zn-based compounds. These are potentially useful in making laser diodes and light emitting diodes in the visible and UV regions. Because of their high melting points and component partial pressures vapor growth has proved popular, but growth from the liquid is also used. Crystal sizes can be up to 80-mm diameter (ZnTe), 50 mm for Zn and 25 mm for ZnS and ZnSe.

The next few chapters cover a wide range of oxide and fluoride materials that are used in numerous and diverse applications. The first material discussed is sapphire, which has a unique blend of high melting point, exceptional hardness, transmission over a wide wavelength band, radiation and chemical resistance and producibility in large and shaped crystals. It is used in lasers, as a substrate for epitaxial growth (of, for example, Si and GaN), shaped crystals in microelectronics, optical windows, etc. Various growth techniques have been applied with the heat exchanger method producing the largest crystals at some 340-mm diameter. The next chapter deals with a range of fluoride materials that are produced for various applications in photonics, medicine, semiconductor processing and optical communications from the vacuum-UV to the mid-IR regions. Device types include lasers, upconversion media, optical amplifiers, diode-pumped and tunable solid-state lasers, etc. Ultrahigh-quality calcium fluoride is widely used as a lens in

photolithography of Si-based integrated circuits. Other fluorides are used in scintillators, holographic media and transparent magnetic systems. Oxide and halide scintillators form the basis of the subsequent chapter. Scintillators convert different forms of ionising radiation into visible light. They are used in nuclear-medicine imaging (e.g. computer tomography), high-energy physics and astrophysics, security systems, environmental control and other industrial uses. Materials include NaI, bismuth germanate, CsI and lead tungstate, and several tons of a particular material might be needed for a specific high-energy physics experiment. Crystal dimensions can reach 600×500 mm in some halide systems, with weights of several hundred kilograms. The final chapter in the series dealing with oxides and fluorides describes the growth and applications of quartz, more specifically α -quartz grown by the hydrothermal technique. Quartz is the main piezoelectric material and its uses are widely spread across industrial and consumer products, including watches and timing circuits for computers and telecommunications. In addition, quartz demonstrates birefringence and optical rotary power, leading to uses in optical filters and waveplates. Some 3000 tons of quartz are produced each year, with up to 5000 kg being produced in a single run, with crystals up to $5 \times 5 \times 15$ cm in size.

The next three chapters are concerned with more Group IV elements and compounds. The first material is diamond, which, besides its obvious uses in jewelry and in mechanical engineering, has applications in electronics. This is due to its unique combination of high hardness, high thermal conductivity, optical transparency and wide bandgap. Bulk growth takes place under conditions of high pressure and high temperature. Commercially available sizes range from 1–10 mm, although the largest is 34.8 carats (~ 7 g) in weight, with dimensions of almost 20 mm on the sides. The next chapter covers SiC, which is set to replace conventional semiconductors in high-power electronics, e.g. motor controllers and power distribution in electric vehicles. Its wide bandgap, high thermal conductivity, high breakdown field strength and chemical stability make it attractive for high-temperature, power-control and high-speed communication devices. Currently, some of the GaN devices used in satellite communications at higher powers are grown on SiC substrates. Crystals have been grown up to 75-mm diameter, depending on polytype and orientation. Silicon is not only used in microelectronic devices, as described in Chapter 1, it is also used in photovoltaic solar cells as described in Chapter 16. Standard Czochralski and float-zone techniques have been used to grow material up to 150-mm diameter, but a range of other techniques have also been used. The largest multicrystalline cast ingots can reach sizes of $690 \text{ mm} \times 690 \text{ mm}$, weighing some 240 kilograms. Various ribbon and sheet crystals are also produced, with widths up to 100–150 mm or 50 mm with lengths of 200 cm, at extremely high production rates, albeit with somewhat lower conversion efficiencies.

The final chapter of the book enters the fascinating area of growth under microgravity conditions, which has been studied for the last 30 years. Initially, the absence of convection in melt- and vapor-grown crystals was expected to produce more homogeneous material. Most experiments were conducted on semiconductors, with a small amount of work on detectors. Residual-gravity effects are still a problem, however, in realizing the goal of larger crystals with improved homogeneity, although some improvements in homogeneity and structural quality have been obtained. A dewetting phenomenon is seen in some systems that dramatically improves the structural quality of crystals, and this has been reproduced on earth.

Finally, I would like to sincerely thank all the contributors to the book, as well as Jenny Cossham, Zoe Jenner and Susan Barclay of John Wiley & Sons Ltd for their help

and patience throughout the course of the book preparation and production stages. I would also like to thank two of my many mentors, Dennis Elwell and Hans Scheel for initiating me into crystal growth, some 30 years ago, and for remaining good friends and colleagues ever since. Thanks are also due to the management of BAE SYSTEMS Infra-Red Limited for their support in this project.

Peter Capper,
Southampton, UK

1 Silicon

TAKETOSHI HIBIYA¹

¹*Tokyo Metropolitan Institute of Technology 6-6, Asahigaoka, Hino 191-0065, Japan*

KEIGO HOSHIKAWA²

²*Faculty of Education Shinshu University, Nishinagano, Nagano 380-8544, Japan*

1.1 Introduction	1
1.2 Crystal-growth method and technology	3
1.2.1 High-purity polycrystalline silicon	3
1.2.2 CZ-Si growth apparatus and related furnace parts	6
1.2.3 CZ-Si crystal growth	11
1.2.4 FZ (float-zone) Si crystal growth	13
1.2.5 Wafer processing	16
1.3 Melt process	18
1.3.1 Analysis of heat- and mass-transfer processes	18
1.3.2 Oxygen transportation process and mechanism	24
1.3.3 Control of oxygen concentration by application of cusp magnetic field	27
1.4 Defect and wafer quality	30
1.4.1 Oxygen precipitation and gettering	30
1.4.2 Grown-in defects	33
1.5 Concluding remarks	39
References	40

1.1 INTRODUCTION

Modern society is being supported by IT (information technology), i.e., the fusion of computer and communication technologies. From the hardware viewpoint, these are based on silicon technology, i.e., systems on chips, where MPUs (microprocessor unit), logic, and memories are fabricated on the same chip, whereas these functions were conventionally separately prepared. The evolution of IT requires high capability in image processing, even in a lap-top computer. This causes an increase in the memory capacity installed within computers. In order to improve throughput and yield of these LSI (large-scale

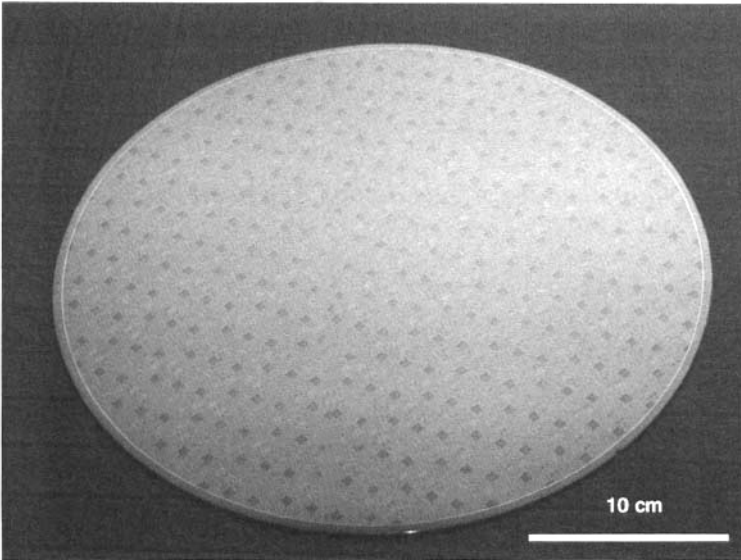


Figure 1.1 Large-scale integration chips on a 300-mm diameter wafer. (Courtesy of NEC)

integration) chips, silicon wafers with large diameter and high quality are required. Figure 1.1 shows LSI chips fabricated on a 300-mm diameter silicon wafer.

Historically, the first transistor was prepared using germanium. However, from the viewpoint of temperature characteristics, silicon is better than germanium due to its wider band gap (1.14 eV at room temperature) than that for germanium (0.67 eV at room temperature), although the mobility of germanium is higher than that of silicon [1]. Nowadays, almost all LSI chips are fabricated on silicon wafers except for high-speed devices and optical devices fabricated on III-V compound semiconductor crystals.

The International Technology Roadmap for Semiconductors (ITRS) 2003 predicted a future trend of LSI chip technology [2]. For example, for DRAM (dynamic random access memory), memory size per chip will be increased from 4 Gbit (2004) to 120 Gbit (2018) for introduction level, and from 1 Gbit (2004) to 32 Gbit (2018) for production level. The performance of chips will also be improved; for example, the on-chip local clock will be increased from 4.2 GHz (2004) to 53 GHz (2018) and power dissipation will be also increased from 158 W (2004) to 300 W (2018). This improvement of chip performance suggests that the chip size will increase with increasing number of transistors per chip, without shrinking device-design rules. Chip size will be almost constant through continuous effort to shrink device-design rules, as follows. Typical specifications of DRAM and MPU (microprocessor unit) are shown in Table 1.1. Conventionally, the specification for DRAM is a kind of index for LSI fabrication technology; however, nowadays the specification for MPU is also a guide of the development of technology. The DRAM half-pitch, which shows the most representative feature of DRAM fabrication technology with respect to scaling, is already as small as 100 nm and will be less than 50 nm in 2010. The physical gate length, which is smaller than the real gate length, will be 7 nm in 2018. This suggests that the area of a gate will also be decreased from 0.065 mm^2 (2004) to 0.0016 mm^2 (2018); consequently, the chip size is also required to be decreased.

Table 1.1 Roadmap for LSI chip fabrication technology

	2004	2007	2010	2013	2018
DRAM Generation (bit/chip)	1G	2G	4G	8G	32G
(Production introduction)	4G	16G	32G	64G	128G
On-chip local clock (GHz)	4.2	9.3	15	23	53
Allowable maximum power (W)	158	189	218	251	300
DRAM half-pitch (nm)	90	65	45	32	18
MPU physical gate length (nm)	37	25	18	13	7
Gate area (mm ²)	0.065	0.028	0.012	0.0061	0.0016
Chip size at production (mm ²)	110	97	83	83	87
Mask levels (MPU)	31	33	35	35	39
Wafer diameter (mm)	300	300	300	450	450

Nevertheless, the size of a chip will not be decreased to any great extent and the numbers of chips per wafer will not be increased, because bit size per chip will be increased at the same time. Corresponding to an improvement of performance, mask levels are increased, e.g. for MPU, from 31 (2004) to 39 (2018). This suggests that yield can be degraded during the chip-fabrication process.

In order to overcome this problem and to decrease the production cost of LSI chip fabrication, an increase in wafer diameter is required. In 2004 silicon wafer size has been converted from 200 mm to 300 mm in diameter (see Fig. 1.1). The ITRS suggests that 450-mm wafers will be used in 2012. In order to respond to such a continuous requirement for large-size wafers from the device-fabrication side, von Ammon [3] and Shiraishi and coworkers [4] tried to grow 400-mm ingots, as shown in Fig. 1.2.

Not only is improvement of throughput by use of large-diameter wafers required but also improvement of yield of LSI chips is needed. As feature size shrinks, the yield of chip fabrication can be affected by defects in wafers whose size is comparable to that of a feature size of 100 nm. This size of defect has not affected yield when the feature size of device design is as large as 1 μm . However, now it becomes a problem.

Consequently, development of LSI chip technology requires large-size, defect-free silicon single crystals. In this chapter, silicon single-crystal growth technology, mainly the Czochralski technology, is reviewed, i.e., raw materials, crystal-growth process, wafer fabrication, the melt process and characterization of defects.

1.2 CRYSTAL-GROWTH METHOD AND TECHNOLOGY

1.2.1 High-purity polycrystalline silicon

Nowadays, silicon crystals for LSI are based on two basic and very important technologies. The first is the manufacturing technology of high-purity raw material that is only realized in silicon, whereas it has never been realized in other materials. The second is dislocation-free crystal-growth technology. High-purity manufacturing technology of polycrystalline silicon with so-called 10 nines (10N: a purity of 99.9999999 %) or 11 nines (11N) will be introduced in this section.

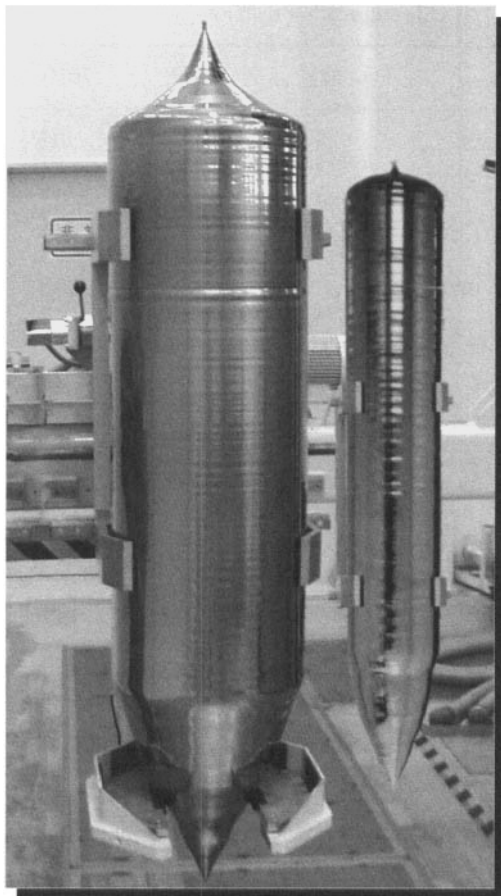


Figure 1.2 400-mm diameter ingot. (Courtesy of SSI)

Manufacturing processes from mineral silica to silicon wafer for LSI are schematically shown in Fig. 1.3. Silicon is the element with the second largest abundance following oxygen on the Earth with a Clarke number of 28.8%. The initial raw materials of silicon single crystal are mineral silica as shown in Fig. 1.3(a). The mineral silica used for manufacturing single-crystal silicon is produced only in Brazil, China and a few other countries, where mineral silica with a very high purity can be mined.

Silicon is obtained by reduction (deoxidation) of SiO_2 , which is one of the stable oxides, as shown in Equation (1.1),



The reduction process is carried out in an arc furnace with graphite electrodes at high temperature (1500–2000 °C). Purity of the obtained silicon lumps is about 98%, as shown in Fig. 1.3(b), and they are called metallurgical-grade silicon, MG-Si. Most of the metallurgical-grade silicon is used in the metallurgical and chemical industries. Only several per cent of the whole amount of the production of metallurgical-grade silicon

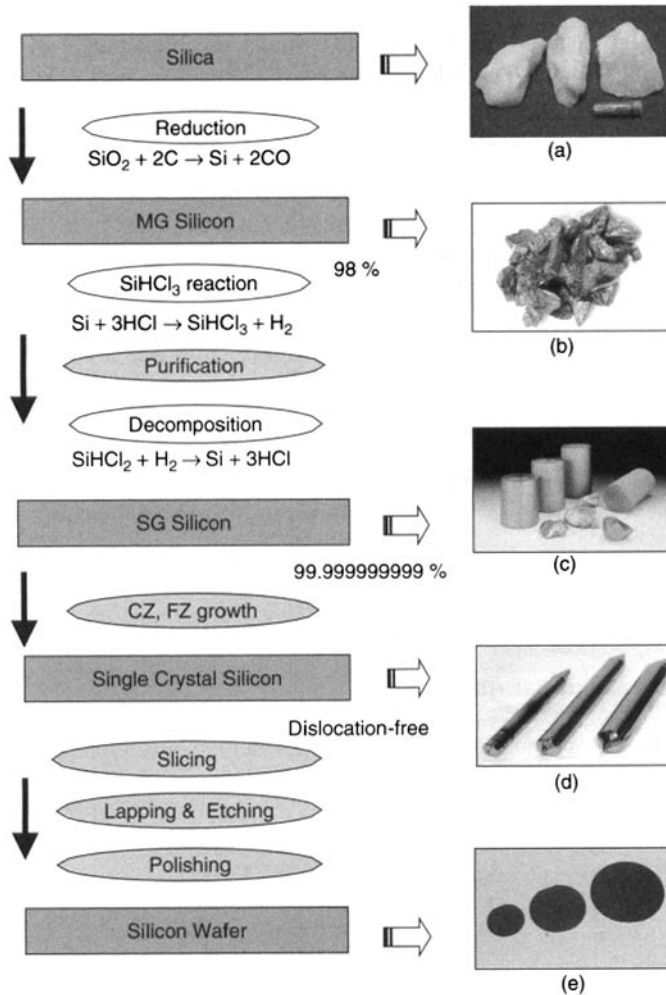
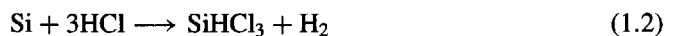


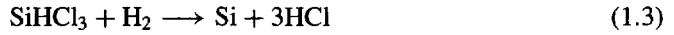
Figure 1.3 Manufacturing processes from mineral silica to silicon wafer for LSI. (a) Mineral silica, (b) metallurgical-grade silicon lumps (Courtesy of Tokuyama Corp.), (c) polycrystalline cut rods and nuggets of semiconductor-grade silicon (Courtesy of Tokuyama Corp.), (d) single-crystal silicon ingots, and (e) silicon wafers

is used for semiconductor fabrication. Semiconductor-grade silicon, SG-Si, is produced by purifying the metallurgical-grade silicon, using the well-known purification process called the Siemens method developed in the early 1960s [5]. In the Siemens method, the following reaction is carried out, in which powdered metallurgical-grade silicon reacts with hydrogen chloride (HCl) to form trichlorosilane (SiHCl_3),



Most of the impurities in the metallurgical-grade silicon are removed by forming chlorides such as BCl_3 , FeCl_3 , etc., during the reaction in Equation (1.2), and then trichlorosilane

(SiHCl_3) of high purity is obtained. For further purification, distillation of trichlorosilane (the boiling point is 31.8°C) is repeated, and finally the high purity of so-called 10 or 11N is realized. The purified trichlorosilane reacts with high-purity hydrogen gas (H_2) and decomposes as polycrystalline silicon of high purity in a chemical vapor deposition (CVD) apparatus according to the following reaction,



Polycrystalline silicon obtained from this method is generally an ingot with a diameter of 100–150 mm. The ingots are processed into rods and nuggets (or chips) for different purposes and they are supplied to the single-crystal growth process as shown in Fig. 1.3(c).

There are other purification processes from metallurgical-grade silicon to semiconductor-grade silicon besides the Siemens method. One example is the method where purification process takes place through a monosilane (HSi_4) as an intermediate having a boiling point of -119.9°C instead of trichlorosilane. This technique was developed in the late 1960s [6]. Furthermore, free-flowing granular polysilicon with diameters ranging from several hundred micrometers to several millimeters was developed in the 1980s and used practically in the industries [7].

1.2.2 CZ-Si growth apparatus and related furnace parts

1.2.2.1 CZ-Si growth apparatus

A typical CZ-Si single-crystal growth apparatus is schematically illustrated in Fig. 1.4, and a photograph of a commercially available CZ-Si growth apparatus for 300-mm diameter

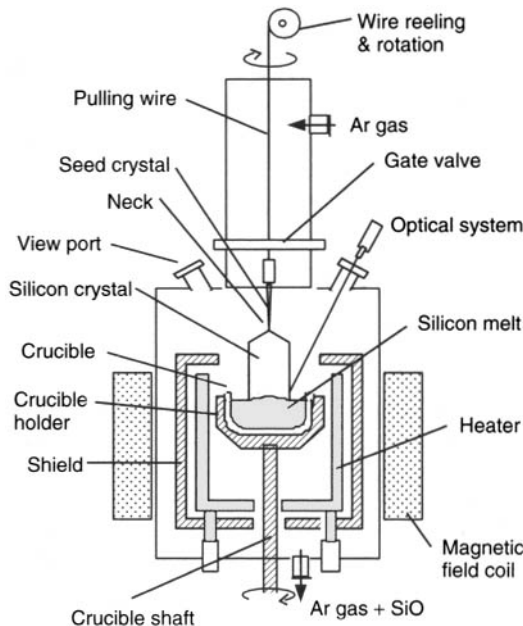
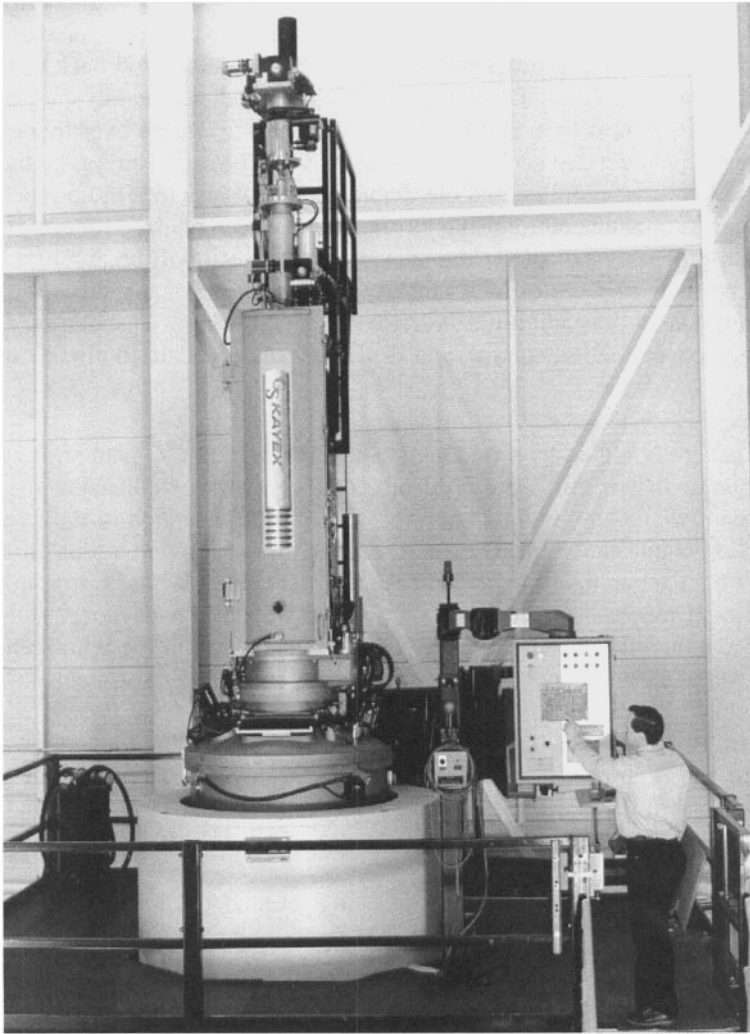


Figure 1.4 Schematic diagram of CZ-Si growth apparatus

ingots is shown in Fig. 1.5. In the apparatus, essential functions for the Czochralski method are incorporated. Silicon crystal is grown gradually with a controlled shape from the silicon melt contained in a silica crucible, using a silicon seed crystal set over the silicon melt. In addition, special equipments and functions are usually provided, as follows.

(1) High airtightness and a reducing atmosphere

It is necessary to keep the chamber of silicon single-crystal growth completely airtight to protect air leakage from an environment atmosphere as low as 1 Pa s^{-1} . Reduced Ar pressure in the chamber is controlled at several thousand Pascals during crystal growth [8] and the purity of the Ar gas used for silicon crystal growth is higher than 99.9995 %.



Courtesy of Kayex Corp.

Figure 1.5 Photograph of a commercially available CZ-Si growth apparatus (Courtesy of Kayex Corporation)

High airtightness and high purity of Ar gas are necessary because the hot-zone parts made of graphite will be damaged at high temperature, even if only a small amount of oxygen exists in the atmosphere. The purpose of reducing the Ar pressure to about 1 kPa is for pumping out SiO gas evaporated from the surface of the silicon melt effectively from the chamber of the CZ-Si apparatus. The reducing Ar atmosphere is important for dislocation-free crystal growth. Ar gas is supplied continuously from the top of the chamber with a certain flow rate, and the gas is pumped out continuously from the bottom of the chamber. Control of Ar gas pressure is realized due to the balance of Ar supply rate and pumping rate.

(2) Automatic control of diameter and growth processes

Silicon crystal growth with a required diameter is realized by successful diameter control, where an optical sensor or an image sensor is used to measure the diameter and/or diameter variation during the crystal growth precisely, and the results are fed back to pulling rate and melt temperature control. Diameter control is carried out mainly by changing the pulling rate over the short term and by changing melt temperature over the long term. A CCD (charge coupled device) camera is now usually used for measuring the diameter of a silicon crystal in a crystal puller, and the diameter control becomes more precise: usually within ± 1 mm. Automatic control using a computer has been realized for almost the whole crystal-growth processes except for the neck process, which will be described later. The position of the melt surface (growth interface) and rotation of crystal and crucible are changed continuously depending on the ratio of crystallization or solidified fraction for precise oxygen concentration control, and these controls are realized also by a computer.

(3) Crystal-pulling system

A crystal is generally pulled by a rotating shaft in the normal CZ method. A wire-reeling and rotating system was also developed in CZ-Si crystal growth, as the silicon crystal becomes large in diameter and in length. The reason for application of the wire system is that a CZ-Si apparatus can be made shorter, especially for growing a long silicon crystal, compared with an apparatus using a shaft. Another advantage is that a wire in the system can absorb small mechanical vibration and keep a silicon crystal more stable than that with a shaft. On the other hand, there are some disadvantages of the wire-reeling system. The crystal rotation rate cannot be set very high because of lack of mechanical strength of a wire, which sometimes is a problem for high-quality crystal growth. Furthermore, resonant vibration occurs when a silicon crystal has some particular length or weight. For the large size and high-quality single-crystal growth, the conventional shaft system still has the possibility to be applied.

(4) Recharge system

Recently, a recharge function has been incorporated within a CZ-Si apparatus as a standard option. Polycrystalline silicon crystals are recharged while keeping the crucible temperature high, after a part of the melt or almost all of the melt is pulled out as a single crystal. Consequently, a new silicon crystal is grown from the increased silicon melt after recharge. The purpose of recharging the melt at high temperature is to use an expensive silica crucible repeatedly, whereas a silica crucible cannot be used again for growth if it is cooled to room temperature. Another reason is to control the resistivity of a whole crystal. Generally, a dopant is distributed along the growth direction according to the

normal-freezing equation as the solidified fraction increases. In the recharge growth system, crystal growth is stopped when the solidified fraction reaches a certain value, i.e., a designed resistivity, and then polycrystalline silicon is recharged into the melt with certain amounts of dopant, if necessary. Then crystal growth is restarted. In this system, the important advantage is that not only can the silica crucible be used repeatedly but also the remaining silicon melt is effectively used. Recharge methods and equipments are being developed by individual companies, but have not yet been disclosed, because of proprietary know-how.

(5) Application of magnetic fields

It was more than 20 years ago when the application of magnetic fields to CZ-Si crystal growth was proposed [9]. The application of magnetic fields was attempted to obtain silicon crystals with low oxygen concentration or to obtain crystals with high resistivity through suppressing impurities dissolving from a crucible into a melt. As shown in Figs. 1.4 and 1.5, nowadays, application of a magnetic field is a standard option for a normal CZ-Si apparatus, so as to grow high-quality crystals with diameters of 200 mm or 300 mm. The application of magnetic fields is not only for controlling oxygen concentration and reducing impurities, but also for maintaining stability of the melt surface, which is very important for dislocation-free CZ-Si crystal growth, because fierce vibration of the melt surface due to oscillatory flow sometimes results in the introduction of dislocations.

1.2.2.2 Hot-zone

The hot-zone is one of the most important parts of a CZ-Si apparatus, and it strongly affects control of crystal quality such as dislocation-free growth, oxygen concentration and point defects, etc., which are major characteristics of silicon crystals. The hot-zone in the chamber of a CZ-Si apparatus is not the same among silicon crystal-growth companies, although the outside of CZ-Si apparatuses look similar to each other. The structure of the hot-zone has been designed by each crystal-growth company, and the details are confidential. Figure 1.6 schematically shows an example of a typical structure of a hot-zone. A gas-flow guide and radiation shield as a part of a hot-zone had been applied when 6-inch silicon crystal growth was attempted. The hot-zone plays an important role in realizing stable dislocation-free crystal growth, oxygen-concentration control and point-defect control, through controlling the convection of the Ar gas and the temperature distribution near the melt surface, although its size, shape and location in a hot-zone are different among silicon crystal companies.

1.2.2.3 Silica crucible

The silica crucible is a very important part of the hot-zone because it contains a silicon melt at high temperature and a large amount of oxygen dissolves continuously from the crucible wall; the supply of oxygen to the crystal is important to assure a sufficient gettering capability of grown crystals, as mentioned in Section 1.4.1. For current crystal-growth systems, the diameter of the silica crucible is designed to be about 3 times larger than that of the crystal. A silica crucible with a diameter of 32–36 inch (800–900 mm)

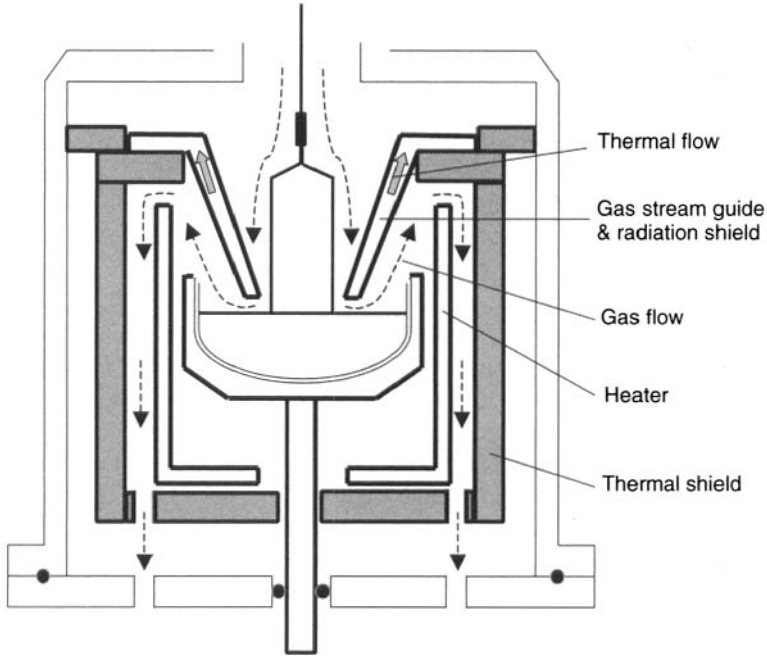


Figure 1.6 Schematic diagram of a typical structure of a hot-zone

is used for 300-mm diameter silicon crystal growth. Figure 1.7(a) shows a typical shape of a silica crucible. Figure 1.7(b) is a micrograph showing a cross section near the inner wall, where the silica crucible contacts the silicon melt. Figure 1.7(b) also shows the structure of the inner wall before heat treatment of the crystal-growth process. A crucible contains many bubbles because crucibles are produced by fusing natural SiO_2 powders in a die made of carbon; numerous bubbles remain in crucibles due to the high viscosity of fused SiO_2 . An inner wall of a crucible (1–3 mm) is made transparent by special treatment at high temperature and in high vacuum, so as to remove bubbles, which can be detached from the crucible when the inner surface is dissolved and are transported to the crystal/melt interface and finally cause a defect in grown crystals. Figure 1.7(b') shows the same area as that in Figure 1.7(b) after being heated at 1500°C for 4 h (simulation of crystal growth). Bubbles in the opaque layer have expanded and some bubbles can be observed even in the transparent layer.

Figures 1.7(c), (d) and (e) schematically show a cross section of practically employed silica crucibles near the inner-wall surface. Figure 1.7(c) shows the surface structure of a typical crucible made of natural silica. As mentioned above, a crucible wall is coated with a transparent layer, whereas numerous bubbles remain inside the crucible body. Figure 1.7(d) shows an example of a crucible whose inner-wall surface is coated with high-purity synthesized quartz glass. This is expected to reduce heavy-metal contamination from the crucible. Figure 1.7(e) shows a silica crucible with a BaO-coating layer on the inner surface [10]. Dissolution of the crucible is expected to be suppressed by this coating.

Crucible material and inner-wall structure treatment are designed to assure high yield of grown crystals, considering viscosity, thermal conductivity, dissolution rate into the silicon melt, influence on dislocation-free crystal growth, and so on.

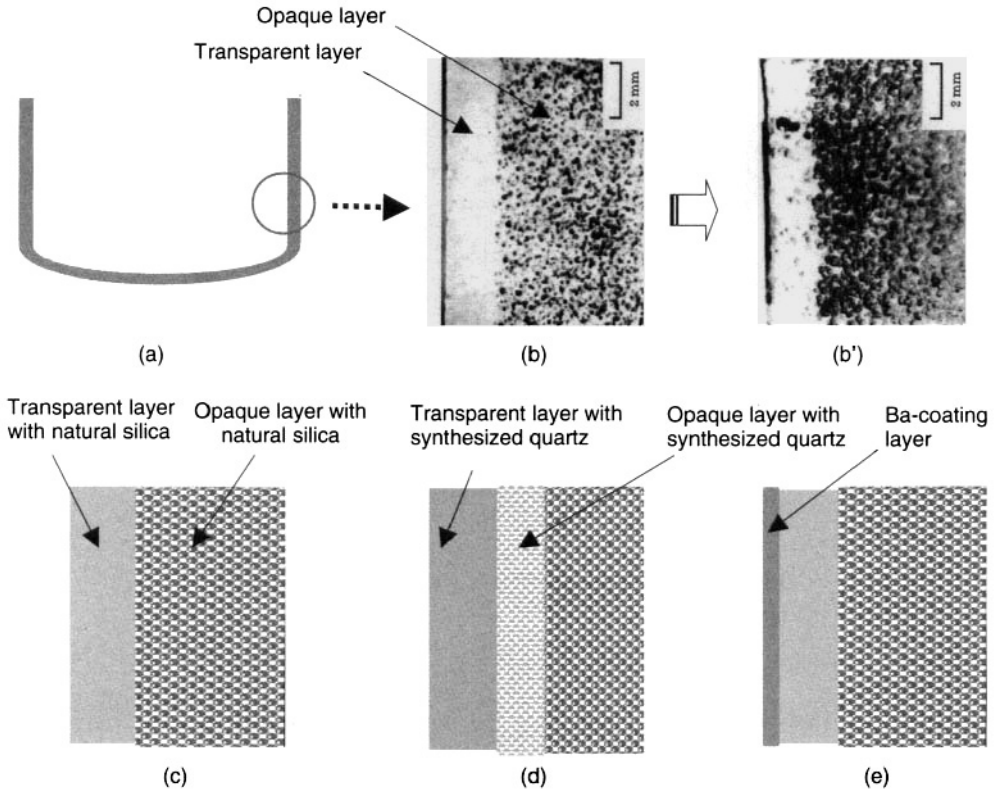


Figure 1.7 Schematic diagrams of microscopic structure near the inner surface of silica crucible

1.2.3 CZ-Si crystal growth

1.2.3.1 Basic process

A basic process of CZ-Si crystal growth is as follows. First, a certain amount of polycrystalline silicon is charged in a silica crucible, and the silicon is melted by a graphite heater at a temperature higher than its melting point, 1420°C . Then, crystal growth is started using a silicon seed (seeding) after adjusting the melt temperature to a certain value. As shown in Fig. 1.8, a thin neck is made followed by shouldering. After that, a body with a certain diameter is grown until the desired amount of silicon melt is crystallized. Finally, a tail is formed before finishing the growth process.

Generally, the shape of a crystal is controlled by controlling the temperature near the melt surface in a silica crucible and the pulling rate of the crystal. The following are considered as a sequence of the crystal-growth process.

(1) Neck: During the seeding process introduction of dislocations must be avoided. There are two origins of dislocations: one is those existing in the seed crystal and the other is those introduced by thermal shock during dipping of a seed crystal into the melt. In order to grow a dislocation-free crystal, a relatively high pulling rate of $1\text{--}5\text{ mm min}^{-1}$

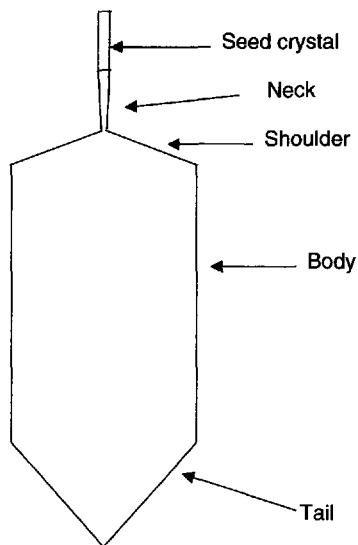


Figure 1.8 Shape of a silicon crystal and nomenclature

and a neck process with a diameter as small as 3–5 mm and length of 100–300 mm are employed.

(2) **Shoulder:** This process is for enlarging the diameter of a silicon crystal from a thin neck to a body with a much larger diameter, such as 200 to 300 mm. The temperature of the silicon melt is decreased and the pulling rate is decreased to $0.1\text{--}0.5\text{ mm min}^{-1}$ at the same time. Then the diameter increases rapidly, and a flat shoulder is formed.

(3) **Body:** This is the effective portion for production of silicon wafers with a certain diameter. The growth of the body is carried out by automatic diameter control (ADC) based on the information of the diameter at the region just after growth, detected by an optical instrument.

(4) **Tail:** The diameter is decreased gradually from that of the body to zero in this portion. This tailing process is necessary to avoid formation of dislocations induced by thermal shock due to sudden detachment of a grown crystal from the melt. Otherwise, a high density of dislocations will be generated and multiplied and then finally will propagate into an already-grown dislocation-free region of the crystal; the length of dislocated part is about 1–2 times the diameter. A photograph of typical dislocation-free silicon crystals is shown in Fig. 1.9.

1.2.3.2 Dislocation-free crystal growth

Nowadays, LSI devices are produced from silicon wafers from a CZ-Si ingot with a diameter of 300 mm after many processes including cutting and polishing, etc., as mentioned later. The fact that a silicon ingot with such a large diameter can be obtained is due to the success of dislocation-free silicon crystal growth. Dislocation-free silicon crystal growth is based on a thin-neck process proposed by Dash 40 years ago (1959) [11, 12], in which a thin (3–5 mm diameter) and long (100–300 mm) neck part is formed



Figure 1.9 Dislocation-free silicon crystals grown recently (diameters of 150, 200 and 300 mm)

as shown in Fig. 1.10(a), and this process is still employed as an industry standard. On the other hand, a silicon crystal with a diameter larger than 300 mm becomes too heavy for the conventional thin neck to support. As alternatives to the conventional technique, new ideas for obtaining dislocation-free crystals with a large diameter and a high weight in the future have been proposed, as shown in Figs. 1.10(b) and (c). Through the investigation by Super Silicon Institute (SSI) Corporation for preparation of 400-kg crystal with a diameter of 400 mm, they proposed introduction of a subsidiary cone after the thin neck process for eliminating dislocations, so that the weight of the grown crystal can be sustained by this cone with a combination of a special mechanical clamp, as shown in Fig. 1.10(b) [13, 14]. Recently, Hoshikawa *et al.* [15, 16] found that no dislocations were generated during dipping by using a heavily B-doped or B- and Ge-codoped seed crystal even though there is a strong thermal shock, and proposed a new technique to obtain dislocation-free CZ-Si crystals without the thin-neck process; see Fig. 1.10(c). An example of a dislocation-free silicon crystal without the thin neck is shown in Fig. 1.11.

1.2.4 FZ (float-zone) Si crystal growth

Figure 1.12 shows a sketch of a float-zone crystal-growth system. Because float-zone crystal growth is a crucible-free technique, contamination is scarcely introduced during the crystal-growth process. Also, the oxygen concentration is as low as 10^{15} atoms cm^{-3} , because there is no oxygen supply. Thus, float-zone-grown silicon single crystals have resistivities as high as $400 \Omega \text{m}$. Due to the high resistivity, float-zone-grown crystals are used for discrete power devices, such as rectifiers, thyristors, power transistors, and so on.

For industrial silicon single-crystal growth, RF (radio frequency: 1–3 MHz) heating is employed. Because silicon has a high resistivity at room temperature, first a carbon ring is

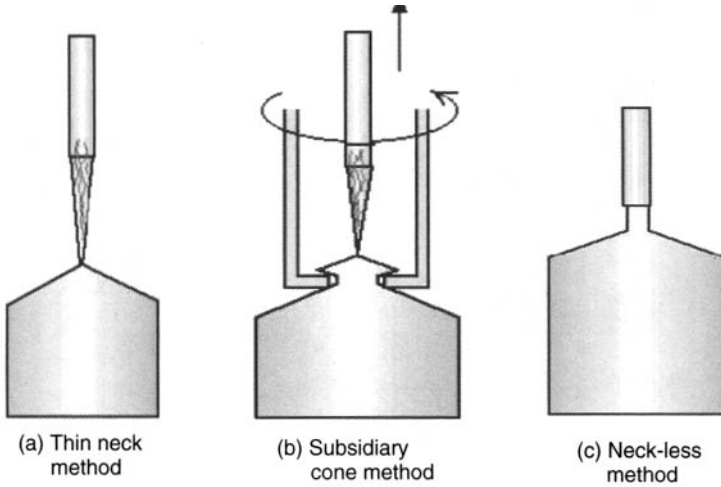


Figure 1.10 Three methods of dislocation-free silicon crystal growth. (a) conventional thin neck, (b) subsidiary cone, and (c) without thin neck

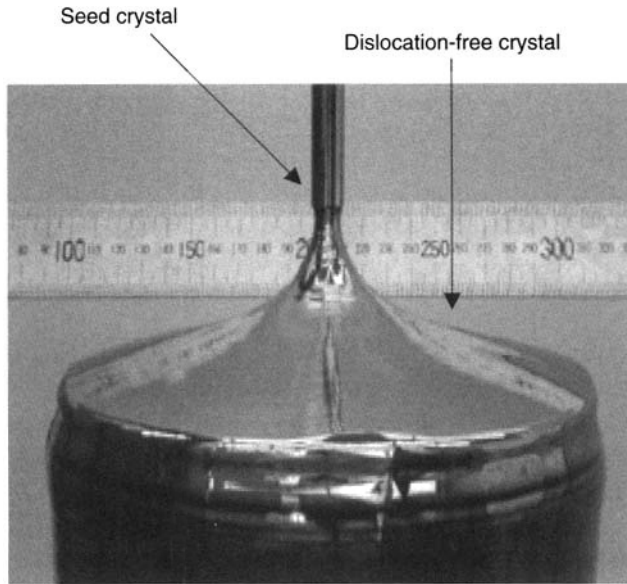


Figure 1.11 A dislocation-free silicon crystal without a thin neck

heated by RF power; see Fig. 1.12(a). Using radiation from the carbon ring, polycrystalline feed rod is heated, so that the electrical conductivity of the rod is sufficiently increased, and then direct RF heating of the feed rod is available; see Fig. 1.12(b). An edge of the feed rod is melted by the RF power and brought into contact with a seed crystal that rotates in the opposite direction and then the molten zone is formed; see Fig. 1.12(c). As shown in Fig. 1.12(d), a molten zone is sustained stably against the gravitational force

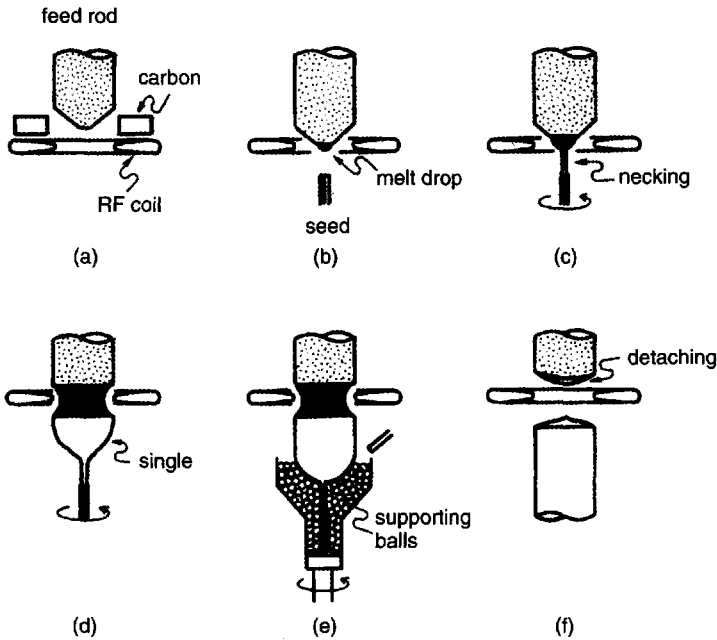
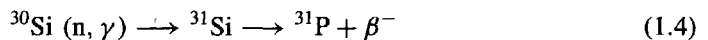


Figure 1.12 Float-zone crystal-growth process

by the electromagnetic force and the surface tension of a silicon melt. The diameter of the grown crystal increases as the crystal grows. However, the diameter of the molten portion is smaller than that of the solid parts; thus this technique is called the 'needle-eye technique'. Because the heat capacity of the total system is smaller than that for the CZ system, crystal growth rates as high as 2 mm min^{-1} can be obtained. Single-crystal growth of silicon 200 mm in diameter has been attempted [17].

A problem in the float-zone crystals is inhomogeneous distribution of resistivity due to that of the dopant. 3D numerical simulation shows that float-zone crystal growth using RF heating is featured with use of a nonaxisymmetric one-turn coil, as shown in Fig. 1.13 [18]. This causes nonaxisymmetric distribution of the input power in the melt, coupled with crystal rotation. Considering buoyancy, electromagnetic and Marangoni forces, the flow and temperature fields were calculated (see Fig. 1.14); they show nonaxisymmetric distributions. Flow instability was found; inhomogeneous distribution of resistivity (dopant) was also calculated and compared with experimental observation. It was concluded that rotation is one of the major origins of growth striations.

Dopants are added from a gas phase using, e.g., PH_3 or B_2H_6 . Neutron transmutation doping (NTD) in an atomic reactor is also used to dope phosphorus into silicon, as follows,



Three per cent of the natural abundance of ^{30}Si captures thermal neutrons and is transmuted into ^{31}Si , which decays with a half-life of 2.62 h by the emission of beta particles to ^{31}P . Use of neutron transmutation doping assures homogeneous distribution of the phosphorus dopant, resulting in uniformly doped n-type silicon with accurately predetermined resistivity, although strong growth striations remain in float-zone crystals.

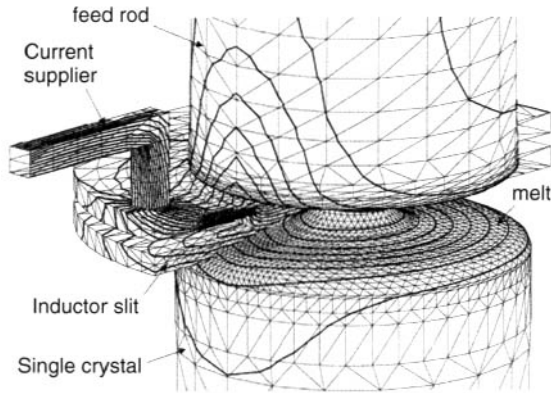


Figure 1.13 Simulation for FZ system (Reprinted from Ratnieks *et al. J. Cryst. Growth* **216**, (2000) 204, copyright (2000) with permission from Elsevier)

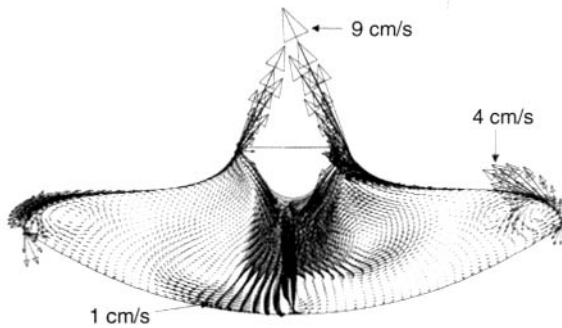


Figure 1.14 Modeling for float-zone crystal growth, showing nonaxisymmetric distribution of flow-field modeling (Reprinted from Ratnieks *et al. J. Cryst. Growth* **216**, (2000) 204, copyright (2000) with permission from Elsevier)

1.2.5 Wafer processing

In order to use silicon crystals as a substrate for LSI chips, single-crystal ingots are sliced, lapped and polished. The quality of the wafer surface, including that of the back-side surface, is required to be guaranteed from the viewpoint of lithography using a stepper. As shown in Table 1.1, because the chip design rule is less than 100 nm, the focus-tracking capability of a stepper during lens-scan is quite sensitive to wafer flatness. The term ‘nanotopography’ is used for this issue instead of flatness. This is affected not only by surface flatness but also by that of the back side, because a chuck is used to hold a wafer from the back side during the resist-exposure process of device fabrication. This is also the case for the chemical-etching process. Etching using alkaline solution is better than that using acidic solution. Conventionally for 200-mm wafers, only the surface side of the wafer is mirror polished. However, from 300-mm wafers onwards, double-side-polished wafers are employed for LSI chip fabrication. This subject is closely related to the assurance of the gettering capability of wafers, in another words control of oxide precipitates, as mentioned later.

After growth of a single-crystal ingot, the shoulder and tail parts are removed using a sawing machine. After the ingot is shaped axisymmetrically, an orientation flat or a notch is introduced by a diamond tool by determining the crystallographic direction using X-ray diffraction. This is necessary for the photolithography process in device fabrication. Up to 200-mm diameter wafers, an orientation flat has been used. From 300-mm wafers onwards, a notch is used. An ingot is sliced into wafers after inspecting the crystallographic direction by X-ray diffraction. Conventional internal-diameter blade (ID-blade) saws have been used, as shown in Fig. 1.15. Nowadays, multiwire saws are used for slicing 300-mm diameter wafers with a thickness of ~ 1 mm. Slurry containing fine particles of abrasive is carried with a fine high-tensile piano wire; ingots are sliced using the abrasive. Since one single wire is wound continuously in multiple loops, the whole ingot is sliced simultaneously into hundreds of wafers. The edge side of sliced wafers is ground by a diamond wheel to circular to prevent mechanical damage, such as chipping in downstream processes. This process is called beveling. This is also effective to prevent edge crowning in the epitaxial-growth process.

Sliced wafers are lapped mechanically using a double-sided lapping machine with corundum abrasive to remove surface irregularities and damage induced by the slicing process, so that wafers will have uniform thickness. Lapped wafers are chemically etched to remove a surface-damaged layer, which remains even after the lapping process.

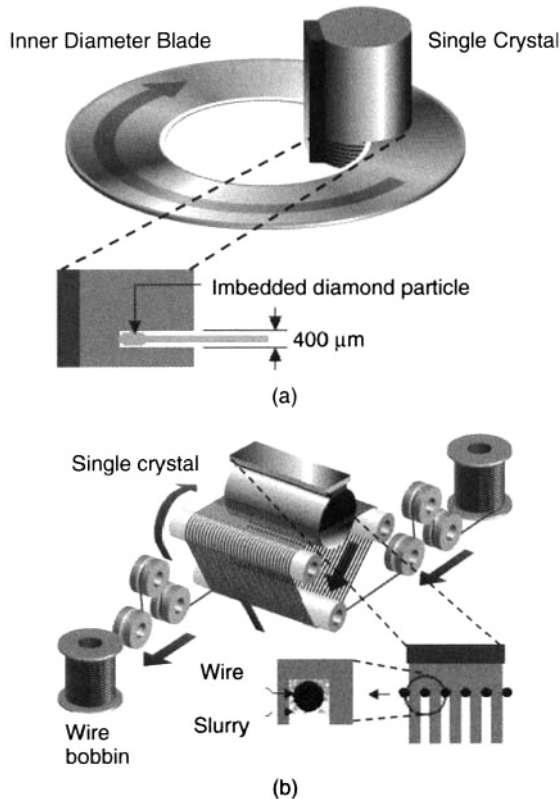


Figure 1.15 Slicing of silicon crystals by internal diameter blade saw and multiwire saw.

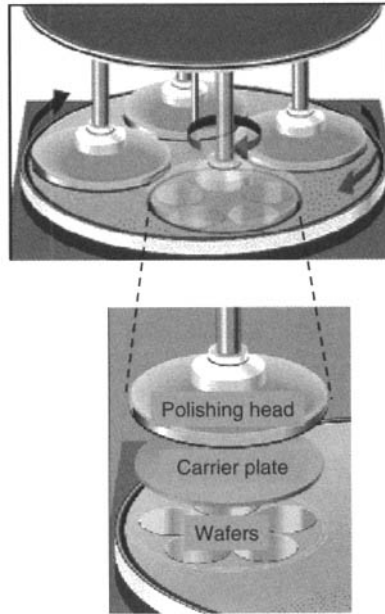


Figure 1.16 Polishing process

As shown in Fig. 1.16, wafers are finally polished mechanochemically using colloidal silica dispersed in NaOH solution. This process is important to obtain damage-free and contamination-free surfaces. Residual damage and contamination degrade the yield of LSI chips, because silicon wafers are processed at high temperatures: over 1000°C . Conventionally, this polishing has been done only on the surface side of wafers, whereas the back side has been used to assure a gettering capability, e.g. back-side damage by sand blasting or deposition of polycrystalline silicon: known as poly-back-seal. However, for 300-mm diameter wafers, both sides are polished to assure flatness, as mentioned in Sections 1.1 and 1.4.1.

1.3 MELT PROCESS

1.3.1 Analysis of heat- and mass-transfer processes

Silicon crystal growth is governed by heat- and mass-transfer processes at the crystal/melt interface. The shape of the crystal/melt interface, the macroscopic distribution of dopants, including oxygen, their microscopic distribution (growth striation), and formation, distribution and coagulation of vacancies are closely related to the above-mentioned processes. Thus, it is essential to understand precisely and to control these processes. However, it is very difficult to analyze these processes experimentally, because silicon melt is opaque in the visible region and chemically reactive, and its temperature is as high as 1400°C . Tools for experimental analysis for this process are temperature measurement (distribution and oscillation), and flow visualization, including surface observation and numerical modeling.

As shown in Fig. 1.17, measurement of the temperature field is a basic tool for diagnostics of melt behavior from the viewpoint of the heat and mass transport [19], because the flow field is difficult to observe directly. This is almost the only way to assess

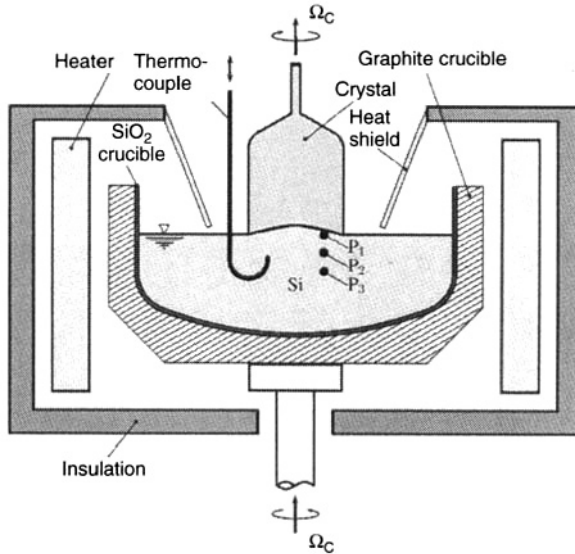


Figure 1.17 Diagnostics of temperature field within a crucible (Reprinted from Enger *et al. J. Cryst. Growth* **230**, (2001) 135, copyright (2001) with permission from Elsevier)

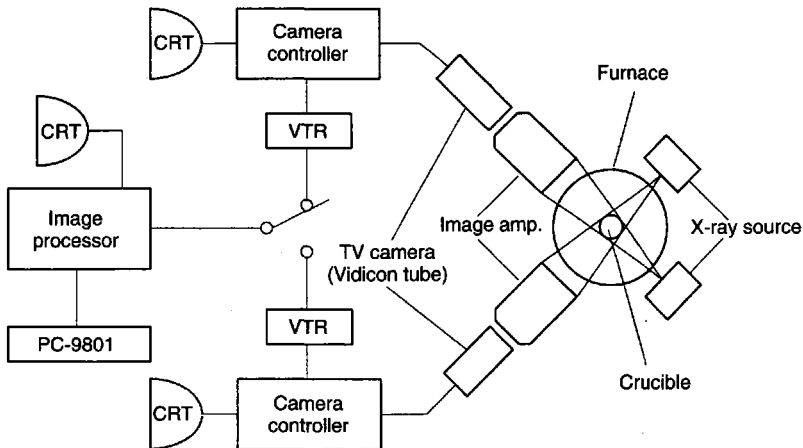


Figure 1.18 Flow-visualization system (Reprinted from Watanabe *et al. Proc. Winter Annual Meeting of American Society of Mechanical Engineers* (1991) copyright (1991) with permission from ASME)

the flow field except for numerical simulation. By measuring the frequency and correlation of temperature oscillations between multiple thermocouples set along the azimuthal direction of the crucible, the existence of a traveling wave was revealed [20]. The temperature field of the silicon melt was precisely measured using thermocouples during Czochralski growth of single crystals and the causality between temperature-field oscillation and the introduction of growth striations was revealed [21]. Efforts have been continuously made to correlate experimentally obtained data with numerical data [19].

Kakimoto *et al.* [22, 23] were the first to visualize the flow field of silicon melt in a 75-mm diameter crucible using X-ray radiography with tracer particles (see Fig. 1.18). Tracer

particles were made of tungsten chips coated with silica glass, so that neutral buoyancy conditions were assured. Due to the difference in absorption between the silicon melt and a tracer particle, the trajectory can be visualized, as shown in Fig. 1.19. Since the crucible size was small, axisymmetric flow was observed when crucible rotation rate was small. The flow-mode transition from axisymmetric flow to nonaxisymmetric flow, i.e. baroclinic instability flow, was observed by the X-ray visualization system, when the crucible/crystal rotation rate was increased, as shown in Fig. 1.20 [24, 25]. This is due to coupling of the

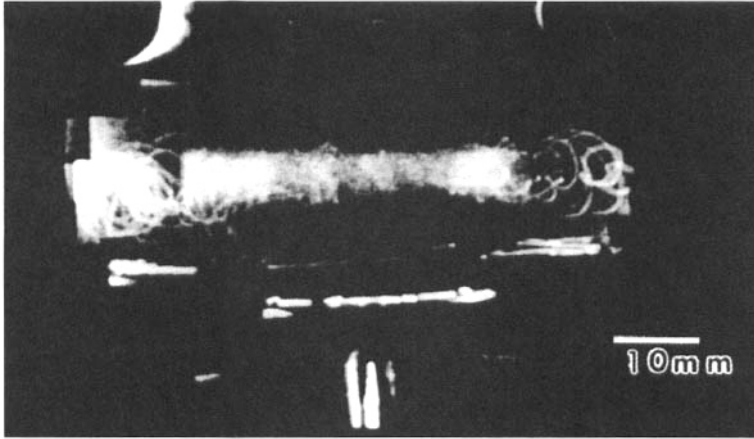


Figure 1.19 Visualized trajectory of tracer particles

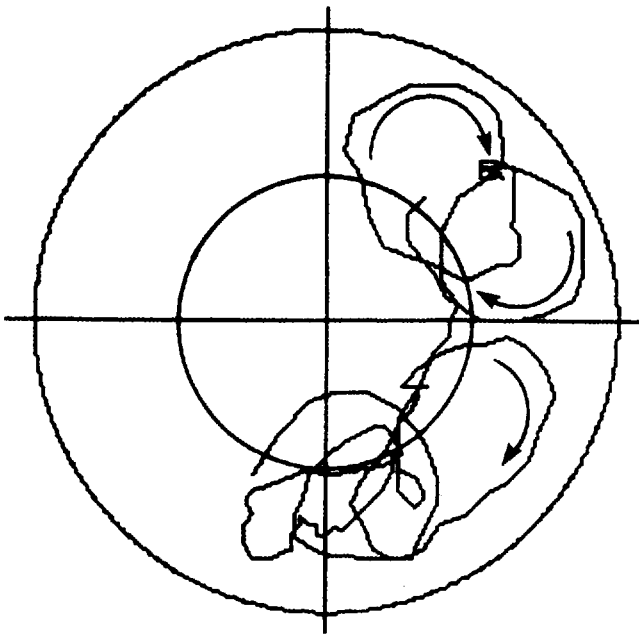


Figure 1.20 Moving cell structure observed by X-ray radiography due to baroclinic instability (Reprinted from Watanabe *et al. J. Cryst. Growth* **128**, (1993) 288, copyright (1993) with permission from Elsevier)

buoyancy force and the Coriolis force induced by crucible and/or crystal rotation. This instability occurs due to the same mechanism as for a large-scale atmospheric circulation; i.e. coupling of the buoyancy force and rotation of the earth resulting in formation of a low-pressure center or a high-pressure center. Criteria to show this instability are the thermal Rossby number Ro_{Th} and the Taylor number Ta , These numbers are defined as follows,

$$Ro_{Th} = \frac{g\beta\Delta Th}{\omega_c^2 r_c^2} \quad (1.5)$$

and

$$Ta = \frac{r_c}{h} \frac{4\omega_c^2 r_c^4}{\nu^2} \quad (1.6)$$

where g , β , ΔT , h , ω_c , r_c and ν are gravitational acceleration, volumetric thermal expansion of silicon melt, temperature difference between the top and the bottom, melt height, crucible rotational rate, crucible radius and kinematic viscosity of silicon melt, respectively.

Silicon crystal growth under the nonaxisymmetric flow condition due to the baroclinic instability flow results in strong temperature oscillations and consequently inhomogeneous oxygen distribution along the growth direction, i.e. oxygen growth striations, as shown in Fig. 1.21 [26]. Oxygen that precipitates as SiO_2 plays an important role to getter heavy-metal contaminants introduced during the chip-fabrication process and to increase mechanical strength, as discussed later. Tanaka *et al.* [27] observed by a CCD camera thermometer that the baroclinic wave is modified by a thermal plume in the high Ta number region, i.e. $Ta = 10^{10}$. However, for silicon melt contained within a crucible with larger diameter, X-rays can no longer penetrate, and the flow structure cannot be visualized. Instead, a combination of temperature-distribution measurement, observation

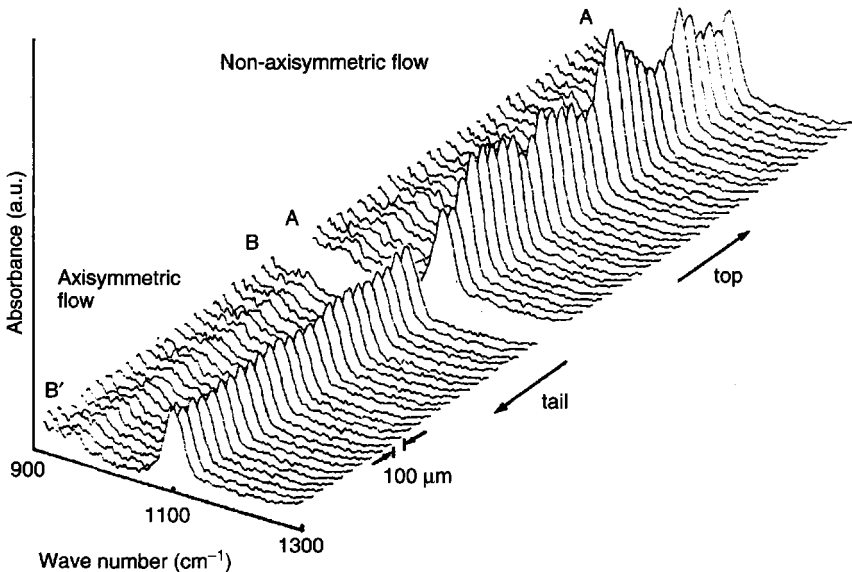


Figure 1.21 Inhomogeneous distribution of oxygen due to flow instability (Reprinted from Watanabe *et al. J. Cryst. Growth* **151**, (1995) 285, copyright (1995) with permission from Elsevier)

of surface thermal patterns and numerical modeling is used to analyze the heat and mass transport within the crucible. Kishida and Okazawa [28] reported that above a Ta value of 10^{11} , the baroclinic instability flow is converted into geostrophic turbulence flow.

Numerical simulations are a powerful tool to overcome difficulties in the experimental approach for diagnostics of the heat- and mass-transfer processes in the melt. A numerical approach is necessary not only to understand the crystal-growth process but also to find an appropriate direction to optimize crystal-pulling conditions in industry. The recent development of computer capability has enhanced the development of numerical studies to a great extent, because use of computer modeling shows a higher cost benefit than an experimental approach, although experiments are required at the final stage. Not only is a better mathematical model required but also accurate and precise thermophysical data must be prepared.

Two numerical methods are currently used; one is the 'bulk-flow model' and the other is 'global heat analysis'. The bulk-flow model handles melt-flow structure in the crucible and the global heat analysis includes heat transfer within the grown crystals, the effect of thermal shield and the effect of gas flow. Usually, the former handles melt flow three-dimensionally and the latter handles the system as axisymmetric.

From the industrial viewpoint, it is preferred to analyze the melt-flow structure using the bulk-flow model. The larger the crystal diameter, the larger the Grashof number becomes, which shows the magnitude of buoyancy-driven convection. This is because large-diameter crystal-growth requires large amounts of melt within a large-diameter crucible, as discussed in Section 1.2.2.3. The Grashof number is defined as follows: $Gr = (\beta g \Delta T r_c^3) / \nu^2$. Here, β , g , ΔT , r_c and ν are the volumetric thermal expansion coefficient, the gravitational acceleration, the temperature difference in the system, the crucible diameter and the kinematic viscosity, respectively. For the 300-mm diameter crystal-growth case, the Grashof number reaches as high as 10^9 to 10^{10} ; this means that melt flow is turbulent. In order to model turbulent flow in the crucible, three numerical models have been proposed; these are RANS (Reynolds-averaged Navier–Stokes), LES (large-eddy simulation) and DNS (direct numerical simulation).

In the RANS method Reynolds-averaged equations of momentum, mass, heat and species are solved after time-averaged operations, using the low Reynolds number form of the $k-\varepsilon$ model, where the Reynolds stress is explained as turbulent kinematic viscosity. In this method, the system is axisymmetric [29]. Due to this condition, a strong down flow beneath the crystal appears. The DNS does not use any turbulent model. Enger *et al.* [19] compared temperature oscillations due to melt convection with those obtained by numerical simulation. 3D and time-dependent simulation was performed by the DNS method for the identical system employed for experimental measurement; i.e., a 20-kg melt contained within a crucible with a diameter of 360 mm. The temperature distribution and oscillation mode showed good agreement with each other. However, for a melt contained within a larger crucible, such as that for the growth of 300-mm wafers, simulation requires tens of millions of grid cells. This requirement exceeds the current computational capability. Recently, the LES method has been employed, where the filtered Navier–Stokes equation is employed. Although this method requires a moderate number of computational cells, unsteady melt motion, such as melt flow affected by crucible rotation and argon gas flow, can be reproduced [30]. Combining the Reynolds-averaged approach with the large-eddy simulation, melt flow under the magnetic field was analyzed, as shown in Fig. 1.22 [31]. The effect of a horizontal magnetic field on the distribution of electric potential, flow

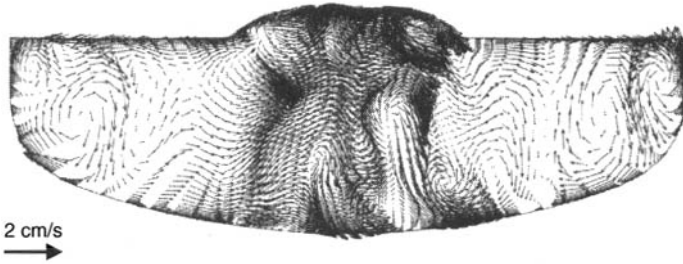


Figure 1.22 Instantaneous velocity distribution in the silicon melt for 100-mm crystal. Crucible rotational rate is 5 rpm (Reprinted from Evstratova *et al. J. Cryst. Growth* **237/239**, (2002) 1757, copyright (2002) with permission from Elsevier)

velocity and temperature was studied by this combined method using the InGaSn eutectic melt, which simulates a Si melt within a 20-inch (500-mm) diameter crucible and 165-mm diameter crystal [32]. The LES can be easily combined with a 2D global model, which treats heat and mass transfer of all the parts of the crystal-growth furnace.

A global model is used to analyze not only melt convection but also the temperature distribution within a puller including a crystal, gas flow, and crystal/melt interface shape. This technique is used to design a hot-zone for a crystal puller in industrial use. Since a global model handles many items, analysis is axisymmetric. This technique is also used to determine the boundary conditions of the model for the bulk-flow model, such as temperature of the crucible wall. Recently, Kalaev *et al.* [33] made a 3D analysis of the total system (see Fig. 1.23) and showed that 3D analysis well reproduces the crystal/melt interface. Furthermore, the defect distribution within a crystal can be analyzed, as shown in Fig. 1.24. The gas-flow effect on global heat transport and melt convection is also analyzed [34].

Marangoni flow is one of the mechanisms for heat and mass transfer during crystal growth. However, this effect has not been recognized for some time. Since a silicon crystal-growth experiment was carried out under microgravity [35], this flow has been the target of research. Recently, this effect has been recognized and has been involved in numerical simulation [18, 36]. The Marangoni flow shows a marked dependence on oxygen partial pressure of an ambient atmosphere, i.e. oxygen concentration in the melt [37]. This flow shows a unique behavior at the surface of the Czochralski melt, because the oxygen concentration is high in the melt adjacent to the crucible wall and low in the vicinity of the growing crystal. Thus, surface tension and its temperature coefficient would not be constant all over the melt surface, instead they change periodically due to an inhomogeneous distribution of temperature and oxygen concentration at the melt surface. In order to include this in numerical simulation, the two-dimensional distribution of surface tension and its temperature coefficient should be measured experimentally.

The capability of numerical modeling has been developed to a great extent in recent years. However, thermophysical property data that is indispensable to numerical modeling have not yet been well established. For example, there is no directly measured thermal conductivity of molten silicon, whereas thermal diffusivity has been measured using a laser-flash method [38]. Even for reported thermophysical property data, there is a large scatter depending on who did the measurements; see, for example, the case for surface tension of molten silicon [39]. Also, the data employed is different depending on who makes the simulation. Thermophysical property data should be critically evaluated and recommended values must be used.

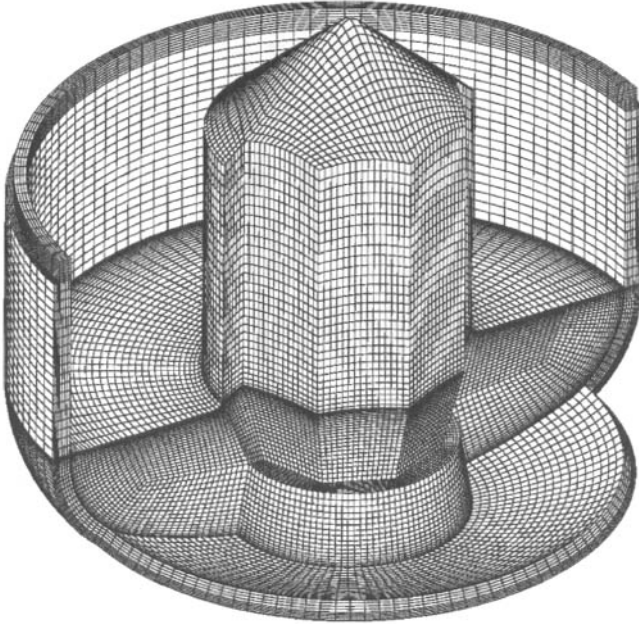


Figure 1.23 3D global computational grid system for 300-mm diameter crystal growth (Reprinted from Kalaev *et al. J. Cryst. Growth* **250**, (2003) 203, copyright (2003) with permission from Elsevier)

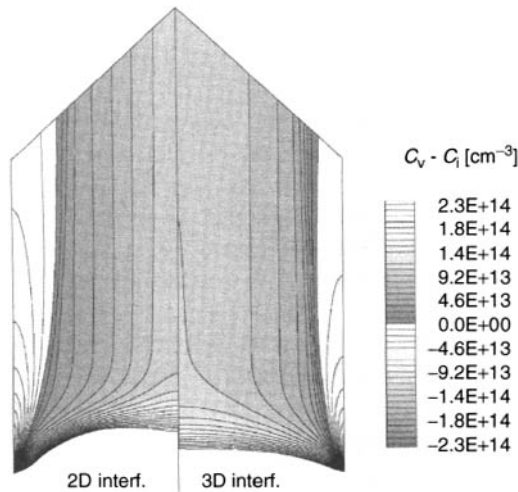


Figure 1.24 Calculated distribution of the difference between vacancy concentration and interstitial concentration; left: two-dimensional calculation; right: three-dimensional calculation (Reprinted from Kalaev *et al. J. Cryst. Growth* **250**, (2003) 203, copyright (2003) with permission from Elsevier)

1.3.2 Oxygen transportation process and mechanism

Oxygen concentration in a CZ-Si crystal strongly affects the yield of LSI fabrication through a gettering process; therefore, oxygen concentration in Si crystals must be controlled at

the most appropriate level depending on the class of device or its fabrication process. In order to control the oxygen concentration incorporated into silicon crystals effectively, it is necessary to understand the processes and mechanisms for oxygen transportation in CZ-Si crystal growth.

It has been reported that there are three methods for measuring silica (or oxygen) dissolution rate in silicon melt, as shown in Fig. 1.25. Figure 1.25(a) shows the first method with a measurement condition similar to practical silicon crystal growth. A silica crucible for practical silicon crystal growth is used for holding the silicon melt. A silicon rod [40, 41] or a plate [42] is dipped into the silicon melt and its dissolution rate is measured. The second method utilizes a small silica crucible, as shown in Fig. 1.25(b) [43], and the third method a silicon drop on a silica substrate, as shown in Fig. 1.25(c) [44]. The oxygen-dissolution rate from silica to silicon melt and its temperature dependence obtained from the different methods are shown in Fig. 1.26. It is evident that the results are divided into three groups depending on the measurement method. This interesting phenomenon results from the fact that the dissolution rates (dissolved oxygen atoms from a unit area of silica to silicon melt in unit time, atoms $\text{cm}^{-2} \text{s}^{-1}$) are calculated from the weight loss of the samples after the dissolution experiment, where oxygen atoms dissolve from the silica into the silicon melt and move in the silicon melt by diffusion and convection, and finally evaporate from the melt surface. This suggests that the difference in dissolution rate among the three methods (Fig. 1.25) is due to the fact that the oxygen-transportation process after dissolution in the silicon melt including evaporation from the melt surface is different. As shown in Fig. 1.25(c), the transportation distance in silicon melt is very short and the evaporation area is much larger for the case of a silicon drop, then a large dissolution rate of about 7×10^{16} atoms $\text{cm}^{-2} \text{s}^{-1}$ was obtained, whereas a much smaller result of about 1×10^{16} atoms $\text{cm}^{-2} \text{s}^{-1}$ was obtained in the case where a silica rod or plate is used.

The mechanism of oxygen transportation during CZ-Si crystal growth can be understood by analyzing the dissolution rate of a silica crucible in which silicon melt is held. The total amount of oxygen evaporation Y from the surface of a silicon melt can be determined, if the total amount of oxygen dissolution X from a silica crucible to a silicon melt is known because the total amount of oxygen incorporated into a silicon crystal Z can be obtained by measuring the oxygen concentration of the grown crystal. Oxygen-transportation processes during CZ-Si crystal growth are schematically shown in

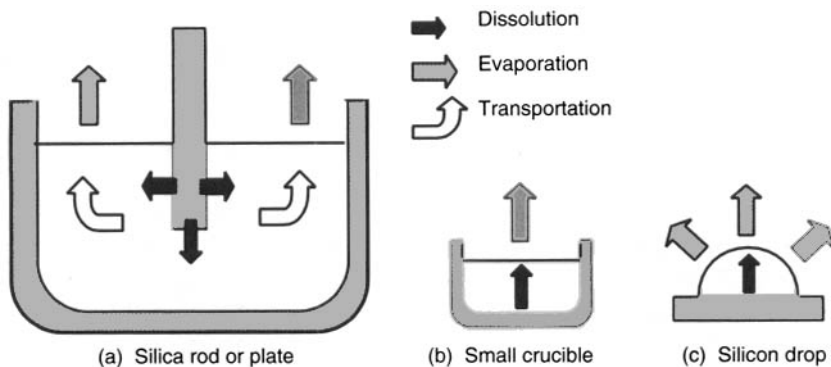


Figure 1.25 Three methods for measuring silica (or oxygen) dissolution rate in silicon melt

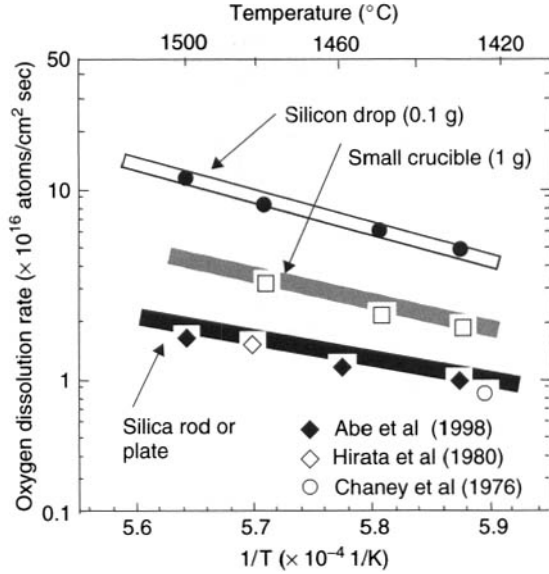


Figure 1.26 Oxygen dissolution rate from silica into silicon melt and its temperature dependence obtained from the different methods

Fig. 1.27. As shown in Fig. 1.27(a), most of the oxygen (more than 99 %) dissolved from a silica crucible in a silicon melt evaporates from the surface of the silicon melt [45]. This behavior of oxygen in CZ-Si crystal growth is very different from that of other impurities, which are conserved in the silicon melt. In the total oxygen flow from a silica crucible by dissolution to a silicon melt, only a small amount Z is incorporated into a silicon crystal; the majority is evaporated from the melt surface Y . Therefore, the following relationship is available.

$$X = Y + Z \approx Y \gg Z \tag{1.7}$$

Figure 1.27(b) shows a distribution of oxygen concentration in silicon melt in a normal CZ-Si crystal growth in which the melt is stirred sufficiently by forced convection [45]. A characteristic of this distribution suggests that there is a diffusion boundary layer with a thickness of δ_s , in which a large gradient of oxygen concentration exists, and dissolved oxygen atoms move to the bulk silicon melt by diffusion. The oxygen concentration in other parts of the melt C_m is due to sufficient stirring by convection. On the other hand, near the melt surface there is another diffusion boundary layer with a thickness of δ_a , in which a large gradient of oxygen concentration also exists. It is supposed that oxygen atoms diffuse through this layer and evaporate to the surrounding atmosphere as a form of SiO. It is easy to understand that the values of δ_s and δ_a strongly affect the amounts of dissolution X and evaporation Y of oxygen, and only very small variations of dissolution X or evaporation Y will effect large changes of oxygen concentration in a silicon melt C_m . It can be understood from Equation. (1.7) that oxygen incorporated into a silicon crystal has almost no affect on the oxygen flow in CZ-Si crystal growth.

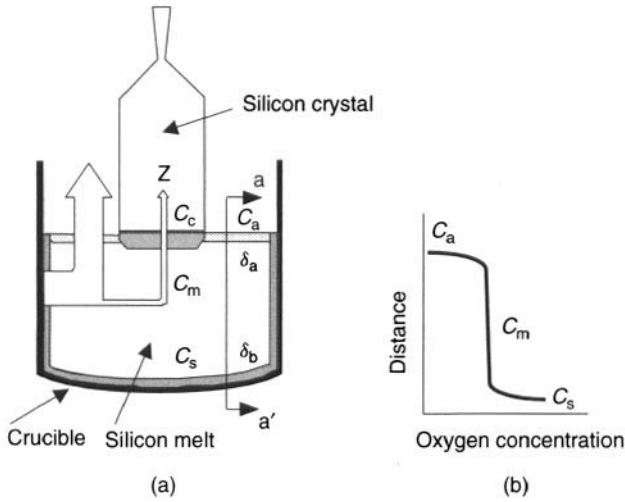


Figure 1.27 Oxygen-transportation processes during CZ-Si crystal growth

The oxygen concentration in a silicon crystal depends on the oxygen concentration in a silicon melt directly as follows,

$$C_c = K C_m \quad (1.8)$$

where K is a phenomenological segregation coefficient of oxygen, which is a variable depending on the effective segregation coefficient k_{eff} and forced convection just below the interface of the crystal and melt caused by rotation of the crystal. Unlike other impurities, K is not the same as k_{eff} for oxygen. This is attributed to the fact that oxygen is not conserved in the melt and that the amount of oxygen evaporated is two orders larger than that incorporated into the crystal.

Based on the knowledge mentioned above, the oxygen-concentration-control technique has progressed markedly in CZ-Si crystal growth. It is no exaggeration to say that oxygen concentration and its distribution have been controlled sufficiently for LSI fabrication.

1.3.3 Control of oxygen concentration by application of cusp magnetic field

According to the quantitative analysis of oxygen transportation in CZ-Si crystal growth mentioned in Section 1.3.2, two parameters are essential for controlling oxygen concentration, i.e., thickness of the diffusion boundary layers in the silicon melt near the crucible wall δ_s and the melt surface δ_a . These parameters are strongly affected by forced convection due to rotations of crystal and crucible and buoyancy-driven convection due to the temperature distribution in the melt. Thus, it is effective to control oxygen concentration in the crystal by controlling melt convection, because it strongly affects the oxygen concentration in the silicon melt C_m . In addition to the conventional methods, such as control of buoyancy-driven convection and forced-flow convection by changing temperature distribution and the rotation rate of the crystal and the crucible, there have been

breakthroughs via introduction of new measures; application of a magnetic field, such as a rotating magnetic field [45, 46], a DC magnetic field [9, 47] and a cusp magnetic field [48]. Recently, the combination of DC magnetic field and direct electric current has been proposed [49].

An example of applying a cusp magnetic field to control oxygen concentration effectively [48, 50] is introduced in this section. Figure 1.28 shows schematic diagrams of a CZ-Si crystal growth system with a cusp magnetic field. Two superconducting coils with counter-rotating electric currents are positioned outside the chamber of the furnace. The distribution of magnetic field when the surface of the silicon melt is in the same position as the center of the two coils is shown in Fig. 1.28(a). Magnetic-field components vertical to the crucible bottom H_z and vertical to the crucible sidewall at the melt free surface H_r are used as typical values for representing the magnitude of the cusp magnetic field. Figure 1.28(b) shows a case where the center of the cusp magnetic-field is inside the melt and a vertical component of magnetic field is applied to the melt surface. In this case, magnetic-field components vertical to the crucible sidewall H_s and vertical to the melt surface H_a are used for representing the magnitude of the cusp magnetic field. The other conditions suitable for crystal growth are shown in Table 1.2.

Figure 1.29 shows the radial distribution of oxygen concentration obtained from four silicon crystals grown with a basic distribution of magnetic field as shown in Fig. 1.28(a) for various magnitudes of magnetic fields ($H_z(0.2)$ and H_r) [48]. Here, the numerical value of 0.2 in ($H_z(0.2)$ and H_r) represents the magnitude of magnetic field at a solidified

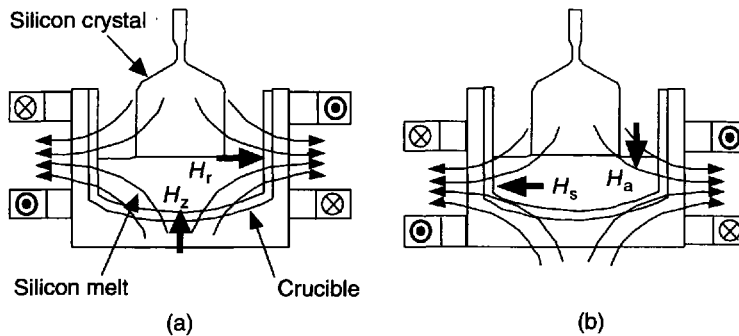


Figure 1.28 Schematic diagrams of CZ-Si crystal growth system with a cusp magnetic field. (a) Surface of silicon melt is in the same position at the center of two coils, (b) the center of the cusp magnetic field is inside the melt

Table 1.2 Growth conditions when using a cusp magnetic field

Crystal diameter:	76 mm
Crucible diameter:	150 mm
Melt weight:	3500 g
Growth direction:	(100)
Crystal pulling rate:	1 mm
Crystal rotation rate:	30 rpm
Crucible rotation rate:	-10 rpm

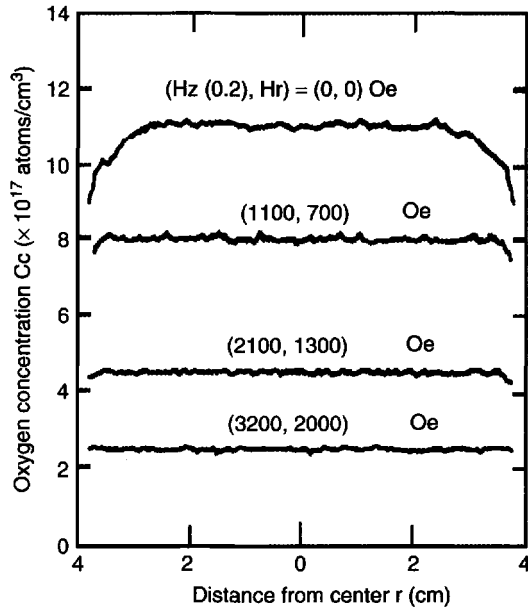


Figure 1.29 Radial distribution of oxygen concentration for various magnitudes of a cusp magnetic field for the configuration shown in Fig. 1.28(a) (Reprinted from Hirata *et al. J. Cryst. Growth* **96**, (1989) 747, copyright (1989) with permission from Elsevier)

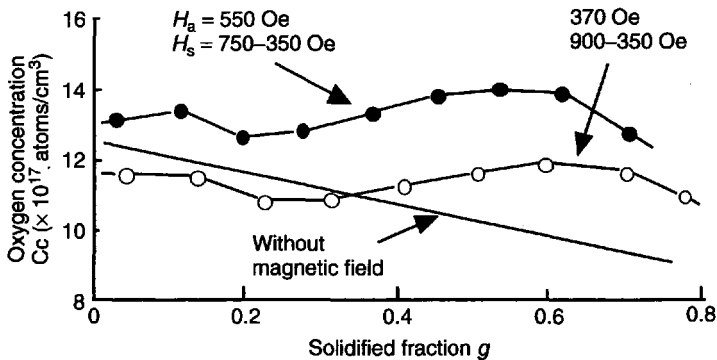


Figure 1.30 Dependence of oxygen concentration on solidified fraction by controlling relative position of center of two coils and melt surface in the configuration as shown in Fig. 1.28(b)

fraction $g = 0.2$. For a crystal rotation of 30 rpm and crucible rotation rate of -10 rpm, the oxygen concentration decreases considerably with an increase in the cusp magnetic field and the radial distribution of the oxygen concentration tends to become homogeneous with an increase in the magnetic field. Figure 1.30 shows the oxygen concentration at the center of a crystal as a function of fraction solidified for two silicon crystals grown within a distribution of magnetic field whose center is inside the melt, as shown in Fig. 1.28(b), where controlled magnetic fields are shown by H_s and H_a . The experimental results indicate that it is much easier to control oxygen concentration in a wide

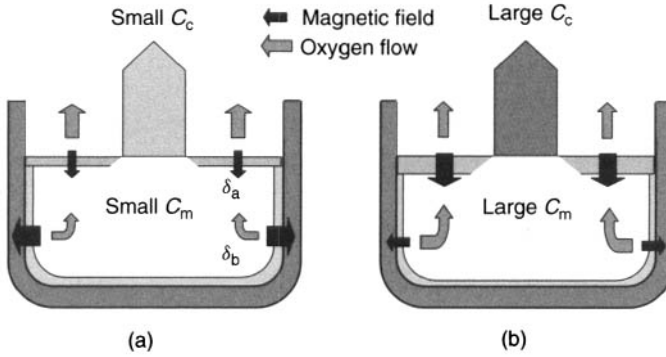


Figure 1.31 Schematic images of oxygen concentration control by application of cusp magnetic field

range and that a homogeneous distribution along the growth direction is available, regardless of the fraction solidified, by changing the magnetic field at the center of the melt surface H_a , compared with crystal growth without a magnetic field. The mechanism of oxygen control by applying a cusp magnetic field can be explained quantitatively by the oxygen distribution in a silicon melt including a diffusion boundary layer as shown in Fig. 1.27 in Section 1.3.2. A cusp magnetic field has a three-dimensional distribution of magnetic flux, as shown in Fig. 1.28. As a result, it is easier to control magnetic-field components vertical to the crucible sidewall H_s , where oxygen dissolution is accelerated, and magnetic-field components vertical to the melt surface H_a , where oxygen evaporation occurs independently. For example, for the configuration shown in Fig. 1.28(a), the component of a magnetic field vertical to the crucible wall increases with an increasing cusp magnetic field, which is due to suppression of convection near the crucible wall, consequently, the average thickness of the diffusion boundary layer δ_s increases. However, there is no change in the vertical component of the magnetic field, thus, no change of average thickness of diffusion boundary layer δ_a near the melt surface occurs. As a result, $\alpha = \delta_a/\delta_s$ decreases, which decreases the oxygen concentration in the silicon melt, and then decreases the oxygen concentration in the silicon crystal, as shown in Fig. 1.29. On the other hand, in the configuration in Fig. 1.28(b), the thickness of the diffusion boundary layers δ_a and δ_s can be controlled by changing the magnitude of the cusp magnetic-field components H_s and H_a independently, as shown in Fig. 1.31. As a result, $\alpha = \delta_a/\delta_s$ can be changed freely and then the oxygen concentration in the melt C_m and in the crystal C_c may decrease, as shown in Fig. 1.31(a), or increase, as shown in Fig. 1.31(b). Consequently, a uniform oxygen distribution with increasing solidified fraction can be realized in comparison with that without applying a magnetic field because the decrease of oxygen concentration in silicon melt C_m is compensated, although the amount of silicon melt decreases as a crystal grows.

1.4 DEFECT AND WAFER QUALITY

1.4.1 Oxygen precipitation and gettering

According to the phase diagram for the silicon-oxygen binary system, a solid silicon phase has a small, but strongly temperature-dependent solubility for oxygen, as shown

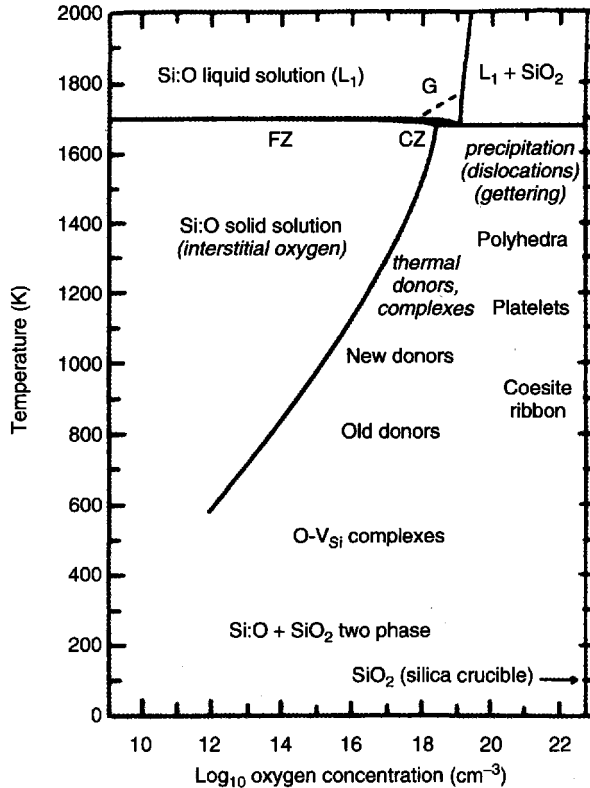


Figure 1.32 Phase diagram for the Si–O system (Reprinted from Mikkelsen in *Oxygen, Carbon, Hydrogen and Nitrogen in Crystalline Silicon* eds. J. C. Mikkelsen *et al.* (1986), copyright (1986) with permission from the Materials Research Society)

in Fig. 1.32. Near the melting temperature the solubility of oxygen is estimated to be 10^{18} atoms cm^{-3} and 10^{17} atoms cm^{-3} at 1200°C , respectively [51]. Oxygen occupies interstitial sites of a silicon crystal. Oxygen atoms in silicon crystals have two important roles, i.e. suppression of introduction of dislocations during high-temperature processing and gettering of heavy-metal contaminants.

During high-temperature annealing processes, such as surface oxidation, formation of slip (dislocations) was observed, which caused warpage of wafers. Formation of dislocations is caused by relief of thermal stress introduced by an inhomogeneous temperature distribution, either at the initial stage of the process just after insertion of wafers into the furnace, or at the final stage just after the withdrawal of wafers from the furnace. Introduction of dislocations is suppressed by oxygen atoms in Si crystals. This is due to so-called impurity hardening; and the required oxygen concentration is of the order of 10 ppm.

The solubility of oxygen in silicon crystals shows a temperature dependence, as shown in Fig. 1.32, the higher the temperature, the larger the solubility becomes. On heat treatment at high temperature but lower than the melting temperature, excess amounts of oxygen can precipitate as SiO_2 , whose crystallographic structure is different from that of silicon. This results in formation of punch-out dislocations near the precipitates in Si crystals, where metallic contaminants precipitate [52]. This is the origin of the intrinsic

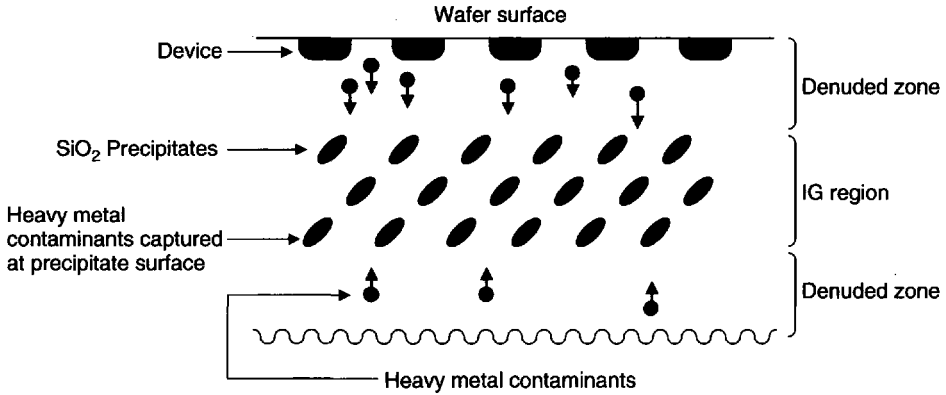


Figure 1.33 Concept of DZIG (denuded-zone intrinsic gettering)

gettering effect. The essential idea of gettering is as follows; a defect in a crystal can getter contaminants that are introduced during the device-fabrication process. These are Fe, Cu and other heavy metals introduced during ion implantation or the plasma process for metallization. Thus, the gettering technique is important to remove these heavy-metal contaminants and to increase the device yield in the production process.

There are several techniques of gettering; i.e., BSD (back-side damage), PBS (poly-back-seal) and IG (intrinsic gettering). When the back side of wafers is sandblasted, many defects are induced; these defects can getter contaminants. Poly-silicon crystals, which have many grain boundaries, formed on the back side of the wafers also getter contaminants. For 300-mm diameter wafers, neither BSD nor PBS can be applied, because both surface and back side must be mirror polished. As mentioned in Section 1.2.5, this is due to the fact that the focus-tracking capability of a stepper during lens-scan is quite sensitive to wafer flatness. An important technique to increase yield of devices fabricated on 300-mm diameter wafers is the denuded-zone intrinsic gettering (DZIG) technique, as shown in Fig. 1.33. This technique can satisfy both requirements for silicon wafers; silicon wafers must have sufficient gettering capability and the surface region of wafers must be free of oxide precipitates.

To assure the gettering capability, silicon wafers must contain sufficient oxygen and oxygen must be precipitated as oxide. The concentration of oxygen in silicon crystals is controlled by the growth conditions, such as crucible/crystal rotation rates. The number and size of oxide precipitates are controlled not only by the oxygen concentration but also by the heat treatment during and after the crystal-growth process, i.e., control of nucleation and growth of oxide precipitates. However, if oxide precipitates exist near the surface region (denuded zone), where devices are fabricated, they cause degradation of device yields. For example, oxide precipitates within this region cause an increase in the possibility of break-down in a gate oxide layer for the MOS (metal oxide semiconductor) structure. Thus the region just beneath the surface must be clean and should not contain any oxide precipitates. After preparing oxide precipitates, silicon wafers are annealed in a reducing atmosphere, so that oxide precipitates can disappear within this area due to decomposition of oxides and out-diffusion of oxygen. This region is called the denuded zone, whose thickness is about 10 μm . Oxide precipitates in the denuded zone can be detected by laser-beam scattering, if they exist. The temperature and time of heat treatment required

for the device-fabrication process varies from factory to factory, line to line and process to process. It also depends on the class of devices. Thus, it is difficult to clearly define the specification of gettering capability. This is proprietary information to each company.

1.4.2 Grown-in defects

There are two classes of intrinsic grown-in point defects in silicon crystals, i.e., self-interstitial silicon atoms and vacancies. Early studies have been carried out for float-zone silicon crystals; A- and B-swirls correspond to interstitial defects and D-type defects to vacancies [53]. According to Voronkov [54], the type of defects incorporated in silicon crystals is controlled by a ratio of v/G , where v is the crystal growth rate and G is the temperature gradient within the crystal near the solid/liquid interface. This simple v/G rule has been generalized to the dislocation-free Czochralski silicon crystals [55]. Below the critical v/G value of $0.13\text{--}0.20\text{ mm}^2\text{ min}^{-1}\text{ K}^{-1}$ interstitials are dominant and above this value vacancies are dominant (Fig. 1.34). This v/G rule means that the type of defects in crystals is governed by recombination of vacancies and self-interstitials in the vicinity of the crystal/melt interface. At low v/G the recombination loss of point defects is partially compensated by the diffusion flux from the interface into the crystal so that the remaining point defects are self-interstitials that have a higher diffusivity. At higher v/G the contribution of diffusion is small and surviving defects are vacancies. Formation of secondary defects such as dislocation loops and void defects follows this rule. Dislocation loops due to interstitial silicon atoms were observed for the low v/G case and void defects resulting from agglomeration of vacancies for the high v/G case. Because, for small-size crystals, the temperature gradient is large, dislocation loops can be observed, whereas, for large-size crystals, void defects appear. For the commercially produced Czochralski crystals, formation of void defects has been a problem for some time, when the growth rate was increased to improve the throughput of production. The mechanism of formation has been clarified recently and optimization of growth conditions for defect-free crystals is a key to improved throughput of silicon crystals.

The behavior of secondary defects, such as ring OSF (oxidation-induced stacking faults) and void defects, is closely related to that of incorporated oxygen, which occupies

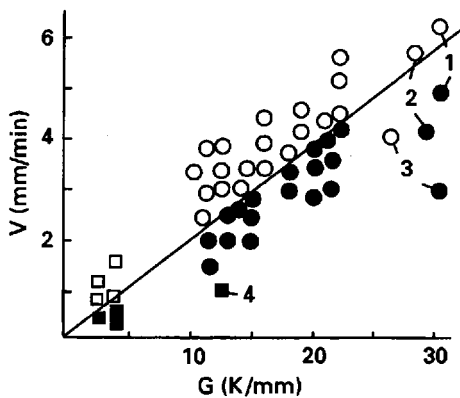


Figure 1.34 Classification of grown-in microdefects (Reprinted from Voronkov and Falster *J. Cryst. Growth* **194**, (1998) 76, copyright (1998) with permission from Elsevier)

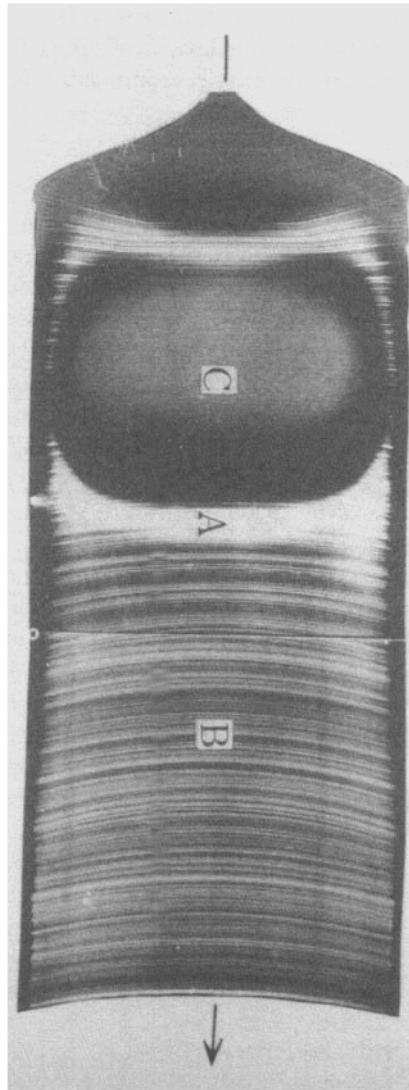


Figure 1.35 Oxidation-induced stacking fault (Reprinted from Harada *et al. Semiconductor Silicon 1986*, copyright (1986) with permission from The Electrochemical Society)

interstitial positions. When silicon crystals grown at various growth rates were annealed at high temperature and oxidized, stacking fault rings were formed. This is shown as the white portion of the X-ray topograph in Fig. 1.35 [56]. Because this OSF looks circular when observed in a wafer, it is also called a ring-OSF. The OSF appears within the vacancy region near the boundary of different types of defect when growth rate is high. As shown in Fig. 1.36, the P-band is converted into OSF through oxidizing annealing. The P-band is located head-on to the B-band, which consists of dislocation loops and was formed when the v/G or the growth rate is small. The OSF was formed during oxidation annealing: particles or small voids in the P-band play a role in the heterogeneous nucleation center

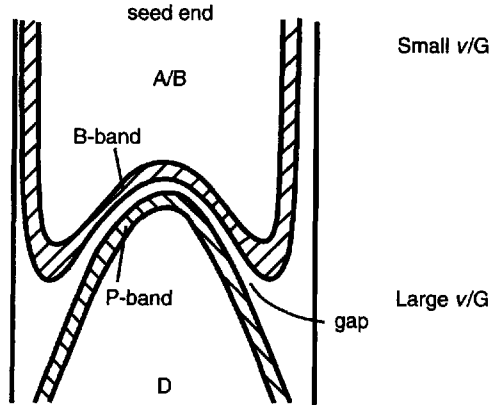


Figure 1.36 Spatial distribution of grown-in microdefects (Reprinted from Voronkov and Falster *J. Cryst. Growth* **194**, (1998) 76, copyright (1998) with permission from Elsevier)

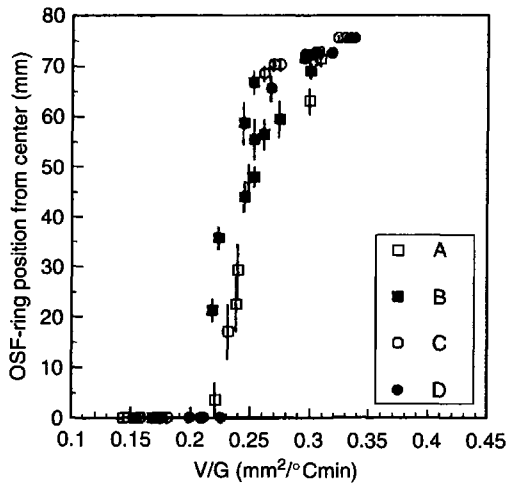


Figure 1.37 OSF-ring position vs. v/G (Reprinted from Hourai *et al. Semiconductor Silicon 1998*, copyright (1998) with permission from The Electrochemical Society)

for stacking faults. The diameter of the OSF depends on growth rate v and the parameter v/G , as well, as shown in Figs. 1.36 and 1.37 [55, 57]. Thus, OSF shrinks when v/G becomes smaller and finally disappears, and then the whole area of the wafer turns into a self-interstitial-defect region. On the other hand, the diameter of OSF becomes larger and finally reaches the outer edge of ingot and then disappears, when v/G becomes larger. The whole area of the wafer is in the vacancy-defect region.

As mentioned previously, silicon crystals contain many vacancies as intrinsic point defects, particularly when v/G or growth rate v is high. Silicon crystals also contain oxygen (see Section 1.3.3), which is supplied from the melt and is necessary for hardening wafers and gettering. Figure 1.38 shows the behavior of vacancies and oxygen in silicon crystals. During the cooling process silicon crystals are saturated with vacancies that agglomerate as the temperature is lowered and finally form octahedral voids, i.e., negative

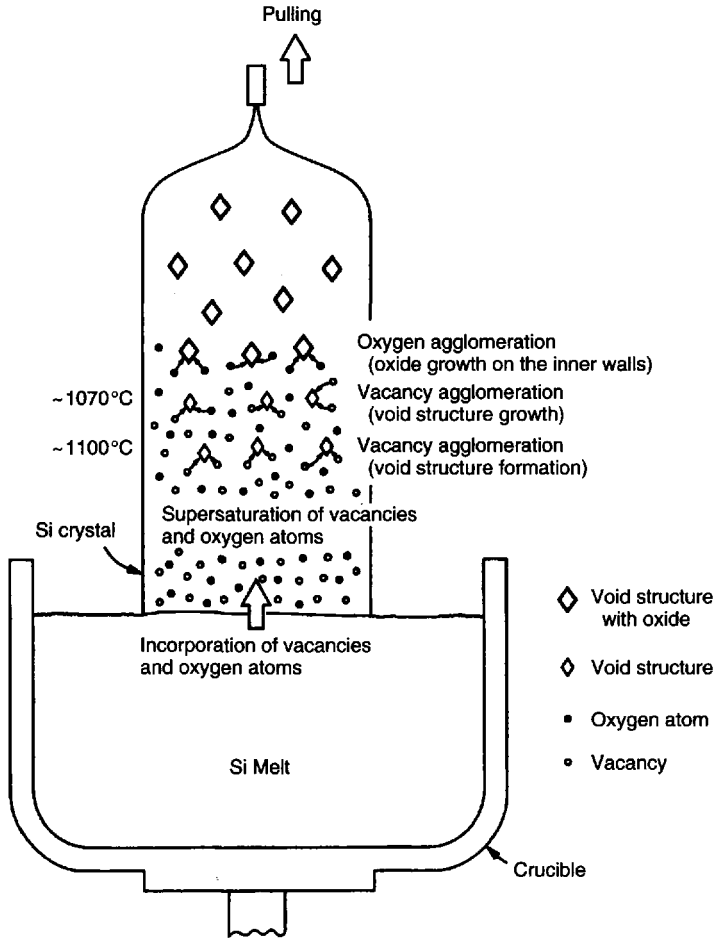


Figure 1.38 Formation of void defects as a result of interaction of vacancies and oxygen (Reprinted from Itsumi in *Crystal Growth Technology*, eds. H. Scheel and T. Fukuda (2003), copyright (2003) with permission from Wiley)

crystals whose size is 100 nm, as shown in Figs. 1.39 and 1.40 [58, 59]. The inside of the void is coated with SiO_2 . Excess amounts of oxygen precipitate at the inside of the void. The SiO_2 -coated voids have been studied for a long time by many researchers. Itsumi and coworkers were the first to report oxide defects [59, 60]. However, the origin and formation mechanism of this defect have not been clarified as yet. Historically, various names were given according to the technique used to find this defect. In 1990 Ryuta and his coworkers found particle-like defects on the wafer surface after SC1 cleaning, i.e., a mixture of aqueous ammonia, hydrogen peroxide and water [61]. This was named the COP (crystal-originated particles) defect. Yamagishi and his coworkers observed FPD (flow-pattern defects) by the Secco etch technique [62]. Since oxide precipitate defects deteriorate the gate-oxide integrity of the MOS structure, the defects were named GOI (gate-oxide integrity) defects [63]. The defects were also detected using light-scattering tomography, thus the defects were named LST (laser-scattering tomography) defects [64].

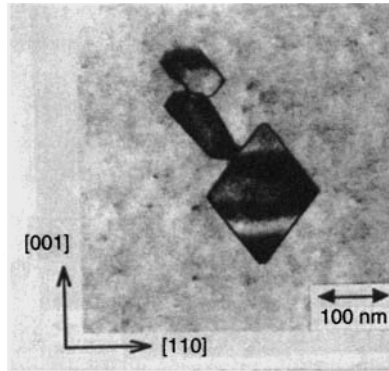


Figure 1.39 Octahedral void defect observed by transmission electron microscope (Reprinted from Kato *et al. Jpn. J. Appl. Phys.* **35**, (1996) 5597, copyright (1996) with permission from Institute of Pure and Applied Physics, Japan)

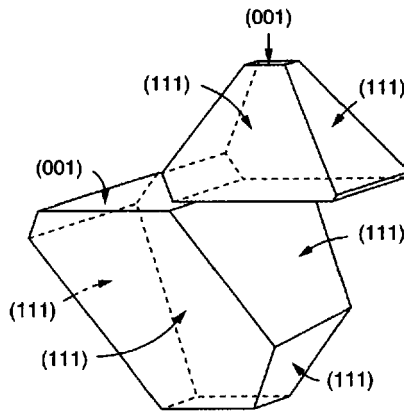


Figure 1.40 Sketch of void defect (Reprinted from Itsumi in *Crystal Growth Technology*, eds. H. Scheel and T. Fukuda (2003), copyright (2003) with permission from Wiley)

Generally speaking, it is very difficult to find the position and to observe the shape of this type of defect simultaneously, because the size is 100 nm and the density is 10^5 – 10^6 cm^{-3} . Conventionally, observation of the defect had been done by chance. A combination of light-scattering tomography (LST) for identifying location [64], focused ion beam (FIB) for sample thinning and transmission electron microscopy (TEM) for shape observation [58] has successfully solved the above problems, and it has been shown that COP and flow-pattern defects are identical, i.e. voids whose inner walls were coated with SiO_2 . Figure 1.40 shows a sketch of void defects; they have an octahedral structure consisting of (111) facets or a truncated octahedron with (001) facets. Dual-type voids were also observed.

From the viewpoint of LSI (large-scale integration) chip fabrication, void defects cause a deterioration in production yield. Void defects in the area of locally oxidized silicon (LOCOS) in the memory cell of MOS RAM cause excessive leakage current between neighboring cells [65]. Voids in the area of a gate oxide also cause problems. Due to down-sizing of the design rule towards 10 nm, as shown in Table 1.1, chip-production

yield could be more seriously affected by defects of this size. Silicon wafers without void defects are needed. From the viewpoint of crystal-production throughput, the faster the crystal is pulled, e.g. at 1 mm min^{-1} , the higher the economical benefit. However, crystals must be pulled at lower pulling rates, as far as formation of void defects is concerned. As countermeasures for this problem, the following alternatives are proposed; use of epitaxial wafer and annealing in hydrogen or nitrogen atmosphere. Nitrogen-doped crystals have been widely discussed [66, 67].

Use of EMCZ (electromagnetic Czochralski) could be one possible solution to overcome the above-mentioned void-defect problem in the crystal-growth process based on Voronkov's model. The EMCZ simultaneously utilizes application of magnetic flux B and electric current I , resulting in Lorentz force $F = I \times B$, which drives the melt azimuthally as shown in Fig. 1.41 [49]. Due to the vertical magnetic field and the rotation of the melt, buoyancy-driven convection is almost suppressed, but heat is transferred from the crucible wall to the crystal horizontally mostly by conduction. From the viewpoint of heat transfer the melt behaves as if it were solid. This suggests that enhanced heat transfer takes place from the crucible to the crystal/melt interface; consequently the interface shape becomes strongly concave. This assures a large thermal gradient G near the crystal/melt interface. Thus, the crystal growth rate v can be increased while keeping the v/G constant, so that defect-free crystals can be grown at even higher growth rate than that for the conventional CZ method, as shown in Fig. 1.42. A homogeneous distribution of oxygen along the radial direction is also assured by the EMCZ technique [68]. Oxygen is efficiently transported by the hydromechanical effect of an electrode immersed into the melt close to the crucible wall. Near the electrode a small counter cell is generated. This counter cell drives oxygen efficiently from the crucible wall to the growing crystal.

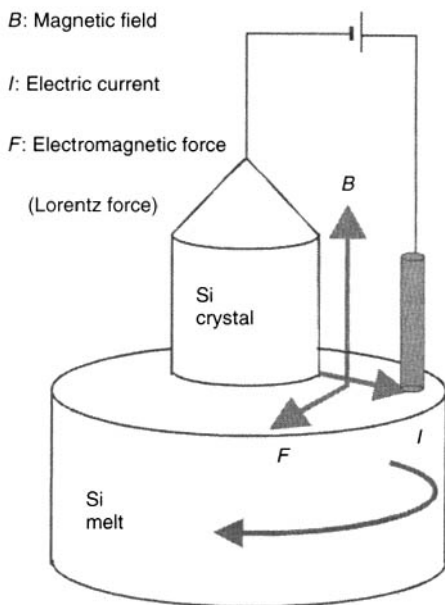


Figure 1.41 Concept of EMCZ (Reprinted from Watanabe *et al. Jpn. J. Appl. Phys.* **38**, (1989) 777, copyright (1989) with permission from Institute of Pure and Applied Physics, Japan)

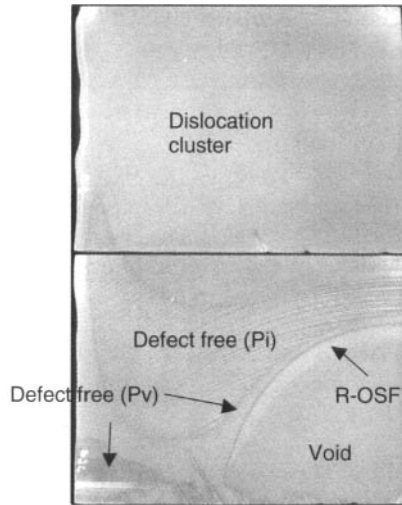


Figure 1.42 Defect-free region by EMCZ

1.5 CONCLUDING REMARKS

In this chapter we have discussed many features of CZ-Si crystal growth. The big driving force of CZ-Si crystal growth is IT (information technology). As long as IT is developing, the demand for large, high-quality, reasonably priced Si wafers will remain. The following are perspectives on this subject.

- **Large crystal:** LSI industries have recently started producing 300-mm wafers. According to the technological trend, 450-mm wafers will be utilized in the future. However, use of 450-mm wafers will be determined not only from the technical view point but also from the business viewpoint.
- **Numerical modeling:** Modeling techniques have been improved year by year due to the development of the capability of computers. Crystal growth had been previously treated in two dimensions. Nowadays, three-dimensional and time-dependent calculation is normal, and turbulent flow can be handled. The contribution of numerical modeling to crystal growth will become much more important.
- **Void defects:** The current problems of bulk Si wafers are connected to void defects. Epitaxial wafers are used for high-end products. However, if bulk wafers are employed, Si wafers can be supplied at a more reasonable price. Crystal growers will hopefully find a new solution, introducing a new technique, such as rotating magnetic field and/or electromagnetic Czochralski (EMCZ).
- **Understanding of crystal-growth process:** From the viewpoint of the science of CZ-Si growth, there are many subjects to be understood. One of these is the surface-tension-driven (Marangoni) flow at the melt surface. The Marangoni effect for the CZ-Si growth system is more complicated than that for the float-zone system. This is a challenging subject for research. The data base for thermophysical properties of the CZ-Si growth system must be improved; currently there is no direct measurement of

thermal conductivity of molten silicon, which is one of the important parameters to govern the growth rate of a single crystal.

REFERENCES

1. *Semiconductors*, ed. N.B. Hannay, (Van Nostrand, Princeton, N.J., 1959).
2. *International Technology Roadmap for Semiconductors 2003*, <http://public.itrs.net>
3. W.V. Ammon, in: H. Richeter *et al.* (eds.), *Proceedings of the Sixth GADEST '95*, (Scitec Publications, 1995) p. 97.
4. Y. Shiraishi, K. Takano, J. Matsubara, T. Iida, N. Takase, N. Machida, M. Kuramoto and H. Yamagishi, (2001) *J. Cryst. Growth* **229**, 17.
5. J.R. McCormic, *Polycrystalline Silicon, Semiconductor Silicon 1986*. pp. 43–60, (The Electrochemical Society, Pennington, USA).
6. P.A. Taylor, (1987) Silane: Manufacture and applications, *Solid State Technol.*, July, 53–59.
7. S.K. Iya, R.N. Flagella and F.S. DiPaolo, (1982) Heterogeneous decomposition of silane in a fixed bed reactor, *J. Electrochem. Soc.* **129**, 1531–1535.
8. C.P. Chartier and C.B. Sibley, (1975) *Solid State Technol. J.*, 31–33.
9. T. Suzuki, N. Isawa Y. Okubo and K. Hoshi, (1981) *Semiconductor Silicon 1981*, (The Electrochemical Society, Pennington, USA), 90.
10. U.S. Patent No 5,976,247.
11. W.C. Dash, (1959) Silicon crystals free of dislocations, *J. Appl. Phys.* **30**, 459.
12. W.C. Dash, (1960) Growth of silicon crystals free from dislocations, *J. Appl. Phys.* **31**, 736.
13. N. Machida, T. Iida, N.T. Akase, K. Takano, J. Matsubara, Y. Shiraishi, M. Kuramoto and H. Yamagishi, (2000) Crystal supporting systems for 400 mm silicon CZ crystal growth., *Proceedings of the 3rd International Symposium on Advanced Science and Technology of Silicon Materials* 195–202.
14. T. Iida, N. Machida, N. Takase, K. Takano, J. Matsubara, M. Kuramoto and H. Yamagishi, (2001) *J. Cryst. Growth* **229**, 31.
15. K. Hoshikawa, X. Huang, T. Taishi, T. Kajigaya and T. Iino, (1999) *Jpn. J. Appl. Phys.* **38**, L1369.
16. X. Huang, T. Taishi, I. Yonenaga and K. Hoshikawa, (2000) *Jpn. J. Appl. Phys.* **39**, L1115.
17. A. Rudevičs, A. Muiznieks, G. Ratnieks, A. Mühlbauer and Th. Wetzel, (2004) *J. Cryst. Growth* **266**, 54.
18. G. Ratnieks, A. Muiznieks, L. Buligins, G. Raming, A. Mühlbauer, A. Lüdge and H. Riemann, (2000) *J. Cryst. Growth* **216**, 204.
19. S. Enger, O. Gräbner, G. Müller, M. Breuera and F. Durst, (2001) *J. Cryst. Growth* **230**, 135.
20. K.-W. Yi, V.B. Booker, M. Eguchi, T. Shyo and K. Kakimoto, (1995) *J. Cryst. Growth* **156**, 383.
21. T. Kanda, M. Hourai, S. Miki, T. Shigematsu, H. Tomokage, T. Miyano, H. Morita and A. Shintani, (1996) *J. Cryst. Growth* **166**, 663.
22. K. Kakimoto, M. Eguchi, H. Watanabe and T. Hibiya, (1988) *J. Cryst. Growth* **88**, 365.
23. M. Watanabe, M. Eguchi, K. Kakimoto and T. Hibiya, *The Winter Annual Meeting of the American Society of Mechanical Engineers*, Atlanta, Georgia, December 1991. Proceedings of the Conference, Experimental and Numerical Visualization, ASME FED-vol. 128, pp. 225–260.
24. M. Watanabe, M. Eguchi, K. Kakimoto, B. Yann and T. Hibiya, (1993) *J. Cryst. Growth* **128**, 288.
25. Y. Kishida, M. Tanaka and H. Esaka, (1993) *J. Cryst. Growth* **130**, 75.
26. M. Watanabe, M. Eguchi, K. Kakimoto, H. Ono, S. Kimura and T. Hibiya, (1995) *J. Cryst. Growth* **151**, 285.
27. M. Tanaka, M. Hasebe and N. Saito, (1997) *J. Cryst. Growth* **180**, 487.

28. Y. Kishida and K. Okazawa, (1999) *J. Cryst. Growth* **198/199**, 135.
29. A. Lipchin and R.A. Brown, (1999) *J. Cryst. Growth* **205**, 71.
30. I.Yu. Evstratova, V.V. Kalaev, A.I. Zhmakin, Yu.N. Makarov, A.G. Abramovc, N.G. Ivanovc, E.M. Smirnovc, E. Dornberger, J. Virbulis, E. Tomzig and W. von Ammon, (2001) *J. Cryst. Growth* **230**, 22.
31. I.Yu. Evstratova, V.V. Kalaev, A.I. Zhmakin, Yu.N. Makarov, A.G. Abramovc, N.G. Ivanov, A.B. Korsakov, E.M. Smirnov, E. Dornberger, J. Virbulis, E. Tomzig and W. von Ammon, (2002) *J. Cryst. Growth* **237/239**, 1757.
32. A. Krauzea, A. Muimnieksa, A. Mühlbauer, Th. Wetzel and W.v. Ammon, (2004) *J. Cryst. Growth* **262**, 157.
33. V.V. Kalaev, D.P. Lukanin, V.A. Zabelin, Yu.N. Makarov, J. Virbulis, E. Dornberger and W. von Ammon, (2003) *J. Cryst. Growth* **250**, 203.
34. V.V. Kalaev, I.Yu. Evstratov and Yu.N. Makarov, (2003) *J. Cryst. Growth* **249**, 87.
35. A. Eyer, H. Leiste and R. Nitsche, (1984) *Proc. 5th European Symposium on Materials Sciences under Microgravity*, Schlot-Elmau 1984 (ESA SP-222), 173.
36. V. Kumar, B. Basu, S. Enger, G. Brenner and F. Durst, (2003) *J. Cryst. Growth* **253**, 142.
37. T. Azami, S. Nakamura and T. Hibiya, (2001) *J. Electrochem. Soc.* **148**, G185.
38. K. Yamamoto, T. Abe and S. Takasu, (1991) *Jpn. J. Appl. Phys.* **30**, 2423.
39. B.J. Keene, (1987) *Surf. Interface Anal.* **10**, 367.
40. R.E. Chaney and C.J. Varker, (1976) *J. Cryst. Growth* **33**, 188.
41. K. Abe, K. Terashima, T. Matsumoto, S. Maeda and H. Nakanishi, (1998) *J. Cryst. Growth* **186**, 557.
42. H. Hirata and K. Hoshikawa, (1980) *Jpn. J. Appl. Phys.* **19**, 1573.
43. X. Huang, K. Saito, S. Sakai, K. Terashima and K. Hoshikawa, (1998) *Jpn. J. Appl. Phys.* **37**, 3188
44. X. Huang, K. Saito, S. Sakai, K. Terashima and K. Hoshikawa, (1998) *Jpn. J. Appl. Phys.* **37**, L193
45. K. Hoshikawa, H. Hirata, H. Nakanishi and K. Ikuta, (1981) *Semiconductor Silicon 1981*, eds. H.R. Huff, R.J. Kriegler and Y. Takeishi (The Electrochem. Soc., Pennington, USA), p. 101.
46. Yu.M. Gelfgat, (1999) *J. Cryst. Growth* **198/199**, 165.
47. K. Hoshikawa, (1982) *Jpn. J. Appl. Phys.* **21**, L545.
48. H. Hirata and K. Hoshikawa, (1989) *J. Cryst. Growth* **96**, 747
49. M. Watanabe, M. Eguchi and T. Hibiya, (1999) *Jpn. J. Appl. Phys.* **38**, L10
50. H. Hirata and K. Hoshikawa, (1989) *J. Cryst. Growth* **98**, 777.
51. J.C. Mikkelsen, Jr., *Oxygen, Carbon, Hydrogen and Nitrogen in Crystalline Silicon*, eds. J. C. Mikkelsen, Jr. *et al.* (MRS Proc. Vol. 59, 1986) p. 19.
52. W.K. Tice and T.Y. Tan, (1976) *Appl. Phys. Lett.* **28**, 564.
53. A.J.R. de Kock, (1973) *Philips Res. Repts Suppl.* **1**, 1.
54. V.V. Voronkov, (1982) *J. Cryst. Growth* **59**, 625.
55. V.V. Voronkov and R. Falster, (1998) *J. Cryst. Growth* **194**, 76.
56. H. Harada, T. Abe and J. Chikawa, *Semiconductor Silicon 1986*, eds. H.R. Huff, T. Abe and B.O. Kolbesen (Electrochemical Society, Pennington, 1986) p. 76.
57. M. Hourai H. Nishikawa, T. Tanaka, S. Umeno, E. Asayama, T. Nomachi and G. Kelly, *Semiconductor Silicon 1998* eds. H.R. Huff, H. Tsuya and U. Gösele (Electrochemical Society, Pennington, 1998) p. 453.
58. M. Kato, T. Yoshida, Y. Ikeda and Y. Kitagawa, (1996) *Jpn. J. Appl. Phys.* **35**, 5597.
59. M. Itsumi, Octahedral Void Defects in Czochralski Silicon, in *Crystal Growth Technology*, eds. H. Scheel and T. Fukuda, (Wiley, Chichester, UK, 2003) p. 214.
60. M. Itsumi and F. Kiyosumi, (1982) *Appl. Phys. Lett.* **40**, 496.
61. J. Ryuta, E. Morita, T. Tanaka and Y. Shimanuki, (1990) *Jpn. J. Appl. Phys.* **29**, L1947.
62. H. Yamagishi, I. Fusegawa, N. Fujimaki and M. Katayama, (1992) *Semicond. Sci. Technol.* **7**, A135.

63. J.G. Park and G. Rozgonyi, (1996) *Solid State Phenom.* **47/48**, 327.
64. K. Moriya, K. Hirai, K. Kashima and S. Takasu, (1989) *Jpn. J. Appl. Phys.* **66**, 5267.
65. F.G. Gonzalez, G.A. Rozgony, B. Gilgen and R. Barbour, *High Purity Silicon IV*, ed. C.L. Glayes *et al.*, (ECS), (Electrochemical Society, Pennington, and USA) 357.
66. W. von Ammon, R. Hölzl, J. Virbulis, E. Dornberger, R. Schmolke and D. Gräf, (2001) *J. Cryst. Growth* **226**, 19.
67. S. Umeno, T. Ono, T. Tanaka, E. Asayama, H. Nishikawa, M. Hourai, H. Katahama and M.U. Sano, (2002) *J. Cryst. Growth* **236**, 46.
68. M. Watanabe, M. Eguchi, W. Wang, T. Hibiya and S. Kuragaki, (2002) *J. Cryst. Growth* **237/239**, 1657.

2 Growth of Gallium Arsenide

M.R. BROZEL

Academic Consultant

I.R. GRANT

Wafer Technology Ltd, Milton Keynes, UK

2.1 Introduction	43
2.2 Doping considerations	45
2.3 Growth techniques	48
2.3.1 Horizontal Bridgman and horizontal gradient freeze techniques	48
2.3.2 Liquid encapsulated Czochralski (LEC) technique	49
2.3.3 Vertical gradient freeze (VGF) technique	53
2.4 Crystalline defects in GaAs	54
2.4.1 Defects in melt-grown, semi-insulating GaAs	54
2.5 Impurity and defect analysis of GaAs (chemical)	59
2.6 Impurity and defect analysis of GaAs (electrical)	61
2.6.1 Introduction to the electrical analysis of defects in GaAs	61
2.7 Impurity and defect analysis of GaAs (optical)	65
2.7.1 Optical analysis of defects in GaAs	65
2.8 Conclusions	67
Acknowledgments	68
References	69

2.1 INTRODUCTION

In the simplest terms, GaAs crystals are synthesized by reacting together high-purity Ga and As. Dopants may be added to produce materials of different conduction type and carrier concentration. However, the growth of compounds from the melt is a thermodynamic process and is characterized by the shape of the phase diagram near the solidus at temperatures just below the melting point of the compound. Hurle has published a thorough reassessment of the thermodynamic parameters for GaAs, with and without doping (Hurle, 1999). The complete phase diagram for Ga-As, showing the GaAs compound, is

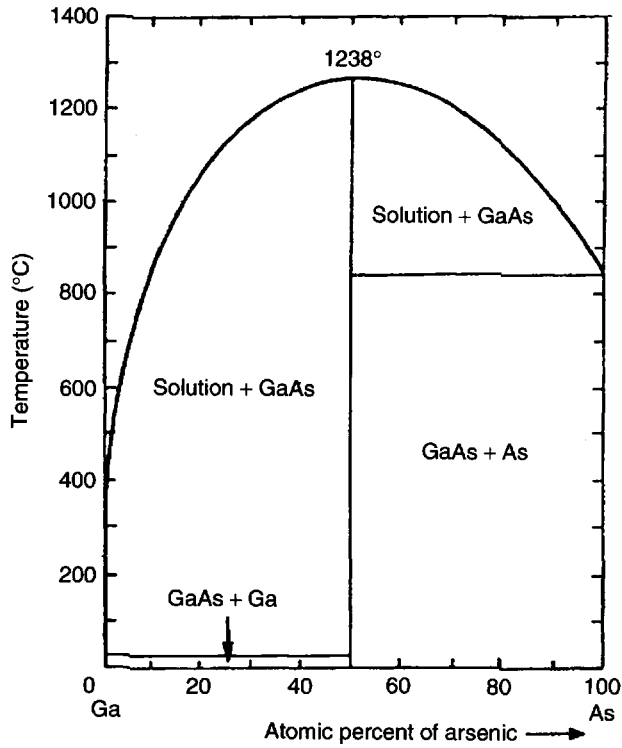


Figure 2.1 The complete phase diagram of the Ga-As system at an assumed pressure of As vapour of about 1 atmos. The vertical line near 50% composition is crystalline GaAs. (Reprinted from *Properties of Gallium Arsenide* p.559, eds, M.R. Brozel and G.E. Stillman, (1996) copyright (1996) with permission from IEE)

shown in Fig. 2.1 (Koster and Toma, 1955). However, details near the GaAs solidus are not revealed at this large scale.

The shape of the GaAs solidus is more complicated than indicated in Fig. 2.1. In particular, the congruent point, the maximum melting temperature, corresponds to a GaAs compound containing more As than exists in stoichiometric material, Fig 2.2.

It follows that growth from a stoichiometric melt results in a solid phase containing an excess of As of approximately $1 \times 10^{19} \text{ cm}^{-3}$. The solidus is retrograde so that, if thermodynamic equilibrium is maintained, this excess As must be lost from the host as the solid cools. If this As supersaturation cannot be relieved by outdiffusion from the crystal, then it will result in the generation of As-rich second phases (precipitates). Growth from a Ga-rich melt will result in the growth of a stoichiometric crystal. However, the melt will become more Ga-rich as growth proceeds leading to the growth of solid GaAs that steadily becomes richer in Ga.

Experimental work has shown that either due to the incorporation of an intrinsic defect, often assumed to be the gallium antisite defect, Ga_{As} , (Holmes *et al.*, 1982a) or a boron-related defect, Ga-rich LEC GaAs is strongly p-type (Elliott, 1983). A possibility for the latter defect is the boron antisite, B_{As} (Hobgood *et al.*, 1982, Yu *et al.*, 1981, Elliott *et al.*, 1982, Elliott, 1983).

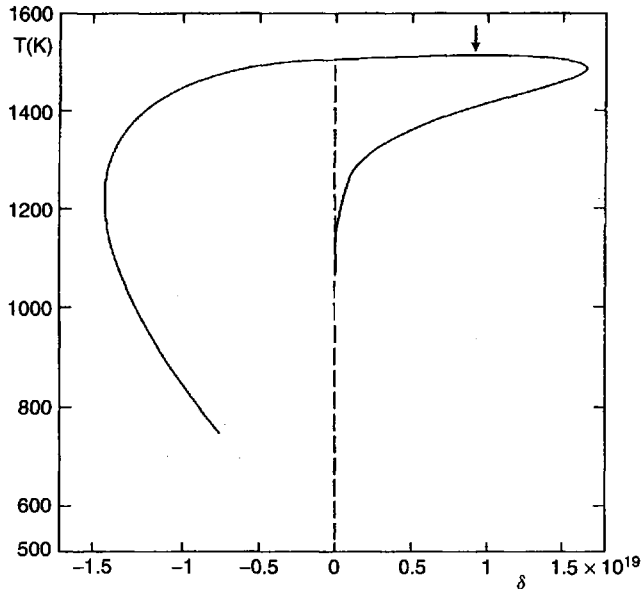


Figure 2.2 The GaAs solidus. The arrow marks the congruent point. (Reprinted from Hurle, *J. Appl. Phys.* **85**, (1999) 6957, copyright (1999) with permission from the American Institute of Physics)

Although As richness is found in melt-grown GaAs, measured concentrations of excess As do not exceed 10^{17} cm^{-3} (Kurusu *et al.*, 1989, Terashima *et al.*, 1984). It is not known how most of the grown-in excess As atoms are lost.

2.2 DOPING CONSIDERATIONS

Unlike group IV semiconductors where shallow donors are group V atoms only, donors in III-V compounds can occur on either sublattice, as IV_{III} or VI_{V} , where the capital letters represent the group in the Periodic Table from which the donor is selected and the subscript is the sublattice occupied. However, only certain group IV atoms have a suitable solubility on the Ga sublattice for them to be useful and the same situation is true for group VI atoms on As lattice sites.

Similarly, acceptors can be of II_{III} or IV_{V} types. (In principle, group IV atoms can be both acceptors and donors, IV_{III} and IV_{V} , respectively, a situation known as 'amphotericity'. Silicon, and to a similar extent germanium, in GaAs behave like this.) Once again not all of these occur in practice.

The choice of dopant depends mainly on its segregation coefficient and solubility (see Hurle, 1999). Figure 2.3 shows most of the known shallow donors and acceptors in GaAs with their ionization energies. Also shown in this figure are two important impurities that generate levels deeper in the bandgap. Cu is an unwanted deep acceptor contaminant but Cr has some technological importance and this element is discussed later.

Table 2.1 shows segregation coefficients for many impurities in melt-grown GaAs, although the data in the first two columns are rather dated. Weisberg *et al.* (1960) doped ingots, mainly polycrystalline, with the relevant impurity and then measured concentrations

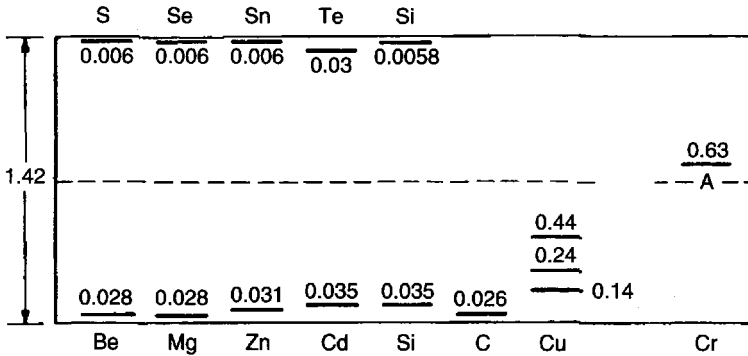


Figure 2.3 Ionization energies, in eV, of the shallow donors and acceptors in GaAs. Also shown are the important deep levels due to Cu and Cr. Cu is an impurity that can be introduced at growth or by processing and causes deleterious effects in devices. Cr was originally used as a deep acceptor to produce semi-insulating GaAs. Its use has fallen since the introduction of LEC and similar growth techniques. (Updated from *Semiconductor Devices, Physics and Technology*, S.M. Sze, John Wiley, 1985, copyright (1985) with permission from John Wiley)

of the impurity at different positions of the ingot by atomic emission spectroscopy. Whelan *et al.* performed similar measurements on a series of zone-refined crystals. However, in their measurements the impurity was tagged with a radioactive tracer, making quantitative estimates of concentration more sensitive and accurate. The third column includes more modern data that has been discussed by Hurle (1999).

It should be noted that there are two 'segregation coefficients' for donors; one corresponds to atomic concentrations while the other describes the manner in which the carrier concentration changes along the crystal axis. Because of autocompensation, these are different. Table 2.1 reports atomic data. It should also be noted that segregation data may be affected by the precise stoichiometry of the melt (Hurle, 1999) although this has been shown not to be the case for Sn doping (Brozel *et al.*, 1987). Additionally, note that segregation coefficients assume that once a solute has been added to the melt, no further additions are made and nothing is lost, i.e. growth takes place in a conservative system. This is not the case for carbon, which in LEC growth, probably enters the melt continuously from the ambient gases (see later). There is, however, a consensus that the segregation coefficient for carbon in GaAs is greater than unity.

In melt-grown GaAs, donors are usually either Si_{Ga} or Te_{As} , as each has a satisfactory segregation coefficient and solubility, although other group VI species have been used. As mentioned above, donors experience some degree of autocompensation with the result that up to a carrier concentration, n , of about $3 \times 10^{18} \text{ cm}^{-3}$ the carrier concentration is only about 80 % of the added dopant concentration. Thermodynamic analysis has demonstrated that for group VI donors this is a result of the formation of [donor - V_{Ga}] pair defects, where V_{Ga} represents the Ga vacancy. Autocompensation for the case of Si doping is a result of the amphotericity of Si with a fraction, about 10 %, of the Si atoms taking up As lattice sites and behaving as shallow acceptors. Above $n = 3 \times 10^{18} \text{ cm}^{-3}$, the carrier concentration tends to saturate and extra donor atoms are involved in vacancy complexes with a drop in electron mobility, the appearance of dislocation loops and a rapid rise in lattice constant (Hurle, 1999).

Table 2.1 Segregation coefficients of selected dopants in melt-grown GaAs. Columns 1 and 2 are from Weisberg *et al.* (1960) and Whelan *et al.*, cited in Skalski (1962). The sources for column 3 are: (1) Edmond, 1959, (2) Kobayashi and Osaka, (1985), (3) Brozel *et al.*, (1987), (4) Willardson and Allred, (1966), (5) Mullin *et al.* (1980), (6) Grinshtein *et al.* (1975), (7) Pelevin *et al.* (1971), (8) Cronin and Haisty (1964), (9) Martin *et al.* (1979, 1980), (10) Gimel'farb *et al.* (1970), (11) Brozel *et al.* (1982)

	Weisberg <i>et al.</i> (1960)	Whelan <i>et al.</i>	Other
Ag	0.1	—	
Al	3	—	
C	—	—	1.44(2)
Ca	< 0.02	—	
Cd	< 0.02	< 0.2	
Cr	—	—	0.00064(8) 0.00089(9) 0.00057(4) 0.00058(10) 0.00075 < k < 0.0011(11)
Cu	—	< 0.002	
Fe	< 0.02	0.003	
Ge	0.03	—	0.0028(5) 0.01(7)
In	0.1	—	
Mg	0.3	—	
Mn	< 0.02	—	
Ni	< 0.02	—	
P	2	—	
Pb	< 0.02	—	
S	0.3	0.5 < k < 1.0	0.3(4)
Sb	< 0.02	—	
Se	—	0.44 < k < 0.55	0.3(4) 0.43(5)
Si	0.1	0.14	0.14(4)
Sn	0.03	—	0.004(3), 0.048(6), 0.08(4)
Te	0.3	0.05 < k < 0.16	0.059(4), 0.068(5)
Zn	0.1	0.27 < k < 0.9	0.36(1), 0.4(4)

The p-type doping of melt-grown GaAs appears to be much easier. There is no auto-compensation and the solubility of Zn, the most common acceptor dopant in melt-grown GaAs, is over 10^{20} cm^{-3} . The segregation coefficient of Zn in GaAs is 0.4.

Although the partial pressure of Ga above a Ga-As melt at all reasonable temperatures is extremely small and can be ignored, the partial pressures of As_2 and As_4 depend sensitively on the melt composition and this can be used to control the ratio of Ga/As in the melt as the crystal grows. Over a stoichiometric GaAs melt at the melting temperature of 1238°C this pressure is approximately 2 atmos (1 atmos above ambient) of which approximately 60% is As_4 . It is necessary to control this pressure to retain melt composition and to impede the loss of As from the melt. This requirement to

compensate for the As dissociation from the melt has resulted in the development of several growth techniques.

2.3 GROWTH TECHNIQUES

2.3.1 Horizontal Bridgman and horizontal gradient freeze techniques

The first growth method to be used commercially was the horizontal Bridgman (HB) technique (Weisberg *et al.*, 1960). In essence, the growth chamber consists of a horizontal quartz tube, at one end of which is a quartz crucible containing the Ga/As melt near the melting temperature (T_m) of 1238 °C, while the other end is cooler, near 617 °C, and contains a small quantity of elemental As, Fig. 2.4.

This As produces the overpressure of As that controls the stoichiometry of the Ga-As melt. The Ga-As melt is often formed by reacting molten, metallic Ga in the growth section with As vapour produced from the As reservoir at the other end. In other processes polycrystalline GaAs is used as the source for the molten Ga-As. The growth can proceed in two ways. In the classical HB technique the initial melt exists in a region at a temperature just above T_m but adjacent to a small temperature gradient. A seed crystal, already placed in the crucible with part of it in the melt while the rest is at a temperature below T_m , will initiate growth. The melt is moved mechanically through the temperature gradient so that the entire melt is gradually cooled below T_m . Eventually, all of the GaAs melt solidifies on the seed as a single crystal and with the same orientation.

In a modification to HB, the mechanical withdrawal of the GaAs melt through the gradient is replaced by slowly reducing the temperature of the growth region electronically.

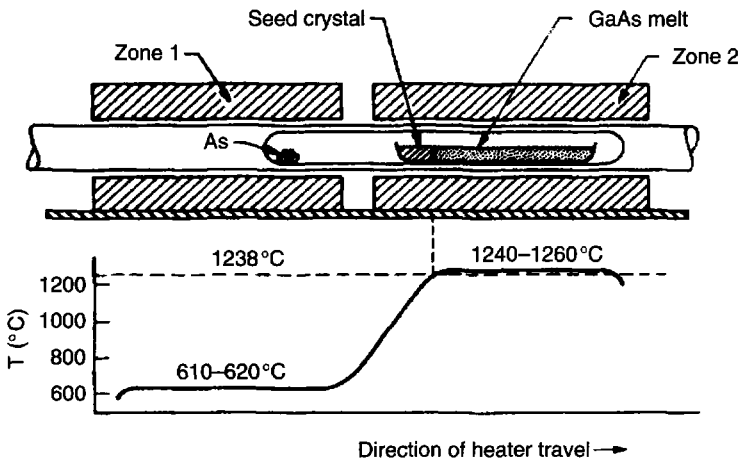


Figure 2.4 Horizontal Bridgman technique for growing GaAs. Growth takes place in the high-temperature region of the furnace, whilst the As vapor pressure is controlled by the presence of elemental As in the low-temperature region. The interface between the melt and the solid is gradually moved until all the GaAs is solidified. (Reprinted from *Semiconductor Devices, Physics and Technology*, S.M Sze, John Wiley, 1985, copyright (1985) with permission from John Wiley)

This is the horizontal gradient freeze (GF) method (Woodall, 1964). It has the advantage of needing less space and is less sensitive to mechanical disturbance.

In both cases, crystals are best grown along $\langle 111 \rangle$ to reduce the occurrence of twinning. $\{001\}$ wafers can be extracted from the $\langle 111 \rangle$ ingot by accurate sawing. Advantages of the HB and horizontal GF methods include the potential for good visibility of the growth interface allowing the operator to make modifications as growth takes place. However, grown crystals have a D-shaped cross section because of the shape of the melt in the crucible and subsequent wafering. Considerable loss of material is incurred if the wafers are edge-ground to make them circular.

HB and horizontal GF GaAs are contaminated with silicon atoms from the quartz growth tube and this renders them n-type. This contamination can be limited to below 10^{16} cm^{-3} and is not a problem if highly doped n-type material is required, as extra Si will be added to the melt anyway. The use of crucibles made of pyrolytic boron nitride (pBN) instead of quartz allows GaAs to be grown with a low residual carrier concentration ($<10^{12} \text{ cm}^{-3}$) but there is a disadvantage in terms of their high cost. Although there are few uses for p-type bulk GaAs, the overdoping of the melt with an acceptor species (usually Zn) effectively renders the crystal p-type. The reduction in hole mobility by compensation of a minority of the Zn atoms by the Si atoms is of little consequence.

However, regardless of the type of crucible material, the advantages of semi-insulating (SI) behaviour can only be obtained after residual donors have been counterdoped by the incorporation of Cr atoms in the melt (Cronin and Haisty (1964), Martinez *et al.* (1981)). Cr atoms act as deep acceptor centers in n-type GaAs and act to pin the Fermi energy just above midgap, see Fig. 2.3. The GaAs so produced exhibits a resistivity that can exceed $10^8 \Omega \text{ cm}$. Such Cr-doped GaAs was the mainstay of the high-speed GaAs device industry for over a decade. However, issues of segregation, low solubility and rapid outdiffusion of Cr atoms from substrates during high-temperature processing, including epitaxy, made these substrates undesirable once high-purity semi-insulating material became widely available. Finally, the combination of poor thermal conductivity and low critically resolved shear stress (CRSS) at elevated temperatures results in the inevitable thermal gradients in the cooling crystal producing plastic deformation by the creation of slip dislocations. In HB and horizontal GF material the dislocation densities are around 10^3 cm^{-2} (see Chen *et al.* (1990)) although these densities can be reduced by over an order of magnitude due to 'impurity hardening' in highly n-type GaAs (Moravec *et al.*, 1991). Dislocations, their generation and their properties will be considered later.

2.3.2 Liquid encapsulated Czochralski (LEC) technique

The Czochralski technique, in which a crystal is pulled from a melt, was originally used for metals and was then modified for the commercial growth of Ge and then Si. The seed and crystal is rotated around a vertical axis as growth proceeds. This results in the immediate advantage of producing ingots of circular cross section. Simultaneous rotation of the melt can result in efficient mixing of the host and dopant, a great advantage for doped crystals.

In the case of compounds, where the partial pressures of one or both components are large, the melt surface must be protected either by incorporating an independent source of the vapour under dissociation (as in HB or GF growth) or by other means. In LEC

growth, the surface is covered by an encapsulant layer of liquid boric oxide, B_2O_3 , (Metz *et al.* (1962), Mullin *et al.* (1968)). This is prepared from boric acid, which is baked under vacuum at high temperature to remove most of the water. The residual water content can be specified from a minimum level of ~ 100 ppm to a few thousand ppm. The water content can be accurately measured by infrared absorption of the OH stretching mode (Shropshall and Skinner, 1984). This value is critical for the chemical reactions that take place during growth. The axially rotating crystal is withdrawn through the encapsulant and then cools naturally by heat radiation, and by conduction and convection via the high-pressure ambient gas, see Fig. 2.5.

LEC pullers use high-purity elements for the in-situ synthesis of GaAs. They are high-pressure growth machines (and, therefore, expensive) because the internal pressure can exceed 60 atmos when the Ga and As are compounded. The boric oxide becomes liquid at temperatures of a few hundred degrees Celsius and floats to the surface of the other materials in the crucible. At all times during the subsequent reaction and growth it protects the surface from As loss. Its water content helps to purify the melt (Oliver *et al.*, 1981). An example of this behaviour is shown in Fig. 2.6 (Wafer Technology Ltd.).

If the crucible is quartz the resulting, nominally undoped, crystal is n-type because of Si incorporation. However, if the crucible is made from pyrolytic boron nitride (pBN) the crystal is SI over its entire length even without the introduction of Cr into the melt (Hobgood *et al.*, 1982).

Nearly all LEC GaAs is contaminated by boron at concentrations up to 10^{18} cm^{-3} depending on the water content of the boric oxide (Holmes *et al.*, 1982). High B concentrations are observed for growth from boric oxide of the lowest water content, see Fig. 2.7.

In all SI material the B atoms take up Ga lattice sites and are electrically inactive (Holmes, 1982b). In Si-doped GaAs some of the B atoms appear to be incorporated as an acceptor species, resulting in some compensation (Laithwaite *et al.*, 1977).

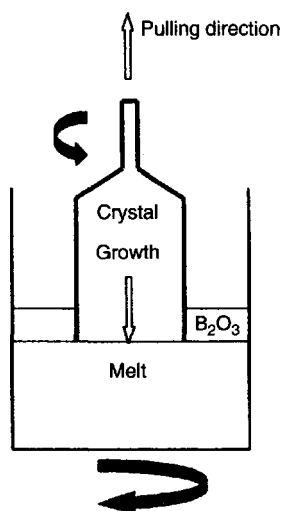


Figure 2.5 LEC growth. The hollow arrow indicates the liquid/solid interface where growth takes place. As the growing crystal is pulled through the molten boric oxide it is rotated, resulting in a cylindrical ingot. The crucible is rotated in the opposite direction to stir the melt efficiently (Courtesy of Wafer Technology plc, UK)

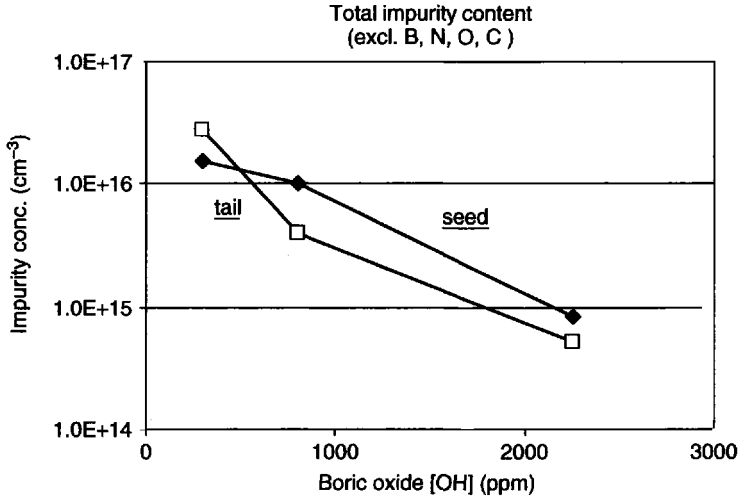


Figure 2.6 Reduction in total impurity content of LEC-grown GaAs crystals as a function of the water content of the boric-oxide encapsulant (Courtesy of Wafer Technology plc, UK)

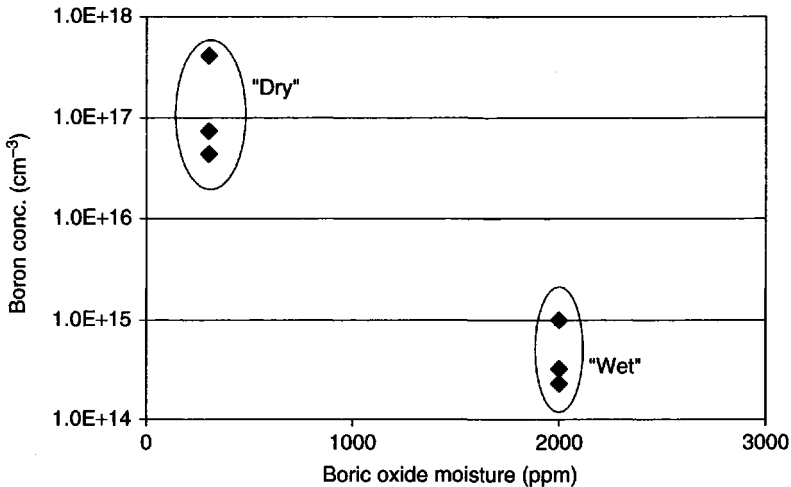


Figure 2.7 Showing the reduction of boron uptake into the growing undoped LEC GaAs crystal when boric oxide of greater water content is used (Courtesy of Wafer Technology plc, UK)

The shape control is also assisted by the presence of large radial gradients limiting the diameter of the crystal through the curvature of the growth interface isotherm. The growth rate is controlled by measuring the rate of weight increase by means of a load cell within the pressure vessel. This information is used to control the furnace temperature within a feedback loop, providing continuous shape control throughout the growth, including the 'grow-out phase' from the seed to the final crystal diameter.

Advantages of LEC growth include the in-situ synthesis of the compound, the fact that the melt is not in contact with the crucible (being separated from it by the boric

oxide) and the high yield of long, single crystals of large diameter. The high yield of large single crystals is aided by the large radial and axial thermal gradients that are a feature of Czochralski growth. As we will show later, the high thermal gradients that assist LEC growth also result in large dislocation densities, up to 10^5 cm^{-2} . Uncontrolled cooling of the LEC crystal causes the outside to contract onto the core, creating slip dislocations at densities from 10^4 to 10^5 cm^{-2} (Jordan *et al.*, 1980). This defect creation occurs just below the crystallisation temperature where dislocation motion by slip is easy. In addition, high concentrations of native point defects, which allow dislocation motion by climb, are also present. As a result, the dislocations are able to polygonise into cells, a rearrangement that reduces their strain energies. The final arrangement of a dislocation cell structure is the situation that is usually seen when a wafer is assessed.

As in HB and HGF growth, the crystal can be doped n-type or p-type. Si or Te is normally used for n-type doping, while Zn is used for p-type material. As mentioned above, a reaction between the melt and the boric oxide has been found to occur with Si doping leading to a reduction in Si uptake and considerable boron contamination of the GaAs (Brozel *et al.* (1978)). In many cases, the concentration of B in the final crystal is comparable to the Si concentration. Nevertheless, Si remains one of the preferred donors for LEC GaAs.

GaAs crystals of mass up to 25 kg and diameter up to 200 mm are easily produced. Wafers of 150 mm diameter are routinely supplied to device manufacturers from LEC crystals: at the time of writing this article 200-mm diameter wafers were being made available to manufacturers for assessment.

2.3.2.1 Growth of SI LEC GaAs

The growth of nominally undoped GaAs by LEC from a pBN crucible results in SI behaviour. Chemical analysis of this type of GaAs always finds a concentration of carbon that is higher than the total concentrations of all other electrically active impurities (Holmes *et al.*, 1982c). The high carbon concentrations are not too surprising because not only is carbon a possible impurity in both Ga and As but there are many components of the LEC puller, namely the heaters and much of the thermal insulation, that are also made of carbon. Much work has shown that the carbon is introduced to the Ga-As melt through the gas phase, probably as carbon monoxide and the control of the partial pressure of this gas, when deliberately introduced, can be used to control the uptake of carbon in the crystal (Doering *et al.*, 1990). Because carbon atoms take up As sites and act as shallow acceptors, the resulting crystal would be expected to be p-type.

Some of the carbon acceptors are compensated by residual concentrations of shallow donors such as silicon and sulfur. The compensation of the rest is performed by native deep donor defects. Most of these occur at low concentration. However, one, known as EL2, occurs at concentrations between 1 and $1.5 \times 10^{16} \text{ cm}^{-3}$. Although it is the partial ionisation of this donor that pins the Fermi energy close to midgap and results in SI behaviour, the final resistivity of the GaAs depends mainly on the carbon concentration (Lambert *et al.*, 1990). The atomic identity of EL2 was a hot topic of research for many years and there still remain questions as to its identity (Baranowski and Trautman, 1996). However, what is not questioned is that the defect involves the As-antisite defect, As_{Ga} .

After growth, high concentrations of EL2 are found associated with dislocations and this results in nonuniformities in electrical properties (Grant *et al.*, 1982, Skolnick *et al.*, 1984a). Microprecipitates of hexagonal As are also found in close association with the dislocations (Cullis *et al.*, 1980). Most manufacturers use ingot anneals at temperatures close to 1000 °C to render EL2 concentrations more uniform and to improve electrical uniformity (Rumsby *et al.*, 1984). Some follow ingot heat treatments with anneals of the individual wafers (Oda, 1996). The schedules of these treatments vary between wafer suppliers but, in general, after these treatments the resistivity is of the order of $10^7 \Omega \text{ cm}$ with a uniformity of better than $\pm 10\%$.

It must be emphasized that the dislocation density cannot be reduced by heat treatments and this has led to the development of improved growth techniques. One of these employs the concept of a hot-wall enclosure to reduce the high thermal gradients seen in conventional LEC growth, the first implementation of which was by Gremmelmaier (1956). These techniques seek to reduce thermal gradients by controlling the ambient gas temperature. The consequence of this is a greater decomposition of the surface due to loss of As that is overcome by the use of a separate As source within the hot-wall chamber. This leads to the term vapour-controlled Czochralski (VCZ) (Pekarek, 1970, Inada *et al.*, 1986, Rudolph and Jurisch, 1999) which produces crystals of reduced dislocation density.

An alternative method to reduce dislocation densities in melt-grown GaAs and one now gaining dominance is the vertical gradient freeze (VGF) method.

2.3.3 Vertical gradient freeze (VGF) technique

This is a modification of the horizontal technique where the melt is contained in a vertical crucible above a seed crystal. The crucible, surrounded by the furnace, is normally pBN and boric oxide is used as the encapsulant to protect the melt and avoid wetting the crucible walls. This arrangement can be employed for heavily doped n- and p-type material as well as high-purity SI crystals. Quartz crucibles can also be used for n-type growth. However, in this case, boric-oxide encapsulant cannot be used due to adhesion to the crucible and crystal, resulting in cracking on cooling. For growth in quartz, the system must be sealed to allow an As vapour-pressure balance. Also, the crucible surface must be specially prepared to avoid melt wetting on the walls. The main motivation for this latter method is to avoid boron contamination from the encapsulant, (Bourret and Merk, 1991).

The growth proceeds from the bottom of the melt upwards with a usual growth direction of $\langle 100 \rangle$ until the melt is exhausted (Monberg *et al.*, 1989). Diameter control of the growing crystal is not an issue with this method allowing smaller temperature gradients to be employed. This results in a crystal with lower dislocation densities, typically between 10^2 and 10^3 cm^{-2} . A VGF growth schematic is shown in Fig. 2.8.

The starting material is polycrystalline GaAs. This must be synthesised in a separate reactor, which can be of similar design to the furnace arrangement in a LEC puller. Allowance can be made for the introduction of a controlled amount of carbon, which will be necessary for SI behaviour in the final ingot. The use of polycrystalline GaAs starting material means that the VGF equipment can be easily fabricated 'in house' as high pressures will not be experienced. Initially the major drawback to VGF was the low growth rate coupled with the inability to see the progress of the growth. In other words, if growth was not progressing correctly, this could not be detected until after the entire

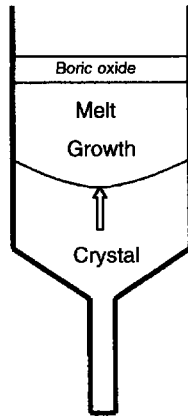


Figure 2.8 VGF growth. The seed crystal, in the narrow section at the bottom of the crucible, is held below the melt and the growth takes place upwards. The hollow arrow indicates the solid/liquid interface where growth takes place. The boric oxide surrounds the liquid and solid and helps in the final extraction of the cooled crystal from the crucible (Courtesy of Wafer Technology plc, UK)

melt was solidified and this was several days in most circumstances. However, after the method is optimized the yield can approach 100%. The usual dopants can be employed if conducting material is required.

The reduced dislocation density in VGF GaAs has made it the material of choice for most applications. This is because the trend towards epitaxial-based structures for both opto and microwave electronic devices has fuelled a requirement for improved structural quality of substrates. This is in contrast to earlier technologies using ion implantation where precise control of point defects in the bulk was the dominant consideration. At the time of writing, SI wafers of 200 mm diameter have been supplied as test wafers to device manufacturers.

2.4 CRYSTALLINE DEFECTS IN GaAs

Crystal defects are crucial in determining the electrical and some optical properties of GaAs. Most of these are incorporated into melt-grown, substrate material but they can be generated in later processing steps.

2.4.1 Defects in melt-grown, semi-insulating GaAs

2.4.1.1 Structural defects

Previously, the problems associated with melt growth were introduced. The growing crystal, cooling from the outside, experiences compressive stresses that cause plastic deformation by the introduction and subsequent motion of dislocations.

In SI GaAs many of the dislocations move by slip and climb to produce a cell-like structure following polygonization. This structure is complex and is best revealed by

specialized chemical etching of the surface (Abrahams and Buiocchi, 1965, Blunt *et al.*, 1982) or reflection X-ray topography (Lang, 1978). Each technique reveals; classical dislocation cells, 'lineage' (the boundary between sections of the crystal that have a small tilt misorientation and caused by dislocation motion) and residual slip that has not resulted in polygonization, possibly because it occurred at lower temperatures. The lineage occurs preferentially along the $\langle 110 \rangle$ diameters. A typical image from a 20-mm² area from a 3-inch diameter {001} SI LEC GaAs is shown in Fig. 2.9.

Selective etching by molten KOH is commonly used by substrate manufacturers in order to reveal dislocations passing through the surface and being revealed as pits. Thus, they obtain an 'etch pit density', or EPD, which corresponds to the dislocation density, (see, for example, Brown and Warwick, 1986). However, TEM is a preferable though much slower method for investigating dislocations (see, for example, Bangert, 1996).

VGF GaAs contains a much lower density of dislocations but even these are found to be in the form of a cell structure (Breivik *et al.*, 1992). n^+ GaAs is much less dislocated and no cell structure is present. It is thought that the slip velocity of dislocations on their glide planes is reduced in highly n-type material, or that impurity hardening by the dopant atoms occurs (Seki, 1978), so that n^+ GaAs contains far fewer dislocations than SI or p-type material. This reduction is very marked in Si-doped GaAs.

Figure 2.10 is a representation of the dislocation density ranges obtained for different growth techniques. In the cases of undoped GaAs, we can see the relative contributions from the growth techniques themselves. For 2-inch diameter undoped VGF GaAs a dislocation density below 10^3 cm^{-2} can be achieved. Within the methodology of the VGF technique itself, Si doping above a threshold level of about 10^{17} cm^{-3} results in a further marked reduction in dislocation density. Two cases are distinguished; growth in a quartz crucible without boric-oxide encapsulant, VGF Si(Q), results in a dislocation density between 1 and $3 \times 10^2 \text{ cm}^{-2}$ but growth in the presence of boric oxide, VGF Si(pBN), leading to the concomitant introduction of B atoms into the crystal, results in a further large reduction to levels below 10 cm^{-2} . The concentration of B introduced into the crystal is shown in Fig. 2.11.

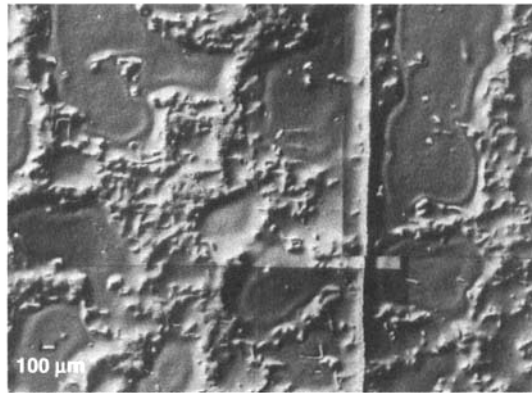


Figure 2.9 A 20-mm² area of a 3-inch diameter {001} SI LEC GaAs after etching to reveal dislocations. Many of the dislocations are arranged in a cellular-wall formation enclosing regions where the dislocation density is small. The nearly vertical line, closely aligned along $[110]$ is lineage where dislocations have interacted to produce a small-angle tilt boundary. (Courtesy of D.J. Stirland.)

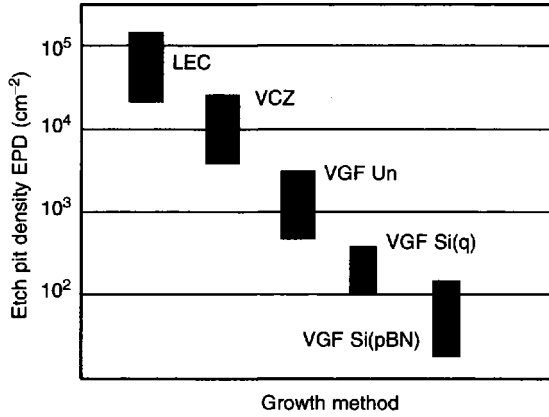


Figure 2.10 This plot demonstrates the improvement of structural quality, in terms of dislocation density as revealed by etch pit density, as a function of growth method, see text (Courtesy of Wafer Technology plc, UK)

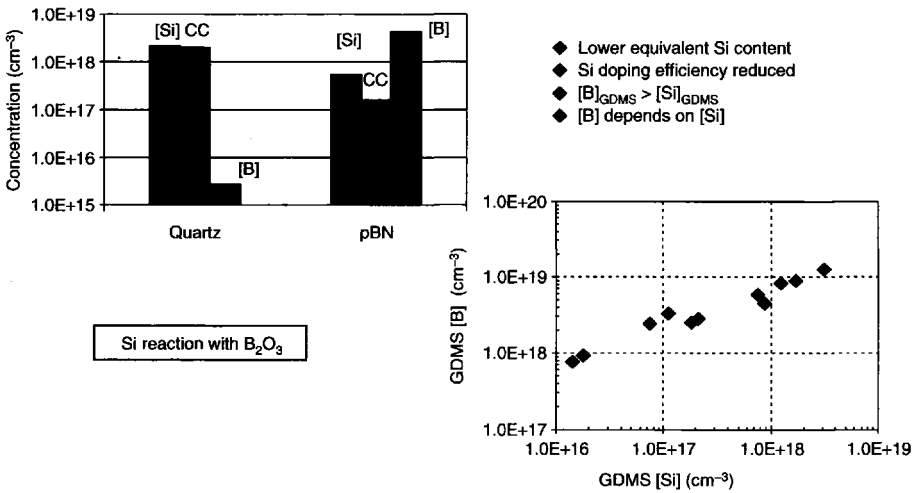


Figure 2.11 This plot demonstrates how the introduction of boron atoms into GaAs depends on the crucible material and the concentration of Si. In the histogram, cc is the carrier concentration measured by Hall effect (Courtesy of Wafer Technology plc, UK)

Boron is introduced into the crystal by a chemical reaction between the Si dopant and the encapsulant. For a given Si-melt concentration, a lower Si level is retained by crystals grown with encapsulation. Also, for similar Si concentrations in the GaAs crystal the electrical activity measured as donor concentration is reduced in the pBN grown material.

However, Te doping at the same level is not as efficient in this hardening process. Moreover, the presence of Si, with or without B, cannot be the only reason for lattice hardening as the addition of neutral atoms such as In at high concentration can also reduce the dislocation density to near zero (Jacob, 1982). There are separate reports of ‘hardening’ of undoped GaAs by boron incorporation at concentrations above $5 \times 10^{17} \text{ cm}^{-3}$ (Tada *et al.*, 1982)

2.4.1.2 Point defects

SI GaAs is a relatively pure material. It contains boron impurities at high concentration but these are neutral, see Section 2.2.3. Silicon and sulfur, both shallow donors, are found at concentrations around 10^{15} cm^{-3} . Concentrations of other electrically active impurities are extremely low and can be ignored.

The exception is carbon, a shallow acceptor, which occurs naturally in LEC GaAs, but that is often added intentionally to VGF GaAs, at concentrations between 10^{14} and 10^{16} cm^{-3} . For this reason carbon is then treated as a dopant and not an impurity. The accurate measurement of the carbon concentration is challenging. The standard method uses the low-temperature, far-infrared absorption due to the localised vibrational modes (LVM) of carbon acceptors, a technique that has a sensitivity of around 10^{14} cm^{-3} (Murray, 1996), see Section 2.5.

However, SI GaAs contains many native defects, and these are listed in Table 2.2.

Table 2.2 Deep electronic levels observed in melt-grown, SI GaAs. EL is an electron level and HL is a hole level. In most commercial material only EL2 exists at concentrations exceeding 10^{15} cm^{-3} and is the only deep level assumed to be involved in the compensation mechanism to give SI properties. (Reprinted from Brozel, *Properties of Gallium Arsenide*, Eds M.R. Brozel and G.E. Stillman, p.377 (1996), copyright (1996) with permission from IEE)

Label	Origin	Concentration (cm^{-3})	Emission energy (eV)	Capture cross section (cm^2)
EL11			Ec - 0.17	3×10^{-16}
EL17			Ec - 0.22	1.0×10^{-14}
EL14			Ec - 0.215	5.2×10^{-16}
EL6	complex defect	$10^{14} - 10^{15}$	Ec - 0.35	1.5×10^{-13}
EL5		$10^{14} - 10^{15}$	Ec - 0.42	10^{-13}
EL3		10^{13} to 10^{15}	Ec - 0.575	1.2×10^{-13}
EL2	native defect	$1 - 1.5 \times 10^{16}$	Ec - 0.825	1.2×10^{-13}
	As _{Ga} or [As _{Ga} - X]		Ec - 0.95 (double donor)	
HL10		below 2×10^{14}	Ev + 0.83	1.7×10^{-13}
HL9			Ev + 0.69	1.1×10^{-13}
HL7		$\sim 10^{15}$	Ev + 0.35	6.4×10^{-15}
'Ga _{As} '	Gallium antisite Ga _{As} or boron antisite B _{As}	3×10^{15} to 3×10^{16} (dependent on Ga-richness of melt)	Ev + 0.077	
			Ev + 0.203 (double acceptor)	

Most native point defects are deep donors, at concentrations between 10^{13} and 10^{15} cm^{-3} with one, EL2, the 'As antisite' defect (As_{Ga}), being dominant, existing at a concentration of between 1 and $1.5 \times 10^{16} \text{ cm}^{-3}$. Compensation of the carbon acceptors by EL2 pins the Fermi level near the centre of the bandgap, the other point defects being fully ionized by this process. The lack of native acceptors at concentrations above those of donors makes the presence of carbon (or other chemical acceptors) mandatory for SI behaviour.

2.4.1.2.1 The EL2 centre

Because of the importance of the EL2 centre, selected important properties are reviewed below.

EL2 is a native deep double donor whose first ionization state is at 0.75 eV above the valence band. This is the level that controls the Fermi level in SI GaAs. A second ionization from + to ++ occurs at an energy at 0.54 eV above the valence band.

Only the singly ionized state is paramagnetic but EPR measurements on this state have clearly demonstrated that EL2 contained the As antisite, As_{Ga} , defect (Wagner *et al.*, 1980).

EL2 exhibits a broad near-infrared absorption band in SI GaAs, which has been separated into components from neutral and singly ionized EL2 (Martin, 1981, Skowronski *et al.*, 1986).

At low temperatures EL2 defects can be excited into an inert metastable state by irradiating the GaAs with subbandgap light (Martin, 1981). In this state EL2 has no observable optical or electrical properties. This process is associated with a photoactivated relaxation of As_{Ga} along a $\langle 111 \rangle$ direction into an interstitial site to produce a $[\text{As}_i - \text{V}_{\text{Ga}}]$ complex (Dabrowski and Scheffler, 1988, Chadi and Chang, 1988). Normal deep-donor behaviour is recovered by warming above 140 K.

The two states of EL2 are shown in Fig. 2.12. (Interestingly, a similar deduction about the motion of donor atoms has been made in highly n-type GaAlAs when the Al content exceeds a critical value, the loss of normal donor behaviour being ascribed to the generation of the 'DX' center. Thus, conduction electrons are lost on irradiating the

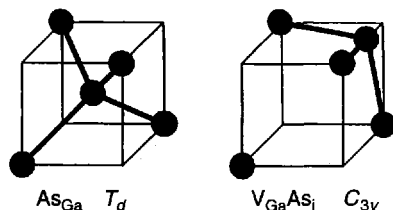


Figure 2.12 The two states of EL2. The dark circles are As atoms. In T_d symmetry the central As atom is tetrahedrally bonded to four nearest-neighbour As atoms as As_{Ga} . In the state represented by C_{3v} symmetry this As atom has been excited to move along the $\langle 111 \rangle$ direction where an uncharged metastable site is present. It is now represented by $[\text{V}_{\text{Ga}} - \text{As}_i]$. Heating above 140 K causes the As atom to return to the stable As_{Ga} structure. (Reprinted from J.M. Baranowski and P. Trautman in *Properties of Gallium Arsenide*, eds M.R. Brozel and G.E. Stillman, p. 353 (1996), copyright (1996) with permission from IEE)

cooled sample with subbandgap light. The recovery from DX-like behaviour is also found by warming the sample.)

High concentrations of EL2 are found in close association with dislocations in as-grown material. Coupled with the presence of As precipitates, this demonstrates that the environments of dislocations are very As-rich. EL2 concentrations are rendered uniform by ingot anneals that, as expected, also improve the uniformity of electrical properties.

Concentrations of EL2 defects are easily determined by measuring their room-temperature infrared absorption at wavelengths near 1 micrometre (Martin, 1981). The use of an infrared-sensitive CCTV camera or photographic film can allow mapping of the concentrations to be made (Brozel, 1996).

Another defect, often referred to as the "reverse contrast", or RC, defect can also be mapped; though at lower sample temperatures, using a small variation of this absorption technique (Skolnick *et al.*, 1984b, Brozel and Skolnick, 1994). RC absorption also reveals dislocations. However, concentrations of RC defects are not completely homogenized by these heat treatments indicating that other point defects may also be resistant to standard anneal protocols. RC defects occur at relative concentrations that are the reverse of EL2 defects in unannealed material (they are high where [EL2] is low, and vice versa) and seem to control minority carrier lifetime in SI GaAs and, thus, their low-temperature luminescence. Their identity as being As vacancies was demonstrated by positron annihilation methods (Le Berre *et al.*, 1995) and their nonuniform distribution was explained, at least in part, by the influence of dislocations on the As Frenkel reaction on the As sublattice as the crystal cools (Brozel and Tuzemen, 1994). The identities of other point defects in SI GaAs have not been determined.

2.5 IMPURITY AND DEFECT ANALYSIS OF GaAs (CHEMICAL)

Because concentrations of impurities in GaAs, with the exceptions mentioned previously, are extremely low and always less than 1 part per million (ppm) or $\sim 4 \times 10^{16} \text{ cm}^{-3}$, secondary ion mass spectrometry (SIMS), or glow-discharge mass spectrometry (GDMS), are the chosen methods for chemical analysis (see, Schroder 1998). In these methods, the surface is ablated and ionised. The secondary ions from the material under investigation are then passed through a mass spectrometer before detection. Sensitivities of better than 10^{13} cm^{-3} are quoted by most GDMS laboratories. Unfortunately, important species like hydrogen, oxygen and carbon are not detected with adequate sensitivity by these techniques unless considerable care is taken to remove these impurities from the vacuum ambient of the mass spectrometer. A typical example of a GDMS analysis is given in Table 2.3.

In bulk GaAs, C and H are best detected using infrared absorption by localised vibrational modes (LVM). This technique exploits the fact that light impurities in a solid have vibrational frequencies that do not couple well to the lattice modes (phonons); they vibrate at frequencies above the maximum optical phonon frequency (Reststrahlen) and lose this energy only slowly to the lattice. This gives them a long lifetime and a narrow bandwidth resulting in sharp absorption bands that fall in the mid- to far-infrared part of the spectrum, usually between 4 and 30 micrometres. Because vibrational frequencies and their absorption strengths depend on the atomic weights of the atoms and their isotopic abundances, respectively, LVM measurements can reveal the atom type unambiguously in many circumstances.

Table 2.3 A typical GDMS analysis of undoped SI GaAs. Concentrations are expressed in parts per billion (ppb) atomic. Note that previous measurements in the GDMS equipment have left some contamination so that some maximum concentrations, such as In, are artificially increased

Element	Ingot 1	Ingot 2	Ingot 3
Li	< 2	< 2	< 2
Be	< 1.6	< 1.2	< 1.3
B	110	31	41
F	< 4	< 4	< 5
Na	< 0.5	< 0.8	10
Mg	1	< 0.5	2
Al	1	1.2	3
Si	20	26	32
P	< 0.7	1.4	2
S	48	44	36
Cl	2	3	6
K	< 10	< 10	< 12
Ca	< 12	< 10	< 12
Ti	< 0.08	0.7	< 0.1
Cr	< 0.5	< 0.7	< 1
Mn	1.3	0.5	1
Fe	4	4	5
Ni	< 0.3	< 0.3	< 0.3
Cu	< 0.7	< 1	< 1
Zn	2	8	12
Ge	< 35	< 35	< 30
Se	< 6	< 7	< 8
Mo	< 0.4	< 0.4	< 0.4
Cd	< 4	< 4	< 5
In	< 100	< 100	< 100
Sn	< 2	< 2	< 2
Sb	< 0.6	< 0.6	1.5
Te	1.3	< 0.7	< 0.8
Pb	< 0.2	< 0.3	< 0.2
Bi	< 0.2	< 0.2	< 0.2

Measurement of these narrow absorption bands, often employing a Fourier transform infrared (FTIR) spectrophotometer and low sample temperatures, provides sensitive information not only of concentrations but also of the atomic environments of the impurity atoms.

Unfortunately, absorption from free carriers is very strong in this spectral region and this must be reduced, usually by irradiation of the sample with high-energy electrons. At suitably low fluences, this produces deep levels that compensate the material, apparently without otherwise affecting the impurities. However, this makes the technique difficult for routine measurements. SI GaAs does not need this treatment, making it the method of choice for the measurement of carbon concentration (Section 2.4.1.2).

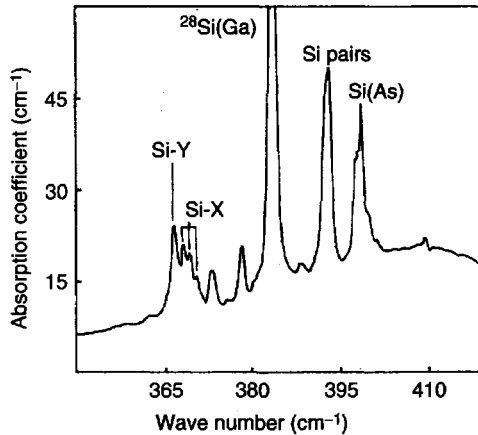


Figure 2.13 An LVM absorption spectrum of GaAs doped with Si at a concentration of around $5 \times 10^{18} \text{ cm}^{-3}$ after high-energy electron irradiation to remove free carriers. (Reprinted from R. Murray in *Properties of Gallium Arsenide*, eds. M.R. Brozel and G.E. Stillman, p. 228 (1996), copyright (1996) with permission from IEE)

As an example, an LVM absorption spectrum from an n^+ GaAs sample containing a high concentration of Si is shown in Fig. 2.13. Lines due to Si_{Ga} donors are present at 384, 379 and 373 cm^{-1} corresponding to vibrations of ^{28}Si , ^{29}Si and ^{30}Si on Ga lattice sites, respectively. Lines from Si_{As} shallow acceptors, $[\text{Si}_{\text{Ga}} - \text{Si}_{\text{As}}]$ nearest-neighbour pairs and complexes labelled Si-X and Si-Y, seen only at high Si concentration are also seen.

An excellent review of LVM analysis has been presented by Newman, 1994.

The importance of oxygen in commercial GaAs has been questioned for many years. However, the maximum concentrations detected in bulk material are usually below the sensitivity limit for chemical techniques or LVM absorption. The only reports of oxygen at relatively high concentration in LEC GaAs were based on a few, carefully prepared crystals (Alt, 1989).

Other methods of chemical analysis are either in disuse or out of the scope of this short section and will not be discussed here.

2.6 IMPURITY AND DEFECT ANALYSIS OF GaAs (ELECTRICAL)

2.6.1 Introduction to the electrical analysis of defects in GaAs

One of the simplest ways of assessing a sample of GaAs is a measurement of carrier concentration and mobility. This is easily achieved in conducting material by Hall-effect analysis. Applications of the Hall effect to GaAs have been discussed in detail by Look, (Look, 1989). This rather simple measurement can give considerable information about concentrations of shallow and deeper electronic levels. However, its sensitivity to the latter is rather limited. Also, measurements in SI GaAs are complicated by the difficulty in passing sufficient current through the material to achieve a measurable Hall voltage and the extremely high source impedance of the latter. There are also complications

resulting from surface-conduction effects and long time-constant photoconductivity that require modified procedures. For these reasons specialist Hall-effect equipment and sample preparation must be used to assess this material. Fortunately, there exist other highly sensitive electrical assessment techniques that can be used to assess SI GaAs.

However, before these are introduced the importance of mapping needs to be emphasized. It is clearly important to reveal variations of electrical parameters across a wafer and changes that may occur from wafer to wafer. These measurements, which must be performed rapidly and preferably without contact to the GaAs wafer, are often limited to resistivity. For conducting materials, eddy-current-loss measurements can be made very rapidly with a resolution of a few mm. This equipment has been available commercially for many years. For SI GaAs the absorption of RF radiation is very small and another technique, time-domain charge measurement, (TDCM) has been developed (Stibal *et al.*, 1991). This method, which measures the dielectric relaxation time in order to give resistivity data, can have a spatial resolution of a few tens of micrometres (Wickert *et al.*, 1999). An example of a resistivity map from a typical 2-inch diameter SI GaAs wafer is shown in Fig. 2.14.

2.6.1.1 Identification of shallow impurities

In p-type GaAs shallow acceptors have an appreciable ionization energy and in nondegenerate material the resulting free holes can often be frozen-out by cooling to temperatures close to 4.2 K. The Hall effect can be very useful here. An Arrhenius plot extracted from carrier-concentration measurements taken as a function of temperature can reveal this activation energy and, therefore, the acceptor. The presence of more than one acceptor makes the analysis more difficult; if compensating donors are present they are not revealed directly but mobility data can indicate their concentration.

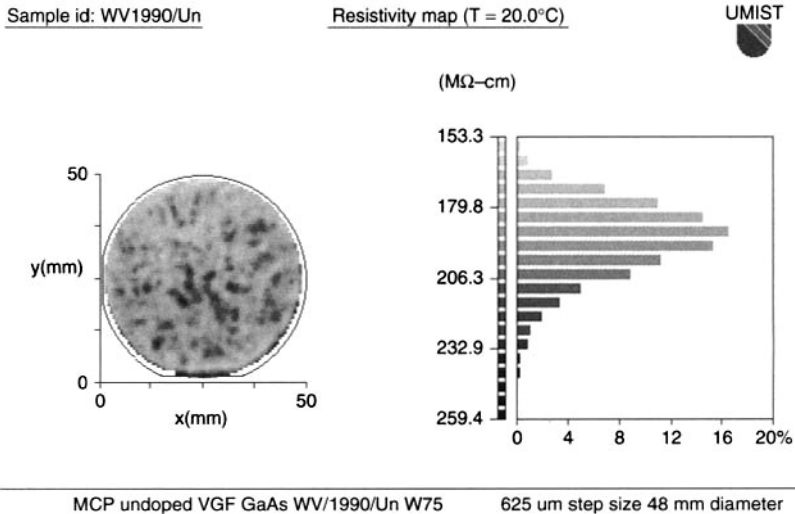


Figure 2.14 A resistivity map of a 2-inch diameter VGF, undoped SI GaAs wafer without anneal. Much of the variation in resistivity is associated with dislocation cell structure (Courtesy of Wafer Technology plc, UK)

This method does not work with n-type material because the ionization energies of shallow donors are very similar and, although total donor concentrations can be established, identification is impossible. Once again, it is assumed that no acceptors act as compensating defects.

However, a more complex technique, photo-thermal ionization spectroscopy (PTIS) can identify donors (Stillman *et al.*, 1977). This is based on the fact that the energy, ΔE , to excite the outermost bound s-electron to its first excited 2p state depends on the donor type. In PTIS, the sample, with Ohmic contacts, is cooled to temperatures near 10 K. Its conductivity is measured under illumination with light from a monochromator. When the photon energy is equal to ΔE , the 1s-electron is excited to the 2p state and very rapidly, ionized thermally to the conduction band where it can be detected as a photocurrent. PTIS is very sensitive (less than 10^{14} cm^{-3} has been cited) but it fails for concentrations much higher than 10^{16} cm^{-3} because overlap of the s-electron wavefunctions causes broadening of the 1s–2p transitions. Extra information can be obtained by application of a magnetic field, stress or other perturbations to the crystal and these are discussed in Asfar *et al.*, 1980.

2.6.1.2 Deep level defects

Deep levels are produced by many impurities and intrinsic point defects. Detection and measurement depends on whether the GaAs is SI or conducting.

2.6.1.2.1 SI GaAs

Deep levels can trap carriers produced by illumination with above-bandgap light, and then release them thermally when the light is removed. The released carriers, electrons or holes, can then produce a current in an external circuit. The temperatures at which different traps release their carriers can be used to determine their ionization energies. This is the basis of thermally stimulated currents (TSC) spectroscopy, a technique that is especially useful for assessing high-resistivity materials such as SI GaAs (see, Blood and Orton (1992) for discussions of this and other electrical assessment techniques). Two Ohmic contacts are placed on the sample. After optical filling of the traps at low temperature and at zero applied bias, the temperature is increased at a constant rate with the GaAs under bias and with a sensitive current meter in series with the voltage supply. The current in the external circuit shows a series of peaks corresponding to trap emptying, the deeper traps requiring higher temperatures before they can contribute. This technique is sensitive (10^{13} cm^{-3}) and can be semiquantitative. It cannot, however, show whether a deep level is an electron or a hole trap, because the emptying of either will produce the same external current. A typical TSC spectrum from a sample of SI GaAs is shown in Fig. 2.15.

A modification of TSC analyses the separate current transients that result from the emptying of different traps. This is photo-induced current transient spectroscopy (PICTS) and uses approaches similar to DLTS, described in the next section. Whilst TSC employs a single filling of the traps, PICTS uses a repetitive filling procedure by pulsing the light as the measurement proceeds. It is, therefore, more sensitive than TSC.

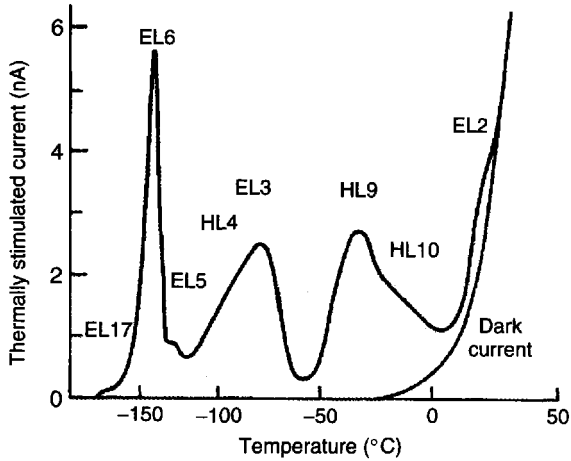


Figure 2.15 TSC spectra recorded on a 350- μm thick sample of SI GaAs. The traps have been filled by illumination with white light for 3 min at 80 K. The reverse bias is 25 V (Reprinted from Martin *et al.*, *J. Appl. Phys.* **51**, (1980) 2840, copyright (1980) with permission from the American Institute of Physics)

2.6.1.2.2 Conducting GaAs

Application of TSC to conducting semiconductors with ohmic contacts is impracticable because of the high, temperature-independent, background current that would flow. However, the filling and emptying of traps is still a useful approach. If a rectifying junction can be formed, applying a forward bias can fill traps; the subsequent application of a reverse bias produces a depletion layer in which the traps can empty thermally. The emptying of each trap produces a current pulse that is exponential with time so that each pulse is a sum of several exponentials with different time constants.

Although the current in an external circuit could be used to perform the subsequent measurement, it is easily shown that more information can be obtained from the change in depletion-layer capacitance because this can reveal whether electrons or holes are being de-trapped. If this capacitance change transient, also a sum of exponentials, is analyzed by applying the 'rate window' concept, (Lang, 1974) the data can be presented as a 'spectrum' of capacitance change in that window versus temperature. This is known as deep level transient spectroscopy (DLTS) and a typical spectrum from a sample of GaAs is shown in Fig. 2.16.

DLTS is quantitative, giving defect concentrations, ionization energies, capture cross sections and the identification of the type of trap (electron or hole). The labeling of the deep levels in Table 2.2 followed the early application of DLTS to GaAs.

DLTS equipment includes a sensitive and fast capacitance meter, usually furnished by Boonton, Inc., and a control box that applies the forward and reverse bias voltages as well as applying the rate-window analyzer to the output. The sample must be placed in a variable-temperature cryostat. As a rule, DLTS is controlled by a computer. Often the fabrication of a p-n junction is inconvenient and a Schottky contact is used. Because minority carriers cannot be introduced into a semiconductor by this means, DLTS will only be sensitive to majority carrier traps. If minority traps are to be investigated using the Schottky-barrier method, minority carriers must be introduced using a pulse of above band gap light instead

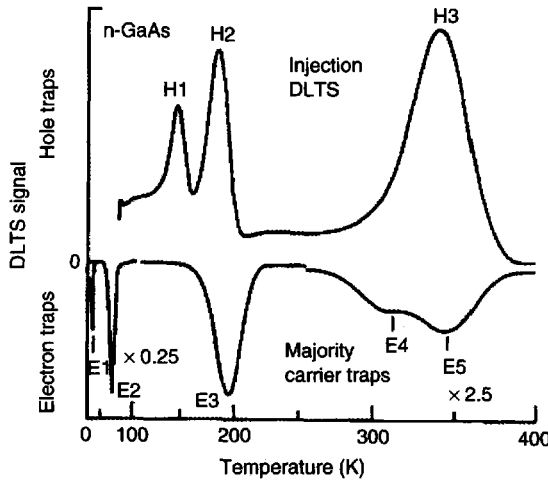


Figure 2.16 Minority and majority traps introduced by high-energy electron irradiation of a sample of n-type GaAs after the fabrication of a $p^+ - n$ diode. (Reprinted from Lang and Kimmerling, *IOP Conf. Ser. No. 23* (1975) 581, copyright (1975) with permission from IOP Publishing). For further details, see Blood and Orton, 1992, 525–596

of forward bias, optical DLTS (ODLTS). The uses of the many variations of DLTS have been discussed by Look (1989), Schroder (1998), Blood and Orton (1992).

The sensitivity of DLTS depends on the carrier concentration, which, for standard operation, must exceed the total deep level concentration by more than an order of magnitude. Within this restriction, the sensitivity is about two orders of magnitude less than the carrier concentration.

Although DLTS is widely used, it has a serious disadvantage; each trap produces a wide peak and several traps of similar emission properties are difficult to distinguish. So-called Laplace-transform DLTS has been developed to overcome this (Dobaczewski *et al.*, 1994). A rate window is no longer used but the transient is analyzed directly in terms of its exponential components by applying an inverse Laplace transform to it. However, this is demanding in terms of temperature control and the linearity of capacitance measurement. Older techniques such as photocapacitance spectroscopy are beyond the scope of this section but are reviewed in the books mentioned above.

2.7 IMPURITY AND DEFECT ANALYSIS OF GaAs (OPTICAL)

2.7.1 Optical analysis of defects in GaAs

For obvious reasons, analytical techniques that do not require electrical contacts to be made to the sample or are otherwise “nondestructive” are attractive to wafer manufacturers. Many of these are optical in nature. The use and limitations of LVM absorption has been addressed in Section 2.5 and that for measuring EL2 concentrations was described in Section 2.2.4. Other absorption techniques are of limited interest; we concentrate on light emission, or luminescence, methods.

2.7.1.1 Photoluminescence

Luminescence in semiconductors results from the radiative recombination of excess carriers. In melt-grown GaAs, luminescence takes place via the mediation of defects (Bebb and Williams, 1972, Dean, 1982). The energies of luminescence bands give information on the defect structures and the intensities are related (albeit in a rather indirect way) to concentrations. However, the total luminescence intensity is decreased by the effects of parallel, nonradiative recombination paths. If the excess carriers are produced optically, often by illumination of the sample with a laser beam, the technique is 'photoluminescence'. Excitation using a beam of high-energy electrons in a SEM results in 'cathodoluminescence', CL. Although the scanning ability of the SEM allows CL to map the luminescence of the material, CL is rarely applied to GaAs.

In either method, excess carriers are produced within the top few micrometres of the surface. However, this is not the only volume that is probed by the technique, as these carriers will diffuse about one diffusion length, L_D , before they recombine. L_D will be greater in material where the minority carrier lifetime is greater; in general, this will be associated with 'better', more luminescent material. It follows that there are restrictions on the spatial information that can be obtained, better resolution being obtained with material of lower L_D . Moreover, excess carriers that diffuse to the surface are lost to the measurement as they recombine there without emission of light. This process is quantified by a 'surface recombination velocity', which is strongly increased as the temperature is raised. PL and CL are usually performed at low sample temperature because this reduces thermal broadening of the emission lines and reduces the diffusion of excess carriers to the sample surface. The emitted light is passed through a high-resolution spectrometer before detection by either a suitable photomultiplier tube or semiconductor (usually Si or Ge) detector. A Ge detector must be cooled, although cooling of all detectors generally results in less noise.

2.7.1.2 Low-temperature luminescence from point defects

Low-temperature luminescence from shallow acceptors often dominates the spectra of SI GaAs, the energy of the lines being approximated by $E_G - E_A$ where E_A is the energy of the acceptor relative to the top of the valence band. Because E_A depends on the acceptor species, the presence of a particular acceptor can be determined. Similar luminescence from donors is less easy to differentiate as they have similar values of E_D (where E_D is the energy level relative to the bottom of the conduction band). Luminescence from intrinsic deep levels is weak because recombination is mostly nonradiative. However, that from EL2 centres can be resolved both at low and at room temperature (Martin *et al.*, 1980, Tajima and Iino, 1989). The situation regarding deep impurity levels, especially transition metals often resulting from contamination, is different with strong luminescence resulting from many. Of interest is the line due to Cu at 1.05 eV that is particularly strong and well resolved and allows this common contaminant to be detected. The PL spectra from GaAs depend very sensitively on the method of growth, subsequent treatments and the presence of impurities. Readers interested in this technique are directed towards the relevant chapters of "Properties of Gallium Arsenide, III edition", 1996.

2.7.1.3 Room-temperature luminescence measurements

The broadening effects of temperature and the increased influence of the surface greatly reduces the use of room-temperature luminescence as an analytical tool. However, if mapping of emission properties across a whole wafer is to be attempted, measurements at room temperature are often attractive because of its relative ease compared to low-temperature studies. It is then a truly nondestructive method giving spatial information of surface properties (that control the surface recombination velocity) and it is often used for assessing substrates and their uniformity (see Fig. 2.17). A review of these techniques has been given by Miner and Moore (1996).

2.7.1.3.1 Mapping of surface properties

The surface quality of GaAs substrates is critical to successful epi-growth. Manufacturers perform special cleaning and oxidation procedures to ensure reproducible surface properties, those being suitable for immediate epi-growth being supplied as 'epitaxial-ready'. A valuable check on these properties is scanning PL as changes to the surface result in changes to the surface recombination velocity. Of course, this assumes that the material is well annealed and that residual nonuniformities in point-defect concentrations do not otherwise affect the recombination kinetics, a situation that is never fully achieved. There is no need for a spectrometer in this measurement as the total PL efficiency is altered by the surface and, in any case, PL line widths are thermally broadened. Collection of all the luminescence means that a relatively large signal is detected giving a large increase in the measurement rate. Small-scale structures are often associated with residual volume nonuniformities (see, for example, Oda *et al.*, 1992) whilst large-scale effects are most often due to polishing and subsequent contamination of the surface (Skromme *et al.*, 1987). A room-temperature PL map of a commercial 3-inch diameter SI GaAs wafer is shown in Fig. 2.17.

Another nondestructive approach for the assessment of the crystalline quality of the near-surface region of a wafer is X-ray diffraction, normally double-crystal X-ray diffraction, DXD. X-rays are emitted from a tube and then 'conditioned' by diffraction from a first crystal of high structural quality GaAs. The radiation is then diffracted again by the sample, which can be tilted to move it in and out of the diffraction condition. This results in a 'rocking curve' that contains information about lattice strain. The diffracted X-rays are detected by either a scintillation counter or semiconductor detector.

For reviews of these techniques, see Tanner and Bowen, 1980 and Tanner, 1988.

Spatial mapping of the rocking curves from substrates to map changes in lattice constant and residual strain is possible, as the rocking curves are simple. An example of a rocking curve from a sample of VGF GaAs is shown in Fig. 2.18.

2.8 CONCLUSIONS

Undoped SI and n^+ -type GaAs represent the two forms of commercial melt-grown GaAs now supplied in bulk to industry.

In this chapter we have presented the commercially important methods of GaAs growth and the physical and chemical means by which they are contaminated by both intrinsic and extrinsic defects. We have introduced some important techniques for the assessment of these materials and have tried to give a feel for the advantages of each.

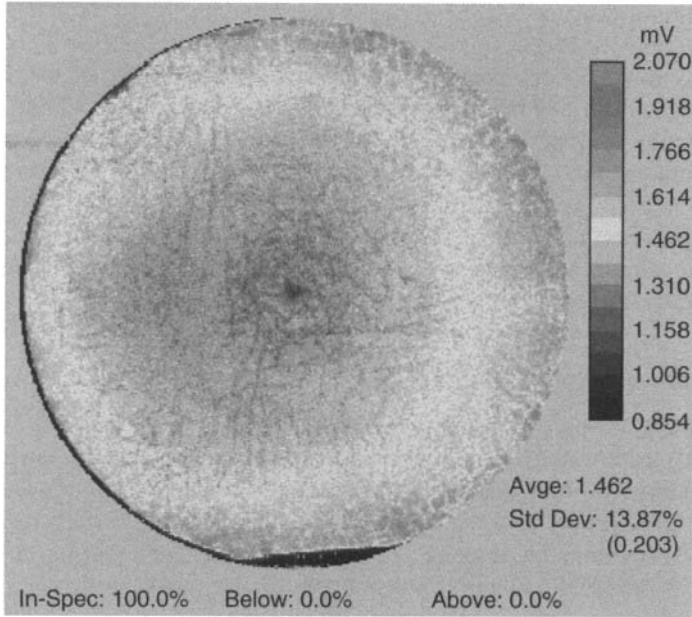


Figure 2.17 (Plate 1) A room-temperature PL map of an unannealed, undoped VGF showing evidence of dislocation cell structure (Courtesy of Wafer Technology plc, UK)

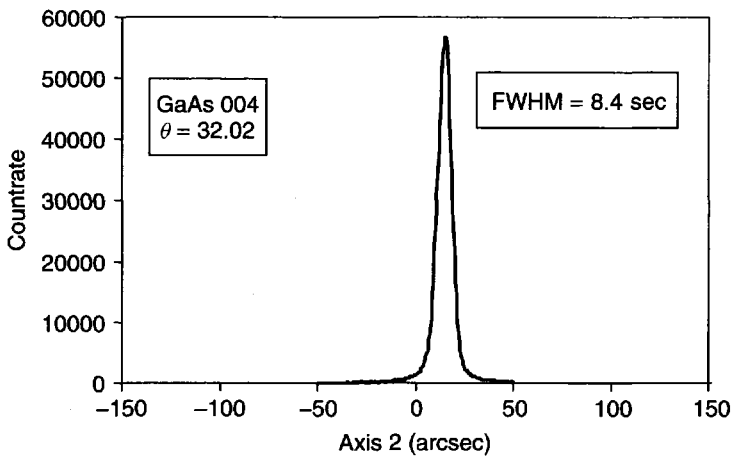


Figure 2.18 X-ray rocking curve from a VGF, Si-doped GaAs wafer. In addition to a narrow rocking curve, such material also exhibits a low EPD (Courtesy of Wafer Technology plc, UK)

ACKNOWLEDGMENTS

The authors are delighted to acknowledge the help given to them over many years by colleagues in academic institutions, government laboratories and in industry.

REFERENCES

- Abrahams M.S. and Buiocchi C.J. *J. Appl. Phys.* **36** (1965) 2855.
- Afsar M.N., Button K.J. and McCoy G.L. *Inst. Phys. Conf. Ser. No 56* (1980) 547–555.
- Alt H.Ch. *Appl. Phys. Lett.* **54** (1989) 1445.
- Bangert U. *Properties of Gallium Arsenide*, Third edition. Eds M.R. Brozel and G.E. Stillman. EMIS Datareview no 16. Publ. INSPEC, IEE London, United Kingdom, 1996, 418–428.
- Baranowski J.M. and Trautman P. *Properties of Gallium Arsenide*, Third edition. Eds M.R. Brozel and G.E. Stillman. EMIS Datareview no 16. Publ. INSPEC, IEE, London, United Kingdom, 1996, 341–357.
- Bebb H.B. and Williams E.W. 'Photoluminescence I: Theory' in *Semiconductors and Semimetals* (Eds. R.K. Willardson, A.C. Beer), 1972. Academic Press, New York; **8**, 181–320.
- Blood P. and Orton J.W. 'The Electrical Characterization of Semiconductors: Majority Carriers and Electron States'. *Techniques of Physics*, Editor N.H. March, 1992. Academic Press, London.
- Blunt R.T., Clarke S. and Stirland D.J. *IEEE Trans. Electron. Dev.* **ED29** (1982) 1039.
- Bourret E.D. and Merk E.C. *J. Cryst. Growth* **110** (1991) 395–404.
- Breivik L., Brozel M.R., Stirland D.J. and Tuzemen S., *Semicond. Sci. Technol.* **7** (1992) A269–A274.
- Brown G.T. and Warwick C.A. *J. Electrochem. Soc.* **133** (1986) 2576.
- Brozel M.R., Clegg J.B. and Newman R.C. *J. Phys. D (Appl. Phys.)* **11** (1978) 1331.
- Brozel M.R., Tuck B., Rumsby D. and Ware R.M. *J. Cryst. Growth* **60** (1982) 113–119.
- Brozel M.R., Foulkes E.J., Grant I.R. and Hurle D.T.J. *J. Cryst. Growth* **80** (1987) 323.
- Brozel M.R. and Skolnick M.S. *Proc. Conf. Semi-Insulating III-V Materials*, Hakone (1986) 109.
- Brozel M.R. and Tuzemen S. *Mater. Sci. Eng (B)*, **28** (1994) 130–133.
- Brozel M.R. *Properties of Gallium Arsenide*, Third edition. Eds M.R. Brozel and G.E. Stillman. EMIS Datareview no 16. Publ. INSPEC, IEE, London, United Kingdom, 1996, 399–408.
- Chadi D.J. and Chang K.J. *Phys. Rev. Lett.* **60** (1988) 2187.
- Chen T.P., Huang T.S., Chen L.J. and Gou Y.D. *J. Cryst. Growth* **106** (1990) 367.
- Cronin G.R. and Haisty. *J. Electrochem. Soc.* **111** (1964) 874–877.
- Cullis A.G., Augustus P.G. and Stirland D.J. *J. Appl. Phys.* **51** (1980) 2256.
- Dabrowski J. and Scheffler M. *Phys. Rev. Lett.* **60** (1988) 2183.
- Dean P.J. *Prog. Cryst. Growth Charact.* **5** (1982) 89–174.
- Dobaczewski L., Kaczor P., Hawkins I.D. and Peaker A.R. *J. Appl. Phys.* **76** (1994) 194.
- Doering P.J. *et al. Proc. 6th Conf. on Semi-Insulating III-V Materials*, Toronto, Canada, 1990 Eds A.G. Milnes, C.I. Miner (IOP Publishing, 1990) 173–181.
- Edmond J.T. *Proc. Phys. Soc. London*, **73** (1959) 622.
- Elliott K.R. *Appl. Phys. Lett.* **42** no 3 (1983) 274–276.
- Elliott K.R., Holmes D.E., Chen R.T. and Kirkpatrick C.G. *Appl. Phys. Lett.* **40** (1982) 898.
- Gimel'farb F.A., Girich B.G., Mil'vidskii M.G., Plevin O.V. and Fistul' V.I. *Sov. Phys.-Solid State*, **11** (1970) 1612.
- Grant I., Rumsby D., Ware R.M., Brozel M.R. and Tuck B. *Proc. Conf on Semi-Insulating III-V Materials*, Evian, France, 1982 (Shiva Publishing, Nantwich, Cheshire, England, 1982: p. 98–106).
- Gremmelmaier R. *Z. Nat. Forsch. A*. **11** (1956) 511.
- Grinshtein P.M., Lipkes M.Ya, Rytova N.S. and Fistul' V.I. *Sov. Phys.-Semicond.* **9** (1975) 725.
- Hobgood H.M., Ta L.B., Rohatgi A., Eldridge G.W. and Thomas R.N. *Proc. Conf on Semi-insulating III-V Materials*, Evian, France, 1982 (Shiva Publishing, Nantwich, Cheshire, England, 1982: p. 30).
- Holmes D.E., Chen R.T., Elliott K.R. and Kirkpatrick C.G. *Appl. Phys. Lett.* **40** (1982a) 46–48.
- Holmes D.E., Chen R.T., Elliott K.R. and Kirkpatrick C.G. *IEEE Trans. Electron. Devices*, **29** (1982b) 1045.

- Holmes D.E., Elliott K.R., Chen R.T. and Kirkpatrick C.G. *Proc. Conf on Semi-insulating III-V Materials*, Evian, France, 1982 (Shiva Publishing, Nantwich, Cheshire, England, 1982c: p. 19–27).
- Hurle D.T.J. A comprehensive thermodynamic analysis of native point defect and dopant solubilities in gallium arsenide. *J. Appl. Phys.* **85** (1999) 6957–7022.
- Inada T., Sato T., Ishida K., Fukuda T. and Takahashi S. *J. Electron. Mater.* **15** (1986) 169.
- Jacob G. *Proc. Conf. On Semi-Insulating III-V Materials*, Evian, France, 1982 (Shiva Publishing, Nantwich, England). 1982: 2.
- Jordan A.S., Caruso R. and von Neida A.R. *Bell Syst. Tech. J.* **59** (1980) 593.
- Kobayashi T. and Osaka, J. *J. Cryst. Growth* **71** (1985) 240.
- Koster W. and Thoma B. *Z. Met. Kd.* **46** (1955) 291.
- Kurusu K., Suzuki Y. and Takami H., *J. Electrochem. Soc.* **136** (1989) 1450–1452.
- Laithwaite K., Newman R.C., Angress J.F. and Gledhill G.A. *Inst. Phys. Conf. Ser. No 33a* (1977) 133.
- Lambert U., Nagel G., Rufer H. and Tomzig E. *Proc. 6th Conf. on Semi-Insulating III-V Materials*, Toronto, Canada, 1990 Eds A.G. Milnes, C.I. Miner (IOP Publishing, 1990) 183–188.
- Lang A.R., 'Recent Applications of X-Ray Topography' in *Modern Diffraction and Imaging Technique in Materials Science*, Eds S. Amelinckx, G. Gevers and J. Van Landuyt, North Holland, Amsterdam, 1978, 407–479.
- Lang D.V. *J. Appl. Phys.* **45** (1974) 3023.
- Lang D.V. and Kimmerling L.C. *IOP Conf. Ser. No 23* (1975) 581.
- Le Berre C. *et al. Appl. Phys. Lett.* **66** (1995) 2534.
- Look D.C. 'Electrical Characterization of GaAs Materials and Devices', *Design and Measurement in Electronic Engineering Series*, 1989. John Wiley and Sons, Chichester, UK.
- Martin G.M. *Appl. Phys. Lett.* **39** (1981) 747.
- Martin G.M., Farges J.P., Jacob G., Hallais J.P. and Poiblaud G. *J. Appl. Phys.* **51** (1980) 2840–2852.
- Martin G.M., Verheijke M.L., Jansen J.A.J. and Poiblaud J. *J. Appl. Phys.* **50** (1979) 467.
- Martin G.M., Jacob C. and Poiblaud J. *Acta. Electron.* **23** (1980) 37.
- Martinez G., Hennel A.M., Szuszkiewicz W., Balkanski M. and Clerjaud B. *Phys. Rev. B* **23** (1981) 3920.
- Metz E.P.A., Miller R.C. and Mazelsky R. *J Appl. Phys.* **33** (1962) 2016.
- Miner C.J. and Moore C.J.L. *Properties of Gallium Arsenide*, Third edition. Eds M.R. Brozel and G.E. Stillman. EMIS Datareview no 16. Publ. INSPEC, IEE, London, United Kingdom, 1996, 320–332.
- Monberg E.M., Brown H. and Borner C.E. *J. Cryst. Growth* **94** (1989) 643–650.
- Moravec F., Stepanek B. and Doubrava P. *Cryst. Res. Technol.* **26** (1991) 579–585.
- Mullin J.B., Heritage R.J., Holliday C.H. and Straughan B.W. *J Cryst. Growth* **3–4** (1968) 281–285.
- Mullin J.B., Royle A. and Benn S. *J. Cryst. Growth* **50** (1980) 625.
- Murray R., *Properties of Gallium Arsenide*, Third edition. Eds M.R. Brozel and G.E. Stillman. EMIS Datareview no 16. Publ. INSPEC, IEE, London, United Kingdom, 1996, 227–234.
- Newman R.C. *Semicond. Sci. Technol.* **9** (1994) 1749.
- Oda O., Yamamoto H., Seiwa M., Kano G., Inoue T., Mori M., Shimakura H. and Oyake M. *Semicond. Sci. Technol.* **7** (1992) A215.
- Oda O. *Properties of Gallium Arsenide*, Third edition. Eds M.R. Brozel and G.E. Stillman. EMIS Datareview no 16. Publ. INSPEC, IEE, London, United Kingdom, 1996, 591–595.
- Oliver J.R., Fairman R.D. and Chen R.T. *Electron. Lett.* **17** (1981) 839–841.
- Pekarek L. and Czech. *J. Phys. B* **20** (1970) 857.
- Pelevin O.V., Shershakova I.N., Gimel'farb F.A., Mil'vidskii M.G. and Ukhorskaya T.A. *Sov. Phys.-Crystallogr.* **16** (1971) 528.
- Rudolph P. and Jurisch M., *J. Cryst. Growth* **198/199** (1999) 325–335.

- Rumsby D., Grant I., Brozel M.R., Foulkes E.J. and Ware R.M. *Proc. Conf. On Semi-Insulating III-V Materials*, Kah-Nee-Ta, OR, USA (Shiva Publishing, Nantwich, England, 1984) 165–170.
- Schroder D.K. *Semiconductor Material and Device Characterization*, 2nd edition. A Wiley Inter-Science Publication, John Wiley, New York, 1998.
- Seki Y., Watanabe H. and Matsui J. *J. Appl. Phys.* **49** (1978) 822.
- Shropshall M.R. and Skinner P.E. *Proc. Conf. on Semi-Insulating III-V Materials*, Kah-Nee-Ta, OR, USA, 24–26 April 1984 (Shiva Publishing, Nantwich, England, 1984) p. 178.
- Skalski S., *Compound Semiconductors* vol. 1, Ch. 43, pp 385–389, eds R.K. Willardson, H.L. Goering, Reinhold Publishing, NY, 1962.
- Skolnick M.S., Brozel M.R., Reed L.J., Grant I., Stirland D.J. and Ware R.M. *J. Electron. Mater.* **13** (1984a) 107–125.
- Skolnick M.S., Reed L.J. and Pitt A.D. *Appl. Phys. Lett.* **44** (1984a) 447–449.
- Skowronski M., Lagowski J. and Gatos H.C. *J. Appl. Phys.* **59** (1986) 2451.
- Skromme B.J., Sandroff C.J., Yablonovitch E. and Gmitter T. *Appl. Phys. Lett.* **51** (1987) 24.
- Stibal R., Windscheif J. and Jantz W. *Semicond. Sci. Technol.* **6** (1991) 995–1001.
- Stillman G.E., Wolfe C.M. and Dimmock J.O. *Semicond. Semimet.* Vol. **21**, 1977 (Academic Press, New York) 169.
- Sze S.M. *Semiconductor Devices*, Physics and Technology, John Wiley, 1985.
- Tada K., Kawasaki A., Kotoni T., Nakai R., Takabe T., Akai S. and Yamaguchi T. *Proc. Conf on Semi-insulating III-V Materials*, Evian, France, 1982 (Shiva Publishing, Nantwich, Cheshire, England, 1982: p. 36–44).
- Tajima M. and Iino T. *Jpn. J. Appl. Phys.* **28** (1989) L841–844.
- Tanner B.K. and Bowen D.K. *Characterization of Crystal Growth Defects by X-Ray Methods*, Plenum, New York, 1980.
- Tanner B.K. *X-Ray Topography and Precision Diffractometry of Semiconductor Materials* (Eds T.J. Shaffner, D.K. Schroder), 1988, Electrochem. Soc., Pennington NJ, 133–149.
- Terashima K. *et al.*, *Jpn. J. Appl. Phys.* **2** **79** (1984) 463–468.
- Wagner R.J., Krebs J.J., Strauss G.H. and White A.M. *Solid State Commun.* **36** (1980) 15.
- Weisberg L.R., Rosi F.D. and Herkart P.G., *Properties of Elemental and Compound Semiconductors*, vol 5 Ed H.C. Gatos (Interscience, New York) 1960, 25–67.
- Whelan *et al.*, see Skalski S.
- Wickert M., Stibal R., Hiesinger P., Jantz W. and Wagner J. *Proc. SIMC-X* (1998) Eds Z. Liliental-Weber and C. Miner, IEEE Publishing, 1999, 21–24.
- Willardson R.K. and Alfred W.P. *Inst. Phys. Conf. Ser* **3** (1966) 35.
- Woodall J.M. *Electrochem. Technol.* **no 2** (1964) 167–169.
- Yu P.W., Holmes D.E. and Chen R.T. *Proc. Conf. GaAs and Related Compounds*, Oiso, Japan. IOP Publishing 1981.

This page intentionally left blank

3 Computer Modelling of Bulk Crystal Growth

ANDREW YECKEL AND JEFFREY J. DERBY

Department of Chemical Engineering and Materials Science, and Minnesota Supercomputing Institute, University of Minnesota, 421 Washington Ave SE, Minneapolis, MN 55455-0132, USA

3.1	Introduction	74
3.2	Present state of bulk crystal growth modelling	75
3.3	Bulk crystal growth processes	77
3.4	Transport modelling in bulk crystal growth	79
3.4.1	Governing equations	79
3.4.2	Boundary conditions	83
3.4.3	Continuum interface representation	84
3.4.4	Radiation heat-transfer modelling	86
3.4.5	Noninertial reference frames	88
3.4.6	Magnetic fields	88
3.4.7	Turbulence	89
3.5	Computer-aided analysis	89
3.5.1	Discretization	89
3.5.2	Numerical interface representation	90
3.5.3	Deforming grids and ALE methods	92
3.5.4	A simple fixed-grid method	94
3.5.5	Quasi-steady-state models	96
3.6	Modelling examples	98
3.6.1	Float-zone refinement of silicon sheets	98
3.6.2	Bridgman growth of CZT: axisymmetric analysis	102
3.6.3	Bridgman growth of CZT: three-dimensional analysis	104
3.6.4	Morphological stability in solution growth of KTP	106
3.7	Summary and outlook	112
	Acknowledgments	113
	References	113

3.1 INTRODUCTION

Bulk crystal growth encompasses a wide variety of physical phenomena that occur over a vast range of length scales, making it among the most difficult of industrial processes to model. On a macroscopic scale, ranging from millimeters to meters, transport of heat, mass, and momentum is always important. At a mesoscopic scale, ranging from tens of nanometers to tens of micrometers, the crystal melt or crystal solution interface can exhibit hillocks, steps, or other structures even though it may appear macroscopically smooth. Mesoscale structure also occurs within the crystal in the form of grain boundaries or extended defects, and even within the melt, where structured complexes of molecular species sometimes appear. At a microscopic scale of nanometers or less, the fundamental mechanisms by which atoms or molecules are incorporated into the growing crystal ultimately determine its final structure.

Bulk crystal growth also encompasses a vast range of time scales. The longest of these is the time of growth, which can range from hours to months, depending on the type of crystal and the system used to grow it. Heat, mass, and momentum transport each have a characteristic time scale, depending on the dominant mechanism of transport and the physical properties of the system. If diffusion dominates transport, these time scales typically range from minutes to hours. Within the solution or melt, however, convective transport usually dominates, and the transport time scale is typically reduced to seconds or less. Phenomena occurring at mesoscopic length scales, such as morphological instabilities, typically evolve over time scales that are comparable to transport time scales. Atomistic events important in bulk growth range from the rate of incorporation of atoms into a solidification of an interface, occurring over time scales on the order of milliseconds or less, to much longer times associated with concerted action, such as nucleation events.

A model that includes all these physical phenomena, spanning at least nine orders of magnitude of length and time scales, is far beyond the capability of today's computers. Moreover, even if the computing capability were available, the existing state of theory remains inadequate to build a comprehensive model of bulk crystal growth. This observation motivates the essential need to formulate a model that includes enough physics to make realistic, usable predictions, yet that is simple enough to remain tractable with today's tools. Model realism and tractability are easy enough to define and evaluate, but the notion of model *usability* depends greatly on purpose.

In the case of bulk crystal growth, the greatest purpose that modelling can serve is to directly connect processing conditions to final outcome. Since bulk crystals usually are incorporated into electronic, optical, or optoelectronic devices, final outcome is most often measured in terms of the crystal properties relevant to these devices. These crystal properties are in turn determined by the chemical composition and structure of the crystal, particularly the types and distributions of various crystalline defects. A significant body of theoretical and empirical knowledge exists that connects material properties to the distribution of crystalline defects and chemical composition, but this aspect of the problem lies outside the scope of crystal *growth* modelling, and therefore outside the scope of this chapter. Thus, for the crystal-growth modeller, the ultimate task is to connect processing conditions to the morphology, chemical composition, and defect structure of the crystal.

Macroscopic transport phenomena always have an important effect on the microscopic structure of bulk crystals. Indeed, the most difficult problem remaining in crystal-growth modelling is to forge a direct connection between the macroscopic and microscopic realms.

Usually those who focus on one realm borrow information gleaned from the other realm to provide guidance in constructing a useful model, but adequate tools simply do not exist to create a model that completely integrates the two realms. By far the greatest progress has been made in transport modelling, although advances are being made piecemeal across the spectrum of microscopic phenomena. A few recent studies have partially integrated macroscopic modelling with microscopic phenomena to tackle problems of predicting growth morphology in melt growth [1–4] and solution growth [5, 6], and in predicting point-defect generation and transport [7, 8] in silicon growth. In most cases, however, modellers have focused on macroscopic transport, relying on criteria derived from simple theories or experimentally derived heuristics to infer outcomes with regard to crystal structure.

Although it is possible to restrict the scope of modelling to the macroscopic realm and still obtain valuable information, this approach generally requires that we somehow distill the physics of phase transformation to a continuum representation, which typically takes the form of boundary conditions to be applied at the growth interface. This approach works well for many systems, particularly melt-growth systems in which growth is not kinetically limited. In such systems a continuum model makes it possible (at least in principle) to accurately determine temperature distribution, flow structure, interface shape, and chemical composition of the crystal. The situation is more complicated in solution-growth systems, which are always operated far from equilibrium. Nevertheless, with some knowledge of crystal-growth habit it is possible to model many important aspects of solution-growth systems using a continuum representation of the interface.

Even restricting a crystal-growth model to a continuum representation of phenomena occurring at macroscopic length scales may not be enough to guarantee model tractability, however. The hydrodynamics problem alone can be daunting. Flow usually exhibits steep boundary layers, is often time dependent and three-dimensional, and in some cases is turbulent. Hydrodynamics is often coupled to the heat-transfer problem, further complicating matters. Modelling of radiation poses a particular difficulty in melt-growth systems, owing to the complicated geometries typical of crystal-growth furnaces, and the inherent complexity of radiation heat transfer. Heat transfer is usually less important in solution-growth systems, but here the appearance of very thin concentration boundary layers at the crystal solution interface can make the mass-transfer problem nearly intractable. To these difficulties we add the complication of a geometry that continuously changes with time, due to the phase transformation of material that defines growth. This moving boundary aspect of the problem dominates crystal-growth modelling in many respects, and thus will be an important focus of this chapter.

3.2 PRESENT STATE OF BULK CRYSTAL GROWTH MODELLING

Prior to the 1980s nearly all crystal-growth modelling consisted of analytical and semianalytical models. These early models provided great insight, but, nevertheless, were highly limited in scope and utility, and no attempt at a review is made here. The 1980s witnessed a flowering of computer-aided analysis of bulk crystal growth, aided by rapid advances in computing hardware. Much of this work is summarized in a review article by Brown [9]. A rapid expansion of commercial software for computational fluid dynamics and

transport phenomena also occurred during this time, allowing nonspecialists to try a hand at modelling. By the end of the 1980s, continuum transport modelling had reached a state where it was routine to solve stationary problems in two space dimensions that included coupled fluid dynamics, heat and mass transport in moderately complicated geometries, for multiphase problems in which the location of the crystal/melt interface position was determined in a self-consistent manner. Developments proceeded apace and within a few years it became feasible to integrate a time-dependent transport model for growth of an entire crystal. Around this time the first significant calculations of three-dimensional transport phenomena also began to appear.

The mid-1990s was a period of great optimism that *accurate* three-dimensional calculations, including time-dependent phenomena, would soon also become routine. This has not been the case, however, and in the past few years there appears to have been a slowing of developments in this area. We attribute this slowdown to three factors, none of which had been anticipated: greater difficulty and overhead in solving three-dimensional problems than expected, disappointing developments in computing hardware, and a surprising lack of progress in algorithm development for solving large sets of algebraic equations. At every stage, ranging from grid generation to visualization, modelling of three-dimensional phenomena has proven exponentially more difficult than for two-dimensional phenomena. This difficulty is also tied in part to slow improvement in usability of the basic tools for development of parallel-computing applications. Several paradigms for parallel-computing development have come and gone, as well as several specialized machine architectures, making it difficult for all but the most determined of developers to keep up with changes. Although the Message Passing Library (MPI) interface has matured into something resembling a portable standard for parallel-code development, a large burden remains on the user to carefully and laboriously design algorithms that are suitable for parallel platforms. Common numerical methods used in computational transport phenomena do not parallelize easily, and the ideal of a compiler that can automatically and effectively parallelize a typical serial code simply has not emerged. Aside from these issues of usability of parallel-computing platforms, even the advance of sheer computing power has been slower than anticipated. Parallel-computing machines have proven an order of magnitude more expensive to build and maintain than was believed a decade ago. This reality, coupled with significant economic problems experienced by supercomputer makers in the post-Cold War era, has resulted in limited availability of clock cycles for many users of these machines, further hampering progress.

Although the issues just described have slowed progress, none has been as troublesome as the lack of a much-needed breakthrough in practical methods of solving very large sets of algebraic equations of the kind encountered in computational transport. Historically, direct methods based on variants of Gaussian elimination have proven practical, robust, and efficient for two-dimensional calculations on serial machines, to the point where the vast majority of two-dimensional problems can be solved with ease using cheap personal computers. Direct methods do not scale well to the sizes required for three-dimensional problems [10], however, making it necessary to use iterative methods [11]. Iterative solvers have two major advantages over direct solvers for solving three-dimensional problems: they are much easier to parallelize, and generally require far less memory to run [12]. Unlike direct methods, however, iterative methods have failed the requirement of robustness: for transport modelling in crystal growth in particular,

significant nonlinearity due to convective transport greatly slows, and sometimes completely halts, convergence to a solution. The key issue is preconditioning of the matrix that describes the set of equations [11]. To date, the robustness of preconditioners has been correlated to complexity, to the point where the most robust preconditioners often resemble direct solvers [13].

We do not wish to sound overly negative about prospects for the day when it is routine to solve three-dimensional problems in bulk crystal growth. We believe that the slowing of development in parallel-computing platforms is of only minor consequence compared to the critical role of solution algorithms. The emergence of MPI seems to have stabilized developments in parallel-code development, and although it appears that a breakthrough all-purpose preconditioner remains over the horizon (and perhaps never to be found), there has been steady and substantial progress in this area in recent years [13]. The state of commercial tools for visualization of solutions is excellent in our view, and we see no fundamental difficulties blocking further development of usable tools for grid generation. We believe that maturation of robust and efficient preconditioning techniques will be the limiting factor, but expect these developments to continue at a rate such that three-dimensional calculations are routine and accurate within the next decade.

3.3 BULK CRYSTAL GROWTH PROCESSES

A great variety of processes are used to grow bulk crystals from melt or solution. Brown [9] has observed that melt-growth methods can generally be classified as one of two types: confined or meniscus-defined growth. Common examples of confined growth methods are vertical and horizontal Bridgman (VB and HB) and vertical gradient freeze (VGF). Common examples of meniscus-defined growth methods are Czochralski and float-zone. Solution-growth methods usually consist of a seed crystal fully immersed in a vessel of solution, the temperature of which is gradually lowered to maintain supersaturation as solute is depleted (an interesting exception to this approach is the travelling heater method (THM) [14], which in some respects resembles confined melt-growth methods). Solution-growth methods are generally simpler to implement than melt-growth methods, but in some respects are more difficult to model for reasons discussed below. It is also possible to grow bulk crystals from the vapor but not commonly done due to low growth rates. Modelling of vapor growth of bulk crystals is reviewed in [15]; we neglect the subject here.

To limit the scope of this work we focus on the three systems shown in Fig. 3.1: (a) vertical Bridgman, (b) Czochralski, and (c) solution growth with agitation.¹ Each of these systems is discussed below with respect to proper formulation of the equations that govern continuum transport phenomena, with particular attention paid to formulation of the moving-boundary problem. Sample calculations drawn from our research will be used to demonstrate state-of-the-art capabilities for modelling transport phenomena in these systems. Brief consideration will also be given to the direct modelling of crystal morphology, for example facet formation in kinetically limited melt growth and step-train dynamics during solution crystal growth, to illustrate recent progress in this area.

¹ The melt-growth systems depicted here are generic, whereas the solution-growth system is a specific technique developed by Bordui and Motakef to grow KTP [16].

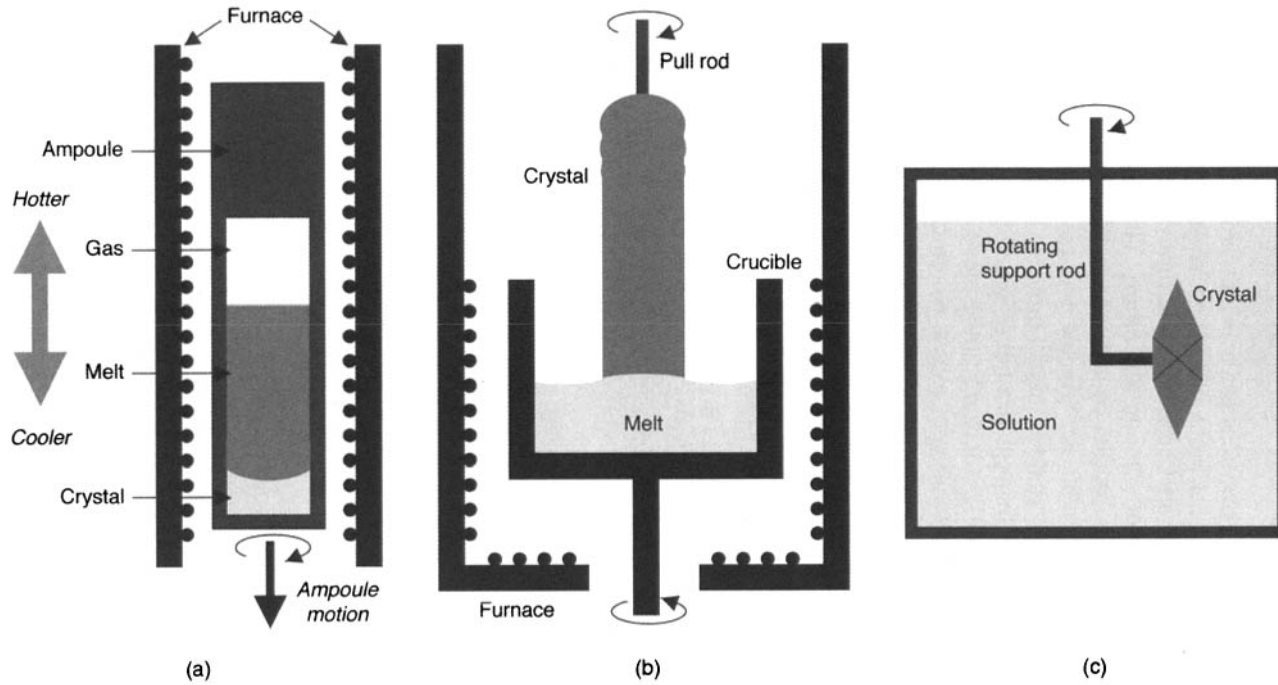


Figure 3.1 Schematic of typical bulk crystal growth systems: (a) vertical Bridgman; (b) Czochralski; (c) solution growth

3.4 TRANSPORT MODELLING IN BULK CRYSTAL GROWTH

Computer modelling of fluid dynamics, heat and mass transport has often been described as an art² as well as a science, to acknowledge the seemingly endless difficulties that arise in the application of numerical methods to this subject. Although numerous choices of highly developed commercial software exist for modelling of transport phenomena, on account of these difficulties none of them can be used blindly with much success, a situation that is likely to persist well into the future. Overcoming these difficulties requires a minimum of two core competencies. One is a thorough grasp of the fundamentals of continuum transport phenomena. The other is a general understanding of the numerical methods that are used to discretize and solve the governing equations of transport phenomena. For the truly serious modeller the need to engage in code development requires additional competencies, including knowledge of modern computer languages and parallel-computing architectures, as well as a solid grounding in at least one numerical method for discretization of partial differential equations.

Continuum transport modelling at macroscopic length scales is the most highly developed aspect of crystal-growth modelling and much has already been written on the subject. The seminal treatise on the general subject of transport phenomena is the textbook of Bird *et al.* [18], which fulfills an essential role as reference material for the equations governing continuum transport phenomena. At least one book devoted to modelling of transport phenomena specific to crystal growth has been published [19], featuring chapters by different authors writing on various topics. A number of chapters on the subject can be found within other works, including a general introduction to the subject by Derby [20], an extensive review of convection in melt growth by Müller and Ostrogorsky [21], and some more recent accounts of specific topics in crystal-growth modelling [22–24]. Although fifteen years old now, the review article by Brown [9] remains remarkably current in many respects and is essential reading for anyone contemplating modelling. The forthcoming review article by Lan [25] will provide a much needed update on recent progress in crystal-growth modelling. Of particular note are the proceedings of the occasional Workshop on Modelling in Crystal Growth [26–28]. These workshops have been immensely successful at bringing together leading crystal-growth modellers from around the world, and their proceedings provide an indispensable resource for tracking the state of developments in modelling of bulk crystal growth.

3.4.1 Governing equations

Since so much has already been written on transport modelling in crystal growth we merely summarize the governing equations commonly used for this purpose. Towards this end Table 3.1 defines the nomenclature used throughout Section 3.4, Table 3.2 shows governing equations of mass, momentum, and energy transport, and Table 3.3 lists some typical boundary conditions. These equations are based on a number of unstated assumptions and by no means are they universally applicable to bulk crystal growth, but in the majority of circumstances they provide an accurate and rigorous account of transport. The

² Maroudas [17] has recently suggested that modellers be referred to as artisans, rather than artists, with the connotation of highly skilled craftsmanship rather than pure creativity.

Table 3.1 Nomenclature for Section 3.4

Symbol	Description	Units
a	absolute acceleration of reference frame	length/time ²
B	magnetic field	mass/(charge × time)
<i>c</i>	species concentration	mass/length ³
<i>c_{eq}</i>	equilibrium solubility	mass/length ³
<i>c_o</i>	species concentration reference value	mass/length ³
<i>C_p</i>	heat capacity	energy/(mass × degree)
<i>D</i>	diffusion coefficient	length ² /time
<i>D_s</i>	diffusion coefficient in crystal	length ² /time
<i>D_l</i>	diffusion coefficient in melt	length ² /time
F	body force per unit volume	mass/(length ² × time ²)
<i>g</i>	gravitational acceleration	length/time ²
g	gravitational acceleration vector	length/time ²
<i>h</i>	heat-transfer coefficient	energy/(length ² × time × degree)
<i>H</i>	mean curvature	length ⁻¹
<i>H_f</i>	enthalpy of fusion	energy/mass
I	identity tensor	—
<i>k</i>	thermal conductivity	energy/(length × time × degree)
<i>k_l</i>	thermal conductivity of melt	energy/(length × time × degree)
<i>k_s</i>	thermal conductivity of crystal	energy/(length × time × degree)
<i>k_a</i>	thermal conductivity of ampoule/crucible	energy/(length × time × degree)
<i>k_B</i>	Boltzmann constant	energy/degree
<i>K</i>	partition coefficient	—
<i>L</i>	characteristic length	length
n	outward normal unit vector	—
<i>p</i>	pressure	mass/(length × time ²)
<i>p_a</i>	ambient pressure	mass/(length × time ²)
q_r	radiant heat flux at surface	energy/(length ² × time)
r	position vector	length
t	unit tangent vector	—
<i>t</i>	time	time
T	stress tensor	mass/(length × time ²)
<i>T</i>	temperature	degree
<i>T_f</i>	temperature profile of furnace	degree
<i>T_i</i>	growth-interface temperature	degree
<i>T_m</i>	equilibrium melting temperature	degree
<i>T_o</i>	reference temperature	degree
<i>v</i>	velocity	length/time
V_b	velocity of boundary	length/time
V_{sl}	velocity of melt crystal interface	length/time
<i>β</i>	thermal compressibility of melt	degree ⁻¹
<i>β_s</i>	solution expansivity of melt	length ³ /mass
<i>β_{kin}</i>	kinetic coefficient	length/time or length/(time × degree)
<i>γ</i>	capillary coefficient	force/length
<i>γ_o</i>	surface tension at reference temperature	force/length
<i>dy/dT</i>	thermal variation of surface tension	force/(length × degree)
<i>dy/dc</i>	compositional variation of surface tension	force × length ² /mass
<i>ε</i>	emissivity of ampoule/crucible	—

Table 3.1 (continued)

Symbol	Description	Units
μ	dynamic viscosity	mass/(length \times time)
μ_g	chemical potential	energy
ξ	thermal boundary condition parameter	—
ρ_l	liquid density	mass/length ³
ρ_o	melt density at reference temperature	mass/length ³
ρ_s	crystal density	mass/length ³
σ	Stefan–Boltzmann constant	energy/(length ² \times time \times degree ⁴)
σ_c	supersaturation	—
Φ	phase-field	—
Φ	electric potential	force/charge
ω	rotation rate	rad/time
$\dot{\omega}$	rotation-rate time derivative	rad/time ²

Table 3.2 Conservation equations for bulk crystal growth from liquids

Type	Form	Conservation equation
Mass	Constant density	$\nabla \cdot \mathbf{v} = 0$ (3.1)
Momentum	Incompressible Navier–Stokes	$\rho_o(\partial \mathbf{v} / \partial t + \mathbf{v} \cdot \nabla \mathbf{v}) - \nabla \cdot \mathbb{T} = \rho_o \mathbf{g} [1 - \beta(T - T_o) + \beta_s(c - c_o)]^\dagger + \mathbf{F}(\mathbf{v}, \mathbf{x}, t)^\ddagger$ where $\mathbb{T} \equiv -p\mathbf{I} + \mu(\nabla \mathbf{v} + (\nabla \mathbf{v})^T)$ (3.2)
Energy	Convective-diffusion	$\rho_o C_p (\partial T / \partial t + \mathbf{v} \cdot \nabla T) = \nabla \cdot (\mathbf{k} \nabla T)$ (3.3)
Species	Convective-diffusion	$\partial c / \partial t + \mathbf{v} \cdot \nabla c = \nabla \cdot (D \nabla c)$ (3.4)

[†]Boussinesq approximation for slightly compressible liquids.

[‡]General body-force term.

principle assumptions behind these equations are that the fluid is only slightly compressible, its flow is Newtonian, and energy and species transport is dominated by forced- or natural-convection effects, rather than diffusion-induced flow. These assumptions are usually valid for bulk crystal growth from the melt. The situation is not so clear in solution crystal growth, where conditions are often nearly isothermal and forced convection is not always used. In this case diffusion-induced convection can be important, particularly at the growth interface. Also, Fick's first law of diffusion, used to derive Equation (3.4), might not be accurate in ionic solutions due to charged transport effects. Caution is warranted under these conditions, therefore.

The equations in Table 3.2 are written for a single phase. Crystal-growth systems always have at least two phases (crystal, and melt or solution), but often more, in which case the equations are applied to each phase using physical parameters appropriate to the material of that phase. Thus it is to be understood that the physical properties and field variables have an implicit index denoting the material of each phase. Also, if there are more than two chemical species of interest, Equation (3.4) has an implicit index denoting

Table 3.3 Common boundary conditions

Equation	Type	Boundary condition	
Momentum	No-slip	$\mathbf{v} - (\mathbf{n} \cdot \mathbf{v})\mathbf{n} = \mathbf{V}_b - (\mathbf{n} \cdot \mathbf{V}_b)\mathbf{n}$	(3.5)
Momentum	No-penetration	$\mathbf{n} \cdot \mathbf{v} = \mathbf{n} \cdot \mathbf{V}_b$	(3.6)
Momentum	Penetration [†]	$\mathbf{n} \cdot \mathbf{v} = \mathbf{n} \cdot [\mathbf{V}_b + \mathbf{V}_{sl}(1 - \rho_s/\rho_l)]$	(3.7)
Momentum	Capillary	$\mathbf{n} \cdot \boldsymbol{\tau} _l = \mathbf{n} \cdot \boldsymbol{\tau} _g +$ $[\gamma_o + (d\gamma/dT)(T - T_o) + (d\gamma/dc)(c - c_o)]2\mathcal{H}\mathbf{n} +$ $(\mathbf{n}\mathbf{n}) \cdot \{(d\gamma/dT)\nabla T + (d\gamma/dc)\nabla c\}$	(3.8)
Energy	Latent heat [†]	$\mathbf{n} \cdot (-k_l \nabla T _l + k_s \nabla T _s) = \rho_s H_f \mathbf{n} \cdot \mathbf{V}_{sl}$	(3.9)
Energy	Furnace [‡]	$\mathbf{n} \cdot (-k_a \nabla T _a) = h(T - T_f(\mathbf{x}, t)) + \sigma \varepsilon (T^4 - T_f^4(\mathbf{x}, t))$	(3.10)
Species	Partitioning	$c _s = K c _l$	(3.11)
Species	Segregation [†]	$\mathbf{n} \cdot (-D_l \nabla c _l + D_s \nabla c _s) = -(K - \rho_s/\rho_l) c _l \mathbf{n} \cdot \mathbf{V}_{sl}$	(3.12)

[†]Solidification velocity \mathbf{V}_{sl} is measured in reference frame of stationary crystal.

[‡] T_f is furnace temperature profile specified external to domain.

each species³ (for a more detailed presentation of the equations for the general multiphase, multispecies situation, see [30]).

The momentum balance in Equation (3.2) includes several contributions to the body force. Forces due to thermal and solutal buoyancy are written explicitly in terms of the Boussinesq approximation, which is standard for slightly compressible liquids. To this we add a general body-force term $\mathbf{F}(\mathbf{v}, \mathbf{x}, t)$, which may have contributions from a variety of effects. These include use of a noninertial reference frame, discussed in Section 3.4.5, and application of a magnetic field to a conducting liquid, discussed in Section 3.4.6. It should be noted that the Boussinesq approximation does not include inertial effects that can arise in certain systems, for example high rotation rates at low gravity [31, 32]. Lee and Pearlstein [32] generalize the Boussinesq approximation to include centrifugal effects for a set of equations written in a rotating reference frame, but the same result can be obtained to first order by applying a variable density throughout Equation (3.2) rather than simply in the body-force terms. Arguably there is no reason to *not* do this when using numerical methods, since the Boussinesq approach of using a variable density only in the body-force term is a legacy of classical methods of analysis.

The equations in Tables 3.2 and 3.3 are written in dimensional form. The equations are easier to interpret and to solve when the variables are scaled to order one, so it is customary to nondimensionalize the equations by scaling each of the variables with a characteristic quantity. Many different dimensionless forms of the equations are possible in models of bulk crystal growth, and many dimensionless parameters can appear (Brown [9] identifies thirteen dimensionless parameters relevant to crystal growth). For example, in buoyancy-dominated flows there is no obvious characteristic velocity and a few different choices are in common use. One example is $v_c = k/\rho C_p L$, which leads to the following

³ To apply Equation (3.4) to multiple species implies pseudobinary transport, which, strictly speaking, is valid only for dilute species. Nondilute multispecies transport can be modelled using either the Stefan–Maxwell equations or Fick’s law of multicomponent diffusion [18], but this is rarely done because little information is available on multicomponent diffusion coefficients. For an example of modelling multicomponent species transport in melt crystal growth, see [29].

dimensionless form of momentum equation:

$$(\partial \mathbf{v} / \partial t + \text{Pr}^{-1} \mathbf{v} \cdot \nabla \mathbf{v}) - \nabla \cdot \mathbb{T} = \text{Ra}(T - 1)\mathbf{g} \quad (3.13)$$

where $\text{Pr} \equiv \mu C_p / k$ and $\text{Ra} \equiv \rho^2 C_p g L^3 \beta T_o / \mu k$. Another velocity scaling, $v_c = \sqrt{\beta g L T_o}$, is suggested by the solution to the problem of a vertical heated plate in an infinite bath. This choice yields the dimensionless form:

$$(\partial \mathbf{v} / \partial t + \sqrt{\text{Gr}} \mathbf{v} \cdot \nabla \mathbf{v}) - \nabla \cdot \mathbb{T} = \sqrt{\text{Gr}}(T - 1)\mathbf{g} \quad (3.14)$$

where $\text{Gr} = \text{Ra}/\text{Pr}$. Other forms are possible, for example setting the characteristic velocity using the rotation rate of the crystal or crucible in systems where rotational effects are dominant. Here we avoid discussing dimensionless forms in detail, only making the point that there is no unique best scaling. It is necessary to apply thought and experience to determine the best characteristic scalings for a given situation.

3.4.2 Boundary conditions

The boundary conditions in Table 3.3 cover most situations likely to occur in bulk crystal growth (some obvious conditions have been omitted from the table, for example matching and symmetry conditions). The equations are written in a general three-dimensional form with surface directions indicated using only the unit normal vector \mathbf{n} and identity tensor \mathbf{I} , to avoid defining tangent directions. The unit normal points outward by convention. For two-dimensional problems it is convenient to use a tangent vector, in which case some obvious modifications apply to Equations (3.5) and (3.8). All variables are written with respect to the computational reference frame except for the solidification velocity, \mathbf{V}_{sl} , which is measured in the reference frame of the stationary crystal. The velocity \mathbf{V}_b is a rigid boundary motion that can include both normal and tangential components. The computational frame may translate at an arbitrary velocity with respect to the laboratory frame, so care must be taken to note that \mathbf{V}_b may have a contribution due to translation of the reference frame in addition to contributions from motion of the boundary within the reference frame.

In many cases simplifications to these boundary conditions will be applicable. For example, the right-hand side of the no-slip and no-penetration conditions will be zero wherever rigid boundaries are stationary with respect to the reference frame. The two conditions taken together are often referred to singly as the no-slip condition, written in vector form $\mathbf{v} = \mathbf{V}_b$, but we separately identify the vector components because there are situations in which it is appropriate to specify only one component. An example is at the growth interface in melt-growth systems in which there is a change of density upon solidification: here the no-slip condition is applied, but the no-penetration condition is replaced by Equation (3.7), which we call the penetration condition. Note that Equation (3.7) reverts to the no-penetration condition if the solid and liquid densities are equal.⁴

⁴ It is occasionally misunderstood that the proper boundary condition for the equal density case is $\mathbf{n} \cdot \mathbf{v} = 0$ when solving the problem in a reference frame fixed with the crystal. The notion that movement of the interface causes

When a free boundary between a gas and a liquid is present, for example in meniscus-defined growth, it is necessary to account for the effects of interfacial tension. Equation (3.8) represents the force balance at the interface: the normal component accounts for capillary pressure and the tangential component accounts for stress caused by the surface tension gradient (known as the Marangoni effect). The condition is often simplified by assuming that the stress induced by the gas phase is negligible. In this case the momentum balance in the gas phase is discarded and the stress term $\mathbf{n} \cdot \mathbb{T}|_g$ is set equal to an ambient pressure (denoted p_a , often simply zero). A tangential stress $\mathbf{n} \cdot \mathbb{T}|_g$ can also be induced by an RF field for electrically conducting melts [33]. When solving a free-boundary problem it is also necessary to apply Equation (3.6), which acts as a constraint that determines the location of the free boundary in a self-consistent manner (in this context it is usually referred to as the kinematic condition). When Equation (3.6) is used in this way, \mathbf{V}_b is unknown and must be calculated as part of the solution. It is worth noting that confined melt-growth systems, e.g. Bridgman systems, often have a free boundary between the melt surface and a gas-filled head space, so to be rigorous the capillary and kinematic conditions should also be applied here. But it is usually reasonable to assume that gravity keeps this free boundary nearly flat, in which case the normal momentum balance is automatically satisfied and only the tangential component of Equation (3.8) is applied.

3.4.3 Continuum interface representation

The manner in which the growth interface is represented is a central feature of bulk crystal growth models from both a physical and a numerical point of view. At its simplest this can mean using an assumed shape, which might for example be based on the known growth habit of a given crystal. But a self-consistent growth model requires that the interface geometry be computed as part of the solution to the transport problem. Doing this requires a model that can describe the shape or velocity of the interface, at least on a macroscopic scale, but there does not appear to be a unique model for this purpose. Both ‘sharp’ and ‘diffuse’ methods have been used to represent interfaces in continuum models of solidification. Strictly speaking, sharp-interface methods are those in which the continuum governing equations treat the interface as a surface of zero thickness across which physical properties are discontinuous. Conversely, diffuse methods are those in which the continuum governing equations treat the interface as a region of finite thickness across which physical properties vary rapidly but continuously from one bulk value to the other.

For a sharp-interface model of melt growth, the normal velocity of the growth interface can be represented in terms of a thermodynamic driving force, an undercooling ΔT :

$$\mathbf{n} \cdot \mathbf{V}_{sl} = \beta_{kin} \Delta T \quad (3.15)$$

flow seems to stem from confusion with the oft-solved problem of an infinitely long system in a reference frame that moves with the interface. But in the equal-density case the liquid simply freezes in place, and therefore no flow is induced in the reference frame fixed with the crystal. When the densities are not equal the situation is more complicated, because there is a net gain or loss of volume proportional to $\rho_s/\rho_l - 1$. Should the solid be denser than the liquid, for example, the melt will translate towards the crystal as a whole to accommodate the loss of volume.

where β_{kin} denotes a kinetic coefficient, and ΔT is usually written in terms of some variant of the Gibbs–Thomson relation at the interface, for example [34]:

$$\Delta T = T_i - T_m \left(1 - \frac{\gamma}{\rho_s H_f} \mathcal{H} \right) \quad (3.16)$$

where T_i is the interface temperature, T_m is the melting temperature of a planar interface, γ is a capillary coefficient, and \mathcal{H} is the local mean curvature of the interface. The relation in Equation (3.15) is quite general, but is written in a form that conceals considerable complexity. The linear form of the kinetic term is misleading because the coefficient β_{kin} often depends strongly on interface velocity. Also, both β_{kin} and the surface tension γ depend on interface morphology and are often anisotropic. The anisotropic nature of these processes can cause faceting, particularly at high growth rates or low temperature gradients.

For an atomically rough interface the kinetic coefficient becomes large enough that the undercooling ΔT goes to zero and $T_i = T_m(1 - \gamma\mathcal{H}/\rho_s H_f)$. Here, the rate of interface movement is controlled by the flow of latent heat away from the interface. Capillary effects are only important when the interface curvature is large compared to the reciprocal of the capillary length, for example in dendritic growth. It is preferable to avoid this situation in bulk crystal growth (although perhaps not always possible), so capillary effects are usually neglected in bulk melt-growth models. Under these conditions Equation (3.15) reduces to its simplest and most widely used form,

$$T = T_m \quad (3.17)$$

commonly referred to as the melting-point isotherm condition.

In certain melt-growth systems, particularly oxides, growth kinetics are important and faceting is observed, but only recently have models been developed that incorporate growth-kinetics-driven faceting into a continuum transport model of bulk crystal growth. Brandon *et al.* [1, 3, 4] use an approach in which Equation (3.15) is solved directly as part of the transport model, with a value of β_{kin} that varies sharply but continuously near to singular orientations of the interface. Lan and Tu [2] use a different approach that is more geometric in nature, in which the locations of facet planes of fixed orientation are iteratively updated until Equation (3.15) is satisfied. These treatments represent a step forward in the use of transport models to predict interface morphology, but come with limitations. It is essential to use the correct form of β_{kin} , which requires that the models be well informed by experiments. The models can predict faceting, but only apply near to equilibrium and are unsuitable for simulating detailed evolution of unstable growth morphologies, for example dendritic growth.

Modelling the growth velocity of a crystalline surface in bulk solution growth is much more problematic than in melt-growth systems, since interfacial kinetics are much more important. Here too the model must be well informed by experiments, so that the growth habit and growth kinetics are known in a form suitable for inclusion in a macroscopic transport model. The simplest sharp-interface representation of growth is given by:

$$\mathbf{n} \cdot \mathbf{V}_{\text{sl}} = \beta_{\text{kin}} \sigma_c \quad (3.18)$$

where supersaturation is the driving force for crystallization. Supersaturation is defined as $\sigma_c \equiv \Delta\mu_g/k_B T = \ln(c/c_{eq})$, where $\Delta\mu_g$ is the change in the chemical potential between the crystal and liquid and k_B is the Boltzmann constant. The kinetic coefficient in this expression varies strongly as a function of the detailed nature of the surface, posing great challenges for realistic modelling. Not enough is presently known to use a model based on Equation (3.18) to *predict* interface morphology in solution growth. Recent efforts [5, 6] to integrate a mesoscale model of step flow with a macroscale model of transport have shown promise in this direction, however, as described below in Section 3.6.4.

Diffuse-interface models have been the subject of intense interest in recent years, particularly phase-field models, the development and use of which have recently been chronicled in a monograph by Emmerich [34]. In phase-field models the material phases are characterized by an order parameter Φ (the phase-field) that varies over an arbitrary range (typically -1 to 1), its value at one extreme representing the solid and at the other extreme representing the liquid. The value of the phase-field varies rapidly but continuously from solid to liquid over a thin interfacial region, as do the physical properties. To construct a phase-field model it is necessary to formulate an equation that governs behavior of the order parameter. Models of Φ are phenomenological in origin, but much emphasis has been placed in recent years on formulation of phase-field models that are thermodynamically consistent and that asymptotically match the sharp-interface limit, putting these models on firm theoretical ground [34]. Diffuse-interface methods are at greatest advantage when the interface is highly deformed or the phase topology is either not known or subject to change. Thus these methods have become popular in recent years for the study of morphological instability, particularly dendritic growth.

Note that the definitions of sharp- and diffuse-interface methods used here are made without any reference to the method by which the continuum equations are discretized, which can have a profound impact on the character and quality of interface representation. We discuss below in Section 3.5 how, upon discretization, sharp-interface methods can take on important characteristics of diffuse methods. Thus, although the definitions of sharp and diffuse are unambiguous, their usefulness as a classification scheme is somewhat limited.

3.4.4 Radiation heat-transfer modelling

The equations presented here treat radiation heat transfer only in the most superficial way: as a boundary condition (Equation (3.10)) that represents the flux of heat in terms of an externally specified temperature profile presumed to be available as a model input. Although this simple approach is often useful, particularly if good experimental measurements of temperature within the furnace are available, it is limiting nonetheless. If it is desired to simulate the coupling of transport phenomena within the growth vessel to furnace heat transfer then it is necessary to consider radiation heat transfer at a significant level of detail, for example by calculation of view factors or ray-tracing techniques. Radiation heat transfer is particularly important in simulation of Czochralski systems, where small changes in crystal and melt shape have a highly nonlinear effect on radiation [35]. For some materials, particularly oxides, internal radiation transfer can also be important [36, 37].

Several models of melt growth have been developed that include detailed calculations of furnace radiation, starting with Brown and coworkers [35, 38, 39]. Two of these

efforts have led to commercial codes, FEMAG [40] and CrysVUN [41, 42]. An evaluation of these models can be found in [43]. Notably all these codes are restricted to solving two-dimensional axisymmetric problems. Modelling of three-dimensional radiation heat transfer in a crystal-growth furnace is a daunting problem, but in many cases appears unnecessary since furnaces are usually designed to be nearly axisymmetric. Three-dimensional flows in the melt are not uncommon, but in many circumstances convective heat transfer is too weak to significantly affect azimuthal heat transfer outside of the growth vessel. Circumstances that favor this situation include low Prandtl number fluids (i.e. metals and most semiconductors), growth vessels made of high-conductivity materials, large thermal mass of furnace components, or any circumstances under which convection is weak, for example in microgravity or under magnetic suppression. Under these circumstances it is reasonable to use an axisymmetric furnace modelled coupled to a three-dimensional model of transport phenomena within the growth vessel [44, 45]. An approach that has become popular in recent years is to compute a global two-dimensional solution, the results of which are used to construct suitable thermal boundary conditions for solving a three-dimensional transport model within the growth vessel [25, 46–49]. Although it is not possible to study three-dimensional furnace heat transfer directly using this approach, we show in Section 3.6.3 that simple perturbations can be used to study the effects of furnace asymmetry on transport.

The 2D–3D coupling approach just described has so far been limited to a one-way communication of information from the two-dimensional outer problem to the three-dimensional inner problem. The outer problem can include heat transfer within the growth vessel at whatever level of approximation is permitted by the software (usually two-dimensional, perhaps without convection), but cannot fully reflect the effects of convective heat transfer within the growth vessel. It is therefore desirable to develop a more fully coupled scheme in which information from the inner problem is used to iteratively update the outer problem. The central issue is the matching of temperature and heat flux at the interface between the inner and outer problems; there are two boundary conditions only one of which can be completely matched. A logical scheme is to use a weighted combination of the two conditions:

$$\xi \mathbf{n} \cdot (k_{\text{inner}} \nabla T|_{\text{inner}} - k_{\text{outer}} \nabla T|_{\text{outer}} + \mathbf{q}_r|_{\text{outer}}) + (1 - \xi)(T_{\text{inner}} - T_{\text{outer}}) = 0 \quad (3.19)$$

where ξ ranges from 0 for pure temperature matching to 1 for pure flux matching. A fixed-point iteration can be constructed by first applying this condition to the inner problem, then applying a similar condition (with ξ and $1 - \xi$ swapped) to update the outer problem. It has been shown for a simple one-dimensional heat-transfer problem that the stability and convergence of this iteration depends on the value of ξ ; our research on the two-dimensional case is ongoing. Note that in going from the inner problem to the outer problem thermal data must be reduced in dimension to construct boundary conditions. This can be done by using a weighted average:

$$T_{2D}^i = \frac{\int_{\Gamma} w_{2D}^i T_{3D} d\Gamma}{\int_{\Gamma} w_{2D}^i d\Gamma} \quad (3.20)$$

where Γ is the interface between inner and outer problems and w_{2D}^i is a weight function, for example standard basis functions when using the finite-element method or delta functions when using the finite-difference method.

3.4.5 Noninertial reference frames

The momentum balance in Equation (3.2) is written for an inertial reference frame. Certain problems are greatly simplified if a noninertial reference frame is used. If the momentum balance is written in a reference frame that translates and rotates at arbitrary velocity with respect to an inertial reference frame, it is necessary to include an apparent body force \mathbf{F} that accounts for the acceleration of the reference frame. For a reference frame with absolute acceleration \mathbf{a} and instantaneous rotation rate $\boldsymbol{\omega}$:

$$\mathbf{F} = \rho(\mathbf{a} + \boldsymbol{\omega} \times (\boldsymbol{\omega} \times \mathbf{r}) + 2\boldsymbol{\omega} \times \mathbf{v} + \dot{\boldsymbol{\omega}} \times \mathbf{r}) \quad (3.21)$$

where \mathbf{r} and \mathbf{v} are position and velocity in the noninertial frame. Noninertial frames are most commonly used to study rotating systems and microgravity crystal growth. An example is the solution-growth system shown in Fig. 3.1c. The crystal and support rotate in the laboratory frame causing the geometry to vary with time. This problem can be solved on a fixed geometry by adopting a reference frame that rotates with the crystal [50, 51]. Then Equation (3.21) with $\mathbf{a} = 0$ is added to the momentum balance. Another example is crystal growth in the microgravity environment of space, where a reference frame attached to the experiment is subject to residual accelerations that vary both in magnitude and direction, known as g-jitter. In modelling of g-jitter effects it is common to use $\mathbf{F} = \mathbf{a}(t)$ and neglect the rotational contributions, unless rotation is specifically used in the experiment.

3.4.6 Magnetic fields

Use of magnetic fields to manipulate convection is an area of ongoing interest in crystal growth and has attracted considerable attention from modellers in recent years. A general review of magnetohydrodynamics in materials processing is given by Davidson [52]. Some examples include use of magnetic fields to suppress convection in microgravity Bridgman experiments [53–55], to control instability in Czochralski growth [24], and to promote mixing in melt-growth systems [56, 57]. A typical model consists of the equations in Table 3.2 with the Lorentz body force included in the momentum balance:

$$\mathbf{F} = \sigma(-\nabla\Phi + \mathbf{v} \times \mathbf{B}) \times \mathbf{B} \quad (3.22)$$

where \mathbf{B} is the magnetic field and σ is the electrical conductivity, and a scalar equation added to determine the electric potential Φ :

$$\nabla^2\Phi = \nabla \cdot (\mathbf{v} \times \mathbf{B}) \quad (3.23)$$

where it has been assumed that the magnetic field is unaffected by the flow. The equations are straightforward to solve, but the magnetic fields cause thin boundary layers that can be challenging to resolve numerically. The behavior of the equations can be nonintuitive due to the complicated interaction of flow kinematics with the flow of electric current, as discussed by Yeckel and Derby [55].

3.4.7 Turbulence

The form of the Navier–Stokes equation given in Table 3.2 is suitable for conditions of laminar flow. Many bulk crystal growth systems exhibit laminar flow, including float-zone and most Bridgman systems, but turbulence is common in Czochralski systems and in some larger solution-growth systems as well. The crudest approach to incorporating turbulent effects is to use enhanced transport properties (e.g. viscosity, thermal conductivity, mass diffusivity) in a laminar-flow model. A more accurate picture of transport can be obtained using a turbulence model. The Reynolds-averaged Navier–Stokes (RANS) approach has been used most often. Robey [58, 59] used a standard $k - \varepsilon$ model to model turbulent transport in solution growth of KDP. A variety of $k - \varepsilon$ models have also been used to model turbulent melt convection in Czochralski growth of silicon. Lipchin and Brown [60] compared three $k - \varepsilon$ models for turbulent viscosity and concluded that a low Reynolds number form worked best. Low Reynolds number $k - \varepsilon$ models have also been used in [47, 61, 62]. An alternative to the RANS approach is large-eddy simulation (LES) [46, 63]. Recently, Ivanov *et al.* [64] have proposed a hybridized method in which RANS-derived equations are applied in wall regions and LES-derived equations are applied in the core region. Each of these attempts to model turbulent transport has been a mixed success, and no clear choice of turbulence model has emerged. Given the importance of turbulent transport to the industrial production of silicon, turbulence modelling likely will long remain an active research area.

3.5 COMPUTER-AIDED ANALYSIS

The model equations described in the previous sections do not yield to traditional mathematical methods and must therefore be studied using computer-aided numerical analysis. There are many methods in use and to describe them all is not feasible, so in the following sections we focus on those issues in numerical analysis that we deem of specialized importance to crystal-growth modelling. We illustrate some of our points with examples drawn from our experience using finite-element methods, but in most cases an analogous situation or procedure applies to other popular discretization methods such as finite volume or finite difference.

Many commercial codes exist that are devoted to solving problems in fluid mechanics and transport phenomena, mostly based on finite-volume or finite-element methods. Two codes specialized for crystal-growth modelling are FEMAG [40] and CrysVUN [41]. Examples of crystal-growth modelling performed using popular general-purpose codes can be found in [58] (CFX4), [65] (FIDAP), [66] (FLUENT), and [67] (CFD-ACE). It is not necessary for users to completely understand the numerical methods used in these codes, but a general understanding will greatly facilitate their correct use. Even when using commercial codes, however, it is always critical to understand the model itself, as embodied in the equations described in Section 3.4.

3.5.1 Discretization

The first step in the numerical solution of the governing equations is to convert the partial differential equations into a set of differential-algebraic equations (DAEs) by discretizing

spatial derivatives. These DAEs can then be integrated in time using any one of several standard methods. The most common techniques for discretizing the equations are the finite-volume and finite-element methods, although finite-difference and spectral methods are also widely used. In our work we have used both the Galerkin finite-element method [68, 69] and the Galerkin/least-squares method [70] to discretize the equations, and a second-order trapezoid rule [71] or the backward Euler method to integrate the resulting DAEs. Regardless of the methods used the result is a set of algebraic equations that must be solved at each time step. The equations are often highly nonlinear and therefore must be solved iteratively. Our approach is to use Newton's method, which reduces the equations to a linear form at each iteration. Solving the linearized equations at each Newton iteration is by far the costliest step in computational terms. As discussed in Section 3.2, it is usually preferable to solve these equations using a direct method based on Gaussian elimination when solving two-dimensional problems, but it is almost mandatory that an iterative method be used when solving three-dimensional problems. Our choice is to use preconditioned generalized minimal residual (GMRES) method [11, 72], a Krylov subspace projection method. Additional details on our methods and software can be found in [12, 30].

3.5.2 Numerical interface representation

Many methods have been devised to represent phase interfaces in discretized transport models. We cannot describe them all here, but we try to make some useful generalizations about their nature. Methods generally are of two basic types: fixed-grid methods and deforming-grid methods. Each type has its advantages and disadvantages, and each introduces its own complexities to constructing the discretized model. In fixed-grid methods all fields (e.g. temperature, flow, etc.) are computed on a fixed grid of computational cells (e.g. finite elements, finite volumes). In general, the interface will pass through the interior of cells, which introduces two complications. Cells at the interface are located partially in each phase, which requires an interpolation of material properties within the cells. Also, interface boundary conditions are to be applied along a curve that does not coincide with the underlying grid used to discretize the field variables, which introduces another interpolation of some sort. These complications are absent from deforming-grid methods, the essence of which are to allow discretizing the interface conditions on the same grid used to represent the field variables. In these methods the grid is deformed so that the interface lies along the edges of computational cells everywhere. Each cell lies entirely inside of one phase and remains in that phase (unless regridding with topology change is needed), allowing material properties to be represented locally without interpolation.

A fixed-grid discretization cannot directly represent the interface, which therefore must be represented with a supplemental discretization. This can take many forms: the phase-field [34], enthalpy [73], and level-set [74] methods all use an implicit representation of the interface, but each has a distinct approach to the problem. The phase-field method is a true diffuse-interface model in which the interface is implicitly represented by the order parameter Φ . Interfacial flux conditions arise naturally as volumetric conditions within the interfacial zone defined by Φ , and physical properties can be represented in terms of simple ad hoc functions of Φ . The enthalpy method resembles the phase-field method in

some superficial respects, but is better described as a sharp-interface method discretized in a diffuse manner rather than as a true diffuse-interface model. The sharp-interface model results in a discontinuous enthalpy field at the phase boundary, but this discontinuity cannot be resolved by the underlying fixed-grid discretization, so in practice the enthalpy varies rapidly but continuously across an interfacial zone of nonzero thickness (sometimes this region takes on physical meaning as a mushy zone). Also, it is not possible to directly implement sharp-interface conditions using the underlying fixed-grid representation, so it is customary to implement interfacial flux conditions as pseudovolumetric conditions within the interfacial zone. In contrast, the level set is a true sharp-interface method, but as with the enthalpy method it is not possible to directly implement sharp-interface conditions using the underlying fixed-grid representation. Hence it holds in common with the enthalpy and phase-field methods an artificial⁵ smearing of interfacial flux conditions, blurring the practical distinction between the terms sharp and diffuse introduced in Section 3.4.3.

Whereas the aforementioned fixed-grid techniques all rely on an implicit characterization of the interface, a host of fixed-grid methods also exist in which the interface is tracked explicitly, for example front-tracking [75], volume-of-fluid [76], and sharp-interface [77] methods. Since the location of the interface is arbitrary with respect to the fixed grid it is necessary to use a discretization scheme to track the interface that is independent of the underlying fixed-grid discretization. Then it is necessary to interpolate material properties and interfacial flux conditions between these discretization schemes. Thus these methods share in common with their implicit fixed-grid cousins some degree of artificial smearing of interfacial flux conditions [78]. Udaykumar *et al.* [77] describe a fixed-grid method that uses special discretization procedures to obtain second-order accurate interpolation of interfacial conditions to avoid this problem, but even so the method represents the interface position with only first-order accuracy, a common characteristic of fixed-grid methods. Methods limited to first-order accuracy demand a high degree of grid refinement to resolve the interfacial region.

Deforming-grid methods make it possible to achieve high accuracy with much less grid refinement than required by fixed-grid methods, provided that the grid can represent the interface without excessive distortion of the computational cells. Interfacial conditions and physical properties are accurately represented, eliminating key sources of error; typically the accuracy of the interface position is comparable to the accuracy of the underlying field variables such as temperature. Figure 3.2 shows a comparison of the enthalpy-based fixed-grid method of CrysVUN to the deforming-grid method employed in Cats2D [30], for a model of GaAs growth by the VGF method. A global furnace model is included in the CrysVUN model. Temperature data at the ampoule wall from the CrysVUN calculations are used to construct thermal boundary conditions for the Cats2D calculations. There is good agreement in the predicted interface shape provided the grids are sufficiently refined, but as shown in Fig. 3.2c, the fixed-grid calculations achieve only first-order convergence in interface position, whereas the deforming-grid calculations achieve nearly second-order convergence with a much lower error in interface position. Deforming-grid methods are subject to failure in many situations, however, several of which are illustrated in Fig. 3.3. The unexpected appearance of a phase interface (Fig. 3.3a), or the motion of an interface around a corner (Fig. 3.3c), might in some circumstances be

⁵ One view is that the diffuse interface of the phase-field model corresponds to a real interfacial transition zone. In practice it is not possible to resolve such a thin region, however, and the 'interface thickness' parameter of the model is chosen based purely on numerical considerations, just as in the enthalpy method.

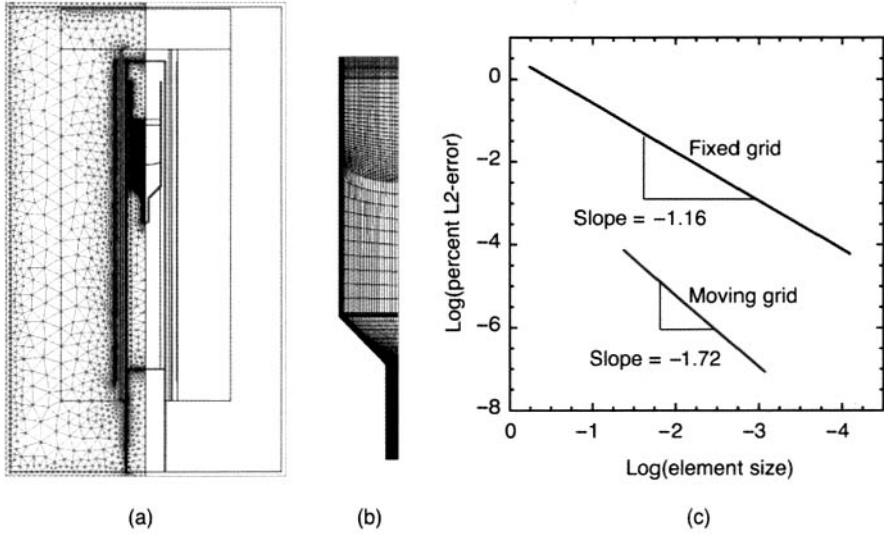


Figure 3.2 Comparison of fixed-grid and deforming-grid methods for growth of GaAs by vertical gradient freeze (VGF) method. (a) Grid for global heat-transfer calculation performed by CrysVUN [41], with interface represented by enthalpy method (fixed grid). (b) Grid for local analysis using Cats2D, with interface represented by deforming grid (ampoule outer-wall temperatures are provided by CrysVUN). (c) Convergence of interface position vs. grid refinement

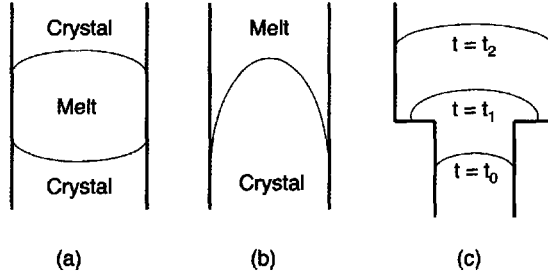


Figure 3.3 Situations likely to cause failure of deforming-grid methods: (a) unanticipated appearance or disappearance of phase interface; (b) extreme distortion of phase interface; (c) travel of phase interface around corners or similar topological changes

viewed as mere inconveniences when using a deforming-grid method, but severe interface distortion (Fig. 3b) is usually fatal because it becomes impossible to align the boundaries of computational cells to the interface. In such cases it becomes necessary to resort to fixed-grid methods.

3.5.3 Deforming grids and ALE methods

When using a deforming-grid method some means of numerical grid generation is required to reposition nodes in a way that avoids excessive deformation of the computational cells.

Grid-generation methods fall into two general categories, algebraic grid generation and partial-differential-equation-based grid generation [79]. Use of algebraic grid generation, for example the method of spines [80], has declined in favor of PDE-based methods such as pseudosolid-domain mapping [81] and elliptic grid generation [79]. In these methods the nodal positions (or computational cell boundaries, depending on the point of view) are characterized by a continuous vector field $\mathbf{x} = (x, y, z)$, which defines a mapping between the physical domain and a reference, or *parent*, domain $\xi = (\xi, \eta, \zeta)$, for example the standard finite element. The vector field $\mathbf{x} = \mathbf{x}(\xi)$ is obtained by solving a system of partial-differential equations, many varieties of which have been contrived to achieve various desired effects in grid generation. These equations can be solved in the same parent domain ξ as field variables such as temperature and flow, a convenient arrangement that simplifies algorithm development.

In the pseudosolid method, \mathbf{x} is not computed directly, but is updated by solving a set of PDEs for displacement δ of a solid body undergoing deformation (usually treated as linear elastic). Given an initial grid \mathbf{x}_0 a new grid is computed from $\mathbf{x} = \mathbf{x}_0 + \delta$. We emphasize that despite the physical basis of these equations, they are used in a purely artificial manner here, as a convenient way to deform the grid in a controlled manner. The method is straightforward to implement, and has the major advantage that it makes no assumptions about the structure of the grid. A disadvantage is the strong tendency of the pseudosolid PDEs to conserve the volume of the computational cells, a property that can cause severe distortion of the cells if there is a large evolution in interface shape. Pseudosolid-domain mapping is used to compute unstructured grids of tetrahedral finite elements in the three-dimensional calculations presented in Section 3.6.3.

Whereas the pseudosolid equations are formulated in the physical domain as $\mathbf{x} = \mathbf{x}(\xi)$, elliptic grid-generation equations are formulated in the parent domain, namely in the form $\xi = \xi(\mathbf{x})$. This parent domain is conceived to be a regular array of uniform computational cells, with cell edges given by uniformly spaced isocurves of ξ , η , and ζ , a construction that restricts elliptic grid generation to structured grids. A typical system of elliptic grid equations is given by [82]:

$$\nabla \cdot \mathbf{D}(\xi) \cdot \nabla \xi = 0 \quad (3.24)$$

where \mathbf{D} is a diagonal tensor. Before solving Equation (3.24) it is necessary to invert it to a form in which \mathbf{x} is the dependent variable and ξ is the independent variable, so that the equations can be solved in the parent domain alongside the physical equations (the form of the inverted equations [30], omitted here, is nonlinear and rather more complicated than Equation (3.24)). The scalar two-dimensional form of Equation (3.24) is given by:

$$\nabla \cdot D_\xi(\xi, \eta) \nabla \xi = 0 \quad (3.25)$$

$$\nabla \cdot D_\eta(\xi, \eta) \nabla \eta = 0 \quad (3.26)$$

These equations are used to compute structured grids of quadrilateral finite elements for most of the two-dimensional calculations in this chapter. The element-size distribution is controlled by a pair of coefficients, D_ξ and D_η . The inverses of these coefficients can be thought of as weights, $w_\xi = D_\xi^{-1}$ and $w_\eta = D_\eta^{-1}$, that are equidistributed along lines of constant ξ and η . Along a line of constant η , for example, $w_\xi dS = c_1 d\xi$, where c_1 is a constant and dS is differential arclength in the physical domain. Similarly, along a line of constant ξ , $w_\eta dS = c_2 d\eta$. Arclength distributions of node spacing along curves

of ξ and η given by $F(\xi; \eta)$ and $G(\eta; \xi)$ can be obtained by setting $D_\xi = \partial F / \partial \xi$ and $D_\eta = \partial G / \partial \eta$. It is possible to avoid making explicit use of distribution functions F and G , however, by using the initial mesh \mathbf{x}_0 to compute [83]:

$$D_\xi = \frac{\partial S}{\partial \xi} = \sqrt{\left(\frac{\partial x}{\partial \xi}\right)^2 + \left(\frac{\partial y}{\partial \xi}\right)^2}, \quad D_\eta = \frac{\partial S}{\partial \eta} = \sqrt{\left(\frac{\partial x}{\partial \eta}\right)^2 + \left(\frac{\partial y}{\partial \eta}\right)^2} \quad (3.27)$$

The effect of computing D_ξ and D_η in this way is to preserve the relative distribution of element sizes of the initial mesh under the influence of domain deformation. A significant consequence is that global information, namely the node-distribution functions F and G , is replaced by local information, $\partial S / \partial \xi$ and $\partial S / \partial \eta$, which greatly simplifies implementation. The result is a robust, parameter-free formulation that is easy to use.

When using deforming-grid methods in time-dependent problems it is important to recognize that the time derivatives in the equations in Tables 3.2 and 3.3 are taken with respect to the computational reference frame, whereas time derivatives of the discretized equations are computed with respect to the reference frame of the parent domain, which moves locally at the velocity of the nodes. In order to evaluate the time derivative of a scalar field f we must convert it to the frame of the parent domain [84]:

$$\frac{\partial f}{\partial t} = \dot{f} - \dot{\mathbf{x}} \cdot \nabla f \quad (3.28)$$

where the overdot indicates time derivatives with respect to the reference frame of the parent domain (this procedure is similar to application of the Reynolds transport theorem). Then the energy equation is discretized in the form (compare with Equation (3.3)):

$$\rho_0 C_p (\dot{T} + (\mathbf{v} - \dot{\mathbf{x}}) \cdot \nabla T) = \nabla \cdot (k \nabla T) \quad (3.29)$$

where the effect of the moving grid appears as a correction to the convective velocity. Analogous changes appear in species- and momentum-conservation equations (Equations (3.2) and (3.4)). Because the reference frame of the parent domain is neither Eulerian nor Lagrangian, the approach described here is often referred to as an arbitrary Lagrangian–Eulerian (ALE)⁶ method [85]. Several excellent references [82, 86, 87] describe the use of ALE methods with elliptic grid generation for solving time-dependent moving-boundary problems in fluid mechanics.

3.5.4 A simple fixed-grid method

The observation that fixed-grid methods usually attain no better than first-order convergence for accuracy of interface position, despite the considerable sophistication of some of these methods, motivates the development of a simple technique for representing the interface and applying interfacial conditions in solidification problems. We have devised a simple procedure in which the transport equations are solved on a fixed grid, with each

⁶ Caution should be exercised to not confuse ALE methods with *mixed Eulerian–Lagrangian* methods, which are a type of fixed-grid method with explicit interface tracking. In these methods the field equations are solved in an Eulerian frame and the interface is tracked in a Lagrangian frame, hence the term *mixed*.

element⁷ assigned to a material (with appropriate physical properties) based on whether or not the average temperature within the element exceeds the melting temperature. The procedure is repeated iteratively until convergence. The interface is defined implicitly by this operation as the boundary between elements of different phases, in effect following the line of element edges that are nearest to the true interface. Since this approximation to the interface lies entirely along element edges, it is natural to impose interfacial boundary conditions using the underlying discretization (for example via the surface integrals in the weak form of the finite-element residuals). The *element-edge-interface method* (EEIM) does not require any interpolation of physical properties or smearing of boundary conditions, and a standard finite-element discretization strictly conserves energy, but it is plain to see that the approximation represents the interface position with accuracy that is no better than first order in element size. The misplacement of the interface will result in local errors in the application of boundary conditions and physical-property interpolation, but these errors appear to be no worse than similar interpolation errors for any first-order fixed-grid method. Figure 3.4a shows a comparison of this method to a deforming-grid method, for a simple two-phase solidification problem. Interface deflection and curvature is caused by a 5 to 1 thermal conductivity ratio between liquid and solid. In this method it is natural to measure convergence by the extent to which the temperature along the element-edge interfaces deviates from the melting temperature, in a root-mean-square sense. Figure 3.4b shows that convergence is nearly first order by this measure, which is consistent with first-order convergence of the spatial error.

The element-edge-interface method is useful for solving problems in which interface-curvature effects are unimportant, and in which it is not necessary to explicitly compute the velocity of the interface. To compute the curvature or velocity would require a smooth representation of the interface, adding a level of complexity that blunts the appeal of

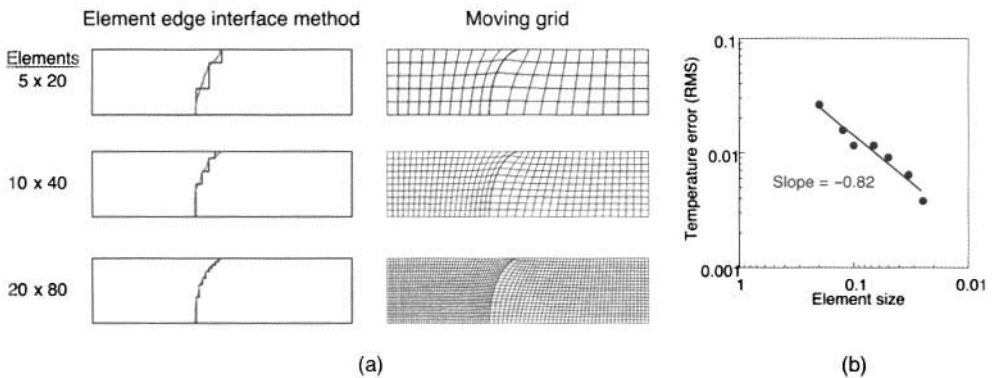


Figure 3.4 Comparison of element-edge-interface method to deforming-grid method. (a) Interface representation. In the EEIM simulations the interface (composed of straight-line segments) and the melting-point isotherm are both displayed. In the moving-grid simulations the interface and melting-point isotherm coincide. (b) Convergence of interface-temperature error vs. grid refinement (error is defined as the root-mean-square deviation of the interface temperature from the melting temperature)

⁷ Although described here in a finite-element context, an analogous procedure would be straightforward to develop for finite-volume methods.

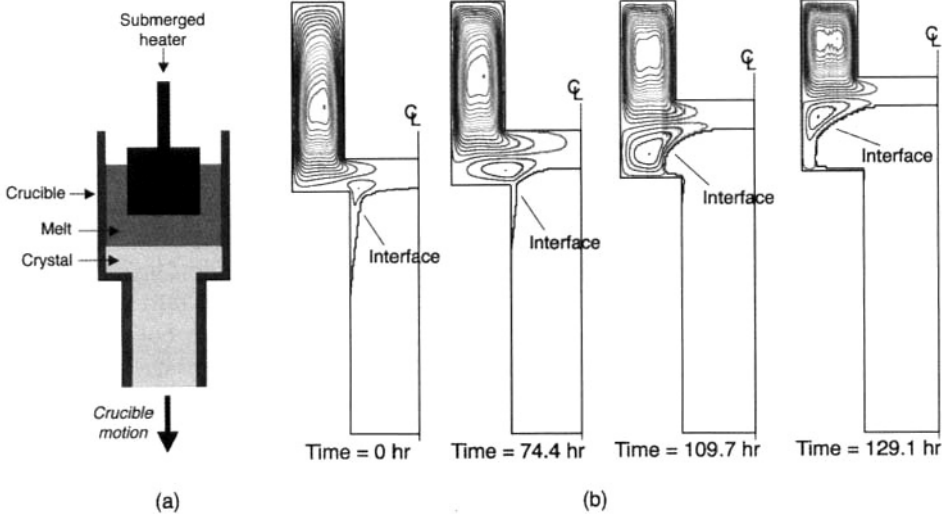


Figure 3.5 Axial heat flux at phase interface: (a) schematic; (b) streamlines and interface shape vs. time

the simple method. Computing the interface velocity to apply interfacial flux boundary conditions (Equations (3.9) and (3.12)) can be circumvented by releasing or consuming discrete amounts of energy or mass when an element changes its phase identity (computing the production of latent heat by this method can destabilize the outer iteration; work is ongoing to develop a scheme to improve the stability and convergence of these iterations).

Figure 3.5 shows results obtained using the element-edge-interface method to solve a problem that exhibits all three of the difficulties illustrated in Fig. 3.3. An AHP⁸ growth system [88] (shown in Fig. 3.5a) is used to grow bismuth germinate (BGO). The crucible has a sudden expansion with a narrow lower region and a wider upper region, separated by a sharp corner. The extreme distortion of interface shape occurs due to radiative heat loss from the interface through a semitransparent crystal. During growth the interface travels around a sharp corner, a change in grid topology that is not easily accommodated by deforming-grid methods. Another change of topology occurs when an isolated region of melt is temporarily formed at the side wall of the lower crucible when the solidification front closes off the mouth of the lower crucible. A significant degree of grid refinement is needed (the calculations in Fig. 3.5b used 58 600 equations), but acceptable accuracy can be obtained at reasonable cost for two-dimensional problems. Additional details on these calculations can be found in [89].

3.5.5 Quasi-steady-state models

Interface motion in bulk crystal growth systems is generally very slow compared to the time scale of transport phenomena [90]. In many systems energy and momentum transport

⁸ Axial heat flux close to phase interface.

undergo large transients at the start of growth, but after a relatively short time these transients decay. Subsequently the transport equations remain nearly at steady state, and the only significant effect of interface motion relates to balances of heat or material across the interface. This observation naturally leads to consideration of a quasi-steady-state (QSS) model, in which the geometric position of the interface is fixed, and the steady-state equations for transport are solved to obtain a snapshot in time. For melt growth an assumed value of interface velocity V_{sl} is applied to account for the release of latent heat in Equation (3.9). After sufficiently long time, V_{sl} reaches a constant value equal to the translation rate of the furnace relative to the growth vessel, under which condition the QSS model is valid. From a computational point of view, this approach is expedient, since one need only solve a set of nonlinear algebraic equations for the model rather than a set of time-dependent DAEs.

After the initial transients of the transport equations have decayed, there is an intermediate stage of growth during which the interface velocity is far from its final value and the conventional QSS model is not valid. Virozub and Brandon [91] have developed a method intermediate between the QSS model and a fully time-dependent model that extends the QSS model to this intermediate stage of growth. The method consists of an outer iteration that starts with an assumed interface velocity. The QSS model is solved twice within each iteration, at two slightly different positions relative to the furnace. The interface positions provided by these two solutions are used to compute the interface velocity by finite differences. The iteration is repeated using the updated interface velocity until the procedure converges. Brandon and Virozub outline conditions under which the method is accurate and show that the method can be used to extend the QSS model to considerably shorter growth times in many systems. For two-dimensional problems, it is by now quite fast to solve the fully time-dependent model using almost any computer, which reduces the attraction of the method. A much greater benefit is expected when solving three-dimensional problems, however.

The situation with species mass conservation in melt growth is somewhat different from that for energy and momentum conservation. During melt-growth processes, energy and momentum are exchanged between the system and the surroundings, but from the standpoint of mass these are closed systems. The effect of partitioning (Equation (3.11)) is to cause either a progressive enrichment or depletion of a species from the melt during growth under most conditions. Thus mass transfer is inherently time dependent in these systems. To formulate a solvable QSS model of segregation, it is necessary to add material to the melt to compensate for depletion of a partitioning species (or remove it to compensate for accumulation). The usual practice for doing this is to imagine that the melt within the computational domain communicates with a far-field condition at uniform concentration [92]:

$$\mathbf{n} \cdot D_1 \nabla c|_l = -V_{sl}(c - c_o) \quad (3.30)$$

where V_{sl} is the QSS interface velocity (usually the furnace translation rate) and c_o is the far-field concentration. This boundary condition applies to long growth vessels in which a well-mixed region at the far-field boundary is isolated from the influence of the interface region. Xiao *et al.* [93] discuss issues with the validity of this boundary condition when these assumptions do not hold. The QSS segregation model can predict radial segregation, but only under conditions of no axial segregation, a significant restriction.

3.6 MODELLING EXAMPLES

We present here a number of examples taken from our research chosen to illustrate some of the finer details of crystal-growth modelling not covered in Sections 3.4 and 3.5. The first example is a model of the ribbon-to-ribbon process, a meniscus-defined growth system for producing photovoltaic silicon. This problem is used to demonstrate two constraints that are commonly applied to meniscus-defined growth systems: the wetting-angle constraint and the global-mass constraint. The next examples are axisymmetric and three-dimensional models of vertical Bridgman systems for growth of cadmium zinc telluride. One is a study of accelerated crucible rotation, a three-dimensional axisymmetric problem that has three velocity components but that requires discretization in only two space dimensions. In the other we couple a global furnace model, solved using CrysVUN, to a three-dimensional model of melt convection to study various situations in which a vertical Bridgman system can deviate from axisymmetric behavior. The final example illustrates an approach that combines macroscale transport modelling with mesoscale simulation of crystal morphology to study step-train dynamics in layer-by-layer growth of KTP.

3.6.1 Float-zone refinement of silicon sheets

The ‘ribbon-to-ribbon’ (RTR) process for sheet growth of silicon [94] is a method used to produce low-cost silicon for photovoltaic applications. The method is illustrated schematically in Fig. 3.6a. A polycrystalline film is scanned by a laser or other focused heat source to form a narrow molten zone, behind which a large-grained silicon crystal is grown. The RTR process bears a strong resemblance to the float-zone process for refinement of cylindrical ingots [9]. The key difference is that the RTR melt zone is two orders of magnitude

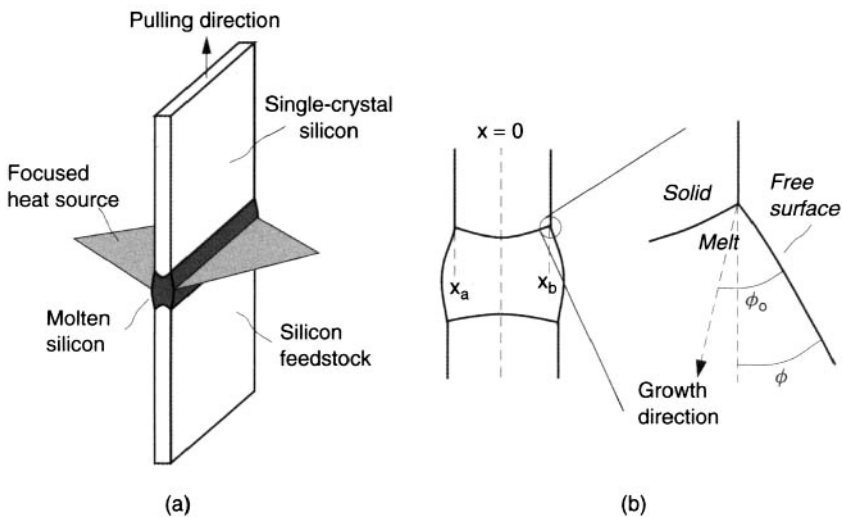


Figure 3.6 Ribbon-to-ribbon process: (a) schematic; (b) growth angles and wetting-line locations under dynamic conditions. (Reprinted from Yeckel *et al.*, *J. Cryst. Growth* **135** (1995) 51, copyright (1995) with permission from Elsevier Science)

smaller than in float-zone growth, due to which gravitational effects are greatly reduced and meniscus shape is controlled by capillary forces. From a modelling standpoint the RTR process also shares important features of Czochralski modelling as discussed below. We describe here a model of RTR growth developed by Yeckel *et al.* [95], focusing on key model-formulation issues that are common to meniscus-defined growth systems. A similar model has also been developed by Lan [96, 97]) to simulate float-zone growth of tube crystals.

It is easiest to solve this problem in a reference frame that is fixed with respect to the heater. The melt is nearly stationary in this frame, which avoids numerical difficulties that can arise if the melt moves a large distance through the computational domain. Equations (3.1)–(3.3) are solved subject to Equations (3.5), (3.7), (3.9), and (3.17) applied at solid/liquid interfaces and Equations (3.6) and (3.8) applied at liquid/gas interfaces. Equation (3.10) is applied to the external domain boundaries to account for the application of an external heating source (an ideal heat source with a Gaussian power distribution is used and thermal conditions at the ends of the sheet are obtained by matching to a one-dimensional far-field analytical solution as described in [95]). It is important to recognize that Equations (3.2) and (3.3) must include convective transport in the feed and crystal to account for motion of the sheet in the computational reference frame, even though these are solid materials without flow. Hence within these materials a uniform convective velocity, $\mathbf{v} = V_T \mathbf{e}_y$, must be imposed. Care must also be exercised to take account of sheet motion when applying boundary conditions to the solid/liquid and liquid/gas interfaces. Velocity boundary conditions at solid/liquid interfaces are given by Equations (3.5) and (3.7) with $\mathbf{V}_b = V_T \mathbf{e}_y$ and at liquid/gas interfaces by Equation (3.6) with $\mathbf{V}_b = V_T \mathbf{e}_y + \dot{\mathbf{x}}$, where $\dot{\mathbf{x}}$ is the velocity of the interface in the computational reference frame.⁹ The velocity of the growth interface \mathbf{V}_{sl} used in Equations (3.7) and (3.9) is defined with respect to a reference frame attached to the crystal and so is given by $\mathbf{V}_{sl} = -V_T \mathbf{e}_y + \dot{\mathbf{x}}$.

The equations just described are insufficient to completely define the model. Additional constraints are needed to determine the locations at which the melt attaches to the feed and crystal (i.e. the locations at which the solid/liquid interfaces intersect the liquid/gas interfaces). Since dewetting of the melt is tantamount to process failure it is generally assumed that the liquid/gas interfaces are pinned at the corners of the feed and the crystal, as shown in Fig. 3.6b. The geometry of the feed is fixed and known, so the pinning locations at the solid/liquid interface between feed and melt will be determined entirely by the melting-point isotherm (Equation (3.17)). The situation is more complicated at the other interface: here the melt resolidifies to form a crystal the precise thickness and position of which is unknown *a priori*. Therefore it is necessary to introduce the lateral positions x_a and x_b defined in Fig. 3.6b as unknowns, the values of which are to be determined as part of the solution. To establish these values it is necessary to add two constraints to the model. The formulation of these constraints is based on the observation that crystallization from the melt occurs in a preferred direction at the solid–liquid–gas trijunction. As shown in the figure, growth occurs at an angle ϕ_0 with respect to the tangent of the liquid/gas interface at the pinning location. Thus we can write that the

⁹ The correctness of these boundary conditions may be easier to see by making the substitution $\mathbf{v} = V_T \mathbf{e}_y + \mathbf{u}$ in Equations (3.1)–(3.3) and specifying boundary conditions on \mathbf{u} rather than \mathbf{v} , i.e. in the reference frame attached to the crystal. In this case $\mathbf{V}_b = 0$ and a simpler and more recognizable form of the boundary conditions emerges.

lateral positions x_a and x_b will vary with time according to

$$\frac{dx_a}{dt} = (\mathbf{V}_{sl} \cdot \mathbf{e}_y) \tan(\phi_a - \phi_o) \quad (3.31)$$

$$\frac{dx_b}{dt} = (\mathbf{V}_{sl} \cdot \mathbf{e}_y) \tan(\phi_b - \phi_o) \quad (3.32)$$

where ϕ_a and ϕ_b are angles on either side of the sheet defined as shown in Fig. 3.6b. At steady state the crystal thickness ($x_a - x_b$) and lateral offset ($x_a + x_b$) are constant and the conditions simplify to $\phi_a = \phi_b = \phi_o$. The growth angle for silicon has been determined experimentally as approximately 11° [98]. Note that the application of this condition to the planar geometry of the RTR process is slightly different from the axisymmetric formulations for float-zone or Czochralski growth where there is only a single meniscus. In these systems only the diameter of the crystal is unknown, and therefore only a single constraint is needed.

We now arrive at a subtle point in the model formulation, common to all meniscus-defined growth processes, which is the relationship between meniscus shape, pressure, and melt volume. The Navier–Stokes equations determine pressure in the melt only to within an unspecified constant. For those flows in which pressure does not enter the problem via boundary conditions the pressure level is arbitrary and can be chosen by setting one of the pressure unknowns equal to the desired value. In the present case, however, the absolute pressure level enters the problem via Equation (3.8) at the liquid/gas interface and its value is needed to determine the shape of the interface. Until now we have said nothing about the volume of the melt, but we note that if the shape of the interface is known then the melt volume is also known. Working backwards it is easy to see that *choosing* a particular melt volume in effect sets the pressure level, by constraining the shape of the interface. This can be done by imposing a global mass constraint:

$$\rho_s A_s(t) + \rho_l A_l(t) = M \quad (3.33)$$

where A_s and A_l are the volumes of solid and liquid silicon and M is total mass. This constraint can be applied in place of Equation (3.1) for one of the pressure unknowns.

The model equations can be solved for growth at steady state by setting all time derivatives to zero and setting $\phi_a = \phi_b = \phi_o$. To determine whether a given steady-state condition can be attained it is necessary to simulate the dynamic process of start-up. The first step is to calculate an initial condition by solving the steady-state problem in which the sheet and heater are held stationary. The initial pool of molten silicon is produced by melting of the sheet without growth; hence all four wetting-line locations are determined from the known geometry of the sheet and Equations (3.31) and (3.32) are not needed. Next the dynamic equations (including Equations (3.31) and (3.32)) are integrated in time with the sheet in motion. In addition to computing the positions of the solid/liquid and liquid/gas interfaces that bound the melt, it is necessary to track the shape of the crystal as it is grown. This can be done by converting the time history of the wetting-line locations x_a and x_b to a traveling wave

$$x(y, t) = x(y - V_T \delta t, t - \delta t) \quad (3.34)$$

according to which the nodes on boundaries corresponding to the crystal/gas interface are repositioned at each time step.

The model equations are solved using the finite-element code Cats2D [30]. The Galerkin finite-element method is employed, with biquadratic basis functions on nine-node quadrilateral elements used to discretize all field variables except pressure, which is discretized using linear discontinuous pressure basis functions. The grid is controlled by elliptic grid generation, using an ALE deforming-grid technique with sharp-interface representation. Grids with up to 2016 elements and 22613 degrees of freedom were used.

Results are shown in Fig. 3.7 for simulations of nonsymmetric heating. The conditions of these simulations can be found in [95]. Figure 3.7a shows steady-state temperature isotherms and streamlines, for two different power ratios. A ratio of 2.02 means that twice as much heater power is applied to one side of the sheet as the other. Due to the conductive nature of silicon the outcome is perturbed only slightly from symmetry when using this power ratio. A ratio of 3.86 has a more dramatic effect, including a

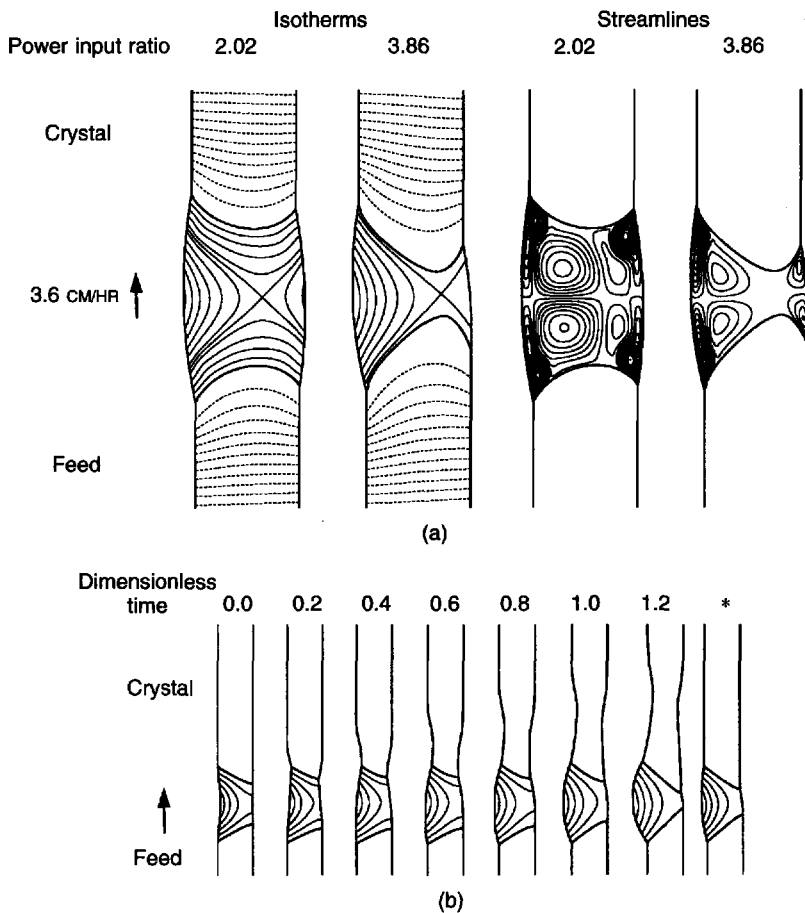


Figure 3.7 Ribbon-to-ribbon dynamics: (a) quasi-steady-state results for asymmetric heating; (b) start-up dynamics for asymmetric heating. (Reprinted from Yeckel *et al. J. Cryst. Growth* 135 (1995) 51, copyright (1995) with permission from Elsevier Science)

visible lateral offset of the crystal. Figure 3.7b shows time-dependent crystal shapes and isotherms during start-up of a process in which heating is applied to one side of the sheet only. Initially the melt contracts as shown at time $t = 0$, since the density of liquid silicon exceeds that of solid silicon at the melting temperature. With reference to Fig. 3.6b, it is easy to see that the initially convex liquid/gas interfaces will cause the crystal to grow sharply inwards. The amount of silicon solidified will be less than that melted, causing mass to accumulate in the melt. The melt expands outward until the angle between the plane of growth and plane of the melted sheet exceeds the equilibrium growth angle, which happens at approximately $t = 0.4$, after which the crystal begins to grow outward. For symmetric heating at this power a strongly damped oscillation in crystal thickness is observed and steady state is achieved within a few periods of the oscillation. For the case shown in the figure, however, the unheated side of the melt freezes over slightly after $t = 1.2$, even though a stable steady-state solution exists under these conditions (marked by an asterisk in Fig. 3.6b).

It should be emphasized again that the manner in which the growth-angle and global-mass constraints are used in this example is generic to models of meniscus-defined growth systems. The use of a moving reference frame is also typical. Thus the formulation of the governing equations for systems such as Czochralski and float-zone is very similar to that presented here.

3.6.2 Bridgman growth of CZT: axisymmetric analysis

We turn now to a confined melt-growth problem, a vertical Bridgman system for growth of cadmium zinc telluride (CZT), a semiconductor crystal used in fabrication of infrared and radiation detectors. CZT is commercially grown by the vertical Bridgman method, but it has not yet been possible to reliably produce CZT in quality and quantity sufficient for mass production of detectors. The principal obstacle to high-yield industrial production of usable CZT is formation of tellurium inclusions [99], which significantly degrade device performance. Instability of the growth interface caused by constitutional supercooling is the leading hypothesis to explain inclusions in CZT [100]. Constitutional supercooling can occur when a gradient of chemical composition exceeds a critical value at the solid/liquid interface during solidification of a compound, and is exacerbated by conditions of low thermal gradient and high growth rate.

It is generally understood that reducing compositional gradients via mixing processes can delay the onset of constitutional supercooling, thereby improving the quality of grown material and allowing higher growth rates. One of the methods used to control mixing in Bridgman growth systems is to rotate the ampoule about its axis during growth, as illustrated in Fig. 3.1a. Both steady [101, 102] and accelerated rotation [103–105] have been studied using computer modelling. Steady rotation is not favored in this situation because it tends to suppress mixing by damping convective flows in the meridional plane (the r, z plane in an r, θ, z cylindrical coordinate system). The accelerated crucible rotation technique (ACRT) [106] is preferred because it *induces* flow in the meridional plane through creation of Ekman boundary layers at solid surfaces. Usually the goal of ACRT is to enhance mixing, so as to improve interface stability and reduce radial segregation, but this goal is not necessarily achieved. ACRT can interact with buoyant forces to create unexpected effects that reduce mixing [104], as discussed below. It is also shown

that certain flow features, when present, can enhance mixing. Thus ACRT significantly increases the range of attainable growth conditions, but care must be exercised in selecting suitable rotation parameters. Computer modelling is ideally suited to explore the wide parameter space of this problem.

The analysis in this section is based on the assumption that the flow is axisymmetric, by which it is meant that all derivatives with respect to the azimuthal coordinate θ vanish. For a stationary ampoule the equations are purely two-dimensional, with only axial and radial velocity components, but under conditions of ACRT the surface of the rotating ampoule generates a third flow component in the azimuthal direction, called swirl. Flow in the meridional plane is generally much weaker than in the azimuthal direction, and is therefore referred to as *secondary* flow. Only this secondary flow is important to mixing under axisymmetric mass transport conditions.

The model equations consist of Equations (3.1)–(3.4), subject to boundary conditions given by Equations (3.5), (3.9)–(3.12) and (3.17). Although the flow is three-dimensional, it depends only on r, z space coordinates and therefore can be discretized on a two-dimensional mesh. The equations are solved using Cats2D with the same methods described in the previous section, using up to 40 734 degrees of freedom. We have studied two growth systems, distinguished primarily by size: a large system for growth of 10-cm diameter crystals [103], and a small system for growth of 1.5-cm diameter crystals [104]. Experimental data suitable for constructing a furnace temperature profile for Equation (3.10) are available for both systems. Some results of these studies are summarized here; further details can be found in [103, 104].

Figure 3.8a shows streamlines of the meridional flow induced by ACRT in the large system, at peak acceleration (left panel) and peak deceleration (right panel). At peak deceleration a Taylor–Görtler-type flow instability is triggered by rotational deceleration near the ampoule wall, as shown by the stack of toroidal vortices along the upper ampoule

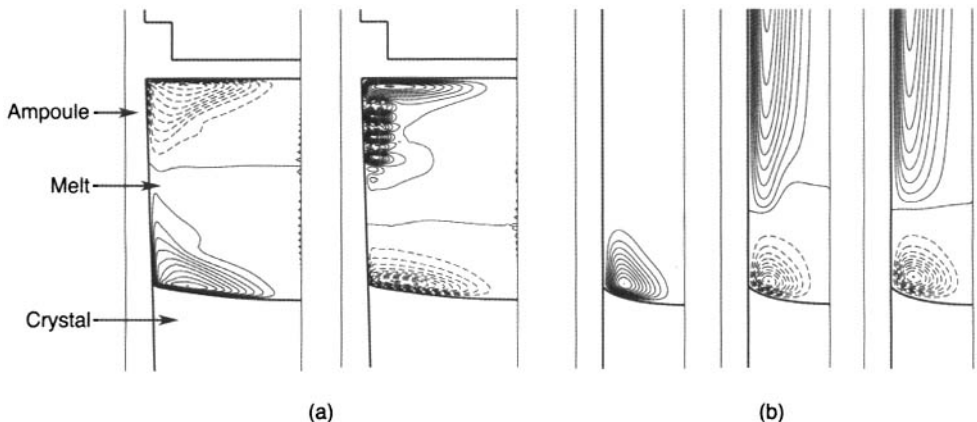


Figure 3.8 Accelerated crucible rotation technique applied to vertical Bridgman growth of cadmium zinc telluride. Streamlines in meridional (r, z) plane: (a) At peak acceleration (left panel) and peak deceleration (right panel), in a large system (10-cm diameter); (b) At peak acceleration (left panel) and intermediate and peak deceleration (middle and right panels), in a small system (1.5-cm diameter). (Reprinted from Yeckel and Derby, *J. Cryst. Growth*, **233** (2001) 599, copyright (2001) with permission from Elsevier Science)

wall. Close spacing of the streamlines show that flow in these vortices is quite strong compared to flow at peak acceleration. Another important dynamic characteristic of the flow is the axial motion of the streamline separating upper and lower flow cells. In contrast, Fig. 3.8b shows that the Taylor–Görtler instability is absent from the small system throughout deceleration (middle and right panels). Note also that the position of the separation streamline is nearly stationary (middle and right panels). Moreover, at peak acceleration in the small system, buoyant forces suppress centrifugal forces, resulting in a very weak flow over most of the ampoule for a period of time (left panel).

The flow effects just described work together to bring about excellent mixing of zinc in the large system, as shown in Fig. 3.9a. Axial motion of the separation streamline, which we refer to as Ekman pumping, allows the zinc-poor region in the lower vortex to capture zinc-rich liquid from the upper zone of the melt. Zinc-poor liquid that is carried into the upper region by Ekman pumping is mixed by the intense flow of the Taylor–Görtler instability. After 25 rotation cycles (2 h) the diffusion layer at the separation streamline has been largely eliminated and zinc concentration in the melt is nearly homogenized. Conversely, in the absence of these effects mixing is not so effective in the small system, as shown in Fig. 3.9b. After two hours (in this case equal to 120 rotation cycles¹⁰) the diffusion layer remains apparent and radial mixing at the interface is worse than in the large system.

3.6.3 Bridgman growth of CZT: three-dimensional analysis

Vertical Bridgman systems are usually designed to favor axisymmetric conditions in the ampoule, but many factors can result in three-dimensional behaviors. These can arise

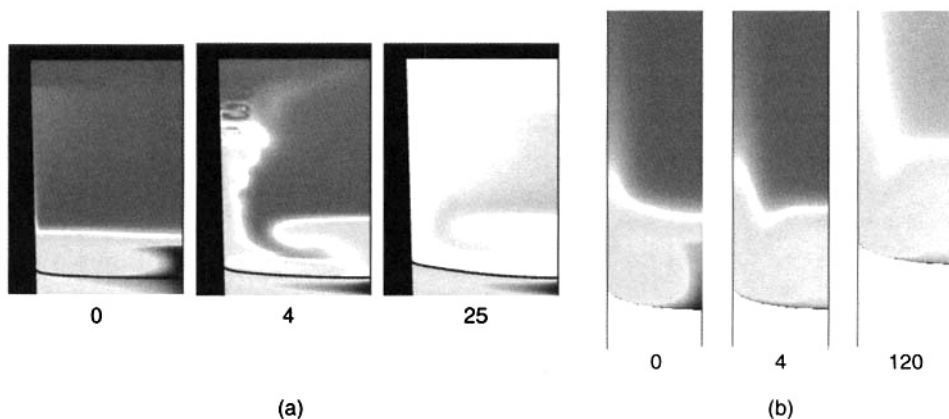


Figure 3.9 Accelerated crucible rotation technique applied to vertical Bridgman growth of cadmium zinc telluride. Zinc distribution in melt vs. number of ACRT cycles completed: (a) large system (10-cm diameter) (b) small system (1.5-cm diameter). (Reprinted from Yeckel and Derby, *J. Cryst. Growth* 233 (2001) 599, copyright (2001) with permission from Elsevier Science)

¹⁰ Optimum rotation cycle length is used in both cases to maximize secondary flow; the difference in cycle length is due to the difference in Ekman time scale [106], $\tau = L(\rho_0/\omega\mu)^{1/2}$, of the large and small systems.

from intrinsic three-dimensional fluid-mechanical instabilities due to nonlinear effects, or from extrinsic system features that violate cylindrical symmetry. We have studied several such extrinsic features, which we refer to as imperfections. These include tilting of the ampoule with respect to gravity, misalignment of the ampoule within the furnace, deviation of ampoule shape from cylindrical, and localized furnace heating [49]. A few of these results are presented here to demonstrate that seemingly minor imperfections can cause large nonaxisymmetric perturbations to radial segregation. Some of these effects have also been studied by Lan and coworkers [107, 108].

To study these effects we extend the model of the previous section to three space dimensions. A two-dimensional axisymmetric base case, in which a cylindrical ampoule is centered within an axisymmetric furnace, is the starting point for the model. We consider only the quasi-steady-state case, applying Equation (3.30) at the top of the ampoule as a far-field concentration boundary condition. A base case temperature profile, $T_c(r, z)$, is obtained using CrysVUN and used to construct a three-dimensional furnace temperature profile according to:

$$T_f(r, \phi, z) = T_c(r, z)(1 + T_{\text{global}}(r, \phi)) + T_{\text{local}}(\phi, z) \quad (3.35)$$

where T_{global} represents a perturbation due to misalignment or noncylindrical shape of the ampoule, and T_{local} represents the effect of a localized heat source (deliberately applied in an attempt to manipulate convection). For cases in which the ampoule is tilted at an angle θ with respect to vertical, the gravity vector is given by

$$\mathbf{g} = -\sin\theta \mathbf{e}_x - \cos\theta \mathbf{e}_z \quad (3.36)$$

where \mathbf{e}_z is the unit vector in the direction of the ampoule axis, and \mathbf{e}_x is a unit vector perpendicular to it ($\theta = 0$ and $\mathbf{g} = -\mathbf{e}_z$ for the base case).

Ampoule rotation at a steady rate ω is added to some of the simulations, to study its benefits in counteracting three-dimensional segregation effects. The equations are solved in a stationary coordinate system attached to the furnace, so care must be taken to note that the crystal and ampoule rotate as a solid body with convective velocity $\mathbf{v} = \omega r \mathbf{e}_\theta$. This velocity must be accounted for in conservation Equations (3.3) and (3.4), and boundary condition Equations (3.5) and (3.6). Also, the velocity of the growth interface \mathbf{V}_{sl} used in Equations (3.9) and (3.12) is given by $\mathbf{V}_{\text{sl}} = -\omega r \mathbf{e}_\theta + \dot{\mathbf{x}}$, where $\dot{\mathbf{x}}$ is the velocity of the interface in the computational reference frame.

The model equations are discretized using the Galerkin-least squares method for the Navier–Stokes equations [70], and the streamline-upwind Petrov–Galerkin method for the energy and species equations [109]. Four-noded tetrahedral elements with linear basis functions are used to represent all field variables. The discretized equations are solved using a portable MPI-based parallel implementation of preconditioned GMRES [11, 72]; more details are available in [12, 110]. A mesh consisting of 512 302 elements with a total of 632 107 degrees of freedom is used.

The two-dimensional examples previously discussed were treated using a direct solver to calculate all equations simultaneously, but for reasons related to convergence of the iterative method, we have found it more effective in our three-dimensional calculations to use a decoupled approach to determine the location of the melt/crystal interface. A procedure is used in which the governing equations are first solved on a fixed mesh, with

Equation (3.17), the melting-point isotherm condition, relaxed. To obtain an estimate of the displacement between the interface and the melting-point isotherm, we use a first-order expansion of the temperature field about the current position of the interface, obtaining:

$$\delta_z = - \left. \frac{T}{\partial T / \partial z} \right|_m \quad (3.37)$$

where δ_z is the displacement in the direction along the ampoule axis. We then solve a set of pseudosolid grid-generation equations [81], applying δ_z as a Dirichlet boundary condition at each node on the interface, to deform the mesh to conform to the estimated location of the melting-point isotherm. The procedure is repeated until δ_z is suitably small at all interface nodes. This procedure works well provided that the axial temperature gradient in the system is not very small, but use of very small gradients is generally forbidden in directional solidification systems anyway, to satisfy physical stability limitations.

Sample results of isoconcentration surfaces and pathlines for a system tilted 5° from the vertical are shown in Fig. 3.10. In a case without ampoule rotation (Fig. 3.10a), the flow is dominated by a large cell that circulates from top to bottom of the ampoule. The departure from axisymmetry is dramatic, even for a modest degree of tilt. The long vertical extent of isoconcentration surfaces indicates that the bulk is well mixed axially, but considerable nonaxisymmetric radial segregation is revealed by the simulations, with higher concentration occurring where zinc-rich material flows downward, and lower concentration occurring where zinc-depleted material flows upward. A significant degree of axisymmetry can be restored by rotating the system, however. When rotation is applied to the ampoule (in the counterclockwise direction, when viewed from above), the isoconcentration surfaces are significantly flattened (Fig. 3.10b). This effect is largely due to azimuthal averaging of mass-transport effects, due to linear superposition of a solid-body rotation on the flow in the system; note that the rotation rates studied here are too weak to significantly modify the secondary flow via nonlinear Coriolis effects.

The other system imperfections described in this section have also proven capable of causing large departures from axisymmetry, the effects of which are not easy to anticipate without use of detailed modelling as demonstrated here. The results urge caution in interpreting results of axisymmetric models and show the importance of three-dimensional transport modelling in bulk crystal growth.

3.6.4 Morphological stability in solution growth of KTP

Solution crystal growth relies on the controlled precipitation of a solute from a metastable liquid phase to a crystal mounted in the system (see Fig. 3.1c). Growth is typically sustained by continually lowering the system temperature to keep the fluid phase in a supersaturated state, even though the solute concentration level decreases with time due to the flux of molecules from the solution phase to the growing crystal. For large crystals, of the size of $\mathcal{O}(\text{cm})$ and larger, growth rates are typically limited by mass transfer through the solution phase, so some means of stirring is needed to achieve high growth rates. However, fluid flows past the three-dimensional, faceted crystals in solution-growth systems can lead to significant inhomogeneity of mass-transfer rates and surface-supersaturation levels. This inhomogeneity often leads to morphological instabilities, manifested by the formation of step bunches (macrosteps) and liquid inclusions [16, 111–114].

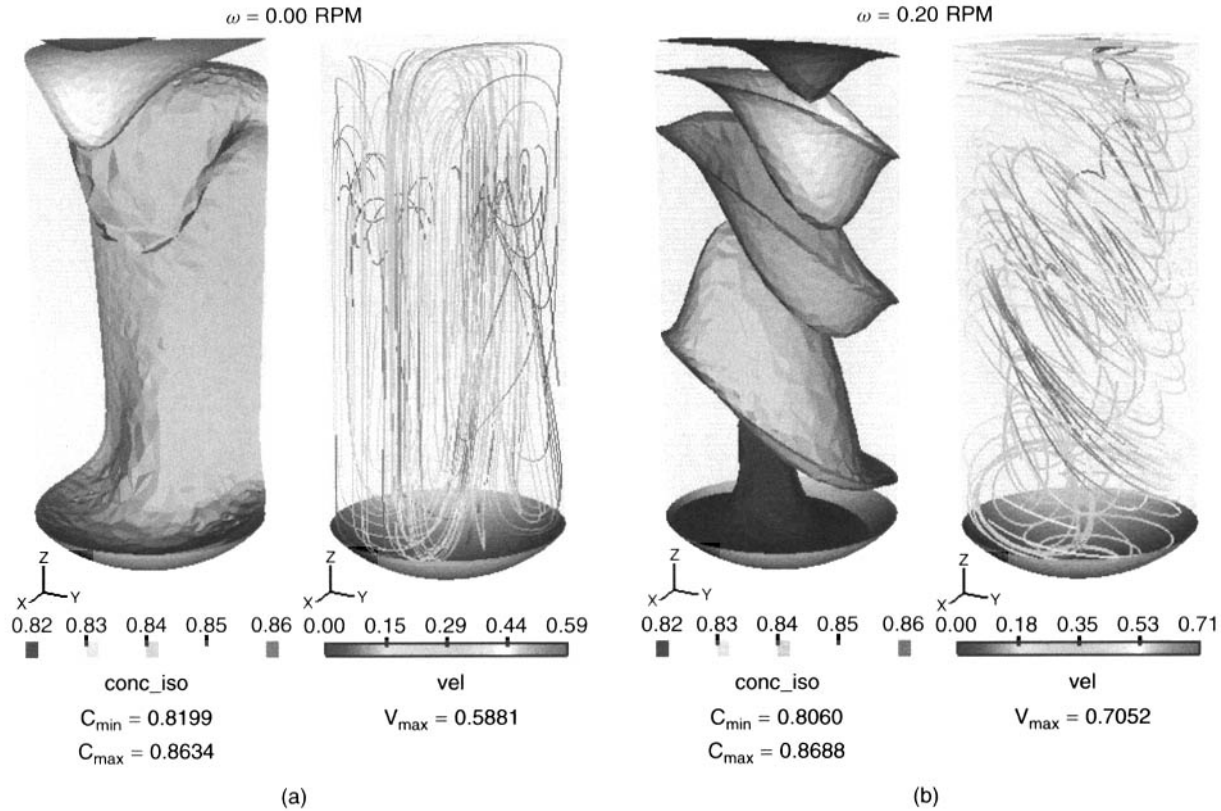


Figure 3.10 Bridgman system tilted 5° from vertical. (a) Without rotation; (b) with slow rotation at 0.2 rpm. (Reprinted from Yeckel *et al. J. Cryst. Growth* **263** (2004) 629, copyright (2004) with permission from Elsevier Science)

To better understand the dynamics of solution growth, we have modelled the system developed by Bordui *et al.* [115, 116] for the growth of potassium titanyl phosphate (KTP) from a high-temperature liquid solution phase. At the macroscopic level, flow and mass transfer are described assuming that the shape of the relatively slow-growing crystal is fixed. We solve the Navier–Stokes equations (Equations (3.1) and (3.2)) for an incompressible, isothermal fluid. The supersaturation field is evaluated by solving the convection-diffusion equation (Equation (3.4)) with suitable flux conditions applied at the surface of the growing crystal. The governing transport equations are written in a rotating, noninertial frame of reference attached to the crystal and its support to obviate the need for a moving mesh (see Section 3.4.5), and solved using the methods described in Section 3.6.3.

A specific example from our prior work [51] is shown in Fig. 3.11a, where pathlines are displayed for steady, three-dimensional flows driven by steady rotation of the crystal (rotation is counter-clockwise when viewed from above). The system is characterized by a rotational Reynolds number of $Re = 252$ and a characteristic Peclet number for mass transfer of $Pe = 8.38 \times 10^6$, where $Re \equiv \rho\omega R^2/\mu$ and $Pe \equiv \rho\omega R^2/D$ (R is the container radius). In this figure the trailing surfaces of the crystal are shown. The supersaturation level on the crystal is represented by varying shades of gray. Bulk supersaturation on a plane that cuts the crystal through the vertical symmetry plane in the longitudinal direction of flow is also shown. Thin boundary layers in concentration through the fluid near the crystal surfaces are evident, as is a depletion plume of low-concentration solution trailing behind the crystal. More results are discussed in [51, 117].

To better understand morphological instabilities in solution crystal growth, a coupled, multiscale, transport-kinetic model is needed that is sufficiently detailed to represent microscopic step growth as well as global transport. The spirit of such a model is presented in Fig. 3.11b, which depicts step motion along the crystal surface coupled with mass transport in the bulk solution above the surface. Along the surface, the mechanisms involved with step motion are depicted in Fig. 3.11c, which schematically shows a series of elementary transport and kinetic processes, starting from material transport in the bulk phase, adsorption and desorption of growth units to and from terraces between steps, followed by surface diffusion and incorporation at discrete step ledges.

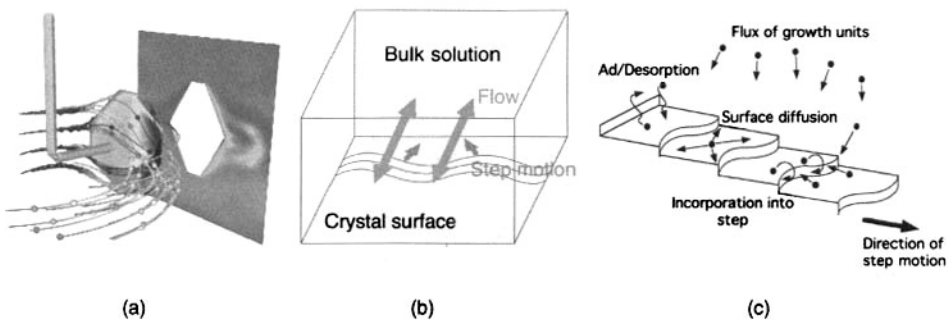


Figure 3.11 (a) Particle paths show flow around a rotating KTP crystal. Varying shades of gray on the crystal, and on the vertical symmetry plane in the longitudinal direction of flow, indicate the supersaturation level. (b) Depiction of coupled surface and bulk transport model for solution crystal growth. (c) Schematic diagram of processes involved with step growth along a vicinal surface of a crystal

This model is represented mathematically using a two-dimensional box containing liquid solution and bounded below by a one-dimensional surface comprised of steps and terraces. Mass transport in the overlying bulk phase and on the crystal surface are modelled together with step kinetics. Mass transport in the bulk phase is described by the convection-diffusion equation written in a dimensionless form for an arbitrary Lagrangian-Eulerian reference frame moving with the step-train:

$$\frac{\partial \sigma_b}{\partial t} - \mathbf{v}_{\text{ref}} \cdot \nabla \sigma_b = -\mathbf{v}_{\text{sol}} \cdot \nabla \sigma_b + \text{Pe}^{-1} \nabla^2 \sigma_b \quad (3.38)$$

where the dimensionless solutal Peclet number is $\text{Pe} = UW/D_b$ with U as the maximum solution velocity in the system, W as the total width of the solution box, and D_b as the bulk diffusivity. The quantities \mathbf{v}_{ref} and \mathbf{v}_{sol} are, respectively, the reference frame and mass average solution velocities. Bulk and surface supersaturations, $\sigma_b = \frac{c - c_e}{c_e}$ and $\sigma_s = \frac{n - n_e}{n_e}$, are defined in terms of c and n , the bulk and surface concentrations per volume and area, respectively, with the subscript e denoting the equilibrium concentration.

Mass transport on the crystal terraces is described by a surface-diffusion equation with explicit adsorption and desorption terms, nondimensionalized with characteristic length and time scales that are consistent with Equation (3.38):

$$\frac{\partial \sigma_s}{\partial t} - \mathbf{v}_{\text{ref}} \cdot \nabla_s \sigma_s = \gamma \text{Pe}^{-1} \left[\nabla_s \cdot \frac{\nabla_s \sigma_s}{1 - \alpha M_1 (\sigma_s + 1)} + L_1^{-2} (\sigma_b^{\text{int}} - \sigma_s) \right] \quad (3.39)$$

where the dimensionless parameter γ is D_s/D_b , the ratio of surface to bulk diffusivities, and α is the adsorption equilibrium constant, defined as $k_{\text{ads}}/k_{\text{des}}$, where k_{ads} and k_{des} are, respectively, the adsorption and desorption rate constants. The surface gradient operator is denoted as ∇_s and σ_b^{int} denotes the bulk supersaturation at the solution/crystal interface. The dimensionless mass parameter M_1 is defined as c_e/ρ_s , with ρ_s as the solution density, and the length parameter L_1 is defined as λ_s/W , with λ_s as the surface diffusion length. In obtaining Equation (3.39), we assume an adsorption layer with a constant density of $\rho_s h$ and a surface equilibrium concentration of $\alpha c_e h$, where h is the height of a step ledge.

Mass balance across the solution/crystal interface at every point on the surface other than a step leads to a boundary condition for Equation (3.38) that simply states that the net flux across the interface is the net adsorption minus the desorption rates:

$$-\frac{\mathbf{n} \cdot \nabla \sigma_b^{\text{int}}}{1 - M_1 (\sigma_b^{\text{int}} + 1)} = \frac{\alpha \gamma L_2}{L_1^2} (\sigma_b^{\text{int}} - \sigma_s) \quad (3.40)$$

where \mathbf{n} is a unit outward normal vector, and L_2 is a dimensionless length parameter defined as h/W .

The motion of individual growth steps is described using a linear kinetic law with asymmetric step kinetics at either side of a step ledge, as well as the direct incorporation from the bulk solution. The dimensionless velocity of the i th step in a train of n steps is written as:

$$u_{\text{step},i} = \text{Pe}^{-1} \left(\frac{\gamma \text{Da}_s^+}{L_1} \sigma_{s,i}^+ + \frac{\gamma \text{Da}_s^-}{L_1} \sigma_{s,i}^- + \text{Da}_b \sigma_{b,i}^{\text{int}} \right), \quad i = 1, \dots, n \quad (3.41)$$

where the surface Damköhler number is $Da_s = k_s \lambda_s / D_s$, with k_s as the step kinetic coefficient. Similarly, the bulk Damköhler number is $Da_b = k_b W / D_b$, which represents the relative rate of direct bulk incorporation versus bulk diffusion. The superscripts + and – denote, respectively, the corresponding values at the front and back of a step ledge.

A mass balance is performed around a growth step to yield additional boundary conditions for Equations (3.38) and (3.39). The boundary condition for direct incorporation, for attachment from the bulk solution directly to a step ledge, is approximated as:

$$-\frac{\mathbf{n} \cdot \nabla \sigma_{b,i}^{\text{int}}}{1 - M_1(\sigma_{b,i}^{\text{int}} + 1)} = \frac{Da_b}{M_2} \sigma_{b,i}^{\text{int}}, \quad i = 1, \dots, n \quad (3.42)$$

where the mass-fraction parameter M_2 is defined as c_e / ρ_c , with ρ_c as the crystal density. Currently, in our initial model development, this material flux is approximated as a one-dimensional flux in a direction normal to the crystal surface over a surface length of h , or the height of a step ledge. Similarly, the surface diffusional fluxes at either sides of the step ledge are written as:

$$-\frac{\mathbf{t}_s \cdot \nabla_s \sigma_{s,i}^{\pm}}{1 - \alpha M_1(\sigma_{s,i}^{\pm} + 1)} = \frac{Da_s^{\pm}}{\alpha L_1 M_2} \sigma_{s,i}^{\pm} \mp \frac{Pe}{\gamma} u_{\text{step},i}(\sigma_{s,i}^{\pm} + 1), \quad i = 1, \dots, n \quad (3.43)$$

where \mathbf{t}_s denotes a unit tangent vector pointing along the surface toward the step and, again, the superscripts + and – denote, respectively, the corresponding values at the front and back sides of a step ledge. The second term in the right-hand side of Equation (3.43) represents the convective-flux contribution due to step motion.

To complete the specification of the problem, we apply a constant value of supersaturation along the top of the bulk domain that is consistent with mass transfer from the far field. Along the sides of the domain, we impose symmetry boundary conditions. Finally, Equations (3.38)–(3.43) are solved simultaneously by an efficient moving-boundary finite-element method.

A sample result from this step-growth model is shown in Fig. 3.12. These computations are for a model system representing an inorganic crystal, such as KTP, where bulk incorporation effects are dominant. Initially, a steady-state solution for an evenly spaced train of 51 steps is computed for no-flow conditions. Then the step spacing is randomly perturbed, a fluid flow is applied either counter to or in the same direction as the step motion, and the system is integrated in time. Figure 3.12a shows the width of a selected terrace as a function of time. Under a fluid flow counter to the direction of step motion, the terrace width eventually approaches its original value and the train of steps is stabilized. For a fluid flow in the same direction of step motion, the initial disturbance first seems to die away but then rapidly grows, as indicated in Fig. 3.12b. Figure 3.12c shows steps at the bottom of the domain underlying the liquid solution above at the final time of the computation. A step bunch of about ten steps clustered closely together is evident in the middle of the crystal surface. The supersaturation in the bulk phase is lowest above the step bunch and higher away from it. The mechanism behind these behaviors is the effect of flow on shifting lateral variations in the supersaturation to be in or out of phase with the distribution of steps along the crystal surface. This mechanism was postulated by the linear stability analyses of Chernov, Corriel, and others [118, 119]. However, as indicated by the temporal behavior in Figure 3.12b, the behavior of this system is quite nonlinear.

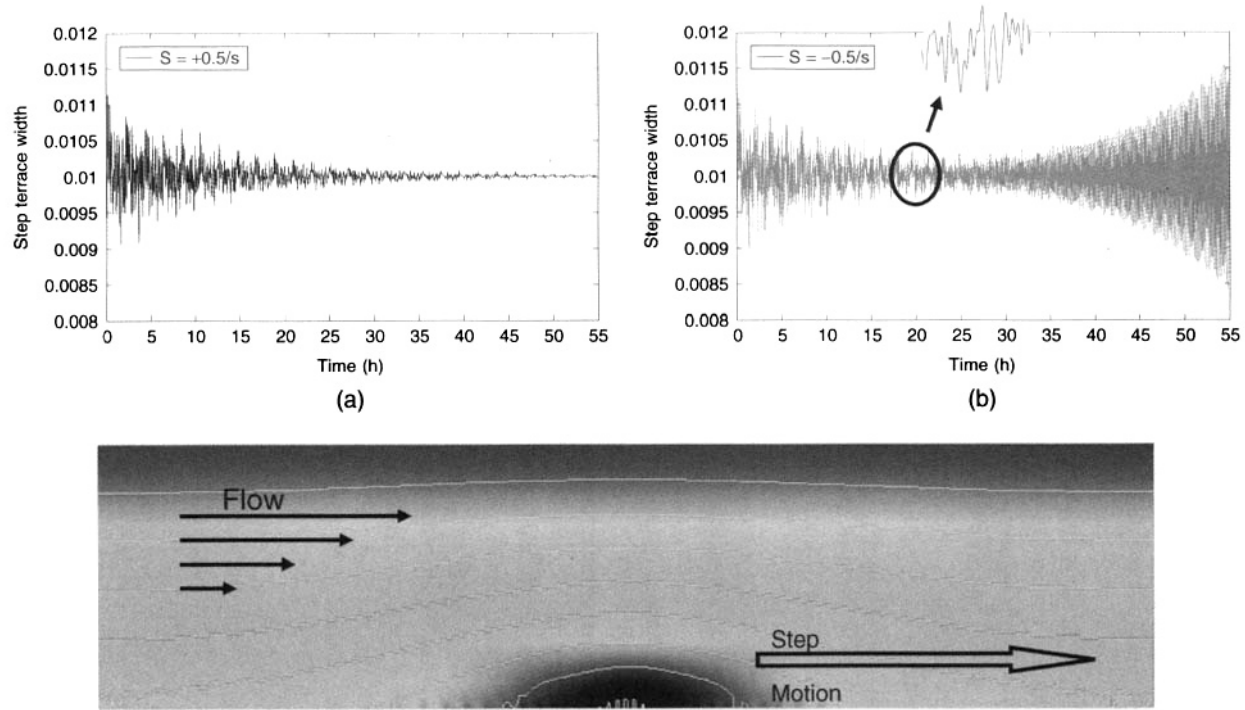


Figure 3.12 The behavior of steps along a vicinal surface in a solution-growth system. A terrace width in the system is tracked with time for an initially perturbed system with a flow (b) counter to the direction and (a) in the same direction of step motion. (c) Supersaturation in the bulk corresponds with a step bunch along the crystal surface (bottom center)

3.7 SUMMARY AND OUTLOOK

The equations governing macroscopic transport phenomena given in Tables 3.2 and 3.3 are firmly established and well understood, excepting turbulence phenomena. The use of these equations to solve problems in melt and solution crystal growth has been illustrated in Section 3.6, using models of representative crystal-growth systems as examples. These continuum transport models can describe the spatial variation of temperature, flow, and chemical composition, and in some cases can predict the macroscopic shape of the interface, but are subject to uncertainty from a number of causes. Perhaps the greatest degree of uncertainty arises from the lack of accurate thermophysical property measurements for many systems, particularly data on high-temperature phase equilibria. Three-dimensional effects in systems modeled as axisymmetric also introduce uncertainty; in Section 3.6.3 we demonstrate that small perturbations to an axisymmetric melt growth system can cause significant three-dimensional effects in mass convection. Another common source of uncertainty is the neglect or oversimplification of radiation heat transfer, which can restrict the model to qualitative predictions. These sources of uncertainty are well defined and the subject of steady improvement in model development. Quantitative furnace modelling has become more common, facilitated by commercial software specialized to this purpose, as discussed in Section 3.4.4. Three-dimensional calculations such as those shown in Sections 3.6.3 and 3.6.4 are not entirely routine, but may soon be so, particularly with breakthroughs in methods to solve large systems of linear equations.

Discretizing or tracking the interface is central to computer modelling of bulk crystal growth. Methods for this purpose exist in such great variety that it is not entirely clear how best to organize and classify them. It is important to identify whether a method is diffuse or sharp, but this characterization is incomplete and perhaps misleading, since as noted in Section 3.5.2, the sharp-interface model can take on characteristics of a diffuse model when discretized, particularly when using fixed-grid methods. Other schemes are possible. In a review of numerical methods in phase-change problems, Idelsohn *et al.* [120] classify methods as either 'front-tracking' or 'fixed-domain' types. In this scheme, fixed-domain types include implicit fixed-grid methods such as phase-field and enthalpy, and front-tracking types include all explicit methods, both on fixed and deforming grids. We prefer a scheme that does not mix fixed- and deforming-grid methods, as is done with the front-tracking classification, because fixed-grid methods are quite different from deforming-grid methods in terms of discretization and implementation. Hence the scheme used here is to make fixed vs. deforming the primary characterization, with explicit (i.e. front tracking) vs. implicit (i.e. fixed domain), and diffuse vs. sharp, used as secondary characterizations. We compare fixed- and deforming-grid methods in Section 3.5.2, using examples based on a sharp-interface model of melt growth. Deforming-grid methods are more accurate than fixed-grid methods (second vs. first order), but can be applied only under a limited range of circumstances. Fixed-grid methods are more flexible, and their use is mandatory under any of the conditions illustrated in Fig. 3.3. Fixed-grid methods have been used to simulate extremely complicated interface shapes, for example phase-field models of dendrite growth [121, 122], but these calculations require complicated adaptive grid methods to circumvent the need for excessive grid refinement.

The models presented here have been largely restricted to a purely macroscopic characterization of the interface shape. In the melt-growth models we have assumed that directional solidification occurs without kinetic limitation, in which case the melting-point

isotherm condition is valid. In the solution-growth model we have used the known growth habit of KTP to prescribe a boundary shape characteristic of an intermediate stage during growth. The major shortcoming of these models is that for the most part they cannot predict growth morphology or microstructure. Recently, a number of efforts have been made to forge a better connection between growth morphology and macroscopic transport. One example is the coupling of a mesoscale model of step flow to a macroscale model of transport for solution growth of KTP, discussed in Section 3.6.4. Other examples are the incorporation of faceting by Brandon *et al.* [1, 3, 4] and Lan and Tu [2] in models of melt crystal growth. Perhaps the most comprehensive model to date is that of Dornberger and Sinno *et al.* [7, 8], which couples a state-of-the-art global transport model with a model of point-defect generation and transport for industrial production of bulk silicon by Czochralski growth. Nevertheless, our present understanding of the connection between macroscopic transport models and crystal structure remains simplistic and incomplete, mostly relying on heuristic or semitheoretical relationships that relate defect formation to interface shape and temperature field. Predicting growth morphology and microscopic defects remains a formidable task, but making this connection lies at the heart of crystal-growth modelling, and thus will remain a principal focus both in terms of theory and numerical practice.

ACKNOWLEDGMENTS

The authors' research programs in crystal-growth modelling have been supported in part by Johnson Matthey Electronics (IRMP, Defense Advanced Research Projects Agency), Lawrence Livermore National Laboratory, the National Aeronautics and Space Administration (Microgravity Materials Science), the National Science Foundation, Sandia National Laboratories, the U.S. Civilian Research and Development Foundation, the University of Minnesota Supercomputing Institute, and the Army High Performance Computing Research Center under the auspices of the Department of the Army, Army Research Laboratory cooperative agreement DAAH04-95-2-0003/contract DAAH04-95-C-0008, the content of which does not necessarily reflect the position or policy of the government, and no official endorsement should be inferred. The authors extend thanks to R.T. Goodwin, J.M. de Santos, H. Zhou, Y.-I. Kwon, B. Vartak, A. Pandey, P. Sonda, B. Dai, and G. Compère for contributions to the research discussed here.

REFERENCES

- [1] Y. Liu, A. Virozub, and S. Brandon. (1999) Facetting during directional growth of oxides from the melt: coupling between thermal fields, kinetics and melt/crystal interface shapes. *J. Cryst. Growth*, **205**:333.
- [2] C.W. Lan and C.Y. Tu. (2001) Three-dimensional simulation of facet formation and the coupled heat flow and segregation in Bridgman growth of oxide crystals. *J. Cryst. Growth*, **233**:523.
- [3] A. Virozub and S. Brandon. (2002) Selecting Finite Element basis functions for computation of large facet formation during the melt growth of single crystals. *Modell. Simul. Mater. Sci. Eng.*, **10**:57.

- [4] S. Brandon, A. Virozub, and Y. Liu. (2003) Interface-kinetics-driven facet formation during melt growth of oxide crystals. In H.J. Scheel and T. Fukuda, editors, *Crystal Growth Technology*, Chapter 3. John Wiley & Sons, West Sussex, UK.
- [5] H. Lin, R.G. Vekilov, and F. Rosenberger. (1996) Facet morphology response to nonuniformities in nutrient and impurity supply. II. Numerical simulations. *J. Cryst. Growth*, **158**:552.
- [6] Y.-I. Kwon and J.J. Derby. (2001) Modeling the coupled effects of interfacial and bulk phenomena during solution crystal growth. *J. Cryst. Growth*, **230**:328.
- [7] E. Dornberger, W. von Ammon, J. Virbulis, B. Hanna, and T. Sinno. (2001) Modeling of transient point defect dynamics in Czochralski silicon crystals. *J. Cryst. Growth*, **230**:291.
- [8] T. Sinno, E. Dornberger, W. von Ammon, R.A. Brown, and F. Dupret. (2002) Defect engineering of Czochralski single-crystal silicon. *Mater. Sci. Eng. Rep.*, **28**:149.
- [9] R.A. Brown. (1988) Theory of transport processes in single crystal growth from the melt. *AIChE J.*, **34**:881.
- [10] A. Yeckel, J.W. Smith, and J.J. Derby. (1997) Parallel finite element calculation of flow in a three-dimensional lid-driven cavity, using the CM-5 and T3D. *Int. J. Numer. Methods Fluids*, **24**:1449.
- [11] Y. Saad. (1996) *Iterative Methods for Sparse Linear Systems*. PWS Publishing Company, Boston.
- [12] A.G. Salinger, Q. Xiao, Y. Zhou, and J.J. Derby. (1994) Massively parallel finite element computations of three-dimensional, time-dependent, incompressible flows in materials processing systems. *Comput. Methods Appl. Mech. Eng.*, **119**:139.
- [13] M. Benzi. (2002) Preconditioning techniques for large linear systems: A survey. *J. Comput. Phys.*, **182**:418.
- [14] G. de Vahl Davis and E. Leonardi. (2000) Crystal growth by travelling heater method in microgravity. In *Modelling of Transport Phenomena in Crystal Growth*, volume 6 of *Developments in Heat Transfer*, Chapter 5. WIT Press, Southampton, England.
- [15] M.V. Bogdanov, S.E. Demina, S.Yu. Karpov, A.V. Kulik, M.S. Ramm, and Yu.N. Makarov. (2003) Advances in modeling of wide-bandgap bulk crystal growth. *J. Cryst. Growth*, **38**:237.
- [16] P.F. Bordui and S. Motakef. (1989) Hydrodynamic control of solution inclusion during crystal growth of KTiOPO_4 (KTP) from high-temperature solution. *J. Cryst. Growth*, **96**:405.
- [17] D. Maroudas. (2003) Multiscale modeling: Status and opportunities in research and education. *AIChE Annual Meeting*, San Francisco, CA, November 16–21.
- [18] R.B. Bird, W.E. Stewart, and E.N. Lightfoot. (1960) *Transport Phenomena*. John Wiley, New York.
- [19] J.S. Szmyd and K. Suzuki, editors. (2000) *Modelling of Transport Phenomena in Crystal Growth*, volume 6 of *Developments in Heat Transfer*. WIT Press, Southampton, England.
- [20] J.J. Derby. (1995) Macroscopic transport processes during the growth of single crystals from the melt. In J.P. van der Eerden and O.S.L. Bruinsma, editors, *Science and Technology of Crystal Growth*, page p. 97. Kluwer Academic Publishers, Dordrecht, The Netherlands.
- [21] G. Müller and A. Ostrogorsky. (1994) Convection in melt growth. In D.T.J. Hurle, editor, *Bulk Crystal Growth, Growth Mechanisms and Dynamics, Handbook of Crystal Growth Vol. 2b*, page 708. North-Holland, Amsterdam.
- [22] A. Yeckel and J.J. Derby. (2003) Computational simulations of the growth of crystals from liquids. In H.J. Scheel and T. Fukuda, editors, *Crystal Growth Technology*, Chapter 6. John Wiley & Sons, West Sussex, UK.
- [23] V.I. Polezhaev. (2003) Modeling of technologically important hydrodynamics and heat/mass transfer processes during crystal growth. In H.J. Scheel and T. Fukuda, editors, *Crystal Growth Technology*, Chapter 8. John Wiley & Sons, West Sussex, UK.
- [24] K. Kakimoto. (2003) Heat and mass transfer under magnetic fields. In H.J. Scheel and T. Fukuda, editors, *Crystal Growth Technology*, Chapter 7. John Wiley & Sons, West Sussex, UK.

- [25] C.W. Lan. (2004) Recent progress of crystal growth modeling and growth control. *Chem. Eng. Sci.*, **59**:1437.
- [26] F. Dupret, J.J. Derby, K. Kakimoto, G. Müller, N. Van Den Bogaert, and A.A. Wheeler, editors. (1997) *Proceedings of the Second International Workshop on Modelling in Crystal Growth*, volume 180 of *J. Cryst. Growth*. Elsevier.
- [27] A. Yeckel, V. Prasad, and J.J. Derby, editors. (2000) *Proceedings of the Third International Workshop on Modelling in Crystal Growth*, volume 230 of *J. Cryst. Growth*. Elsevier.
- [28] C.W. Lan, editor. (2004) *Proceedings of the Fourth International Workshop on Modelling in Crystal Growth*, *J. Cryst. Growth*, **266**.
- [29] J.J. Derby, N. Ponde, V.F. de Almeida, and A. Yeckel. (2000) Modeling segregation and convection during the growth of ternary alloys under terrestrial and microgravity conditions. In A. Ródsz, M. Rettenmayr, and D. Watring, editors, *Solidification and Gravity 2000*, volume 329–330 of *Mater. Sci. Forum*, page 93. Trans Tech Publications Ltd, Zurich.
- [30] A. Yeckel and R.T. Goodwin. (2003) Cats2D (Crystallization and Transport Simulator), User Manual. Unpublished (available at <http://www.msi.umn.edu/~yeckel/cats2d.html>).
- [31] C.W. Lan. (2001) Effects of centrifugal acceleration on flows and segregation in vertical Bridgman crystal growth. *J. Cryst. Growth*, **229**:595.
- [32] H. Lee and A.J. Pearlstein. (2002) Effect of steady ampoule rotation on radial dopant segregation in vertical Bridgman growth of GaSe. *J. Cryst. Growth*, **240**:581.
- [33] A.D. Sneyd. (1979) Fluid flow induced by a rapidly alternating or rotating field. *J. Fluid Mech.*, **92**:35.
- [34] H. Emmerich. (2003) *The Diffuse Interface Approach in Materials Science: Thermodynamic Concepts and Applications of Phase-Field Models*. Springer-Verlag, Heidelberg.
- [35] L.J. Atherton, J.J. Derby, and R.A. Brown. (1987) Radiative heat exchange in Czochralski crystal growth. *J. Cryst. Growth*, **84**:57.
- [36] S. Brandon and J.J. Derby. (1992) A finite element method for conduction, internal radiation, and solidification in a finite axisymmetric enclosure. *Int. J. Num. Meth. Heat Fluid Flow*, **2**:299.
- [37] S. Kuppurao and J.J. Derby. (1993) Finite element formulations for accurate calculation of radiant heat transfer in diffuse-gray enclosures. *Numer. Heat Transfer, Part B: Fundamentals*, **24**:431.
- [38] R.A. Brown, T.A. Kinney, P.A. Sackinger, and D.E. Borside. (1989) Toward an integrated model in Czochralski growth. *J. Cryst. Growth*, **97**:99.
- [39] D.E. Borside, T.A. Kinney, R.A. Brown, G. Kim, J. Stenzenberger, and B. Weinert. (1990) Finite element/Newton method for the analysis of Czochralski crystal growth with diffuse-grey radiative heat transfer. *Int. J. Numer. Methods Eng.*, **30**:133.
- [40] F. Dupret, P. Nicodème, Y. Ryckmans, P. Wouters, and M.J. Crochet. (1990) Global modelling of heat transfer in crystal growth furnaces. *Int. J. Heat Mass Transfer*, **33**:1849.
- [41] M. Kurz, A. Pusztai, and G. Müller. (1999) Development of a new powerful computer code CrysVUN++ especially designed for fast simulation of bulk crystal growth processes. *J. Cryst. Growth*, **198**:101.
- [42] R. Backofen, M. Kurz, and G. Müller. (2000) Process modelling of the industrial VGF crystal growth process using the software package CrysVUN++. *J. Cryst. Growth*, **199**:210.
- [43] E. Dornberger, E. Tomzig, A. Seidl, S. Schmitt, H.-J. Leister, Ch. Schmitt, and G. Müller. (1997) Thermal simulation of the Czochralski silicon growth process by three different models and comparison with experimental results. *J. Cryst. Growth*, **180**:461.
- [44] A. Yeckel, A. Pandey, and J.J. Derby. (2001) Representing realistic complexity in numerical models of crystal growth: Coupling of global furnace modeling to three-dimensional flows. In G. De Vahl Davis and E. Leonardi, editors, *Advances in Computational Heat Transfer II*, pages 1193–1200. New York Academy of Sciences.
- [45] J.J. Derby, P. Daoutidis, Y.-I. Kwon, A. Pandey, P. Sonda, B. Vartak, A. Yeckel, M. Hainke, and G. Müller. (2003) High-performance-computing, multi-scale models for crystal growth

- systems. In M. Breuer, F. Durst, and C. Zenger, editors, *High Performance Scientific and Engineering Computing*, Lecture Notes in Computational Science and Engineering. Springer Verlag, Berlin.
- [46] I.Yu. Evstratov, V.V. Kalaev, A.I. Zhmakin, Yu.N. Makarov, A.G. Abramov, N.G. Ivanov, E.M. Smirnov, E. Dornberger, J. Virbulis, E. Tomzig, and W.v. Ammon. (2001) Modeling analysis of unsteady three-dimensional turbulent melt flow during Czochralski growth of Si crystals. *J. Cryst. Growth*, **230**:22.
- [47] J. Virbulis, Th. Wetzel, A. Muiznieks, B. Hanna, E. Dornberger, E. Tomzig, A. Mühlbauer, and W.v. Ammon. (2001) Numerical investigation of silicon melt flow in large diameter CZ-crystal growth under the influence of steady and dynamic magnetic fields. *J. Cryst. Growth*, **230**:92.
- [48] W. Miller and W. Schröder. (2001) Numerical modeling at the IKZ: an overview and outlook. *J. Cryst. Growth*, **230**:1.
- [49] A. Yeckel, G. Compère, A. Pandey, and J.J. Derby. (2004) Three-dimensional imperfections in a model vertical Bridgman growth system for cadmium zinc telluride. *J. Cryst. Growth*, **263**:629.
- [50] A. Yeckel, Y. Zhou, M. Dennis, and J.J. Derby. (1998) Three-dimensional computations of solution hydrodynamics during the growth of potassium dihydrogen phosphate II. Spin down. *J. Cryst. Growth*, **191**:206.
- [51] B. Vartak, Y.-I. Kwon, A. Yeckel, and J.J. Derby. (2000) Fluid flow and mass transport during solution growth of potassium titanyl phosphate (KTP): I. Steady rotation. *J. Cryst. Growth*, **210**:704.
- [52] P.A. Davidson. (1999) Magnetohydrodynamics in materials processing. *Annu. Rev. Fluid Mech.*, **31**:273.
- [53] N. Ma and J.S. Walker. (1996) Magnetic damping of buoyant convection during semiconductor crystal growth in microgravity. Continuous random g-jitters. *Phys. Fluids*, **8**:944.
- [54] C.W. Lan, I.F. Lee, and B.C. Yeh. (2003) Three-dimensional simulation of dopant segregation in vertical Bridgman crystal growth under axial and transversal magnetic fields. *J. Cryst. Growth*, **254**:503.
- [55] A. Yeckel and J.J. Derby. (2004) Dynamics of three-dimensional convection in microgravity crystal growth: g-jitter with steady magnetic fields. *J. Cryst. Growth*, **263**:40. (Erratum—*J. Cryst. Growth*, **267**:751)
- [56] R.U. Barz, G. Gerbeth, U. Wunderwald, E. Buhrig, and Yu.M. Gelfgat. (1997) Modelling of the isothermal melt flow due to rotating magnetic fields in crystal growth. *J. Cryst. Growth*, **180**:410.
- [57] N. Ma, D.F. Bliss, and G.W. Iseler. (2003) Vertical gradient freezing of doped gallium-antimonide semiconductor crystals using submerged heater growth and electromagnetic stirring. *J. Cryst. Growth*, **259**:26.
- [58] H.F. Robey and D. Maynes. (2001) Numerical simulation of the hydrodynamics and mass transfer in the large scale, rapid growth of KDP crystals. Part 1: Computation of the transient, three-dimensional flow field. *J. Cryst. Growth*, **222**:263.
- [59] H.F. Robey. (2003) Numerical simulation of the hydrodynamics and mass transfer in the large scale, rapid growth of KDP crystals—2: computation of the mass transfer. *J. Cryst. Growth*, **259**:388.
- [60] A. Lipchin and R.A. Brown. (1999) Comparison of three turbulence models for simulation of melt convection in Czochralski crystal growth of silicon. *J. Cryst. Growth*, **205**:71.
- [61] V.V. Kalaev, I.Yu. Evstratov, and Yu.N. Makarov. (2003) Gas flow effect on global heat transport and melt convection in Czochralski silicon growth. *J. Cryst. Growth*, **249**:87.
- [62] A. Krauze, A. Muiznieks, A. Mühlbauer, Th. Wetzel, and W. von Ammon. (2004) Numerical 3D modelling of turbulent melt flow in large CZ system with horizontal DC magnetic field—I: flow structure analysis. *J. Cryst. Growth*, **262**:157.

- [63] V.V. Kalaev, D.P. Lukanin, V.A. Zabelin, Yu.N. Makarov, J. Virbulis, E. Dornberger, and W. von Ammon. (2003) Calculation of bulk defects in CZ Si growth: impact of melt turbulent fluctuations. *J. Cryst. Growth*, **250**:203.
- [64] N.G. Ivanov, A.B. Korsakov, E.M. Smirnov, K.V. Khodosevitch, V.V. Kalaev, Yu.N. Makarov, E. Dornberger, J. Virbulis, and W. von Ammon. (2003) Analysis of magnetic field effect on 3D melt flow in CZ Si growth. *J. Cryst. Growth*, **250**:183.
- [65] J.L. Santallier, T. Duffar, F. Théodore, P. Boiton, C. Barat, B. Angelier, N. Giacometti, P. Dusserre, and J.P. Nabot. (1997) Some features of two commercial softwares for the modeling of bulk crystal growth processes. *J. Cryst. Growth*, **180**:698.
- [66] G. Ratnieks, A. Muižnieks, and A. Mühlbauer. (2001) Numerical 3D study of FZ growth: dependence on growth parameters and melt instability. *J. Cryst. Growth*, **230**:48.
- [67] Th. Wetzel, A. Muiznieks, A. Mühlbauer, Y. Gelfgat, L. Gobunov, J. Virbulis, E. Tomzig, and W.v. Ammon. (2001) Numerical model of turbulent CZ melt flow in the presence of AC and CUSP magnetic fields and its verification in a laboratory facility. *J. Cryst. Growth*, **230**:81.
- [68] T.J.R. Hughes. (1987) *The Finite Element Method*. Prentice Hall, Englewood Cliffs, NJ.
- [69] P.M. Gresho and R.L. Sani. (1998) *Incompressible Flow and the Finite Element Method*. John Wiley and Sons, West Sussex, England.
- [70] T.J.R. Hughes, L.P. Franca, and G.M. Hulbert. (1989) A new finite element formulation for computational fluid dynamics: VIII. The Galerkin/Least-squares method for advective-diffusive equations. *Comput. Methods Appl. Mech. Eng.*, **73**:173.
- [71] P.M. Gresho, R.L. Lee, and R.L. Sani. (1980) On the time-dependent solution of the incompressible Navier-Stokes equations in two and three dimensions. In C. Taylor and K. Morgan, editors, *Recent Advances in Numerical Methods in Fluids*, volume 1, page p. 27. Pineridge Press, Ltd., Swansea, U.K.
- [72] Y. Saad and M.H. Schultz. (1986) GMRES: A generalized minimal algorithm for solving nonsymmetric linear systems. *SIAM J. Sci. Stat. Comp.*, **7**:856–869.
- [73] V.R. Voller, A.D. Brent, and C. Prakash. (1989) The modeling of heat, mass and solute transport in solidification systems. *Int. J. Heat Mass Transfer*, **32**:1719.
- [74] J.A. Sethian and P. Smereka. (2003) Level set methods for fluid interfaces. *Annu. Rev. Fluid Mech.*, **35**:341.
- [75] J. Glimm, J.W. Grove, X.L. Li, K.M. Shyue, Y. Zeng, and Q. Zhang. (1998) Three-dimensional front tracking. *SIAM J. Sci. Comput.*, **19**:703.
- [76] M.V. Bogdanov, S.E. Demina, S.Yu. Karpov, A.V. Kulik, M.S. Ramm, and Yu.N. Makarov. (1981) Volume of fluid (VOF) method for the dynamics of free boundaries. *J. Comput. Phys.*, **39**:201.
- [77] H.S. Udaykumar, R. Mittal, and W. Shyy. (1999) Computation of solid-liquid phase fronts in the sharp interface limit on fixed grids. *J. Comput. Phys.*, **153**:535.
- [78] H. Ji, D. Chopp, and J.E. Dolbow. (2002) A hybrid extended finite element/level set method for modeling phase transformations. *Int. J. Numer. Methods Eng.*, **54**:1209.
- [79] J.F. Thompson, Z.U.A. Warsi, and C.W. Mastin. (1985) *Numerical Grid Generation*. Elsevier, New York.
- [80] S.F. Kistler and L.E. Scriven. (1984) Coating flow theory by finite element and asymptotic analysis of the Navier-Stokes system. *Int. J. Num. Meth. Fluids*, **4**:207.
- [81] P.A. Sackinger, P.R. Schunk, and R.R. Rao. (1996) A Newton-Raphson pseudo-solid domain mapping technique for free and moving boundary problems: A finite element implementation. *J. Comput. Phys.*, **125**:83.
- [82] J.M. de Santos. (1991) *Two-phase cocurrent downflow through constricted passages*. PhD thesis, University of Minnesota. Available through University Microfilms, Inc. (www.umi.com).
- [83] R.T. Goodwin. (1992) University of Illinois, personal communication.

- [84] D.R. Lynch and K. O'Neill. (1981) Continuously deforming finite elements for the solution of parabolic problems, with and without phase change. *Int. J. Num. Meth. Eng.*, **17**:81.
- [85] T.J.R. Hughes, W.K. Liu, and T.K. Zimmerman. (1981) Lagrangian-Eulerian finite element formulation for incompressible viscous flows. *Comput. Meth. Appl. Mech. Eng.*, **29**:329.
- [86] K.N. Christodoulou, S.F. Kistler, and P.R. Schunk. (1997) Advances in computational methods for free-surface flows. In S.F. Kistler and P.M. Schweizer, editors, *Liquid Film Coating*, page 297, London, Chapman and Hall.
- [87] K.N. Christodoulou and L.E. Scriven. (1992) Discretization of free surface flows and other moving boundary problems. *J. Comput. Phys.*, **99**:39.
- [88] V.D. Golyshev, M.A. Gonik, and V.B. Tsvetovsky. (2002) In situ measurement of Bi(4)Ge(3)O(12) interface supercooling during melt crystal growth. *J. Cryst. Growth*, **237–239**:735.
- [89] S.V. Bykova, V.D. Golyshev, M.A. Gonik, V.B. Tsvetovsky, V.I. Deshko, A.Ya. Karvatskii, S. Brandon, O. Weinstein, A. Virozub, J.J. Derby, A. Yeckel, and P. Sonda. (2004) Experimental and numerical analysis of coupled interfacial kinetics and heat transport during the axial heat flux close to the phase interface (AHP) growth of BGO single crystals. *J. Cryst. Growth*, **266**:46.
- [90] S. Kuppurao, S. Brandon, and J.J. Derby. (1995) Modeling the vertical Bridgman growth of cadmium zinc telluride I. Quasi-steady analysis of heat transfer and convection. *J. Cryst. Growth*, **155**:93.
- [91] A. Virozub and S. Brandon. (2003) Revisiting the quasi-steady state approximation for modeling directional crystal growth, the growth rate can and should be calculated! *J. Cryst. Growth*, **254**:267.
- [92] C.J. Chang and R.A. Brown. (1983) Radial segregation induced by natural convection and melt/solid interface shape in vertical Bridgman growth. *J. Cryst. Growth*, **63**:343.
- [93] Q. Xiao, S. Kuppurao, A. Yeckel, and J.J. Derby. (1996) On the effects of ampoule tilting during vertical Bridgman growth: Three-dimensional computations via a massively parallel, finite element method. *J. Cryst. Growth*, **167**:292.
- [94] R.W. Gurtler, A. Baghdadi, R.J. Ellis, and I.A. Lesk. (1978) Silicon ribbon growth via the ribbon-to-ribbon (RTR) technique: Process update and material characterization. *J. Electron. Mater.*, **7**:441.
- [95] A. Yeckel, A.G. Salinger, and J.J. Derby. (1995) Theoretical analysis and design considerations for float-zone refinement of electronic grade silicon sheets. *J. Cryst. Growth*, **152**:51.
- [96] C.W. Lan. (1994) Thermal-capillary analysis of floating-zone growth of tube crystals: Steady-state and conduction dominated calculations. *J. Cryst. Growth*, **135**:606.
- [97] C.W. Lan. (1994) Heat transfer, fluid flow, and interface shapes in the floating-zone growth of tube crystals. *J. Cryst. Growth*, **141**:265.
- [98] T. Surek and B. Chalmers. (1975) The direction of growth of the surface of a crystal in contact with its melt. *J. Cryst. Growth*, **29**:1.
- [99] C. Szeles, S.E. Cameron, S.A. Soldner, J.O. Ndap, and M.R. Reed. (2004) The development of high-pressure electro-dynamic gradient crystal growth technology for semi-insulating CdZnTe growth for radiation detector applications. *J. Electron. Mater.*, **33**:742.
- [100] P. Rudolph. (1998) Melt growth of II-VI compound single crystals. In M. Isshiki, editor, *Recent Development of Bulk Crystal Growth*. Research Signpost, Trivandrum, India.
- [101] A. Yeckel, F.P. Doty, and J.J. Derby. (1999) Effect of steady crucible rotation on segregation in high-pressure vertical Bridgman growth of cadmium zinc telluride. *J. Cryst. Growth*, **203**:87.
- [102] C.W. Lan. (1999) Effects of ampoule rotation on flows and dopant segregation in vertical Bridgman crystal growth. *J. Cryst. Growth*, **197**:983.
- [103] A. Yeckel and J.J. Derby. (2000) Effect of accelerated crucible rotation on melt composition in high-pressure vertical Bridgman growth of cadmium zinc telluride. *J. Cryst. Growth*, **209**:734.

- [104] A. Yeckel and J.J. Derby. (2001) Buoyancy and rotation in small-scale vertical Bridgman growth of cadmium zinc telluride using accelerated crucible rotation. *J. Cryst. Growth*, **233**:599.
- [105] C.W. Lan and J.H. Chian. (1999) Effects of ampoule rotation on vertical zone-melting crystal growth: steady rotation versus accelerated crucible rotation technique (ACRT). *J. Cryst. Growth*, **203**:286.
- [106] E.O. Schulz-Dubois. (1972) Accelerated crucible rotation: Hydrodynamics and stirring effect. *J. Cryst. Growth*, **12**:81.
- [107] M.C. Liang and C.W. Lan. (1996) Three-dimensional convection and solute segregation in vertical Bridgman crystal growth. *J. Cryst. Growth*, **167**:320.
- [108] C.W. Lan, M.C. Liang, and J.H. Chian. (2000) Influence of ampoule rotation on three-dimensional convection and segregation in Bridgman crystal growth under imperfect growth conditions. *J. Cryst. Growth*, **212**:340.
- [109] A.N. Brooks and T.J.R. Hughes. (1982) Streamline Upwind/Petrov-Galerkin formulations for convection-dominated flows with particular emphasis on the incompressible Navier-Stokes equations. *Comput. Methods Appl. Mech. Eng.*, **32**:199.
- [110] A. Yeckel and J.J. Derby. (1997) Parallel computation of incompressible flows in materials processing: Numerical experiments in diagonal preconditioning. *Parallel Comput.*, **23**:1379.
- [111] W.R. Wilcox. (1983) Influence of convection on the growth of crystals from solution. *J. Cryst. Growth*, **65**:133–142.
- [112] R. Janssen-van Rosmalen and P. Bennema. (1977) The role of hydrodynamics and supersaturation in the formation of liquid inclusions in KDP. *J. Cryst. Growth*, **42**:224–227.
- [113] R. Janssen-van Rosmalen, W.H. van der Linden, E. Dobbinga, and D. Visser. (1978) The influence of the hydrodynamic environment on the growth and the formation of liquid inclusions in large potassium dihydrogen phosphate (KDP) crystals. *Krist. Tech.*, **13**(1):17–28.
- [114] W.J.P. van Enckevort, R. Janssen-van Rosmalen, H. Klapper, and W.H. van der Linden. (1982) Growth phenomena of KDP crystals in relation to the internal structure. *J. Cryst. Growth*, **60**:67–78.
- [115] P.F. Bordui and J.C. Jacco. (1987) Viscosity and density of solutions used in high-temperature solution growth of KTiOPO_4 (KTP). *J. Cryst. Growth*, **82**:351–355.
- [116] P.F. Bordui, J.C. Jacco, G.M. Loiacono, R.A. Stolzenberger, and J.J. Zola. (1987) Growth of large single crystals of KTiOPO_4 (KTP) from high-temperature solution using heat pipe based furnace system. *J. Cryst. Growth*, **84**:403–408.
- [117] B. Vartak and J.J. Derby. (2001) On stable algorithms and accurate solutions for convection-dominated mass transfer in crystal growth modeling. *J. Cryst. Growth*, **230**:202.
- [118] A.A. Chernov. (1992) How does the flow within the boundary layer influence morphological stability of a vicinal face? *J. Cryst. Growth*, **118**:333–347.
- [119] A.A. Chernov, S.R. Coriell, and B.T. Murray. (1993) Morphological stability of a vicinal face induced by step flow. *J. Cryst. Growth*, **132**:405–413.
- [120] S.R. Idelsohn, M.A. Storti, and L.A. Crivelli. (1994) Numerical methods in phase-change problems. *Arch. Comput. Methods Eng.*, **1**:49.
- [121] N. Provatas, N. Goldenfeld, and J. Dantzig. (1999) Adaptive mesh refinement computation of solidification microstructures using dynamic data structures. *J. Comput. Phys.*, **148**:265.
- [122] C.W. Lan, Y.C. Chang, and C.J. Shih. (2003) Efficient phase field simulation of non-isothermal free dendritic growth of a binary alloy. *Acta Mater.*, **51**:1857.

This page intentionally left blank

4 Indium Phosphide Crystal Growth

IAN R. GRANT

*Wafer Technology Ltd, 34 Maryland Rd, Tongwell, Milton Keynes,
MK 15 8HJ, UK*

4.1 Introduction	121
4.2 Material properties	122
4.3 Hazards	123
4.4 Crystal structure	124
4.5 Synthesis	125
4.6 Single-crystal growth	129
4.7 Defects	132
4.7.1 Twins	132
4.7.2 Dislocations	133
4.8 Dislocation reduction	135
4.9 VGF growth	136
4.10 Crystal-growth modelling	139
4.11 Dopants	141
4.11.1 N-type InP	141
4.11.2 P-type InP	142
4.11.3 Semi-insulating InP	142
4.12 Conclusion	145
Acknowledgements	145
References	145

4.1 INTRODUCTION

InP belongs to the group of III–V compound semiconductor materials, the most notable of which is GaAs, which have established versatile and varied roles for themselves in a wide range of electronic and optoelectronic applications. The history of research in these materials extends across virtually the entire semiconductor era, from the invention of the Ge transistor through the rise to global economic importance of Si-based electronics. The most prominent early investigator was Welker at Siemens in the early 1950s, [1, 2] who studied and first synthesised many of this family of semiconductors. However, significant commercial impact of the compound materials has awaited increased performance

demands in technology where full exploitation of some of their advantageous crystal properties could be realised.

InP first established itself as a substrate material for the epitaxial growth of alloys such as $\text{In}_x\text{Ga}_{1-x}\text{As}$ and $\text{Ga}_x\text{In}_{1-x}\text{As}_{1-y}\text{P}_y$. These ternary and quaternary alloy structures have a composition optimised to achieve suitable energy bandgaps for the emission and detection of infrared light at the wavelengths required for transmission through optical fibres. InP offers a good lattice parameter match to those alloys selected for operation at the standard wavelengths of 1.3 μm and 1.55 μm where fibres exhibit minimum attenuation and dispersion characteristics. InP-based semiconductor lasers have therefore become key to the operation of high-density trunk networks supporting the explosive growth in internet usage as well as other very high data rate telecommunications.

High-speed electronic devices are also a prerequisite for fibre optic and mobile communications. III-V compounds such as GaAs and InP have intrinsically better high-frequency performance compared with Si due to their relatively high electron mobilities and peak carrier velocities. In addition to this, however, the ability to deposit multiple thin layers of different compositions within a continuous crystal structure offers great latitude to modify the effective materials properties in the active device. Heterojunctions formed between epitaxial layers with different energy band structures can be combined to produce energy-band offsets, potential wells or lattice strain. 'Quantum wells' may be formed in which carriers are confined and their energy quantised. Multiple quantum wells, organised in periodic superlattice structures offer carrier transport and recombination behaviour unavailable in the bulk material. The heterojunction bipolar transistor (HBT) exploits such properties to already provide the best-available microwave device performance for mobile-phone applications, implemented in GaAs in high-volume production. InP HBTs offer the potential for further performance improvement and seem set to enable the next generation of millimetre-wavelength electronic devices [3, 4].

4.2 MATERIAL PROPERTIES

InP is a brittle, silver-coloured crystalline material. Table 4.1 lists some of its important material properties, from the consideration both of its preparation and use.

Table 4.1 InP material properties at 300 K

Property	Units	
Crystal structure		Zincblende
Melting temperature	$^{\circ}\text{C}$	1062
Dissociation pressure	bar	27
Lattice constant	\AA	5.86
Energy gap (25 $^{\circ}\text{C}$)	eV	1.35
Atomic density	cm^{-3}	3.96×10^{22}
Density	g cm^{-3}	4.79
Bulk modulus	dyn cm^{-2}	7.1×10^{11}
Thermal conductivity	$\text{W cm}^{-1} \text{ } ^{\circ}\text{C}^{-1}$	0.68
Electron effective mass	m_0	0.078
Electron mobility	$\text{cm}^2 \text{V}^{-1} \text{s}^{-1}$	≤ 5400
Intrinsic resistivity (25 $^{\circ}\text{C}$)	$\Omega \text{ cm}$	8.2×10^7

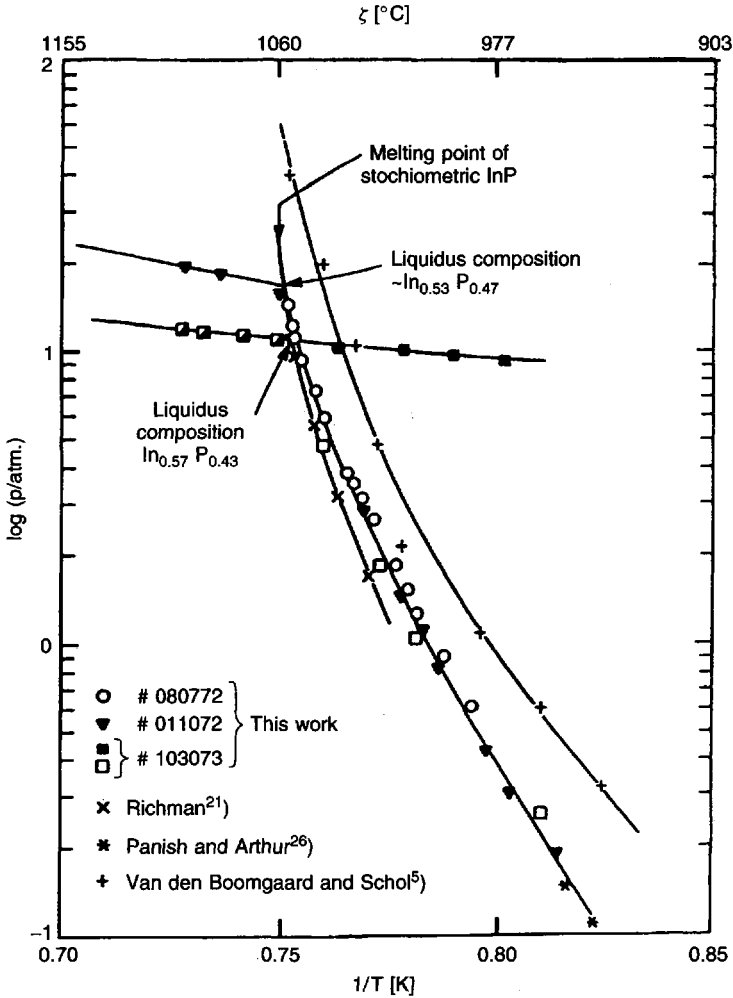


Figure 4.1 InP pressure-temperature characteristic

The melting temperature is moderate (1060 °C) and well within the range of conventional resistance-furnace techniques and materials. The dominant high-temperature property is the tendency to dissociate by the loss of phosphorus. Figure 4.1 shows the temperature dependence of the saturated vapour pressure for both P_2 and P_4 species [5]. At the melting temperature the phosphorus dissociation pressure is around 27 bar. This is a critical factor in the approach to all high-temperature processing of the compound, including synthesis and crystallisation from the melt.

4.3 HAZARDS

The acute toxicity of the material is very low and it can be currently classified as harmful rather than toxic. The main hazards arise from situations where it can be subjected to high

temperature or chemical attack. Phosphorus evolution in air due to thermal decomposition will form a dense white smoke of P_2O_5 , which is acidic and a severe respiratory irritant. Decomposition in the absence of oxygen may result in the condensation of different phosphorus allotropes, including toxic white phosphorus that can spontaneously ignite on exposure to air. Reaction with acids may form PH_3 gas that is both pyrophoric and highly toxic.

Mechanical processing giving rise to finely divided material or airborne dust must be monitored and controlled through the use of suitable liquid coolants and extraction systems. Dust inhalation has been demonstrated to cause damage to the lungs, liver and blood in studies carried out on rodents [6].

4.4 CRYSTAL STRUCTURE

In common with the other III–V semiconductors, InP crystallises in the zincblende (ZnS) structure, belonging to the cubic space group $F43m$. This is a modified form of the diamond structure in which the group IV semiconductors Ge and Si crystallise. It can be described as consisting of two interpenetrating face-centred cubic (fcc) sublattices, one composed of group III In atoms only, the other of the group V, P atoms. The two sublattices are translated with respect to each other by a distance $(-1/4, -1/4, 1/4) a_0$ (where a_0 is the lattice-parameter value). There is no centre of symmetry in this structure and this gives rise to some piezoelectric and nonlinear optical effects.

The chemical bonding within the crystal is tetrahedral. In atoms have three outer electrons in an s^2p^1 configuration, while the P atoms have 5 outer electrons in an s^2p^3 configuration. This contributes an average of four valence electrons per atom to the bonding. The bonding is principally covalent but partly ionic in character due to charge transfer between the two species. The degree of charge transfer depends on the electronegativity difference. Phosphorus is more electronegative than In resulting in a bond polarisation with a net positive In charge and negative P charge. The amount of this charge transfer for InP is $0.421e$.

The concept of two separate sublattices is seen in the occurrence of crystallographically equivalent but chemically distinct $\{111\}$ planes. This is illustrated in Fig. 4.2, where the $\{111\}$ In, designated $\{111\}A$, planes are indicated, consisting entirely of In atoms. Parallel and closely spaced to this is an equivalent $\{111\}P$, or $\{111\}B$ plane. The polar bonding in the $[111]$ direction is fully aligned making these very strong with respect to cleavage. The lowest energy cleavage planes are $\{110\}$ in these materials.

Exposed $\{111\}$ surfaces are chemically distinct, either of In or P type. This has some influence on the behaviour of the bulk material in crystal growth where it can be experimentally observed that for a $\langle 111 \rangle$ growth axis the seed face presented to the melt can result in differences in single-crystal yield depending on whether it is of $\{111\}A$ or $\{111\}B$ type. Facets form on $\{111\}$ planes with different growth rates and hence allow some visual differentiation of the A and B planes on the grown crystal. For the usual growth axis of (001) , the facets are normally seen most easily on the section of the crystal that is growing out to full diameter from the seed. This 'cone growth' is also the region in which the facets can have a strong influence on twin formation.

Because the material does not exhibit a fully four-fold symmetry with respect to its chemical composition, it is necessary to determine and label the orientation of the $\{111\}A$

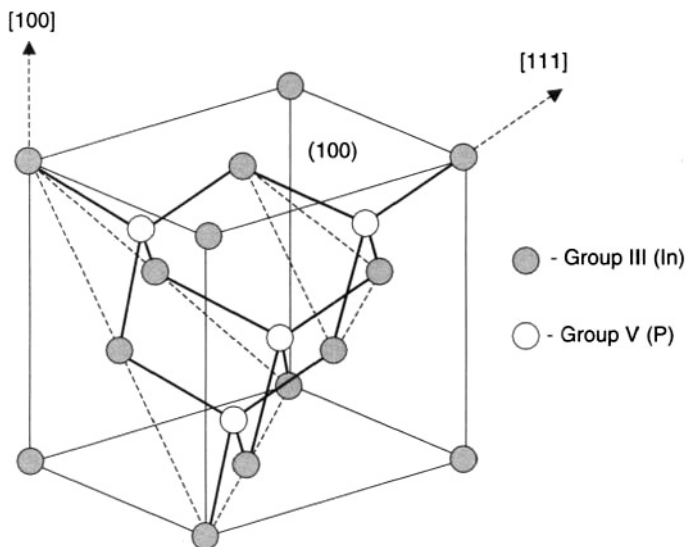


Figure 4.2 Zincblende crystal structure. $\{111\}$ A planes, comprising only In atoms are shown dotted

and B planes within both the bulk and wafer material during processing. In the case of the wafers, this is achieved by adopting a convention for the placement of flats on the wafer periphery that defines both the surface orientation and the position of particular $\{110\}$ planes as a reference for cleavage.

4.5 SYNTHESIS

Both indium and phosphorus raw materials are sourced as high-purity elements with a specification better than 6N (99.9999 %). The specification is normally supported and certified by batch analysis using a technique such as glow discharge mass spectroscopy (GDMS). This has detection limits better than 1 ppba and is also commonly used for the analysis of the crystalline material.

Both the elemental constituents are abundant and their use in semiconductor manufacture represents a small fraction of overall consumption, whereas Ga, for example, has few uses outside of semiconductor processing and any fluctuation of demand in this sector can strongly influence the price and availability. Although In and P are readily available in lower purity (4N), refining capability does restrict choice for the high-purity grades. This is particularly true for phosphorus. There is an intermittent market for scrap InP, for In recycling, and the compound material therefore tends to be collected and stored for processing in bulk.

Indium is supplied in the form of cast metal ingots each weighing of the order of 100 g. Phosphorus is specified as the red phosphorus allotrope and is supplied in large granular form (5–20 mm) sealed under argon in glass bottles. Although red phosphorus is less hazardous than other forms, handling still presents a very significant risk of ignition and nitrogen purging must be used to provide a safe ambient for the dispensing, weighing and loading of phosphorus into the reaction vessels.

The compound is formed by direct exothermic reaction of the elements at high temperature. The elements are combined by transport of the phosphorus to react with molten indium held at a temperature above the melting point of the compound. The high dissociation pressure requires a phosphorus vapour pressure of about 30 bar as a minimum.

Figure 4.3 is a schematic of a high-pressure reaction system used for the synthesis of polycrystalline InP [7]. In order to achieve containment of the P component during the synthesis and cooling, the reaction is carried out inside a sealed vessel or by encapsulating the melt to avoid dissociation. In the system illustrated the indium and phosphorus are loaded separately into a silica glass ampoule. The indium is placed at one end and is held in a boat-shaped crucible also made of silica glass with a special surface treatment to avoid adhesion of the melt or of pyrolytic boron nitride, pBN, which may also have received a surface pretreatment, such as high-temperature baking in air to form a thin boric-oxide surface layer. The phosphorus is loaded at the other end of the ampoule and is separated from the indium by a silica-glass obstruction, forming a diffusion baffle to control the subsequent high-temperature transport of the P vapour feeding the reaction. The ampoule is evacuated to a pressure of around 10^{-6} torr and sealed by flame welding. The whole system is loaded inside a resistance tube furnace, contained inside an outer stainless-steel pressure vessel. The furnace is segmented to provide two main temperature zones. The high-temperature zone is held above the melting point of the compound, while the cooler zone surrounds the phosphorus source and its temperature is controlled to achieve a steady sublimation of the phosphorus and to maintain an adequate P vapour pressure.

An excess weight of P is included in the charge to sustain a P overpressure at the end of the reaction phase. The total charge weight may be between 7 and 10 kg of synthesised compound.

The internal P vapour pressure is well in excess of that which could be supported by the quartz ampoule alone. This is balanced, therefore by the pressure of an inert gas ambient, argon or nitrogen, maintained inside the containment vessel. Precise pressure balance is vital in order to avoid rupture of the ampoule. This is achieved by direct monitoring and control of the gas pressure and by varying the internal pressure in the ampoule by means of temperature control of the solid P source. Accurate vapour-pressure monitoring is difficult, but the differential pressure across the ampoule can be measured by the attachment of transducers. Nonetheless, strong reliance is placed on the reproducibility of the process in terms of furnace set up, heat transfer and a consistent sublimation behaviour of the phosphorus as a function of temperature. Modern high-purity red phosphorus offers good reproducibility in this respect, although differences in behaviour may still be observed between batches from different suppliers, reflecting some differences in manufacturing.

A period of melt stabilisation is allowed after complete reaction, before the cooling and crystallisation cycle begins. A gradient is then formed over the molten InP and the temperature is lowered until nucleation occurs at the coolest end of the boat, nearest the P source. The aim is then to achieve a progressive crystallisation at a constant and controlled rate by ramping the furnace temperatures. In this way, a homogeneous, stoichiometric polycrystalline ingot of InP is formed, having large grain structure and free of inclusions and voids.

The main complexity in the process is in achieving the necessary pressure balance throughout all stages of heating, reaction and cooling where the thermal characteristics of

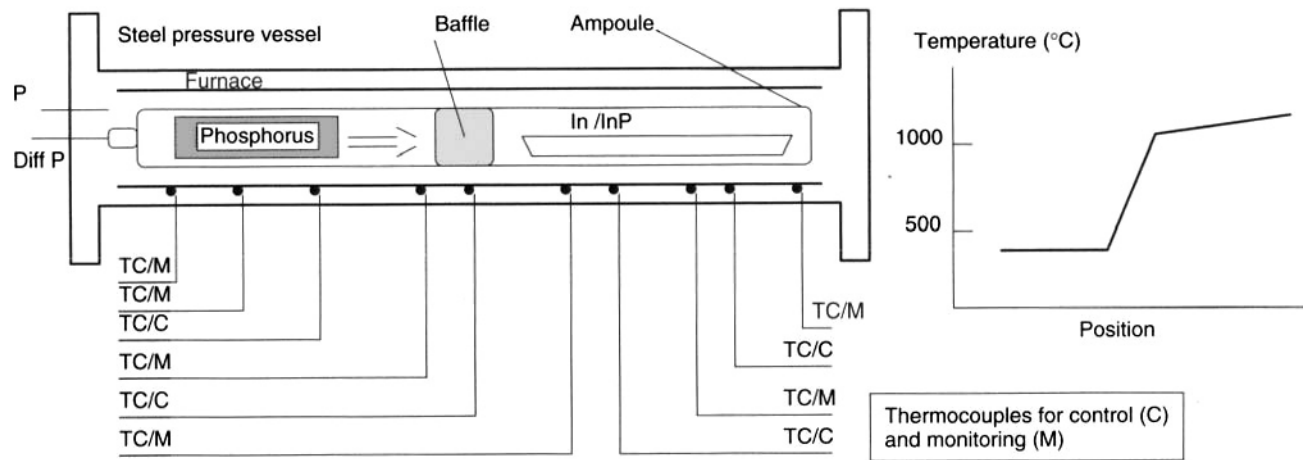


Figure 4.3 InP polycrystalline synthesis system

the load are continually changing. If a rupture of the ampoule does occur then hot phosphorus vapour is suddenly released into the containment vessel. This will generally destroy the furnace components and condense on the water-cooled vessel wall. The vessel is designed to withstand an explosion of the process and therefore the main hazard in these circumstances is faced on opening the system to air after cool down. Rapidly condensed white phosphorus will ignite and its waxy liquid form adds to the hazard of cleaning. Systems for high-volume production of InP have to be designed to cope with such occurrences, leading to a need for relatively inexpensive and easily replaceable furnaces.

An alternative synthesis method involves bubbling a stream of phosphorus vapour through an indium melt maintained at high temperature. Phosphorus is contained in an independently heated ampoule, with an open-ended dip tube immersed in the molten indium. In this case the resultant charge is encapsulated by a layer of liquid boric-oxide glass (B_2O_3) and again an inert-gas ambient is used to balance the compound dissociation pressure across the encapsulant layer. In principle, the use of liquid seals in this system should allow any excess P pressure simply to be released by an increased bubbling rate through the charge. However, pressure fluctuations can cause material to be sucked into the dip tube and solidified, for example. In principle, both methods allow a degree of stoichiometry control via the vapour pressure of P maintained over the melt. The bubbling technique has the advantage of forming the polycrystalline material in-situ in the crucible [8] and usually also in the system that will be used for single-crystal growth, saving the time and costs of extra processing stages. However, this also commits a crystal-growth furnace and prevents testing of the synthesised-material purity prior to growth.

An important consideration in the quality of polycrystal produced is the background purity. This is assessed electrically for residual carrier concentration. Figure 4.4 is a plot of the carrier concentration at room temperature for the first-to-freeze ends of a large number of polycrystalline ingots.

The material is n-type with a carrier concentration typically well below 10^{16} cm^{-3} and usually specified at $< 5 \times 10^{15} \text{ cm}^{-3}$. The usual range for high-purity undoped InP is $2-4 \times 10^{15} \text{ cm}^{-3}$ with a room-temperature Hall mobility of $4000-5500 \text{ cm}^2 \text{ V}^{-1} \text{ s}^{-1}$.

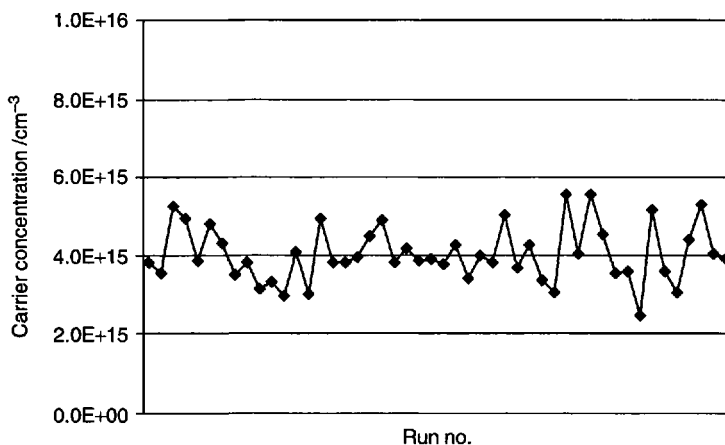


Figure 4.4 Seed-end carrier concentration for high-purity polycrystalline ingots

Table 4.2 GDMS Impurity analysis of polycrystalline InP (concentrations in ppba)

Element	Conc.	Element	Conc.	Element	Conc.
Li	< 2	Mn	< 0.4	In	Major
Be	< 1	Fe	< 0.2	Sn	< 1
B	8	Co	< 0.2	Sb	< 0.8
C	4000	Ni	< 0.6	Te	< 3
N	300	Cu	< 3	I	< 4
O	3000	Zn	< 2	Cs	< 25
F	< 70	Ga	< 20	Ba	< 0.3
Na	< 1	Ge	< 2	La	< 0.1
Mg	< 1	As	85	Ce	< 0.1
Al	< 0.6	Se	< 8	Hf	< 0.2
Si	35	Br	—	Ta	—
P	Major	Rb	< 0.5	W	< 0.3
S	< 10	Sr	< 0.4	Pt	< 0.7
Cl	15	Y	< 0.3	Au	< 10
K	< 80	Zr	< 0.2	Hg	< 2
Ca	< 20	Nb	< 500	Tl	< 0.5
Sc	< 0.5	Mo	< 0.9	Pb	< 0.7
Ti	< 0.5	Pd	—	Bi	< 0.3
V	< 0.5	Ag	< 4	Th	< 0.2
Cr	< 1	Cd	< 15	U	< 0.1

Table 4.2 shows a full GDMS analysis of a polycrystalline ingot and indicates that the dominant detected donor species are Si and S [9]. Background carrier levels in the bulk material of below 10^{15} and down to mid- 10^{14} cm^{-3} have been reported using synthesis from In-rich solution [10] and improvements in residual carrier concentration have also been reported by recrystallising from In-rich melts [11]. At carrier concentrations around 2×10^{15} cm^{-3} or below it is suggested the conduction may be dominated by native donor species [12].

4.6 SINGLE-CRYSTAL GROWTH

Liquid encapsulated Czochralski (LEC) growth has been the main single-crystal production method for InP since its initial uptake for device manufacture. The principal elements of LEC growth are well known and InP was one of the first materials for which it was proposed, in essentially its present form [13].

Figure 4.5 is a schematic of a commercial (Metals Research) high-pressure LEC puller. This illustrates the main features of the method. The equipment itself is representative of the first generation of commercial production of 2-inch diameter crystals with a weight of 1 to 1.5 kg.

The polycrystalline charge is contained in a silica glass or pBN crucible. A solid disc of boron-oxide glass is placed on top of the charge. The crucible is located inside a graphite resistance heater. After an evacuation and purging sequence the chamber is pressurised

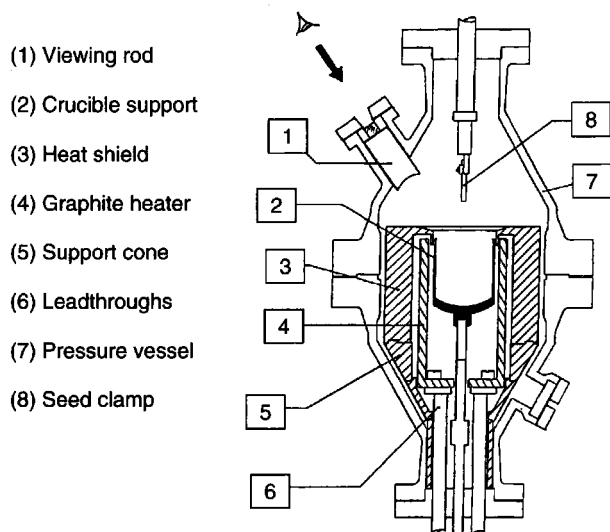


Figure 4.5 LEC crystal puller—schematic

with inert gas (nitrogen or argon) to a minimum of 30 bar. As the charge is heated the boric oxide begins to flow and encapsulate the solid InP while the temperature is still low enough to avoid phosphorus loss. Heating continues until the InP mass is molten and completely encapsulated by a layer of boric-oxide glass. The melt is left to stabilise for a period before crystal growth is initiated.

The crucible is supported by a solid metal shaft that can be rotated and translated vertically within the heater. Special high-pressure seals are designed to transmit the drives to the crucible support rod. Another solid metal pull rod holds the seed crystal suspended over the melt. The pull rod itself is connected, inside the pressure vessel, to a load cell that monitors the total weight of the rod, seed and growing crystal.

The seed is lowered to penetrate the transparent glass layer and to make contact with the melt. The temperature is then adjusted so that the melt attaches to the seed crystal and a meniscus is drawn up. In the arrangement illustrated, the seed is held in a clamp and has a square cross section with the sides normally cut on {110} planes.

Growth takes place by withdrawing the partially melted seed up through the boric-oxide layer, while varying the furnace temperature to increase the diameter of the attached single crystal forming an extension to the original seed-crystal structure. Both the growing crystal and the crucible are rotated. The relative sense, co- or counter-rotation, and the rotation rates are determined by experiment to establish an optimum mixing in the melt for material homogeneity. This can affect the temperature gradients and instabilities, influencing the control of crystal shape as well as a number of key properties in the bulk of the grown crystal. The pull rate is typically in the range $5\text{--}10\text{ mm h}^{-1}$. In the case of the smallest weight of 2-inch crystal the growth phase for the process can be completed within one day. However, the overall growth cycle can be considerably longer when heating, cooling and melt stabilisation periods are taken into account.

Control of the crystal shape is important in achieving efficient conversion of the ingot to standard-diameter circular wafers. The normal objective is to establish a regular cylindrical

shape by expanding the seed-equivalent diameter up to a size slightly greater than the final wafer diameter while minimising the weight of material contained in the cone-shaped transition section at the seed. In a thermally stable and reproducible furnace setup the shape control can be derived experimentally and maintained through a sequence of programmed ramps of the main furnace heater. Diameter control can also be achieved by means of closed-loop feedback acting on the furnace temperature [14]. The input is the weight signal obtained from the load cell during the course of the growth. In the first approximation, the rate of change of the measured weight is proportional to the diameter of the crystal, growing at a constant rate. However, there are a number of variable contributions to the net weight signal arising from effects experienced at different stages of the growth. For example, the material expands on freezing providing an anomalous apparent weight reduction. As the crystal expands from the seed, and while still immersed in the encapsulant it displaces a varying amount of boric oxide of much lower density and hence there arises a varying buoyancy force that also changes the net apparent weight. Both of these effects are particularly influential in the early stages of the growth when the total weight signal is small. The net growth rate is the combination of the pull rate and any change in the meniscus height such as might be caused by the depletion of the melt level in the crucible and hence the detail of the crucible shape towards the end of the growth. A programmed crucible-lift adjustment might also be applied to ensure that the melt surface and growth interface remain at a fixed position within the furnace throughout the run. All of these factors need to be allowed for in setting up any automatic-diameter control system based on crystal weighing. However, the computational demands in implementing such a system are quite modest due to the long time constants of the various contributions.

Figure 4.6 shows an example of a 2-inch diameter ingot demonstrating the degree of diameter stability achievable over an extended growth length. Figure 4.7 shows a standard 3-inch diameter crystal, also grown with automatic diameter control.

Diameter control by direct observation of the crystal has never been successfully achieved due to the optical distortions caused by the boric-oxide layer and the turbulent

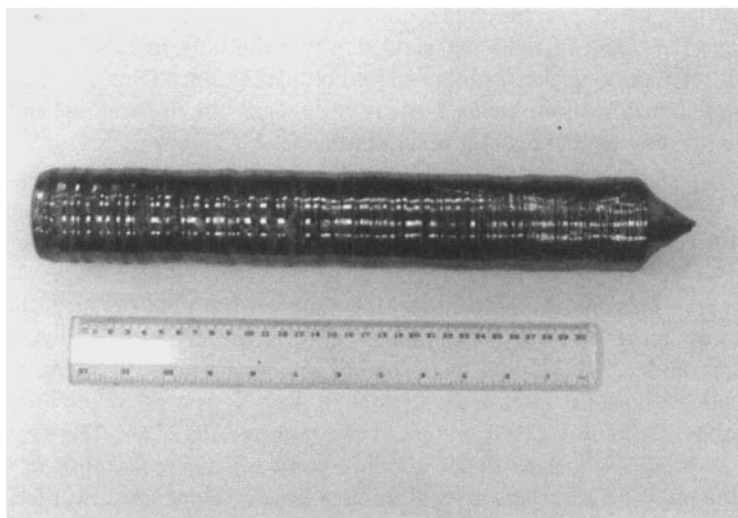


Figure 4.6 Automatic diameter control on 2-inch InP growth

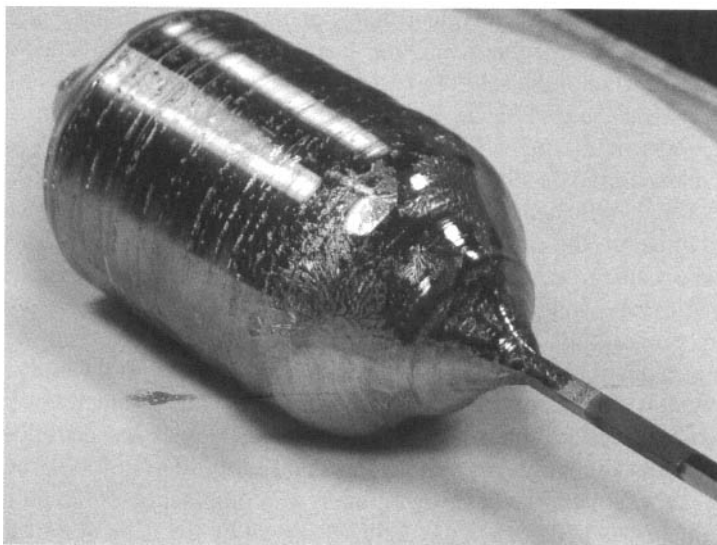


Figure 4.7 3-inch diameter InP crystal

high-pressure gas within the chamber. However, visual monitoring of the melt and early stages of grow out is an important facility to ensure satisfactory seeding and to allow intervention and possible regrowth on the detection of twin formation. A quartz light pipe conveys an image of the melt surface and interface through a pressure-resistant sapphire window onto a CCTV system.

4.7 DEFECTS

The success of the growth process can be limited by the occurrence of a number of defects. These can have the effect of reducing yield, limiting the bulk material specification that can be offered or rendering the resultant ingot completely unusable.

Examples of such defects are twins, polycrystalline growth, dislocations and dislocation clusters, dopant inhomogeneities and precipitates.

4.7.1 Twins

Twinning occurs via a 60° rotational stacking fault on the (111) plane. This results in a twin boundary lying along a (111) plane, splitting the crystal into two regions oriented on (001) and $\langle 221 \rangle$ vertical axes, before and after the twin plane, respectively. The twin boundary usually bisects the crystal in such a way as to provide little or no material capable of yielding (100) wafers at the required diameter. The growth process is normally adjusted to operate under conditions where the probability of twinning is minimised. InP may be regarded as exhibiting a greater tendency towards twin formation than the other III-V compounds due to its lower stacking fault energy [15]. Hurle [16] has described the factors influencing twin formation in encapsulated growth. These

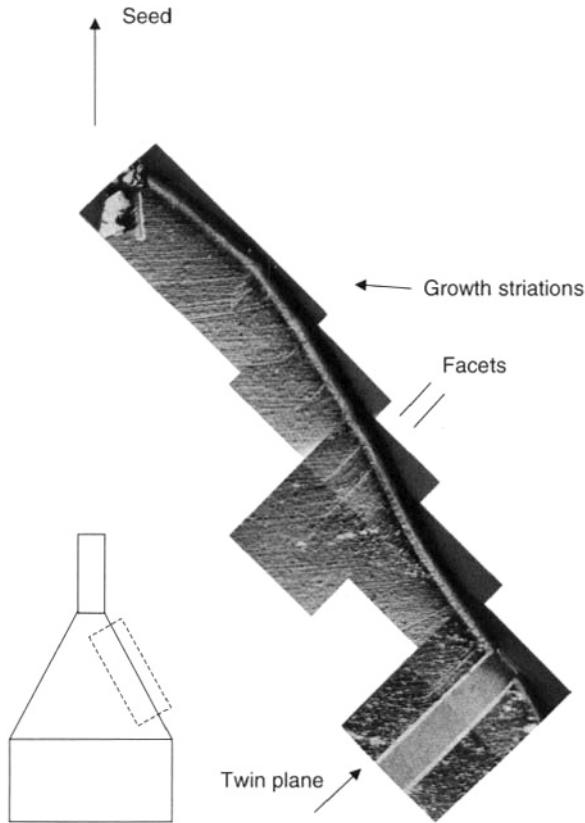


Figure 4.8 Cross section of crystal seed cone

include the form of the solid/melt interface and its intersection with the crystal surface, especially in the cone section at the start of the growth, faceting of the growth interface close to the surface and temperature instabilities that give rise to fluctuating growth rate.

Figure 4.8 is a micrograph of the near-surface region in the cone section of a crystal. This has been etched to reveal dopant striations arising from temperature oscillations in the melt, labelling the instantaneous interface position and shape throughout the growth. The inflexion of the interface close to the surface, conforming with the $\{111\}$ facet plane, is clearly visible. Also revealed by the etching are two closely spaced $\{111\}$ twin planes, bounding a lamellar twin region, which have formed in a strongly faceted part of the growth.

4.7.2 Dislocations

Dislocations are produced by plastic deformation of the crystal at high temperature. Both radial and axial temperature gradients exist during the growth process. Indeed, these are required to achieve controlled crystallisation and to impose a stable shape on the growing crystal. However, the gradients can be large, nonlinear and time dependent at any point

in the crystal during solidification and cool down, resulting in differential contraction and cooling stresses. Above a critical stress value, which is also temperature dependent, dislocations are formed and in InP these are mainly arranged in linear arrays parallel to $\langle 110 \rangle$ directions due to slip on $\{111\}$.

Figure 4.9 is a plot of the axial temperature measured in an LEC growth system, prior to growth, from the melt surface, through the encapsulant layer and up into the ambient gas. It is evident that the peak gradient occurs at the boric-oxide surface where the crystal emerges into the much colder gas.

Dislocation density is measured by counting etch pits revealed on cut wafers using the H-etch [17], consisting of $\text{HBr}:\text{HNO}_3$ (1 : 1) at room temperature. Typical etch pit densities (EPD) around $5 \times 10^4 \text{ cm}^{-2}$ are found in 2-inch diameter crystals grown in an unmodified LEC puller. The distribution of etch pits over the wafer shows an approximate W-shape (Fig. 4.10b), with higher density at the edges and the centre, reflecting the development of the cooling stresses during growth. These are larger as the crystal diameter increases and this is seen in the increased dislocation density with average values above $1 \times 10^5 \text{ cm}^{-2}$ measured in equivalent 3-inch crystals.

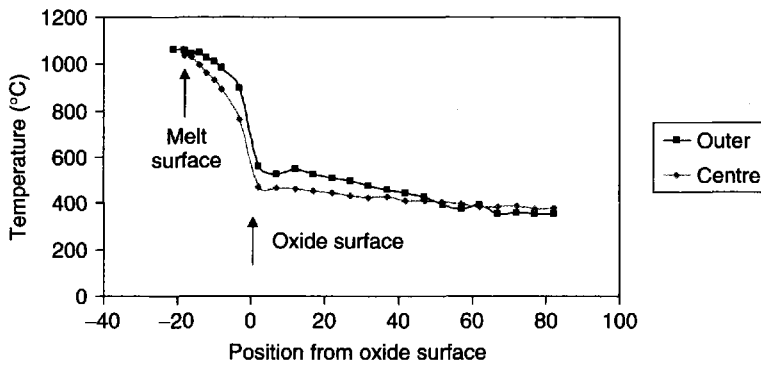


Figure 4.9 Axial temperature gradients

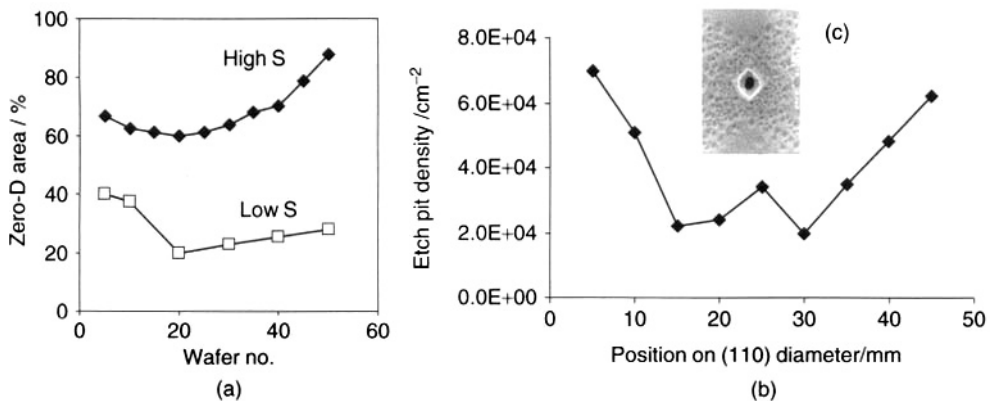


Figure 4.10 (a) Dislocation-free area as a function of wafer position and doping, (b) radial distribution of dislocation density in low-doped InP, (c) SEM micrograph of 'grappe' defect

Dopants such as sulfur and zinc, when added in high concentration can act to reduce the dislocation density by exerting a 'hardening' effect [18–20]. In the case of S doping, 'dislocation-free' material, with densities less than 500 cm^{-2} can be obtained. Again this is more readily achievable in smaller-diameter wafers and with increasing doping concentration (Fig. 4.10a). However, it is generally necessary to moderate the dopant content to avoid issues of outdiffusion from the substrate during epitaxy and dopant inhomogeneities. The typical carrier concentration range specified for InP:S is $3\text{--}8 \times 10^{18} \text{ cm}^{-3}$. High dopant concentration can also influence the crystal-growth behaviour with, for example, strong facet development and the consequently greater risk of twinning. The threshold doping concentration to achieve significant dislocation-density reduction depends strongly on the control of thermal gradients in the growth system. Since EPD is one of the main specification requirements on InP wafers and in particular a dominant demand is for low-EPD or dislocation-free substrates, then much of the effort in single-crystal growth is concerned with optimised low-gradient furnace arrangements for each diameter produced.

Certain characteristic forms of dislocation structure can also influence the yield and usefulness of a crystal. Figure 4.10c is a micrograph of a dislocation cluster, often referred to in InP as 'grappes', made up of a series of prismatic loop dislocations crystallographically aligned and propagating along (110) slip directions for distances up to $100 \mu\text{m}$ from a localised stress centre caused by an included core [21]. The precise origin of these features has not been identified, although the presence of excess In and voids have both been proposed. The general conditions under which they may arise in the growth can be experimentally determined. A strong factor influencing their occurrence is the boric-oxide moisture content and this has to be carefully specified and limited to a low concentration.

Where the grown-in dislocation density is rather high and the form of the growth-interface shape allows a convergence to the dislocation lines into dense clusters or entanglements, these can form into subgrain boundaries and lead to an eventual breakdown into polycrystalline growth.

4.8 DISLOCATION REDUCTION

Dislocation control by means of doping alone has a limited effectiveness and gives rise to limiting problems of its own. The main approach has therefore been to design the growth system to achieve much lower temperature gradients while still maintaining conditions for stable growth. Gradient reduction can be readily obtained by heat shielding in the space immediately above the melt/encapsulant. By preventing both the strong gas flow and direct radiative losses from transporting heat from the growing crystal to the water-cooled chamber walls, the ambient temperature experienced by the crystal above the protective encapsulant layer can be dramatically increased (by a few hundred degrees). The corresponding reduction in gradients results in a much lower dislocation density in the grown crystal.

Figure 4.11 shows a sequence of seed-end wafers from different crystals. These have been etched to reveal the overall pattern of dislocations and convey an impression of their density. Each crystal was grown in a progressively lower gradient system and the effect on EPD is evident. The dislocation-free area increases sharply with gradient reduction.

The benefits of simple heat shielding are limited, however, since raising the temperature of the unprotected region of the crystal increases the surface P loss, eventually

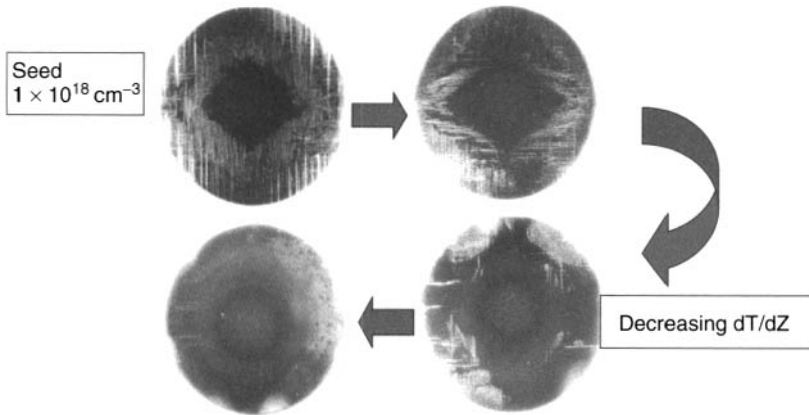


Figure 4.11 Seed-end EPD reduction with reduced temperature gradients

producing strong surface decomposition and the presence of a significant amount of free In that can disrupt the growth. In order to impose the level of gradient desired, various modifications to the LEC method have been devised, including increasing the thickness of the boric-oxide layer and enclosing the whole furnace in a sealed hot-wall chamber. This latter approach, although not simple to implement, has proved the most successful on a production scale and has been promoted by InP manufacturers under the designations of PC-LEC (pressure-controlled-LEC) and VCZ (vapour-controlled Czochralski) [22]. In each case the compensating partial pressure of P, preventing surface decomposition of the crystal, is provided throughout the run by a separately controlled P source. The inner enclosure acts to maintain this overpressure although it does not have to provide a perfect gas-tight chamber. In fact some pressure-balancing connection between the inner and outer chambers is highly desirable in order to avoid catastrophic imbalances at the high pressures used.

Undoped InP produced in such systems has a dislocation density of less than 10^4 cm^{-2} at 2-inch diameter, and the threshold S doping concentration for dislocation-free material can be reduced to a level corresponding to a carrier concentration of $1 \times 10^{18} \text{ cm}^{-3}$ or less.

4.9 VGF GROWTH

The vertical gradient freeze (VGF) growth method [23] has become an important production platform for III-V materials, especially GaAs. The principle of the technique involves in-situ crystallisation within a crucible. The growth is seeded and proceeds from bottom to top in a vertical orientation. Figure 4.12 shows a VGF furnace and schematic in a system designed specifically for InP.

The furnace itself may consist of multiple heating zones configured to impose a controlled temperature gradient over the melt. The crucible can be quartz, or more usually pBN and has to be designed to accommodate the seed crystal in the base. A common arrangement is to have a small-diameter tube for the seed crystal, opening via a cone-shaped section to the full-diameter cylindrical, or slightly tapered cylindrical, section. The melt is encapsulated with boric oxide and in the case of InP, the whole system must be

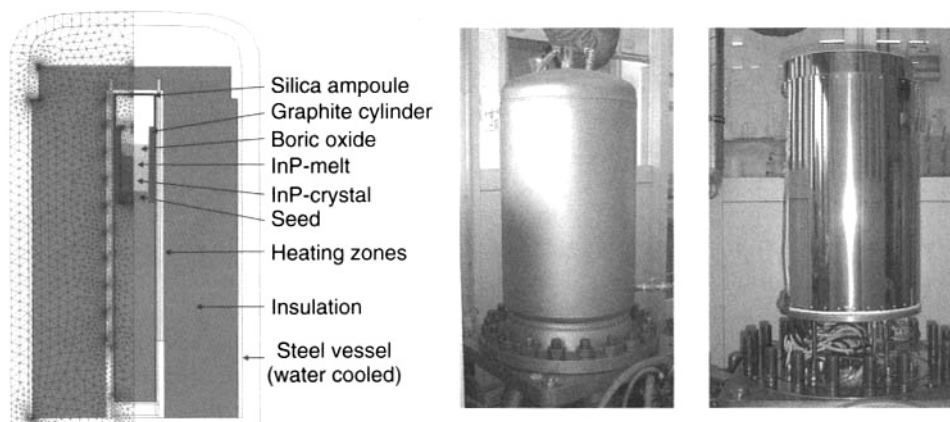


Figure 4.12 VGF furnace schematic and photos

contained within a pressurised and water-cooled vessel operating at the same pressures as an LEC puller.

The growth sequence after loading of the crucible is to heat the charge to achieve a temperature distribution that maintains the top of the melt at a higher temperature than the base and that establishes a position for the melting isotherm part way down the seed. At this point the seed crystal will be partly melted and wetted by the molten charge, forming a stable and well-behaved interface. The temperature distribution over the melt is arranged so that a controlled linear gradient exists at the interface and that the rise in temperature towards the top surface of the melt is limited to avoid overheating and decomposition problems. The objective in the crystallisation phase is to programme the furnace heaters to move the melt isotherm position upwards at a constant rate and to maintain a uniform and low thermal gradient over the grown crystal as it cools.

The major advantage of the method is that the crystal is formed inside the crucible and hence there are no issues of shape control. This allows the use of very low temperature gradients during growth and hence much lower thermal stresses, potentially, than for the LEC system. The free surface of the melt is also well separated from the growth interface minimising the possibility of incorporation of surface contaminants. However, this also means that there is no possibility of visual monitoring of the critical seeding and grow-out phases and hence no opportunity to detect twins and restart the growth. The growth process itself is performed by an automated sequence of furnace ramps.

The growth system can be less expensive than an LEC puller since there is no need for lift and rotation mechanisms or any diameter-control system. The high-pressure requirements of InP do limit the cost-saving potentials, however. Typical growth rates are around 2 mm h^{-1} . The crystal must also be recovered from the crucible undamaged at the end of the run. This involves dissolving the very thin layer of solidified B_2O_3 between the crystal surface and the crucible. The usual solvent is hot methanol. Equally, because of its high value, the pBN crucible has to be recovered intact for reuse.

The overall growth cycle is therefore much longer for VGF than for LEC and hence the productivity for the same yield, is much reduced.

The other factor that strongly affects output is the single-crystal yield. There are a number of influences on this, including failure to seed properly, sticking to the crucible

walls and the formation of twins. Low temperature gradients tend to allow a stronger facet influence on the growth interface and the same factors involved in the LEC case become more critical in this kind of regime. Thus the shape of the crucible cone section, the rate of growth, the detailed shape of the solid/melt interface, particularly at the crystal surface and the stability of the melt temperature with regard to localised supercooling can all influence the yield. These issues can be variously addressed, by thermal design of the furnace to provide the desired interface shape, by ensuring that the high-pressure gas volume for turbulent flow is minimised and that the melt environment is thermally stable, and by selection of a suitable crucible design to achieve the transition between the seed diameter and the final crystal diameter without generating twin growth in the cone section, which is in practice where the greatest risk occurs. One approach is to eliminate the grow-out section completely by using a simple cylindrical-shaped crucible with a seed of the same diameter as the final crystal [24, 25]. Figure 4.13 shows an example of a 2-inch diameter VGF crystal grown in this way.

The seeding position can be accurately and reproducibly established even in a large-area, short-length seed of this type. Although it might be expected that without the ability to expand the interface area that any defects such as dislocations in the seed would directly propagate at the same density into the grown crystal. This is not necessarily the case and significant dislocation reduction can be achieved between the seed and the VGF-grown crystal.

In the ingot shown in Fig. 4.13, the carrier concentration was in the range of mid- 10^{17} cm^{-3} . The EPD of the LEC grown seed crystal was around $5 \times 10^4 \text{ cm}^{-2}$, whereas the dislocation density in the VGF crystal was reduced by about an order of magnitude. This is illustrated in Fig. 4.14 where an EPD map of a seed-end wafer is shown. The general form of the W-shaped EPD distribution is still maintained in the VGF growth.

VGF growth has shown itself capable of providing InP of the best structural quality, with respect to dislocations and residual stress, at diameters of 2, 3 and 4 inches and across all commonly required dopants. There remain some questions concerning the achievable yield and competitive cost performance of the method.

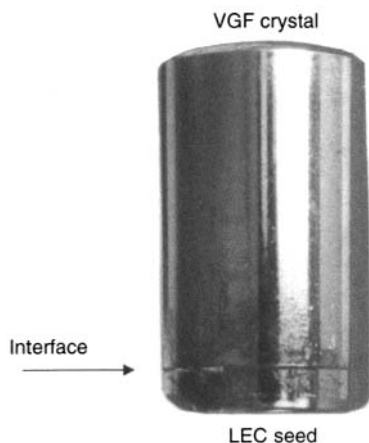


Figure 4.13 VGF single crystal, S-doped

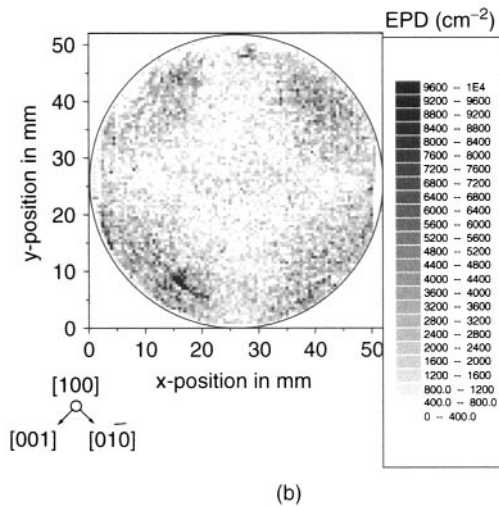
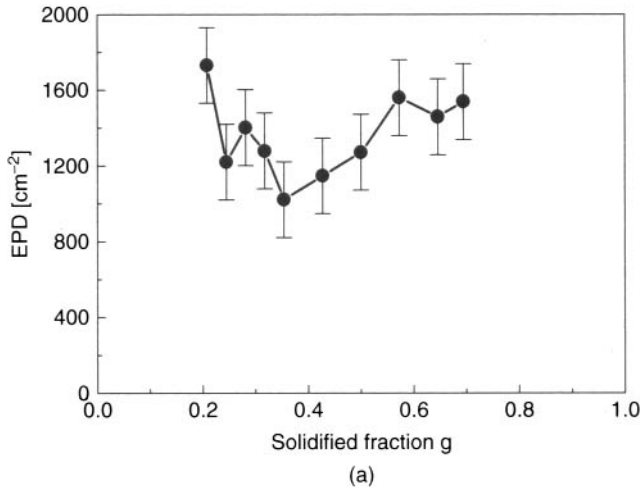


Figure 4.14 (a) Average EPD for wafers along a VGF-grown crystal, (b) seed-end EPD map on a 2-inch wafer

4.10 CRYSTAL-GROWTH MODELLING

The experimental development of high-temperature, high-pressure furnaces is expensive and slow. Tools that can assist in predicting the effects of changes in hot-zone components, materials and basic furnace dimensions are of enormous potential importance when tackling issues such as scaling up to larger-diameter crystals. Complete simulation of the growth system to take into account all the processes of heat transfer, including radiation losses, convective effects in the gas phase, melt flow and mixing, distributed in time and in full three-dimensional space remains an ambitious task. However, numerical computational packages such as CrysVUn⁺⁺ have been developed [26] that offer a time-dependent and 2-dimensional simulation of a growth environment. This has proved particularly useful for the physically much simpler arrangement found in a VGF furnace and has been

demonstrated to be a valuable tool when used in conjunction with furnace design. Using known material thermophysical properties and with measured furnace temperatures as the boundary conditions, quasistationary and time-dependent modelling of the heat transfer via radiation and conduction, taking into account latent heat, can be performed. From this the temperature distribution within the crystal can be determined at any given point in time, providing predictions of the interface position and form throughout the growth. In addition, the von Mises stresses can be calculated from the temperature field experienced by the crystal and simulations can be tested for the avoidance of exceeding the critical stress for dislocation generation at any point.

Figure 4.15 shows a sequence of quasistationary stress maps calculated for the case of a 2-inch diameter InP VGF growth at different time intervals. Experimental verification of the interface position and hence growth rate, and of its detailed form can be made by sectioning the grown crystal and etching to reveal dopant striations marking the interface. Since there is normally no rotation applied in the VGF system and there are no strong

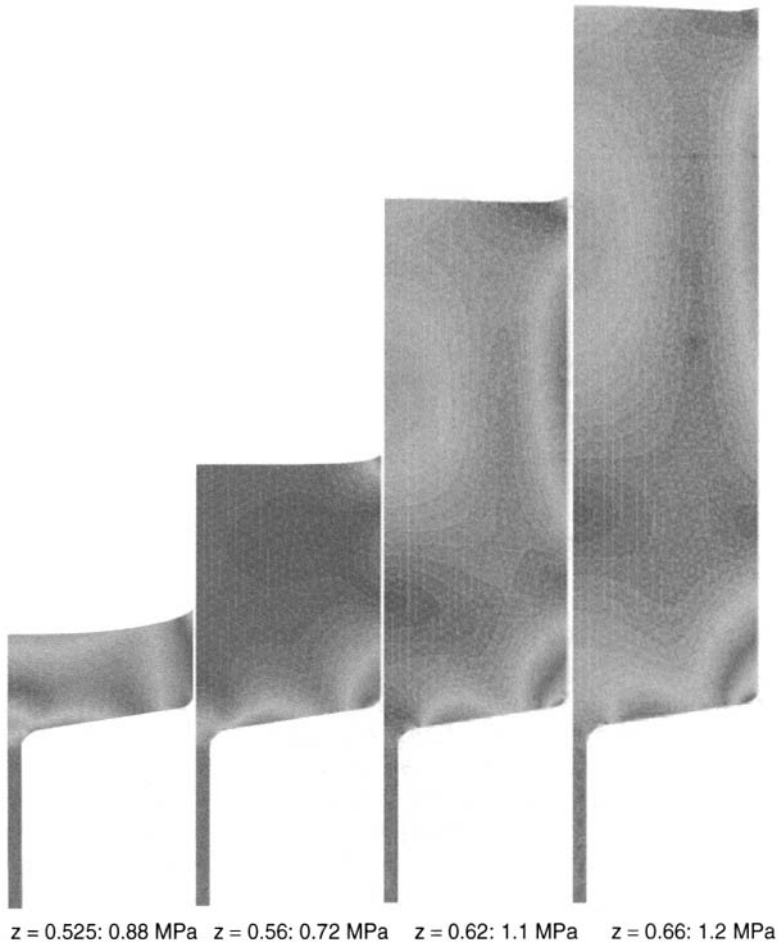


Figure 4.15 (Plate 2) Calculated von Mises stress at different stages of the VGF growth

natural striations due to melt buoyancy-driven convective oscillations, then striations are artificially introduced. A perturbation in the furnace temperature, caused by a sudden and deliberate change in heater power, gives a corresponding change in growth rate and hence in the dopant incorporation at the interface at that moment. By correlating the timing of such events with their appearance in the sectioned crystal the predictions of the simulation can be tested.

4.11 DOPANTS

Table 4.3 lists the main dopants used for control of electrical and dislocation properties. The effective segregation coefficient for each impurity is also listed [27, 28]. This gives some indication of the axial nonuniformity that can be expected in the electrical behaviour in normal directional growth.

4.11.1 N-type InP

N-type low-EPD wafers are obtained by S doping. These make up the largest portion of the substrate market for InP and are used for fabrication of infrared emitters and detectors, such as lasers and PIN diodes. The material can be specified to have an average EPD below a certain figure or to yield a minimum area of wafer below a 'dislocation-free' threshold value. Limits on average EPD of 1000 cm^{-2} and 'dislocation-free' threshold values of 500 cm^{-2} , are commonly applied.

A distribution of EPD is determined by full-wafer mapping. The standard method being to measure 69 positions over a 2-inch wafer in a grid arrangement with each measurement point 5 mm apart. For 3-inch diameter material the pattern is based on a 10-mm grid requiring 37 measurement points.

As the crystal diameter increases it becomes much more difficult to maintain low dislocation content even with the hardening effect of the dopant. Increasing the dopant content is usually not an acceptable option and it is at sizes above 2-inch diameter where the modified LEC variants and VGF growth methods offer distinct advantages in preserving the dislocation specification.

Sn doping is also used for n-type material. Typical concentrations are in the range $1-3 \times 10^{18} \text{ cm}^{-3}$. Sn has no significant effect on dislocation content and typical EPD

Table 4.3 Dopant types and applications

Dopant	Seg. coeff. (k_{eff})	Application	Crystal properties	Market (%)
Undoped	—	LPE source	n-type; $< 1 \times 10^{16} \text{ cm}^{-3}$	~1
Fe	0.0016	OEIC, mm wave	n-type; SI; $> 1 \times 10^7 \Omega \text{ cm}$	~20
S	0.47	LD, LED, PD	n-type; $> 1 \times 10^{18} \text{ cm}^{-3}$ 'zero-D'; $< 500 \text{ cm}^{-2}$	~50
Sn	0.02	LD, LED, PD	n-type; $> 1 \times 10^{18} \text{ cm}^{-3}$	~20
Zn	~1	LD, LED, PD	p-type; $1-10 \times 10^{18} \text{ cm}^{-3}$ low EPD	~10

values would be in the range of $3-5 \times 10^4 \text{ cm}^{-2}$. Low-EPD material can only be obtained in this case by low-gradient growth.

4.11.2 P-type InP

Zn is the only commercially available p-type dopant. It can be incorporated at concentrations above 10^{19} cm^{-3} and at such levels it also has a lattice-hardening effect, yielding dislocation-free material. Its segregation coefficient is close to unity. Zn is volatile in elemental form and this can give rise to variable loss of dopant when it is directly added to the melt. Care must be taken in how the charge is loaded in the crucible so that the dopant is protected up until the point when it is incorporated in the melt. Another approach is to use a measured quantity of well-characterised, predoped InP mixed in the correct proportion with the undoped charge.

4.11.3 Semi-insulating InP

Fe forms a deep acceptor state in InP that acts to compensate the residual shallow donors and when present in a dominant concentration pins the Fermi level near midgap to give intrinsic-like semi-insulating behaviour.

Fe has a small segregation coefficient, no lattice-hardening effect and a limited solubility in the crystal. The minimum concentration required to achieve semi-insulating behaviour depends strongly on the background purity of the compound. For typical undoped InP an Fe concentration in the solid in excess of 10^{16} cm^{-3} is required.

Figure 4.16 is a plot of measured resistivity as a function of the Fe concentration in the same wafer, assessed by mass spectroscopy. A threshold level around $1 \times 10^{16} \text{ cm}^{-3}$ is evident above which the resistivity achieves the accepted 'semi-insulating' minimum

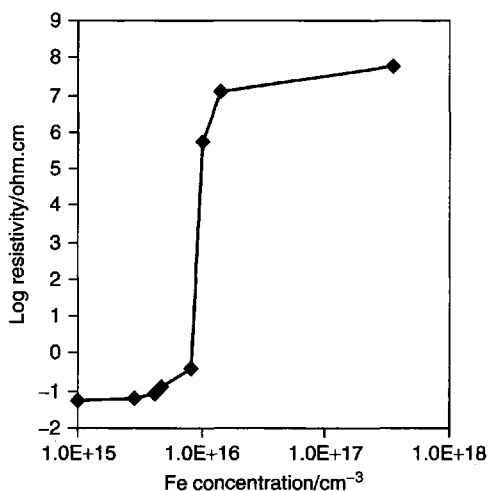


Figure 4.16 Resistivity dependence on Fe-doping concentration

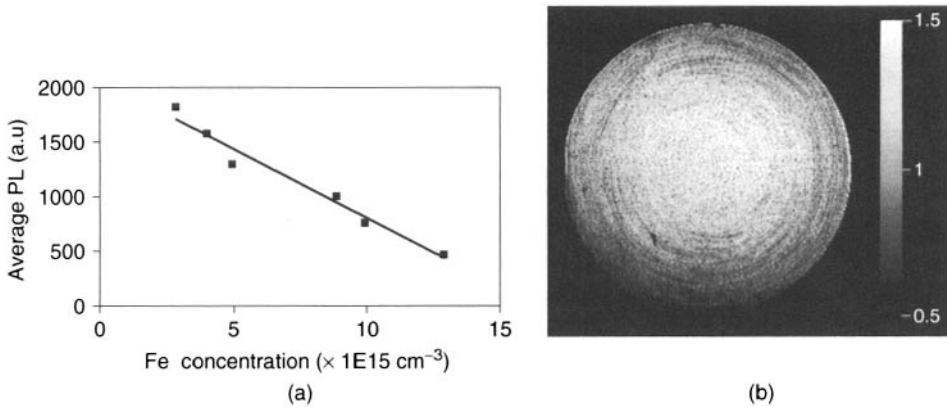


Figure 4.17 (a) PL intensity as a function of Fe-doping concentration, (b) PL intensity map of a semi-insulating InP:Fe wafer

of 10^7 ohm cm and then increases steadily towards 10^8 ohm cm with further increasing Fe content.

The limit on useful Fe doping content is set by the solubility of the impurity. At levels around 10^{17} cm^{-3} FeP_2 precipitates begin to appear as large inclusions in the crystal [29], making that part of it unusable. Due to the low segregation value the Fe concentration increases sharply towards the last-to-freeze end of the crystal and nodular precipitates can be observed in the extreme base of some InP:Fe crystals. The Fe concentration can also be correlated with the photoluminescence response of the bulk material [30]. Figure 4.17a shows the inverse relationship between PL intensity and Fe content. This can be used to provide a detailed distribution map of doping concentration through high-resolution PL mapping, as shown in Fig. 4.17b. The nonuniformity of Fe content exhibited as growth striations and other features is also reflected in variations in electrical resistivity measured by a noncontact capacitance transient method [31]. An example of this is shown in Fig. 4.18a.

Additionally, Fe is a fast diffuser in InP [32], which is a concern for outdiffusion into epitaxial structures. There has consequently been a strong interest in attempting to produce undoped semi-insulating InP, analogous to the GaAs case, where conduction is controlled by native deep level defects. Investigations have involved heat treatments of high-purity undoped InP and some success has been achieved in semi-insulating behaviour in low residual carrier concentration material [33]. However, detailed analysis of such samples has indicated that the required compensation balance has been achieved through a reduction in native shallow donor levels as a result of annealing, together with inadvertent low concentration contamination of the samples with Fe, probably from the furnace and ampoule.

The limiting role of native shallow donors has been suggested in the cases where precise analysis of the chemical donor impurities has shown these to be insufficient to account for the measured carrier concentration [12]. Growth from In-rich melts [11] and synthesis from In solution [10] has resulted in the lowest carrier concentration material, suggesting a stoichiometry-related influence. There is evidence that the defect complex $V_{\text{In}} - \text{H}_4$ that is known to be a shallow donor [34] is at least partly responsible for the

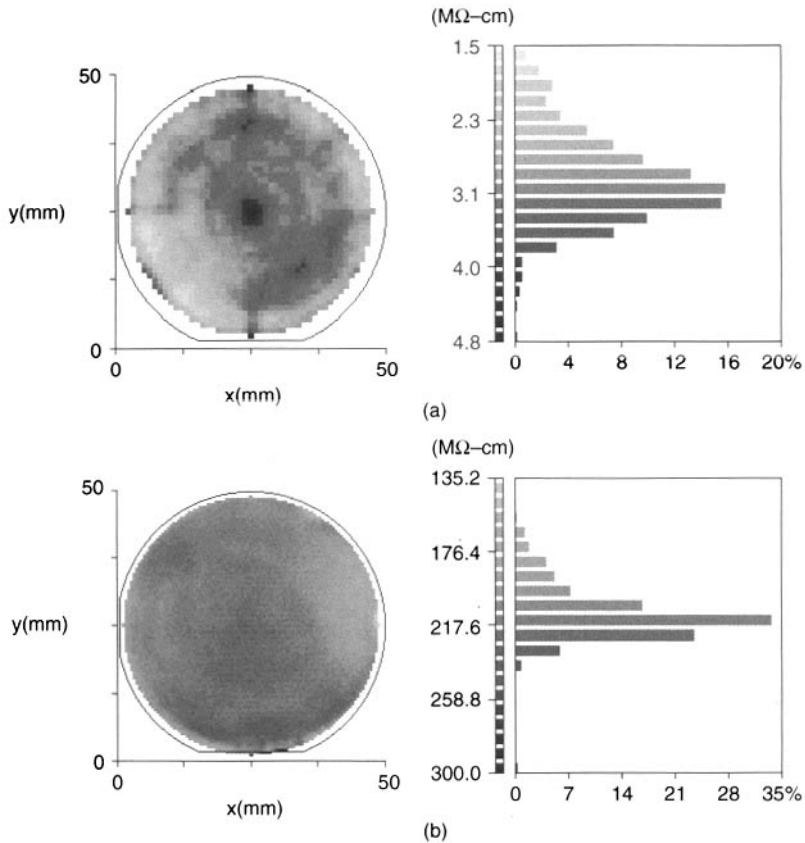


Figure 4.18 (Plate 3) (a) Resistivity map of Fe melt-doped wafer, (b) resistivity map of Fe diffusion-doped wafer

background carrier concentration. The defect concentration can be determined from its infrared local vibrational mode signature and has been shown to have a value around $1.5 \times 10^{15} \text{ cm}^{-3}$ in annealed crystals [12].

Hydrogen can be introduced into the melt from the puller atmosphere through gas-phase reactions of the water content of the boric oxide. During heat treatment these hydrogen-related complexes can be dissociated and redistributed depending on the thermal history. Heat treatment can therefore play an important role in the control of the electrical uniformity of semi-insulating InP, as is the case for undoped GaAs. However, whereas in GaAs the anneal acts only on native point defects, in InP there can also be an Fe-redistribution effect in addition to the observed reduction in donor complexes. Thus the resistivity and Hall mobility are both enhanced by the heat treatment of Fe-doped InP at temperatures between 750 and 1000 °C, for treatment times of several hours. In this way also it is possible to lower the critical threshold concentration of Fe for semi-insulating behaviour [35, 36].

One approach to achieving very uniform semi-insulating wafers of relatively low and constant Fe concentration, and hence avoiding the effects of segregation seen in a melt-doped crystal, has been to diffuse Fe through the material [37, 38]. This is usually done in

wafer form at high temperature using either a FeP_2 vapour ambient or a surface-deposited source. Figure 4.18b shows a resistivity map of a semi-insulating wafer obtained by Fe diffusion into undoped InP.

4.12 CONCLUSION

InP is an important semiconductor material with established niche markets in fibre-optic telecommunications devices. It is also a contender for new high-performance communication devices due to its potential advantages in high-frequency operation. Extensive experience has been gained in the processing of large-area 'non-silicon' wafers for high-speed integrated circuits and microwave devices for consumer applications. This has created an infrastructure, acceptance and technology base for compound materials and InP can potentially benefit from this as a perceived next-generation product to GaAs microwave devices.

Volume manufacturing of InP integrated circuits and electronic devices will require the availability of semi-insulating wafers with diameters of 100 mm or larger. Such substrates are already available and 150 mm wafers have been demonstrated in both VGF and VCZ-type growth. Currently such wafers are, relatively, extremely expensive; a factor of 5 times or more compared with equivalent-area GaAs substrates. Since raw material costs are broadly similar, the burden and focus of the cost pressures will fall on the efficiency of the crystal-growth processes. It remains to be seen which of the available growth methods will offer the optimum combination of productivity and specification for consumer markets.

ACKNOWLEDGEMENTS

The author gratefully acknowledges U. Sahr, University of Erlangen for results on VGF growth and also colleagues at Wafer Technology Ltd.

REFERENCES

- [1] H. Welker, (1952) 'On new semiconducting compounds', *Z. Naturforsch.*, **7a**, 744–749.
- [2] H. Welker, (1955) 'Optical and electrical properties of GaAs, InP and GaP', *J. Electron.*, **1**, 181–185.
- [3] L. Nguyen 'DC to 100 GHz high-speed and mixed-signal integrated circuits', *RF Design*, Oct. 2003.
- [4] D. Yu, K. Lee, K. Bumman, D. Ontiveros, K. Vargason, J.M. Kuo, and Y.C. Kao (2003) 'Ultra high-speed InP–InGaAs SHBTs with f_{max} of 478 GHz', *IEEE Electron. Dev. Lett.*, **24**, No. 6, 384–386.
- [5] K.J. Bachman and E. Buehler, (1974) 'Phase equilibria and vapour pressures of pure phosphorus and of the indium/phosphorus system and their implications regarding crystal growth of InP', *J. Electrochem Soc.*, **121**, 835–846.
- [6] 'Toxicology and carcinogenesis studies of InP' NTP Technical Report 499, NIH publication No. 01-4433, July 2001, U.S. Dept of Health.
- [7] J.E. Wardill, D.J. Dowling, R.A. Brunton, D.A.E. Crouch, J.R. Stockbridge and A.J. Thompson, (1983) 'The preparation and assessment of indium phosphide', *J. Cryst. Growth*, **64**, 15–22.

- [8] S.B. Hyder and C.J. Holloway Jr., (1983) 'In-situ synthesis and growth of indium phosphide', *J. Electron. Mater.*, **12**, 575–585.
- [9] P.J. Dean, M.S. Skolnick, B. Cockayne, W.R. MacEwan and G.W. Iseler, (1984) 'Residual donors in LEC Indium Phosphide', *J. Cryst. Growth*, **67**, 486–494.
- [10] E. Kubota and K. Sugii, (1981) 'Preparation of high-purity InP by the synthesis, solute diffusion technique', *J. Appl. Phys.*, **52**, 2983–2986.
- [11] I. Grant, L. Li, D. Rumsby and R.M. Ware, (1983) 'Growth of indium phosphide from indium rich melts', *J. Cryst. Growth*, **64**, 32–36.
- [12] R. Ware, (2001) 'Perspective for large semi-insulating indium phosphide substrates', *Proc. Int. Conf. on InP and Related Compounds*, IPRM-13, Nara, Japan, 121–124.
- [13] J.B. Mullin, A. Royle and B.W. Straughan, (1970) 'The preparation and electrical properties of InP crystals grown by liquid encapsulation', *Symp. on GaAs and Related Compounds*, Aachen, 41–49.
- [14] W. Bardsley, G.W. Green, C.H. Holliday, D.T.J. Hurlle, G.C. Joyce, W.R. MacEwan and P.J. Tufton, (1975) *Inst. Phys. Conf. Ser. No. 24*, 355.
- [15] H. Gottschalk, G. Patzer and H. Alexander, (1978) 'Stacking fault energy and ionicity of cubic III-V compounds', *phys. stat. sol. (a)*, **45**, 207–217.
- [16] D.T.J. Hurlle, (1995) 'A mechanism for twin formation during Czochralski and encapsulated vertical Bridgman growth of III-V compound semiconductors', *J. Cryst. Growth*, **147**, 239–250.
- [17] A. Huber and N.T. Linh, (1975) 'Révélation métallographique des défauts cristallins dans InP', *J. Cryst. Growth*, **29**, 80–84.
- [18] Y. Seki, J. Matsui and H. Watanabe, (1976) 'Impurity effect on the growth of dislocation-free InP single crystals', *J. Appl. Phys.*, **47**, 3374–3376.
- [19] Y. Seki, H. Watanabe and J. Matsui, (1978) 'Impurity effect on grown-in dislocation density of InP and GaAs crystals', *J. Appl. Phys.*, **49**, 822–828.
- [20] G.T. Brown, B. Cockayne and W.R. MacEwan, (1981) 'The growth of dislocation-free Ge-doped InP', *J. Cryst. Growth*, **51**, 369–372.
- [21] G.T. Brown, B. Cockayne, C.R. Elliott, J.C. Regnault, D.J. Stirland and P.D. Augustus, (1984) 'A detailed microscopic examination of dislocation clusters in LEC InP', *J. Cryst. Growth*, **67**, 495–506.
- [22] M. Tatsumi, T. Kawase, Y. Iguchi, K. Fujita and M. Yamada, (1994) 'Characterisation of semi-insulating III-V materials grown by vapor pressure controlled Czochralski method', in *Proc. of 8th Conf. on Semi-insulating III-V Materials*, Warsaw, ed. M. Godlewski, 11–18.
- [23] W. Gault, E.M. Monberg and J.E. Clemans, (1986) 'A novel application of the vertical gradient freeze method to the growth of high quality III-V crystals', *J. Cryst. Growth*, **74**, 491–506.
- [24] P. Rudolph, F. Matsumoto and T. Fukuda, (1996) 'Studies of interface curvature during vertical Bridgman growth of InP in a flat-bottom container', *J. Cryst. Growth*, **158**, 43–48.
- [25] U. Sahr, I. Grant and G. Muller, (2001) 'Growth of S-doped 2" InP crystals by the Vertical Gradient Freeze technique', *13th Int. Conf. on InP and Related Materials*, Nara, 533–536.
- [26] M. Kurz and G. Muller, (2000) 'Control of thermal conditions during crystal growth by inverse modeling', *J. Cryst. Growth*, **208**, 341–349.
- [27] G.W. Iseler (1991) 'Resistivity of bulk InP', in *Properties of InP*, EMIS Datareview Series No.6, INSPEC, IEE, 25–32.
- [28] J. Wei, (1995) 'Analysis of dopant distributions in LEC-InP', *Cryst. Res. Technol.*, **30**, 8, 1169–1178.
- [29] D. Rumsby, R.M. Ware and M. Whittaker, (1980) 'The growth and properties of large semi-insulating crystals of indium phosphide', in *Proc. of Semi-insulating III-V Materials*, Nottingham, 59–67.
- [30] M. Erman, G. Gillardin, J. Le Bris, M. Renaud and E. Tomzig, (1989) 'Characterization of Fe-doped semi-insulating InP by low temperature and room temperature spatially resolved photoluminescence', *J. Cryst. Growth*, **96**, 469–482.

- [31] R. Stibal, J. Windscheif and W. Jantz, (1991) *Semicond. Sci. Technol.*, **6**, 995–1001.
- [32] I. Harrison, (1991) 'Diffusion of Fe into InP', in *Properties of InP*, EMIS Datareview Series No.6, INSPEC, IEE, 266–267.
- [33] G. Hirt, D. Wolf and G. Muller, (1994) 'Diffusion mechanisms controlling the preparation of annealed semi-insulating InP', in *Proc. of 8th Conf. on Semi-insulating III-V Materials*, Warsaw, ed. M. Godlewski, 19–22.
- [34] R. Darwich, B. Pajot, B. Rose, D. Robein, B. Theys, R. Rahbi, C. Porte and F. Gendron, (1993) 'Experimental study of the hydrogen complexes in indium phosphide', *Phys. Rev. B*, **48**, 17776–177790.
- [35] Y.W. Zhao, S. Fung, C.D. Beling, N.F. Sun, T.N. Sun, X.D. Chen and G.Y. Yang, (1999) 'Effects of annealing on the electrical properties of Fe-doped InP', *J. Appl. Phys.*, **86**, 981–984.
- [36] R. Fornari, A. Zappettini, E. Gombia, R. Mosca, K. Cherkaoui and G. Marrakchi, (1997) 'Conductivity conversion of lightly Fe-doped InP induced by thermal annealing: A method for semi-insulating material production', *J. Appl. Phys.*, **81**, 7604–7611.
- [37] R. Fornari, T. Gorog, J. Jimenez, E. De la Puente, M. Avella, I. Grant, M. Brozel and M. Nicholls, (2000) 'Uniformity of semi-insulating InP wafers obtained by Fe diffusion', *J. Appl. Phys.*, **88**, 5225–5229.
- [38] M. Uchida, T. Asahi, K. Kainosho, Y. Matsuda and O. Oda, (1999) 'Fe doping and preparation of semi-insulating InP by wafer annealing under Fe phosphide vapor pressure', *Jpn. J. Appl. Phys.*, **38**, 985–988.

This page intentionally left blank

5 Bulk Growth of InSb and Related Ternary Alloys

W.F.H. MICKLETHWAITE

Firebird Technologies Inc., 2950 Highway Drive, Trail, BC, Canada, V1R 2T3

5.1 Introduction—a little history	149
5.2 Why the interest?	150
5.3 Key properties	151
5.3.1 Crystallography	151
5.3.2 Growth-critical material parameters	154
5.3.3 Common growth conditions	154
5.3.4 Impurities and dopants	154
5.4 Czochralski growth	155
5.4.1 Challenges	156
5.4.2 Choice and implications of growth axis	162
5.4.3 Size evolution and its drivers	163
5.5 Bridgman and VGF growth	164
5.6 Other bulk growth methods	165
5.7 InSb-related pseudobinary (ternary) alloys	165
5.7.1 (Ga,In)Sb	166
5.7.2 (In,Tl)Sb	168
5.7.3 In(As,Sb)	168
5.7.4 In(Bi,Sb)	168
5.8 Conclusion	169
References	169

5.1 INTRODUCTION—A LITTLE HISTORY

The binary intermetallic compound indium antimonide or InSb, with a ZnS crystal structure was first identified in 1929 [1] with the In-Sb phase diagram being fully defined by 1952 [2]. That this material was a semiconductor with a very narrow bandgap and extremely high electron mobility began to emerge in the early 1950s, within years of the earliest development of semiconductor silicon. Si has evolved in the intervening decades into a billion-dollar, thousands of tonnes-per-year, major industry. InSb has matured much more slowly into the niche markets for costly, very high performance detectors of 3–5 micrometer infrared radiation with sales of a few \$million annually and much more

numerous but inexpensive magnetic sensors. There are also specialty applications in X-ray monochromation, infrared filters and detector optical-immersion lenses.

Many laboratories participated in the early definition of InSb's characteristics over the following decade with several hundred papers being published. Much of this work defining material preparation, properties and its basic applications was summarized by Hulme and Mullin [3] and Liang [4] in 1962. Most of the key material parameters were summarised by Neuberger in 1965 [5] and again in 1971 [6]. Many of these early data remain unchallenged to the present.

5.2 WHY THE INTEREST?

InSb has the narrowest bandgap of the III-V binary compound semiconductors. The E_0 gap is 235 meV at 0 K and 172 meV at 300 K [7] with the gap increasing nearly linearly from 300 K at 0.27 meV K^{-1} to about 232 meV at 77 K, the temperature range of greatest interest. The gap is direct throughout this interval, which means infrared emitters and detectors made from InSb tend to have high quantum efficiencies throughout this entire span. Figure 5.1 shows this dependency.

InSb infrared detectors have evolved from the earliest photoconductive single-element devices, to linear and now large (1024×1024) photovoltaic focal plane arrays. While other materials are used in other applications, the 'producibility' (ability of material and fabrication technology to reliably and reproducibly make arrays of whatever required size and performance) and high 'operability' (low count of dead pixels) of InSb has led to its domination of the cooled, sensitive, rapid-scan applications in the mid-infrared. While its rather high ($\sim 2E16 \text{ carriers cm}^{-3}$) intrinsic carrier concentration at 300 K constrains

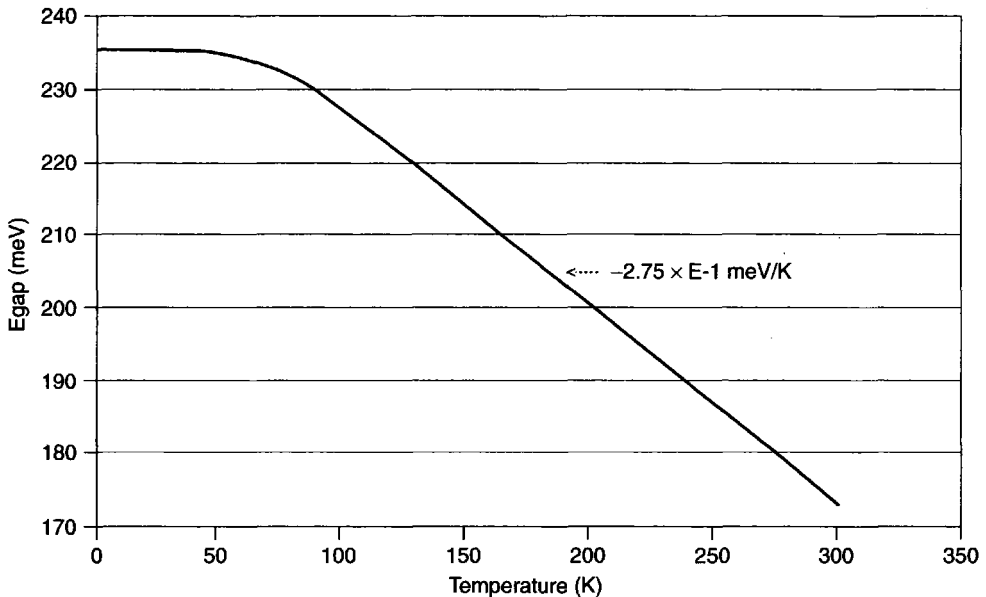


Figure 5.1 InSb bandgap vs. temperature (after Camassel and Auvergne [7])

the development of high-speed transistors and other devices at room temperature, recent developments [8, 9] using InSb as substrate have overcome this limitation using 'carrier exclusion or extraction' devices. The reader is referred to Micklethwaite and Johnson [10] for a review of these technologies.

InSb has the highest room-temperature mobility ($\sim 7-8E4 \text{ cm}^2 \text{ V}^{-1} \text{ s}^{-1}$) of any semiconductor. Since the signal response from a change in transverse magnetic field in the Hall configuration is proportional to the square of the carrier mobility, InSb thin films are widely used in magnetic sensors.

The atomic numbers of In (49) and Sb (51) are both high when compared with those of Si (14), Ge (32), Ga(31) and As(33) with which most readers will be more familiar. This results in a strong interaction with X-radiation. Strong diffraction and the excellent crystalline perfection available make InSb a material of choice for doubly or multiply diffracted X-ray beam monochromators.

5.3 KEY PROPERTIES

Before launching into a discussion of InSb growth technologies, a basic understanding of InSb physics, chemistry and properties is required.

5.3.1 Crystallography

5.3.1.1 ZnS lattice

InSb crystallizes in the ZnS structure (space group F-43m) that comprises two interpenetrating, face-centred cubic sublattices relatively displaced a quarter of the primary-cell body diagonal. All of the III-V semiconductors share this lattice that differs from C(diamond), Ge and Si only in that the two sublattices are solely populated by Group III and Group V atoms, respectively, while the elemental materials are entirely one species. In all these cases every atom is surrounded by four nearest neighbours and covalently shares an average of four electrons.

Figure 5.2 shows three views of this lattice:

- (a) showing tetrahedral coordination around each atom
- (b) showing the alternating In- and Sb-populated {111} planes
- (c) showing 'clear channels' in the $\langle 110 \rangle$ direction

NOTE: in this paper (hkl) refers to the single plane hkl, (pqr) to a direction [normal to (pqr)] and {xyz} is the set of planes like (xyz), i.e. (xyz), (-x,yz), (zxy), etc.

5.3.1.2 Polarity

The {111} planes have the densest atomic packing in this lattice but alternate between totally In and totally Sb atoms populating these planes in hexagonal arrays. This alternation results in distinctly different chemical and mechanical properties for the two sides of all

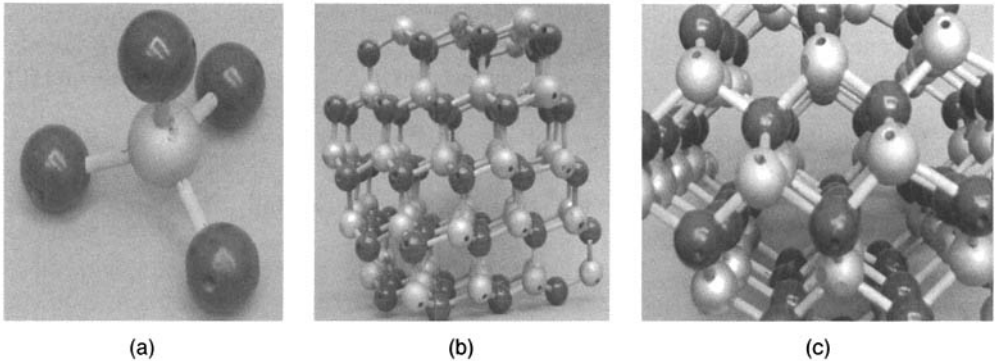


Figure 5.2 InSb lattice (a) tetrahedral coordination (b) $\{111\}$ A and B species planes (c) $\langle 110 \rangle$ clear interstitial channels. The light and dark balls represent In and Sb, respectively

planes of the class $\{h11\}$ (where h is any integer) and requires that this polarity be taken into account during growth. The four $\{111\}$ planes with an even number of negative indices are commonly called** the ‘A, head or In’ planes with the remaining four designated ‘B, tail or Sb’. The polar notation is also applied to $\{211\}$ and $\{311\}$ although the polarity effects decrease quite noticeably as the highest index increases.

This polarity has many effects, notably that damage depth and chemical-attack rates on $\{111B\}$ planes are about twice what they are on $\{111A\}$. It also dictates the choice of seed orientation; for seeds of the $\{h11\}$ type, the $\{h11B\}$ plane must be toward the melt to avoid growth twins [11].

5.3.1.3 Slip

These same four pairs of $\{111\}$ planes are also the slip habit of InSb when exposed locally or generally to stress levels exceeding the critical resolved shear stress or ‘CRSS’. The slip direction is in one of the 12 $\langle 110 \rangle$ directions of the shortest translation vectors in this lattice [12]. If crystals of InSb are stressed by compression, bending or excessive thermal stresses during growth, arrays of slip dislocations result that can be viewed as etch pit arrays defining the traces of the $\{111\}$ planes on the cut plane.

5.3.1.4 Twinning

During growth, a 60° lattice rotation about any III-V bond in a $\langle 111 \rangle$ direction preserves the tetrahedron of opposite species but in a lattice mirroring the parent across the (111) plane. Since both the nearest and second-nearest neighbours remain at their normal distances, the energy required for this ‘twinned’ growth is exceptionally low. For this reason twinning across the set of $\{111\}$ planes is the principal complication in growing single-crystal InSb. The $\{211\}$ and $\{110\}$ twinning reported in other IV and III-V semiconductors is not found in InSb [13].

** [It is worth noting that in the pre-1970 literature there are both this and the reverse notations for ‘head and tail, etc.’ so these early papers must be read with care to ensure correct interpretation].

5.3.1.5 Cleavage

Being a rather weakly bound material; InSb demonstrates pronounced cleavage on all twelve $\{110\}$ planes. The older literature [14] also indicates that the $\{111\}$ and even the $\{332\}$ planes will cleave but the author has never seen this in InSb. Inadvertent cleavage has ended the working life of far too many InSb wafers in processing so great care must be exercised in all handling steps. Conversely, deliberate cleavage offers a ready means to separate device dice from the parent wafer without damage in the last stages of fabrication. Typically, two (110) edges for (111)- and (211)-oriented wafers, sometimes four in the case of (100) wafers, are defined by oriented scribing to initiate cleavage.

5.3.1.6 Diffusion

The vast majority of InSb infrared focal planes are fabricated as diffused- or implanted-junction devices, usually on (111)-oriented wafers. Notably faster diffusion for some species exists in the $\langle 110 \rangle$ directions because these correspond to the clearest interstitial 'channels' in the lattice (see Fig. 5.2c). There is little difference between most other orientations although subtle polarity effects are suggested for $\langle 111 \rangle$ directions.

5.3.1.7 Defects

InSb is among the most perfect materials available commercially. The author has seen defect densities as low as 1 etch-defined pit in a 50-cm² wafer, although higher levels of 10–100 defects cm⁻² are normally specified. Figure 5.3 shows conical etch-pit patterns

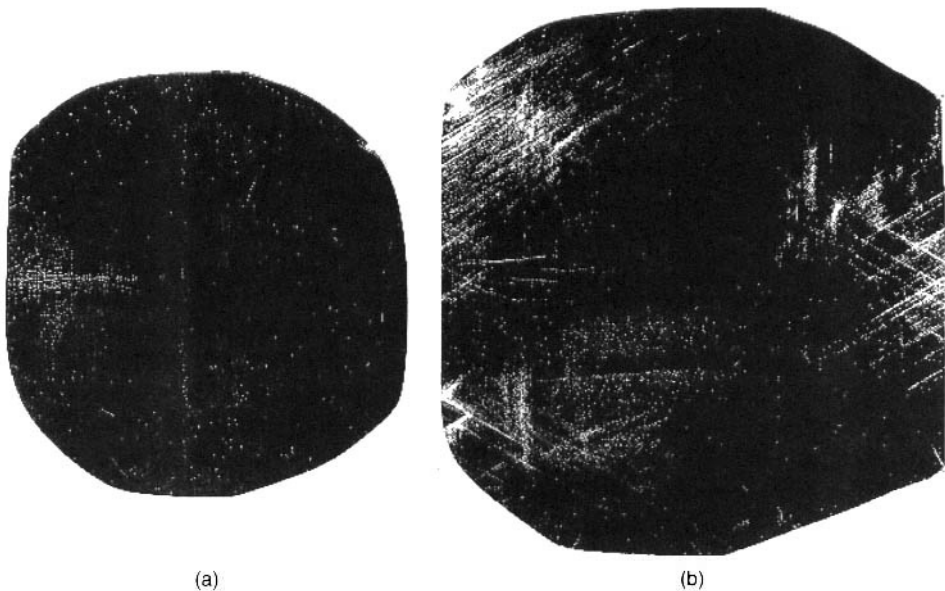


Figure 5.3 InSb conical etch pit patterns (a) typical (b) showing slip

developed by etching with dilute CP4 etchant (HF:HNO₃:HAcetic: water = 3:5:3:20) for (a) a typical production wafer and (b) an early 100-mm wafer showing excessive slip.

5.3.2 Growth-critical material parameters

InSb is the extreme of all the III-V compounds semiconductors in virtually all its material properties. Some of these (the low melting point) assist crystal growers, while others make the growth of high-quality material an exceptional challenge (for example the *very* low CRSS). A knowledge of these and an understanding of their implications is crucial to growing acceptable material—very much a ‘moving target’ in the commercial materials world. Table 5.1, below, summarizes key parameters taken from almost fifty year’s of the literature. The author has given the most evidently reliable data and rejected others; please feel free to contact him to discuss these choices.

5.3.3 Common growth conditions

The key to the very high quality of InSb materials readily available commercially lies in the low (525 °C/798 K) melting point and meticulous attention to detail by growers.

Atypically for metals, InSb *expands* approximately 12.9% on freezing, among the greatest of such expansions (Si 9.6%, Ge 4.9%, GaSb 7.5%) [21]. If the freezing interface is taken as the frame of reference, there is a net flow *away from* the interface at 13% of the freezing rate (termed ‘density effusion’ by the author) which must be explicitly accounted for in any modelling of the crystallizing interface and its dynamics.

Although hydrogen should not (thermodynamically) reduce floating InO_x, in practice it does in the presence of the InSb melt, thus hydrogen is the atmosphere of choice for InSb crystal growth. Vacuum processing is not feasible as it leads to unacceptable Sb losses, while argon cannot be scrubbed sufficiently free of oxygen and water to preclude oxidation. The literature [22] suggests nitrogen may be electrically active.

5.3.4 Impurities and dopants

With its narrow bandgap and applications typically near 77 K where intrinsic carriers are suppressed, the importance of InSb starting material purity cannot be overemphasized. With few exceptions, crystals are grown from precompounded and zone-refined feed. Deportment and control of impurities is too complex a topic for full treatment here but a few generalities may be useful. Elements that displace In (Groups I and II of the periodic table) are doubly and singly ionized acceptors, respectively. Those displacing Sb (Groups VI and VII) are singly and doubly ionized donors. Group IVs are amphoteric, generally behaving as compensating acceptors, while the transition elements have little effect on carrier concentration but are catastrophic to mobility and lifetime. Interestingly, the isoelectronic elements from groups III and V all seem to behave as low-efficiency acceptors.

The great majority of impurities have distribution coefficients ($K = C_s/C_l$) less than unity and segregate to the last-to-freeze portions of the ingot. The exceptions are Zn, Ge

Table 5.1 InSb: significant parameters for growth ([15] except as noted)

Parameter	Value	SI units
Melting temperature [3]	798.4	K
Latent heat of solidification	1.3×10^9	J m^{-3}
Thermal conductivity of liquid @ T_{freezing}	9.23	$\text{W m}^{-1} \text{K}^{-1}$
Thermal conductivity of solid @ T_{freezing}	4.57	$\text{W m}^{-1} \text{K}^{-1}$
Heat capacity of liquid @ T_{freezing}	1.7×10^6	$\text{J m}^{-3} \text{K}^{-1}$
Heat capacity of solid @ T_{freezing}	1.5×10^6	$\text{J m}^{-3} \text{K}^{-1}$
Density of liquid @ T_{freezing}	6.47×10^3	kg m^{-3}
Density of solid @ T_{freezing}	5.64×10^3	kg m^{-3}
Coefficient of liquid volume expansion	1×10^{-4}	K^{-1}
Liquid thermal diffusivity	6×10^{-6}	$\text{m}^2 \text{s}^{-1}$
Liquid dynamic viscosity	3.3×10^{-7}	$\text{m}^2 \text{s}^{-1}$
Surface tension @ 823 K [16]	4.34×10^{-1}	N m^{-1}
Variation in surface tension [15]	-8×10^{-5}	$\text{N m}^{-1} \text{K}^{-1}$
Elastic constants @ T_{freezing} [17]		
C_{11}	5.3×10^{10}	$\text{N m}^{-2} = \text{Pa}$
C_{12}	2.5×10^{10}	$\text{N m}^{-2} = \text{Pa}$
C_{44}	2.8×10^{10}	$\text{N m}^{-2} = \text{Pa}$
Young's modulus @ T_{freezing} (111) [17]	6.8×10^{10}	$\text{N m}^{-2} = \text{Pa}$
Poisson's ratio @ T_{freezing}	0.428	-
Critical resolved shear stress (CRSS)		
491 K [18]	5×10^6	$\text{N m}^{-2} = \text{Pa}$
@ T_{freezing} [19]	2.5×10^5	$\text{N m}^{-2} = \text{Pa}$
Growth meniscus angle [20]	25	degrees
Wetting angle on [16]		
Graphite	124	degrees
BN	134	degrees
Sapphire	111	degrees
Quartz	112	degrees

[Note: for many of these, temperature dependence has been established.]

[Note added in proof: recently, the Ioffe Institute has posted a rather complete set of material parameters for InSb online at www.ioffe.rssi.ru/SVA/NSM/Semicond/index.html].

and the isoelectronic elements. The last is consistent with the fact that InSb has the lowest melting point of all the III-V compounds.

Few commercially significant crystals are grown without deliberate doping to achieve desired electronic characteristics. Te is the donor of choice because of its modest segregation ($K \sim 0.6$) with Zn (~ 2.5), Cd (~ 0.8) or Ge (~ 1.2) being used for acceptors according to application.

5.4 CZOCHRALSKI GROWTH

The Czochralski crystal-growth method is *the* method of choice for commercial InSb production as it readily produces the large volume of near-perfect material required for

modern infrared devices. Ingots producing wafers to 100 mm (4 inch) diameter have recently entered commercial production with defect densities as low as 10 etchable dislocations per square centimetre being regularly achieved. Virtually all the critical details of production for such large ingots are proprietary but there are reasonable references [3] that give basic information.

Growth is usually performed with an unfluxed melt (*not* LEC) under a pure hydrogen cover gas. Since the vapour pressure of Sb at 525 °C at $\sim 5\text{E}-6 \text{ g cm}^{-2} \text{ s}^{-1}$ is very low [3], there is no need for an evaporation-suppressing flux cover. The hydrogen atmosphere is required to reduce the InO_x scum that otherwise forms on the melt, preventing single-crystal growth. A quartz crucible is employed to reduce carbon incorporation. The seed is withdrawn at speeds $\sim 25 \text{ mm h}^{-1}$, giving growth times $\sim 16 \text{ h}$ from seedon. Seed and crucible rotation rates, while critical to the process, are typically low at 2–12 rpm.

InSb growth more closely resembles the growth of silicon and germanium than its more commercialized cousins InP and GaAs. However, there are significant differences in heat transfer due to much-reduced radiative transfer (lower temperature) and increased convective transfer (ultrafluid hydrogen atmosphere). Fluid mechanics in the melt are complicated by faceting and ‘density effusion’ as well as the more usual convection interacting with stirred flows from crucible and seed rotations.

5.4.1 Challenges

5.4.1.1 Twinning

Anyone who has ever grown InSb crystals will have seen more than their fair share of growth twins to the extent that the true art of bulk single-crystal growth is largely that of twin avoidance. The great majority of these arise at the three-phase boundary ring forming the perimeter of the growth interface.

Hurle [23] has examined the incidence and triggering of twins in III-V compound semiconductors, formulating a theory for the nucleation of a twin at an ‘edge’ facet (one touching the crystal circumference) when local conditions thermodynamically favour nucleation in the twinned orientation over the chosen one. Over a certain range of growth angles (angle of the crystal sidewall to the vertical), edge facets can reach the three-phase boundary permitting nucleation to occur preferentially there where the nucleation energy is lowest. Since the surface free energy on {111} (twin) planes is the lowest of all orientations in this lattice, for small nuclei (large supercooling) thermodynamics favours the twinned orientation as the surface energy saved exceeds the incremental twin volume free energy of the differently oriented nucleus. Thus the combination of facet and three-phase boundary readily forms a new crystal in twinned rather than the target orientation. The balance between growth angle, surface tension and supercooling dictates whether twinning will occur for any given seed orientation. While twinning is predicted to be unlikely for {111} in Ge and Si, it *is* likely for InSb and other III-Vs. The increased twinning onto $\langle h11A \rangle$ vs $\langle h11B \rangle$ seed orientations ({111B} and {111A} edge facets) can be explained by subtle changes in melt surface tension against these planes.

Hulme and Mullin [3] offer a good discussion of the twinned crystal orientation as a function of seed orientation. Of all the seed possibilities, {311} is the most interesting as it twins to itself ($\langle 311 \rangle \rightarrow \langle -1-31 \rangle$) while all other orientations twin to higher-index planes that quickly degrade into polycrystalline growth. In the author’s laboratory, the

(211B) growth direction is preferred. This can twin at 19.5, 62 or 90 degrees from the (211) growth plane. In the first case, the new crystal will frequently 'twin back' to the original orientation, leaving a buried twin lens. In the 62° case, disastrous polycrystallinity always results, while the 90° case can take the form of a relatively innocuous, shallow 'edge twin' plate that will propagate vertically through the remaining length of the ingot. Which variant emerges is a sensitive gauge of the melt thermals.

Twin avoidance requires an absolutely stoichiometric melt, free of oxide scum or particulates; an appropriate seed orientation and growth angle (avoiding facets); low (but sufficient) solid thermal gradient and melt thermal control to flatten the interface, minimize supercooling and remelting.

5.4.1.2 Faceting

Anyone who has seen naturally occurring crystals such as quartz or raw diamonds is immediately struck by their tendency to form large flat faces at characteristic angles to each other—'facets'. Figure 5.4 shows the tetrahedrally arranged facets of natural diamonds. These are exactly the {111} set of planes of the diamond cubic lattice, identical to the ZnS lattice of the III-V compounds semiconductors, except for the latter's alternating species on the two sublattices.

In Czochralski-grown InSb, these tetrahedral {111} will always express themselves if geometry and growth conditions permit. Their presence materially affects the distribution of impurities and dopants. The prime determinant in faceting is the number and orientation of the {111} planes that can intersect the growth interface. Table 5.2 sets out this geometry for common growth directions.



Figure 5.4 Naturally occurring {111} facets on diamonds (Photo, DeBeers Group)

Table 5.2 Faceting geometry in the ZnS lattice

Pull direction	{111A} facets	{111B} facets	Angle to growth plane	Rotational spacing
(100)	2	2	54.7°	0/90/180/270°
(110)	1	1	35.3°	0/180°
(111A)		3	70.5°	0/120/240°
(111B)	3		70.5°	0/120/240°
(211A)	1		19.5°	—
(211B)		1	19.5°	—

One of the earliest discussions of the facet effect in InSb was given by Mullin and Hulme [24]. They noted that seed orientations at or near (111) orientation resulted in large flats having {111} orientations (facets), that these were displaced to one side and distorted the expected three-fold boule symmetry when there was a deviation from exact (111) orientation, and that all these were associated with anomalous impurity distributions. Hurle *et al.* [25] demonstrated that interface breakdown of a (100) crystal grown with excess In by constitutional supercooling resulted in a ‘factory roof’ surface of {111} facets. Ivleva *et al.* [26] extended this work to (100), (110), (211) and (511)-grown crystals, finding facets in each case; two, opposed for (100) and (110), one for (211) and two ‘hardly discernible’ ones for the (511). Comparing these results with Table 5.2 demonstrates the apparent asymmetry between possible {111A} and {111B} facets (only the latter developed on the (100) growth face at 54.7°) while both (111A) and (111B) appeared on the (110) face.

Noting that the facet-dominated ingots grown under flat-interface conditions and developed in the central portion of ingots with convex (solid) interfaces but were absent for concave(solid) interfaces, Hulme and Mullin [3] explained the facets as resulting from the requirement for significant supercooling to maintain (111) [facet] growth—thus approximate tangency to the melt isotherms was required for facet development. The reader is referred to Sangster [27] for development of the theory that nucleation on the (111) is the most difficult and a discussion of facet-growth mechanics.

5.4.1.3 Segregation by ‘normal freeze’

The slow withdrawal of a crystal from the melt is the equivalent of a ‘normal freeze’ [28] during which $K < 1$ dopants tend to remain with the melt while $K > 1$ are preferentially incorporated into the growing crystal. This results in an automatic impurity gradient along the ingot length that must be taken into account when targeting doping levels—the large-diameter portion of the ingot comes late in growth where the axial impurity gradient is steepest.

5.4.1.4 Segregation to ‘striations’

Very early in InSb growth experimentation it was noted that smooth, repeating structures could be discerned by etching after the growth of heavily doped ($> 1E18 \text{ cm}^{-3}$) crystals.

Termed 'striations', there was prolonged and vigorous debate over what they were and their origins. Radiotracer experiments revealed that they were periodic, major (factor of 2–10) variations in the dopant concentrations. Their origin was postulated to be periodic variations in melt temperature due to convective cycling or asymmetry between the rotation and thermal axes.

Work to characterize these is typified by three papers by Morizane *et al.* [29–31]. They found that striations persisted without using seed/crucible rotation and hence they were derived from convective effects. This was confirmed more recently by directed-freezing experiments in microgravity [32] in which striations were not present under conditions that created them on earth. The Morizane papers established that the striations reflect the exact shape of the growth interface, could be made to show the shape and size of growth facets and could be turned on/off by the presence/absence of thermal asymmetry or convective melt currents in the growth system.

The striation mechanism is explained by temporal variations in growth rate and their accompanying changes in solute incorporation. In the presence of a segregating impurity, the melt ahead of the growth interface has a solute-enriched (assuming $K < 1$) boundary layer whose thickness is controlled by the interaction of mixing, diffusion and growth rate. Burton *et al.* [33] is the seminal paper for this topic. If the interface accelerates, $K_{\text{effective}}$ more closely approximates unity and more solute is incorporated into the crystallizing material; and vice versa. Thus a cyclic temperature causes a cyclic growth rate and results in cyclic impurity incorporation that can be revealed as striations by etching. In extreme cases, the interface may even melt back ('remelt') causing the effective growth rate to cycle between zero and some high rate.

While these striations are not seen in more lightly doped material, it is probable that the mechanisms that trigger their formation are still at work. Accordingly, great care is taken to maintain thermal symmetry and to control convective currents within the melt to obviate these cyclic impurity variations. For intermediate cases (doped $\sim 1\text{E}17\text{ cm}^{-3}$) striations may appear only on facets where they manifest themselves with a characteristic iridescence after etching. Striations also offer a means of monitoring the variation in interface shape throughout growth as conditions are experimentally adjusted, thus they form a useful tool for improving growth conditions.

5.4.1.5 Segregation to facets

Anomalous (factor of 2–8) segregation of impurities to certain regions of grown crystals was an early puzzle in InSb growth. Mullin [3, 24, 34] did much of the early work to resolve this. Using electrical measurements and radiotracer studies he established that Te ($K \sim 0.6$) was apparently segregating to regions of (111) growth, the facets, as if K were ~ 4 . Other workers found similar effects for Se, Ge and other elements. Initially this was attributed to $K_{\text{effective}}$ being six times greater on-facet than off, making $K_e \sim 3-4$. Similar ratios were found for other elements. Mullin's [34] autoradiographs (Fig. 5.5) for Te segregation for four growth directions remain one of the best illustrations of the facet-segregation effect. It is worth noting that the (111B) case has a single, central facet; the (111A) has 3 strong peripheral facets and a weak central one; the (110) two, one weak and one strong; and the (100) two weak and two strong. This is an excellent demonstration of the different degree of segregation between (111A) and (111B).

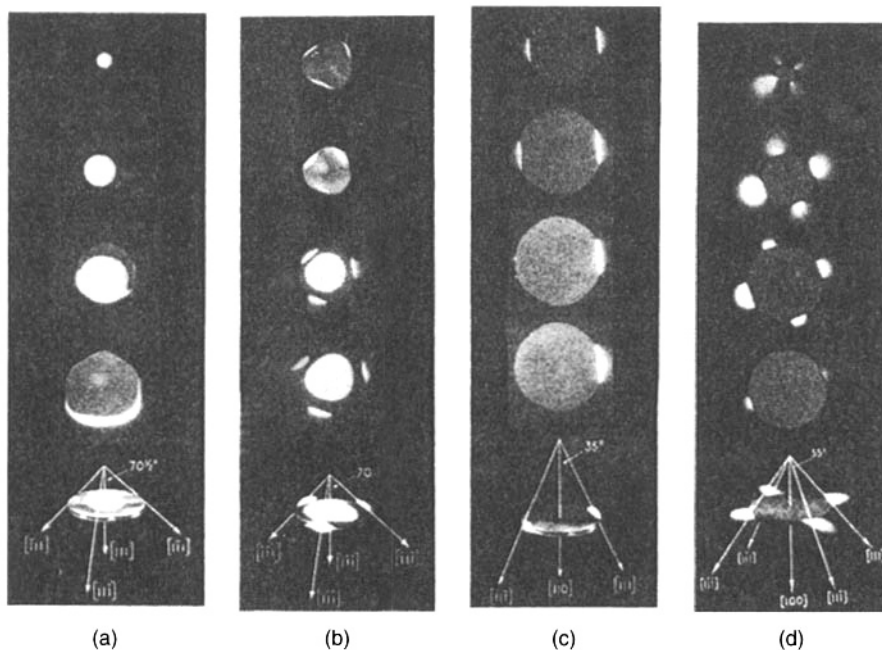


Figure 5.5 Autoradiographs [34] of InSb [Te] wafers cut perpendicular to growth in the (a) $\langle 111B \rangle$ (b) $\langle 111A \rangle$ (c) $\langle 110 \rangle$ (d) $\langle 100 \rangle$ directions. (Note: original figure uses *reverse* notation.) (Reproduced with permission from J.B. Mullin)

Mullin [34] initially explained this effect by considering the possibility of differential stirring on- and off-facet as altering the boundary layers but later settled on a requirement for higher supercooling on facets with their presumed nucleation difficulties. Using the phase diagram for InSb-Te and invoking equilibrium, only part of the differential segregation could be explained. He further postulated that differential growth rate on- and off-facet might be the cause.

This last has been shown [35] to be the probable cause. The geometry of the species populating the $\{111\}$ planes is such that it requires double-atom nucleation to form a 2-D nucleus [27], parallel to the parent plane. Such nucleation has a probability that is approximately the square of the probability of nucleation on a (110) plane under equivalent circumstances. This nucleus then proceeds to grow in these same two dimensions, that is to say strictly laterally rather than adding height steps concurrently. Thus each (111) step nucleates and grows sideways to the limiting isotherm before the addition of the next step. This is unique among all orientations, as all other planes are much more easily nucleated then grow by further 3D nucleation (a combination of (111) , (100) and (110) steps) and expansion. Since all planes have about the same volume growth rate under given circumstances, the lateral growth of the (111) planes must be exceptionally rapid. Using lateral growth rates of $1E5$ and $1E-3$ cm s^{-1} (on- and off-facet), Hayakawa was able to explain $K_{\text{on}} \sim 6.9$ and $K_{\text{off}} \sim 0.63$ for Te. The explanation of the extraordinary facet impurity incorporation then is this huge difference of effective growth rate—bulk vs monostep-lateral. The latter's rapidly advancing sidewalls trap impurities much more completely than the quasiequilibrium off-facet process resulting in the large disparity in K_{eff} .

Reflecting this reality, the literature now typically quotes either or both of 'on-facet' and 'off-facet' segregation coefficients.

5.4.1.6 Defects and slip

The crystalline perfection of seeded melt growth is initially constrained by the quality of the seed crystal employed. While measures such as 'Dash' necking may be required to minimize these defects in Si and Ge, careful mining of standard InSb ingots typically yields seeds with fewer than 10 etchable defects per square centimetre, so this is *not* a problem in InSb Czochralski growth.

The most common defects in CZ InSb are screw dislocations propagating in the direction of growth. These may be revealed as conical etch pits on {111}, teardrop-shaped pits on {211} or indistinct blobs on {100} by the appropriate choice of etchant. The one:one correspondence of these has been verified in the author's laboratory and several others. A typical (111) wafer from a < 80-mm (211)-grown ingot is shown in Fig. 5.3a. This wafer also shows the characteristic 'eagle' pattern (cluster in the centre of the major edge growth facet, central 'T' shape plus (sometimes) two curved arcs originating from the centre of the same edge) and a scattering of random pits. Typical etch pit densities (EPD) are in the range of 1–100 pits cm⁻², averaged over the wafer surface. Given their low number, they are simply counted under a ×25 microscope. Under adverse growth conditions this count may rise several orders of magnitude, resulting in lineage with a 'zipper' appearance. This class of defect is normally strictly limited by device manufacturers' specifications as they correlate with defective pixels in photovoltaic IR focal plane arrays.

Not visible but present on most wafers etched in this way are a much larger number of roughly hemispheric pits not correlated with dislocations. Similar structures have been discussed by Iizuka [36] for GaP who wondered if they might be vacancy aggregates or small dislocation loops. Work in the author's laboratory has established that they are not precipitates. So far, no correlation to device performance has been made with these and they are not subject to specification.

At several times during the author's career, ingots grown under experimental conditions have revealed a type of defect that presents itself as 'star' arrays of etch pits. On a (111) plane these present as one very large central etch pit with chains of barely resolved etch pits radiating up to 100 micrometres outward on the six arms of the intersecting traces of {110} planes at 60° intervals around this central pit. In less severe cases there may be just the central pit and fewer radial pits on just one opposed {110} trace pair 'saturns'. Similar features were reported by Ol'khovikova *et al.* [37] who estimated the cause to be the result of compressive stress from a second-phase inclusion. While these authors correlated the defects with oxides of Al and Si, in our laboratory these are believed to be the result of Sb precipitates; charges that initially showed them did not when regrown and other charges that did not show them when first grown showed them in a subsequent growth. Stable entrained oxides would not likely have been removed or created by these treatments. Device manufacturers cannot tolerate the intensely damaged areas surrounding star defects so growth conditions must be adjusted to eliminate them. As device manufacturers' demands for ever-larger wafers occasion the growth of ever-larger ingots it is inevitable in every growth system that thermal gradient/stress limits will be reached. For any given configuration, thermal stresses deriving from differential

lattice expansion due to existing thermal gradients will inevitably exceed the critical resolved shear stress (CRSS). Once this occurs, the solid relaxes this stress by slip (see Section 5.3.1.3) on {111}.

Mil'vidskii and Bochkarev [19] discuss the key issues of thermal stress generation, localization and the concept of the 'critical' stress. Many other authors describing most commercial crystal growth systems have considerably elaborated this topic, most notably making the point that it is the portions of the general (von Mises) stress resolved onto the {111}(110) slip system that governs whether slip relaxation will occur—hence the term 'critical *resolved* shear stress'.

Mil'vidskii and Bochkarev make many good points: (i) the probability of slip is governed more by peak stress than the duration of stress application (ii) the critical stress climbs quickly as temperature falls (iii) the maximum heat flux in a Czochralski crystal is within a crystal diameter of the growth interface, as is the peak thermoelastic stress (iv) slip can only be avoided by reducing thermal gradients or doping (so-called 'solution hardening').

5.4.2 Choice and implications of growth axis

5.4.2.1 (100) and (110) growth

Many early workers grew InSb crystals in (100) or (110) orientations as they were familiar with the behaviour of the better-known Si and Ge work that preceded. At least two commercial InSb suppliers still offer (100)-grown material. Sangster [27] gave an early but lucid analysis of growth mechanics at an atomic level on low-index planes. For (100) there are minimal nucleation problems but considerable difficulties in maintaining stoichiometry on a flat interface that can cause 'increased dendritic growth, vacancies' and other defects. For (110) nucleation is a greater problem but, once nucleated, these planes can readily expand.

The presence of one/two pairs of asymmetric {111 x } facets on (110)/(100) growth interfaces leads to spatially separated, nonuniform dopant distributions. An early paper by Strauss [38] reported not only the four {111} facets but also a small central (100) facet, the only reference the author has seen to {100} faceting. The technologically significant (111) wafer orientations require oblique cutting at 35.3/54.7° from these orientations. Facets and waste make these growth orientations uncommon today.

5.4.2.2 (111)

The (111B) growth plane has the difficult nucleation—rapid lateral growth pattern and severe facet segregation already described. Some attempts to trade the awkward central facet for three edge facets by inverting the seed to (111A) resulted in myriad twins and polycrystallinity. The (111B) orientation remains the easiest orientation in which to grow single crystals and from which to fabricate (111) wafers, *provided segregation is not an issue*. While one could, in theory, suppress the edge twins in the (111A) orientation by exquisite control of melt thermals, no practical examples of this have been reported.

5.4.2.3 (211)

Sangster notes that $\{h11\}$ planes offer an interesting compromise between $\{111\}$ and $\{100\}$ as the $\{111\}$ double layers propagate by combinations of difficult $\{111\}$ and easy $\{100\}$ lateral steps with the latter mitigating the former. Given the single side facet that can be minimized by growth controls and the shallow cutting angle to the desired $\{111\}$, the $\langle 211B \rangle$ orientation is now used for the bulk of commercial production. Some caution is still required as the electrical evaluation of $\langle 211 \rangle$ -sourced wafers and fabrication of the final wafer must exclude the facet-grown region ($\sim 5\text{--}8\%$ of diameter).

5.4.2.4 Other orientations

Higher-index planes are generally unfavorable for quality single-crystal growth. While $\langle 311 \rangle$ and $\langle 511 \rangle$ growth has been reported, no commercial-scale use is made of these orientations.

5.4.3 Size evolution and its drivers

Since InSb is used primarily for the fabrication of rectilinear, infrared-sensitive focal plane arrays that are increasing steadily in size, there is a strong trend to ever-larger wafer sizes at a rate limited only by improvements to growth technology and economics. For a current 480×640 array at 20 micrometre pitch, the yield from a 71-mm wafer is 13 raw dice but a 100-mm wafer yields 39 with only slightly increased costs, a huge yield/cost improvement. InSb is not alone in this evolution; Si, GaAs and more recently SiC (for blue LED substrates) have all followed this same path. Figure 5.6 shows the

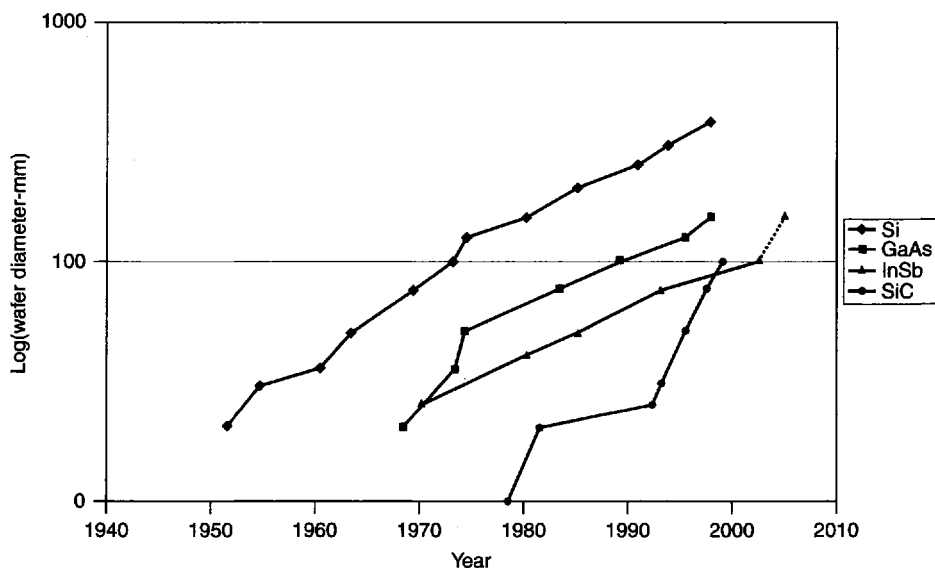


Figure 5.6 The evolution of wafer size. (Si/GaAs/SiC data IEEE [39], InSb from Firebird Technologies)

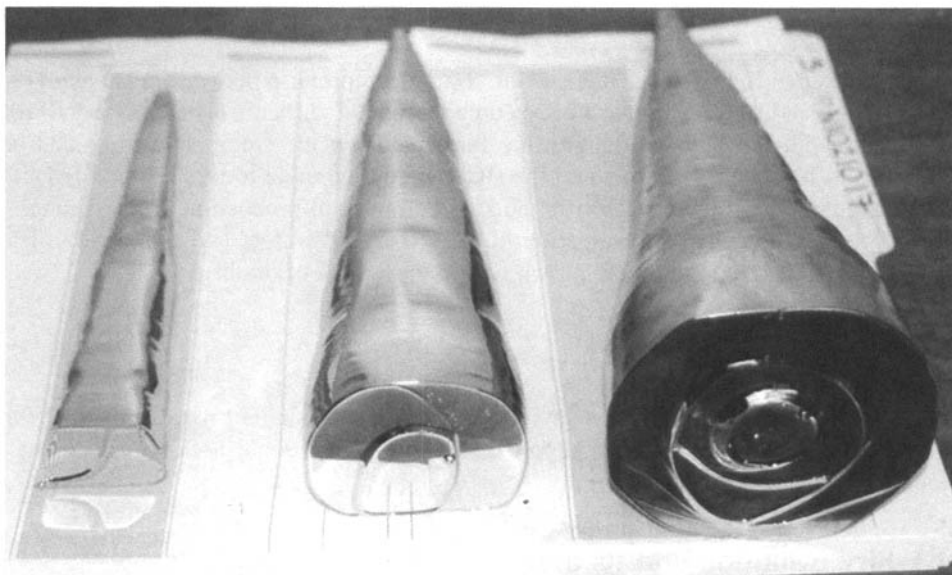


Figure 5.7 The evolution of ingot size: 25/50/100mm-yielding (211B) InSb ingots (Firebird Technologies)

evolution of these. It seems likely that pressure will build for 150-mm InSb wafers in the next few years.

To yield these wafers, a steady increase in ingot dimensions has been required. Each size increment requires both new equipment (crystal mass rises as approximately the cube of the wafer dimension, polishers for 50 mm cannot handle 75 mm, etc.) and better understanding and control of the growth processes. The biggest challenge in crystal growth is management of the grower environment to minimize crystal thermal gradients and avoid the occurrence of ruinous slip. While smaller crystals can be grown by skilled practitioners using empirical methods, the cost and complexity of failed growth runs has led to increasingly sophisticated thermal modelling of the grower systems. The performance of existing systems can be explored, improvements made and then tested in an evolutionary improvement cycle. In the author's laboratory, the 50-mm standard wafer of ~ 1990 was supplanted in 1993 by 75 mm and recently by 100-mm wafers as the leading-edge commercial product. The rise in ingot size and mass from 25 mm/1 kg to 100 mm/18 kg is shown in Fig. 5.7.

5.5 BRIDGMAN AND VGF GROWTH

Directed solidification in quartz ampoules contained within pressurized chambers provided the technology that permitted the early development of GaP, InP and GaAs that require many atmospheres of overpressure to suppress spontaneous decomposition. While techniques such as vertical gradient freeze (VGF) remain important to these material technologies, they were not required for InSb whose commercial development quickly settled onto and evolved along the Czochralski growth route.

However, the simplest means of obtaining small single crystals of InSb for experimentation is to grow them by the horizontal Bridgman method: a graphite or quartz boat, with or without an isolating coating (such as lampblack or graphite) is filled with molten InSb and caused to freeze slowly from one end. Done in a zone-refining apparatus, the process can be repeated an arbitrary number of times with crystallinity improving at each pass until single crystal is achieved. A variant of this has the first-to-freeze end of the ingot seeded with a single crystal of desired orientation. Left unseeded, there were reports that the $\langle 311 \rangle$ direction was the commonest resulting orientation.

While much of the single crystal used in the first decade of InSb experimentation was grown this way, the notorious uncontrolled nucleation of spurious crystals at the boat-triphase intersection greatly limits the probable yield of single crystal. The other serious limitation of this method is the high resulting dislocation count—typically $0.1\text{--}1\text{E}6$ dislocations cm^{-2} vs the $1\text{--}100$ yielded by the Czochralski process. The use of low-wetting containers such as BN or deliberately rough container surfaces relieves but does not eliminate these problems. No commercial production has been made in this way for thirty years.

In recent history, the sequential-freeze technologies have mainly been used to study segregation, see Hui *et al.* [40] or growth-interface mechanics Campbell and Koster [41] where InSb is a convenient materials system and directed-freeze a handy technology. This system has also been used (Duffar *et al.* [42] and Redden *et al.* [43]) to test the effects of growth in microgravity. Some recent use to generate small amounts of device material inexpensively (Mohan *et al.* [44]) has also been reported. These are only a few of the more recent citations but they provide referential access to older work.

5.6 OTHER BULK GROWTH METHODS

Simply put, there are no other commercially significant bulk growth means. For example, while low-temperature growth from solution has been found to reduce dislocations or alter stoichiometric defects in other materials systems, the product of fully developed, modern Czochralski InSb growth does not suffer from these problems so there is no incentive to use the more complicated technologies.

5.7 InSb-RELATED PSEUDOBINARY (TERNARY) ALLOYS

Despite InSb having the narrowest bandgap of the III-V binary compounds, there remains considerable interest in the bulk growth of materials having still narrower gaps. Others are interested in optimized device response at bandgaps between those of the binary III-Vs. To achieve these, many researchers have investigated ternary antimonides, closely related to InSb. Some of these are briefly discussed below.

For these systems, there is generally complete mutual solubility of the pseudobinaries as liquids, suggesting that growth from the melt should be feasible. The challenge lies in the broad freezing range (widely spaced liquidus and solidus), significant tendency to segregate when slowly cooled and the resulting inhomogeneity. Unless sufficient control can be achieved, there tends to be an impractically high spatial variation in composition. Given the moderately strong variation of lattice parameter with composition, this creates strain and stress. In these relatively low-strength (low-CRSS) materials high defect counts,

massive slip or outright shattering of the grown ingots can result. Rapid solidification minimizes these effects.

Unfortunately, growth of single crystals usually requires slow growth. The challenge for these systems then becomes finding an optimal compromise between crystallinity and acceptable uniformity. With a few exceptions these are seldom found in bulk-growth systems, rather in epitaxial technologies (which have their own problems and compromises).

Growth in these systems is further complicated by the broad freezing range (furnace thermal designs must be a compromise instead of optimized), sometimes the presence of more than one preferred crystal structure and occasionally a miscibility gap in the solid state.

5.7.1 (Ga,In)Sb

Interest in (Ga,In)Sb began early and continues actively as this system offers compositionally tunable access to the infrared spectrum in the 1.5–7-micrometer range of great interest for communications, emission control monitoring and thermophotovoltaics.

The phase diagram of the pseudobinary system was established by Woolley and Lees [45]. Their data has been fitted by the author to the following equations; the phase diagram is reproduced as Fig. 5.8 below with these fitted lines.

$$\begin{aligned} \text{Liquidus:} & \quad T_l = 524 + 278 \times x - 94.4 \times x^2 \\ \text{Solidus (0 < } x < 0.75): & \quad T_s = 524 + 55.2 \times x + 49.9 \times x^2 \\ \text{Solidus (0.75 < } x): & \quad T_s = 1091 - 1510 \times x + 1128 \times x^2 \end{aligned}$$

The critical features of this diagram are the divergence between liquidus and solidus that translates to an estimated segregation coefficient of $K_{\text{GaSb}|x \sim 0} \sim 4$ and $K_{\text{InSb}|x \sim 1} \sim 0.2$,

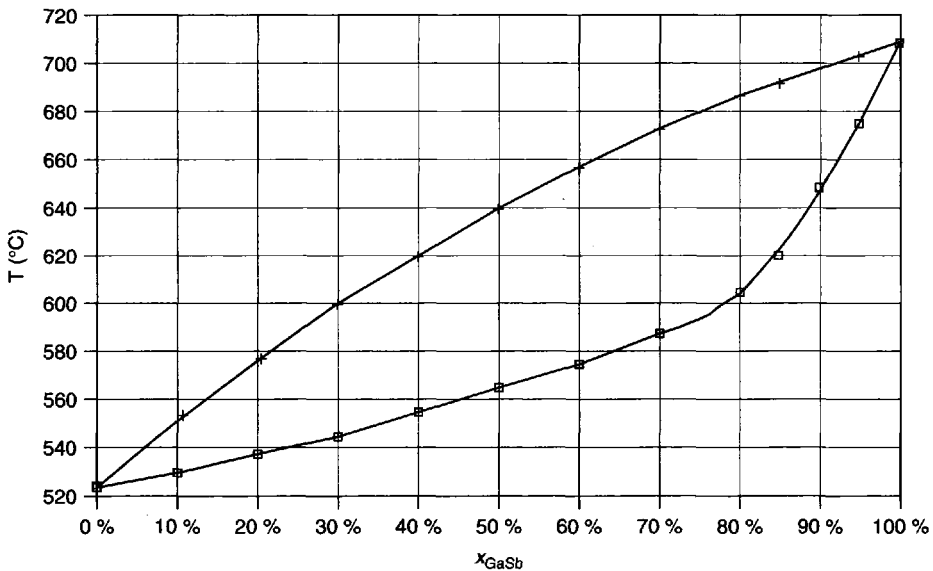


Figure 5.8 The $\text{Ga}_x\text{In}_{1-x}\text{Sb}$ phase diagram

suggesting significant but manageable segregation at both extremes. The ternary phase diagram was generated by Blom and Plasket [46] and confirmed by Ansarsa *et al.* [47].

Some of the earliest growth work was conducted by zone leveling in horizontal boats. It was immediately noted [48] that growth rates greater than $\sim 1 \text{ mm h}^{-1}$ caused interface breakdown due to what is now known as ‘constitutional supercooling’. Bachmann *et al.* [49] characterized the extreme segregation found and flagged the serious strain gradient arising from this compositional gradient.

The Bridgman growth scheme has been used [50] periodically to generate electrical data over a broad compositional range or to study segregation behaviour with/without gravity [51]. The latter found vertical Bridgman segregation at 4 mm day^{-1} in gravity followed the normal freeze equation ($x_{\text{InSb}} = kx_0(1 - g)^{1-k}$, g = fraction frozen) with $k = 0.28$. None of more than twenty papers reviewed reported significant single-crystal yield, the result of the usual problems of heterogenous nucleation on the ampoule walls and twinning.

Other laboratories have used the travelling heater method (aka travelling solvent zone) to improve x uniformity. In 1995 Venkrbec *et al.* [52] achieved excellent homogeneity of $\pm 0.2\%$ for $x \sim 0.95$ but on very polycrystalline ingots. In 1996 Redden [53] achieved single-crystal growth at $\sim 90\%$ GaSb on GaSb seeds with a somewhat greater composition spread. While this work appears promising, it has not apparently been followed up.

Over the past twenty years many laboratories have attempted growth using variants of the Czochralski technique. The simplest approach is the so-called ‘semi-infinite melt’ scheme in which only a relatively small fraction of the charge is withdrawn to avoid excess InSb loading of the remaining melt. Working from the high- x (GaSb-rich) end, the author’s laboratory was able to grow crystals up to 30 mm in diameter by 100 mm long with $0.94 < x < 1$. All of these suffered from a compositional strain gradient and spontaneously cracked upon etching or fabrication despite prolonged strain-relief anneals. One such crystal (6-mm GaSb seed) is shown in Fig. 5.9.

Avoidance of interface breakdown due to segregation requires high rotation rates for seed and crucible and/or the imposition of axial vibration [54]. Avoidance of gross segregation requires other measures: ‘solute-feeding’ [55] (melt is GaSb-replenished from a solid feed slug of matched composition, isolated by a narrow channel) or a ‘floating crucible’ [56] (flow of melt from the reservoir chamber into the growth pool is carefully controlled by a capillary channel through a floating inner crucible). Using these techniques, viable single crystals at 20+ mm diameter with $0 < x < 0.06$ and $0.95 < x < 1$ have been grown.

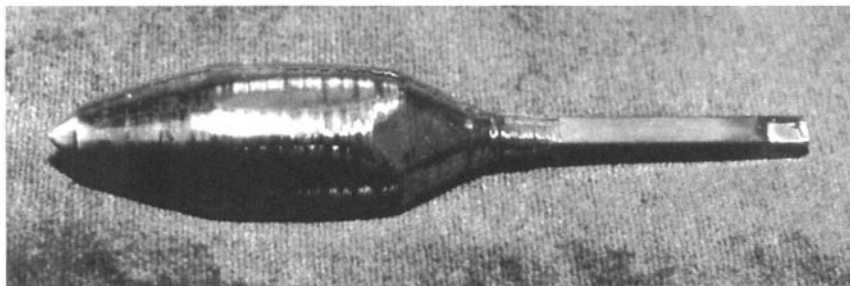


Figure 5.9 A CZ-grown $\text{Ga}_x\text{In}_{1-x}\text{Sb}$ ($x \sim 0.95$) crystal (Firebird Technologies)

5.7.2 (In,Tl)Sb

In 1993 van Schilfgaarde *et al.* [57, 58] considered the possibility of using Tl-substituted InSb as a means of achieving infrared detector response into the 8–12-micrometer range using III-V rather than II-VI (CdHgTe) technology. They calculated that, despite the CsCl crystal structure of TlSb, that there might be solid solubility in the ZnS-type InSb lattice to some 15 mole %. However, their analysis and postulated pseudobinary phase diagram predicted serious problems achieving even 1 mole TlSb using any liquid–solid equilibrium growth process.

Accordingly, there has been no reported work on bulk growth in this system, rather many efforts to grow by MOCVD and MBE. Early work challenged the 15 % solubility (finding 1 % max) but more recently modest success and results to 4 % (11-micrometre cutoff at 77 K) were demonstrated [59]. The reader is directed to Razeghi [60] for a survey of related papers.

5.7.3 In(As,Sb)

This ternary has had a similar, if somewhat longer, history. The phase diagram was roughed-in by Shih and Peretti [61] in 1953. Woolley and Warner [62] established the variation of bandgap with composition, noting the interesting minimum of ~ 100 meV at ~ 60 mole % InSb. This, with the expectation of high mobility makes the In(As,Sb) system potentially attractive for 8–12-micrometre radiation detectors and high-mobility devices. The full ternary phase diagram was published by Stringfellow and Greene [63].

The shape of the liquidus/solidus lines (flat solidus, steep liquidus near InSb; vice versa near InAs) predicts extreme segregation from liquid–solid equilibrium growth methods. While in In(As,Sb) both constituent binaries are ZnS structured, there is evidence [64] for a miscibility gap in the solids between 5 and 70 % InSb (after 2-month anneals) that further bodes ill for equilibrium growth methods. This effect was attributed to strain energy arising from differing atomic sizes.

Accordingly, most experimentation has been confined to epitaxial growth on a variety of III-V substrates, primarily at the low-InSb end of the range to improve lattice matching. While some good device properties have been demonstrated, there is not yet a definitive growth process.

One recent paper [65] reports some success in achieving homogeneity in thin foils by rapid quenching. If this work can be broadened to create single crystals, there may yet be hope for a bulk-growth technology.

5.7.4 In(Bi,Sb)

One of the known limits on this system is the tetragonal crystal structure of the InBi compound that limits the miscibility range of the pseudobinary system to the low-Bi end. A limited amount of work on this system has been reported. Shepelevich [66] reported work on quenched foils and electrical data in the range 77–300 K. Several authors [67–69] report growth of small crystals using the ‘rotary’ Bridgman technique (accelerated crucible rotation or ACRT) to improve interface solute clearing for InBi contents up to ~ 7 %. At

the other end of the compositional range, for InBi of $\sim 80\%$, coarse polycrystals were grown by zone leveling [70].

There is some evidence of abnormal segregation or a solubility limit with reports of Bi or Bi-rich inclusions [71]. The InBi segregation was found to be reduced in microgravity [72], suggesting a strong influence of the differing InSb and InBi densities.

5.8 CONCLUSION

InSb has evolved through the same rich technology stages as the Group IV and 'cousin' III-V semiconductors. Today it makes a contribution modest in scale but significant in impact to a broad spectrum of imaging and sensing devices. Its low melting point makes it a useful material with which to experiment or test new growth systems but the definitive commercial production technology remains the Czochralski growth technique. While InSb's unique material properties make it the material of choice for several key applications; the material's softness, tendency to cleave and ease of succumbing to thermal stress damage make it exponentially more challenging to produce as ingot dimensions increase.

There is no end in sight to this evolution. Focal plane device manufacturers continue to expand the size and capabilities of their arrays, always challenged to provide better sensor resolution, speed and functionality. At least the author's laboratory is already committed to delivering a 150-mm wafer generation within five years and stands willing to help the user community better understand and improve their products through cooperative science. The references listed below are only a small sampling of the over 3500 citations in the author's reference database on antimonide semiconductor technology. Reader queries and discussions are welcome.

REFERENCES

- [1] V.M. Goldschmidt, (1929) *Transactions of the Faraday Society*, **25**, 253–83.
- [2] T.S. Liu and E.A. Peretti, (1952) *Transactions of the American Society of Metals*, **44**, 539–45.
- [3] K.F. Hulme and J.B. Mullin, (1962) Indium Antimonide—A Review of Its Preparation, Properties and Device Applications, *Solid-State Electronics*, **5**, 211–247.
- [4] S.C. Liang, (1962) 'Preparation Indium Antimonide', Chapter 27 of *Compound Semiconductors—Volume 1*, Rheinhold Publishing, New York, R.K. Willardson and H.L. Goering Eds.
- [5] M. Neuberger, (1965) *Indium Antimonide*, NTIS ADA 47667S, 1–201.
- [6] M. Neuberger, (1971) *III-V Semiconducting Compounds*, New York-Washington-London: IFI/Plenum, 77–92.
- [7] J. Camassel and D. Auvergne, (1975) *Physical Review B*, **12**(8), 3258.
- [8] T. Ashley, C.T. Elliott *et al.*, (1997) *Applied Physics Letters*, **70**, 931.
- [9] T. Ashley, C.T. Elliott *et al.*, (1998) *IEEE Proceedings—Optoelectronics*, **145**, 265.
- [10] W.F. Micklethwaite and A.J. Johnson, (2000) Chapter 7 of *Infrared Detectors and Emitters: Materials and Devices*, edited by P. Capper, Kluwer Academic Publishers, Boston.
- [11] R.K. Mueller and R.L. Jacobsen, (1961) *Journal of Applied Physics*, **32**, 550.
- [12] J.W. Allen, (1957) *Philosophical Magazine "A"*, **2**, 1475.
- [13] P. Haasen, (1957) *Journal of Metals*, **209**, 31.
- [14] R.K. Willardson and H.L. Goering, (1962) *Preparation of III-V Compounds*, New York: Reinhold Publishing, 34–45.
- [15] T. Duffar, C. Potard and P. Dusserre, (1988) *Journal of Crystal Growth*, **92**, 467.

- [16] I. Harter, P. Dusserre and T. Duffar, (1993) *Journal of Crystal Growth*, **131**, 157.
- [17] R.F. Potter, (1956) *Physical Review* **103**(1), 47.
- [18] A.R. Chaudhuri, J.R. Patel and L.G. Rubin, (1962) *Journal of Applied Physics*, **33**, 2736.
- [19] M.G. Mil'vidskii and E.P. Bochkarev, (1978) *Journal of Crystal Growth*, **44**, 61–74.
- [20] V. Tatarchenko, (1994) in *Handbook of Crystal Growth, Vol 2b*, D.T.J. Hurle Ed., North Holland, Amsterdam 1011.
- [21] N.N. Sirota, (1978) in *Semiconductors and Semimetals*, **4**, Academic Press, New York, 132.
- [22] S. Nagata, (Toshiba Corp.), (1995) *Japanese Patent* JP 07 33358.
- [23] D.T.J. Hurle, (1995) *Journal of Crystal Growth*, **147**, 239.
- [24] J.B. Mullin and K.F. Hulme, (1960) *Journal of Physics and Chemistry of Solids*, **17**, 1.
- [25] D.T.J. Hurle, O. Jones and J.B. Mullin, (1961) *Solid State Electronics*, **3**, 317.
- [26] V.S. Ivleva, E.V. Kiseleva, R.S. Mitrofanova and V.I. Selyanina, (1969) *Izvestiya Akademii Nauk USSR, Neorganicheskie Materialy*, **5**, 727.
- [27] R.C. Sangster, (1962) Model Studies of Growth Phenomena in the III-V Semiconducting Compound, Chapter 28 of *Compound Semiconductors—Volume 1*, Rheinhold Publishing, New York, R.K. Willardson and H.L. Goering Eds.
- [28] W.G. Pfann, (1958) *Zone Melting*, John Wiley & Sons, New York.
- [29] K. Morizane, A.F. Witt and H.C. Gatos, (1966) *Journal of the Electrochemical Society*, **113**, 51.
- [30] K. Morizane, A.F. Witt and H.C. Gatos, (1966) *Journal of the Electrochemical Society*, **113**, 808.
- [31] K. Morizane, A.F. Witt and H.C. Gatos, (1967) *Journal of the Electrochemical Society*, **114**, 738.
- [32] A.F. Witt and H.C. Gatos, (1975) *Journal of the Electrochemical Society*, **122**, 276.
- [33] J.A. Burton, R.C. Prim and W.P. Slichter, (1953) *Journal of Chemistry and Physics*, **21**, 1987.
- [34] J.B. Mullin, (1962) 'Segregation in Indium Antimonide', Chapter 41 of *Compound Semiconductors—Volume 1*, Rheinhold Publishing, New York, R.K. Willardson and H.L. Goering Eds.
- [35] Y. Hayakawa, M. Nishimura, K. Ishikawa and M. Kumagawa, (1985) *Journal of Crystal Growth*, **73**, 48.
- [36] T. Iizuka, (1971) *Journal of the Electrochemical Society*, **118**, 1191.
- [37] T.I. Ol'khovikova, I.L. Shil'pina, V.S. Ivleva, V.I. Selyanina and V.G. Fomin, (1971) translated from *Fizika Tverdogo Tela*, **3**, 609.
- [38] A.J. Strauss, (1962) *Solid-State Electronics*, **5**, 97.
- [39] Institute of Electrical, Electronic Engineers (2002) as reported in *Compound Semiconductors*, **8**, 45.
- [40] M-j Hui, K. Beatty, K. Blackmore and K. Jackson, (1997) *Journal of Crystal Growth*, **174**, 245–9.
- [41] T.A. Campbell and J.N. Koster, (1998) *Crystal Research Technology*, **33**, 717–31 {and their prior papers listed within}.
- [42] T. Duffar, C. Potard and P. Dusserre, (1988) *Journal of Crystal Growth*, **92**, 467–478.
- [43] R.F. Redden, W.F. Micklethwaite *et al.*, (1998) *Final Report to the Canadian Space Agency: Contract 9F007-4-6027/01-ST*.
- [44] P. Mohna, N. Senguttuvan, S.M. Babu, P. Santhanaraghavan and P. Ramasamy, (1999) *Journal of Crystal Growth*, **200**, 96–100.
- [45] J.C. Woolley and D.G. Lees, (1959) *Journal of the Less-Common Metals*, **1**, 192.
- [46] G.M. Blom and T.S. Plasket, (1971) *Journal of the Electrochemical Society*, **118**, 1831.
- [47] I. Ansara, M. Gabino and J.P. Bros, (1976) *Journal of Crystal Growth*, **32**, 101.
- [48] V.I. Ivanov-Omskii and B.T. Komiets, (1959) *Soviet Physics:Solid State*, **1**, 834.
- [49] K.J. Bachmann, F.A. Thiel, H. Schreiber and J.J. Rubin, (1980) *Journal of Electronic Materials*, **9**, 445.
- [50] A. Jouille, J. Allegre and G. Bougnot, (1972) *Material Research Bulletin*, **7**, 1101.

- [51] S. Sen and W.R. Wilcox, (1978) *Material Research Bulletin*, **13**, 293.
- [52] J.J. Venkrbec *et al.*, (1995) *Journal of Thermal Analysis*, **43**, 399.
- [53] R.F. Redden, (1996) Amistar Research, *private communication*.
- [54] T. Tsuruta *et al.*, (1991) *Japan Journal of Applied Physics*, **31(Suppl 1)**, 23.
- [55] A. Watanabe, A. Tanaka and T. Sukegawa, (1993) *Japan Journal of Applied Physics*, **32**, Letters: 793.
- [56] T. Ashley, J.A. Beswick, B. Cockayne and C.T. Elliott, (1995) *private communication*.
- [57] M. vanSchilfgaarde, A. Sher and A-B Chen, (1993) *Applied Physics Letters*, **62**, 1857.
- [58] A-B Chen, M. vanSchilfgaarde and A. Sher, (1993) *Journal of Electronic Materials*, **22**, 843.
- [59] J.J. Lee and M. Razeghi, (2000) *Journal of Crystal Growth*, **221**, 444.
- [60] M. Razeghi, (1996) *Optoelectronic Properties of Semiconductors and Superlattices*, **1**, Gordon & Breach, New York, 453.
- [61] C. Shih and E.A. Peretti, (1953) *Journal of the American Chemical Society*, **74**, 608.
- [62] J.C. Woolley and J. Warner, (1964) *Canadian Journal of Physics*, **42**, 1879.
- [63] G.B. Stringfellow and P.E. Greene, (1971) *Journal of the Electrochemical Society*, **118**, 805.
- [64] K. Ishida *et al.*, (1989) *Journal of the Less-Common Metals*, **155**, 193.
- [65] V.M. Glazov and K.B. Poyarkov, (2000) *Inorganic Materials*, **36**, 991.
- [66] V.G. Shepelevich, (1991) *Neorganicheskie Materialy*, **27**, 2505.
- [67] Y. Hayakawa *et al.*, (1993) *Shizuoka Daigaku Denshi Kogaku Kenkyusho Kenkyu Hokoku*, **28**, 7.
- [68] V.K. Dixit, B.V. Rodrigues and H.L. Bhat, (2000) *Journal of Crystal Growth*, **217**, 40.
- [69] P. Mohan, S.M. Babu, P. Santhanarangan and P. Ramasamy, (2000) *Material Chemistry and Physics*, **66**, 17.
- [70] G.R. Pandya, C.F. Desai, R.C. Shah and K.R. Shah, (1998) *Crystal Research and Technology*, **42**, 979.
- [71] M.C. Wagener, R.E. Kroon, J.R. Botha and A.W.R. Leitch, (1998) *Proceedings of the Microscopy Society of South Africa*, **28**, 38.
- [72] V.S. Zemskov, M.R. Raukhan and V.P. Shalimov, (2001) *Cosmic Research (translation of Kosmicheskie Issledovaniya)*, **39**, 359.

This page intentionally left blank

6 GaN Bulk Substrates Grown under Pressure from Solution in Gallium

I. GRZEGORY, M. BOĆKOWSKI AND S. POROWSKI

Polish Academy of Sciences, High Pressure Research Centre, Al. Sokolowska 29/37, 01-142, Warsaw, Poland

6.1 Introduction	173
6.2 Phase diagrams and growth method	175
6.2.1 Thermodynamic properties of GaN-Ga-N ₂ system	175
6.2.2 The role of high pressure	178
6.2.3 Crystallization of GaN from solution	179
6.2.4 Experimental	182
6.3 Results of spontaneous crystallization in temperature gradient: crystals and physical properties of the crystals	183
6.3.1 Morphology	183
6.3.2 Physical properties of the pressure-grown GaN crystals	185
6.4 Discussion of crystallization in a temperature gradient	188
6.5 Crystallization on the free gallium surface	192
6.6 Directional crystallization on GaN and foreign substrates	194
6.6.1 Seeded growth of GaN from solutions in gallium on GaN substrates	195
6.6.2 Seeded growth of GaN from solutions in gallium on GaN/sapphire substrates	197
6.7 Applications of pressure-grown bulk GaN substrates	201
6.8 Summary and conclusions	203
References	205

6.1 INTRODUCTION

GaN (and its alloys with Al and In) recently became the basic materials for short-wavelength optoelectronics and also for high-power, high-temperature electronic devices. This is because of their large direct bandgap, high thermal stability, high electron velocities

and other physical properties. The energy gaps in the considered compounds (6.2, 3.4 and 0.7 eV for AlN, GaN and InN, respectively) cover the whole visible spectrum and a large part of the UV range. At present, high-brightness blue and green light emitting diodes (LEDs) and low-power blue laser diodes (LDs) are commercially available [1]. On the other hand, however, the development of GaN-based technology was and still is, strongly limited by difficulties in obtaining large, high-quality crystals that could be used as substrates for epitaxial deposition of multilayer quantum structures necessary for devices. This is a direct consequence of the thermodynamic properties of GaN [2] (and also AlN [3]) in particular, its melting conditions that are so extreme that the application of the common growth methods from stoichiometric liquids is technically impossible.

The spectacular development of GaN-based optoelectronic devices was possible due to elaboration of the two-step metal organic chemical vapor deposition (MOCVD) processes for the growth of both n- and p-type (GaAlIn)N epitaxial structures on highly mismatched sapphire substrates [1, 4]. In these structures dislocation densities are as high as 10^8 – 10^{10} cm⁻² but nevertheless, very efficient luminescence is possible especially if the structures contain InGaN [5]. So, it was suggested that GaN and its alloys are much more 'tolerant' to the presence of structural defects than the conventional III-V systems due to the much lower minority carrier diffusion length and the relative immobility of structural defects in these strongly bonded crystals [6]. It is, however, well established [7] that the structural defects present in heteroepitaxial nitrides influence the optical and electrical properties of GaN-based epitaxial layers and quantum structures, which lowers the efficiency and lifetime of some important classes of devices. Therefore the lack of defect-free, lattice-matched and available substrates for GaN-based epitaxial structures is still a serious obstacle to the further development of some important classes of optoelectronic and electronic devices. For instance, the presence of structural defects in structures deposited on foreign substrates impedes extension of the power and the lifetime of the blue-violet InGaN-based lasers. Recently, considerable effort has been devoted to solving the substrate problem for III-V nitrides.

The important methods, considered already as the classic ones in nitride technology, are based on controllable variations of the relative normal and lateral growth rates of GaN epitaxial layers deposited on foreign substrates that have been patterned in different ways. These methods, called ELOG (epitaxial lateral overgrowth) [8], give quasi-bulk large-diameter GaN substrates with areas that are locally almost dislocation free. Usually the resulting substrates consist of stripes a few μm wide that are nearly dislocation free but are separated by stripes of similar width with a dislocation density of about 10^7 cm⁻². The ELOG-type substrates were very important for the development of violet InGaN-based lasers since only the application of these substrates allowed the lifetime of the devices to be increased beyond 10 000 h and their further commercialization. Despite the great advantages of the ELOG methods, there are some drawbacks, like strong bending of the substrates or quite complicated processing necessary for fabrication of both the substrates themselves and the devices on them.

Another 'epitaxial' approach becoming recently more and more attractive, is the use of hydride vapor phase deposition (HVPE) to grow thick (few hundreds of μm) GaN layers on foreign substrates [9–12]. Then the substrates can be removed [13–15] and large-diameter free-standing GaN wafers can be obtained. Due to interactions between dislocations during the growth of the thick GaN layer, their density drops to values

as low as 10^6 cm^{-2} [16]. Among these free-standing quasi-bulk GaN substrates those developed by Sumitomo Electric [17] enabled the first demonstration [18] of high-power laser diodes and diode arrays. The method of fabrication of the substrates is a multistep deposition of GaN on GaAs wafers [19] including defect-selective etching of the nitride and subsequent regrowth on the surface containing large pits, the result of the etching.

The most direct solution of the problem is to grow perfect bulk GaN crystals. Several groups are working toward this crucial result. The simplest (ideologically, not technically) method for growing nitrides at temperatures and pressures much less extreme than are required for melting, is growth from solutions. At present, there are two basic approaches to the solution growth of GaN: crystallization from solutions in supercritical NH_3 [20–22] (the so-called ammonothermal method) and crystallization from solutions in liquid gallium. Both methods require the use of high pressure. The typical pressure and temperature ranges for the ammonothermal method are 1–3 kbar and 400–600 °C, respectively. Both the spontaneous growth resulting in crystals a few mm in size and seeded growth with the free-standing HVPE-GaN wafers have been studied. The main problem encountered in this approach is the low growth rates of the order of 0.1 mm day^{-1} . An acceleration of the growth has been reported [20] for the ammonothermal processes performed at pressures as high as 20 kbar. Typical dislocation densities in the GaN crystals obtained from supercritical ammonia are 10^4 cm^{-2} .

The best structural quality GaN crystals are grown from solutions of atomic nitrogen in liquid gallium under high N_2 pressure. This technique has been extensively developed in the High Pressure Research Center, Warsaw, Poland [23, 24] and also in Japan Energy Corporation and Yamaguchi University [25].

In the following, the process of GaN crystallization from solutions of atomic nitrogen in liquid gallium under high N_2 pressure will be described on the basis of the results obtained in Warsaw. The most important problems encountered in this technique are strong anisotropy of the growth at the conditions allowing stable crystallization, difficult control of the nucleation rates on the polar {0001} surfaces and difficult control of the mass-transport mechanisms in the growth solution. Better understanding of these phenomena should lead to improvement of the crystallization results in terms of the number and size of these high-quality crystals.

6.2 PHASE DIAGRAMS AND GROWTH METHOD

6.2.1 Thermodynamic properties of GaN-Ga- N_2 system

Table 6.1 compares melting temperatures and pressures of most typical semiconductor materials. The melting temperature of GaN has been calculated by the use of Van Vechten's quantum dielectric theory of chemical bonding [26]. The corresponding pressure followed from the extrapolation of the experimental equilibrium data [2, 27]. Only very recently have the melting conditions for GaN been determined experimentally by the in situ X-ray–high-pressure–high-temperature measurements performed at the Synchrotron Radiation Research Center of the Japan Atomic Energy Research Institute by Utsumi *et al.* [28]. The table shows that both temperature and pressure at melting of GaN

Table 6.1 Melting conditions of semiconductors

Crystal	T^M , °C	p^M , atm.
Si	1400	< 1
GaAs	1250	15
GaP	1465	30
GaN	2520	45 000*
	2220	60 000**
diamond (synthesis)	1600	60 000

*theoretical estimation by Van Vechten [26], pressure extrapolated from the experimental equilibrium data of [2, 27]

**experiment reported in [28]

are much higher than for typical semiconductors. They are rather similar to the conditions used for high-pressure synthesis of diamond.

Due to these extreme melting conditions, GaN (like AlN and InN) cannot be grown from its stoichiometric melt by the Czochralski or Bridgman methods commonly used for typical semiconductors. It has to be crystallized by methods allowing lower temperatures and pressures

Gallium nitride is a strongly bonded compound (with bonding energy of 9.12 eV (atom pair)⁻¹ [13]) in comparison with typical III-V semiconductors like GaAs (bonding energy of 6.5 eV (atom pair)⁻¹). Consequently, the free energy of the crystal is very low in relation to the reference state of free N and Ga atoms. On the other hand, the N₂ molecule is also strongly bonded (4.9 eV atom⁻¹). Therefore, the free energy of GaN constituents in their normal states, Ga and N₂, becomes quite close to that of the crystal. This is illustrated in Fig. 6.1 where the free energy of GaN (1 mole) and the free energy of the system of its constituents (Ga + 1/2N₂) is shown as a function of temperature and N₂ pressure.

With increasing temperature, $G(T)$ of the constituents decreases faster than $G(T)$ of the crystal and at higher temperatures, the nitride becomes thermodynamically unstable. The crossing of $G(T)$ curves determines the equilibrium temperature where GaN coexists with its constituents at a given N₂ pressure. The application of pressure increases the free energy of the constituents to a much higher degree than $G(T)$ of the crystal. As a consequence, the equilibrium point shifts to higher temperatures and the GaN stability range extends. The equilibrium p_{N₂}-T conditions for GaN have been studied by several groups [2, 27, 29–32]. The most complete and consistent results have been obtained by Karpinski *et al.* [2, 27] by direct synthesis and decomposition experiments performed by both a gas-pressure technique (for pressures up to 20 kbar) and a high-pressure anvil technique (up to 70 kbar). The curve following from these data is shown in Fig. 6.2.

The crystallization processes discussed in this paper have been carried out at N₂ pressures up to 20 kbar, which corresponds to the GaN stability limit of 1960 K. These conditions are marked in Fig. 6.2. For the temperature range of 1100–1690 °C (corresponding to the pressure range of 0.1–20 kbar), the curve was described by the van't

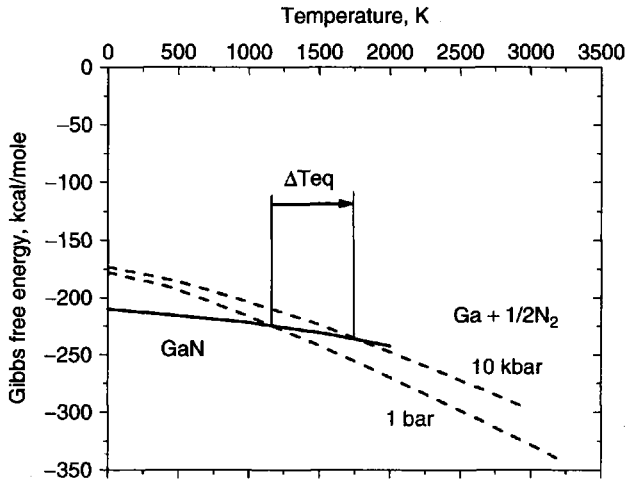


Figure 6.1 Gibbs free energy of GaN and its constituents

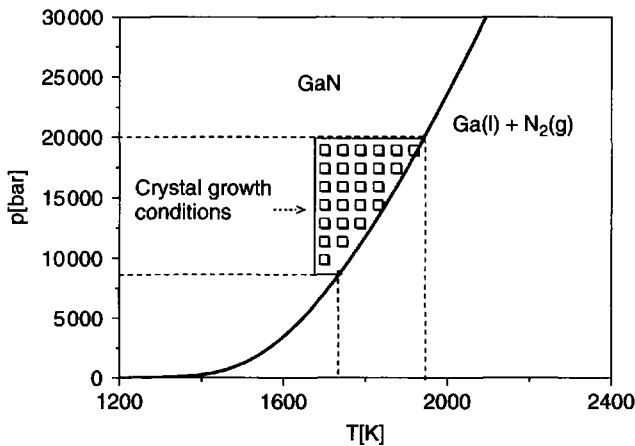


Figure 6.2 Equilibrium curve and crystal-growth conditions for GaN

Hoff equation:

$$\Delta H_F = \frac{1}{2} R \frac{d \ln a_{N_2}}{d(1/T)} \tag{6.1}$$

where ΔH_F is the formation enthalpy of GaN, a_{N_2} is the equilibrium activity of N_2 gas with ΔH_F constant and equal to $-37.7 \text{ kcal mole}^{-1}$.

The extension of the GaN stability range by the application of pressure allows the growth of GaN crystals from solution in liquid Ga. In Fig. 6.3 we show the N solubility data resulting from the annealing of Ga in N_2 atmosphere at the three-phase equilibrium conditions. Even the highest available temperature of 1960 K is quite far from the melting temperature of GaN (Table 6.1). Therefore the N concentrations are not high (below 1 at %) and the growth experiments have to be long to get high-quality crystals with

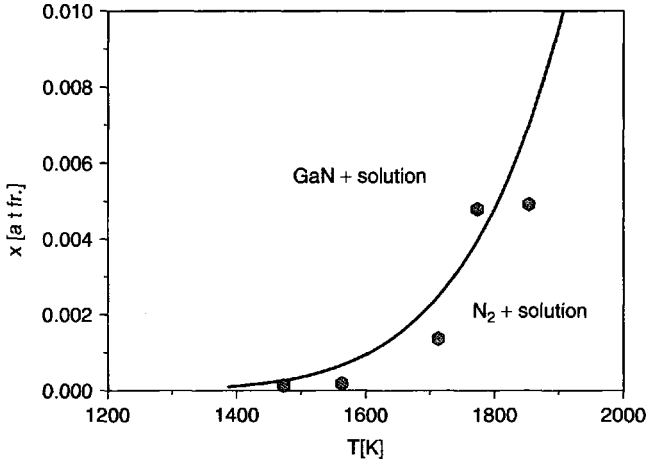


Figure 6.3 Liquidus line for Ga–GaN system: the solid line was calculated in the ideal-solution approximation

dimensions appropriate for research and applications. Therefore a long time (of the order of 100 h) of stable operation is an additional requirement for the growth system.

The solid line in Fig. 6.3 is the liquidus line for the Ga–GaN system calculated in the ideal-solution approximation [33] with Van Vechten’s melting temperature of 2790 K. For this approximation the solubility can be expressed as follows:

$$n = n_0 \exp \frac{\Delta H_{\text{sol}}}{kT} \quad (6.2)$$

where ΔH_{sol} is the heat of dissolution. For GaN, $\Delta H_{\text{sol}} = 44.7 \text{ kcal mole}^{-1} = 0.49 \text{ eV bond}^{-1}$ and expresses the bonding energy in the crystal in relation to its mother phase—the solution. It is equivalent to the heat of crystallization since $\Delta H_{\text{sol}} = -\Delta H_{\text{cryst}}$. This parameter will be used in the following for the description of crystal growth from solution.

6.2.2 The role of high pressure

The analysis of thermodynamical properties of GaN and the system of its constituents explains the role of high pressure as a factor that increases the thermodynamical potential of the constituents that makes the crystal stable at temperatures necessary for crystallization. The pressure, however, is important also for the kinetics of GaN synthesis. The synthesis of GaN from its constituents is possible due to dissociative chemisorption of N_2 molecules on the Ga surface, as was shown by Krukowski *et al.* [34] by density functional theory calculations. The nitrogen molecule dissociates on the Ga surface only if it overcomes the potential barrier of about 3.5 eV. Therefore, the density of the interacting gas is of crucial importance.

Both the increase of thermodynamic potential of gaseous nitrogen and the enhancement of N_2 dissociation by lowering of the potential barrier can be achieved by other (not compression) methods, like the excitement of N_2 plasma or the use of species containing

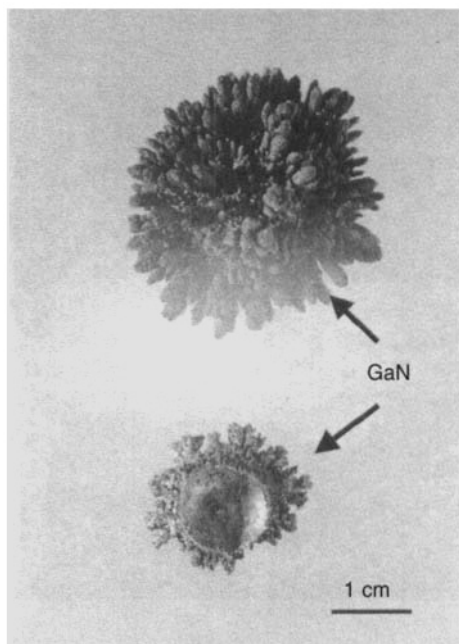


Figure 6.4 Result of GaN synthesis from the liquid Ga and N_2 plasma. The liquid has been pushed out from the initial droplet covered by a GaN crust, by the growing N_2 bubbles

nitrogen atoms bonded weaker than in the N_2 molecule. It was demonstrated [35, 36] that in a microwave nitrogen plasma of 60 Torr and a temperature as low as 1100°C , a very efficient GaN (and even InN!) synthesis is possible. The excited N_2 gas was a very efficient source to saturate a Ga droplet with atomic nitrogen and to form a GaN crust on the droplet surface. However, since the pressure in the system was much lower than the equilibrium one (about 100 bar for 1100°C), the N_2 gas phase started to nucleate and grow in the liquid. This resulted in the formation of the structure shown in Fig. 6.4, which was an empty 'Ga droplet' covered with irregular polycrystalline GaN.

The formation of N_2 bubbles in the supersaturated Ga:N liquid was also observed if the pressure in the system containing GaN crystals dipped in the Ga:N solution was intentionally decreased below the equilibrium value. Then the N_2 bubbles nucleated on the surface of the crystals and the crystals, being locally in contact with the gas, started to decompose until the pressure in the bubbles reached equilibrium. During cooling of the system, the interface between the gas bubbles and the surrounding liquid covered with GaN crystallized from the supersaturated solution. An example of a GaN crystal with local decomposition features on its surfaces is shown in Fig. 6.5.

6.2.3 Crystallization of GaN from solution

If the concentration of atomic nitrogen in the liquid gallium exceeds the equilibrium value, the excess nitrogen is removed from the liquid by formation of N-rich phases: N_2 , if the

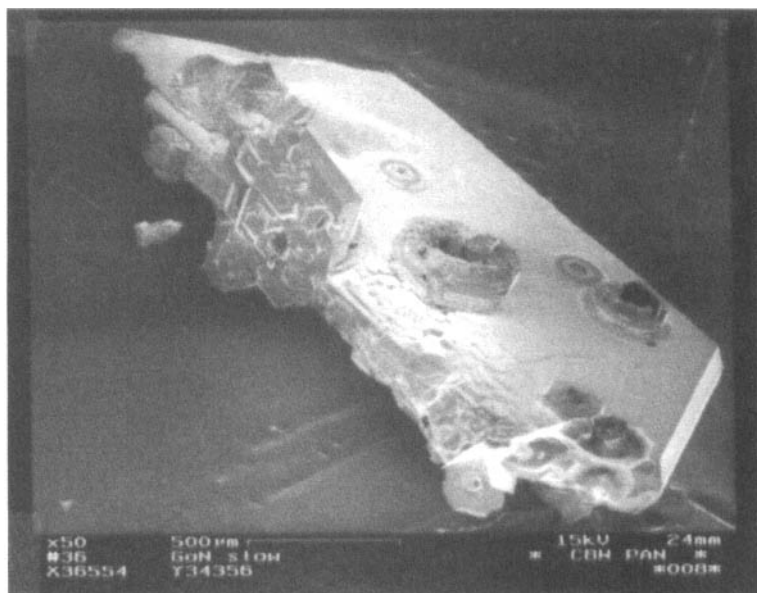


Figure 6.5 Decomposition of GaN in the supersaturated Ga:N solution if the pressure in the system drops below the equilibrium value. Local decomposition features supporting the proposed mechanism are visible on the crystal surfaces

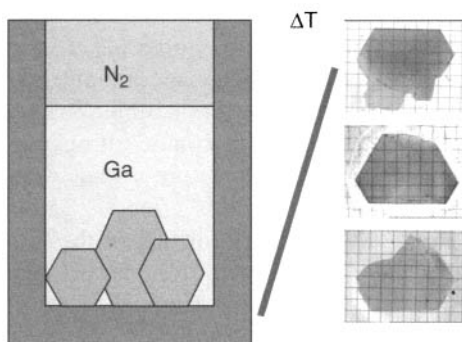


Figure 6.6 Schematic illustration of the crystallization of GaN from solution in a temperature gradient

pressure in the system is lower than required for GaN at a given T , or GaN crystals if the pressure is high enough for stability of GaN.

At the p - T conditions corresponding to the GaN stability range, the solubility of nitrogen in gallium is an increasing function of temperature (Fig. 6.3). So, if a temperature gradient is maintained in the system, crystal growth is expected in the cooler part of the solution, which is schematically shown in Fig. 6.6. This is because nitrogen dissolved in the hotter part (higher equilibrium concentration) is transported by diffusion and convection, which leads to the appearance of excess nitrogen in the cooler part (lower equilibrium concentration).

Below, some basic definitions and elements of the simple nucleation theory are given since, in the following, they will be used for the analysis of the experimental results.

The supersaturation of the solution is defined as the excess concentration related to the equilibrium value, which is the driving force for crystallization. If one assumes that both dissolution and mass-transport processes in the solution are much faster than the crystallization, the supersaturation reaches its maximum possible value and can be expressed as:

$$\sigma_{\max} = \frac{X_{\text{Neq}}(T_2) - X_{\text{Neq}}(T_1)}{X_{\text{Neq}}(T_1)} \quad (6.3)$$

where T_1 is the temperature of crystallization (cold end of the solution), T_2 is the temperature of the hot part of the solution, and X_{Neq} are corresponding equilibrium concentrations.

For a crystal growing in solution by a two-dimensional nucleation mechanism, according to the nucleation theory of Becker–Döring [37], the free-energy change related to the formation of the cylindrical nucleus on the given crystal face is:

$$\Delta G(r) = 2\pi r \gamma_e - \pi r^2 a \Delta G_V \quad (6.4)$$

where ΔG_V is the difference in free energy (for the unit volume) between the solid and liquid phase and γ_e is the specific edge energy of the nucleus.

The nucleus achieves its critical radius at the maximum of the function (6.4). The free-energy change ΔG^* , related to the formation of the critical nucleus can therefore be evaluated. Since ΔG^* is the barrier for the formation of the critical nuclei, their density on the surface can be expressed as:

$$n_s^* = x_s \exp\left(-\frac{\Delta G^*}{kT}\right) \quad (6.5)$$

where x_s is the density of solute atoms on the growth surface.

The rate of nucleation, defined as the number of the critical nuclei on the unit surface created in unit time, is:

$$I = n_s^* z^* A^* \quad (6.6)$$

where z^* is the frequency of attachment of the growth units (atoms) to the unit edge of the nucleus and A^* is the length of the nucleus edge. For expressing the time scale of the processes of incorporation of atoms into the growing GaN crystal, we assume that if the supersaturation of the solution is not very high, the rate of attachment of atoms is close to the rate of their detachment. The atoms in the crystal lattice vibrate with frequencies measured in the phonon spectra. The frequency of the longitudinal optical mode (most crucial for breaking the bond) is $750 \text{ cm}^{-1} = 2.3 \times 10^{13} \text{ s}^{-1}$. Therefore the frequency of detachment (attachment) of an atom from the nucleus edge can be estimated as:

$$\nu = \nu_{\text{LO}} \exp\left(\frac{-2\phi}{kT}\right) = 2.28 \times 10^{10} \text{ s}^{-1} \quad (6.7)$$

where ϕ is the bond energy in the crystal relative to the solution. It is equivalent to the heat of dissolution and equal to $0.49 \text{ eV bond}^{-1}$. So, the frequency of attachment of atoms to the nucleus edge is:

$$z^* A^* = V^+ \geq \nu q \quad (6.8)$$

where q is the number of atoms on the nucleus edge.

The approach just reviewed will be used for modeling of the real crystallization process by expressing the nucleation rates on the dominating crystal faces as functions of supersaturation in the growth solution. For this, the shape (geometry) of the critical nuclei on particular crystallographic faces should be properly chosen to reflect the experimental observations.

The experiments of GaN crystallization were performed mostly in the vertical configuration corresponding to Fig. 6.6, at temperatures of 1700–1850 K. The temperature difference between the hot and the cold zones of the solution was usually 20–50 K. The pressure of N₂ exceeded the equilibrium value corresponding to the highest temperature in the system to keep the solubility relation in agreement with the Ga-GaN liquidus shown in Fig. 6.3. In such a configuration, dissolved nitrogen is transported to the crystallization zone by diffusion and convection. We think that under the typical conditions of our experiments, the convection mechanism plays a dominant role. This follows from the simple estimation based on comparison of nitrogen flows induced by diffusion and convection:

$$j_D = D\rho\nabla x = D\rho\frac{x_1 - x_2}{l} = \rho v_c x_A = j_c \quad (6.9)$$

where j_D is the N flow induced by diffusion, D —diffusion coefficient of N in Ga (for the estimation we used the experimental value for diffusion of N in Al [17]), x_1 and x_2 —nitrogen concentration in the hot and cold zone, respectively, x_A —average N concentration, v_c —velocity of the solution induced by convection and j_c —the N flow induced by the convection. For typical experimental conditions, the convection velocity necessary to create the N flow equivalent to the diffusional one is of the order of 10^{-3} mm s⁻¹. The average velocities resulting from modeling are usually higher than this value.

6.2.4 Experimental

At present, GaN is crystallized in gas pressure chambers with an internal volume of 1500 cm³ and 4500 cm³, allowing crucibles with working volumes of 25 and 100 cm³, respectively. The high-pressure–high-temperature reactor consisting of the pressure chamber and the multizone furnace is equipped with additional systems necessary for: in situ annealing in vacuum, electronic stabilization and programming of pressure and temperature, cooling of the pressure chamber. Pressure in the chamber is stabilized with a precision better than 10 bar. The temperature is measured by a set of thermocouples arranged along the furnace and coupled with the standard input-power control electronic systems based on Eurotherm units. This allows stabilization of temperature to ± 0.2 deg and programmable changes of temperature distribution in the crucible.

GaN crystals presented in this chapter were grown from solutions in pure liquid gallium and in Ga alloyed with 0.2–0.5 at % of Mg or Be at pressures in the range of 8–20 kbar and temperatures of 1400–1600 °C. Magnesium and beryllium, as the most efficient acceptors in GaN, were added to the growth solutions in order to reduce the concentration of free electrons in the crystals by compensation of residual donors.

If the crystallization experiments were performed without intentional seeding, the crystals nucleated spontaneously on the crucible walls at the cooler zone of the solution. The typical duration of the processes was 80–150 h.

6.3 RESULTS OF SPONTANEOUS CRYSTALLIZATION IN TEMPERATURE GRADIENT: CRYSTALS AND PHYSICAL PROPERTIES OF THE CRYSTALS

6.3.1 Morphology

The dominant morphological form of GaN crystals grown by the high-pressure method is thin hexagonal platelets—Fig. 6.7. The large hexagonal surfaces of the platelets correspond to {0001} polar crystallographic planes of the wurtzite structure. The side faces of the crystals are mainly the polar {10–11} and also nonpolar {10–10} planes. The maximum lateral size of the platelets for 100–150 h processes, is 10–14 mm whereas the thickness is 80–120 μm .

The crystals in the form of hexagonal platelets grown slowly, with a rate $< 0.1 \text{ mm h}^{-1}$ into {10–10} directions (perpendicular to the c -axis), are usually single crystals of perfect morphology suggesting stable layer-by-layer growth. They are transparent, with flat mirror-like faces. The habit of the crystals does not change for solutions containing Mg or Be.

As one can deduce from the form of the crystals the growth is strongly anisotropic being much faster (about 100 times) in directions perpendicular to the c -axis. This relation is valid at supersaturations corresponding to the average growth rate in {10–10} directions of $0.05\text{--}0.1 \text{ mm h}^{-1}$.

The supersaturation in the growth solution is determined mainly by the growth temperature, temperature gradients, mass-transport mechanisms in gallium and also by the local surroundings for a particular crystal (neighbouring crystals).

The significant increase of ΔT (i.e. up to 100 K) does not lead to a spectacular increase of the growth rates but rather to growth instabilities on the {0001} polar surfaces of the crystals. The most frequently observed features of the unstable growth are cellular structures (Fig. 6.8a), accelerated growth at the edges exposed to the N flow (Fig. 6.8b) and in the extreme case, the hollow needles elongated into the c -directions (Fig. 6.8c,d).

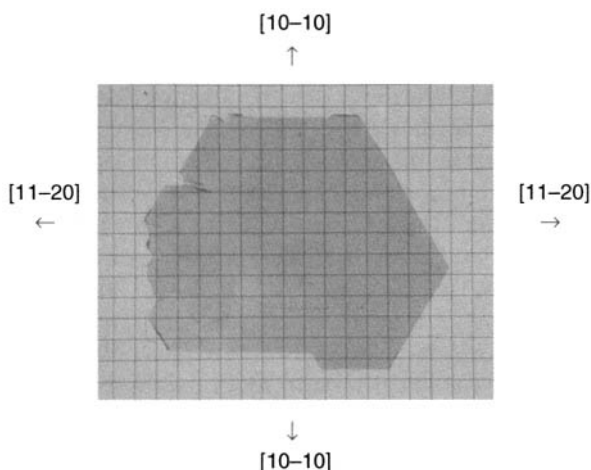


Figure 6.7 Typical GaN crystal grown from solution in liquid gallium

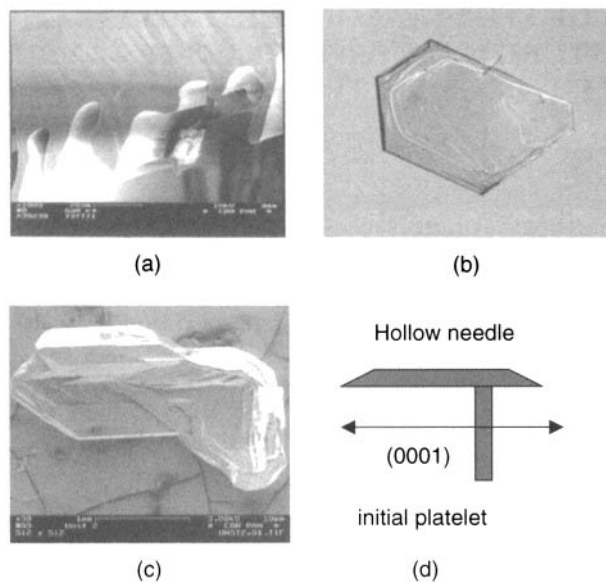


Figure 6.8 Growth instabilities: (a) cross section of the platelet showing the Ga-polar (0001) surface with cellular structure due to the unstable growth, (b) GaN platelet with accelerated growth features at the three edges due to nonuniform supersaturation across the (0001) surface, (c) change of the growth direction from $\langle 10\text{-}10 \rangle$ to the $\langle 0001 \rangle$ due to an abrupt increase of axial temperature gradient in the solution, (d) schematic explanation for (c)

Figure 6.8a shows the cross-sectional SEM scan of the n-type GaN platelet. Periodic structure is visible on the Ga-polar (0001) surface of the crystal. Such features are often observed in many of the solution-grown crystals as a result of constitutional supercooling of the growth solution at the crystallization front. If the supersaturation is too high, the edge nucleation on hexagonal faces of GaN platelets is often observed, which is the first step to unstable growth on that face. The result of such a growth is shown in Fig. 6.8b.

In the extreme cases of very high supersaturations, the growth into the c -direction nucleated at the edges of the plate, becomes very fast, which leads to the formation of well-developed $\{10\text{-}10\}$ faces. Since the lateral growth on the c -face is still slow, the resulting crystals are hollow needles elongated into the c -directions (Fig. 6.8c,d).

The tendency for the unstable growth is stronger for one of the polar $\{0001\}$ faces of the platelets. On this side the morphological features like macrosteps, periodic inclusions of solvent or cellular growth structures are observed. The opposite surface is mirror-like and often atomically flat. For crystals grown without intentional doping (strongly n-type—see the next section) the unstable surface always corresponds to the Ga-polar (0001) face of GaN, whereas for crystals doped with Mg (semi-insulating—see the next section) it is always the opposite N-polar (000-1) face. The polarity of the crystal surfaces was identified by etching in hot alkali water solutions since the Ga-polar surface is inert to etching, whereas the N-polar one etches well for both types of crystals. The method was calibrated by convergent-beam electron diffraction (CBED) [38, 39] and XPS [40] measurements. Therefore doping with Mg (if sufficient to compensate free electrons) changes the microscopic growth mechanisms on the $\{0001\}$ polar surfaces of GaN.

If the doping level is too low and the resulting crystals are still n-type, the morphology is as for crystallization without doping. This suggests that the position of the Fermi level in the crystal influences the microscopic processes occurring on the growing surfaces. Such a suggestion is consistent with the results of *ab initio* calculations [41] showing that the formation energies of both native and impurity-related point defects in GaN are very sensitive to the position of the Fermi level in the crystal.

6.3.2 Physical properties of the pressure-grown GaN crystals

As was already mentioned, the N_2 molecules dissociate on contact with the Ga surface. However, to approach the surface they have to overcome quite a high (about 3.5 eV) potential barrier that lowers substantially the rate of nitrogen dissociation and its further dissolution in the metal. For oxygen interacting with Ga, there is no potential barrier for dissociation [42] and therefore even traces of this impurity in the growth system are a source of unintentional oxygen doping of GaN. Consequently, the crystals are strongly n-type with free electron concentration of about $5 \times 10^{19} \text{ cm}^{-3}$ (metallic conductivity) and mobility of about $60 \text{ cm}^2 \text{ V}^{-1} \text{ s}^{-1}$ [43]. These free carriers can be fully eliminated by Mg acceptors added into the growth solution. Then the resistivity of the crystals becomes as high as 10^4 – $10^6 \Omega \text{ cm}$ at 300 K. Usually the GaN:Mg crystals become p-type with an activation energy of 150 meV, at temperatures slightly exceeding 300 K. More detailed analysis of the electrical properties of pressure-grown Mg-doped GaN crystals can be found in ref. [44].

The presence of the native point defects in the crystals has been checked by positron annihilation measurements [45]. A high concentration of Ga vacancies V_{Ga} has been found in the conductive crystals in contrast to the Mg-doped samples where no Ga vacancies have been observed. This agreed with theoretical predictions that the formation energy of V_{Ga} decreases with the increase of the Fermi-level energy [41] suggesting that the creation of these defects is thermodynamically controlled. The difference in the PL spectra of the conductive (strong yellow emission) and Mg-doped crystals (no yellow emission, blue Mg-related signal) supported the view that V_{Ga} is involved in yellow luminescence in GaN.

Quite a different picture is observed for doping with beryllium [46]. The GaN:Be crystals are also highly resistive with the constant activation energy of 1.46 eV at temperatures up to at least 1000 K. But their PL spectra are dominated by a very strong yellow luminescence and the crystals contain many gallium vacancies [45] like the highly conductive crystals grown without intentional doping. So it is very probable that these crystals are n-type during high-temperature growth and become semi-insulating only during cooling down. Such behaviour can be related to the two possible configurations of Be atoms in GaN lattice (Be_{Ga} —acceptor and Be_{i} —donor) and their redistribution as a function of temperature.

Some faces corresponding to the polar low-index {0001} and {10–11} crystallographic planes in wurtzite structure, appearing in the pressure-grown GaN crystals are nonequivalent regarding their atomic structure. This is reflected in the asymmetry of the physical properties of the plate-like crystals grown without intentional seeding. In Fig. 6.9 an example of such an asymmetry is shown. The figure shows that the material grown with N-polarity differs in its PL properties [47] from the material grown with the Ga-polarity,

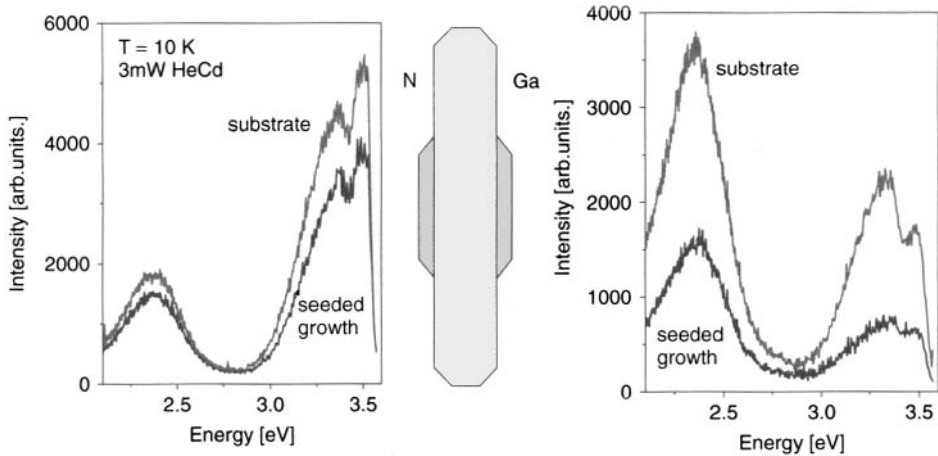


Figure 6.9 Photoluminescence of GaN grown on different sides of polished platelet grown without intentional seeding (substrate) and the platelet (substrate) itself

which indicates that the point defects incorporate into the crystal in different ways. Additionally, the spectra coming from the material grown on the $\{0001\}$ N- or Ga-polar surfaces (seeded growth) are of similar character to the spectra from corresponding surfaces of the substrate. Since the platelets were polished before being used as seeds, the suggestion arises that the platelets themselves also demonstrate a polar character, despite the fact that they were grown mainly in the fastest growth $(10\text{--}10)$ directions that follows from their morphology.

The strong support for this are the measurements of the free-electron concentration distribution across the cleaved, as-grown GaN platelet by the micro-Raman scattering technique [48]. Figure 6.10 shows that the border between materials of higher (N-side) and lower (Ga-side) electron concentration is situated inside the crystal dividing it into two parts. This suggests that the microscopic (on the atomic scale) processes responsible for the formation of both native and impurity-related point defects occur mainly on the $\{10\text{--}11\}$ polar faces of growing GaN crystals independently if the growth is perpendicular or parallel to the c -axis.

The structure of the pressure-grown GaN crystals has been studied by X-ray diffraction (XRD) [49], transmission electron microscopy (TEM) [50, 51], defect-selective etching (DSE) [52] and atomic force microscopy (AFM) of the homoepitaxial layers [53].

For the conductive crystals, the shape of the X-ray rocking curves ($(0002)\text{CuK}\alpha$ reflection) depends on the size of the crystal. The full widths at half-maximum (FWHM) are 20–30 arcsec for 1-mm crystals and 30–40 arcsec for 1–3 mm ones. For larger platelets the rocking curves often split into a few $\sim 30\text{--}40$ arcsec peaks showing the presence of low-angle ($1\text{--}3$ arcmin) boundaries separating grains of a few mm in size. Misorientation between grains increases monotonically from end to end of the crystal [19]. It has been suggested [19] that this can be also related to the polar character of the platelets growth leading to some strain and its subsequent relaxation through the formation of the low-angle boundaries.

It was shown by Liliental-Weber *et al.* [51], by TEM examination that the N-polar $(000\text{--}1)$ surface of the n-type pressure-grown GaN crystals (especially for the smaller

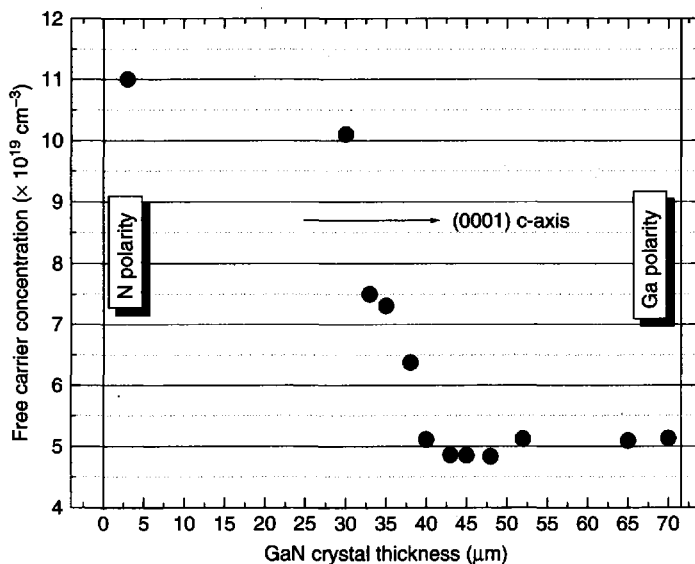


Figure 6.10 Distribution of free-electron concentration across the GaN platelet [48]

ones) is often atomically flat (2–3 monolayer steps present) and that the crystals under this surface are practically free of extended defects. Under the opposite conditions, a rough surface with a number of extended defects like stacking faults, dislocation loops and Ga microprecipitates was observed. The relative thickness of this part usually consists of 10% of the entire thickness of the platelet. It seems that the presence of these defects is related to the growth instabilities often observed on the Ga-polar surface of the crystals grown without intentional doping.

The detailed TEM studies of Mg-doped crystals are reported in [54]. In particular they have shown that the introduction of Mg induces the formation of a set of specific extended defects, being mainly the stacking faults situated at the {0001} polar surfaces of the investigated crystals.

For the use of the crystals as substrates for epitaxy, the near-surface part of the material, being often the result of unstable growth, has to be removed by polishing and subsequent reactive ion etching (Ga-side) [55] or mechanochemical polishing (N-side) [56] procedures. Usually the extended defects are not observed by TEM in the crystals used as substrates for both N- and Ga-polarity epitaxial growth. Figure 6.11 shows two examples of the TEM scans of dislocation-free multilayer structures grown on pressure-grown GaN substrates of both polarities.

Unfortunately, the TEM technique allows only a very small area of samples to be analyzed. Therefore, in order to measure dislocation densities in GaN, defect-selective etching methods have been developed [58]. It was shown that etching in molten KOH–NaOH eutectics reveals dislocations in both GaN heteroepitaxial layers and GaN pressure-grown single crystals. Examples are presented in Fig. 6.12. Figure 6.12a shows the result of DSE of a typical GaN heteroepitaxial layer grown on sapphire substrate. The high density of etch pits is visible. The same method applied for bulk crystals gives a very small ($10\text{--}100 \text{ cm}^{-2}$) number of etch pits.

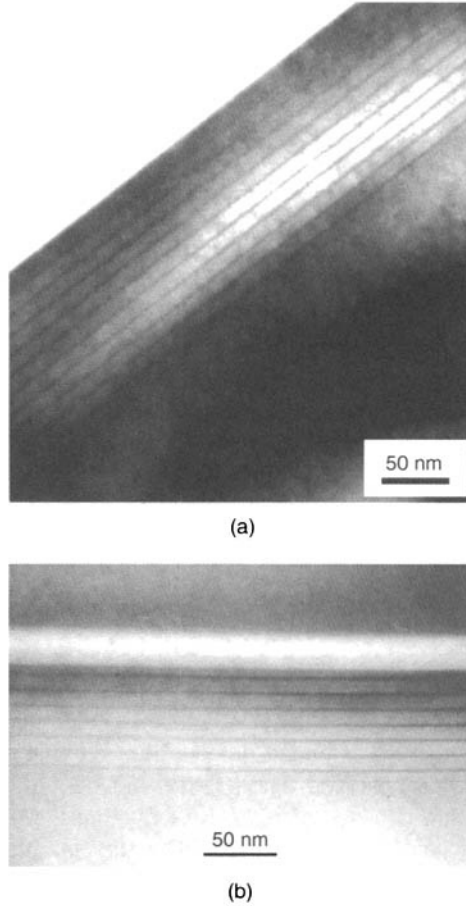


Figure 6.11 TEM cross sections of (a) GaN/Al_{0.1}Ga_{0.9}N multilayer structure grown by PAMBE on the N-polar surface of GaN substrate [50] and (b) GaN/InGaN/AlGaIn multilayer structure grown by MOCVD [57] on the Ga-polar surface of GaN substrate. No extended defects are observed in either the substrates or the layer structures. (TEM: Courtesy of M. Albrecht)

A typical pit observed on both heteroepitaxial layers and crystals is shown in Fig. 6.12c. The pattern in Fig. 6.12b is the result of DSE of a GaN crystal with dislocations generated intentionally by indentation with a diamond. The etch pits surround the imprint of the diamond, showing the area where dislocations are present and that the remaining material is dislocation free.

6.4 DISCUSSION OF CRYSTALLIZATION IN A TEMPERATURE GRADIENT

At the applied conditions where the platelets characterized in the previous section are crystallized, the growth of GaN is strongly anisotropic, being about 100 times faster in directions perpendicular to the *c*-axis of the crystal than parallel to *c*. This indicates

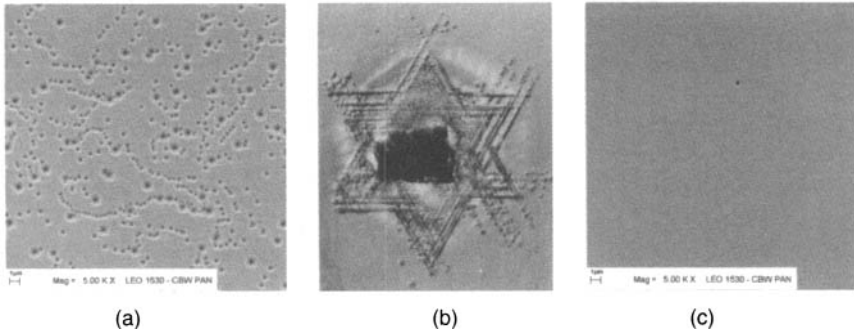


Figure 6.12 Defect-selective etching of GaN: (a) GaN/sapphire heteroepitaxial layer after etching in molten KOH–NaOH eutectics, (b) GaN pressure-grown single crystal after indentation with diamond and etching in molten KOH–NaOH eutectics, (c) etch pit (EP) on the GaN crystal surface after etching in molten KOH–NaOH eutectics, observed density of EP— $10\text{--}10^2\text{ cm}^{-2}$

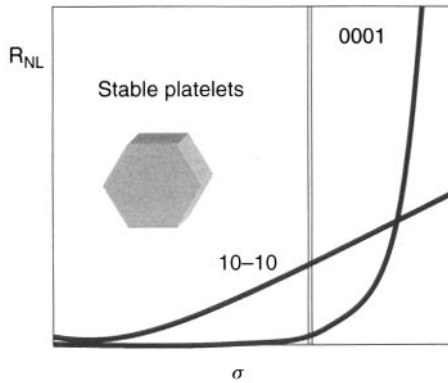


Figure 6.13 Schematic illustration of the dependence of the nucleation rates on supersaturation during crystallization of GaN from the solution

that the nucleation rates on the polar $\{0001\}$ surfaces are extremely small. The observed changes in the crystal morphology at the increased supercooling of the solution suggest that at higher supersaturations the nucleation on these surfaces becomes very fast and its rate is very sensitive to changes of the growth conditions (Fig. 6.13). In this case, the nucleation is difficult to control. In the applied configuration, where a set of crystals is growing simultaneously, it is impossible to control precisely the conditions for a particular crystal or, moreover, for a particular face. The only solution to enhance the growth on the $\{0001\}$ surfaces in a stable way is to apply methods of directional crystallization (see Section 6.6).

If the growth proceeds by the 2-dimensional nucleation mechanism, the observed anisotropy and the dependence of the nucleation rates at different crystal faces on supersaturation suggested by the experimental results, can be consequences of the differences in geometry of the nuclei. To check this, the dependence of the nucleation rates I , on supersaturation σ , for $\{0001\}$ and $\{10\text{--}10\}$ faces of a GaN crystal growing from solution at a temperature of 1800 K has been estimated [23]. The shapes and the arrangements of

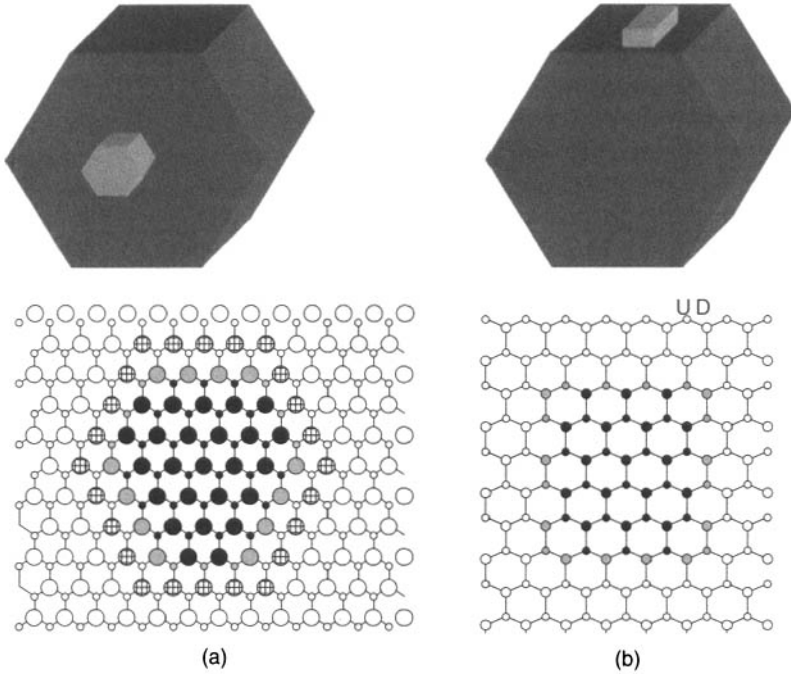


Figure 6.14 2D nuclei on the (0001) and (10–10) surfaces of GaN, respectively. Gray atoms belong to the edges of the nuclei

atoms in the corresponding 2D nuclei chosen for the estimation are shown in Fig. 6.14. The size of the nuclei can be described by the number of atoms along their sides, m . Therefore the total number of atoms n , in the nucleus as well as the number of the broken bonds q , on the nucleus edge can be expressed as functions of m . Each atom at the edge of a nucleus has one broken bond belonging to the same monolayer as the nucleus itself. For the hexagonal nucleus: $n = 3m^2 - 3m + 1$ and $q = 6m - 3$, whereas for the square one: $n = 0.5m_k m_w$, where m_k is the number of columns and m_w is the number of rows. For the nucleus of Fig. 6.7b: $m_w = m_k = 1$ and $q = 2m_k$.

The nucleation rate will be therefore (see Equations (6.5), (6.6) and (6.8)):

$$I = x_s q \nu \exp\left(-\frac{\Delta G^*}{kT}\right) \tag{6.10}$$

as defined in Section 6.2. The free-energy change related to the formation of the nucleus containing n atoms will be:

$$\Delta G = -n\Delta\mu + q\phi \tag{6.11}$$

where $\phi = \Delta H_{sol}/4$, is the average energy of the broken bond and $\Delta\mu$ is the molar free-energy difference between the solution and the crystal, and for an ideal solution is defined as:

$$\Delta\mu(T, x) = RT \ln\left(\frac{x}{x_{cq}}\right) = RT \ln(1 + \sigma) \tag{6.12}$$

The nucleus reaches its critical size once the function (6.11) passes through its maximum:

$$\frac{\partial(\Delta G)}{\partial n} = 0 \text{ or } \frac{\partial(\Delta G)}{\partial m} = 0 \quad (6.13)$$

Therefore, the size of the critical nuclei m^* , as well as the free-energy changes related to their formation can be calculated and the dependences of the nucleation rates on supersaturation obtained.

For the polar (0001) surface, the nucleation rate is:

$$I = \nu x_s \left(\frac{6\phi}{\Delta\mu} + 6 \right) \exp \left[-\frac{1}{RT} \left(\frac{3\phi^2}{\Delta\mu} - \frac{3\Delta\mu}{4} \right) \right] \quad (6.14)$$

whereas for the (10-10), the nucleation rate is:

$$I = \nu x_s \left(\frac{4\phi}{\Delta\mu} - 1 \right) \exp \left[-\frac{1}{RT} \left(\frac{2\phi^2}{\Delta\mu} - \frac{\Delta\mu}{8} \right) \right] \quad (6.15)$$

These dependences are graphically presented in Fig. 6.15.

Despite many simplifying assumptions like the ideal-solution approximation, the choice of nuclei having similar numbers of N and Ga atoms at the edges (to justify the use of ΔH_{sol} as a measure of the broken-bond energy) and selection of the (10-10) face as the rate-determining one for the growth perpendicular to the c -axis, the estimation reflects quite well the most important features of the solution growth of GaN.

The difficulty in increasing the lateral size of the crystals by increasing the duration of the process, suggests that the transport of nitrogen in the gallium becomes slower in time. The crystals appearing in the solution can stop the convection in the crystallization zone and thus change the boundary conditions for the remaining, 'mobile' part of the solution.

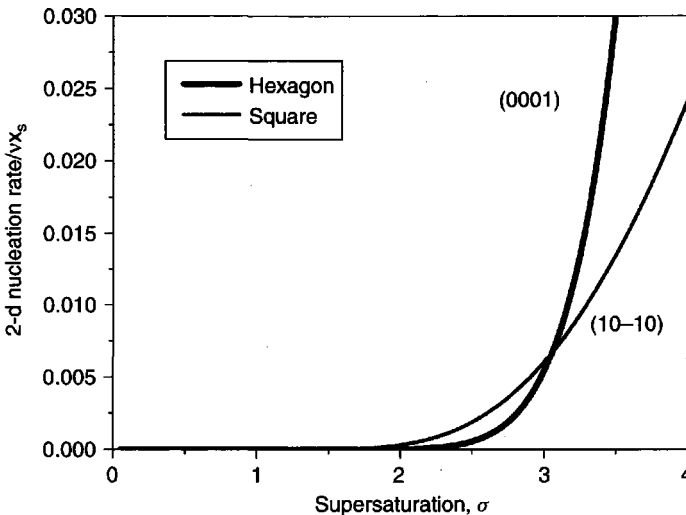


Figure 6.15 Relative 2D nucleation rates on the (0001) and (10-10) surfaces of GaN estimated with the use of heat of dissolution following from the experimental solubility data

Usually, the radial temperature distribution inside the solution is more uniform than at the bottom of the crucible. Therefore the presence of a 1-cm layer of immobile gallium with GaN crystals at the bottom of the crucible, can induce a significant decrease of the convection velocities.

However, on the other hand, the crystals grown in the long-duration processes (150–200 h) are often unstable, exhibiting morphological features similar to the case of the crystallization at high supercooling (see Fig. 6.8). This suggests a quite opposite reason for the limitation of the lateral size of the platelets: the increase of supersaturation in time up to the values where the growth on the (0001) surface dominates thus consumes most of the nitrogen arriving at the crystallization zone. Such an interpretation can be justified taking into account that only a small part of the platelets starting to grow at the beginning of the process reaches the maximum size. Then, if the growth is limited by nitrogen transport, the local supersaturation for a small number of the dominating (large) crystals can be higher than at the beginning of the process when a similar quantity of nitrogen has to be distributed among many crystals.

Therefore, the main drawback of the method where the GaN crystals are grown without intentional seeding is a poor control of supersaturation for a particular crystal.

6.5 CRYSTALLIZATION ON THE FREE GALLIUM SURFACE

A stable growth of large single crystals from solution requires very uniform and supersaturations that are not too high. In the case of growth in a temperature gradient, the uniformity is perturbed by several factors, like: the maintained temperature gradient, convectional flows in the solution or the neighbouring crystals (if the growth is unseeded). This can be avoided to some extent, for a free gallium surface being in direct contact with compressed nitrogen, under isothermal conditions. Until the metal surface is not covered with GaN, the solubility of N follows Ga-N₂ isobars [59] as shown in Fig. 6.16.

If the N₂ pressure becomes higher or the temperature lower than required for three-phase equilibrium, the solution at the surface can be uniformly supersaturated. Then, nucleation and growth can be expected on the gallium surface. The final conditions for such a process starting from the conditions corresponding to Ga + N₂ area of the phase diagram, can be created by lowering the temperature or increasing the pressure in the system. If the supersaturation is created by cooling, the surface crystallization should depend on the cooling rate, final supercooling, geometry and nonintentional temperature gradients in the system. We have shown that the result of the surface crystallization depends mainly on the final supercooling, whereas the cooling rate in the range of 0.5–20 °C/h, is not crucial for this process. Typically, a GaN crystalline crust consisting of grains of different size was obtained in 50–100 h processes. The examples of the surface crystals grown at different supercoolings, at 6 kbar are shown in Fig. 6.17. At small supercoolings, single-crystalline GaN with lateral size reaching 1–2 cm was quite often observed.

Morphologically, these relatively large crystals are similar to those grown in a temperature gradient. They are hexagonal platelets with the N-polar surface flat and the Ga-polar surface rough, showing features of the unstable growth. Also, the crystallographic quality is comparable. In particular, a very small dislocation density (100 cm⁻²) has been revealed by defect-selective etching. From the point of view of GaN substrate technology, the method is worth further development since it gives larger GaN single-crystalline platelets

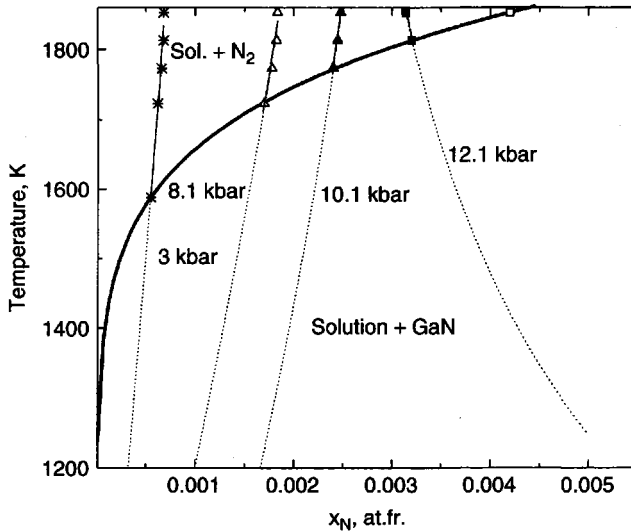


Figure 6.16 Solubility of nitrogen in liquid gallium: Ga-N₂ isobars calculated, solid curve calculated in ideal solution approximation for GaN-Ga system. Experimental solubility data—Fig. 6.3

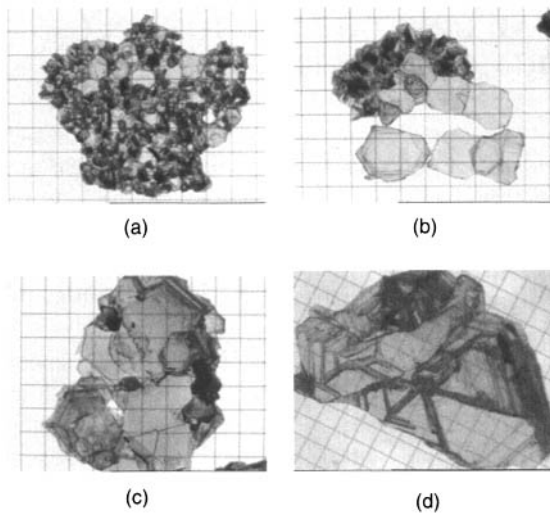


Figure 6.17 GaN crust crystallized on the free gallium surface at 6 kbar (corresponding $T_{eq} = 1400^\circ\text{C}$) at different supercoolings: (a) 70°C , (b) 40°C , (c) 15°C , (d) 10°C

than growth in a temperature gradient, described in the previous sections. Figure 6.18 compares both methods showing the configuration of the experiment and typical resulting crystals. It seems that after an optimization, the surface crystallization can be a source of large single-crystalline GaN platelets to be used as seeds (substrates) for directional crystallization described in the next section.

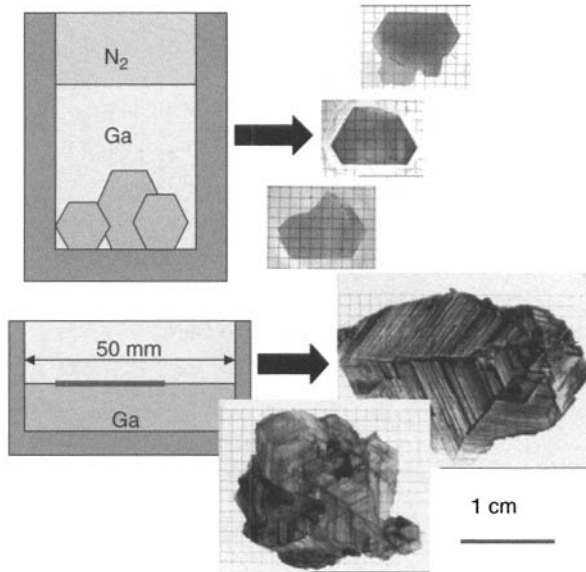


Figure 6.18 Typical results of high-pressure crystallization of GaN without intentional seeding: (a) by temperature gradient method, (b) by crystallization on free gallium surface

6.6 DIRECTIONAL CRYSTALLIZATION ON GaN AND FOREIGN SUBSTRATES

As follows from the previous sections, the most important problems encountered, at present, in the growth of GaN crystals from diluted solutions of atomic nitrogen in the liquid gallium are: the strong anisotropy in growth rates, difficulty with the enhancement and the control of growth in the c -direction due to the steep dependence of the nucleation rate at higher supersaturations and the limitation of the lateral size of the GaN platelets due to the still insufficient control of the mass transport in the solution during the crystallization.

The application of directional crystallization methods (i.e. deposition of GaN on the substrate to force the growth in the particular direction), including low-pressure deposition from the vapor, like HVPE, is a way to increase the rate of stable growth of near-dislocation-free GaN in the c -direction. It is obvious that the best substrates to be used in this approach are the near-dislocation-free GaN crystals. The only but important drawback is the limited size of these substrates.

On the other hand, an interesting alternative is the use of GaN epitaxial layers grown by MOCVD (or HVPE) on sapphire. As was already mentioned, sapphire is the most common substrate for GaN heteroepitaxy where the nitride is deposited at a relatively low temperature of 1050 °C by MOCVD and HVPE or even lower by molecular beam epitaxy (MBE). Under N_2 pressure, the growth temperature can be as high as 1400–1500 °C therefore new phenomena in the crystallization process can be expected. The MOCVD–GaN/ Al_2O_3 substrates can also be useful for optimization of the experimental configuration of GaN directional solution growth especially under the conditions where the growth is limited by nitrogen transport to the crystallization front (not by surface kinetics).

Since our high-pressure equipment allows 2-inch diameter substrates and such GaN/Al₂O₃ substrates are available, the studies of directional solution growth of GaN can be significantly extended regarding the size of the final GaN crystal. However, one has to remember that heteroepitaxial GaN contains dislocations, often being the source of the growth steps that can significantly change the surface kinetics in comparison to the growth on dislocation-free GaN substrate.

6.6.1 Seeded growth of GaN from solutions in gallium on GaN substrates

The thin GaN platelets described in the previous sections can be used for further crystallization as seed crystals. As was already mentioned, the growth on the {0001} polar surfaces of GaN is very slow (usually less than $1 \mu\text{m h}^{-1}$) and often unstable. The main features of the surface morphology, like macrosteps at the edges and the periodic cellular structures, suggest possible mechanisms for the unstable growth.

For macrosteps at the edges the quite obvious reason is the accelerated growth at the edges exposed to the nitrogen flux coming from the hot part of the solution. This can be avoided by proper configuration of the intentional seeding experiment, like the one shown in Fig. 6.21. Such a configuration also allows much more uniform supersaturation across the growing surface to be achieved, which is a very important condition for stable solution growth especially if the growing surfaces are relatively large and when the dependence of the nucleation rate on supersaturation is very steep, which is the case for {0001} surfaces of GaN.

The cellular growth is often a result of constitutional supercooling (Tiller *et al.* 1953) [60] of the solution, which is graphically explained in Fig. 6.19a and b. The analysis of the phenomenon summarized below shows that a temperature gradient perpendicular to the growing surface is the necessary condition for a stable crystallization front.

If the crystallization takes place at the given crystal surface, from a solution of concentration C_N , a depleted zone at the crystallization front is created due to the incorporation of the solute into the crystal (Fig. 6.19a). The concentration profile at the growth front can be transformed onto the temperature profile (T_L on Fig. 6.19b) via the liquidus relation. This

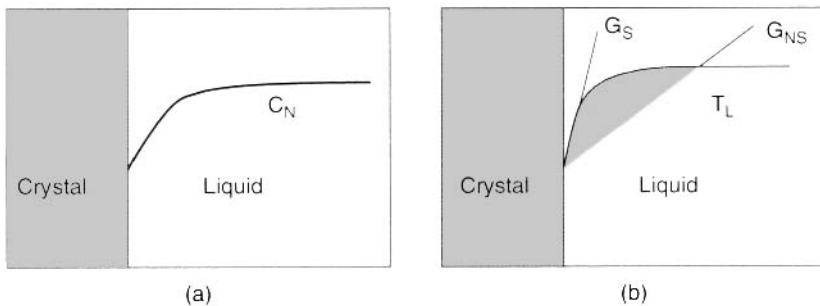


Figure 6.19 Schematic illustration of constitutional supercooling at the crystallization front: (a) creation of the depleted zone at the crystallization front due to incorporation of the solute into the growing crystal, (b) different temperature gradients applied at the crystallization front related to the equilibrium liquidus temperature profile corresponding to the concentration profile of Fig. 6.19a

temperature profile can be related to the real temperature gradient at the crystallization front. If the gradient is relatively small—like the one labeled G_{NS} —the supersaturation in front of the growing surface can be larger than at the surface itself. Then, each local acceleration of the growth results in its further enhancement, local depletion at the sides of the growing cell and the formation of a periodic cellular structure. The condition for stable growth can be expressed by the relation [61]:

$$\frac{G_L}{V} > -\frac{C(1-k)(-m)}{kD} \quad (6.16)$$

where G_L is the temperature gradient at the crystallization front, V —growth rate, k —distribution coefficient, m —diffusion coefficient of the solute in the growth solution. The parameters on the left-hand side of Equation (6.16) can be controlled experimentally if the configuration of the experiment corresponds to the scheme of Fig. 6.21.

The n-type GaN platelets have been used for seeded crystallization in order to suppress the cellular growth on the Ga-polar (000-1) surface. The N-polar (000-1) surfaces have also been used for comparison. The surfaces were prepared as for epitaxy: they were polished mechanically and then the subsurface damage was removed by mechanochemical polishing for the N-polar surface and by reactive ion etching for the Ga-polar surface.

The experiments were performed in a vertical configuration similar to that in Fig. 6.21. Large positive temperature gradients of the order of $100^\circ\text{C cm}^{-1}$ have been applied at an average crystallization temperature of about 1500°C . After 20–50 h processes the substrates with the new crystals deposited on the (0001) surfaces were removed from the solution and investigated.

Some typical results of the growth on the Ga-polar surface are shown in Fig. 6.20 where both the optical and SEM images of the substrate with the newly grown crystals are presented. The new material was transparent, colourless and grown as a single hillock of 6 mm in diameter (maximum size allowed by the experimental configuration)—Fig. 6.20a, b and c. The periodic cellular structures were no longer present. However, typically, the final surface was not flat. The dominant morphology of such crystals were macrosteps of a few tens of micrometers in height, spreading from the hillock center—Fig. 6.20d. This suggests that the growth mechanism was the propagation of the steps from the hillock centre and the subsequent step bunching due to the radial supersaturation gradients. The position of the hillock center most probably corresponds to the minimum supersaturation, being the result of the radial temperature gradients in the growth solution. Apparently, the supersaturation gradients on the growth surface were larger for the crystal in Fig. 6.20c than for the crystal in Fig. 6.20b. The macrosteps are often observed for crystallization from solutions since the surface diffusion is strongly limited in comparison to growth from the vapor phase where the growth often proceeds by the propagation of monoatomic steps.

The mechanism of the growth on the N-polar surface was also the propagation of the macrosteps, however, the presence of several growth centers has been observed for similar conditions of the experiment. It is still not clear if this is related to differences in nucleation mechanisms on the surface of different polarity or to the imperfect preparation of the surface, which, in contrast to the Ga-polar one, is chemically active.

The average rates of the growth in the c -direction observed in these experiments were $4\text{--}8\ \mu\text{m h}^{-1}$ for both polarities, depending on supersaturation at the growth front being a function of temperature gradient and the height of Ga over the substrate. The microscopic

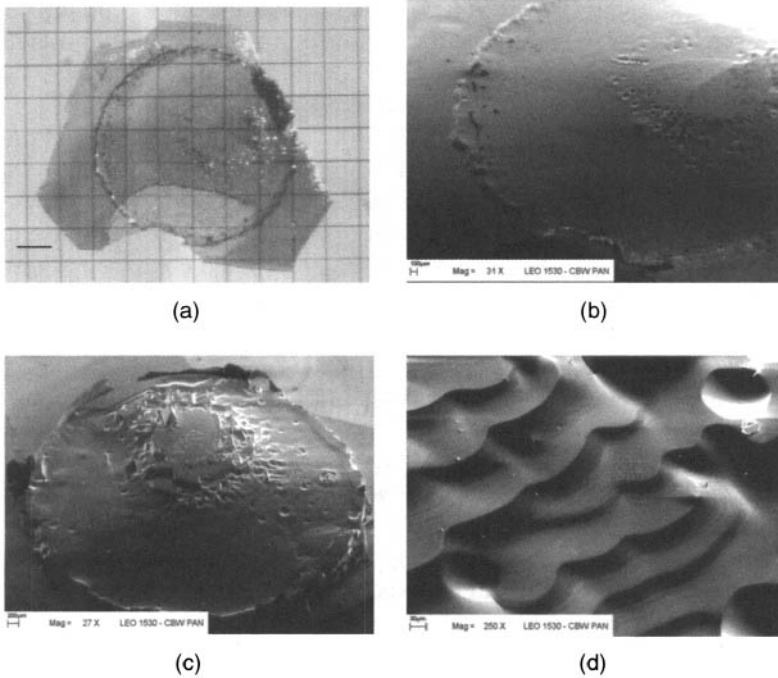


Figure 6.20 GaN substrate with the newly grown material on the Ga-polar surface: (a) optical image (distance between the grid lines = 1 mm), (b–d) SEM images

observation of the cross sections of the samples showed that the growth was stable in terms of continuity of the newly grown material. The inclusions of the solvent and/or voids were not observed. The interfaces between substrates (80–100 μm thick) and the newly grown crystals were not visible, indicating that the surface preparation and the wetting procedures before seeding were performed correctly. The XRD, TEM and DSE analyses [24] show that the material grown by the method just described is of similar structural quality to the substrate used. Therefore, the method is optimized towards higher growth rates, reduction or elimination of step bunching and improvement of the crystallization front. The use of GaN/ Al_2O_3 substrates is helpful in this optimization.

6.6.2 Seeded growth of GaN from solutions in gallium on GaN/sapphire substrates

The GaN/ Al_2O_3 substrates were 2–5- μm thick GaN epilayers grown by the MOCVD method on sapphire substrates by the standard procedure based on the low-temperature buffer-layer concept [1]. Such GaN had a dislocation density of about 10^9 cm^{-2} as determined by defect-selective etching.

The growth experiment consisted of the ‘wetting’ procedure and growth on the substrate in a temperature gradient. The wetting is a short annealing of the substrate immersed in liquid gallium at a temperature exceeding the equilibrium one for a given pressure. Under these conditions gallium slightly etches the surface of the substrate. This is to avoid

access of the N_2 gas to the Ga/GaN interface and to assure a good coupling between the solution and the substrate. The wetting is performed in situ just prior to establishing the temperature gradient.

Some typical configurations used in these experiments are shown in Fig. 6.21. The axial temperature gradients of the order of $20\text{--}100^\circ\text{C cm}^{-1}$ of two different orientations: direct and reversed (substrate on the bottom or on the top of the crucible, respectively) have been used. The maximum temperature in the crucible of 1450°C , the height of the gallium covering the substrate and the diameter of the substrate (10 mm) were constant in most of the experiments. The baffle shown in Fig. 6.21b and c was introduced in order to improve the uniformity of the nitrogen concentration field at the growing surface. The typical duration of the process was 100 h, however, some shorter runs have been made to check the evolution of the growth rate with time.

The conclusions drawn from the experimental results were as follows:

1. The morphology of the newly grown material was similar to the case of crystallization on GaN substrates described in the previous section: GaN deposited on GaN/ Al_2O_3 substrates was transparent, having the form of a single growth hillock covered by macrosteps. The introduction of the baffle significantly improved the shape of the crystallization front making it macroscopically flat for almost the whole growth surface without a marked change of the growth rate. Figure 6.22a and b shows a typical result of the experiments in a configuration as in Fig. 6.21b. The same configuration was applied with GaN substrates, which also resulted in the significant improvement of the final shape of the crystal—Fig. 6.22 c and d.

2. For experiments at a supercooling of 50°C , the inversion of the axial gradient (change configuration from Fig. 6.21b to 6.21c) resulted in a significant increase (twice) of the growth rate, which suggested that the transport of nitrogen across the solution was the rate-limiting factor in the considered processes, at least for supercoolings up to 50°C . This suggestion was supported by the dependence of the mass of the crystallized material on supercooling ΔT (Fig. 6.23a). However, as can be seen from the diagram, the dependence saturates at ΔT exceeding $60\text{--}70^\circ\text{C}$. Under these conditions, the nitrogen coming to the growing surface is not entirely incorporated into the crystal, probably due to a change in surface morphology and unwanted spontaneous nucleation beside the seed. The changes in

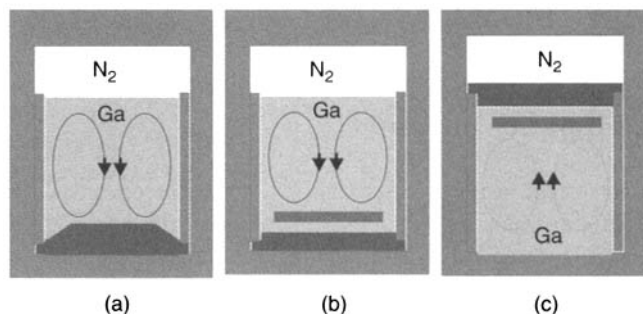


Figure 6.21 Typical configurations used for the growth of GaN on GaN/ Al_2O_3 substrates: (a) direct temperature gradient, no baffle, (b) direct temperature gradient, with baffle, (c) reversed temperature gradient with baffle

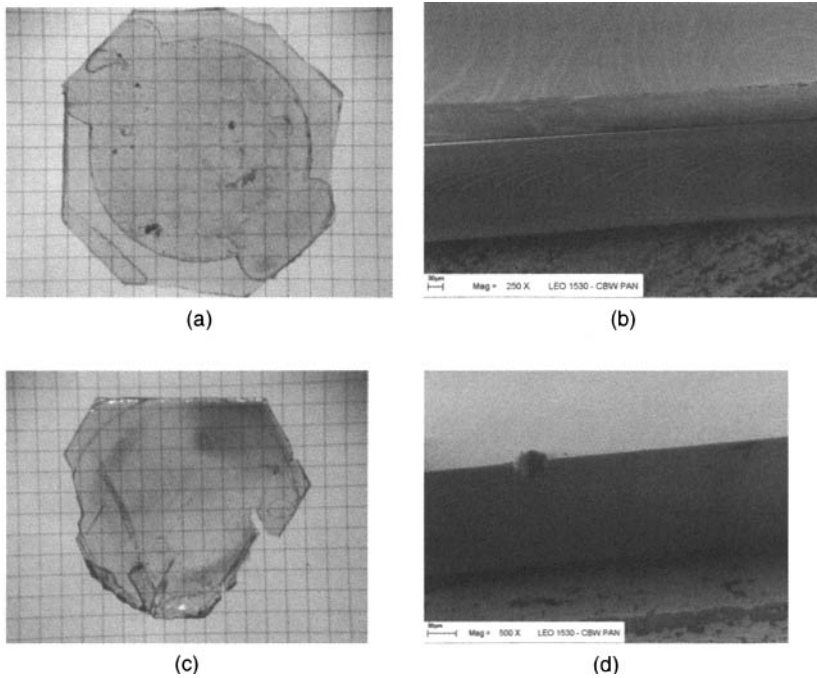


Figure 6.22 General view of GaN deposited on both GaN/Al₂O₃ and single-crystalline GaN substrates: (a) optical image of GaN on the GaN/Al₂O₃, (b) SEM image of the sample (a) with its cross section, (c) optical image of GaN deposited on GaN substrate, (d) SEM image of the sample (c) with its cross section

the surface morphology during the growth are most likely a reason for the decrease of the average growth rate observed as a function of the duration of the experiment—Fig. 6.23b.

Figure 6.24 compares the as-grown surfaces of two 40- μm thick GaN deposited in the experiments of different duration. Development of terraces can lead to the observed hindering of the growth illustrated in Fig. 6.23b. Some other factors, like a change in the heat removal from the substrate with increasing GaN thickness, were considered. However, the experiments of the smoothening of the as-grown surfaces by polishing and the subsequent re-growth on the thick but smooth GaN giving similar results to the growth on the initial substrate strongly supported the concept of the influence of the surface morphology—Fig. 6.25.

3. The initial results of GaN deposition on the substrates as large as 2 inches in diameter indicates that the growth proceeds by similar mechanisms as on the 10-mm substrates. The main difference is that several growth hillocks consisting of steps of different height are observed. Figure 6.26 shows a 2-inch substrate covered with 150- μm thick GaN, obtained in a 100-h experiment, in the nonoptimized configuration corresponding to Fig. 6.21a.

4. Dislocation densities in the material grown on the GaN/Al₂O₃ substrates as checked by defect-selective etching were usually of the order of 10^7 cm^{-2} , which was over one order of magnitude lower than in the initial GaN/Al₂O₃ substrates. It seems that after optimization of the wetting procedure and the start of the growth, dislocation densities

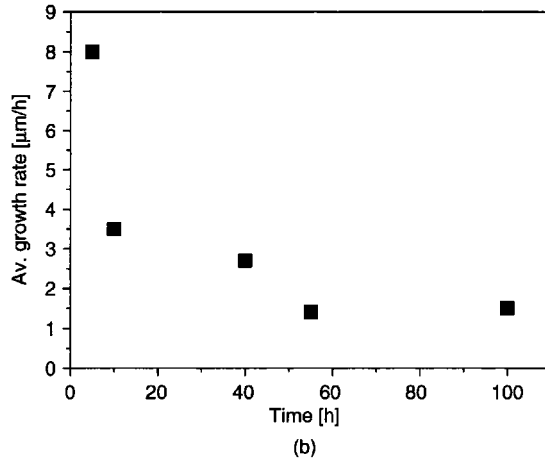
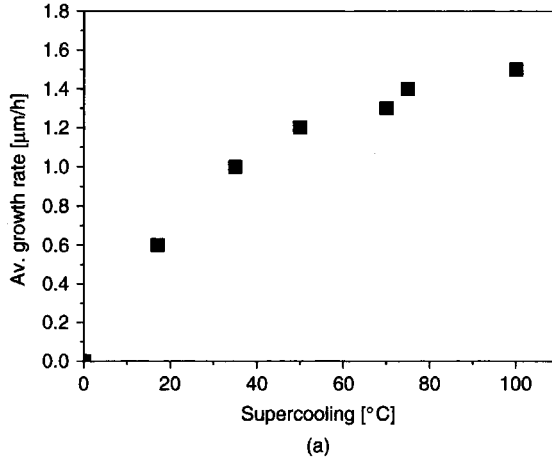


Figure 6.23 Dependence of the average growth rate of GaN crystallized on GaN/ Al_2O_3 substrates on: (a) supercooling for 100 h runs and (b) duration of the process for supercooling of 100°C

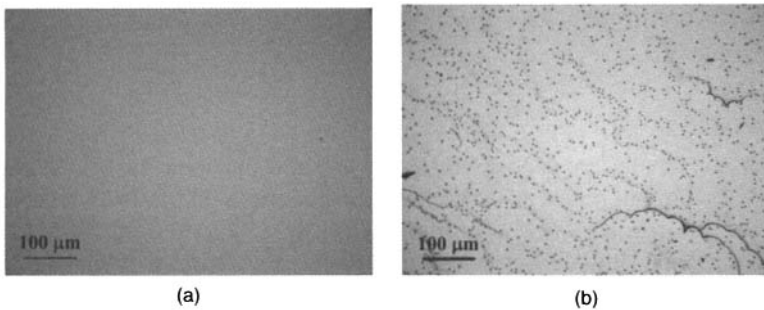


Figure 6.24 Morphology (using differential interference contrast microscopy, DIC) of the as-grown surfaces of 40- μm thick GaN deposited in the experiments of different duration time and supercooling: (a) time: 100 h supercooling: 25°C , (b) time: 5 h supercooling: 100°C , macrosteps decorated with small gallium-oxide crystals precipitated during rapid cooling of the system

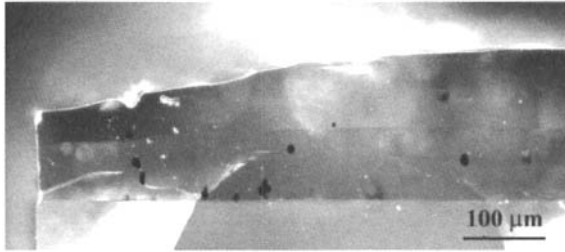


Figure 6.25 The optical image of the cross section of GaN deposited on GaN/Al₂O₃ substrate: the 100- μ m thick GaN was deposited twice on the substrate in the subsequent pressure solution 100-h growth runs. The surface of the first layer was polished between the runs. Preparation of the cross-sectional specimen—J. Borysiuk



Figure 6.26 150- μ m thick GaN grown on GaN/Al₂O₃ substrate

can be even lower. Obviously the use of the free-standing large-diameter GaN quasi-bulk substrates (mentioned in the Introduction) instead of the substrates containing sapphire could lead to a further improvement of the material quality.

6.7 APPLICATIONS OF PRESSURE-GROWN BULK GaN SUBSTRATES

The crystals described in Section 6.3 have been used as substrates for epitaxy of nitride layers and quantum structures by both MOCVD [57, 62, 63] and MBE [50, 64, 65] methods. The influence of the lack of the threading dislocations in the material on its optical properties has been demonstrated for both low and high excitations. Two examples are given in Fig. 6.27.

In Fig. 6.27a, the integrated intensities of the photoluminescence coming from similar structures (8-monolayer GaN single quantum well with Al_{0.1}Ga_{0.9}N 50-nm barriers) grown

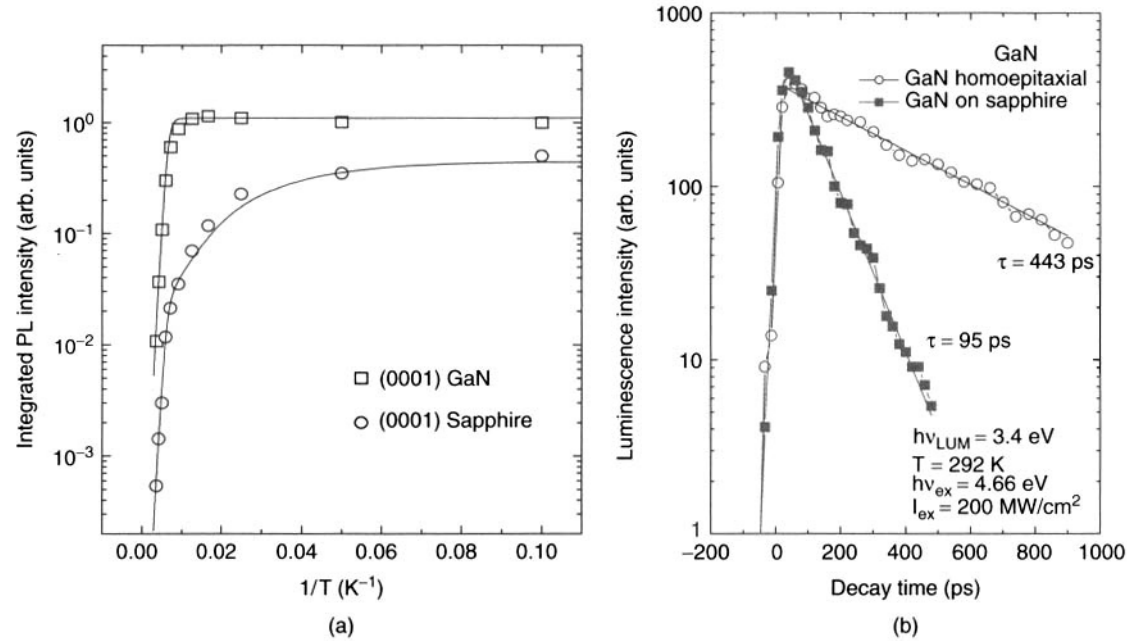


Figure 6.27 Optical properties of near-dislocation-free nitride layers and structures: (a) Temperature dependence of the integrated PL intensity of homoepitaxial (squares) and heteroepitaxial (circles) GaN/Al_{0.1}Ga_{0.9}N QWs (Reprinted from Grandjean *et al. Semicond. Sci. Technol.*, **16** (2001) 358–361, copyright (2001) with permission from the Institute of Physics.) (b) Spontaneous luminescence transients for GaN films grown on sapphire (solid squares) and on GaN substrates (open circles)

by reactive MBE [64] on sapphire and bulk pressure-grown GaN substrates are compared. It is shown that for the structure deposited on GaN, the PL is much stronger, especially at RT. For the structure grown on GaN substrate, the PL intensity starts to decrease with temperature only at about 100 K, mainly due to the thermal escape of carriers from the quantum well towards the AlGaIn barriers, as was observed for classical III-V QW heterostructures with dislocation densities lower than 10^3 cm^{-2} [66]. For heteroepitaxial structures, the presence of dislocations strongly influences the nonradiative recombination processes. The PL intensity starts to decrease at much lower temperatures due to delocalization of excitons and their further interaction with dislocations.

The PL decay has been studied at high excitations [67] for GaN layers grown by MOCVD on sapphire and pressure-grown GaN substrates. The decay time (at RT) of 450 ps measured for homoepitaxial material was five times longer than for corresponding heteroepitaxial layer grown under the same conditions. Figure 6.27b shows the decay of spontaneous luminescence measured at high excitation, close to the stimulated emission threshold for homo- and heteroepitaxial GaN.

Therefore, despite their relatively small size, the pressure-grown GaN crystals should be excellent substrates for blue-violet laser diodes. Other encouraging factors for using these crystals for lasers are the easy cleaving along $\{10\bar{1}0\}$ planes and high electrical conductivity, enabling much simpler processing than for substrates based on sapphire. In particular, the mirrors of the laser resonator can be made simply by cleaving instead of complicated dry-etching procedures. Due to the good electrical conductivity of the substrate, the contact for the n-type part of the laser (see Fig. 6.28) can be made on the back side of the structure. Figure 6.28 shows schematically the structure of one of the laser diodes fabricated recently in the High Pressure Research Center PAS on the bulk pressure-grown substrates [68]. This is a separate confinement heterostructure laser with AlGaIn cladding layers and Mg- and Si-doped GaN waveguides. The structures are grown by MOCVD without any special steps to match AlGaIn with the substrate. Even this simple solution resulted in a very low dislocation density (about 10^5 cm^{-2}) structures. This allowed fabrication of pulsed-current-operated laser diodes of the record high power output exceeding 2.5 W in 30-ns pulses. The current-voltage and current-light characteristics of such a diode are shown in Fig. 6.29.

The semi-insulating GaN:Mg substrates have been used for growth of GaN/AlGaIn heterostructures with a two-dimensional electron gas (2DEG) by both plasma-assisted and reactive (with ammonia) MBE [65, 69]. Very high mobilities of the 2D electron gas have been achieved by both methods. A Hall mobility for the 2DEG as high as $109\,000 \text{ cm}^2 \text{ V}^{-1} \text{ s}^{-1}$ at 1.5 K (the highest ever reported for a GaN/AlGaIn heterostructure) has been measured for samples grown by plasma-assisted MBE.

6.8 SUMMARY AND CONCLUSIONS

The GaN crystals grown from solution in liquid gallium under high pressure of nitrogen are the best quality crystals regarding their structure, in particular the density of threading dislocations being lower than 100 cm^{-2} . The crystals can be of both high and low electrical conductivity and they cleave easily along $\{10\bar{1}0\}$ crystallographic planes. Despite their limited size they can be applied as substrates for epitaxy and processed for making devices.

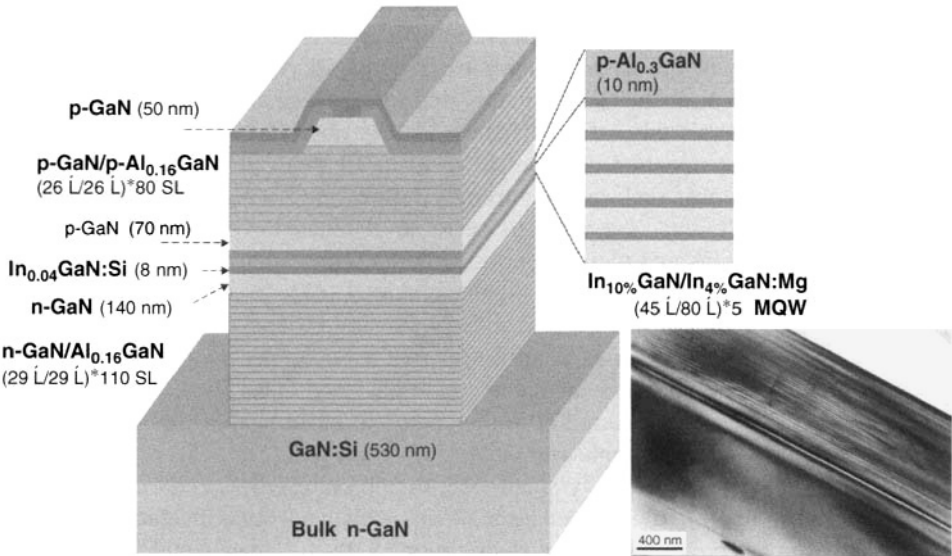


Figure 6.28 Structure of GaN laser diode grown on the pressure-grown GaN substrate. The micrograph is a TEM image of the epitaxial structure corresponding to the scheme

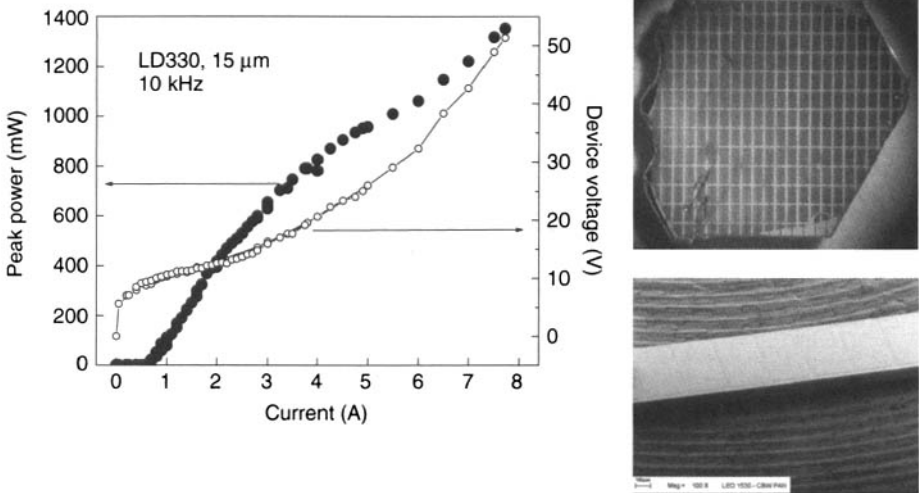


Figure 6.29 The current–voltage and current–light characteristics of high-power, pulse-current-operated laser diode constructed on the pressure-grown GaN crystal. Photos: GaN crystals with several laser diode chips after processing and set of lasers cleaved from the crystal

The increase of the size of the crystals is technically possible since the high-pressure–high-temperature chambers can accommodate 2-inch crystals. However, there are phenomena in the crystallization process itself that limit both the lateral size and the thickness of the crystals. For the lateral size of the individual platelets it seems that the

appropriate changing of the temperature gradients during the crystallization process can enforce the continuation of the growth in {10–10} directions giving platelets of larger diameter. For directional growth, the crucial factor is to avoid the observed decrease of the growth rate with time. If this is related to development of a particular structure of the growth front, the periodic interruptions of the growth or addition of impurities to the solution should be helpful.

REFERENCES

- [1] S. Nakamura and G. Fasol, (1997) Eds. Springer, *The Blue Laser Diode*, 277–300, Springer-Verlag Berlin
- [2] J. Karpinski and S. Porowski (1984) *J. Cryst. Growth* **66**, no. 1, 11–20.
- [3] G.A. Slack and T.F. McNelly, (1976) *J. Cryst. Growth* **34**, 263–279
- [4] S. Nakamura, T. Mukai, M. Senoh and N. Iwasa (1992) *J. Appl. Phys. Part 2-Lett.* **31**, no. 2B, L139–42
- [5] S. Nakamura (2000) *IEICE Trans.* Vol. E83-C, n.4, 529–535
- [6] J.S. Speck and S.J. Rosner, (1999) *Physica B* **273–274**, 24–32
- [7] T. Sugahara and S. Sakai (2000) *IEICE Trans.* Vol. E83-C, n.4, 598–604
- [8] K. Hiramatsu and A. Usui (1999) *EMIS Datareview Series* No. 23, published by INSPEC, The Institution of Electrical Engineers, London, 440–444.
- [9] H.P. Maruska and J.J. Titjen, (1969) *Appl. Phys. Lett.* **15**, 327
- [10] W. Seifert, G. Fitzl and E. Butter, (1981) *J. Cryst. Growth* **52**, 257
- [11] A. Usui, H. Sunakawa, A. Sakai and A. Yamaguchi, (1997) *Jpn. J. Appl. Phys.* **36**, L899.
- [12] T. Shibata, H. Sone, K. Yahashi, M. Yamaguchi, K. Hiramatsu, N. Sawaki and N. Itoh, (1998) *J. Cryst. Growth* **189/190**, 67
- [13] Y. Melnik, A. Nikolaev, L. Nikitina, K. Vassilevski and V. Dmitriev, (1998) *Mater. Res. Soc. Symp. Proc.* **482**, 269
- [14] S.T. Kim, Y.Y. Lee, D.C. Moon, C.H. Hong and T.K. Yoo, (1998) *J. Cryst. Growth* **194**, 37
- [15] M.K. Kelly, R.P. Vaudo, V.M. Phanse, L. Gorgens, O. Ambacher and M. Stutzmann, (1999) *Jpn. J. Appl. Phys. Part 2* **28**, no. 3A, L217
- [16] A. Usui, H. Sunakawa, A. Sakai and A.A. Yamaguchi, (1997) *Jpn. J. Appl. Phys. Part 2* **36**, no. 7B, L899
- [17] Sumitomo website: www.sei.co.jp
- [18] S. Goto, M. Ohta, Y. Yabuki, Y. Hoshina, S. Uchida and M. Ikeda, in *Proc. ICNS 5*, May 2003, Nara, Japan
- [19] Y. Kumagai, H. Murakami, H. Seki and A. Koukitu, (2002) *J. Cryst. Growth* **246**, 215–222
- [20] H.C. Hong, D.S. Park, K.J. Narang, S.F. LeBoeuf, M.P. D'Evelyn, P.R. Tavernier, D.R. Clarke and R.J. Molnar, presented at 8th *Wide Bandgap III-Nitride Workshop*, Sept. 29–Oct. 1, (2003), Richmond, Virginia, USA
- [21] D.R. Ketchum and J.W. Kolis, (2001) *J. Cryst. Growth* **222**, 431
- [22] A. Yoshikawa, E. Ohshima, T. Fukuda, H. Tsuji and K. Oshima, (2004) *J. Cryst. Growth* **260**, 67–72
- [23] I. Grzegory, M. Boćkowski, B. Łuczniak, S. Krukowski, Z. Romanowski, M. Wróblewski and S. Porowski, (2002) *J. Cryst. Growth* **246**, 177–186
- [24] M. Bockowski, I. Grzegory, S. Krukowski, B. Łuczniak, Z. Romanowski, M. Wróblewski, J. Borysiuk, J. Weyher, P. Hageman and S. Porowski, (2002) *J. Cryst. Growth* **246**, 194–206
- [25] T. Inoue, Y. Seki, O. Oda, S. Kurai, Y. Yamada and T. Taguchi (2000) *Jpn J. Appl. Phys.* **39**, 2394
- [26] J.A. Van Vechten (1973) *Phys. Rev. B* **7**, 1479–507
- [27] J. Karpinski, J. Jun and S. Porowski, (1984) *J. Cryst. Growth* **66**, 1–10

- [28] W. Utsumi, H. Saitoh, H. Kaneko, T. Watanuki, K. Aoki and O. Shimomura, (2003) *Nature Mater.* **2**, 735–738
- [29] J.B. Mac Chesney, P.M. Bridenbaugh and P.B. O'Connor, (1970) *Mater. Res. Bull.* **5**, 783
- [30] C.D. Thurmond and R.A. Logan, (1972) *J. Electrochem. Soc.* **119**, 622
- [31] R. Madar, G. Jacob, J. Hallais and R. Fruchard, (1975) *J. Cryst. Growth* **31**, 197
- [32] J. Unland, B. Onoderka, A. Davydov and R. Schmid-Fetzer, (2003) *J. Cryst. Growth* **256**, 33–51
- [33] I. Grzegory, in *Proc. of Joint XV AIRAPT and XXXV EHPRG Conference*, edited by W. Trzeciakowski, (World Scientific, Singapore 1996) p. 14–21.
- [34] S. Krukowski, Z. Romanowski, I. Grzegory and S. Porowski, (1999) *J. Cryst. Growth* **189/190**, 159
- [35] S. Porowski and J. Jun, unpublished
- [36] B. Lucznik, J. Adamczyk, J. Jun, S. Krukowski and I. Grzegory, unpublished
- [37] D. Elwell and H.J. Schell, *Crystal Growth from High-Temperature Solutions*, (Academic Press, London, 1975)
- [38] Z. Liliental-Weber, (1999) *EMIS Datareview Series* No. 23, published by INSPEC, The Institution of Electrical Engineers, London, 230
- [39] J.L. Rouviere, J.L. Weyher, M. Seelmann-Eggebert and S. Porowski, (1998) *Appl. Phys. Lett.* **73**, no. 5, 668–670.
- [40] M. Seelmann-Eggebert, J.L. Weyher, H. Obloh, H. Zimmermann, A. Rar and S. Porowski, (1997) *Appl. Phys. Lett.* **71**, (18)
- [41] J. Neugebauer and C.G. Van de Walle, (1994) *Phys. Rev. B* **50**, 8067
- [42] S. Krukowski, M. Bockowski, B. Łucznik I. Grzegory, S. Porowski T. Suski and Z. Romanowski, (2001) *J. Phys. Condens. Matter* **13**, 8881
- [43] P. Perlin, J. Camassel, W. Knap, T. Talercio, J.C. Chervin, T. Suski, I. Grzegory and S. Porowski, (1995) *Appl. Phys. Lett.* **67**, 2524
- [44] E. Litwin-Staszewska, T. Suski, R. Pietrkowski, I. Grzegory, M. Bockowski, J.L. Robert, L. Konczewicz, D. Wasik, E. Kaminska, D. Cote and B. Clerjaud, (2001) *J. Appl. Phys.* **89**, 7960
- [45] K. Saarinen, T. Laine, S. Kuisma, P. Hautojarvi, L. Dobrzyński, J.M. Baranowski, K. Pakuła, R. Stępniewski, M. Wojdak, A. Wysmotek, T. Suski, M. Leszczyński, I. Grzegory and S. Porowski, (1997) *Phys. Rev Lett.* **79**, 3030
- [46] S. Porowski, M. Bockowski, B. Lucznik, I. Grzegory, M. Wroblewski, H. Teisseyre, M. Leszczyński, E. Litwin-Staszewska, T. Suski, P. Trautman, K. Pakuła and J.M. Baranowski, (1997) *Acta Phys. Polon. A* **92**, no. 5, 958
- [47] PL measured by H. Teisseyre
- [48] E. Frayssinet, Ph.D. Thesis 'Elaboration et etude d'heterojonctions GaN/AlGaN deposees sur GaN massif', Universite Montpellier II, Montpellier (2000)
- [49] M. Leszczyński, I. Grzegory, H. Teisseyre, T. Suski, M. Bockowski, J. Jun, J.M. Baranowski, S. Porowski and J. Domagala, (1996) *J. Cryst. Growth* **169**, 235–242.
- [50] S.H. Christiansen, M. Albrecht, H.P. Strunk, C.T. Foxon, D. Korakakis, I. Grzegory and S. Porowski, (1999) *Proc. ICNS'99*, Montpellier, France, in *phys. stat. sol. (a)* **176**, no. 1, 285
- [51] Z. Liliental-Weber, (1999) *EMIS Datareview Series* No. 23, published by INSPEC, The Institution of Electrical Engineers, London, 230
- [52] J.L. Weyher, P.D. Brown, J.L. Rouviere, T. Wosinski, A.R.A. Zauner and I. Grzegory, (2000) *J. Cryst. Growth* **210**, 151
- [53] M. Leszczyński, P. Prystawko and G. Nowak, private communication
- [54] Z. Liliental-Weber, M. Benamara, W. Swider, J. Washburn, I. Grzegory, S. Porowski, R.D. Dupuis and C.J. Eiting, (1999) *Physica B* **273–274**, 124
- [55] F. Karouta, J.L. Weyher, B. Jacobs, G. Nowak, A. Presz, I. Grzegory, L.M.F. Kaufmann (1999) *J. Electron. Mater.* **28**, no. 12, 1448–51
- [56] J.L. Weyher, S. Müller, I. Grzegory and S. Porowski (1997) *J. Cryst. Growth* **182**, 17–23

- [57] M. Leszczyński, P. Prystawko, R. Czernecki, *et al.*, (2000) in *Proc. Of International Conference on Solid State Crystals*, Zakopane, Poland, Oct.9–13, 2000
- [58] J.L. Weyher, P.D. Brown, J.-L. Rouviere, T. Wosinski, A.R.A. Zauner and I. Grzegory, (2000) *J. Cryst. Growth* **210**, no. 1–3, 151–6
- [59] I. Grzegory, 1995 PhD Thesis, Warunki krystalizacji związków $A^{III}N$ w wysokim ciśnieniu azotu, Warszawa
- [60] W.A. Tiller, K.A. Jackson, J.W. Rutter and B. Chalmers, (1953) *Acta Met.* **1**, 428
- [61] W.A. Tiller, (1968) *J. Cryst. Growth* **2**, 345
- [62] C. Kirchner, V. Schwegler, F. Eberhard *et al.*, (1999) *Appl. Phys. Lett.* **75**, 1098
- [63] P. Prystawko, R. Czernecki, M. Leszczyński, P. Perlin, P. Wiśniewski, L. Dmowski, H. Teisseyre, T. Suski, I. Grzegory, M. Boćkowski, G. Nowak and S. Porowski, (2002) *phys. stat. sol. (a)* **192**, 320
- [64] N. Grandjean, B. Damilano, J. Massies, G. Neu, M. Teissere, I. Grzegory, S. Porowski, M. Gallart, P. Lefebvre, B. Gil, M. Albrecht (2001) *Semicond. Sci. Technol.* **16**, 358–361
- [65] C. Skierbiszewski, Z. Wasilewski, M. Siekacz, A. Feduniewicz, B. Pastuszka, I. Grzegory, M. Leszczyński and S. Porowski, (2004) *phys. stat. sol. (a)* **201**, no. 2, 320–323
- [66] J.D. Lambkin, D.J. Dunstan, K.P. Homewood, L.K. Howard and M.T. Emeny (1990) *Appl. Phys. Lett.* **57**, 1986–8
- [67] S. Jursenas, N.N. Kurilcik, G. Kurilcik, *et al.*, (2001) *Appl. Phys. Lett.* **78** (24), 3776–3778
- [68] P. Perlin, M. Leszczyński, P. Prystawko, R. Czernecki, P. Wiśniewski, J.L. Weyher, G. Nowak, J. Borysiuk, L. Gorczyca, T. Świetlik, G. Franssen, A. Bering, C. Skierbiszewski, I. Grzegory, T. Suski and S. Porowski, (2004) in *Proc. of Photonics West*, San Jose, California, USA.
- [69] N. Grandjean, B. Damilano and J. Massies, (2002) in *Low-Dimensional Nitride Semiconductors*, ed. by B. Gil, Clarendon Press, Oxford.

This page intentionally left blank

7 Bulk Growth of Cadmium Mercury Telluride (CMT)

P. CAPPER

BAE SYSTEMS Infrared Ltd., PO Box 217, Millbrook, Southampton, S015 OEG, UK

7.1 Introduction	209
7.2 Phase equilibria	210
7.3 Crystal growth	211
7.3.1 SSR	212
7.3.2 THM	217
7.3.3 Bridgman	222
7.4 Conclusions	238
References	238

7.1 INTRODUCTION

It is ~ 45 years now since the first development of the ternary compound cadmium mercury telluride (CMT) for infrared (IR) applications. In the early days of CMT production (1960s and 1970s) bulk-growth techniques were the predominant ones. As time progressed into the 1980s and 1990s the various epitaxial techniques, particularly liquid phase epitaxy (LPE), metal-organic vapour phase epitaxy (MOVPE) and molecular beam epitaxy (MBE) took over the major role of CMT production, particularly for photovoltaic devices, due to their greater flexibility. However, in some centres bulk-growth developments have continued during the latter two decades and material grown by several bulk-growth techniques is still used for first-generation IR detectors based on photoconductivity and for windows for some IR detector applications. Because of the sensitive nature of much of the research and development work associated with the material the history of CMT is one of most centres developing their own particular routes to its production somewhat independently of their counterparts in other countries.

There are two main types of bulk-growth technique, namely growth from the liquid and growth from the vapour, however, most work on CMT growth has been from the liquid phase and growth from the vapour phase will not be discussed in this chapter. Of the many bulk growth techniques applied to CMT three are seen to dominate. These are solid-state recrystallisation (SSR), the travelling heater method (THM) and Bridgman/ACRT (accelerated crucible rotation technique). This chapter will cover the major developments

in these three techniques, but first the key area of phase equilibria will be discussed. These equilibria are critical to establish the understanding and limitations of all growth techniques.

Central to the successful use of these materials are the dual issues of elemental purity and cleanliness in all stages of preparation and handling, particularly prior to high-temperature heat treatments. A wide variety of assessment techniques have also been developed to characterise the compositional, electrical and structural properties as well as chemical purity, and these will be described.

7.2 PHASE EQUILIBRIA

Two types of equilibria are of interest. One is the solid compound in equilibrium with the gaseous phase (vapour growth) and the other is solid-liquid-gaseous equilibria (growth from liquid/melt). These phase equilibria also help in understanding post-growth heat treatments, either during cool-down to room temperature or during annealing processes to adjust the stoichiometry, and hence electrical properties of the material. Solid-liquid-gaseous equilibria are described by three variables, temperature (T), pressure (P) and composition (x) in $\text{Cd}_x\text{Hg}_{1-x}\text{Te}$. It is, however, easier to understand the interrelations between these parameters by using 2-dimensional projections such as $T-x$, $P-T$ and $P-x$ plots. A superposition of the $T-x$ plots for HgTe and CdTe is given in Fig. 7.1 [1] where congruent melting points of 670 and 1092 °C, respectively, can be seen.

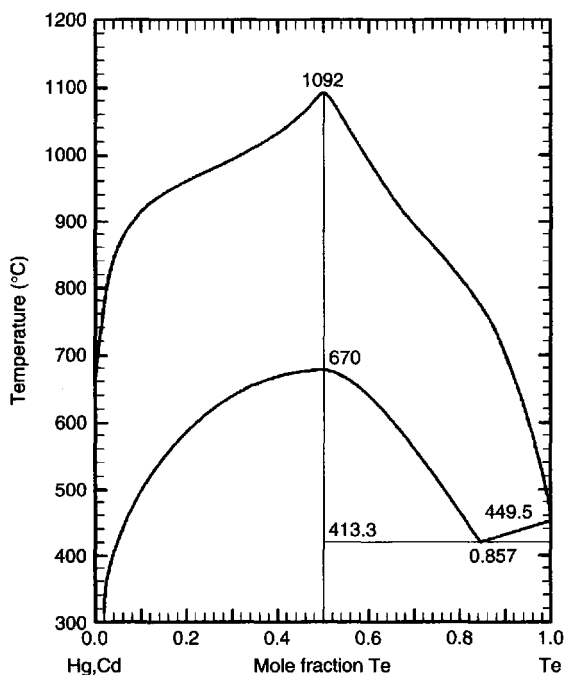


Figure 7.1 $T-x$ phase diagram for HgTe (lower curve) and CdTe (upper curve) (Reprinted from Brebrick in *Properties of Narrow Gap Cadmium-based Compounds* (1994) 55, copyright (1994) with permission from IEE)

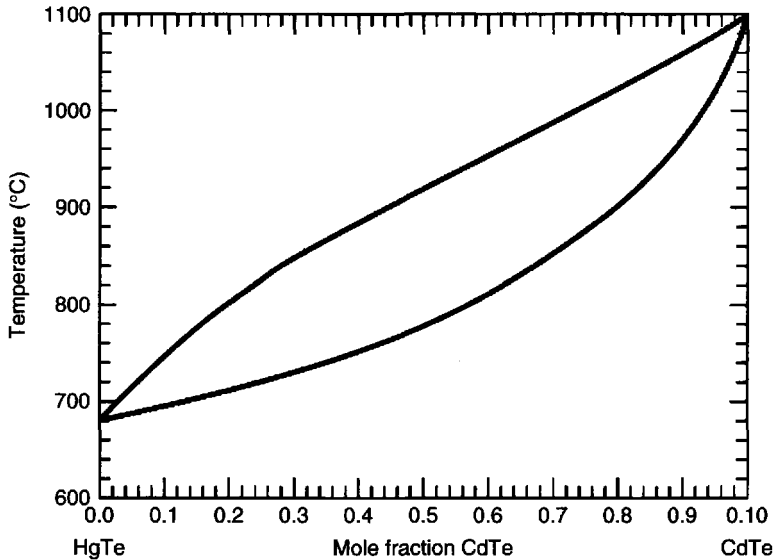


Figure 7.2 T - x phase diagram for the pseudobinary CdTe–HgTe (Reprinted from Brebrick in *Properties of Narrow Gap Cadmium-based Compounds* (1994) 56, copyright (1994) with permission from IEE)

CMT is the third most studied semiconductor after Si and GaAs and a great deal of work has been carried out on the various phase equilibria ([1, 2] contain reviews in this area). The liquidus and solidus lines in the pseudobinary HgTe–CdTe system are shown in Fig. 7.2 [1]. The wide separation between the liquidus and solidus, leading to marked segregation between CdTe and HgTe, was instrumental in the development of all the bulk-growth techniques applied to this system. In addition to the solidus–liquidus separation high Hg partial pressures are also influential both during growth and postgrowth heat treatments. A full appreciation of the $P_{(\text{Hg})}$ – T diagram, shown in Fig. 7.3 is therefore essential. Curves are the partial pressures of Hg along boundaries for solid solutions of composition x where the solid solution is in equilibrium with another condensed phase as well as the vapour phase. For $x = 0.1$ and $10^3/T = 1.3$ (K^{-1}) CMT exists for Hg pressures of 0.1 (Te-saturated) and 7 (Hg-saturated) atm. The atomic fraction of Te decreases, as the Hg partial pressure increases, over a small but nonzero range near to 0.5 atomic fraction. Even at $x = 0.95$ and Te-saturated conditions, Hg is the predominant vapour species and no solid solution contains exactly 0.5 atomic fraction Te. These features are highly significant in controlling the native-defect concentrations and hence electrical properties in CMT. There is also some evidence of a miscibility gap with a critical point at $x = 0.54$ and 457 K, although it could be linked to a surface phase rather than to the bulk phase [1].

7.3 CRYSTAL GROWTH

The vast majority of work on bulk growth of CMT has been from the melt. Although rapid progress has taken place in the epitaxial growth techniques for CMT, material grown by

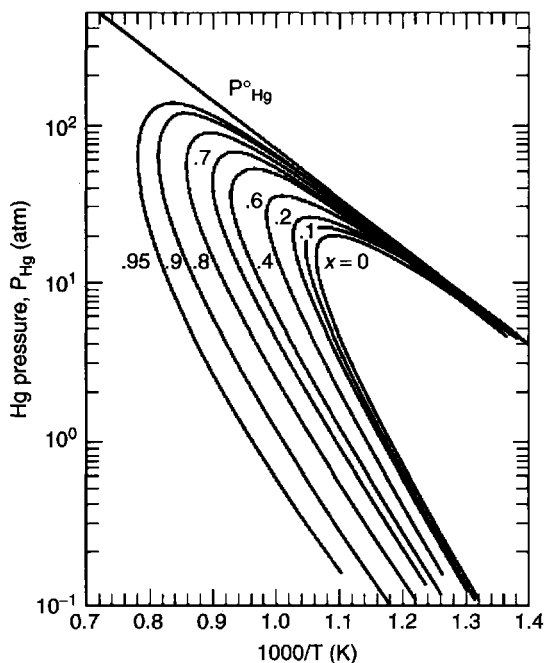


Figure 7.3 P - T diagram for $\text{Cd}_x\text{Hg}_{1-x}\text{Te}$ (CMT) (Reprinted from Brebrick in *Properties of Narrow Gap Cadmium-based Compounds* (1994) 59, copyright (1994) with permission from IEE)

several bulk methods is still in use for infrared detection, particularly for photoconductive detectors. Several historical reviews of the development of bulk CMT have been published [3–8]. Micklethwaite [3] and Kruse [4] gave comprehensive information on the growth techniques used prior to 1980. Many techniques were tried in the early years but three prime techniques survived: SSR, THM and Bridgman; all of which were at one time in production in the USA, Israel and Germany, in the UK and in France and Israel, respectively. Tennant *et al.* [9] provided an authoritative view of the then current major issues in growth techniques and noted that several countries still employed bulk-growth methods. They concluded that the electrical performance had only recently (at that time) been matched by LPE but pointed to the problems of structural defects and size limitations for use in second-generation infrared detectors. This chapter continues with reviews of the three basic bulk-growth techniques, mainly using the more recent reviews of Tregilgas [10], Triboulet [11] and Capper [7, 8], although updates on developments in these basic techniques are also given, where applicable.

7.3.1 SSR

7.3.1.1 Introduction

Tregilgas [10] has given a detailed review of the SSR process and this section will take much of its content from that excellent review. Other names that have been used for this process are quench anneal (QA) and cast recrystallise anneal (CRA). The term anneal is

used in the first case to define a high-temperature grain-growth process, while in CRA it is a low-temperature process to adjust stoichiometry. Strictly speaking SSR is crystal growth from the solid phase at temperatures close to the melting point. The technique was initially commercialised for the production of photoconductive detectors but was also used for second-generation focal plane arrays based on metal-insulator-semiconductor (MIS) detectors. These MIS detectors rely on minority carriers rather than the majority-carrier-type photoconductive devices, thus necessitating greater uniformity and fewer defects. Particularly for long-wavelength devices, this meant that much lower dislocation and subgrain densities and no major grain boundaries were fundamental requirements, necessitating major improvements in recrystallisation to be achieved. Work on the SSR technique also contributed greatly to establishing the basic understanding of many of the features seen in subsequent epitaxial films.

In the basic technique, pure elements are loaded into an etched silica ampoule (it is critical to avoid contact between the mercury and the cadmium during loading to prevent an amalgam forming) and the charge is melted and rocked to ensure complete mixing. Charges are then normally quenched rapidly, into air or oil, to room temperature in either the vertical or near-horizontal orientation, see Fig. 7.4. This produces a dendritic structure that is reduced/removed by the recrystallization step, which occurs at temperatures just below the solidus temperature (i.e. at $\sim 670^\circ\text{C}$) for many days. Grain growth occurs and microinhomogeneities in composition are removed. Care must be taken in the quenching stage to avoid pipes/voids that cannot be removed by the recrystallization step. A low-temperature annealing step, in the presence of mercury, is then used to convert the as-grown p-type material to n-type for subsequent use in detector fabrication. Many modifications were found necessary to reduce the defect densities to levels sufficient to make the MIS devices.

7.3.1.2 Compounding and quenching

During compounding, mercury is lost from the melt to the vapour space above and results in excess tellurium in the quenched ingot. Excess Hg can be added to the initial charge

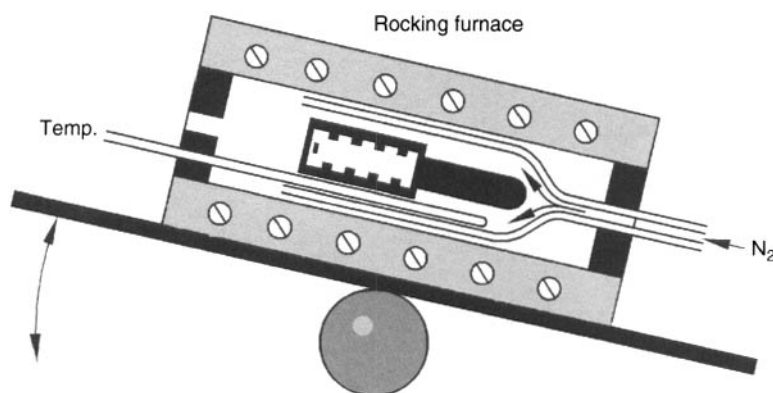


Figure 7.4 Schematic of rocking furnace with gas-quenching tube (Reprinted from Tregilgas, *Prog. Cryst. Growth Charact.* **28** (1994) 57, copyright (1994) with permission from Elsevier Science)

to compensate for this, although too high an excess can lead to Hg inclusions. It is therefore desirable to control both the Hg excess and the ampoule void space/seal-off length. Ingot diameters are limited by the burst pressures of the silica ampoules and the Hg vapour pressure (> 40 atmos) during elemental compounding. This necessitates thick-walled ampoules, but there are limits to this otherwise heat transfer during quenching is reduced and voids, holes and even 'piping' can occur. For internal diameters of 8–12.5 mm wall thicknesses vary from 2–3 mm.

Compressed gas cooling of the end of the ampoule is used to quench the ingot and the flow rate of this gas can be adjusted to vary the grain size and the dendrite-arm spacing in the ingot, with $40\text{--}501\text{ min}^{-1}$ being optimum. Figure 7.5 shows a typical as-quenched microstructure with dendrites and misfit dislocations. If quenching rates become too high then voids, shrinkage pipes and/or compositional 'coring' can all result [12]. The centres of the dendrite arms are CdTe-rich, while the surfaces of the dendrite arms are HgTe-rich. Subgrain boundaries can result from the misalignments between the dendrite arms, and entrapped Te can also be present in these regions.

7.3.1.3 Secondary recrystallisation

Following quenching the ingots are held near to the HgTe melting point for several days to allow homogenisation of dendrites and grain growth to occur. The ingot can be left in its original ampoule (reducing the possibility of additional contamination) or transferred to another etched ampoule with additional Hg before this step in the process. The process that occurs during this step is one of secondary recrystallisation, i.e. grain growth, rather than primary recrystallisation, i.e. where new grains are nucleated and grow at the expense of older grains. On cooling following recrystallisation Te often precipitates within the ingot. The precipitation of Te has been studied extensively. Its extent is governed by the initial stoichiometry of the charge prior to cooling and by the Hg vapour pressure at the recrystallisation temperature. Increasing the Hg partial pressure and slow cooling can be used to minimise Te precipitation.



Figure 7.5 As-quenched microstructure showing dendrites and misfit dislocations (Reprinted from Tregilgas, *Prog. Cryst. Growth Charac.* **28** (1994) 57, copyright (1994) with permission from Elsevier Science)

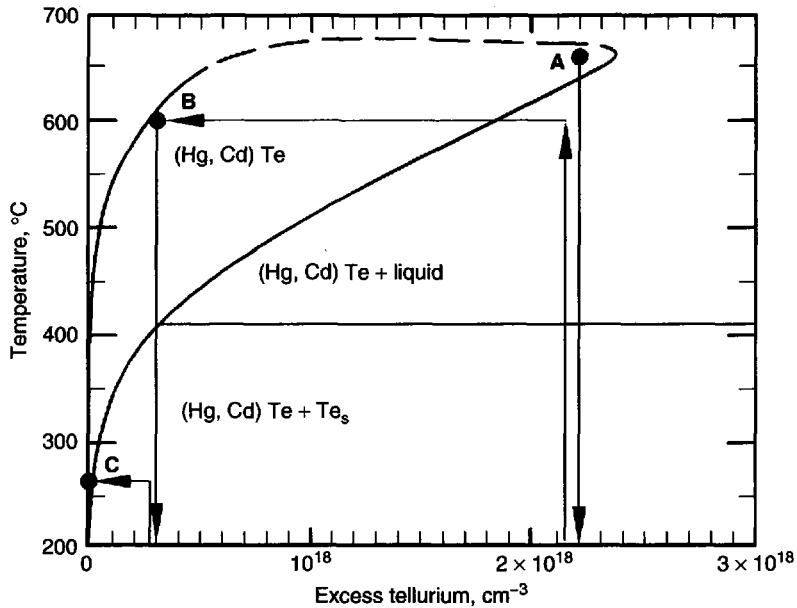


Figure 7.6 Schematic phase diagram showing DRA process (Reprinted from Tregilgas, *Prog. Cryst. Growth Charac.* 28 (1994) 57, copyright (1994) with permission from Elsevier Science)

Dislocation multiplication can result from the elimination of Te precipitates during this process step. Dislocation densities can be 8–10 times higher as a result of this effect. Figure 7.6 shows a schematic of a process to reduce these dislocations. This dislocation-reduction anneal (DRA) process starts from position A, the recrystallisation temperature. Upon cooling Te precipitation occurs. Re-encapsulation of the slices from such an ingot together with additional Hg is followed by reheating and the excess Te is reduced by indiffusing Hg, at point B in Fig. 7.6. Upon cooling from B fewer Te precipitates form and the normal low-temperature type-conversion anneal, at C, occurs without dislocation multiplication. Such a DRA step can lead to a net reduction in dislocation density of a factor of up to 100. This led to a major reduction in dark current in MIS devices made in such material.

7.3.1.4 Annealing to effect type conversion

After recrystallisation the ingot is p-type due to a high metal vacancy concentration. The ingot is then sliced and the slices are annealed in Hg vapour to reduce Te precipitation and to fill the metal vacancies, leaving the material n-type, due, it is believed, to residual donor impurities. The temperatures are normally in the range of 200–300 °C and the anneal duration is selected to control the depth of the p/n junction, i.e. the thickness of the n-type surface layer. This surface layer is related to the Te excess in the material and the annealing temperature. Care must be exercised with the anneal duration as too long an anneal run may lead to release of fast-diffusing impurities, e.g. Cu, which can reconvert the material back to, in this case, extrinsically doped p-type material. Following annealing, Hall-effect measurements are used to assess the carrier concentration and mobility of the

material and hence its suitability for photoconductive device manufacture. Care must be taken here to use the correct thickness of the n-type region if erroneous values for carrier concentration are not to be obtained. Using the full slice thickness in the Hall calculations will somewhat underestimate the true value of carrier concentration although the mobility value will not be affected.

There are several sources of residual impurities in the final material. These include the raw elements, the silica ampoule, chemical etching of the elements and the silica ampoule, the loading environment, surface contaminants on slices after etching prior to annealing and the diffusion of fast-diffusing species, e.g. Na and Cu, through the silica ampoule during low-temperature annealing. Ingot-to-ingot variations in residual background impurities suggest that only some of the impurities are fully electrically active in undoped material.

7.3.1.5 Doping

Doping can be accomplished either by native-defect control or deliberate addition of extrinsic impurities. By varying the Hg partial pressure during the low-temperature annealing step, e.g. by adding Hg or using a vacuum, the material can be annealed under Hg-rich or Hg-deficient conditions, leading, respectively, to n-type or p-type conduction. For extrinsic doping, noble metals such as Cu, Ag and Au are preferred due to their ease of activation and their distribution can be made homogeneous. Acceptor doping with Group V elements, e.g. P, As and Sb, shows inhomogeneous distributions that are difficult to homogenise due to the inherent low diffusion coefficients of these elements. In addition to which, Hg-rich annealing above 400 °C or the DRA process is necessary to activate these impurities. Doping with Cu at high levels was used successfully to manufacture MIS devices. Donor doping with In, Si and iodine have all been accomplished, although Vydyanath [13] has shown that In is only partially active. Donor doping using Al, Ga, In and Br has also been accomplished by indiffusion into slices, although high levels of In and Ga doping can be achieved by melt doping.

7.3.1.6 Variations on the basic technique

Alternatives to the basic SSR process have included 'slush' growth [14], high-pressure growth [15], incremental quenching [16] and horizontal casting [17]. In the 'slush' process the initial homogenous charge is held across the liquidus–solidus gap with the lower end solid and the upper end liquid. High-pressure growth (30 atm He gas) was used in an attempt to reduce structural defects by improved heat-flow control and using intergranular Te as a moving liquid zone during the recrystallization step [15]. Larger-diameter crystals could be produced with this high-pressure technique but uniformity of composition was poor and the technique was not subsequently developed. Incremental quenching involves extruding molten drops from an orifice onto a crucible base, and subsequently on the growing crystal [16]. The 'slush' technique was used in production in the USA, until quite recently, while the incremental quenching technique has been used to provide large-diameter feed material for THM growth [18]. Other developments have been made in the basic process [19, 20] but details available in the open literature are sketchy, due to proprietary constraints.

7.3.1.7 Summary

The SSR technique was used, predominantly in the US, for first-generation photoconductive and second-generation MIS IR detectors. It has now largely been superseded by the various epitaxial techniques and is no longer actively researched, at least to this author's knowledge.

7.3.2 THM

7.3.2.1 Introduction

Triboulet [11] has given a detailed review of the THM process and this section will take much of its content from that excellent review. Triboulet's premise for starting work on THM was that the alternative existing methods all suffered to varying degrees from the particulars of the HgTe–CdTe phase diagram, or required high pressures and/or their implementation could be complex. As a result of this crystals had limited compositional uniformity and/or restricted size. He concluded that what was needed was to achieve a growth process at lower temperatures, and hence lower pressures, reduced contamination, reduced defect levels and less departure from stoichiometry, that also led to a purification effect and ideally would facilitate seeding of growth. The THM method combines the purity advantages of zone refining and the low temperatures necessary to give large-area growth, uniform composition, low defects and defined crystal orientation.

In essence, the method involves moving a molten zone through a solid homogeneous source material by slow movement of the ampoule relative to the heater, as shown in Fig. 7.7. Matter is transported by convection and diffusion across the solvent zone in a

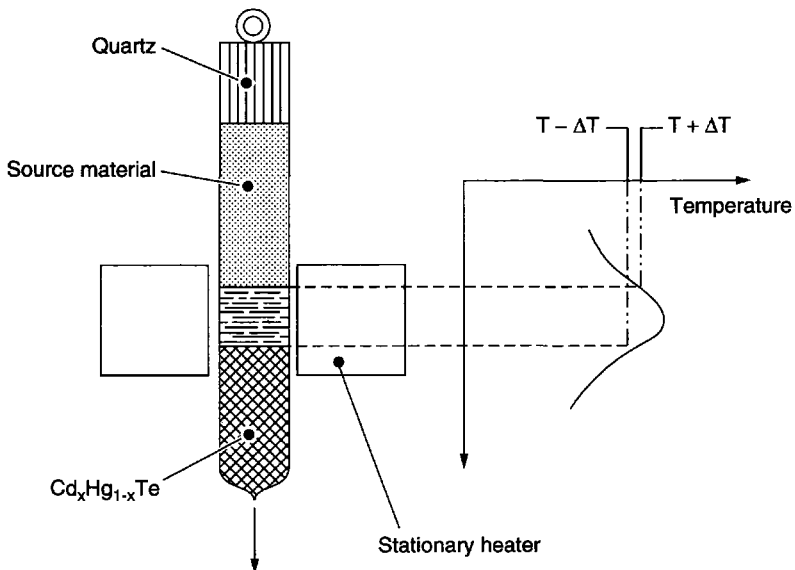


Figure 7.7 Principle of THM process (Reprinted from Triboulet, *Prog. Cryst. Growth Charac.* 28 (1994) 85, copyright (1994) with permission from Elsevier Science)

temperature gradient that results from the ampoule movement. For alloys, a steady state can be reached where the solvent zone dissolves a solid of composition C_0 at the upper hot interface then deposits, at near equilibrium, a material of the same composition at the lower growth interface. Growth occurs at a constant temperature that is lower than the maximum solidus temperature of the material, with all the consequent advantages of low-temperature growth. The Te solution also serves to purify the material during the growth process. Seeding is relatively straightforward to arrange, leading to improved structure and orientation control. Finally, THM allows the growth of longer and larger diameter material, up to 40 mm for CMT.

7.3.2.2 Experimental arrangement

The required temperature profile must have a sharp temperature peak, producing a narrow molten zone (approximately the same dimension as the crystal diameter) and a high temperature gradient at the growth interface to prevent constitutional supercooling. A simple furnace arrangement was used successfully, in which an isothermal plane was arranged at the lower end of a nickel heating ring, i.e. at the growth interface position. Thermal stability was found to be critical to prevent the growth of parasitic nuclei. A stability of at least $\pm 0.1^\circ\text{C}$ was deemed mandatory for successful growth. Multizone furnaces were also attempted but with no real advantage seen.

7.3.2.3 Feed material

Several solutions have been applied to the problem of producing suitable feed material. The most successful appeared to be that of using a cylindrical charge consisting of two segments, one CdTe and the other HgTe, with cross sections in a ratio corresponding to the desired alloy composition. Figure 7.8 shows this scheme, which accomplished crystal diameters of up to 40 mm. These cylindrical segments were obtained from ingots grown by a 'cold-THM' process, by cutting followed by chemical polishing. The fit of these cylinders into the graphite-coated silica ampoule was required to be $\sim 100\ \mu\text{m}$. As the ternary liquid solution cannot be in equilibrium with both binaries, and also because of the high Hg pressures, coring can occur at the Hg-dissolving interface, which is moved to a lower temperature than that of the CdTe, leading to small composition fluctuations.

7.3.2.4 Segregation

Using Te as the solvent steady-state growth is attained asymptotically after an initial transient, providing the source material is macroscopically homogeneous and that the temperature and travelling rate of the solvent zone are constant. Very slow growth rates ($0.1\ \text{mm h}^{-1}$) are typical (Triboulet *et al.* [5]). Figure 7.9 shows a typical axial composition profile of a CMT ingot. The initial transient causes the x value to decrease from its original value down to the desired $x \sim 0.2$ region over a couple of centimetres. From a log plot of this x variation a segregation coefficient k of 3.2 was obtained, compared to the value of ~ 2.5 from the CdTe–HgTe pseudobinary phase diagram. Thus, to avoid the initial transient in the growth the solvent-zone composition was adjusted to be C_0k

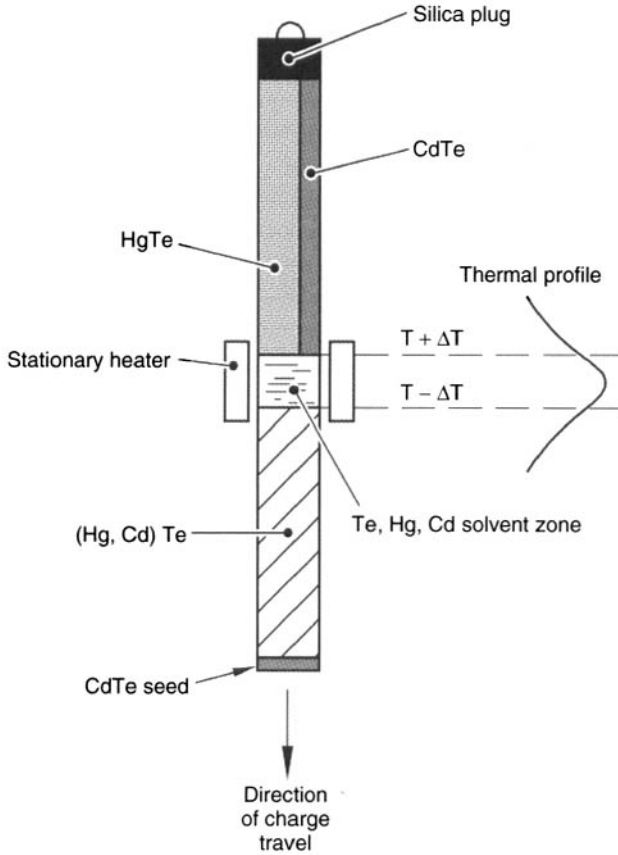


Figure 7.8 Principle of CMT THM growth process using a cylinder of 2 cylindrical segments of HgTe and CdTe as feed material (Reprinted from Triboulet *et al. J. Vac. Sci. Technol. A* 3 (1985) 96, copyright (1985) with permission from AIP)

to yield the desired composition from the start of growth. The required composition is determined from the Te-rich corner of the HgCdTe phase diagram, and is found to depend on the growth temperature and the temperature gradient (and hence the travelling rate). This is akin to growth by zone levelling and steady-state conditions are found to be obtained from the onset of growth.

7.3.2.5 Purification

There is a marked purification effect produced by solution zone refining, particularly when Te is used. The segregation of many impurities has been shown to be higher in liquid Te than in liquid CdTe, and there is less backdiffusion due to the lower growth temperature. A doping experiment, using gold, showed the marked purification obtained in THM growth. A segregation coefficient of 0.003 was obtained, compared with ~ 0.03 from the pseudobinary growth using Bridgman/ACRT (Triboulet *et al.* [5]), i.e. THM does

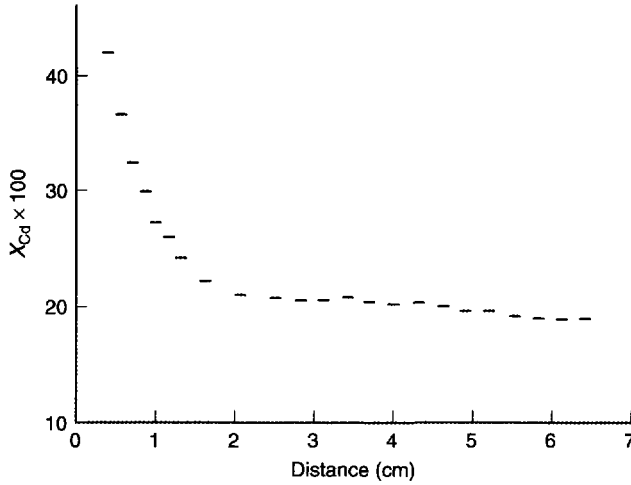


Figure 7.9 Compositional profile of THM CMT crystal using Te as solvent, for $x = 0.2$ (Reprinted from Triboulet *et al. J. Vac. Sci. Technol. A* 3 (1985) 96, copyright (1985) with permission from AIP)

indeed lead to better impurity segregation. Low impurity levels were found from mass-spectrometry measurements and the background donor levels were also low, indicating high purity.

7.3.2.6 Doping

Donor doping has been achieved by using an In-doped CdTe crystal and an undoped HgTe crystal as the starting materials. An alternative of doping the molten zone with HgBr gave a uniform distribution of carrier concentrations at $\sim 1 \times 10^{15} \text{ cm}^{-3}$.

7.3.2.7 Mass and heat transport

Natural convection is expected to be the dominant mechanism of mass transport in THM growth of CMT. This made it sensible to add ACRT to the THM process, as it had already been shown to improve the growth of Bridgman CMT (see Section 7.3.3). In the case of THM a virtual 'saw-tooth' variation of rotation rate was used and good agreement was seen between the model and the optimised growth conditions. A significant improvement in both radial and axial compositional homogeneity was obtained. ACRT also allowed higher growth rates, up to 8.5 mm day^{-1} , to be obtained [21]. In another study this same group used horizontal rotation and compared the results with ACRT. Both were found to produce similar homogeneity and to allow similar higher growth rates.

A recent report by Senchenkov *et al.* [22] showed how a rotating magnetic field can be used to control heat and mass transport. Crystals were 25 mm in diameter, 60 mm long and the crystals were grown at a rate of $2.5 \mu\text{m min}^{-1}$. Magnetic fields of 2–6 mT were used and growth periods were up to 200 h. For the crystal grown with a 2-mT magnetic field the radial composition uniformity was seen to be 0.003–0.007 in x . After low-temperature

Hg annealing the material was n-type with carrier concentration $\sim 1 \times 10^{15} \text{ cm}^{-3}$ and mobility $\sim 1 \times 10^5 \text{ cm}^2 \text{ V}^{-1} \text{ s}^{-1}$, demonstrating the high purity of the material.

7.3.2.8 Structural properties and seeding

Oriented seed crystals of CdTe have been used to produce CMT crystals up to 30 mm diameter in both [111] and [100] orientations. Whether CdTe or CMT seeds were used resulted in little difference in the growth process, nor were marked differences seen when using (111)A or (111)B oriented seeds. Without seeding crystals usually consisted of some large grains, the lower the Cd content the larger the grains. A flat or convex interface is crucial to producing crystals with fewer extended defects, a low temperature gradient at the interface also helps.

Higher etch pit densities (dislocations) and small twins are observed at the periphery of slices. Secondary nucleation at the ampoule walls, resulting from the local concavity of the growth interface, is the probable cause of the twins. These types of defects, and subgrain densities, become progressively more common towards the tail end of THM crystals. However, careful control of the interface shape, low temperature gradients, low temperatures and suppression of constitutional supercooling can lead to subgrain-free material.

7.3.2.9 Electrical properties and device results

As-grown material shows a conductivity type that is controlled by the growth temperature. This is understandable based on phase-equilibria diagrams, the higher the growth temperature the more nearly stoichiometric the material. Also from these phase-equilibria diagrams it is predicted that at a given growth temperature the departure from stoichiometry will be greater for high- x material. Experimental results for $x = 0.22$ showed the material to be p-type for a growth temperature of 600°C and n-type for 700°C , under otherwise identical growth conditions. In addition, as the x was varied from 0.2 to 0.7 the material went from n-type to p-type.

For as-grown p-type material low-temperature annealing in Hg vapour has been shown to lead to n-type conductivity, proving that deviations from stoichiometry, i.e. metal vacancies, are responsible for the p-type conductivity. Carrier concentrations of $2\text{--}5 \times 10^{14} \text{ cm}^{-3}$ with mobilities of 1.6×10^5 to $5 \times 10^4 \text{ cm}^2 \text{ V}^{-1} \text{ s}^{-1}$ were found for $x = 0.2$ and 0.3 material, together with high minority carrier lifetimes of 3 and 30 μs , respectively. These data indicate highly pure material.

Both photoconductive and photovoltaic detectors with BLIP (background limited) performance have been reported for various compositions. Planar-technology photodiodes were diffusion-limited down to 50 or 30 K even out to 20 μm cutoff wavelengths. High quantum efficiencies and reverse resistances were seen and the diodes had low noise levels. Material with $x = 0.44$ and low carrier concentration was used to make p-i-n and avalanche diodes operating at 1.6–2.5 μm . Fibre-optic telecommunication detectors were also made in this material, operating out to 1.33–1.5 μm . Room-temperature photoconductive detectors made in THM material were equivalent to those measured in both LPE and MOVPE material, although the performance degraded somewhat on cooling to 200 K.

7.3.2.10 Summary

THM was developed predominantly in France, and has produced some of the largest, highest-purity CMT crystals. Both photoconductive and photovoltaic detectors, the latter out to telecommunications wavelengths of $1.3\ \mu\text{m}$, have been made in this material. Work is still underway in Russia on this technique, although not now in France, again to the best of this author's knowledge.

7.3.3 Bridgman

7.3.3.1 Introduction

Historically, the first technique used in the UK was the Bridgman process. However, work in the USA concentrated on the cast-recrystallise-anneal (CRA), or solid state recrystallisation (SSR) as it was termed there. Some progress was made on the CRA process in the UK but only for small-diameter material. Emphasis switched to the Bridgman process and, in about 1980, to the accelerated crucible rotation technique (ACRT), a modification of the Bridgman process. The following subsections give details of these two growth techniques. Reviews of bulk growth can be found in Capper [7, 8, 23].

Two fundamentally different approaches were initially followed to improve the basic Bridgman process. These are based on control of melt mixing and of heat flows, respectively. The former has been studied by this author and coworkers (Capper [24]) while the latter includes the work of Szofran and Lehoczky [25], among others. In the Bridgman process, elemental Cd, Hg and Te are loaded into a clean silica ampoule, homogenized by melting/rocking and then frozen slowly from one end in a vertical system to produce a single crystal or, more normally, a large-grained ingot. Marked segregation of CdTe with respect to HgTe occurs in the axial direction but this leads to an advantage of the Bridgman process over other techniques, i.e. material in both ranges of interest ($3\text{--}5$ and $8\text{--}12\ \mu\text{m}$, for $x = 0.3$ and 0.2 , respectively) is produced in a single run.

A novel modification to the Bridgman process was developed by Bittner *et al.* [26] and Hoschl *et al.* [27] who floated a piece of CdTe on the top of the melt. This had the effect of producing uniform material in both axial and radial directions, but still not as uniform as ACRT material; as concluded in Hoschl *et al.* [27].

7.3.3.2 Elemental purification (mercury and tellurium)

All bulk-growth processes for CMT use pure elements as the starting materials and silica ampoules. Despite this, experience at this author's laboratory has shown that problems can occur using bought-in elements directly, even when such material is the purest grade available, i.e. 99.99999% (7N). These problems manifest themselves as charges sticking to silica ampoules, believed to be due to oxygen on Te and/or Cd surfaces, or as high background donor levels in the resulting CMT. For these reasons, and to maintain a consistent and controlled product, facilities to in-house purify both Te and Hg prior to use were established some years ago.

Bought-in Hg, in triply distilled form, is passed through a sub-boiling point vacuum distillation process in a high-purity, all-silica apparatus. From an initial batch of $\sim 9\ \text{kg}$

the first fraction (~ 3 kg) is used for low-temperature Hg annealing processes, while the second fraction (the purest) is used in both bulk and epitaxial growth processes. The remaining fraction is recycled to the supplier for redistilling. We believe that the amounts of Cu and/or Ag (both acceptors in CMT) are significantly reduced by this process and possibly other elements also.

Tellurium purification is by zone refining in flowing hydrogen at $\sim 500^\circ\text{C}$. Again, bought-in material is loaded into a cleaned silica boat in 5-kg batches. This is then placed into a silica tube in a 5-zone furnace arrangement. After flushing with argon, hydrogen is introduced and the furnaces ramped to temperature. The temperatures and furnace spacings have been adjusted to ensure that there is still solid Te between each molten zone. Zones are traversed down the boat at $\sim 25\text{ mm h}^{-1}$ and 5 passes of 5 zones each are carried out. This has the effect of moving impurity elements with segregation coefficients, k , of < 1 to the tail of the bar, while those with $k > 1$ segregate to the tip of the bar. The furnaces are then slowly moved off the bar to give the material the correct 'longitudinal' structure for subsequent cleaving prior to use. On removal, the tip and tail sections are removed, for recycling, while the central section (~ 4 kg) is ready for use with no further chemical cleaning necessary.

7.3.3.3 Bridgman growth of CMT

In the author's laboratory, elemental Cd (unetched), plus in-house purified Hg and Te are loaded, in a nitrogen-purged glove box into an etched, washed, heavy-wall (3 mm) silica ampoule (diameter 12–13 mm). A start composition of $x = 0.12$ is used and homogenization is by melting/rocking. Charges are placed in a vertical grower, remelted and then frozen slowly (0.5 mm h^{-1}) from one end in a vertical system to produce a large-grained ingot. Each growth unit is housed in a semisealed cell to manage the occasional explosions resulting from the ~ 70 atm pressure caused by the free Hg (see Fig. 7.10). Slow rotation about the vertical axis is used to reduce radial temperature variations. Slices cut from the resulting crystals are assessed for x uniformity with infrared transmission (IRT) measurements and Hall measurements at 77 K for the electrical parameters.

In Capper [8] it was shown how radial x variations decreased as the distance from the first-to-freeze end increased and as the growth rate decreased. The extent of the radial x variation was due to the combination of a concave growth surface (with respect to the solid) and density-driven convective flow within a boundary layer close to the interface. This, added to the normal segregation of the low melting point HgTe to the centre of the concave interface, leads to the observed variation. There is marked segregation of HgTe down the length of the crystals that represents an advantage of the Bridgman process over other techniques, i.e. material in both ranges of interest (3–5 and 8–12 μm) is produced in a single run.

Photoconductive devices require low carrier concentration n-type material and this was produced by improving the purity of the starting materials. Low n-type levels ($\ll 1 \times 10^{15}\text{ cm}^{-3}$) were achieved in the as-grown state for $x = 0.2$ – 0.3 , an obvious advantage in terms of reduced handling for Bridgman growth as no annealing stage was required—unlike other bulk methods. Bridgman material was used (Jones *et al.* [29]) to establish the pressure–temperature diagram, by a combination of isothermal and two-temperature annealing. On the Hg-rich side at temperatures below 320°C the n-type

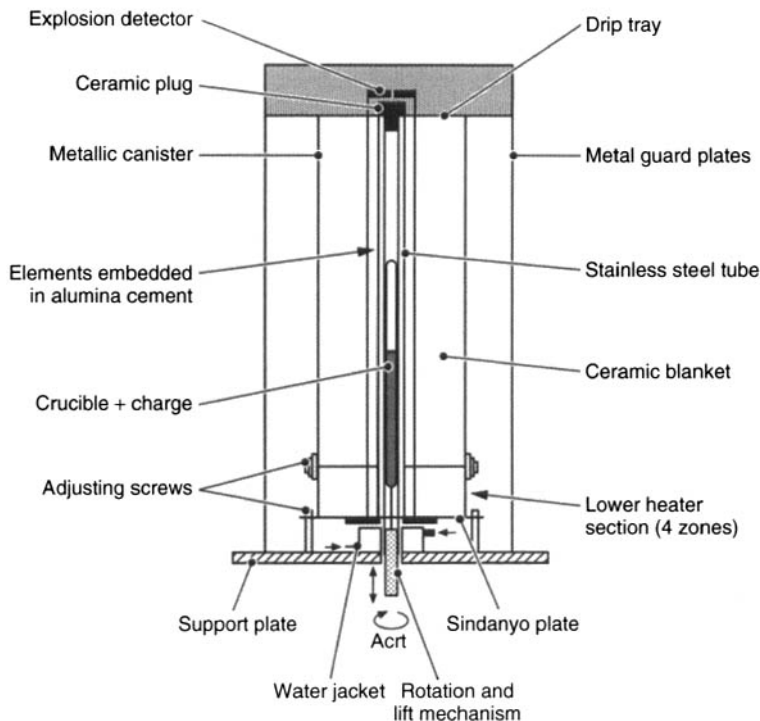


Figure 7.10 Schematic diagram of Bridgman grower for use with Hg-based compounds (Redrawn from Capper *et al. J. Cryst. Growth* **46** (1979) 575, copyright (1979) with permission from Elsevier Science)

carrier concentration is controlled by residual impurities. The $p \rightarrow n$ conversion is due to Hg filling metal vacancies. Conversion from $n \rightarrow p$ was achieved by two-temperature annealing with the Hg at a lower temperature than the CMT slice, in order to introduce metal vacancies.

Bridgman crystals contain several major grains and numerous subgrains within each major grain. No correlations were seen between the nature or density of these grains and the various growth parameters. A Berg-Barrett X-ray topography study of Bridgman material showed it to contain grains of size 0.2–0.6 mm, near to the crystal centre, and 0.05–0.2 mm near to the crystal periphery. Large temperature gradients during growth may explain the relatively large misorientations, compared to CRA material grown in the same laboratory.

Most impurity elements are electrically active in accordance with their position in the periodic table (Capper [30]). This behaviour is linked to stoichiometry at growth, i.e. those elements that substitute on Te lattice sites have to be forced into the correct sites in Te-rich material. Group I and III elements are acceptors and donors, respectively, on the metal sites. There is evidence, however, that some Group I elements can migrate at low temperatures to grain boundaries or to the surface of samples. Segregation of impurities in CRA (SSR) is very limited due to the initial fast quench step. By contrast, Bridgman benefits from marked segregation of impurities due to its slow growth rate, leading to very low levels of impurities.

7.3.3.4 Accelerated crucible rotation technique (ACRT)

Limits on controlling melt mixing in the Bridgman process necessitated a means of stirring melts contained in sealed, pressurised ampoules. The ACRT of Scheel [31] was utilised as it increased the size of crystals, eliminated unwanted phases and increased stable growth rates. The first report of the use of ACRT in CMT Bridgman growth was given in Capper and Gosney [32]. These effects were developed and discussed in more detail in later papers (see Capper [8] for a review) and are outlined here.

Three processes that are fast by comparison with buoyancy-driven convection and occur on acceleration/deceleration are:

- a) Transient Couette flow, which occurs on rapid deceleration (spin-down) particularly in tall containers. Liquid adjacent to the container walls decelerates faster than liquid in the bulk and centrifugal forces drive the inner portions of liquid towards the wall. Horizontal vortices form in counter-rotating pairs. This only occurs beyond a critical rotation rate, given by a value of 270 for the dimensionless Reynolds number:

$$Re = R^2 \Delta \Omega_c \sigma / \eta \quad (7.1)$$

where $\Delta \Omega_c$ = step change in rotation rate (rpm)

R = container radius (cm)

σ = fluid density (g cm^{-3})

η = dynamic viscosity of fluid ($\text{g cm}^{-1}\text{s}^{-1}$)

- b) Spiral shearing flow, which occurs on both spin-down and spin-up and is again caused by fluid at the walls changing its velocity faster than liquid in the bulk. It is characterised by the thickness, d , of a layer close to the wall where the rotation rate is half its initial value and by τ_1 , the time taken by the central part of the fluid to reduce to this level.

$$d = R(E\Omega_o t)^{0.5} \approx (\eta t / \sigma)^{0.5} \quad (7.2)$$

$$\tau_1 = 0.1(E\Omega_o)^{-1} \approx 0.1\sigma R^2 / \eta \quad (7.3)$$

where t = time after container stops rotating (s)

Ω_o = maximum rotation rate (rpm)

E = Ekman number ($\eta / \Omega_o R^2 \sigma$)

Spin-up/spin-down times should be $< \tau_1$ to maximise stirring.

The number of spiral arms is given by:

$$N = \Omega_o \sigma R^2 / 16\pi \eta \quad (7.4)$$

with separation,

$$\Delta r = 4\pi \eta / \sigma \Omega_o r \quad (7.5)$$

where r is the radius of the point in question.

(Δr should be kept at 0.01–0.1 cm to ensure diffusion can act as the mixing process.)

- c) Ekman flow, which occurs above a solid boundary, placed perpendicular to the axis of rotation. During spin-up, fluid adjacent to the boundary is forced to the side walls and returns diffusely and more slowly through the bulk, with the reverse occurring on spin-down.

The Ekman layer thickness is given by:

$$d_E = (\eta/\Omega_o\sigma)^{0.5} \quad (7.6)$$

with maximum radial fluid velocity of:

$$V = \Omega_o R \quad (7.7)$$

and maximum vertical fluid velocity of:

$$W = (\eta\Omega_o/\sigma)^{0.5} \quad (7.8)$$

The flow decreases within a time:

$$\tau_E = R(\sigma/\eta\Omega_o)^{0.5} \quad (7.9)$$

Figure 7.11 depicts these flows as seen in water-simulation trials. All three predicted flow patterns were seen and showed qualitative agreement with the parameters given in Equations (7.2)–(7.9). The most vigorous stirring arose due to Ekman flow for distances of $\sim R$ to $2R$ from the container base (Ekman volume), particularly when a flat-based container was used. Implications drawn from these simulations, for CMT growth, included improvements in radial x variations and a reduction in the number of crystallites propagating from the crucible walls as a result of Ekman flows near to the interface.

Bidirectional rotation is employed and rapid acceleration/deceleration (in 1–2 s) is easily achieved at any rotation rate. Ekman layer thickness, d_E , from earlier flux growth, should be < 0.05 cm, which necessitates rotation rates > 20 rpm. Horizontal and vertical flow velocities, V and W , are $\gg R/\tau_E$ for all rotation rates, ensuring that the Ekman volume passes through the Ekman layer each ACRT cycle. Rotation rates > 20 rpm will ensure that Δr is within the preferred range of 0.1–0.01 cm to homogenise the fluid body by diffusion. Both run (at maximum rate) and stop times, τ_r and τ_s , can be set to values close to the Ekman time, τ_E , to ensure mixing occurs for as long as possible and that decaying Ekman flow is minimised.

Brice *et al.* [33] reviewed the models developed for flows induced by ACRT and summarised by identifying three distinct flow regimes as the acceleration/deceleration rate increased. For small accelerations, axially symmetric fluid flows increase the symmetry of heat and mass flows. Moderate accelerations produce axial and radial fluid flows at the base of the column (R – $2R$) that stir the fluid in this region only. Large accelerations give rise to unstable asymmetric flows. The system is characterised by the Reynolds number and Table 7.1 lists the critical Reynolds numbers and the corresponding rotation rates for the values of R (0.65 cm) and η/σ ($0.006 \text{ cm}^2 \text{ s}^{-1}$) typical of CMT melts. These values of Re_c are superimposed onto the interface depth versus rotation rate plot of Fig. 7.12. For points a) and b) Ekman flow is delayed as the ampoule base is not perpendicular to the rotation axis in the conical-based ampoules used for growth. Once Ekman flow

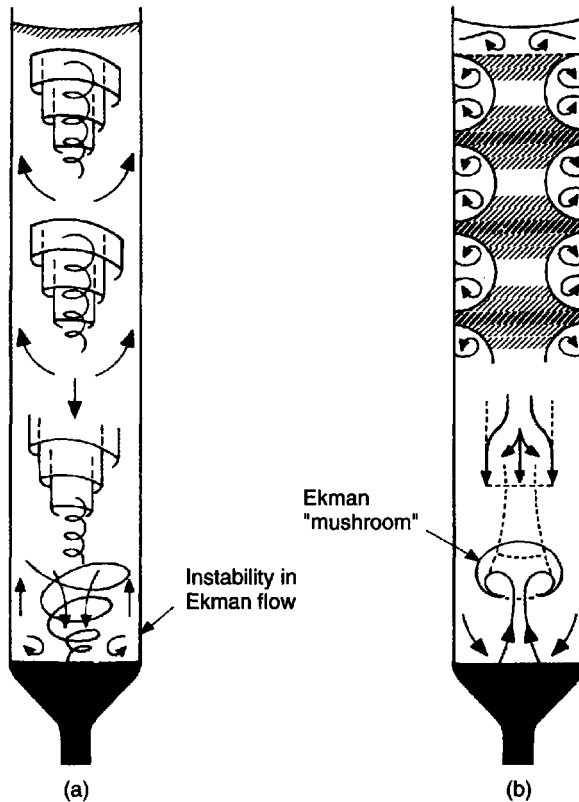


Figure 7.11 Flows in a flat-based container during (a) spin-up and (b) spin-down (Reprinted from Capper *et al. J. Electron. Mater.* **15** (1988) 361, copyright (1988) with permission from The Minerals, Metals and Materials Society)

Table 7.1 Critical Reynolds number (Re_c) and corresponding critical rotation rates (in rpm) for ACRT in 13, 50 and 75 mm diameter ampoules. ($\nu = \eta/\sigma = 0.006$, kinematic viscosity in $\text{cm}^2 \text{s}^{-1}$)

Event	Re_c	Rotation rate (rpm)		
		13 mm	50 mm	75 mm
Ekman flow starts a)	15	≥ 2	0.1	0.05
Ekman flow fully developed b)	70	10	0.6	0.25
Couette flow unstable c)	270	38	2.4	1.1
Ekman flow unstable d)	500	69	4.5	2.1

is fully established, the interface depth decreases to a minimum. Couette instabilities are predicted to occur at point c) and were seen in the simulations. As the Reynolds number increases further, Ekman flow will become unstable and interface depth increases. Too much melt mixing can be introduced by certain ACRT conditions and this can lead to a deterioration in crystal properties.

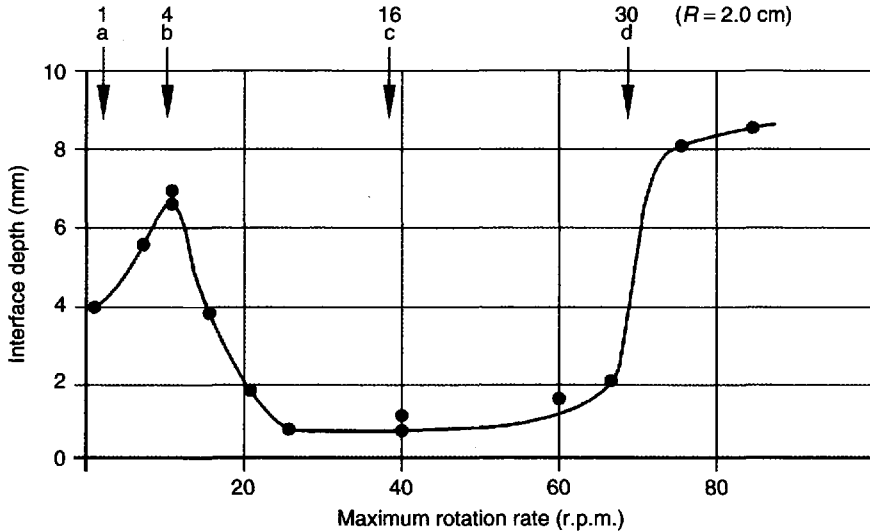


Figure 7.12 Interface depth versus ACRT maximum rotation rate. Points a–d refer to Table 7.1 (Modified from Capper *et al. J. Cryst. Growth* **89** (1988) 171, copyright (1988) with permission from Elsevier Science)

A Chinese group (Liu Jungcheng *et al.* [34] and references therein) have carried out detailed numerical modelling of the ACRT flows obtained when using a trapezoidal sequence, as used above, and compared them to water-simulation results carried out in their laboratory. The two sets of results agreed well in the lower part of the liquid, where Ekman flow is strongest, giving confidence in the applicability of the model to ACRT flows.

Various rotation sequences and start compositions were investigated and x uniformity and crystal structure determined. After comparing results, $x = 0.19$ was chosen as the preferred start composition. For these crystals grown with short run and stop times (8 and 1 s) there was a region (several cm long) of $x = 0.21$ material with axial and radial x uniformity of ± 0.002 . A similar Bridgman crystal would produce < 0.8 cm of similar x material with considerably larger radial x variations, i.e. ACRT gives a five- to ten-fold increase in potentially usable material. Figure 7.13 depicts the radial x variations for 4 crystals grown in a 4-furnace grower under identical conditions. For all four, the radial x variations are ± 0.002 at all wavelengths (i.e. $0.19 < x < 0.34$). This demonstrates the reproducibility of the process and suggests that relatively flat interfaces are present throughout the growth process—a marked improvement over normal Bridgman growth particularly for high- x material.

A secondary benefit obtained from ACRT was a decrease in the number of major grains, typically from 10 to 1 in the $x = 0.2$ region. Subgrain structure was, however, unchanged by the addition of ACRT. A Berg–Barrett X-ray topography study of ACRT samples showed that the misorientations of subgrains was reduced, compared to Bridgman, but the density was essentially unchanged.

Application of ACRT opened up a large number of possible parameter combinations. Quenching studies of crystals grown under a wide variety of conditions showed interface

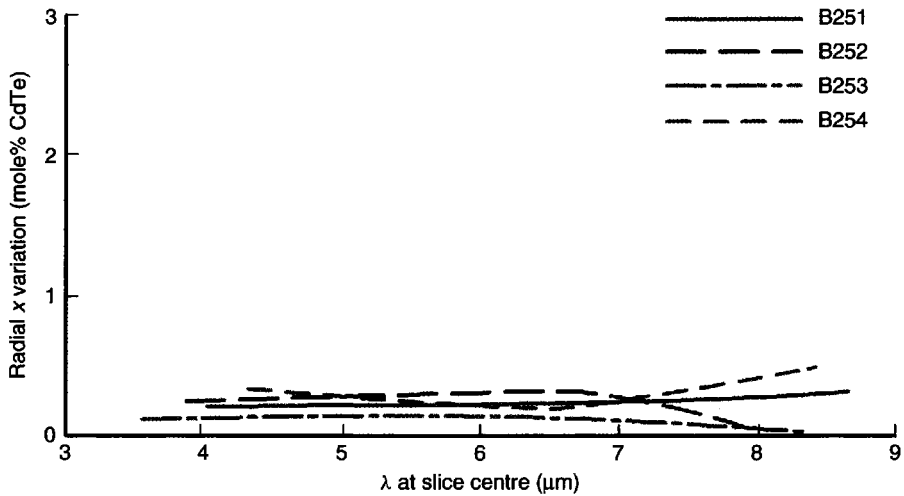


Figure 7.13 Radial x variations for 4 ACRT crystals from a 4-furnace grower (Reprinted from Capper *et al. J. Electron. Mater.* **15** (1988) 371, copyright (1988) with permission from The Minerals, Metals and Materials Society)

depths of ≈ 1 mm for $x = 0.12$ and 0.19 start crystals, unlike the 1 and 4 mm, respectively, seen in equivalent standard Bridgman crystals. Increasing the maximum rotation rate produced the interface depths shown in Fig. 7.12. The preferred region in which to operate is $25 < \Omega_0 < 60$ rpm, for a 13-mm diameter crystal. As growth rate increased, interface depth altered less than in Bridgman growth, suggesting that faster stable growth rates are possible with ACRT. From the simulation studies, it was apparent that a small stagnant region occurred in the tip of a conical-based ampoule. Quenching studies in flat-based ampoules revealed not only a flat interface but also that the slow-grown material, produced prior to quenching, was single crystal for the entire 2.5 cm length. This demonstrated the power of Ekman stirring and the importance of initiating the growth of a single crystal grain. Because of the small radial variations in composition growth of larger-diameter crystals (up to 20 mm) is also possible using ACRT and the radial variation in wavelength for a 20-mm diameter slice from a crystal grown with a maximum rotation rate of 25 rpm was $\sim 0.2 \mu\text{m}$, i.e. small, as predicted to maintain stable Ekman flow for this diameter.

Recently, work has been undertaken in the author's laboratory to extend the basic ACRT process to produce near-IR material, where higher starting x values are used (Capper *et al.* [35]). An improved ampoule seal-off procedure was developed to enable us to grow at the higher temperatures (hence higher pressures) needed for these higher- x start crystals.

Figure 7.2 shows the pseudobinary phase diagram of the HgTe–CdTe system. This demonstrates the fundamental problem in the near-equilibrium growth of CMT by melt growth methods, i.e. the wide separation between the liquidus and the solidus. However, this is actually a benefit when we are trying to produce higher x material. As the starting x is increased the first-to-freeze material also increases in x , although not at quite the same rate due to the relative curvatures of the liquidus and solidus. The initial goal was to produce material of $x \sim 0.7$, i.e. ~ 1.3 – $1.4 \mu\text{m}$ cutoff wavelength. Figure 7.2 shows that this necessitates using starting x values of 0.33–0.35.

Figure 7.3 shows the pressure–temperature phase diagram for various x values. The region above the P°_{Hg} line is essentially Hg vapour, with solid of the indicated x values existing in the loops on the lower right and liquid to the left of the loops. This amply demonstrates how the maximum growth temperature and hence the Hg vapour pressure increases as x increases.

Standard bidirectional rotation ACRT was employed with rapid acceleration/deceleration (in 1–2 s). From considerations of the simple model (Capper [36]) it was seen that maximum rotation rates for the currently grown 20-mm diameter crystals should be between 10 and 30 rpm and we normally used between 25 and 30 rpm to maximize Ekman flow. Also for these crystals short run and stop times (8 and 1 s, respectively) were used as for standard 13-mm diameter crystals.

Figure 7.14 shows the axial composition profiles of some of the crystals grown. As expected, as the start x value increases so does the ‘plateau’ region of near-constant composition, although not necessarily linearly with start x due to variations in ampoule shape and diameter, note we are only plotting against slice number and not normalized distance. The plots in Fig. 7.14 also show some evidence of growth transients in the first-to-freeze sections of some of the crystals. This could be caused by constitutional supercooling in the tip regions, possibly linked to a lack of adequate stirring in these conically shaped regions.

Figure 7.15 shows the FTIR (Fourier transform infrared) map of a short-wavelength slice ($\lambda \sim 1.4 \mu\text{m}$) demonstrating excellent radial uniformity. The small nonuniform regions are associated with edge cracks in this slice; cracking is still a problem in these high- x crystals.

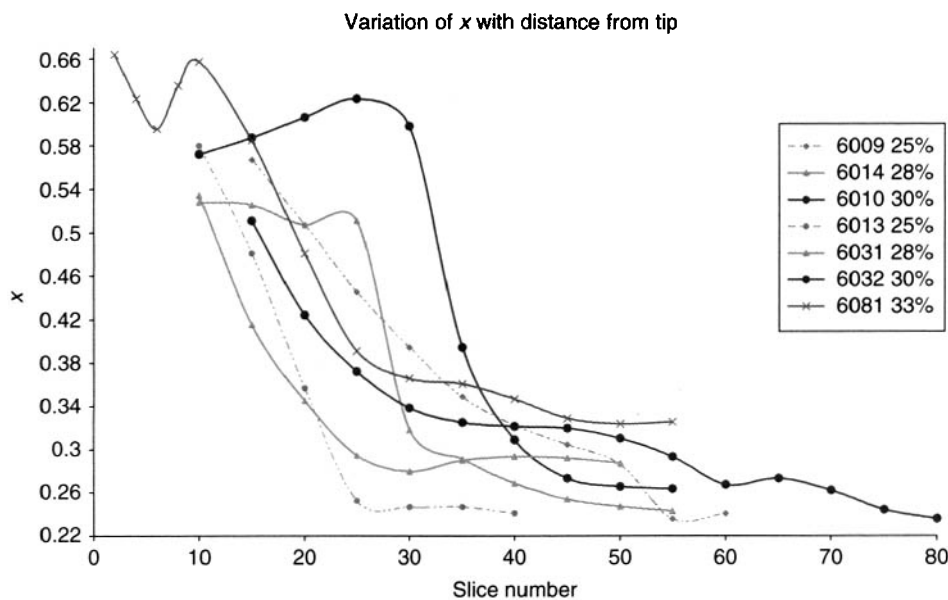


Figure 7.14 Axial composition profiles of high- x ACRT crystals (Reprinted from Capper *et al.*, *J. Mater. Sci.:Mater. Electron.* **15** (2004) 721, copyright (2004) with permission from Kluwer Academic Publishers)

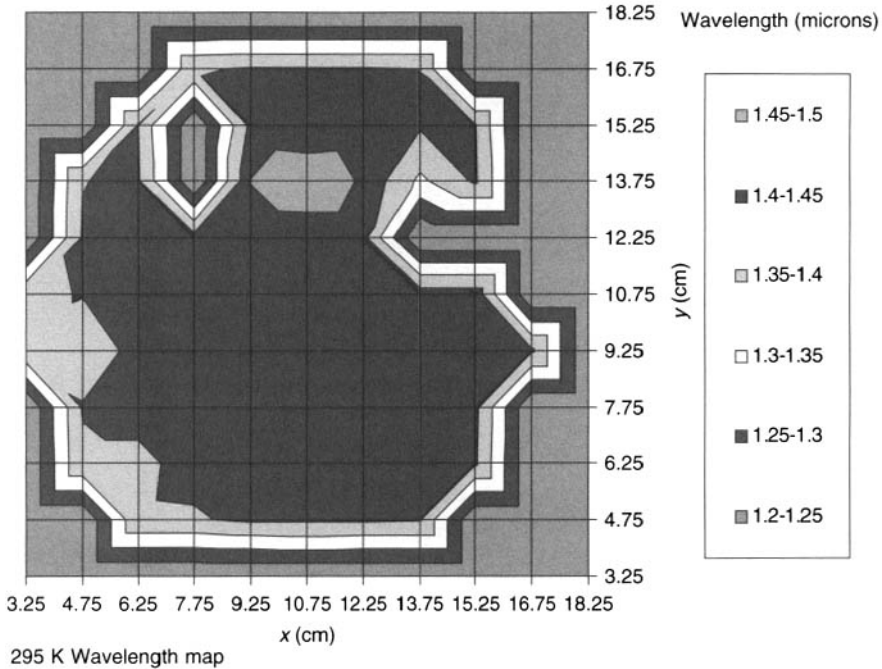


Figure 7.15 Radial distribution of wavelength (in μm at room temperature) in high- x slice (Reprinted from Capper *et al. J. Mater. Sci.:Mater. Electron.* **15** (2004) 721, copyright (2004) with permission from Kluwer Academic Publishers)

To try to simultaneously assess the radial and axial uniformity we sliced an axial plank, $\sim 20 \times 40$ mm in size, and mapped the wavelength variations. Figure 7.16 shows the results of this measurement and it can be seen that at the lower (first-to-freeze) end the ‘interface depth’ is small and the shape is slightly convex (not ideal). As growth proceeds the interface shape takes on a ‘seagull wing’ shape, although the uniformity is still good. In the upper half of the plot the sample is again uniform in both the axial and radial directions ($\pm 0.1 \mu\text{m}$ over a 20×20 mm area). This is the plateau region for this particular start x crystal.

To further investigate the interface region in these high x crystals we have carried out quenching studies in several crystals. Figure 7.17 shows the interfaces delineated by quenching followed by axial sectioning and etching to reveal the differences in structure for the grown and the cast material. Three different crystals were quenched at positions 5, 90 and 190 mm from the first-to-freeze position. It can be seen that flat (~ 1 mm) convex interfaces are present near to the first-to-freeze end and in the $x \sim 0.2$ – 0.3 regions, i.e. at 5 and 90 mm, respectively, mirroring the excellent compositional uniformity in these regions. At the 190-mm position the interface depth is large (> 10 mm) but it should be noted that this is approaching the HgTe-rich section of the crystal, i.e. where the Cd content is very low. Under these conditions it is not expected that ACRT will be effective in stirring the melt.

A new assessment tool that we have just started to use for these high- x crystals is that of IR imaging. By placing a blackbody on one side of the slice (polished on both sides to

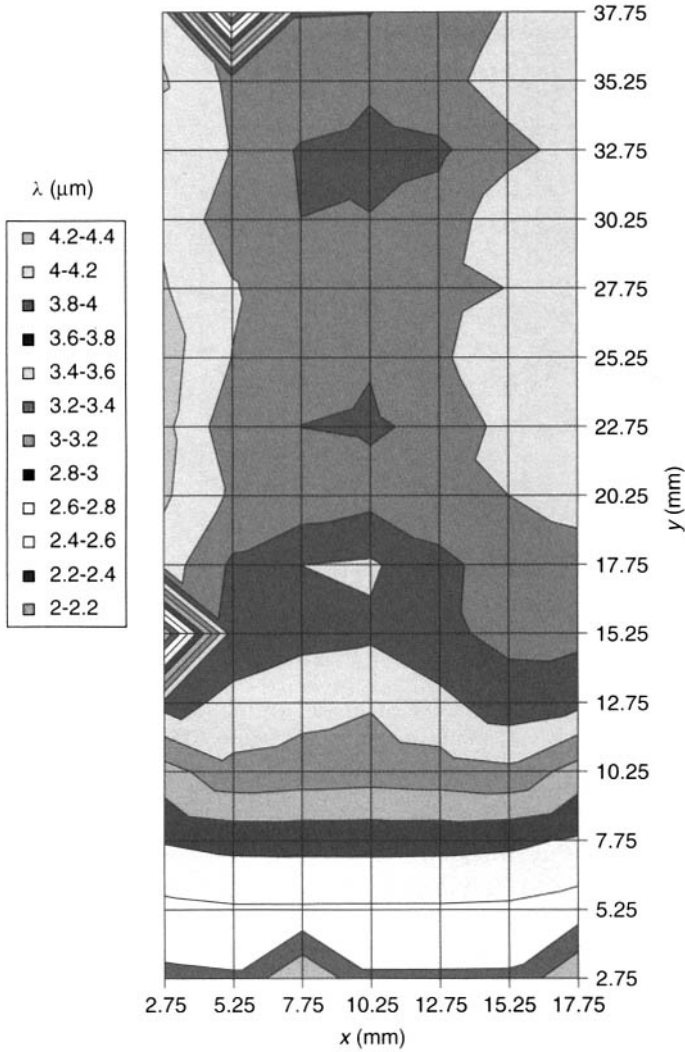


Figure 7.16 Variations in wavelength (in μm at room temperature) in high- x ACRT axially sliced plank (Reprinted from Capper *et al. J. Mater. Sci.:Mater. Electron.* **15** (2004) 721, copyright (2004) with permission from Kluwer Academic Publishers)

~ 1 mm thickness) and a MW (midwave) camera system (CEDIP) on the other, images can be taken that show up IR-absorbing defects. This is a rapid, noncontact assessment method that can be used for all slices with cutoff wavelengths less than that of the camera system's detector. Figure 7.18 shows several such images from slices taken from different positions in one crystal, although the features seen are also observed in other crystals. The low-numbered slices are from the first-to-freeze end of the crystal and it can be seen that they are essentially free of absorbing defects. As the slice number increases, first edge cracks (slices 21 and 22) and finally second-phase inclusions (slices 34 and 37) probably of Te, and 'swirl-like' patterns of light/darker contrast, rather than black/white, appear.

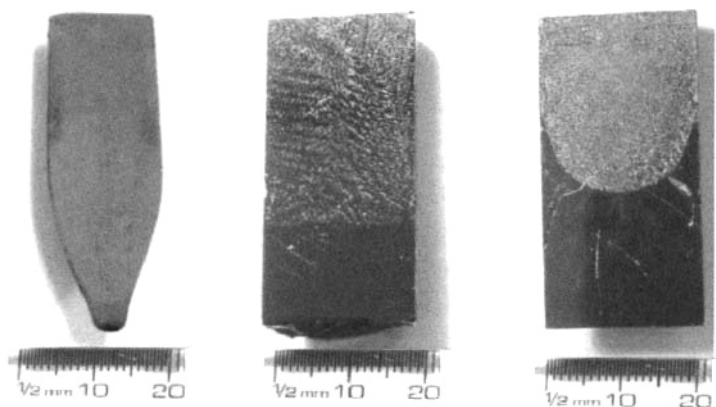


Figure 7.17 Solid/liquid interfaces in quenched high- x ACRT crystals (Reprinted from Capper *et al. J. Mater. Sci.:Mater. Electron.* **15** (2004) 721, copyright (2004) with permission from Kluwer Academic Publishers)

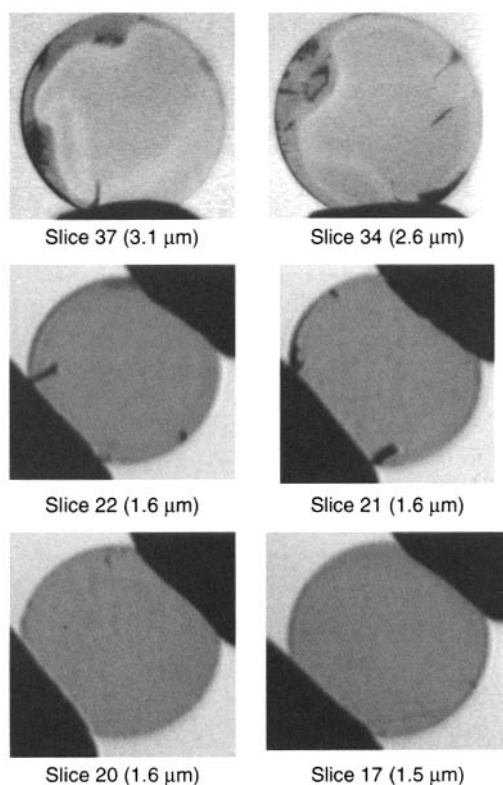


Figure 7.18 IR camera images in high- x ACRT slices (number in brackets = cutoff wavelength of slice) (Reprinted from Capper *et al., J. Mater. Sci.:Mater. Electron.* **15** (2004) 721, copyright (2004) with permission from Kluwer Academic Publishers)

The origin of the latter patterns is unknown at present. Possible causes include ACRT stirring flow patterns frozen in, p-type regions in an otherwise n-type slice (these crystals are known to change from n-type in the first-to-freeze sections to p-type at some distance from the tip (Capper [24]) and stress caused by cracking. Work is continuing in this area of assessment to understand the origin and extent of these IR-absorbing defects.

The electrical properties of ACRT material differ markedly from those of equivalent Bridgman crystals (Capper [30]). Material with $x > 0.3$ is n-type as-grown, at a level above that found for Bridgman crystals but, at $x < 0.3$, the material is p-type. Such material converts to low ($< 1 \times 10^{15} \text{ cm}^{-3}$) n-type on the standard anneal treatment (Jones *et al.*, [29]) indicating that metal vacancies are the cause of the p-type behaviour. Groups I and III elements are acceptors and donors, respectively, on the metal sites as they are in Bridgman, with the exception of Au. Groups V and VII are inactive dopants in those portions of ACRT crystals that are Te-rich as-grown, i.e. $x < 0.3$, but are active dopants for $x > 0.3$ where metal-rich conditions prevail, as found in Bridgman material. Impurity-segregation behaviour in ACRT material was also found to be different from Bridgman growth (Capper [8]). In general, impurity segregation coefficients decrease in ACRT crystals, when compared to standard Bridgman.

Samples have been assessed for purity using laser scan mass spectrometry (LSMS) and Table 7.2 gives results for Bridgman and ACRT crystals. Segregation effects lead to highly pure regions near to the first-to-freeze end. Very low levels of all impurities (including C and O) can be seen in addition to Cu in the ACRT sample, which was deliberately added to dope this crystal p-type.

7.3.3.5 Uses in IR devices

The low n-type carrier levels and high lifetime of Bridgman/ACRT material is well suited to give high-performance SPRITE (signal processing in the element) detectors

Table 7.2 LSMS impurity survey in Bridgman and ACRT bulk CMT samples ($\times 10^{15}$ atoms cm^{-3} , precise to factor of 3, accurate to factor of 2)

Element	Bridgman	ACRT
Li	<0.005	0.6
C	3	30
O	<0.05	0.1
F	0.06	<0.2
Na	0.03	0.6
Al	0.2	<0.09
Si	1	<0.3
S	1	<0.06
K	0.03	0.6
Cr	0.2	<0.06
Cu*	<0.5	30

*Intentional dopant

(Elliott [37]). In this type of device the image is scanned along the CMT strip at a rate similar to that at which carriers diffuse under bias. On thinning to $\sim 10\ \mu\text{m}$, the slice is cut into strips (monoliths) and these are mounted on sapphire carriers prior to metallisation and dicing to delineate the elements. In a study of far-IR detection at $350\text{--}1200\ \mu\text{m}$, Kimmitt *et al.* [38] found that ACRT CMT ($0.39 < x < 0.53$ and $3 \times 10^{13}\text{--}2 \times 10^{14}\ \text{cm}^{-3}$ n-type) acted as an impurity photoconductor. Charlton *et al.* [39] listed the various space applications that have used bulk material to make discrete IR detectors, both photoconductive and photovoltaic. Ashley *et al.* [40] demonstrated room-temperature operation in photoconductors made in ACRT-grown material using excluding contacts to suppress Auger-generated noise. ACRT was also critical in producing sufficient material of the required composition and carrier concentration for several large photoconductive detector programmes. There are some 5000–6000 UK Common Module imagers in service worldwide that are based on this bulk material. This bulk material is still used at BAE SYSTEMS for a wide range of single and multi-element photoconductive arrays of IR detectors, including several types of SPRITEs and US Common Module detectors.

The first staring array imagery in the $8\text{--}14\ \mu\text{m}$ band (77 K) was demonstrated (Ballingall *et al.* [41]) using ACRT CMT as the detector material. Ballingall *et al.* [42] discussed the effects of major grain boundaries on 2-dimensional array performance. Baker *et al.* [43] also reported that such structure leads to anomalous crosstalk between adjacent diodes. Uniformity of diode properties can be high, however, in 32-element linear arrays. Despite the potentially damaging subgrain structure, a 32×32 array ($4.5\ \mu\text{m}$ cutoff) with only a single defective element was made in ACRT material. Both $3\text{--}5$ and $8\text{--}14\ \mu\text{m}$ band arrays of 64×64 elements have been made in bulk ACRT material (Baker *et al.* [43]). Yields of these larger arrays, however, are low due to the subgrain structure, hence the move to using epitaxial material.

7.3.3.6 Other developments

Hoschl *et al.* [27] developed a modified Bridgman process in which a melt of constant composition is arranged above the growing crystal. As growth proceeds the CdTe removed by the crystal growth is replaced above the melt by a piece of CdTe floating on the melt surface. Initially, a HgTe charge is prepared in the normal way. This ampoule is then carefully opened and a suitably sized CdTe ingot is placed in the ampoule above the HgTe. The combined charge is then placed in a vertical Bridgman furnace and heated at the melting point of the desired x value for several days. This step produces a melt of the desired composition and is the critical step in the entire process. The temperature gradient between the hot and cold zones was 10°C cm^{-1} with the former at $\sim 707^\circ\text{C}$ and the latter at 520°C . The growth rate is chosen to avoid the effects of constitutional supercooling and was $\sim 1.16 \times 10^{-6}\ \text{cm s}^{-1}$. Normally single crystals were obtained. The radial x variations, determined by electron-probe microanalysis was estimated as ± 0.005 , being higher at the edge of slices, as in normal Bridgman. Diodes made in this material were comparable to those made in THM material. The disadvantages of the technique include the long growth time, 2–3 months, and the inferior compositional uniformity, compared to ACRT (Hoschl *et al.* [27]). However, it is a simpler process in the sense that it only requires binary compounds to be formed initially, and it produces material of equivalent purity to THM and ACRT.

In a series of recent papers, this material has been used to study various effects of p-n junction formation, and also to study some of the fundamental properties of the material. The latter have included minority carrier diffusion lengths and lifetimes (Franc *et al.* [44]), galvanomagnetic and thermoelectric parameters (Moravec *et al.* [45]) and native point defects (Belas *et al.* [46]). In [47] the temperature dependence of the depth of p to n conversion during argon milling was shown. Cooling of the substrate to ~ 100 K was suggested as a means of avoiding unwanted type conversion during processing. This effect was also discussed in relation to reactive ion etching using H_2/CH_4 mixtures (Belas *et al.* [48]). In [44] the diffusion lengths of minority holes in n-type material were found to vary between 20 and 120 μm at 80 K decreasing with temperature to 8–35 μm at 130 K. For p-type material, the values were between 6 and 12 μm at 80 K but increased with temperature. The study of galvanomagnetic and thermoelectric parameters (Moravec *et al.* [45]) consisted of Hall-effect measurements over the range 4.2 to 300 K with magnetic fields up to 0.23 T. The Seebeck coefficient was measured by two methods, yielding both hole concentration at 77 K and the Seebeck coefficient over the temperature range from 10 to 280 K. Good agreement was seen between the activation energy levels of defects determined theoretically and experimentally, and these also agreed with values from previous work on standard Bridgman material of equivalent properties. In Belas *et al.* [46] changes in electrical conductivity with time after reactive ion etching have been interpreted in terms of release and diffusion of Hg interstitials with a diffusion coefficient of $> 10^8 \text{ cm}^2 \text{ s}^{-1}$. Two trap levels are associated with complexes formed by extrinsic acceptors and bound Hg interstitials.

A recent report has been made of a new method of producing CMT crystals using a high-pressure modification to the Bridgman process (Yue Wang *et al.* [49]). In this technique two stages are used to produce the starting material. In the first stage the composition is fixed at 0.04–0.06. This is melted, clearly at a relatively low temperature, and then a second charge with a composition of ~ 0.4 is loaded on top of the initial charge (see Fig. 7.19). Crystal growth then takes place at a slow rate of $\sim 0.21 \text{ mm h}^{-1}$ in a low temperature gradient (5°C cm^{-1}) at a low growth temperature of $\sim 710^\circ\text{C}$. Thin-walled ampoules can be used because a nitrogen pressure of 30–40 atm is applied to the ampoules during processing. A schematic of the diffusion of CdTe within the melt is depicted in Fig. 7.20, together with the relevant composition profile. Crystals up to 40 mm in diameter have been produced and the uniformity of composition in the axial direction, albeit only from density measurements that give an average figure, is good. Uniformity in the radial direction is quoted as ± 0.001 in composition, again albeit over only the central $6 \times 6 \text{ mm}$ area. No electrical data were given but this is clearly a promising technique to produce large-area bulk slices of CMT.

7.3.3.7 Summary

In the Bridgman growth of CMT, a controlled increase in melt mixing, produced by ACRT, leads to an improvement in radial compositional variations and good axial uniformity resulting in a factor of ten increase in overall material yield over normal Bridgman growth. Large-diameter crystals (13–20 mm) have been grown with a high degree of radial x uniformity by ACRT. Crystals of 20 mm diameter with a length of 200 mm weighing $\sim 0.5 \text{ kg}$ are now routinely produced. Electrical and chemical characterisation

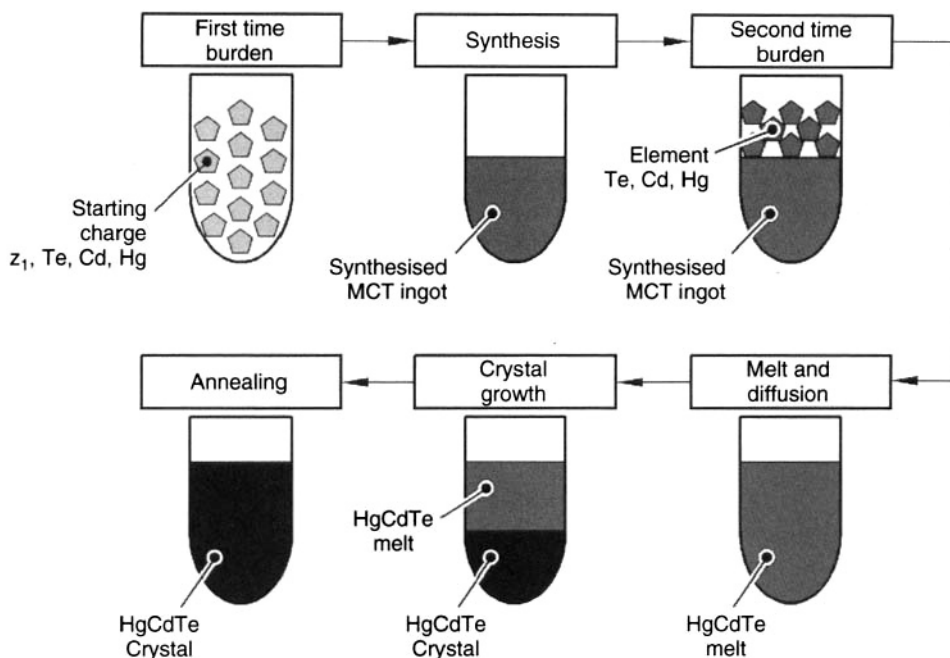


Figure 7.19 Growth procedure for CMT by high-pressure Bridgman technique (Reprinted from Yue Wang *et al. J. Cryst. Growth* **263** (2004) 273, copyright (2004) with permission from Elsevier Science)

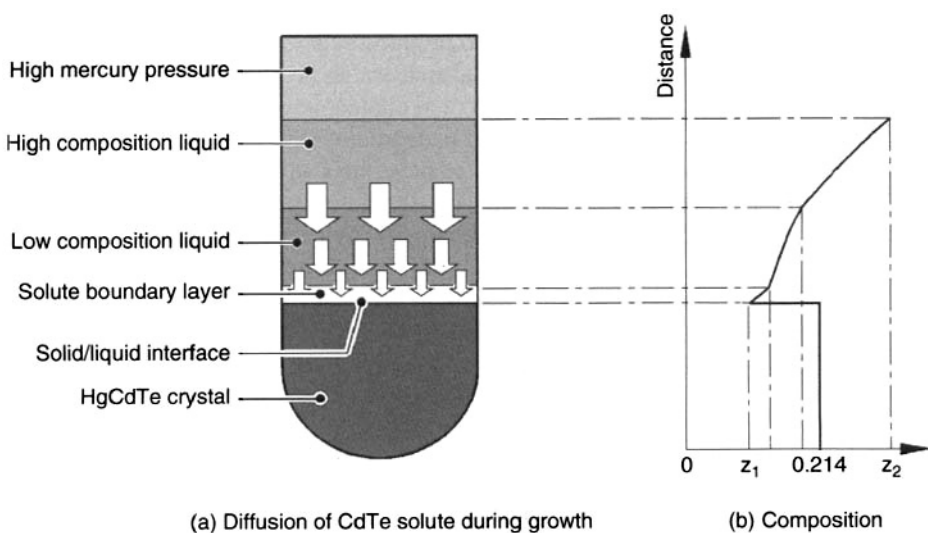


Figure 7.20 Diffusion of CdTe in CMT liquid during high-pressure Bridgman growth (Reprinted from Yue Wang *et al. J. Cryst. Growth* **263** (2004) 273, copyright (2004) with permission from Elsevier Science)

shows that high-purity material is obtained (when pure elements are used) and this allows the manufacture of a wide variety of high-performance photoconductive infrared detectors. Bulk-growth techniques for CMT are still in production and continue to satisfy the needs of the first-generation IR detectors, based on photoconductors, for both military and commercial use. The use of ACRT at BAE SYSTEMS also made possible the fabrication of early 2-dimensional arrays of photodiodes with a high degree of uniformity of response. This type of material has also been used to demonstrate nonequilibrium detector operation. Grain structure prevents it from being useful in larger-area detector arrays. The quality and costs of epitaxial material are improving continuously but it will be some years yet before bulk-grown material ceases entirely to be produced, for photoconductive applications.

Other groups, notably Czech and Chinese, have developed modifications to the basic Bridgman process that produce usable material. The former group use a piece of CdTe floating on the melt to act as the replenishment source, while the latter group use a 2-stage process to achieve the same effect, i.e. to replenish the CdTe taken out of the melt during crystal growth. IR devices have been made in the material of the former group but it is still too early to tell if the Chinese technique will produce suitable material for device fabrication.

A new company has recently been set up in New Zealand (Spitfire Semiconductors) to grow and sell bulk CMT material. They use a modified Bridgman technique but no growth details are available in the open literature, as yet.

7.4 CONCLUSIONS

Despite the use of the various epitaxial growth techniques to produce CMT material for second- and third-generation IR devices, bulk-grown material continues to be used for some first-generation device types based on the photoconductive effect. This chapter has summarised the three main techniques used to produce bulk CMT material, namely, solid-state recrystallisation, travelling heater method and Bridgman, together with their variants. This material was mainly used for first-generation photoconductive IR detectors, although the first small focal plane arrays, i.e. second-generation devices were also made in bulk material in the early days. All three techniques have their advantages and disadvantages, which have been detailed above. Currently, it is thought that only material grown by modifications of the Bridgman process are being actively researched and/or in production in several sites throughout the world although THM work may be progressing in Russia. It will probably be several more years before bulk material is made completely redundant by epitaxial processes.

REFERENCES

- [1] R.F. Brebrick, (1994) in *Properties of Narrow Gap Cadmium-based Compounds*, P. Capper (Ed.), EMIS Datareview Series No. 10, IEE, London.
- [2] J.C. Brice, (1986) *Prog. Cryst. Growth Charact.*, **13**, 39.
- [3] W.F.H. Micklethwaite, (1981) *Semicond. Semimet.*, **18**, Ch. 3.
- [4] P.W. Kruse, (1981) *Semicond. Semimet.*, **18**, Ch. 1.
- [5] R. Triboulet, T. Nguyen Duy, and A. Durand, (1985) *J. Vac. Sci. Technol. A*, **3**, 95.
- [6] H. Maier, (1988) *N.A.T.O. Advanced Research Workshop on the Future of Small-gap II-VI Semiconductors*, Liege, Belgium.

- [7] P. Capper, (1994) in *Properties of Narrow Gap Cadmium-based Compounds*, P. Capper (Ed.), EMIS Datareview Series No. 10, IEE, London, 55.
- [8] P. Capper, (1994) *Prog. Cryst. Growth Charact.*, **28**, 1.
- [9] W.E. Tennant, C.A. Cockrum, J.B. Gilpin, *et al.*, (1992) *J. Vac. Sci. Technol. B*, **10**, 1359.
- [10] J.H. Tregilgas, (1994) *Prog. Cryst. Growth Charact.*, **28**, 57.
- [11] R. Triboulet, (1994) *Prog. Cryst. Growth Charact.*, **28**, 85.
- [12] B.E. Bartlett, P. Capper, J.E. Harris and M.J.T. Quelch, (1979) *J. Cryst. Growth*, **47**, 341.
- [13] H.R. Vydyanath, (1996) *J. Cryst. Growth*, **161**, 64.
- [14] T.C. Harman, (1972) *J. Electron. Mater.*, **1**, 230.
- [15] A.W. Vere, B.W. Straughan, D.J. Williams, *et al.*, (1982) *J. Cryst. Growth*, **59**, 121.
- [16] L. Colombo, A.J. Syllaios, R.W. Perlaky, and M.J. Brau, (1985) *J. Vac. Sci. Technol. A*, **3**, 100.
- [17] R.K. Sharma, V.K. Singh, N.K. Mayyar, *et al.*, (1987) *J. Cryst. Growth*, **131**, 565.
- [18] L. Colombo, R.R. Chang, C.J. Chang, and B.A. Baird, (1988) *J. Vac. Sci. Technol. A*, **6**, 2795.
- [19] J. Ziegler, (1986) US Patent 4,591,410.
- [20] W.M. Higgins, G.N. Pultz, R.G. Roy, and R.A. Lancaster, (1989) *J. Vac. Sci. Technol. A*, **7**, 271.
- [21] R.U. Bloedner and P. Gille, (1993) *J. Cryst. Growth*, **130**, 181.
- [22] A.S. Senchenkov, I.V. Barmin, A.S. Tomsa, and V.V. Krapukhin, (1999) *J. Cryst. Growth*, **179**, 552.
- [23] P. Capper, (1987) *Properties of Mercury Cadmium Telluride*, J.C. Brice and P. Capper (Eds) EMIS Datareview Series No. 10, IEE, London.
- [24] P. Capper, (1989) *Prog. Cryst. Growth Charact.*, **19**, 259.
- [25] F.R. Szofran, and S.L. Lehoczky, (1984) *J. Cryst. Growth*, **70**, 349.
- [26] H. Bittner, P. Hoschl, and B. Schubert, (1991) *Cryst. Res. Tech.*, **26**, 667.
- [27] P. Hoschl, R. Grill, J. Svoboda, P. Hlidek, P. Moravec, J. Franc, and E. Belas, (1994) *J. Cryst. Growth*, **138**, 956.
- [28] P. Capper, J.E. Harris, D. Nicholson, and D. Cole, (1979) *J. Cryst. Growth*, **46**, 575.
- [29] C.L. Jones, M.J.T. Quelch, P. Capper and J.J.G. Gosney, (1982) *J. Appl. Phys.*, **53**, 9080.
- [30] P. Capper, (1991) *J. Vac. Sci. Technol. B*, **9**, 1667.
- [31] H.J. Scheel, (1972) *J. Cryst. Growth*, **13/14**, 560.
- [32] P. Capper and J.J.G. Gosney, (1981) U.K. Patent 8115911.
- [33] J.C. Brice, P. Capper, C.L. Jones and J.J.G. Gosney, (1986) *Prog. Cryst. Growth Charact.*, **13**, 197.
- [34] Liu Jungcheng, Jie Wanqu and Zhou Yaohe (1997) *Prog. Nat. Sci.*, **7/2**, 215
- [35] P. Capper, C.D. Maxey, C. Butler, M. Grist and J. Price, (2003) *J. Mater. Sci.:Mater. Electron.*, **15**, 721.
- [36] P. Capper, (2002) *J. Mater. Sci.:Mater. Electron.*, **12/8**, 423.
- [37] C.T. Elliott, (1994) in *Properties of Narrow Gap Cadmium-based Compounds*, P. Capper (Ed.), EMIS Datareview Series No. 10, IEE, London, p. 311.
- [38] M.F. Kimmitt, G.C. Lopez, J.C. Giles, M. Takai, H.P. Roser, B.T. McGuckin, and A. Black, (1985) *Infrared Phys.*, **25**, 767.
- [39] D.E. Charlton, L.G. Moore and W.I. McMillan, *Proceedings of the ESA Symposium on Photon Detectors for Instrumentation*, ESTEC, Noordwijk, Netherlands (Nov. 1992).
- [40] T. Ashley, C.T. Elliott and A. Harker, (1986) *Infrared Phys.*, **26**, 303.
- [41] R.A. Ballingall, *Conference on Advanced IR Detectors and Systems*, (IEE, London, 1981) p. 70.
- [42] R.A. Ballingall, I.D. Blenkinsop, D.J. Lees, I.M. Baker, M.D. Jenner and R. Lockett, *Conference on Advanced IR Detectors and Systems*, (IEE, London, 1983) p. 6.
- [43] I.M. Baker, J.E. Parsons, J.H.W. Lewis, R.A. Lockett and J.T.M. Wotherspoon, (1985) *Proc. SPIE*, **588**, 16.

- [44] J. Franc, E. Belas, A.L. Toth, H. Sitter, P. Hlidek, P. Moravec and P. Hoschl, (1999) *J. Cryst. Growth*, **197**, 593.
- [45] P. Moravec, R. Grill, J. Franc, K. Varghova and E. Belas, (2001) *Semicond. Sci. Technol.*, **16**, 7.
- [46] E. Belas, R. Grill, J. Franc, P. Moravec, K. Varghova, P. Hoschl, H. Sitter and A.L. Toth (2001) *J. Cryst. Growth*, **224**, 52.
- [47] E. Belas, R. Grill, J. Franc, A.L. Toth, P. Hoschl, H. Sitter and P. Moravec, (1996) *J. Cryst. Growth*, **159**, 1117.
- [48] E. Belas, J. Franc, A.L. Toth, P. Moravec, R. Grill, H. Sitter, and P. Hoschl, (1996) *Semicond. Sci. Technol.*, **11**, 1116.
- [49] Yue Wang, Quanbao Li, Qinghim Han, Bingwen Song, Jie Wanqu, Zhou Yaohe and Yuko Inatomi, (2004) *J. Cryst. Growth*, **263**, 273.

8 Bulk Growth of CdZnTe/CdTe Crystals

R. HIRANO AND H. KURITA

*Nikko Materials Co., Ltd, Compound Semiconductor Materials Production
Dept. Isohara Plant, 187-4 Usuba Hanakawa-cho Kitaibaraki-shi, Ibaraki
319-1535 Japan*

8.1 Introduction	241
8.2 High-purity Cd and Te	242
8.2.1 Cadmium	242
8.2.2 Tellurium	243
8.3 Crystal growth	243
8.3.1 Polycrystal growth	243
8.3.2 VGF single-crystal growth	244
8.4 Wafer processing	260
8.4.1 Process flow	261
8.4.2 Characteristics	264
8.5 Summary	266
Acknowledgements	266
References	266

8.1 INTRODUCTION

CdZnTe crystals are widely used as substrates to grow epitaxial layers of HgCdTe infrared detector arrays. Infrared imaging has evolved from its high performance to become a useful technology in a variety of applications. These include night sights, fire fighting, search and rescue, industrial or building maintenance, medical imaging and astronomy, and these applications require high-quality CdZnTe substrates. Many studies have been made on the growth of CdTe bulk crystals having a low defect density with higher purity. For several years research activities have mainly been concentrated on growing large-diameter crystals to obtain larger single-crystal regions. The need for large focal plane array (FPAs) is driving the move towards larger-diameter crystal growth greater than 100 mm. We are now developing 5-inch CdZnTe crystals. On the other hand, in order to grow high-quality HgCdTe epilayers, high-quality substrates with smaller precipitates, lower impurity concentrations and uniform Zn concentrations are required. In addition, it is also important to obtain high-quality polished surfaces, especially for MBE growth.

The goal of this chapter is to present recent developments in CdZnTe crystals for subsequent HgCdTe epitaxial growth.

8.2 HIGH-PURITY Cd AND Te

8.2.1 Cadmium

Distillation efficiently eliminates impurities such as Zn, Mg and As, which have relatively high vapor pressures. Table 8.1 shows the purity of 6N-Cd that was produced by our group, analyzed by glow discharge mass spectrometry (GDMS) at the National Research Council of Canada (NRC). It is seen that most of the elements are present below the detection limits, except for Zn.

Table 8.1 GDMS results of Cd and Te analyzed at NRC (ppba)

	6N-Cd (CS2000OA5)	6N-Te (ZR3-99-Z02)		6N-Cd (CS2000OA5)	6N-Te (ZR3-99-Z02)
Li	<1	<1			
Be	<0.4	<1	Rb	<0.1	<0.7
B	<0.8	<3	Sr	<0.1	<0.3
C			Y	<0.1	<0.3
N			Zr	<0.1	<0.3
O			Nb	<0.2	<0.2
F	<6	<9	Mo	<0.4	<0.6
Na	<1	<3	Pd	<6	<2
Mg	<0.5	<2	Ag	<8	<1
Al	<0.3	<0.6	Cd	Matrix	<4
Si	<0.8	24	In	<30	<0.4
P	<0.5	<1	Sn	<4	<3
S	<0.6	<2	Sb	<0.5	<75
Cl	2	<1	Te	<2	Matrix
K	<2	<6	I	<0.8	<790
Ca	<4	<40	Cs	<0.2	<5
Sc	<0.3	<0.7	Ba	<2	<4
Ti	<0.1	<0.4	La	<2	<0.9
V	<0.06	<0.2	Ce	<2	<4
Cr	<0.3	<1	Hf	<0.1	<0.4
Mn	<25	<0.8	Ta		
Fe	<20	<0.5	W	<0.1	<0.5
Co	<0.1	<0.5	Pt	<0.1	<1
Ni	<0.6	<0.8	Au	<5	<10
Cu	<0.8	<2	Hg	<1	<2
Zn	26	<5	Tl	<0.2	<0.7
Ga	<0.4	<1	Pb	<0.2	<0.7
Ge	<0.7	<4	Bi	<0.2	<0.5
As	<10	<1	Th	<2	<0.08
Se	<5	60	U	<0.03	<0.09

8.2.2 Tellurium

In order to obtain 6N-Te, a combination of two purification processes is needed, such as distillation and zone refining. Zone refining is an effective purification technique for Te because a majority of the impurity segregation coefficients are much less than unity. Table 8.1 also shows the purity of 6N-Te that was also produced by our group, analyzed by GDMS at NRC. It can be seen that Se is a difficult impurity to remove compared to other impurities.

8.3 CRYSTAL GROWTH

A wide variety of techniques, such as Bridgman, THM and VGF, have been used for CdTe crystal growth [1]. Generally, the single-crystal growth charges are both compounded prior to introduction into the single-crystal growth furnace and compounded from the elemental Cd and Te in situ. In our group, using ex situ compounding, the elemental Cd and Te are reacted in a separate ampoule in a different furnace and the compounded CdTe is then loaded into the growth pBN crucible to prevent explosion during a reaction process in the VGF furnace.

8.3.1 Polycrystal growth

High-purity 6N Cd and 6N Te metals were heated to temperatures higher than the melting point in a high-pressure furnace to synthesize polycrystal CdTe source materials. The 2.5–5 kg polycrystals were grown using quartz or pBN boats (quartz-polycrystal or pBN-polycrystal), respectively. Figure 8.1 shows the carrier concentrations of polycrystals. Most of the polycrystals grown using quartz boats show n-type conductivity at about $(1-10) \times 10^{15} \text{ cm}^{-3}$. On the other hand, the carrier concentrations of polycrystals grown using pBN boats show both n- and p-type conductivity.

Impurity concentrations in polycrystals were analyzed using the glow discharge mass spectrometry (GDMS) method at the National Research Council of Canada (NRC). Samples were cut from the first-to-freeze, middle-to-freeze and last-to-freeze ends. Table 8.2 shows the GDMS results of quartz-polycrystals and pBN-polycrystals. For some elements, such as Li and Na, there are marked differences between the concentrations in the quartz-polycrystals and the pBN-polycrystals. The concentrations of both Na and Li in the pBN-polycrystals are much lower than those in the quartz-polycrystals. For Cu and Si, the concentrations in the pBN-polycrystals are also low. On the other hand, B concentrations in the pBN-polycrystals are much higher than those in the quartz-polycrystals. For Li, Na and Cu, the effective segregation is clearly seen toward the last-to-freeze end of crystals in the quartz-polycrystals, as shown by Tower *et al.* [2]. In CdZnTe crystals, it is well known that the common acceptor impurities are from Group I (Li, Na, Cu) [2]. The sum of these three impurity concentrations ($[\text{Li}] + [\text{Na}] + [\text{Cu}]$) in the quartz-polycrystals is about $(5-20) \times 10^{16} \text{ cm}^{-3}$ as shown in Table 8.2. The present results have shown that the electrical carrier concentrations of quartz polycrystals shown in Fig. 8.1(a) are strongly dependent on the p-type impurity concentrations, such as Li and Na. Hence high-purity CdTe polycrystals are grown using pBN boats, instead of quartz boats.

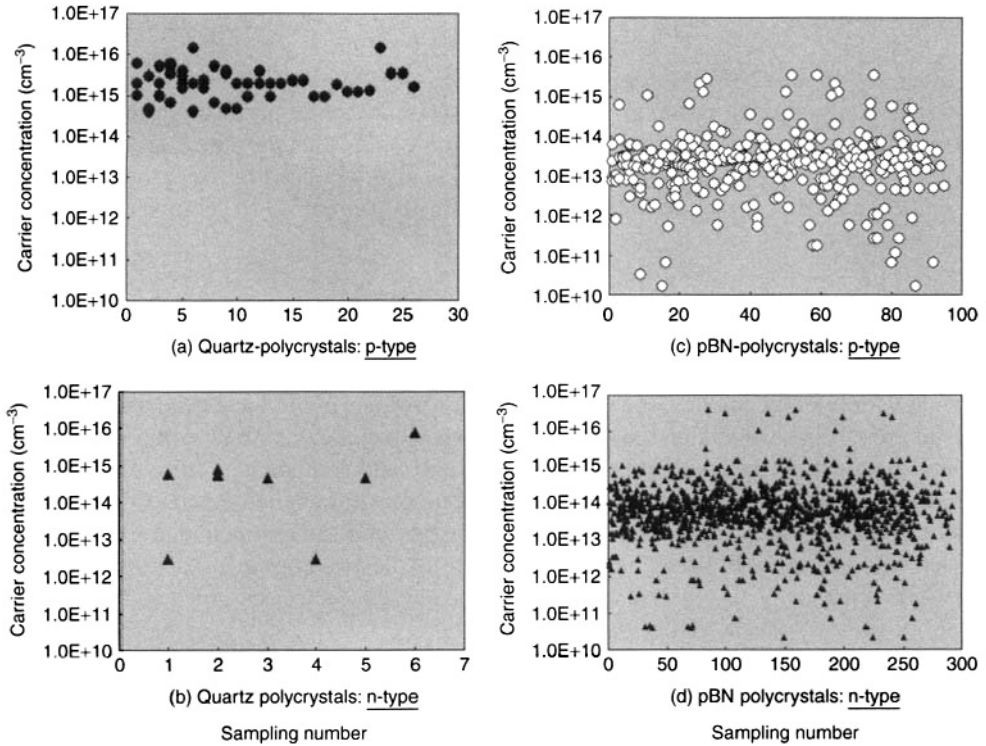


Figure 8.1 Carrier concentration of CdTe polycrystals, (a) Quartz polycrystals: p-type conductivity (b) Quartz polycrystals: n-type conductivity, (c) pBN polycrystals: p-type conductivity and (d) pBN polycrystals: n-type conductivity

8.3.2 VGF single-crystal growth

The polycrystals of (1.5–4.0) kg and 6N ZnTe of 40–90 g were charged in pBN crucibles and these were then sealed in a quartz ampoule that had a Cd reservoir in its lower part for controlling the Cd pressure, and thereby minimizing stoichiometric defects (precipitates). Figure 8.2 shows a typical example of a 5-inch CdZnTe (Zn = 3 %) crystal after grinding. The crystal was grown in the $\langle 111 \rangle$ direction. There were neither grain boundaries nor twins from top to tail, except for the tail part with a length of 5 mm, which shows polycrystals with an average grain size of 10–20 μm^2 .

8.3.2.1 Purity

Carrier concentrations of CdZnTe crystals were measured by the van der Pauw method. Most CdZnTe substrates showed p-type conductivity. Figure 8.3 shows typical examples of carrier concentrations for CdZnTe single crystals that were grown by the VGF method, as a function of the solidified fraction g . It is clearly seen that the carrier concentration of CdZnTe crystals grown by the VGF method can be decreased drastically using the polycrystals grown in pBN boats. It seems that p-type impurities from the quartz are the

Table 8.2(a) GDMS results of CdTe polycrystals grown in quartz boat (ppba)

	Quartz boat				Quartz boat		
	Top	Center	Tail		Top	Center	Tail
Li	< 1	220	480				
Be	< 0.7	< 0.6	< 0.7	Rb	< 0.2	< 0.1	< 0.2
B	< 2	< 1	< 1	Sr	< 0.2	< 0.2	< 0.1
C				Y	< 0.08	< 0.09	< 0.09
N				Zr	< 0.1	< 0.2	< 0.2
O				Nb	< 0.2	< 0.2	< 0.2
F	< 5	< 5	< 6	Mo	< 0.6	< 1	< 0.6
Na	< 2	44	67	Pd	< 15	< 10	< 15
Mg	< 0.9	34	< 2	Ag	< 15	< 8	< 10
Al	< 0.6	39	< 0.6	Cd	Matrix	Matrix	Matrix
Si	17	23	26	In	< 75	< 50	< 40
P	< 0.8	7	< 1	Sn	< 10	< 9	< 10
S	5	13	8	Sb	< 30	< 35	< 25
Cl	4	6	9	Te	Matrix	Matrix	Matrix
K	< 30	< 10	< 15	I	< 140	< 180	< 140
Ca	140	< 15	< 15	Cs	< 2	< 1	< 2
Sc	< 0.2	< 0.2	< 0.2	Ba	< 1	< 5	< 2
Ti	< 0.3	1200	< 0.4	La	< 0.05	< 5	< 0.05
V	< 0.1	< 0.08	< 0.2	Ce	< 0.05	< 18	< 0.2
Cr	4	< 2	< 0.9	Hf	< 0.2	< 0.2	< 0.1
Mn	< 10	< 10	< 10	Ta			
Fe	< 5	< 5	< 5	W	< 0.3	< 0.3	< 0.2
Co	< 0.3	< 0.2	< 0.3	Pt	< 1	< 1	< 1
Ni	< 0.7	< 1	< 1	Au	< 5	< 5	< 5
Cu	3	4	7	Hg	< 1	< 1	< 1
Zn	< 4	5	7	Tl	< 0.3	< 0.3	< 0.5
Ga	< 1	< 1	< 0.9	Pb	< 0.4	< 0.3	< 0.5
Ge	< 2	< 2	< 2	Bi	< 0.2	< 0.2	< 0.3
As	< 4	< 3	< 4	Th	< 0.4	< 0.3	< 0.3
Se	< 10	40	30	U	< 0.6	< 0.5	< 0.5

main source of contamination. Figure 8.4 shows the carrier concentrations of CdZnTe single crystals as a function of Na and Li concentrations measured by SIMS (secondary ion mass spectrometry). A clear relation between the carrier concentrations and the sum of Na and Li concentrations is found [3]. A similar result was also obtained by GDMS analysis. These results imply that the quartz material used in the growth process is a possible source for the contamination of Na and Li. No marked difference of B and Si concentrations between the VGF crystals grown using pBN-boat polycrystals and those grown using quartz-boat polycrystals was found. Triboulet *et al.* [4] also showed that silica is the source of contamination and mainly from acceptors that have been identified from PL (photoluminescence) experiments to be Cu. However, in the present work, no dependence of the carrier concentration on the Cu concentration analyzed by GDMS was found. Becker *et al.* [5] have shown that the carrier concentration of p-type ingots increases in the

Table 8.2(b) GDMS results of CdTe polycrystals grown in pBN boat (ppba)

	pBN boat				pBN boat		
	Top	Center	Tail		Top	Center	Tail
Li	<0.4	<0.8	<1	Rb	<0.1	<0.2	<0.2
Be	<0.5	<0.9	<1	Sr	<0.06	<0.2	<0.2
B	130	58	140	Y	<0.05	<0.1	<0.1
C				Zr	<0.1	<0.2	<0.2
N				Nb	<0.06	<0.2	<0.1
O				Mo	<0.4	<0.6	<0.7
F	<4	<6	<6	Pd	<16	<23	<19
Na	<1	<2	<2	Ag	<18	<17	<15
Mg	<1	<2	<2	Cd	Matrix	Matrix	Matrix
Al	<0.6	<1	<0.6	In	<50	<60	<35
Si	5	5	3	Sn	<10	<18	<15
P	2	<1	5	Sb	<30	<25	<20
S	11	7	20	Te	Matrix	Matrix	Matrix
Cl	50	5	7	I	<150	<200	<240
K	<15	<20	<10	Cs	<2	<3	<3
Ca	<7	<7	<15	Ba	<2	<4	<4
Sc	<0.2	<0.4	<0.4	La	<0.05	<0.1	<0.1
Ti	<0.2	8	<0.5	Ce	<0.07	<0.1	<0.4
V	<0.07	<0.2	<0.2	Hf	<0.1	<0.3	<0.3
Cr	<0.3	<0.7	<0.8	Ta			
Mn	<10	<10	<10	W	<0.1	<0.4	<0.3
Fe	<5	<5	<5	Pt	<1	<2	<2
Co	<0.2	<0.4	<0.4	Au	<5	<5	<5
Ni	<0.6	<2	<2	Hg	<0.8	<2	<2
Cu	1	<2	<2	Tl	<0.3	<0.7	<0.6
Zn	6	12	15	Pb	<0.3	<0.6	<0.6
Ga	<0.9	<2	<2	Bi	<0.2	<0.5	<0.4
Ge	<1	<3	<3	Th	<0.5	<0.7	<0.6
As	<3	<4	<2	U	<0.7	<0.9	<0.8
Se	20	20	40				

growth direction. They concluded [5] that part of the vacancies would become occupied by impurity atoms, thereby mainly producing acceptor-type centers. These centers (possibly together with unoccupied vacancies that also have acceptor character) are the source of the p-type conductivity [6]. Despite some differences in the technical details, the predominant acceptor defect has been assumed to be the cadmium vacancy V_{Cd} and this is responsible for the p-type conductivity [7]. However, the present results have shown that the p-type carrier concentration is strongly dependent on the Li and Na impurity concentrations in CdZnTe crystals. In 1998, Fiederle *et al.* [8] showed the possible defect structure by the following steps:

- CdTe is usually grown under Te-rich conditions and crystals are generally p-type with a resistivity of the order of 1×10^3 to $1 \times 10^5 \Omega \text{ cm}$.



Figure 8.2 A 5-inch CdZnTe crystal

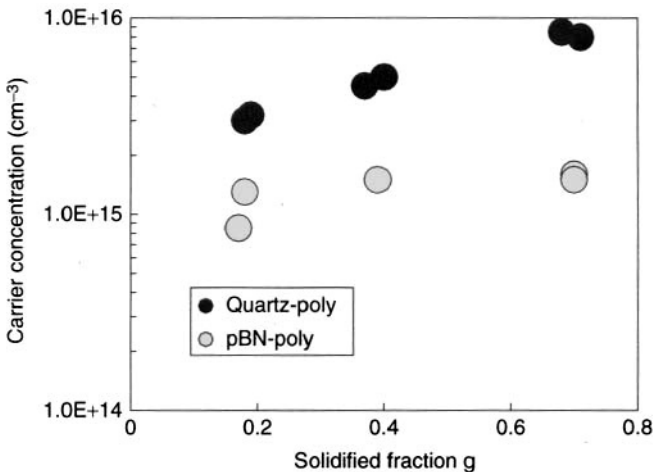


Figure 8.3 Carrier concentration of CdZnTe crystals grown by the VGF method. Dependence of the carrier concentration on the polycrystals is also shown. (Reprinted from A. Koyama *et al.* *J. Electron. Mater.* **28** (1999) 683, copyright (1999) with permission from The Minerals, Metals & Materials Society)

- It was assumed that these growth conditions would lead to a high concentration of cadmium vacancies of the order of $1 \times 10^{16} \text{ cm}^{-3}$, which are responsible for the low resistivity and the p-type conductivity.
- However, positron annihilation measurements of such material show that the vacancy concentration is only in the range of $1\text{--}3 \times 10^{15} \text{ cm}^{-3}$, whereas residual acceptor impurities can be found in concentrations above $1 \times 10^{16} \text{ cm}^{-3}$.

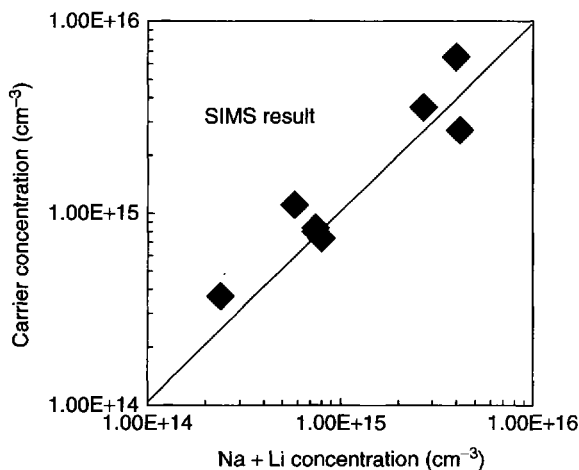


Figure 8.4 Carrier concentration of CdZnTe crystals as a function Li plus Na concentration. (Reprinted from A. Koyama *et al. J. Electron. Mater.* **28** (1999) 683, copyright (1999) with permission from The Minerals, Metals & Materials Society)

- With residual impurity concentrations of this order of magnitude, the resistivity should be well below $1 \times 10^3 \Omega \text{ cm}$.

Therefore, it has to be assumed that undoped CdTe is partially compensated by other deep level defects. They finally concluded that the Te-antisite defect is a good candidate for the deep level, which is responsible for the compensation in CdTe. As shown in Fig. 8.4, we found that the p-type carrier concentration is strongly dependent on the Li and Na impurity concentrations. It seems that the electrical carrier concentration of p-type CdZnTe crystals can be determined by the concentrations of Cd vacancies, p-type impurities and n-type impurities (halogen or group III metals). As Fiederle *et al.* [8] pointed out, we also have found that a little higher resistivity CdZnTe crystals with about 1×10^3 to $1 \times 10^5 \Omega \text{ cm}$ can be grown by lightly doping with halogens (Cl) or group III metals (Ga, Al, In).

Figure 8.5 shows the carrier concentration of CdZnTe crystals as a function of difference of impurity concentrations between p-type and n-type impurities:

$$\Delta = [\text{Ga} + \text{In} + \text{Al} + \text{Cl}] - [\text{Na} + \text{Li}]$$

The results have shown that the carrier concentration of CdZnTe crystals is strongly dependent on the concentrations of p-type impurities (Na and Li) and n-type impurities (halogen or group III metals), as shown by Fiederle *et al.* [8].

We found that the carrier concentration was reduced further if the single-crystal growth was stopped at the half-way solidified fraction position ($g \approx 0.5$), because of the reduction of impurity concentrations. The result suggests that the impurities will diffuse and be redistributed during the crystal-growth process. It is generally considered that the segregation coefficients of Li, Na and Cu in CdZnTe crystal are less than 1.0 [2]. However, GDMS analyses conducted by Tower *et al.* [2] have shown that the axial distribution of these impurities is different among the crystal growers. In the present work, we also

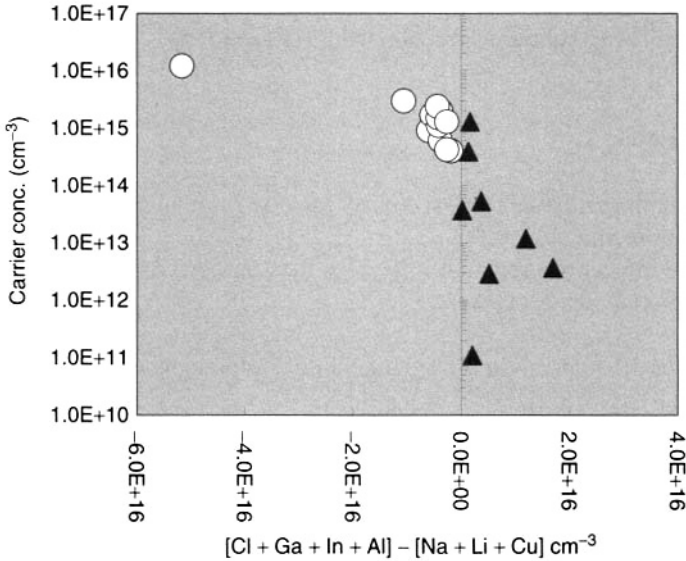


Figure 8.5 Carrier concentration of CdZnTe crystals as a function of the difference of p-type and n-type impurity concentrations

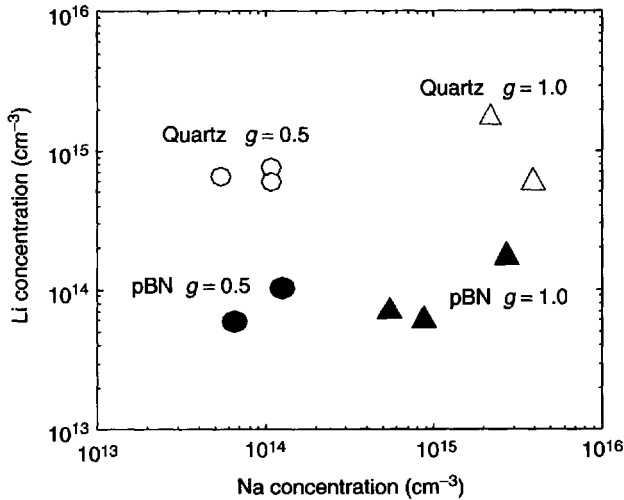


Figure 8.6 Correlation between Li and Na concentrations in CdZnTe Crystals. The 'g = 0.5' label means that the crystal growth was stopped at g = 0.5

found that the distribution of these impurities depends on the growth process. The results also imply that these impurities will be re-distributed during the crystal-growth process. Figure 8.6 shows the correlation between the Na and Li concentrations in CdZnTe crystals grown under the different conditions. As a result, we found that Li concentrations in CdZnTe crystals can be reduced by growing the crystals using pBN-polycrystals. On

the other hand, the Na concentrations can be markedly reduced by stopping the crystal growth at the half-way solidified fraction position ($g = 0.5$).

8.3.2.2 Precipitates

When nonstoichiometric CdZnTe is cooled rapidly from high temperature, the grown crystals contain precipitates.

What are the effects of precipitates in substrates on device performance?

Previously discussed effects were

- Increase of the IR transmission by reduction of Te precipitates [9].
- Improvement of the LWIR device R_0A performance by eliminating Te precipitates [6].
- Growing on substrates with a high concentration of Te precipitates resulted in low concentration of Cu in HgCdTe epilayers [10].
- Improvement of surface quality after polishing the substrates with low density of Te precipitates [3].

After polishing the substrates, surface defects can be seen with distinct crystallographic shapes as shown in Fig. 8.7. It has been speculated that the surface defects are the result of a crystalline-shaped Te precipitate that intersects the surface being removed during polishing. Figure 8.8 shows the correlation between the surface defect density and the Te-precipitate density. There can be seen to be a good correlation between the surface defect density and the precipitates. The present result shows that there is a need to improve the Te precipitates in order to prepare a high-quality surface for MBE growth.

In order to reduce the Te precipitates, Vydyanath *et al.* [6, 11] carried out wafer annealing of CdZnTe containing Te precipitates, over the temperature range of 500–900 °C, using Cd/Zn pressures appropriate to stoichiometry, and postulated that the reported removal of large Te precipitates could result from migration of the second-phase material under the action of temperature gradients if the Te melting point is exceeded during the wafer annealing. However, it is noted that this process may be at the expense of an increase in

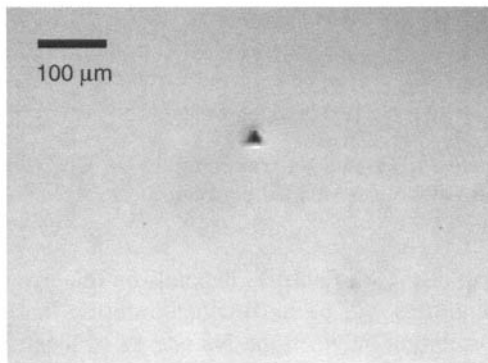


Figure 8.7 Surface void defect observed by Nomarski microscopy

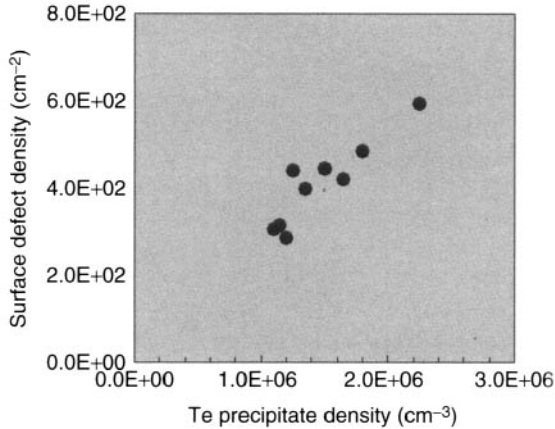


Figure 8.8 Surface defect density as a function of Te-precipitate density

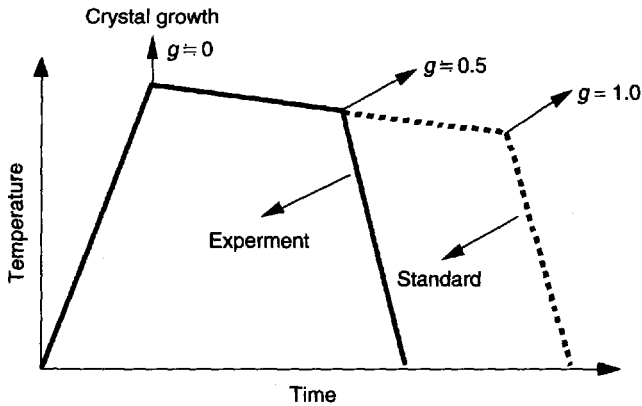


Figure 8.9 Schematic process of the postgrowth ingot annealing methods

dislocation density and rocking curve width. In addition, concerning the production cost, a postgrowth annealing method is desirable. In our group, the crystals were annealed in the VGF furnace at about 950°C for more than 10h under a Cd pressure in order to reduce the Te precipitates [3]. The precipitates were mainly evaluated by IR microscopy. Figure 8.9 shows the schematic process of the postgrowth ingot annealing.

Figure 8.10 shows the postgrowth ingot annealing temperature of Cd reservoir and that of CdZnTe crystals. The crystal growth and the cooling conditions are also shown in this figure. The crystals show p-type conductivity and the precipitate size was about $2\ \mu\text{m}$ (postgrowth ingot annealing-1) as shown in Fig. 8.11(b) by the postgrowth ingot annealing method. The size became smaller and precipitate-free (ppt-free) substrates, examined by IR transmission microscopy, can be obtained by paying attention to controlling the cooling rate after the ingot annealing, as shown in Fig. 8.11(c) (postgrowth ingot annealing-2). No increase in the rocking curve width and dislocation density was seen by this method. However, in the case of incomplete annealing, the crystal showed n-type conductivity with a large size ($10\ \mu\text{m}$) of Cd precipitates.

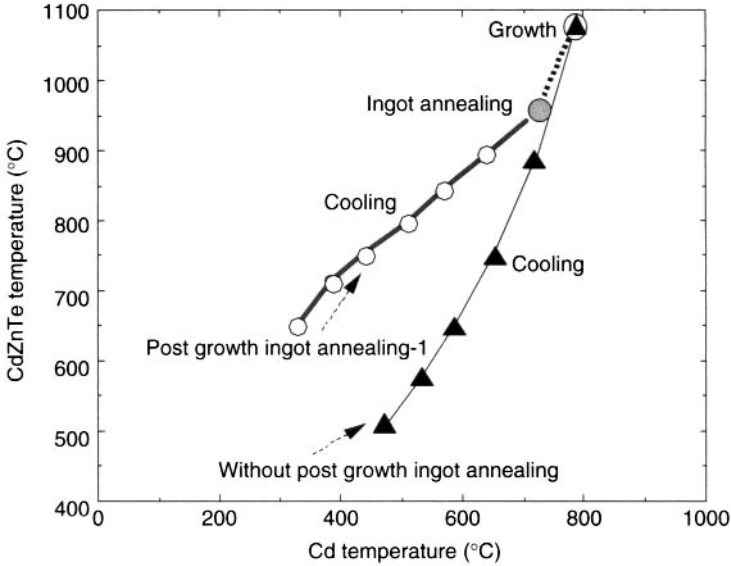


Figure 8.10 Postgrowth ingot annealing temperature of Cd reservoir and that of CdZnTe crystals. (Reprinted from A. Koyama *et al. J. Electron. Mater.* **28** (1999) 683, copyright (1999) with permission from The Minerals, Metals & Materials Society)

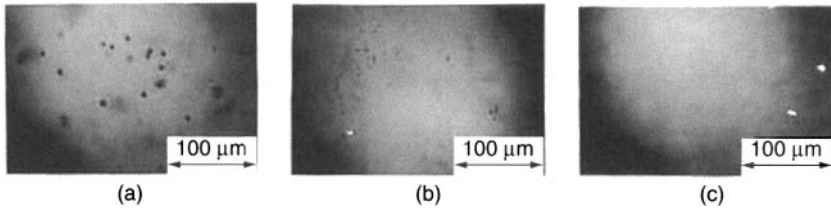


Figure 8.11 IR transmission micrographs of (a) without postgrowth annealing, (b) postgrowth annealing-1 and (c) postgrowth annealing-2. (Reprinted from A. Koyama *et al. J. Electron. Mater.* **28** (1999) 683, copyright (1999) with permission from The Minerals, Metals & Materials Society)

Figure 8.12 shows the correlation between the electrical conductivity and the ingot-annealing condition. The size of Te precipitates is also shown in this figure. These data show that the conductivity and the precipitate size were changed by postgrowth ingot annealing.

Vydyanath *et al.* [6, 11] have shown that the existence of a temperature gradient in the CdTe wafers is necessary for the process of Te precipitate thermomigration to occur during the annealing. However, the present postgrowth ingot annealing was performed at the same temperature from top to tail of the ingots. The present results suggest that the postgrowth ingot annealing effect on the precipitates cannot be explained solely by thermomigration of liquid Te. Zanio [12] showed the chemical diffusion coefficients of CdTe is expressed by

$$D(\text{CdTe}) = 4 \exp(-1.15/kT) \text{ cm}^2/\text{s}^{-1} \quad (8.1)$$

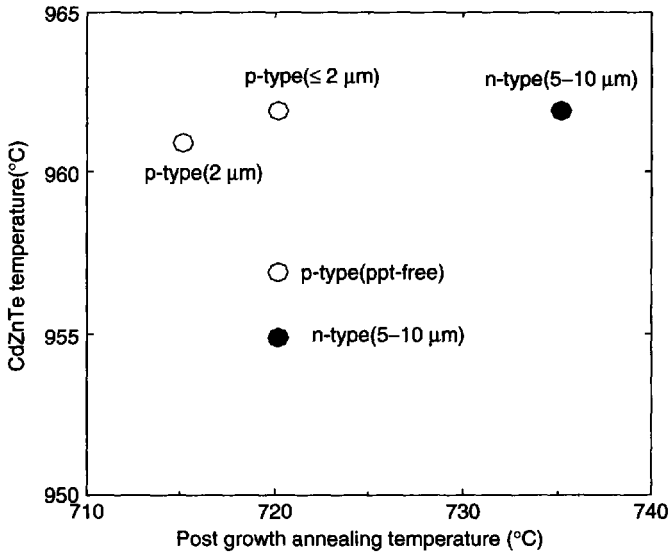


Figure 8.12 Postgrowth ingot-annealing temperature of Cd reservoir and that of CdZnTe crystals showing the electrical conductivity and the precipitate size. (Reprinted from A. Koyama *et al. J. Electron. Mater.* 28 (1999) 683, copyright (1999) with permission from The Minerals, Metals & Materials Society)

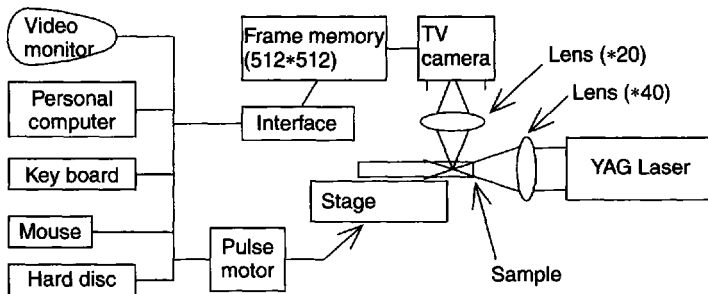


Figure 8.13 Optical-evaluation methods

where D is the chemical diffusion coefficient, k is Boltzmann's constant and T is the crystal temperature. The diffusion distance at 950 °C for 20 h annealing is about 20 mm and this corresponds to the bulk size. It seems that the change of stoichiometry during the postgrowth ingot annealing is one of the most probable reasons for the reduction of the precipitate size. We have also investigated the precipitates by other methods, such as laser-scattering tomography (LST) and surface light scattering observation (S-LS). These evaluation methods are shown in Fig. 8.13. The LST investigation was carried out at room temperature using mirror-polished substrates. A 300-mW YAG laser beam was focused on a cleaved face of the substrates. The S-LS observation was performed under a narrow, strong beam light source with a 1–2-cm focused light intensity of more than 20 000 lux. Figure 8.14 shows the precipitates in the different grades of substrates, such as conventional, ppt-improved-1st and ppt-free grades, observed by IR microscopy

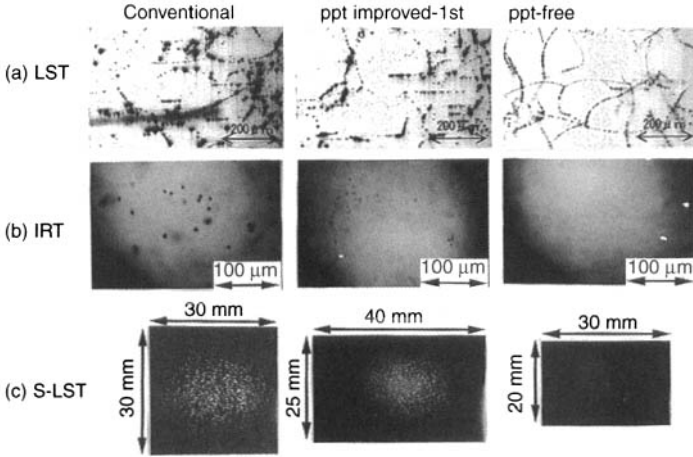


Figure 8.14 Precipitates observations by (a) LST, (b) IRT and (c) S-LST methods

(IRT), LST and the unaided visual observation methods. The ppt-free grade means that the precipitates are not seen by the IR transmission (IRT) method. We found that if the precipitates were not seen by the IRT method, smaller precipitates can be observed by the LST method. The LST observation results also imply that the precipitates are arranged along the cell network. On the other hand, the S-LS method shows that the number of particles on a precipitate-free (ppt-free) substrate decreased markedly compared with that of a conventional substrate. In fact, we could not observe the surface void defects on the ppt-free substrates as shown in Fig. 8.7 by Nomarski microscopy.

8.3.2.3 IR transmittance

It has been thought that there is definitely a correlation between the presence of precipitates and optical transmittance. However, free-carrier absorption must also be considered. Yang *et al.* [13] suggested that the extinction of infrared light is dominated at higher energy (shorter wavelength) by scattering of precipitates, and at lower energy (longer wavelength) by the absorption of free carriers. We also believe that it is important to distinguish between the IR transmittance in the shorter wavelength and that in the longer wavelength. Figure 8.15 shows the IR transmittance of as-grown p-type CdZnTe crystals including 2–5 μm Te precipitates [3]. It is obvious that the IR transmittance increases with decreasing carrier concentration. Figure 8.16 shows the correlation between the IR transmittance at 16 μm and the carrier concentration [3]. The IR transmittance of n-type ingots was higher than that of p-type ingots, since the carrier concentration of n-type ingots was lower than that of p-type ingots. The effect of wafer annealing on the precipitates in CdZnTe crystals has been widely studied. Vydyanath *et al.* [6] showed that the IR transmittance is increased by eliminating the Te precipitates after annealing at 800–900 $^{\circ}\text{C}$ under Cd and Zn overpressure. It has been shown that the annealing can modify the electrical properties, increase the IR transmittance and reduce the precipitate density. Li *et al.* [9] have shown that the IR transmittance of nonstoichiometric CdZnTe wafers that were annealed at 700 $^{\circ}\text{C}$ for 5 h increases dramatically. They concluded that

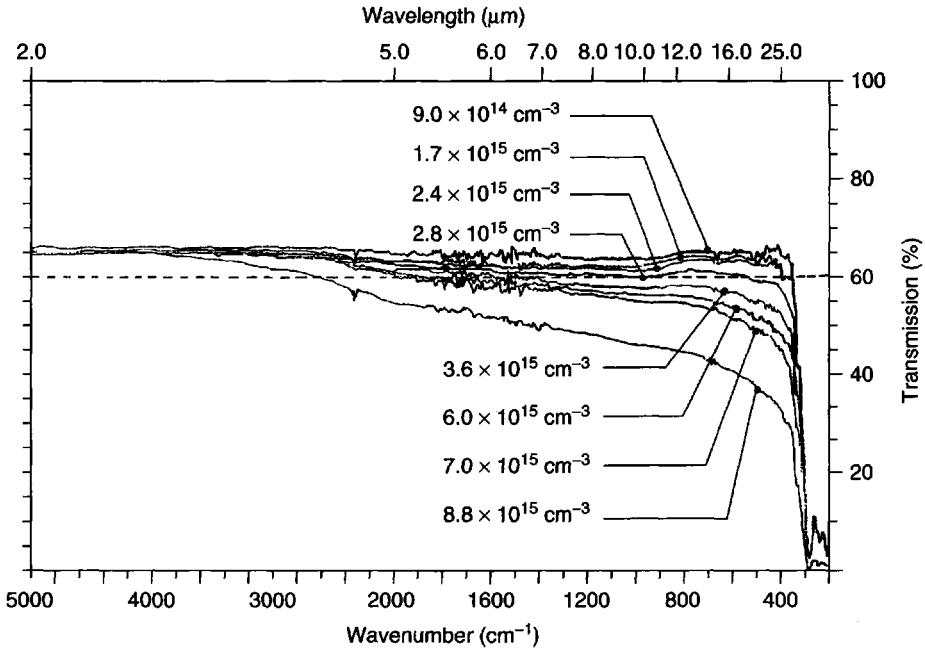


Figure 8.15 IR transmittance of CdZnTe crystals. Dependence on the carrier concentration is also shown in this figure. (Reprinted from A. Koyama *et al. J. Electron. Mater.* **28** (1999) 683, copyright (1999) with permission from The Minerals, Metals & Materials Society)

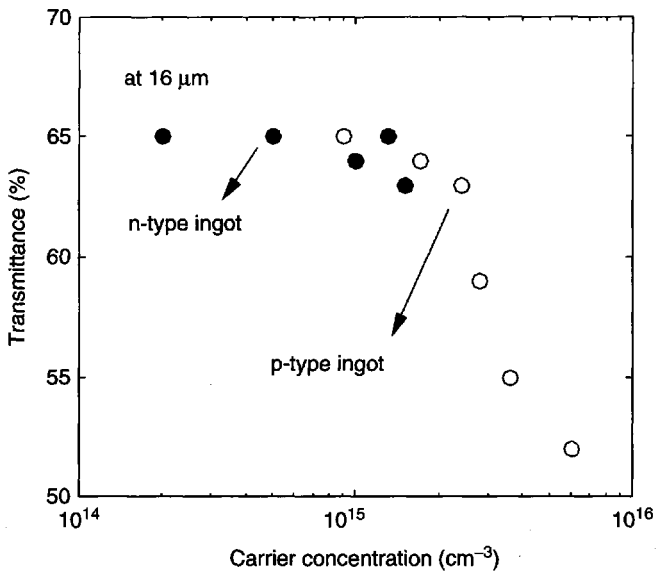


Figure 8.16 Correlation between the IR transmittance at 16 μm and the carrier concentration. (Reprinted from A. Koyama *et al. J. Electron. Mater.* **28** (1999) 683, copyright (1999) with permission from The Minerals, Metals & Materials Society)

the density of Te precipitates and Cd vacancies is low after the annealing; therefore the IR transmittance was increased. Triboulet *et al.* [4] have shown that the annealing step makes the impurities electrically active and allows the conductivity type of the samples to be generally converted from p- to n-type, when achieved under Cd-rich conditions at 700 °C for 5 h. Lee *et al.* [14] found that the increase in the hole concentration and the type conversion from semi-insulating CdTe to p-type CdTe after annealing are caused by the increase in the carrier concentration of the Cd vacancies and its complexes. We have also studied the change of IR transmittance of n-type, p-type and highly resistive substrates after annealing at 500 °C under N₂ atmosphere. All substrates show the reduction in the IR transmittance after annealing, as shown in Table 8.3. Only the No. 1 sample, with high resistivity in the as-grown state, shows the proper IR transmittance above 60 % after the annealing, since the carrier concentration was low enough even after the annealing. In the case of the No. 2 sample, despite the elimination of Cd precipitates after the annealing, the IR transmittance at the longer wavelength (16 μm) was decreased. No marked change in the IR transmittance at the shorter wavelength (2 μm) was observed. In conclusion, this study shows that to clarify the effect of wafer annealing on the IR transmittance one needs to investigate both carrier concentration and precipitate density.

8.3.2.4 EPD and X-ray FWHM

In order to measure the dislocation density (EPD) in CdZnTe crystals, the Nakagawa etchant [15] is the best method, though this etchant can only reveal the etch pits on the (111) A surface with rounded pits. Figure 8.17 shows the correlation between the X-ray FWHM and the average EPD of 3-inch diameter CdZnTe crystals that were grown using pBN or quartz crucibles. It is clearly seen that the low-EPD crystals can be grown using pBN crucibles and there is a strong correlation between the EPD and the X-ray FWHM.

8.3.2.5 Zn concentration and uniformity

The production of large-area and homogeneously lattice-matched HgCdTe (MCT) is a key requirement for the manufacture of infrared focal plane arrays (IRFPAs). In order to grow the homogeneously lattice-matched MCT it is important to grow the bulk CdZnTe crystals

Table 8.3 Annealing effects on the carrier concentration and the IR transmittance. Annealing conditions: 500 °C, 2 h, N₂

Sample No.	Before annealing					After annealing				
	Carrier conc. (cm ⁻³)	ρ (Ω cm)	μ (cm ² V ⁻¹ s ⁻¹)	p or n	IRT (%) (at 16 μm)	Carrier conc. (cm ⁻³)	ρ (Ω cm)	μ (cm ² V ⁻¹ s ⁻¹)	p or n	IRT (%) (at 16 μm)
No. 1	2.0E+08			p	65	5.0E+10	2.0E+06	63	p	64
No. 2	3.1E+12	2.8E+04	74	p	63.5	2.6E+15	2.8E+01	85	p	59
No. 3	2.0E+14	3.5E+01	919	n	64	5.0E+14	1.3E+01	944	n	56
No. 4	3.8E+14	1.9E+02	85	p	66	7.3E+14	1.1E+02	82	p	52
No. 5	3.4E+14	2.3E+02	79	p	63	3.5E+15	1.9E+01	96	p	52

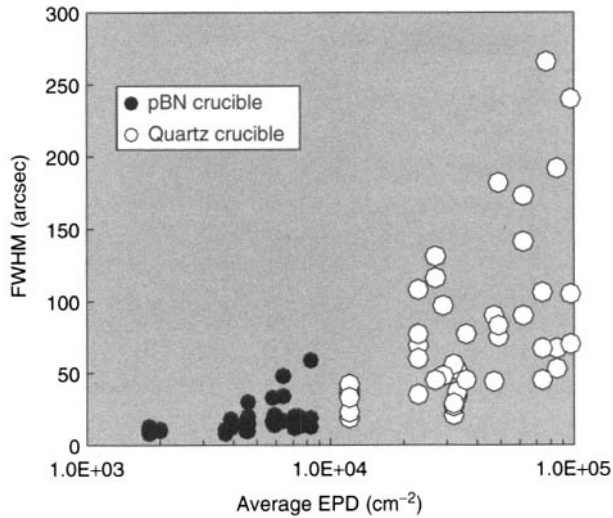


Figure 8.17 Correlation between the X-ray FWHM and the average EPD of 3-inch CdZnTe crystals

with uniform Zn concentrations. To evaluate the Zn concentration of CdZnTe substrates, NIR transmission spectroscopy employed extrapolation techniques to determine a cutoff wavelength [16, 17]. However, it was very difficult to do automatic measurements, since such techniques rely on individual interpretation of the linear portion. Maxey *et al.* [18] have reported a study of the NIR band edge cuton, defined by the wavelength corresponding to an absorption coefficient (α) = 10 cm^{-1} , which automatically corrects for thickness or transmission variations. In our group, a new Zn concentration mapping system using a Carl Zeiss Si diode array spectrometer, which can make the mapping of Zn concentration within a very short time, was developed using the Maxey *et al.* method [19]. Four-inch diameter CdZnTe crystals, with uniform Zn concentration were grown under the more uniform temperature distribution in the furnace [19].

A NIR instrument for Zn concentration mapping was developed using a diode-array-type spectrometer produced by Carl Zeiss (MMS 1 NIR enh spectrometer). The diode arrays can simultaneously record a complete spectrum within a fraction of a second. The system is shown in Fig. 8.18. NIR spectra were analyzed by the Maxey *et al.* [18] method. The surface-condition dependence on the NIR shape was also investigated. Figure 8.19 shows the typical spectra of samples, which have mirror-polished and Br₂-methanol etched surfaces. Since the surface on the etched sample is rougher than that of the polished sample, scattering losses from surfaces can dramatically alter the maximum NIR transmittance. Figure 8.20 shows the correlation between the wavelength $\lambda(\alpha = 10 \text{ cm}^{-1})$, measured at 24 °C, and the Zn concentration analyzed by the ICP (inductively coupled plasma) method. As a result, the Zn concentration of polished substrates is expressed as

$$\text{Zn (\%)} = 285.43 - 0.3343\lambda(\alpha) \quad (8.2)$$

and the Zn concentrations of Br₂-methanol etched (after cutting) substrates is expressed as

$$\text{Zn (\%)} = 288.93 - 0.3386\lambda(\alpha) \quad (8.3)$$

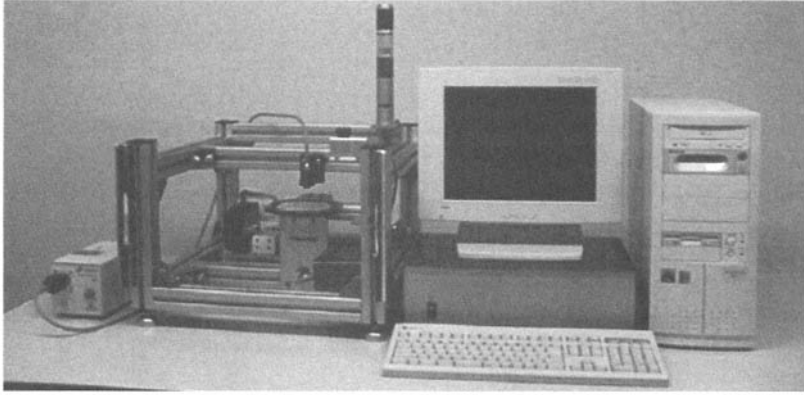


Figure 8.18 Photograph of the NIR mapping system

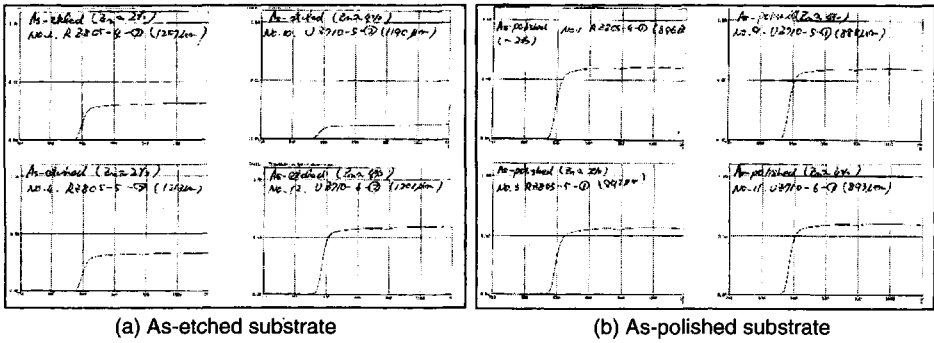


Figure 8.19 NIR transmission spectra (a) as-etched and (b) as-polished substrates. (Reprinted from R. Hirano *et al. J. Electron. Mater.* 29 (2000) 654, copyright (2000) with permission from The Minerals, Metals & Materials Society)

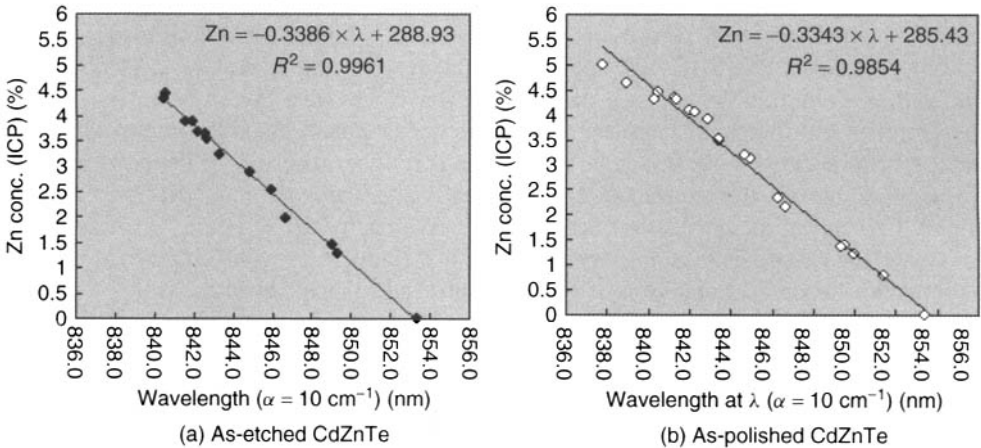
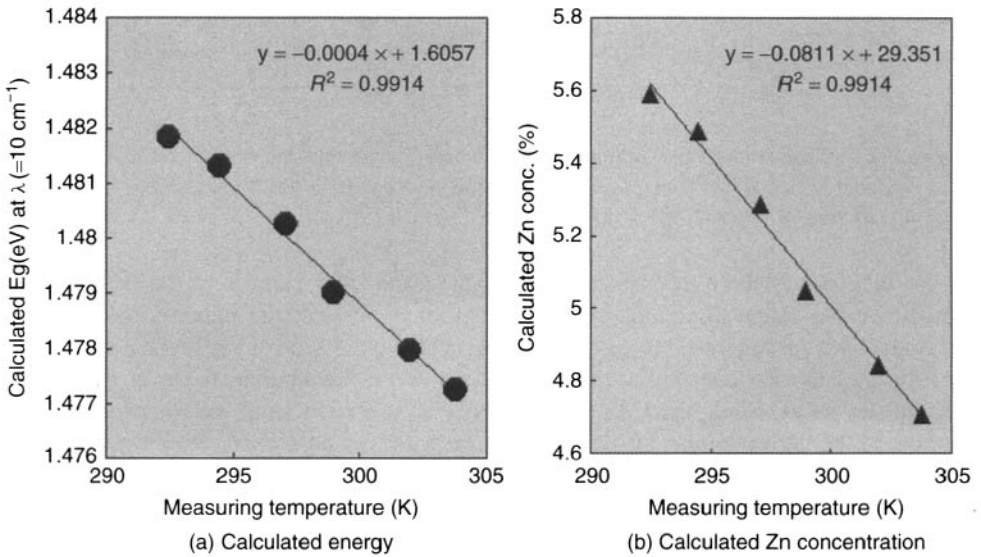


Figure 8.20 Correlation between Zn concentration analyzed by ICP and wavelength

Table 8.4 Temperature dependence of the NIR measurement

Temp (K)	Wavelength λ at $\alpha = 10 \text{ cm}^{-1}$	Calculated E_g (eV)	Calculated Zn conc. (%)
292.5	836.8	1.482	5.59
294.5	837.1	1.481	5.49
297.1	837.7	1.480	5.28
299	838.4	1.479	5.05
302	839	1.478	4.84
303.8	839.4	1.477	4.71

**Figure 8.21** Temperature dependence of NIR measurement (a) calculated energy and (b) calculated Zn concentration

The results have shown that the correlation between the Zn concentration measured by chemical analysis and the $\lambda(\alpha = 10 \text{ cm}^{-1})$ is strongly dependent on the surface conditions.

These expressions are different from Maxey *et al.*'s results [19]. This shows the importance of establishing local calibrations when new systems are used to measure the Zn concentration. Another important point is the temperature, since the optical $\lambda(\alpha = 10 \text{ cm}^{-1})$ will change with changing measuring temperature. Table 8.4 shows the wavelength $\lambda(\alpha = 10 \text{ cm}^{-1})$ as a function of measuring temperature. The calculated energy E_g at $\lambda(\alpha = 10 \text{ cm}^{-1})$ and the calculated Zn concentration are also shown. As shown in Fig. 8.21, the temperature dependence of the calculated energy dE/dT of about $4.0 \times 10^{-4} \text{ eV K}^{-1}$ is in good agreement with the previously reported values of the temperature dependence of the CdTe bandgap [20]. The calculated Zn concentration is expressed as

$$\text{Zn (\%)} = -0.0811 \times T(\text{K}) + 29.351 \quad (8.4)$$

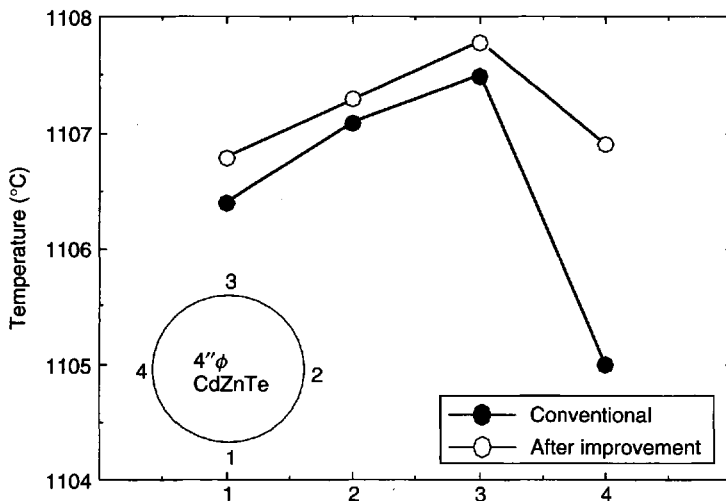


Figure 8.22 Temperature distribution of VGF furnace at the outside of the crucible. (Reprinted from R. Hirano *et al. J. Electron. Mater.* **29** (2000) 654, copyright (2000) with permission from The Minerals, Metals & Materials Society)

Figure 8.22 shows the temperature distribution of the VGF furnace at the outside of the crucible in the radial direction. In the conventional furnace, the maximum temperature difference was more than 2°C . Large and deep voids were seen at the highest temperature position and the Zn concentrations near the voids are lower than those at the position without the voids. Since the CdZnTe melt will be solidified from the lower temperature position to the higher temperature position at the same axial position, the Zn concentration should be low at the lower-temperature position with the voids. In our observations, nonuniformity of the temperature distribution in the radial direction was mainly due to the heat loss at the connector ends of the heaters. By improving the growth furnace, especially the heater structure, the maximum temperature difference was reduced to less than 1°C as shown in Fig. 8.22. The size of voids observed on the outside of the crystals became small and the distribution has become uniform.

Figure 8.23 shows the Zn concentration mappings of 4-inch (111) substrates, which were cut from the improved and the conventional crystals, investigated by the NIR instrument. The solidified fraction g is also shown in this figure. It can be confirmed that the Zn concentrations near the voids are lower than those of the positions where voids are not observed. Reduction of the temperature difference in the growth furnace can produce large substrates with uniform Zn concentration.

8.4 WAFER PROCESSING

Recent advancement in MBE growth technology demands CdZnTe substrates with high surface quality, especially surface roughness and orientation accuracy. In addition, larger substrates over 50 mm square are being used in the production stages, as FPAs get larger. Under such trends, flatness and thickness variations on the substrates have become more important factors than before in successful device processing.

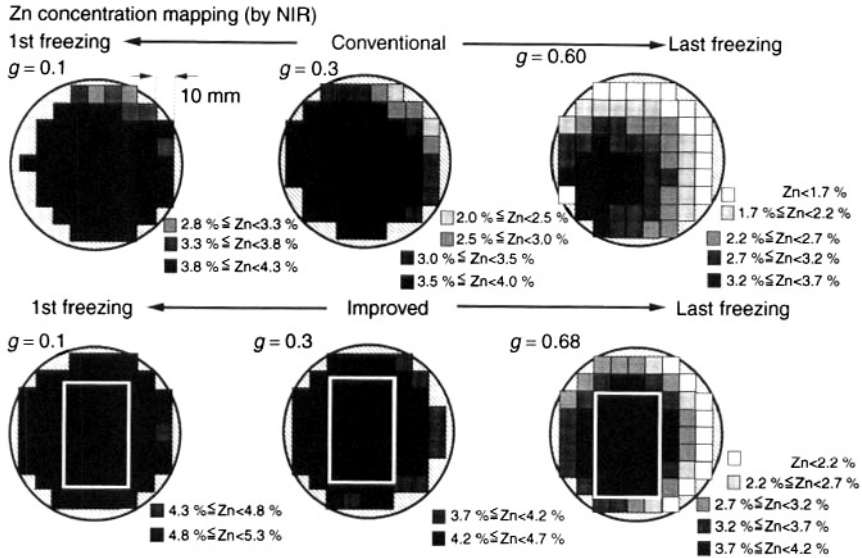


Figure 8.23 Zn concentration maps of 4-inch CdZnTe. (Reprinted from R. Hirano *et al. J. Electron. Mater.* **29** (2000) 654, copyright (2000) with permission from The Minerals, Metals & Materials Society)

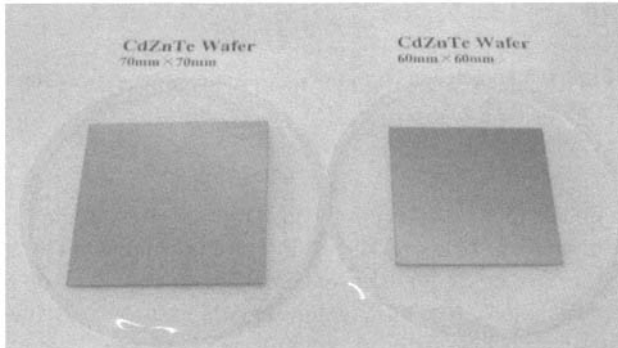


Figure 8.24 Polished CdZnTe substrates of 70 mm and 60 mm square

To satisfy such strict demands, the quality of CdZnTe substrates has been improved in terms of wafer possessing such as slicing and polishing. Now high-quality substrates up to $70 \times 70 \text{ mm}^2$ are available from 5-inch crystals (Fig. 8.24.)

The processing technology for CdZnTe substrates is almost the same as that of Si and other compound semiconductor substrates. In this section, various characteristics of the wafer processing based on state-of-the-art technology are presented.

8.4.1 Process flow

Figure 8.25 shows the schematic flow of CdZnTe substrates production. The following is the detailed information on each process.

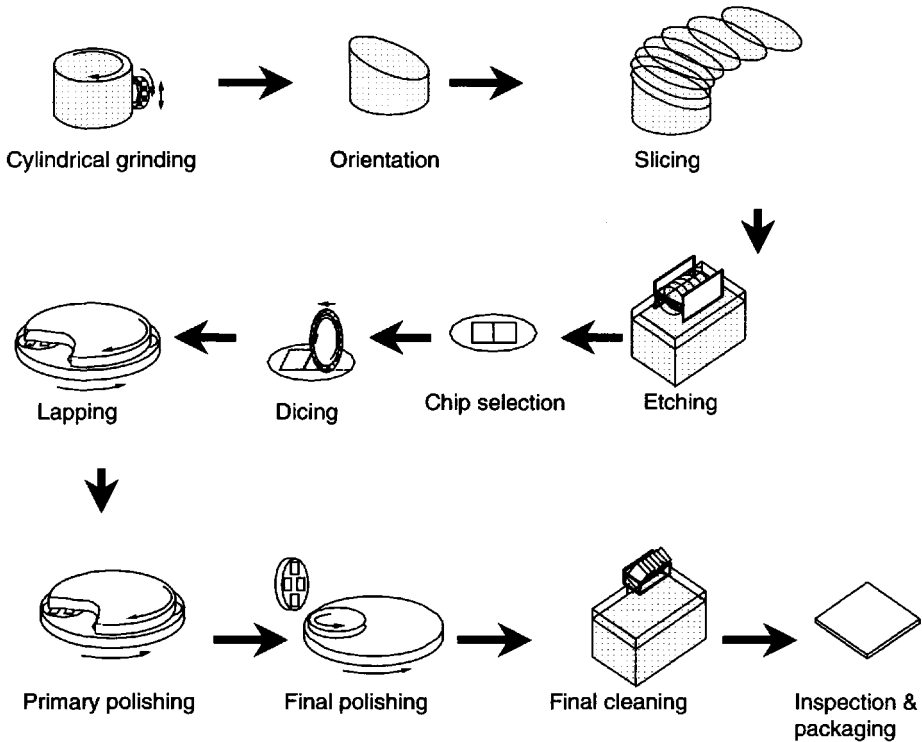


Figure 8.25 Schematic flow of CdZnTe wafer processing

8.4.1.1 Slicing

After grinding, the end of the crystal is cut by an ID saw, corresponding to specific crystallographic orientation such as (111) or (211). It is well known that (111) and (211) oriented CdZnTe substrates are preferred for LPE and MBE, respectively, for HgCdTe epitaxial growth. As mentioned above, the VGF single crystal is grown in the $\langle 111 \rangle$ direction. Therefore the crystal is cut diagonally to obtain the (211) face.

After the end cutting, the crystal is sliced into wafers parallel to the end face. Multiwire saws are employed in the slicing process for CdZnTe crystals as well as Si crystals, because of reduced slicing damage and kerf loss. Now crystals up to 5-inch diameter can be sliced.

8.4.1.2 Etching

The sliced wafers are etched by bromine-methanol to remove slicing damage. Then they are etched by another solution that reveals defects such as dislocations and microtwins. The etchant proposed by Nakagawa is popular and reliable for the (111) face [15]. Other etch solutions proposed by Inoue *et al.* [21] and Everson *et al.* [22] are also used. However, the consistency of dislocation-density measurements between the methods is still controversial.

8.4.1.3 Dicing

After etching, squares or rectangles corresponding to the specified size are marked out on the single-crystalline area. Then they are cut along the lines by dicing machines. The dicing machine is generally used for Si-based device processing. However, CdZnTe wafers are so fragile that they are easily chipped when standard blades for Si wafers are used. Furthermore, latent damage by dicing sometimes causes breakage of CdZnTe wafers in the following processes.

Therefore it is very important to select blades with the proper bond type, bonding strength, grit size, concentration and thickness for CdZnTe wafers. In addition, machining conditions such as blade rotation and table speed should be optimized.

8.4.1.4 Lapping

The purpose of lapping is to reduce the thickness variations from wafer to wafer and to improve flatness on each wafer. The both-sides lapping method is suitable for this purpose rather than the single-side lapping method. The both-sides lapping method is widely used not only for semiconductor wafers such as Si and GaAs but also other substrates such as glass, quartz and oxide single crystals.

Glass platens and alumina-based powders are employed.

8.4.1.5 Polishing

After lapping, CdZnTe substrates are finished by two or three steps of polishing processes. In the primary polishing process, colloidal silica and hard polishing pads for stock removal are employed to make mirror-like surfaces without degrading flatness.

In final polishing, soft pads with a pore structure are employed. Generally, colloidal silica is also used in final polishing for Si substrates. On the contrary, no colloidal or powdered silica is applied to final polishing for compound semiconductors, since those substrates are easily scratched or damaged by colloidal silica. Bromine-methanol is well known as a solution for chemical polishing of compound semiconductors including various III-V and II-VI materials. However, in our experience the polishing process by bromine-methanol is sometimes less reproducible and gives haze or an orange-peel-like surface on CdZnTe wafers. Furthermore, bromine-methanol corrodes polishing machines and eventually shortens the life of machines. We have developed our unique chemical solution for final polishing instead of bromine-methanol. Surface properties given by our polishing processes are described later.

8.4.1.6 Inspection

Thickness and thickness variation in a wafer are measured after polishing. Then the finished surface is inspected with the unaided eye. By illuminating the surface with an intense light, defects are detected as light-scattering points. Next, the surface is observed under diffuse light illumination to detect larger defects.

8.4.2 Characteristics

Characteristics of CdZnTe wafers produced by optimizing the above-mentioned processes were evaluated. In this section, details of characteristics including misorientation, thickness variation and surface roughness are described.

8.4.2.1 Crystallographic misorientation

Crystallographic misorientation affects the morphology of epitaxial layers. Both the end-cutting and slicing processes play a key role in accurate orientation. In the end-cutting process, a sample wafer is first sliced. Then the misorientation of the sample is measured by an X-ray diffractometer. Finally, on the basis of the sample measurements, the cutting face is retilted on the slicing machine so that the error can be offset. Such a trial-and-error method cannot be applied to a multiwire saw. Therefore, it is very important to adjust the oriented end face of the crystal parallel to the cutting face, which will be generated by wire tracks. Stiffness of the machine itself is also indispensable for accurate slicing. Figure 8.26 shows the misorientation on (111) CdZnTe substrates prepared by optimized slicing processes. The misorientation is less than 0.1 deg.

8.4.2.2 Thickness variation and warp

As mentioned above, thickness variation in a wafer is an important factor in successful device processing. Thickness variation in a wafer is defined as the difference between the maximum and minimum values of the thickness measurements on the five points as shown in Fig. 8.27(b). Generally speaking, it is more difficult to reduce thickness variation on the larger substrates. Figure 8.27(a) shows thickness variation on CdZnTe wafers of

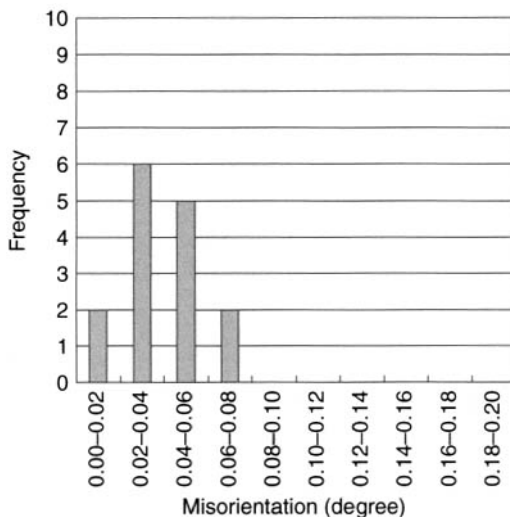


Figure 8.26 Crystallographic misorientation on (111) CdZnTe substrates

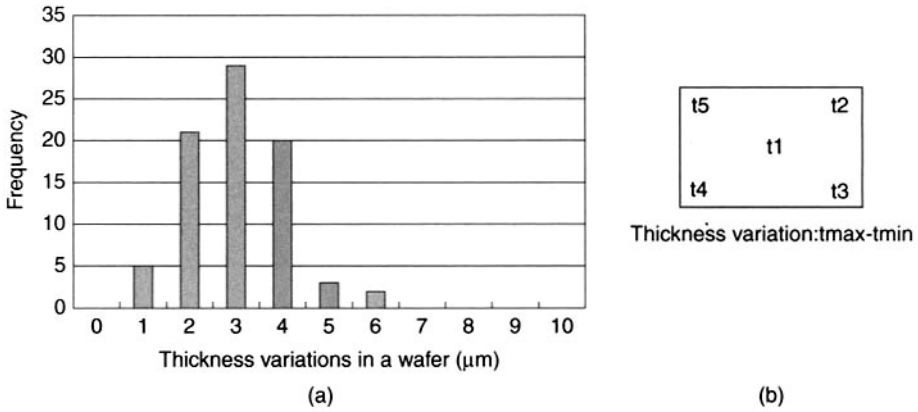


Figure 8.27 Thickness variation (TV) on CdZnTe substrates (a) TV histogram on $50 \times 50 \text{ mm}^2$ CdZnTe substrates and (b) the definition of TV

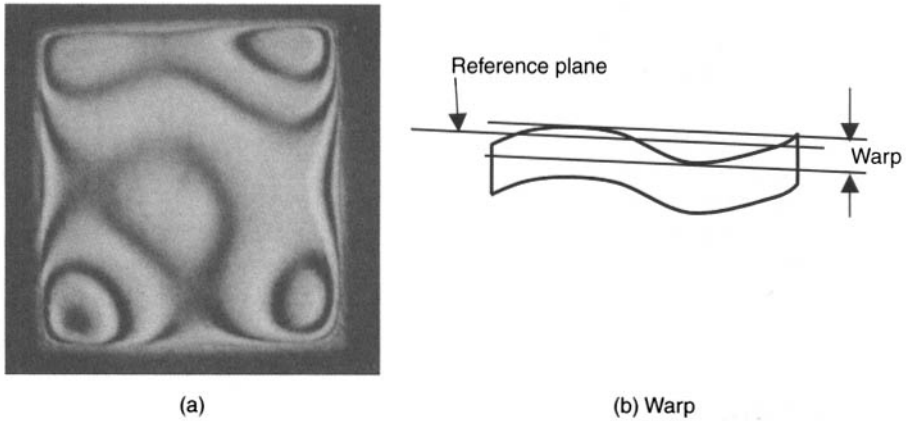


Figure 8.28 Warp on a CdZnTe substrate of 70 mm square, (a) Warp on a CdZnTe substrate of $70 \times 70 \text{ mm}^2$ ($1 \mu\text{m fringe}^{-1}$) and (b) the definition of warp

$50 \times 50 \text{ mm}^2$. As a result of optimizing each polishing step, the thickness variation in each wafer has been reduced to $6 \mu\text{m}$ or less.

On the other hand, warp of a substrate is another important parameter for device processing. It is defined as the maximum distance between the highest and lowest point on the surface of an unclamped wafer from a reference plane. Figure 8.28 shows the warp on a $70 \times 70 \text{ mm}^2$ wafer.

8.4.2.3 Surface roughness

Surface roughness of CdZnTe substrates affects the morphology on HgCdTe epitaxial layers. Figure 8.29 shows the surface roughness (a) after primary polishing and (b) after finishing by our unique chemical solution. The finished surface is literally featureless and suitable for sophisticated epitaxial growth, especially MBE.

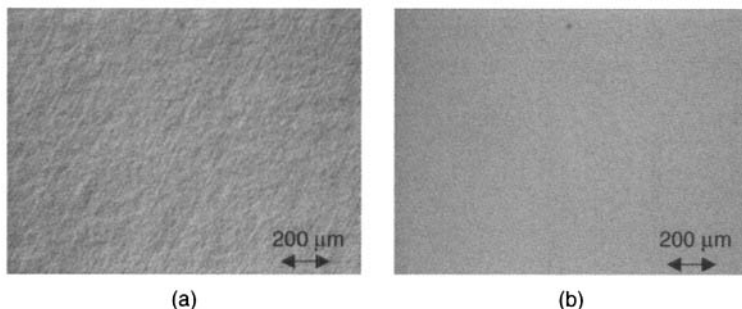


Figure 8.29 Nomarski micrographs on CdZnTe substrates, (a) after primary polishing with chemical solution and colloidal silica; (b) after final polishing by our unique chemical solution

8.5 SUMMARY

As mentioned above, use of purer starting CdTe polycrystals is the key factor to prepare high-quality substrates, with lower precipitate density, lower impurity concentrations, uniform Zn concentration and high surface smoothness. Especially for MBE growth, high-quality substrates with better surface properties are needed. We believe that the surface quality does not depend only on the polishing conditions but also on the crystal qualities. For example, if the crystals have large-sized precipitates, they will produce defects after MBE growth, as shown by the Rockwell group.

It is also important to prepare large-sized substrates. In our group, we have recently succeeded in growing single CdZnTe crystals with 5-inch diameter. From these ingots, large-sized substrates more than 70×70 mm in size can be obtained. No difference has been found between the crystal properties of 5-inch CdZnTe crystals and those of 4-inch crystals.

ACKNOWLEDGEMENTS

The authors wish to thank K. Suzuki, A. Noda, A. Arakawa, A. Hichiwa and H. Taniguchi of Nikko Materials for their technical contributions and their valuable discussions. In addition, we wish to thank T. Shibata and T. Ohhashi for their management guidance and encouragement. We thank Mr. Miura for his English guidance.

REFERENCES

- [1] P. Capper. (1997) *Narrow-gap II-VI Compounds for Optoelectronic and Electromagnetic Applications*, edited by P. Capper (Chapman & Hall, London).
- [2] J. P. Tower, S. P. Tobin, M. Kestigian, P. W. Norton, A. B. Bollong, H. F. Schaaque and C. K. Ard, (1995) *J. Electron. Mater.* **24** 497.
- [3] A. Koyama, A. Hichiwa and R. Hirano, (1999) *J. Electron. Mater.* **28**, 683.
- [4] R. Triboulet, A. Aoudia and A. Lussion, (1995) *J. Electron. Mater.* **24**, 1061.
- [5] U. Becker, P. Rudolph, R. Boyn, M. Winecke and I. Utke, (1990) *phys. stat. sol.* **120**, 653.
- [6] H. R. Vydyanath, J. A. Ellsworth, J. B. Parkinson, J. J. Kennedy, B. Dean, C. J. Johnson, G. T. Neugebauer, J. Speich and Pok-Kai Liao, (1993) *J. Electron. Mater.* **22**, 1073.

- [7] M. A. Berding, (1999) *Appl. Phys. Lett.* **74**, 552.
- [8] M. Fiederle, C. Eiche, M. Salk, R. Schwarz, K. W. Benz, W. Stadler, D. M. Hofmann and B. K. Meyer, (1998) *J. Appl. Phys.* **84**, 6689.
- [9] B. Li, J. Zhu, X. Zhang and J. Chu, (1997) *J. Cryst. Growth* **181**, 204.
- [10] R. Korenstein, R. J. Olson, D. Lee, P. K. Liao and C. A. Castro, (1995) *J. Electron. Mater.* **24**, 511.
- [11] H. R. Vydyanath, J. A. Ellsworth, J. B. Parkinson, J. J. Kennedy, B. Dean, C. J. Johnson, G. T. Neugebauer, J. Sepich and P. K. Liao, (1992) *J. Vac. Sci. Technol. B* **10**, 1476.
- [12] K. Zanio, (1970) *J. Appl. Phys.* **41**, 1935.
- [13] B. Yang, Y. Ishikawa, Y. Doumae, T. Miki, T. Ohyama and M. Isshiki, (1997) *J. Cryst. Growth* **172**, 370.
- [14] H. I. Lee, Y. D. Woo, H. S. Kang, C. K. Chang and T. W. Kim, (1999) *J. Mater. Sci. Lett.* **18**, 695.
- [15] K. Nakagawa, K. Maeda and S. Takeuchi, (1979) *Appl. Phys. Lett.* **34**, 574.
- [16] S. M. Johnson, S. Sen and W. H. Konkel, (1991) *J. Vac. Sci. Technol. B* **9**, 1897.
- [17] P. Capper, J. E. Harris, E. S. O'Keefe and C. L. Jones, (1995) *Adv. Mater. Opt. Electron.* **5**, 101.
- [18] C. D. Maxey, J. E. Gower, P. Capper, E. S. O'Keefe, T. Skauli and C. K. Ard, (1999) *J. Cryst. Growth* **197**, 427.
- [19] R. Hirano, A. Hichiwa, H. Maeda, and T. Yamamoto, (2000) *J. Electron. Mater.* **29**, 654.
- [20] K. Zanio, (1978) *Semicond. Semimet.* **13**, 99.
- [21] M. Inoue, I. Teramoto, S. Takayanagi, (1963) *J. Appl. Phys.* **34**, 404.
- [22] W. J. Everson, C. K. Ard, J. L. Sepich, B. E. Dean, G. T. Neugebauer, H. F. Schaake, (1995) *J. Electron. Mater.* **24**(5), 505.

This page intentionally left blank

9 Bulk Crystal Growth of Wide-Bandgap II-VI Materials

M. ISSHIKI, J.F. WANG

Institute of Multidisciplinary Research for Advanced Materials Tohoku University Japan

9.1 Introduction	269
9.2 Physical and chemical properties	270
9.3 Phase diagrams	270
9.4 Crystal-growth methods	270
9.4.1 Growth from vapor phase	272
9.4.2 Growth from liquid phase	276
9.4.3 Crystal growth from solid phase	280
9.5 Crystal growth of wide-bandgap compounds	280
9.5.1 ZnS	280
9.5.2 ZnO	282
9.5.3 ZnSe	284
9.5.4 ZnTe	291
9.6 Conclusions	294
References	294

9.1 INTRODUCTION

II-VI compound semiconductors are one of the most important optoelectronic materials. Wide-gap II-VI compounds, especially, ZnS, ZnSe, ZnO and ZnTe, are promising materials in fabricating laser diodes (LDs) and light-emitting diodes (LEDs) operating in the visible and ultraviolet spectral ranges. The recent challenge for their application is the development of sizable high-purity and high-quality bulk crystals as substrates for fabricating devices. Progress has been made in the past several decades in the areas of bulk crystal growth with regard to stoichiometric control, uniformity, reproducibility, thermal stability, diameter control, and impurity and dopant control. Sizable ZnO, ZnSe and ZnTe single crystals have conventionally been grown by seeded physical vapor transport (SPVT), the hydrothermal method, Bridgman methods, and so on. These advances have attracted much attention for the development of future optoelectronics.

In this chapter, the main physical and chemical properties as well as phase diagrams of these wide-gap materials are firstly introduced. Then the growth methods and results are reviewed. The crystals can be grown from a liquid phase, a vapor phase or a solid phase. There are many variations within each of the three techniques, which will be discussed in detail. The single-crystal growth of the above-mentioned compounds is assessed and the direction of future activity is outlined.

This chapter also highlights the recent results concerning large-size bulk ZnO, ZnSe and ZnTe crystal growth. ZnO bulk single crystals have been commercially grown by chemical vapor transport (CVT) or seeded chemical vapor transport (SCVT) and hydrothermal methods. It has been expected that ZnO growth will be developed more rapidly than any of the bulk single crystal including GaN growth. In the case of ZnSe, a closed, double-crucible method has been proved to be very suitable for preventing the deviation from the stoichiometric compositions of the melt in the process of ZnSe Bridgman growth. Twin-free high-quality ZnSe single crystals using a polycrystalline seed have been grown. Furthermore, low-resistivity n- and p-type ZnSe single crystals have been successfully grown by changing the compositions of the starting materials.

9.2 PHYSICAL AND CHEMICAL PROPERTIES

Since wide-gap II-VI compounds have higher ionicity, higher melting points and higher vapor pressures at the melting point than those of III-V and element semiconductors, it is difficult to grow their bulk crystals from the melt, compared with III-V compounds. Furthermore, the superheating phenomenon occurs when heating them to the melting point; on the other hand, it is possible that the bulk crystals can be grown from vapor phase.

Therefore, before introducing bulk crystal growth, it is helpful to review their physical and chemical properties. Table 9.1 shows the properties of some of the main II-VI compound semiconductor materials [1–17]. Unlike elemental and III-V compound semiconductors, the parameter measurements of the wide-gap II-VI compounds often have to be carried out at high temperature and pressure. So, it can often be found that the values of thermodynamic parameters are different in different references. This reflects the measurement difficulty.

9.3 PHASE DIAGRAMS

It is necessary to understand phase diagrams very well for growing high-quality single crystals of wide-bandgap II-VI compounds. Figure 9.1 shows the phase diagrams of some of the main wide-bandgap II-VI compounds, ZnS [18], ZnSe [18, 19] and ZnTe [18]. Although many studies have been done, there is still a lack of exact thermodynamic data, especially the details of phase diagrams near the congruent point, and a suitable phase diagram of ZnO cannot yet be given. These features show the complexity of II-VI compounds. Therefore, these materials need to be explored further.

9.4 CRYSTAL-GROWTH METHODS

Bulk crystal growth has been the most important subject studied in the past several decades. It may be thought that the application of II-VI compound semiconductors began

Table 9.1 Properties of some wide-bandgap II-VI compound semiconductors

Property	Material	ZnS	ZnO	ZnSe	ZnTe
Melting point (K) [10]		2038 (WZ, 150 atm)	2248	1797	1513
Energy Gap E_g at 300 K (eV)(ZB*/WZ*) [11]		3.68/3.911	—/3.4	2.8215	2.394
dE_g/dT ($\times 10^{-4}$ eV K $^{-1}$) ZB/WZ		4.6/8.5	—/9.5	4.0/—	5.5/—
Structure		ZB/WZ	WZ	ZB/WZ	ZB
Bond length (μm) [12]		2.342 (WZ)	1.977 (WZ)	2.454 (ZB)	2.636 (ZB)
Lattice constant (ZB) a_0 at 300 K (nm)		0.541	—	0.567	0.610
ZB nearest-neighbor dist. at 300 K(nm)		0.234	—	0.246	0.264
ZB Density at 300 K (g cm $^{-3}$)		4.11	—	5.26	5.65
Lattice constant (WZ) at 300 K (nm)					
$a_0 = b_0$		0.3811	0.32495	0.398	0.427
c_0		0.6234	0.52069	0.653	0.699
c_0/a_0		1.636	1.602	1.641	1.637
WZ density at 300 K (g cm $^{-3}$) [11]		3.98	5.606	—	—
Symmetry ZB/WZ		C 6 me/F 43 m	—/C 6me	—/F 43 m	—/F 43 m
Electron affinity χ (eV)				4.09	3.53
Phase stable at 300 K [13]		ZB & WZ	WZ	ZB	ZB
Solid-solid phase transition temperature (K)		1293	—	1698	—
Heat of crystallization ΔH_{LS} (kJ mol $^{-1}$)		44	62	52	56
Heat capacity C_p (cal mol $^{-1}$ K $^{-1}$)		11.0	9.6	12.4	11.9
Ionicity (%)		62	62	63	61
Equilibrium pressure at cmp (atm)		3.7	—	1.0	1.9
Minimum pressure at mp (atm)		2.8	7.82	0.53	0.64
Specific heat capacity (J g K)		0.469	—	0.339	0.16
Thermal conductivity (W cm $^{-1}$ K $^{-1}$)		0.27	0.6	0.19	0.18
Thermo-optical coefficient $(dn/dT)(\lambda = 10.6 \mu\text{m})$		4.7	—	6.1	—
Electro-optical coefficient r_{41} (m/V) ($\lambda = 10.6 \mu\text{m}$)		2×10^{-12}	—	2.2×10^{-12}	4.0×10^{-12} ($r_{41} = r_{52} = r_{63}$)
Linear expansion coefficient (K $^{-1}$) [13]					
ZB structure		—	2.9×10^{-6}	7.6×10^{-6}	8.0×10^{-6}
WZ structure		6.9×10^{-6}	7.2×10^{-6}	—	—
Poisson ratio		0.27		0.28	
Dielectric constant $\epsilon_0/\epsilon_\infty$		8.6/5.2	8.65/4.0	9.2/5.8	9.3/6.9
Refractive index [10] ZB/WZ		2.368/2.378	—/2.029	2.5/—	2.72/—

(continued overleaf)

Table 9.1 (continued)

Property	Material			
	ZnS	ZnO	ZnSe	ZnTe
Absorption coefficient (including 2 surfaces) ($\lambda = 10.6 \mu\text{m}$) (cm^{-1})	≤ 0.15	—	$1-2 \times 10^{-3}$	—
Electron effective mass (m^*/m_0) [2]	—0.40	—0.27	0.21	0.2
Hole effective mass m^*_{dos}/m_0	—	—	0.6	Circa 0.2
Electron hall mobility at 300 K ($\text{cm}^2 \text{V}^{-1} \text{s}^{-1}$) [11]	165	125	500	340
Hole hall mobility at 300 K ($\text{cm}^2 \text{V}^{-1} \text{s}^{-1}$) [11]	5	—	30	100
Exciton binding energy (meV) [14–17]	36	60	21	10
Average phonon energy (meV) [14–17] ZB/WZ	16.1/17.1	—	15.1/—	10.8/—
Elastic Constant (10^{10}N m^{-2})				
C_{11}	1.01 ± 0.05	—	8.10 ± 0.52	0.72 ± 0.01
C_{12}	0.64 ± 0.05	—	4.88 ± 0.49	0.48 ± 0.002
C_{44}	0.42 ± 0.04	—	4.41 ± 0.13	0.31 ± 0.002
Knoop hardness (N cm^{-2})	0.18	0.5	0.15	0.13
Young's modulus (M_{psi})	10.8	—	10.2	—

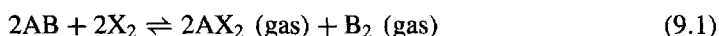
here. To date, many growth methods have been developed for growing high-quality crystals. According to the phase balance, the crystals can be grown from vapor phase, liquid (melt) phase and solid phase.

9.4.1 Growth from vapor phase

Crystal growth from the vapor phase is a basic method. One of the advantages is that the growth can be performed at lower temperature. This can prevent undesirable phase transitions. Therefore, this method was widely used to grow II-VI compound semiconductors. According to the transport mechanism, the crystal-growth method from vapor phase can be divided into chemical vapor transport (CVT) and physical vapor transport (PVT).

9.4.1.1 CVT technique

CVT is based on the chemical transport reactions that occur in a closed ampoule having two different temperature zones. Figure 9.2 shows a typical schematic diagram of a CVT system. In the high-temperature region, the source AB (A: II elements; B: VI elements) reacts with the transport agent X. If the transport agent is a Group VII element, the following reaction occurs,



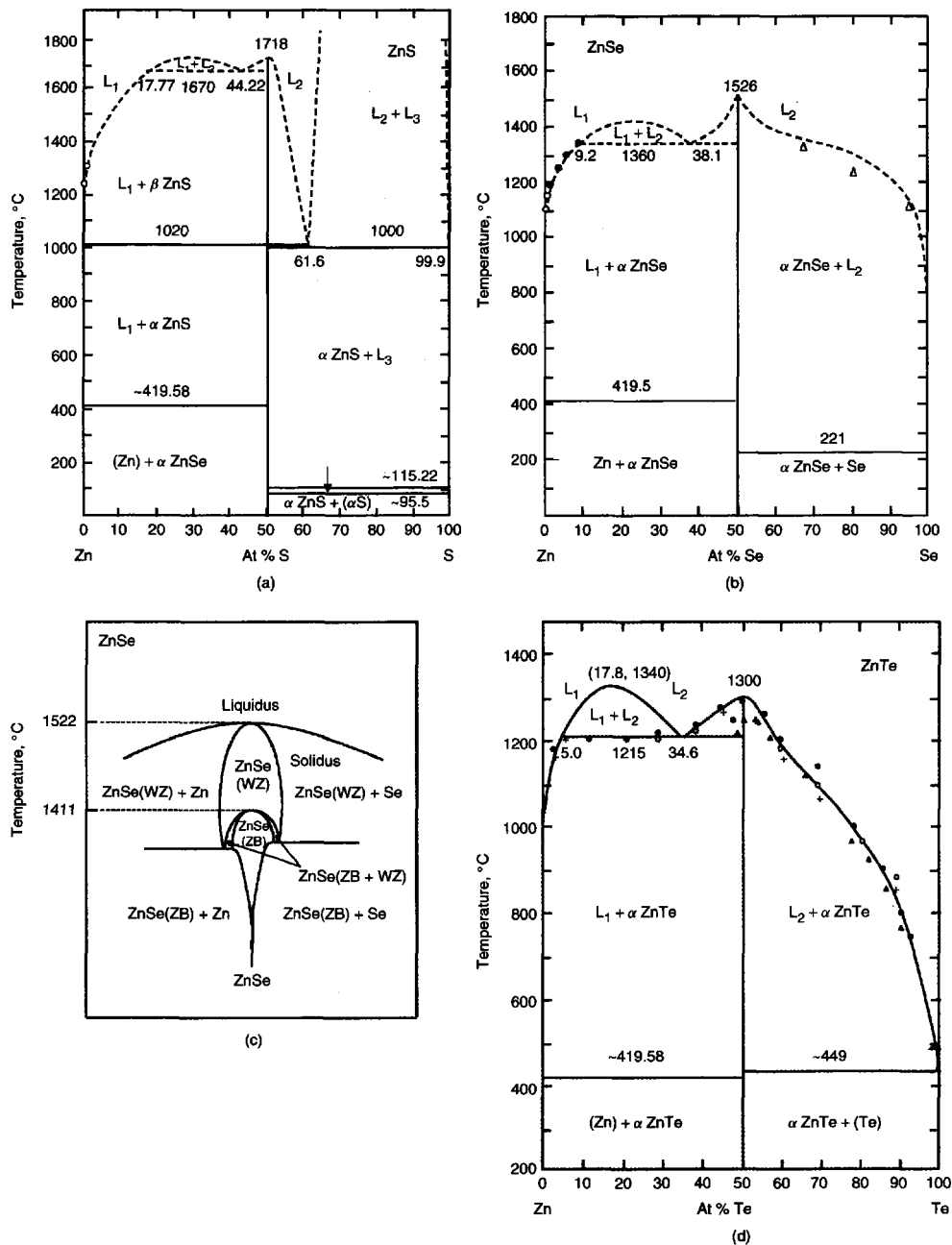


Figure 9.1 Phase diagrams of some main wide-bandgap II-VI compounds: (a) ZnS (Reprinted from Sharma and Chang *J. Cryst. Growth* **88** (1988) 192, copyright (1988) with permission from Elsevier), (b) ZnSe (Reprinted from Sharma and Chang *J. Cryst. Growth* **88** (1988) 192, copyright (1988) with permission from Elsevier), (c) ZnSe phase diagram near the congruent point (Reprinted from Okada *et al. J. Cryst. Growth* **165** (1996) 31, copyright (1996) with permission from Elsevier), (d) ZnTe (Reprinted from Sharma and Chang *J. Cryst. Growth* **88** (1988) 192, copyright (1988) with permission from Elsevier)

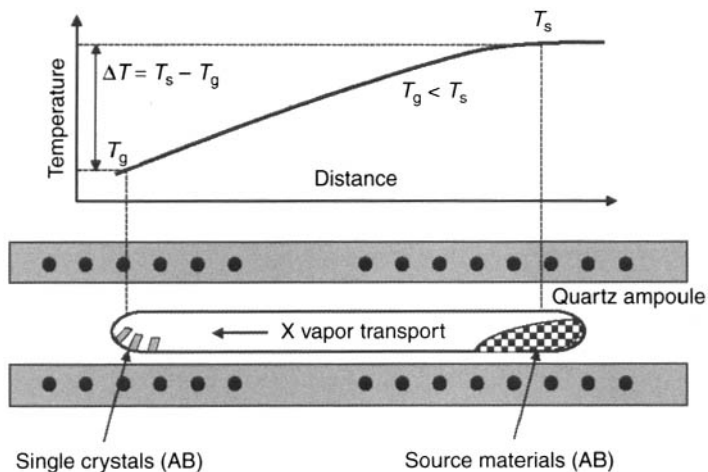


Figure 9.2 Schematic diagram of a conventional chemical vapor transport (CVT) system

In the low-temperature region, the reverse reaction takes place. The whole process continues by back diffusion of the X generated in the lower-temperature region. The transport agents X usually employed are hydrogen (H_2), halogens (I_2 , Br_2 , Cl_2), halides (HCl , HBr), etc. For example, I_2 has been widely used as a transport agent of ZnS , $ZnSe$, $ZnTe$ and CdS [20]; HCl , H_2 , Cl_2 , NH_3 [21] and C , CH_4 [22] as the transport agents of ZnO . In CVT growth, crystallographic perfection and morphological stability of the grown crystals are strongly related to growth temperature, temperature difference (ΔT) between source and crystal-growth zone, concentration of the transport agent, system pressure, and the aspect ratio (length/diameter) of the ampoule. Some typical growth parameters are summarized in Table 9.2 [20–22].

9.4.1.2 PVT technique

The PVT method is similar to CVT, but the transport agent is not used. This technique is based on the dissociative sublimation of compounds. In early work, the Piper–Polich

Table 9.2 Typical growth parameters of ZnS , ZnO , $ZnSe$ and $ZnTe$ crystals grown by CVT

	Growth temperature (K)	ΔT (K)	Transport agent concentration ($mg\ cm^{-3}$)	Ampoule diameter (mm)	Aspect ratio of ampoule (L/D)
ZnS	1075–1173	5–50	0.5–5	10–20	5–17
ZnO	1228–1273	5–10	> 0.3		
$ZnSe$	1023–1073	5–50	0.5–50		
$ZnTe$	973–1073	5–50	0.5–50		

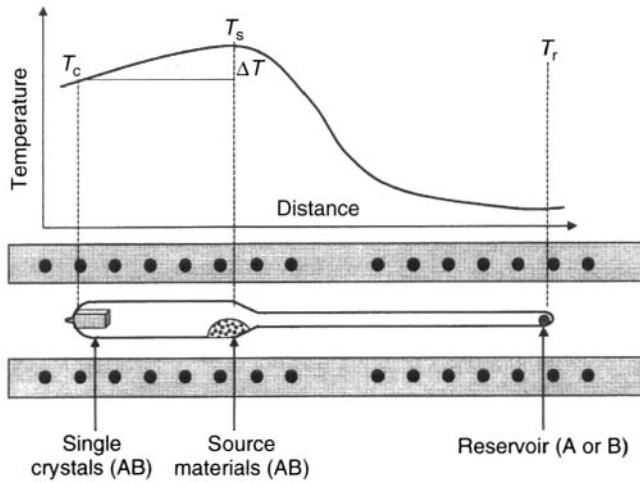
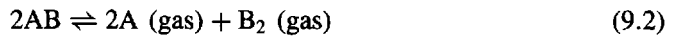


Figure 9.3 Schematic diagram of physical vapor transport (PVT) method

method was a typical PVT technique used. By this method, crystals of centimeter size can be grown.

Prior [23] improved the above growth method, using a reservoir to control the deviation from stoichiometry. The experimental arrangement is shown in Fig. 9.3. The constituent element is placed in a reservoir. The reservoir temperature can be calculated according to the solid–vapor equilibrium,



The total pressure (P) in the ampoule is given by

$$\begin{aligned} P &= P_A + P_{B_2} \\ &= P_A + K \cdot P_A^{-2} \\ &= (K/P_{B_2})^{1/2} + P_{B_2} \end{aligned} \quad (9.3)$$

where P_A and P_{B_2} are the partial pressures of group II and VI elements, respectively, and $K = P_A^{-2} \cdot P_{B_2}$ is the equilibrium constant of Equation (9.2). At any temperature, there is minimum total pressure (P_{\min}), which corresponds to the condition,

$$P_A = 2 P_{B_2} = 2^{1/3} \cdot K^{2/3} \quad (9.4)$$

Under this condition, the vapor-phase composition is stoichiometric and the growth rate is maximum [24]. After modifying this method to use a closed ampoule, it can be applied to grow high-purity and high-quality crystals of II-VI compounds.

In the PVT process (Fig. 9.3), an ampoule containing a polycrystalline source of the desired II-VI compound is heated to a temperature that causes the compound to sublime at a rate leading to crystal growth. The ampoule is typically placed in a furnace that provides a temperature gradient over the length of the ampoule, so that the polycrystalline source

material sublimates at the higher temperature and deposits at the end of the ampoule where the temperature is lower. This temperature difference (ΔT) causes the material transport from the charge to eventually deposit at the cooler end. Due to the difference of vapor pressures of the constituent elements, a reservoir is used to control the partial pressure. By selecting the proper growth conditions, the rate of deposition can be set to a value leading to growth of high-quality crystals.

PVT growth of II-VI compounds can be carried out at temperatures much lower than their melting points. This gives benefits in reducing defects such as voids and/or inclusions of excess components, which are often found in melt-grown crystals, and also reducing the contamination of the growing crystal from the equipment. The PVT process also has a purifying effect. Volatile impurities can deposit at the reservoir and impurities with low vapor pressures remain in the source material. Other effects, such as reduction of point defects, are also typically found when crystals grown by PVT are compared to crystals grown by melt techniques. Although claims have been made that the lower temperatures of PVT crystal growth should also reduce the twinning found in most of the cubic II-VI compound crystals, the reduction is not usually realized in practice. The assumption that the twinning is a result of cubic/hexagonal phase transitions is not confirmed to be the determining factor in twin formation.

9.4.1.3 SCVT/SPVT

The PVT process has always shown the capability to produce high-quality II-VI compound single crystals, however, crystal volume is usually limited to several cm^3 , and grain boundaries and twins readily form during growth. In order to solve these problems, the seeded chemical vapor transport (SCVT) and seeded physical vapor transport (SPVT), the so-called 'modified-Lely method', have been developed [25]. The difference between SCVT/SPVT and CVT/PVT is that a single-crystal or polycrystal seed is set in the crystal growth chamber before growth starts. The most successful means of eliminating twin formation has been realized by using these two methods. The diameter of the grown crystal is dependent on the geometric condition of the ampoule and temperature profiles eliminating spurious nucleation on the walls are required. Since the use of a seed crystal provides better control over the nucleation process, high-quality single crystals can be grown [26, 27].

9.4.2 Growth from liquid phase

Crystal growth from liquid phase has two routes, from the melt and from the solvent. All the methods of growth from the melt and solvent rely on cooling the liquid below its melting point and liquidus point, respectively. From the viewpoint of industrial production, melt growth is more useful than vapor growth for obtaining large single crystals.

9.4.2.1 Bridgman method

The most straightforward melt-growth technique is a normal freezing. When freezing is achieved by the use of a two-zone furnace, it is called the Bridgman or Bridgman–Stockbarger method. The usual configuration is vertical and the ampoule is lowered

from the hot zone to the cooler zone, which is below the melting point of the grown material. This is called the vertical Bridgman (VB) method. On the other hand, a horizontal configuration using a boat has also been applied to grow crystals. This is called the horizontal Bridgman (HB) method. Bridgman growth can be simply understood that the molten charge passes a temperature gradient at a slow speed and solidifies when the temperature is lower than the melting point of this material.

There are three ways to move the solid/liquid interface: 1. The ampoule moves through the temperature gradient. 2. The furnace moves and the ampoule is stationary. 3. The ampoule and furnace are stationary and the temperature is gradually reduced by keeping the temperature gradient at the interface constant. The latter is called the gradient freezing (GF) method.

Single crystals can be grown using either seeded or unseeded ampoules or crucibles. Twinning and deviation from stoichiometric composition are the main problems preventing the growth of crystals with good crystallinity. Growth can be controlled by the movement rate and the shape of the solid/liquid interface.

In the case of growth from a solid solution or impurity doping, a distribution effect between liquid and solid should be taken into consideration. If the distribution coefficient k is not close to unity, the doping element segregates through the crystal and a uniform concentration cannot be obtained.

The Bridgman method has been most extensively used to grow single crystals of II-VI wide-bandgap compounds like ZnS, ZnSe and ZnTe. This is because of the simplicity of the growth apparatus, high growth rate and the possibility to obtain crystals of usable size and quality. There are two Bridgman techniques for preparing II-VI wide-bandgap compound single crystals. One is the high-pressure technique [28, 29] and the other is the closed technique [30, 31]. In the former, it is inevitable that compositional deviation from stoichiometry occurs during melting. Since the properties and structural perfection of these compound crystals are correlated very strongly with the nonstoichiometry [32, 33], compositional deviation must be controlled during melt growth. Omino and Suzuki [31] and Wang *et al.* [34, 35] adopted a closed double-crucible to prevent the deviation from the stoichiometric compositions of the melt during Bridgman growth. Figure 9.4 shows a typical vertical Bridgman growth furnace and its temperature profiles [36].

9.4.2.2 Hydrothermal growth

The hydrothermal technique is a method for growing crystals in an aqueous solvent at low temperature [37]. It has been used to grow many compound crystals [38, 39]. The most successful example in obtaining II-VI compounds is the growth of ZnO single crystals. Figure 9.5 shows a schematic diagram of the hydrothermal method.

Since the middle of the last century, this technique has been used to synthesize large crystals and employed for large-scale synthesis of piezoelectric, magnetic, optical, ceramic, and many other special materials. The hydrothermal method of crystal growth has several advantages. 1) Due to the use of a closed system, it is easier to control oxidation and to maintain the conditions that allow the synthesis of phases that are difficult to obtain by other methods. 2) A crystal grows under less thermal strain, and thus may lead to a lower dislocation density than the crystal grown from a melt. 3) The method has proven to

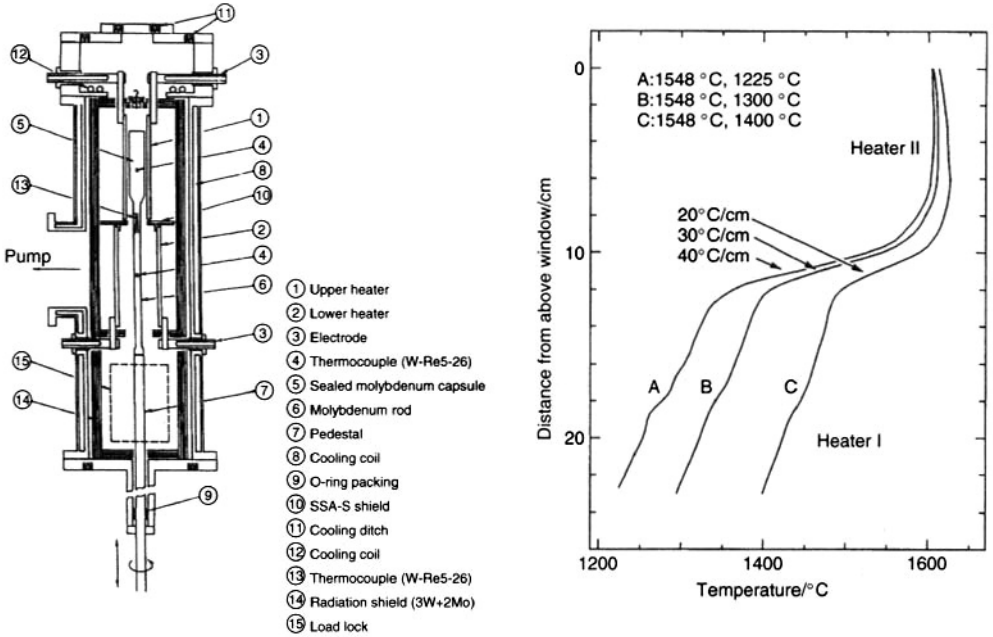


Figure 9.4 Schematic of the vertical Bridgman growth system (a), and its temperature profiles (b)

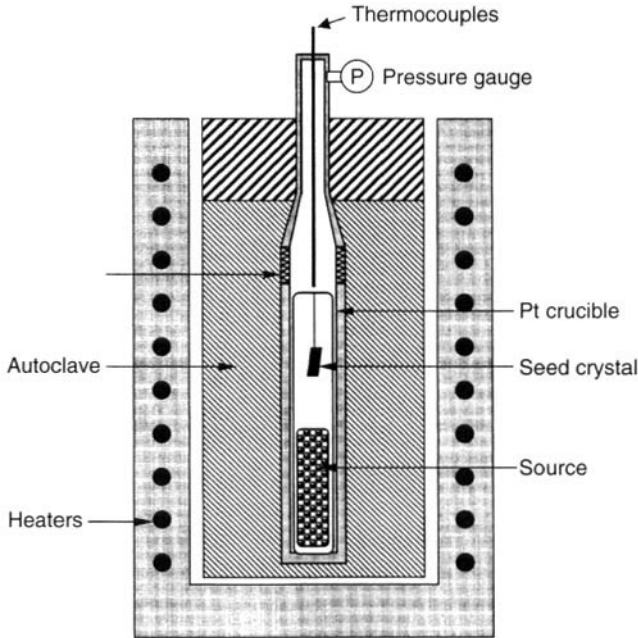


Figure 9.5 Schematic diagram of a typical hydrothermal technique for growing ZnO single crystals

be very useful for the synthesis of the so-called low-temperature phases. 4) Hydrothermal synthesis proceeds with rapid convection and very efficient solute transfer, which results in comparatively rapid growth of larger, purer, and dislocation-free crystals.

9.4.2.3 Traveling heater method (THM)

A schematic illustration of the traveling heater method (THM) is shown in Fig. 9.6. A molten solvent zone is moved slowly through a solid source material. In this process, the dissolution of feed material occurs at the receding liquid/solid interface (T_2) and the crystallization of dissolved feed material occurs continuously at the advancing interface (T_1). The major advantage of this method is a lower growth temperature as compared with the growth from the near-stoichiometric melt. Low growth temperature reduces possible contamination and the defect density in the crystals. In addition, THM produces a purification effect by the solvent. The drawbacks of this method are low growth rate (about 5 mm day^{-1}) and difficulty in obtaining near-stoichiometric compounds. The selection of the solvent material is important in THM growth.

9.4.2.4 Liquid encapsulation czochralski (LEC)

In the LEC method, the melt is contained in a crucible but the crystals are grown at the free top surface of the melt so that there is no contact between the crystal and the crucible. In order to prevent evaporation of constituent elements, an encapsulant is needed. The encapsulant must, of course, be made of a material that is less dense than the material in the crucible and must not be dissolved in the melt. As the crystal grows, it is slowly pulled upwards so that the solid/liquid interface is just above the level of the liquid surface. The melt temperature and pulling rate depend upon the rate at which the heat is removed and they can be changed independently. By the rotation of the crucible and the crystal, asymmetries in temperature gradient of the melt are reduced and a better mixing of the melt is achieved.

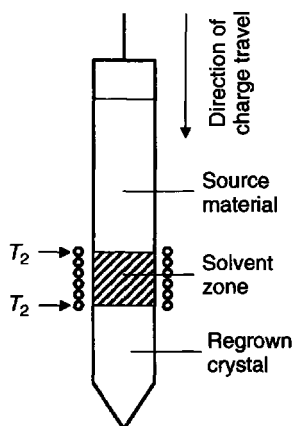


Figure 9.6 Schematic of traveling heater method (THM)

This method has been widely used to grow silicon and III-V compounds in industry. II-VI compounds have also been attempted by this method [40–42]. In the case of II-VI compounds, the growth of single-crystal ZnSe has been proved to be impossible using B_2O_3 due to reactivity [42]. Asahi *et al.* [43] have proved that B_2O_3 is a suitable encapsulant in ZnTe melt growth. Thus, it is hopeful to grow ZnTe single crystals by the LEC technique.

9.4.3 Crystal growth from solid phase

Conventional melt growth of II-VI materials such as ZnS and ZnSe has generally resulted in material containing low-angle grain boundaries and high levels of twinning owing to the phase transition between the high-temperature wurtzite phase and the low-temperature cubic structure. Other problems of melt growth include contamination of the material from the container at the high temperature and parasitic nucleation arising from the high degree of association in the melt. A method has been developed whereby polycrystalline material is annealed at high temperatures, but below the phase-transition temperature. This is called solid-state recrystallization (SSR) or solid-phase recrystallization (SPR). This method has been used for growing wide-gap II-VI compounds [44].

In SSR/SPR growth, the starting materials are polycrystals with small crystal grains. When these materials are annealed at high temperature under the component atmosphere, the energy stored in the polycrystalline material is released by recrystallization. By controlling the annealing temperature and duration, single crystals can be grown.

9.5 CRYSTAL GROWTH OF WIDE-BANDGAP COMPOUNDS

9.5.1 ZnS

9.5.1.1 Growth from liquid phase

Zinc sulfide has a phase transition from the cubic zinc-blende structure (3C) to hexagonal wurtzite structure (2H) [45–47]. The stable form of ZnS at low temperature is the cubic structure and transformation to wurtzite structure occurs at 1293 K [45]. Owing to the small difference of free energy between the two phases, it is very difficult to observe the phase conversion [47]. Addamiano and Aven [48, 49] grew ZnS crystals by controlled cooling of molten ZnS using pure and activated ZnS powder source material. Although the result showed good optical properties, the crystals were proved to be pure hexagonal wurtzite structure. Ebina and Takahashi [50] found that the ZnS single crystals grown from the melt contain a considerable amount of stacking disorder, although the crystals showed a cubic structure. These results indicate that the growth of cubic ZnS single crystal is difficult from the melt.

Cubic ZnS single crystals have been grown from solvents such as Te [51] and some halides [52, 53] at temperatures significantly lower than its melting point. Washiyama *et al.* [51] grew ZnS single crystals using Te solvent. The Te solvent, in which ZnS was dissolved at 1373–1473 K, was slowly cooled to 773–823 K at a rate of 15–40 K h⁻¹. They grew plate-like transparent cubic crystals with dimensions of 3 mm × 3 mm × 1 mm and found that the grown crystal contained 0.1–0.8 at % Te.

Linares [52] grew optically isotropic ZnS crystal from PbCl₂ solvent at temperatures of 773–1073 K. Colorless crystals free from birefringence or flux inclusions can be grown at a slow growth rate. Parker and Pinnell [53] investigated the optimum solvent growth composition of K(I/Cl)-(Zn/Cd)Cl₂ at temperatures of 723–1173 K. They grew crystals up to 10 mm from a solvent of KI (20 wt %)-ZnCl₂ and found the change of crystal morphology from dendritic, thin platelets to thicker platelets with increasing growth temperature. The thick crystals had a low dislocation density, but the thin-platelet and well-faceted crystals frequently showed twinning.

9.5.1.2 Growth from vapor phase

Cubic ZnS single crystals have been grown by CVT methods using HCl [54, 55], NH₄Cl [56] and I₂ [56–58] as transport agents. Although the crystals grown below 1273 K usually have a cubic structure and those grown above 1273 K have a hexagonal structure [56], Dangel and Wuensch [57] reported that the hexagonal structure predominates at iodine concentrations below $5 \times 10^{-4} \text{ g cm}^{-3}$, where surface reactions are rate controlling.

Fujita *et al.* [58] grew ZnS single crystals as large as 24 mm × 14 mm × 14 mm by the SCVT method using iodine as a transport agent. The average linear growth rate was about $1.0 \times 10^{-6} \text{ cm s}^{-1}$. The crystal size depended strongly on the ampoule geometry and the temperature difference between seed and solvent. The study of electrical properties showed that the crystals annealed in molten Zn at 1223 K for more than 48 h were low-resistivity n-type.

Ohno *et al.* [59] grew cubic ZnS single crystals by the iodine-transport method without seeding. By means of a Zn-dip treatment, a low-resistivity crystal was obtained and used as a substrate for homoepitaxial MOCVD growth. Fabricated MIS-structured blue LEDs yielded external quantum efficiency as high as 0.05%. They found that crystal quality was significantly improved by prebaking the ZnS powder in H₂S gas prior to growth. The growth rate also increased three-fold.

On the other hand, the PVT method seems to be unsuitable for growing cubic ZnS single crystals compared with the CVT method. Some groups [60, 61] tried, but only small-size hexagonal ZnS crystals were obtained due to the high growth temperature.

9.5.1.3 Growth from solid phase

Cubic ZnS single crystals were also grown using the SSR/SPR technique [44, 62–65]. The crystal growth depended on both annealing temperature and atmosphere. Lemason *et al.* [44] studied the dependence of grain size on annealing temperature using the microcrystalline sources of cubic structure prepared by CVD. The results showed that SSR annealing for 288 h under a sulfur atmosphere (5 atm) led to submillimetric grains at a temperature of 1273 K, millimetric grains at 1373 K and centimetric grains at 1423 K. Large-size ZnS single crystals (about 40 cm³) were obtained after annealing at 1373 K under a sulfur vapor pressure of 10 atm for 21 days. On the other hand, SSR growth was also carried out under Zn vapor pressure (2.1 atm) [44]. When the annealing temperature is 1273 K, growth did not occur. When annealing was carried out at 1423 K, millimetric grains were obtained. Since this annealing temperature was higher than the

hexagonal/cubic phase-transition temperature, a high density of twins was found in the crystals. In order to suppress this twinned structure, different cooling rates were used. But the result was not satisfactory.

Yoneta *et al.* [65] studied the dependence of ZnS grain size on annealing atmosphere (Zn or S) and temperature. Compared with the grain size of starting materials, the annealed grain size in sulfur was larger than that of samples annealed in a Zn atmosphere. This can be interpreted as being due to the large difference in diffusion coefficients between S and Zn [66]. The experimental results showed that the grain size reduced with decreasing annealing temperature and did not change below 1073 K compared with that of the starting material. This is consistent with the grain-growth model in that the grain growth is affected by zinc self-diffusion through the zinc vacancy generated at higher temperature under the sulfur atmosphere. The above results are consistent with that of Triboulet's group [44].

9.5.2 ZnO

Since ZnO has a wide bandgap of 3.4 eV at room temperature and a very high exciton binding energy of 60 meV, it is attractive for optoelectronic application in the blue and violet regions. It also has the potential as a substrate material for the growth of GaN epilayers. This is because it has the same crystallographic structure as GaN with a lattice mismatch less than 1.8% as well as a small difference in thermal expansion coefficients. Furthermore, ZnO crystals are considered extrinsic n-type piezoelectric semiconductors. Undoped crystals have a typical resistivity of 0.1–100 Ω cm and drift mobility of 10 to 125 $\text{cm}^2 \text{V}^{-1} \text{s}^{-1}$. Low-resistivity ZnO crystal can be prepared by special growth and annealing methods. ZnO crystal is quite transparent in the 0.4–6.0 μm range. A slight absorption is sometimes found around 2.2 to 2.3 μm and an additional slight absorption is found at 3.42 μm . Since 1953, Walker [67] and many other researchers [68–71] have grown large-size ZnO single crystals by a different method.

9.5.2.1 Growth from liquid phase

Hydrothermal growth has been widely adopted in preparing sizable ZnO crystals. Figure 9.5 shows the schematic diagram of the hydrothermal technique. Suscavage *et al.* [70] grew high-quality bulk ZnO crystals using a (0001) seed. The crystals showed anisotropy between $[000\bar{1}]$ (C^+) and $[0001]$ (C^-) planes, and have a different color. The former is light green and high resistivity, and latter is dark green and low resistivity. These differences were thought to be due to a difference in impurity incorporation between the two sectors. Anisotropy is also seen in the surface quality of polished slices. For slices cut and polished on both sides of the basal plane, sharper and more intense room-temperature PL peaks, and a narrower X-ray rocking curve were measured. The PL spectra at 2.1 K showed ground state Γ_5 (3.3758 eV) and Γ_6 (3.3740 eV) and their excited states $n = 2$ and $n = 3$ were observed. These data demonstrate that high-quality ZnO can be grown by the hydrothermal technique.

Sekiguchi *et al.* [72] grew ZnO single crystals by the hydrothermal method using a mixture of KOH and LiOH aqueous solution. The seed crystal, suspended by a Pt wire, and sintered ZnO as a source material (nutrient), together with a KOH (3M) and LiOH

(1M) aqueous solution, were put into a Pt crucible [73] (the hydrothermal conditions are different in different papers). The seed crystals and the source material were separated by a Pt baffle. The crucible was sealed by welding and put into an autoclave made of high-strength steel. Then, the autoclave was put into a vertical furnace. The temperature of the autoclave was raised to about 673 K, which produced 0.1 GPa of pressure. The growth temperature was monitored by a thermocouple inserted in the autoclave. Seed crystals grew to about 10 mm or larger after 2 weeks. These crystals were transparent, pale green or pale yellow in color depending on the growth conditions. The crystal habit of hydrothermal ZnO crystals grown on basal plane seeds shows that growth in the [0001] direction is 3 times faster than in the $[000\bar{1}]$ direction [72].

9.5.2.2 Growth from vapor phase

Since the melting point of ZnO is 2248 K, it is very difficult to grow a single crystal from the melt. For this reason, growth from the vapor phase is especially important for this material. The vapor pressure of ZnO is very small at about 1273 K that is usually used to grow semiconductor crystals. Therefore, CVT or SCVT is extensively used to grow ZnO single crystal [74–80].

Shiloh and Gutman [75] grew ZnO single crystals in a closed system using transport agents of HCl, NH₃, NH₄Cl, H₂, Cl₂ and HgCl₂. The results showed that NH₃, NH₄Cl and HgCl₂ were efficient. Using these transport agents, extremely pure ZnO single crystals of 2 mm diameter and 8 mm length have been grown. Hassani *et al.* [22] demonstrated that carbon and hydrocarbons such as methane acted as efficient chemical transport agents for ZnO. The transport rate was shown to be independent of the initial amount of carbon, but roughly proportional to the temperature difference between the source and crystal. The control of the growth mechanisms of ZnO by CVT and the knowledge of the volatility and stability of all the species in the vapor phase was made possible through a thermodynamic approach that allowed identification of the dominant vapor species. ZnO single crystals with centimeter sizes were grown after adjusting the main growth parameters. Neither carbon nor residual H₂ were detected in the crystals by SIMS measurements. The PL spectra at 1.6 K were essentially dominated by a narrow (D⁰,X) line at 3.359 eV. A rocking-curve FWHM of 28 arcsec was obtained, which showed very good crystal quality.

Recent progress in growing large ZnO single crystals is very inspiring [80, 81]. Look *et al.* [80] grew ZnO single crystals by SCVT. Pure ZnO powder, synthesized through the reaction of high-purity Zn vapor and O₂, was used as the starting source, which was placed at the hot end (1423 K) of the ampoule and transported by using H₂ as a carrier gas. At the cool end (1373 K) of the ampoule, a single-crystal seed was fixed. In order to maintain the proper stoichiometry, a small amount of water vapor was also added. The growth duration was 150–175 h. Crystals with 2-inch diameter and about 1-cm thickness were obtained. The Hall measurement at 300 K showed that carrier concentration and mobility were about $6 \times 10^{16} \text{ cm}^{-3}$ and $205 \text{ cm}^2 \text{ V}^{-1} \text{ s}^{-1}$, respectively. The maximum value of the mobility was obtained at 50 K at about $2 \times 10^3 \text{ cm}^2 \text{ V}^{-1} \text{ s}^{-1}$, comparable to the highest value reported in the past for ZnO. The PL spectra at 2 K showed five kinds of emission related to impurities. In addition, the weak emission centered at 3.374 eV was detected and confirmed as the A-band free exciton by reflectivity spectra. This confirmed the high

quality of the ZnO crystals. Currently, it is available in wafers up 2 inch grown by SCVT [81]. On the other hand, Cermet [82] has demonstrated the feasibility of growing high-purity ZnO bulk crystals by a seeded melt growth method. The melt growth of ZnO single crystals will possibly be realized in the not too distant future.

9.5.3 ZnSe

9.5.3.1 Growth from liquid phase

There are several methods to grow ZnSe crystals from liquid phase. Here, special emphasis is focused on the vertical Bridgman (VB) method because it is hopeful to prepare large single crystals. However, the compositional deviation from the stoichiometry during melting, superheating and supercooling [32], and phase transformations [83] produce ZnSe bulk crystals containing twins and grain boundaries in very high density [84]. To solve these problems, Omino *et al.* [31] and Wang *et al.* [34, 35, 85] adopted a closed double-crucible assembly consisting of an inner pBN crucible and an outer molybdenum capsule in order to control the compositional deviation of melting ZnSe from stoichiometry. A polycrystal seed was used to avoid supercooling and the optimum temperature gradient at the growth interface and growth rate were determined.

Polycrystalline 6N ZnSe synthesized by the CVD method was used as the starting material. About 13 g of ZnSe was placed into a pBN crucible of 75 mm length and 12 mm diameter. Then this crucible was inserted into a Mo crucible of 120 mm length and 15 mm outer diameter. This double crucible was loaded into the chamber of the electron-beam welder for sealing. The sealed Mo crucible was mounted on the pedestal of the vacuum furnace and heated below 2.0×10^{-4} Pa. Before growing the ZnSe crystal, the melt was held at the highest temperature of 1827 K [86] for 8 h in order to guarantee complete melting, homogenization and breaking up of possible melt complexes.

From the viewpoint of growth thermodynamics, a stable smooth growing interface is a prerequisite for preparing high-quality ZnSe single crystals by the Bridgman method. The shape of the growing interface is determined by the temperature gradient (G) on the growth interface and the growth rate (R). The stability of the solid/melt interface can be described by the ratio of G/R [87]. The maximum growth rate can be estimated by selecting suitable parameters when the temperature gradient is given. Some groups [32, 84, 85, 88–92] have studied the relationship of G/R . The results showed that a ZnSe single crystal could be grown when the value of G/R is greater than 65 K h cm^{-2} and less than 187 K h cm^{-2} .

To determine the optimum growth conditions, ZnSe crystals were grown at three different temperature gradients and different growth rates. The examined ranges of temperature gradient and growth rate were $20\text{--}40 \text{ K cm}^{-1}$ and $1.8\text{--}10.8 \text{ mm h}^{-1}$, respectively. By evaluating these crystals by low-temperature PL spectra and FWHM of XRD rocking curves, a temperature gradient at the growth interface of 30 K cm^{-1} and a growth rate of 3.6 mm h^{-1} were thought to be optimum.

In order to describe the relationship between growth rate and the temperature gradient at the growth interface, the experimental results are summarized in Fig. 9.7. The experimental results show that it is necessary for growing a ZnSe single crystal that the G/R value should be limited in the range of $57\text{--}175 \text{ K h cm}^{-2}$. The suitable value of G/R assessed

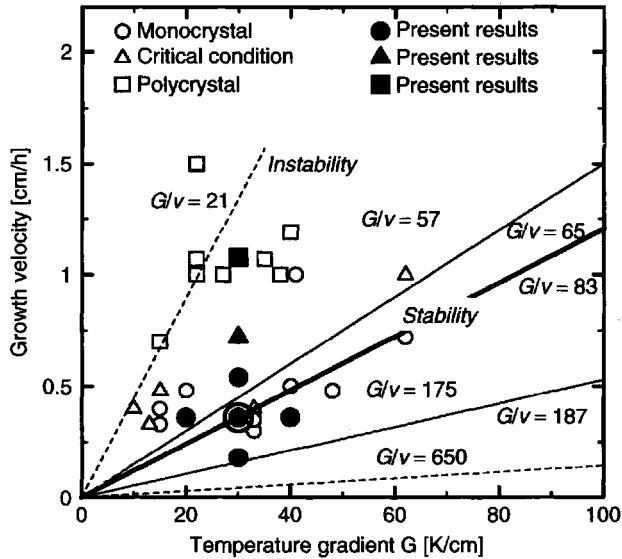
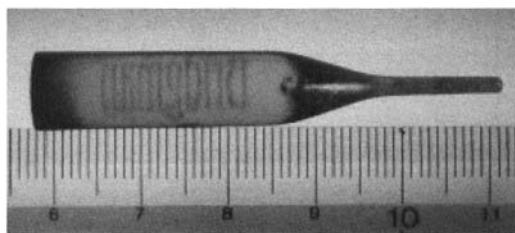


Figure 9.7 Relationship between growth velocity and temperature gradient at the growth interfaces (our data are plotted with those of Rudolph *et al.* [92])

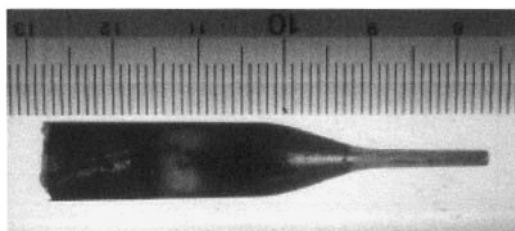
from the determined optimum temperature gradient and growth rate is 83 K h cm^{-2} . This value agrees with the result concluded in ref. [92]. The optimized conditions concluding a special temperature program [93], an overheating temperature of 76 K, and temperature gradient of 30 K cm^{-1} and growth rate of 3.6 mm h^{-1} as marked by \odot in Fig. 9.7 are recommended for growing twin-free high-quality ZnSe single crystals.

Figure 9.8(a) shows a photograph of a ZnSe crystal grown by the Bridgman method under the above-described optimum conditions. It appears to be transparent, and greenish-yellow in color. The structural defects such as precipitates, inclusions, lamella-shaped twins and microtwins cannot be observed in this ZnSe crystal by reflection and transmission microscopy. For the purpose of comparison, the photograph of ZnSe grown at the growth rate of 11 mm h^{-1} is shown in Fig. 9.8(b). This crystal shows an opaque orange-brown color. The clear lamella twins are observed even on the surface of the ingot. The observation of the polished surface by microscopy also shows numerous twin boundaries. Furthermore, the results of XRD revealed that it is a polycrystal. It is thought that random nucleation occurs at the phase-transition temperature, as too great a growth rate leads to an unstable growth interface. This means that structural imperfections, such as low-angle grain boundaries and precipitates, are produced during the growth of the crystal. For the ZnSe crystal in Fig. 9.8(a), chemical etching was carried out on the (110) cleavage plane. An average value of EPD of $2.0 \times 10^5 \text{ cm}^{-2}$ was obtained. The FWHM of 4-crystal XRD curves yields 19 arcsec using the (440) diffraction.

In general, the excess metal in interstitial sites or chalcogen vacancies act as donors, while chalcogen in interstitial sites or metal vacancies are acceptors in II-VI compounds. Kikuma *et al.* [94] grew low-resistivity ZnSe crystals from Zn-rich melts under argon pressure by controlling the Zn partial pressure. Wang *et al.* [85] investigated the effect of melt compositions on crystal quality and electrical properties in order to prepare low-resistivity n- and p-type ZnSe single crystals. The range of composition ratio (Zn/Se)



(a)



(b)

Figure 9.8 Two typical ZnSe crystals grown by vertical Bridgman method: (a) Twin-free ZnSe single crystal grown at optimized conditions, (b) Polycrystal ZnSe grown at a rate of 10 mm h^{-1}

is 0.98–1.03 in mole fraction. The grown crystals show a transparent greenish-yellow color. But in the case of Se excess, the color in the tail is brown, and the greater the ratio of Se/Zn, the deeper the color. This phenomenon can be attributed to the distribution of excess Se. Figure 9.9 shows the band-edge emissions of ZnSe samples with different Zn/Se ratios. The emission peaks from all the samples are very sharp. This indicates that the ZnSe crystals are of high quality. When the ratio of Zn/Se is just 1, I_1^d emission from an exciton bound to a zinc vacancy as a neutral acceptor is dominant. This is a feature of ZnSe crystals with high resistivity. With increase of the ratio of Zn/Se, I_2 emission related to excitons bound to neutral donors becomes intensive and I_1^d emission weak. This can be interpreted by the decrease in Zn vacancy concentration. This shows the emission features of low-resistivity n-type ZnSe. On the other hand, when the ratio of Zn/Se is smaller than 1, I_1 emission originated from excitons bound to neutral acceptors becomes dominant. This might imply that they are from low-resistivity p-type ZnSe.

The results of FWHM of X-ray rocking curves, EPD, Hall and $C-V$ measurement are summarized in Table 9.3 [85]. When the ratio of Zn/Se > 1 or < 1 , the values of FWHM and EPD are greater than that of Zn/Se = 1. The greater the deviation from stoichiometry, the greater the values of FWHM and EPD. These results prove that the compositional deviation leads to degradation of crystallinity, even to polycrystals. The results of Hall measurement show almost insulating behavior for the sample of Zn/Se = 1. On the other hand, the carrier (electron) concentrations become larger with an increase of added Zn content. The highest electron concentration is $8.8 \times 10^{17} \text{ cm}^{-3}$. The electron mobilities are of the order of $300 \text{ cm}^2 \text{ V}^{-1} \text{ s}^{-1}$ for all samples of Zn excess. For the samples of Zn/Se < 1 , $C-V$ measurement shows p-type conductivity, and the highest acceptor concentration is $1.8 \times 10^{17} \text{ cm}^{-3}$. Independent of whether samples are n- or p-type, the electron or hole concentration and their Hall mobility depend on the Zn or Se excess degree in the

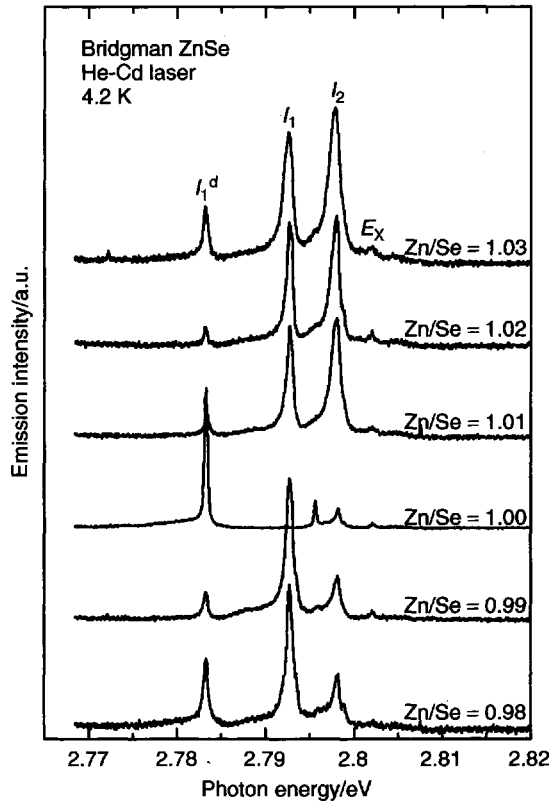


Figure 9.9 Band-edge emission of ZnSe single crystals grown from different mole ratios of Zn to Se

examined range. The carrier concentration is in direct proportion to the content of excess Zn or Se. On the contrary, the mobility of carriers is in inverse proportion.

The difficulty in growing low-resistivity p-ZnSe crystals lies in the existence of Se vacancies at high concentration [95]. They play the role of donors and compensate the shallow acceptor. As excess Se was added to the starting materials, the concentration of Se vacancies is predicted to be decreased in grown ZnSe crystals. Therefore, it is beyond doubt that the decrease of Se vacancy concentration creates a favorable environment for enhancing the net acceptor concentration. As a result, the acceptor impurities existing in

Table 9.3 Summary of the experimental values for the ZnSe crystals with composition ratio (Zn/Se) of 0.98–1.03

	Zn/Se = 1.03	Zn/Se = 1.02	Zn/Se = 1.01	Zn/Se = 1.00	Zn/Se = 0.99	Zn/Se = 0.98
FWHM (arcsec)	90	70	60	19	108	154
EPD (cm^{-2})	2×10^7	5×10^6	6×10^6	2×10^5	9×10^6	1×10^7
Mobility ($\text{cm}^2 \text{V}^{-1} \text{s}^{-1}$)	370	342	322	—	—	—
Carrier Conc. (cm^{-3})	8.8×10^{17}	2.9×10^{17}	2.2×10^{17}	$< 1 \times 10^{12}$	—	1.8×10^{17}
Conductive type	n	n	n	n	—	p

the starting material can work as an active acceptor. On the other hand, it might also be a possible reason to lead to p-type ZnSe that the incorporation of a large number of added Se atoms in interstitial positions generates a more stable acceptor state. The more detailed mechanism will be clarified in future experiments. If ZnSe crystals with higher acceptor concentration is desired, acceptor impurities should be doped into the starting material of excess Se.

9.5.3.2 Growth from vapor phase

ZnSe single crystals were grown by the iodine transport method [96–99]. Typical growth temperatures and ΔT values were 1023–1223 K and 10–20 K, respectively. Koyama *et al.* [99] obtained ZnSe single crystals with values of FWHM of 6.2 arcsec and etch pit density (EPD) of $8 \times 10^2 \text{ cm}^{-2}$, respectively. This value is close to the ideal value of 4.5 arcsec [100]. Fujiwara *et al.* [101] grew ZnSe single crystals by the CVT method using iodine as the transport agent. The optimum growth temperature, seed orientation associated with the angle at the conical tip and iodine concentration were determined from the viewpoint of high growth rate and morphological stability. A ZnSe single crystal with 1 inch diameter was successfully grown under the determined growth conditions.

PVT is the most general method used for growing ZnSe single crystals. Kiyosawa *et al.* [102] grew ZnSe single crystals with the shape of a hexagonal prism constructed by {110} planes. They measured the transport rate as a function of Zn or Se partial pressure and compared it with the theoretical calculation. Experimental data obtained using a Zn reservoir are shown in Fig. 9.10. The transport rate is constant in the low- P_{Zn} region and starts to decrease with increasing P_{Zn} at the value of P_{Zn} corresponding to the minimum total pressure (P_{min}).

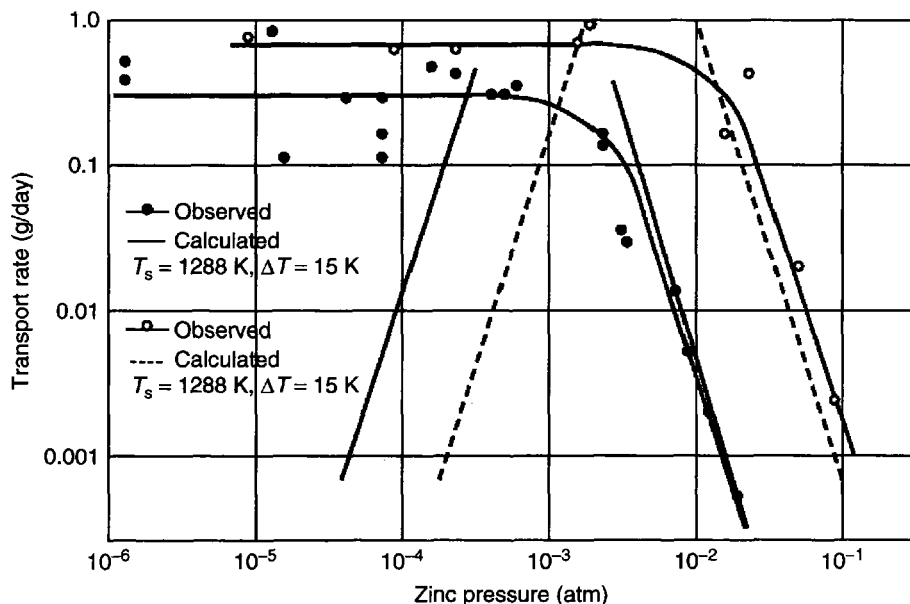


Figure 9.10 Relationship between transport rate and partial pressure of Zn

Assuming that the rate-determining process is a diffusion process caused by the difference in the vapor-phase composition between the source chamber and the growth chamber, they obtained the following equation to express the transport rate J for the Zn reservoir.

$$J = \frac{A \cdot P_{\text{Zn}}(KT_s - KT_c)}{[(P_{\text{Zn}}/2) - P_{\text{Se}_2}][P^3_{\text{Zn}} - 2KT_c]} \quad (9.5)$$

where J represents the transport rate (g day^{-1}), T_s and T_c the temperatures at the growth chamber and at the source chamber, respectively. K is the equilibrium constant of Equation (9.5). A is given by

$$A = 227S \cdot W \left[\frac{T^3(M_{\text{Zn}} + M_{\text{Se}_2})}{2M_{\text{Zn}} \cdot M_{\text{Se}_2}} \right]^{1/2} \frac{2}{N \cdot k \cdot T \Delta X (\sigma_{\text{Zn}} + \sigma_{\text{Se}_2})} \quad (9.6)$$

where S is the cross-sectional area of the ampoule, W the molar weight of ZnSe, M the molar weight of gas molecules, N the Avogadro number, k the Boltzmann constant, σ the molecular diameter and ΔX the distance between source chamber and growth chamber, T' is $(T_s + T_c)/2$.

When P_{Zn} is high and predominant in the total pressure, the measured transport rate is proportional to P^3_{Zn} . On the other hand, the transport rate is constant and independent of P_{Zn} . Calculated results are also showed in Fig. 9.10. Good agreement between experimental and calculated results in the high- P_{Zn} region indicates that the diffusion process is the rate-determining process and that the P_{Zn} can be controlled by the Zn reservoir in this region. On the other hand, this deduction cannot explain the experimental results in the region of P_{Zn} lower than that corresponding to P_{min} . In this region, another process should be the rate-determining process and the P_{Zn} cannot be controlled by the Zn reservoir. The P_{min} condition has been selected to grow single crystals, because this condition gives maximum growth rate in the region where the deviation from stoichiometric composition can be controlled.

Huang and Igaki [103] grew high-quality ZnSe single crystals, starting from the purification of the selenium. Before the synthesis, selenium was purified by a distillation method. ZnSe polycrystals were synthesized at about 1273 K by chemical reaction of commercial Zn (6N grade) with refined Se. Before growth, ZnSe polycrystals were purified by a sublimation method under a partial pressure corresponding to P_{min} . The growth temperature and ΔT were 1273 K and 3–5 K, respectively. They adopted necking in the growth ampoule and increased considerably the reproducibility of obtaining high-quality single crystals. The PL spectra measured on their crystals showed a strong emission due to the radiative recombination of free excitons and very sharp donor-bound exciton lines.

Isshiki *et al.* [104] purified zinc by a process consisting of vacuum distillation and overlap zone melting in pure argon. Using refined zinc and commercial high-purity Se, high-quality ZnSe single crystals were grown [105] by the same method as reported by Huang and Igaki [103]. The PL spectra near the band-edge region [106] are shown in Fig. 9.11. The emission intensities of donor-bound excitons (I_2) are remarkably small. The emission intensities of the radiative recombinations of free excitons (E_X) are very strong. These intensities indicated that the crystal had a very high purity and a very low donor concentration, and they suggest that purity of the grown crystal strongly depends on the purity of the starting materials. This method is suitable for preparing high-purity

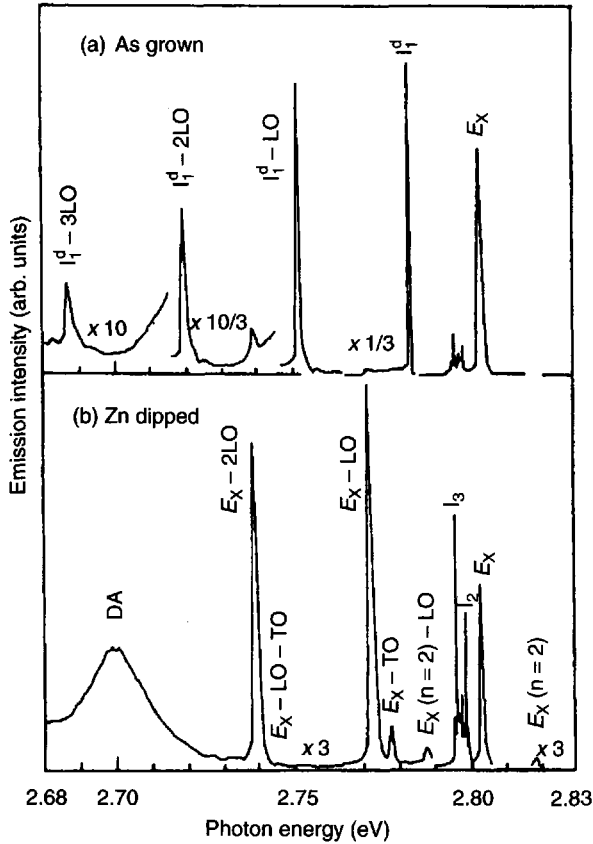


Figure 9.11 Band-edge emission of high-purity ZnSe grown by the PVT method

crystals, since a purification effect is expected during growth. Impurities with higher vapor pressure will condense at the reservoir portion and those with lower vapor pressure will remain in the source crystal. This effect was confirmed by the PL results [107]. In these crystals, photoexcited cyclotron resonance measurements have been attempted and cyclotron resonance signals due to electrons [108, 109] and heavy holes [110, 111] have been detected for the first time. The cyclotron mobility of electrons under $B = 7T$ is $2.3 \times 10^5 \text{ cm}^2 \text{ V}^{-1} \text{ s}^{-1}$. This indicates that the quality of the grown crystals is very high. Furthermore, the donor concentration in the crystal is estimated to be $4 \times 10^{14} \text{ cm}^{-3}$ by analyzing the temperature dependence of the cyclotron mobility [107].

9.5.3.3 Growth from solid phase

Terashima *et al.* [112] studied the grain growth of polycrystalline ZnSe by annealing starting materials in zinc or selenium atmospheres. It has been found that grains grew from $10 \mu\text{m}$ to 10 mm in diameter by annealing in a selenium atmosphere for two weeks at 1273 K , while samples annealed under zinc ambient grew up to 2 mm in size. The color of the crystals changed markedly; the selenium-annealed samples became pure

green, whereas those annealed under zinc ambient remained yellow. The residual impurity concentrations in the annealed samples measured by ICP (inductively coupled plasma) have been found to be less than those obtained by other techniques. These results show feasibility for application in optical devices. Wright [113] investigated the microstructure of ZnSe single crystal grown by SPR. Optical and scanning electron microscopy reveals the presence of considerable numbers of micrometer-sized tetrahedral-shaped features in the crystals. Micro-Raman spectroscopy reveals that these are crystalline selenium precipitates. TEM observation reveals a low dislocation density inner part of the bulk but much higher density in the vicinity of the surface.

Triboulet *et al.* [114–116] studied the SSR growth mechanism and the conditions of ZnSe single crystals in detail. CVD microcrystalline ZnSe was used as source material. SSR experiments were carried out under different pressure regimes at temperatures below 1373 K in order to reduce the contamination occurring at high temperature. Large single crystals ($\sim 20 \text{ cm}^3$) were obtained after annealing in 1273–1373 K for 20 days under Se partial pressures. On the other hand, the crystallization rate was found to be significantly reduced under a Zn vapor pressure. This can be explained by the fact that the solubility of ZnSe is high on the chalcogen side and very limited on the metal side [114]. The grain boundaries should be decorated by the fast-diffusing selenium during annealing under selenium pressure, and grain-boundary migration could then occur by some kind of solution growth on the microscopic scale. Besides, it has been thought that vacancies enhance migration and grain-boundary velocity. Zn vacancies created during the fast diffusion of Se could actively participate in the grain-boundary migration. Another interesting result in ref. [114] is that the growth rate of single crystal is influenced by the purity of starting materials. The growth rate is 10^3 times faster for the purer starting material than those of less pure materials [115].

The crystals grown by SSR showed good structural quality. Crystals with rocking-curve FWHM of 14 arcsec have been obtained [114, 116]. A dislocation density as low as 10^2 cm^{-2} was estimated from SEM observations and X-ray synchrotron measurements. The low-temperature PL spectra showed that I_1^d , I_1 , and free-exciton emission E_X were dominant [116, 117]. The as-grown SSR ZnSe crystals were found to be semi-insulating. After these single crystals were annealed in a mixture of Zn + Al at 1133 K [118], low-resistivity substrates with high structural quality were obtained. XRD rocking curves showed a FWHM of 35 arcsec, and the exciton peak was observed in cathodoluminescence (CL) spectra. Hall-effect measurement showed free-electron concentrations of $5 \times 10^{17} \text{ cm}^{-3}$, and an electron mobility of $200 \text{ cm}^2 \text{ V}^{-1} \text{ s}^{-1}$ (resistivity $6.3 \times 10^{-2} \Omega \text{ cm}$) at 300 K. These make it possible to achieve a conductive contact on the back face of devices. ZnSe layers grown by MBE onto these recrystallised substrates have been reported to have excellent structural perfection [119]. PL spectra showed that near-band-edge emission was dominant and no deep-level emission was observed [120].

9.5.4 ZnTe

9.5.4.1 Growth from liquid phase

Crystal growth from the melt of nearly stoichiometric composition was reported by Fischer *et al.* [121]. The crucible containing a melt with a slight excess of Zn was passed through a temperature gradient from about 1553–373 K in 5 h under 30–50 atm of argon pressure.

A transparent red ingot was obtained; this consists of crystals with average dimensions of 5–8 mm. Using the gradient freeze technique, Lynch [122] grew single crystals from a near-stoichiometric melt in a graphite crucible under controlled Zn pressure. The ingots were about 12 mm in diameter and 25 mm long. There were several runs where 80–90 % of the ingots were in the form of a single crystal.

Title *et al.* [123] reported crystal growth from solutions containing up to 50 % excess tellurium. The excess tellurium lowers the melting point to 1470 K so that unsupported quartz ampoules can be used without softening. Steininger and England [124] grew ZnTe single crystals with dimensions up to 35 mm × 20 mm × 10 mm from a Te-excess solution using a sealed quartz ampoule.

Sato *et al.* [125] used (0001) sapphire substrates as a seed material for the solution and melt growth of ZnTe crystal. The stability of the sapphire crystal allows successive growth from the melt just after the material is synthesized in the same crucible. Polycrystalline 6N ZnTe and 6N Te were used as starting materials. The crucible consisted of a graphite outer and a pBN inner tube. In the case of solution growth, the starting materials were charged in the crucible with the composition of Zn:Te = 3:7. The crucible was sealed in a vacuum quartz ampoule. The moving rate of the ampoule was 0.9 mm h⁻¹, and the temperature gradient was about 10 K cm⁻¹. In spite of lattice mismatch of 9.3 % between (0001) sapphire and (111) ZnTe, a crystal with a 25-mm diameter and 55-mm length was grown. At the bottom of the ingot, a single crystal of about 10 mm length was obtained. The remainder was polycrystalline material containing Te precipitates. Furthermore, crystals with 50 mm diameter were also grown on the sapphire substrates in the same growth conditions. Most of the crystal was single crystal.

In the case of melt growth, a high-pressure furnace was used [125]. A (0001) sapphire substrate with 50 mm diameter was used as a seed. 184 g of 6N Zn and 360 g of 6N Te metal were charged in the crucible with 40 g of B₂O₃. The crucible was heated to 1623 K and held for 20 h in order to obtain a uniform composition melt. Then, the temperature was lowered at a rate of 2.9 K h⁻¹ to 1373 K. The temperature gradient was about 18 K cm⁻¹. The furnace pressure was kept at 10 kg cm⁻² during growth. On the other hand, a single crystal with a length of 20 mm and with more than 70 % area of the grown crystal could be successfully grown. The FWHM of the XRD rocking curve was 20 arcsec. This value is half of the ZnTe single crystal grown from the solution. GDMS results showed that high-purity crystals, except for boron atoms, were formed. The most interesting result is that the lowest EPD was 2000 cm⁻². This is the lowest for ZnTe crystals with sufficiently large sizes for practical application. From the above results, this growth method is special, effective and hopeful.

Asahi *et al.* [126] grew ZnTe single crystals with a diameter of 80 mm and a length of 50 mm by the vertical gradient freezing (VGF) method. In this method, a high-pressure furnace was used and the melt was encapsulated by B₂O₃ during crystal growth. The growth direction was nearly (111) or (110). When long ZnTe crystals were grown, polycrystals were found at the tail. It seems to be difficult to grow on ingot longer than 50 mm. They thought that this is because the solid/liquid interface shape easily becomes concave against the liquid at the tail owing to the low thermal conductivity of ZnTe.

Furthermore, Asahi *et al.* [127] successfully grew ZnTe single crystals with 80 mm diameter and 40 mm length using a combination of GF and Kyropoulos methods (Fig. 9.12). In the growth process, a ZnTe seed was used to pull the ZnTe crystal. Before growth

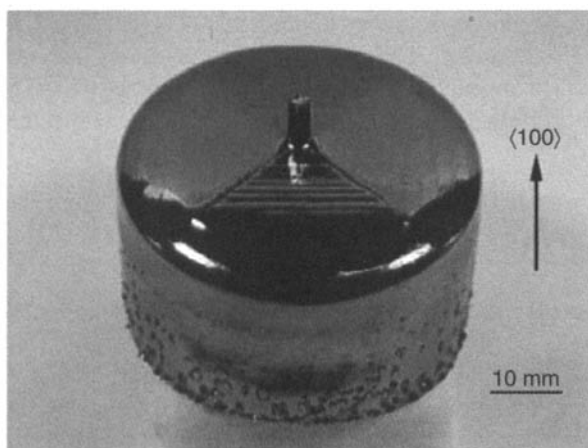


Figure 9.12 ZnTe single crystal grown by the method of the combination of GF and Kyropoulos methods

started, the starting materials were heated to 1573 K and held at this temperature for several hours. The pressure in the growth furnace was kept at 1.5–2 MPa using Ar gas during growth. The temperature gradient on the solid/liquid interface was about $10\text{--}20\text{ K cm}^{-1}$. The growth rate was $2\text{--}4\text{ mm h}^{-1}$. The characterisation of crystals showed that the FWHMs of the rocking curve measured by XRD were about 20 arcsec, and EPDs were $5 \times 10^3 - 1 \times 10^4\text{ cm}^{-2}$. The results show that the crystal has high quality.

9.5.4.2 Growth from vapor phase

Growth by CVT in the ZnTe-I₂ and ZnTe-Ge-I₂ systems was experimentally and thermodynamically studied by Kitamura *et al.* [128]. In the former system, they observed the simultaneous growth of Te crystals as well as ZnTe crystals and a decrease in transport rate with growth time below 1173 K. In this system, the convection flow greatly affected the transport process and caused deposition of Te. In the latter system, neither the growth of Te nor Ge inclusions was observed in the crystals grown. The transport rate of ZnTe was large enough and almost independent of the growth time. A large ZnTe crystal was grown at a relatively low temperature (937 K) in this system.

Taguchi *et al.* [129] used sublimation THM to grow high-purity ZnTe single crystals from the vapor phase. The temperature of the sublimation interface was fixed at 1080 K and that of the growth interface was varied from 1058 to 1073 K. The growth rate was 3 mm day^{-1} . The grown crystals showed the strong free exciton emission at 4.2 K in PL spectra. Te precipitates, which were often observed in ZnTe crystals grown by other methods, were hardly detected in the crystals in this study.

Korostelin *et al.* [130] grew twin-free ZnTe single crystals with diameters of 40–50 mm in sealed-off or quasi-closed quartz ampoules using PVT with He at $T = 1353\text{ K}$. To improve the crystal quality a small-area wafer ($1\text{--}2\text{ cm}^2$) was used as a seed. The best results were achieved under the conditions providing simultaneous growth in axial and radial directions with optimum growth rates of $30\text{--}50\text{ }\mu\text{m h}^{-1}$. The EPD of the ZnTe

wafers cut from the grown crystals was about $1 \times 10^4 \text{ cm}^{-2}$. The FWHM of the X-ray rocking curve was 18–22 arcsec. The Te precipitates observed in as-grown crystals were removed by post-growth annealing in liquid Zn or Zn vapor at 1073–1173 K. The removal of the Te precipitates correlated with the increase of the free-exciton emission line intensity in the CL spectrum.

9.6 CONCLUSIONS

Although great progress has been made in preparing II-VI bulk single crystals, there are still many problems to be solved. First, the basic properties should be explored further, especially phase diagrams. Secondly, in order to grow high-quality and large-diameter crystals from the melt, the component deviation from stoichiometry should be effectively controlled. Thirdly, reversion of conductivity type must be realized. For this reason, it is necessary to control the concentration of intrinsic defects. Meanwhile, acceptor or donor elements should be effectively doped into crystals. These are important study projects for further application of wide-gap II-VI compound semiconductors.

REFERENCES

- [1] Harmann, H., Mach, R. and Sell[†], B. (1982) In *Current Topics in Materials Science*, Vol. 9, (ed. Kaldis, E.), North-Holland Publishing, Amsterdam.
- [2] Rudolph, P. (1994) *Prog. Cryst. Growth Charact.*, **29**, 275.
- [3] Rudolph, P., Schäfer, N. and Fukuda, T. (1995) *Mater. Sci. Eng.*, **R15**, 85.
- [4] Shetty, R., Balasubramanian, R. and Wilcox, W.R. (1990) *J. Cryst. Growth*, **100**, 51.
- [5] Kulakov, M.P., Kulakovskii, V.D., Savchenko, I.B. and Fadeev, A.V. (1976) *Sov. Phys.-Solid State*, **18**, 526.
- [6] Ivanov, Yu.M. (1996) *J. Cryst. Growth*, **161**, 12.
- [7] Böer, K.W. (1990) in *Survey of Semiconductor Physics*, Vol. 1: *Electrons and Other Particles in Bulk Semiconductors*, Van Nostrand, New York.
- [8] Wolf, C.M., Holonyak, N. and Stillman, G.E. (1989) in *Physical Properties of Semiconductors*, (Prentice Hall, New York).
- [9] Smart, L. and Moore, E. (1995) in *Solid State Chemistry*, (Chapman & Hall: 2nd Edition).
- [10] *Handbook of Chemistry & Physics*, Edition 53 (CRC Press, 1972–1973).
- [11] Singh, J., (1993) in *Physics of Semiconductors and Their Heterostructures* (New York: McGraw-Hill).
- [12] Yamamoto, N., Horinaka, H. and Miyauchi, T. (1997) *Jpn. J. Appl. Phys.*, **18**, 225.
- [13] Neumann, H. (1980) *Krist. Tech.*, **15**, 849.
- [14] Camassel, J., Auvergne, D. and Mathieu, H. (1974) *J. Phys. Colloq.*, **35**, C3–67.
- [15] Shan, W., Song, J.J., Luo, H. and Furdyna, J.K. (1994) *Phys. Rev. B*, **50**, 8012.
- [16] Dmitrenko, K.A., Shevel, S.G., Taranenko, L.V. and Marintchenko, A.V. (1986) *phys. stat. sol. (b)*, **134**, 605.
- [17] Logothetidis, S., Cardona, M., Lautenschlager, P. and Garriga, M. (1986) *Phys. Rev. B*, **34**, 2458.
- [18] Sharma, R.C. and Chang, Y.A. (1988) *J. Cryst. Growth*, **88**, 192.
- [19] Okada, H., Kawanaka, T. and Ohmoto, S. (1996) *J. Cryst. Growth*, **165**, 31.
- [20] Hartmann, H., Mach, R. and Selle, B. (1982) in *Current Topics in Materials Science*, Vol. 9, (Ed. E. Kaldis) North-Holland, Amsterdam.
- [21] Shiloh, M. and Gutman, J. (1971) *J. Cryst. Growth*, **11**, 105.

- [22] Hassani, S., Tromson-Carli, A., Lusson, A., Didier, G. and Triboulet, R. (2002) *phys. stat. sol. (b)*, **229**, 835.
- [23] Prior, A.C. (1961) *J. Electrochem. Soc.*, **108**, 106.
- [24] Kiyosawa, T., Igaki, K. and Ohashi, N. (1972) *Trans. Jpn. Inst. Metal.*, **13**, 248.
- [25] Tairov, Y.M. and Tsvetkov, V.F. (1978) *J. Cryst. Growth*, **43**, 209.
- [26] Cantwell, G., Harsch, W.C., Cotal, H.L., Markey, B.G., McKeever, S.W.S. and Thomas, J.E. (1992) *J. Appl. Phys.*, **71**, 2931.
- [27] Korostelin, Yu.V., Kozlovsky, V.I., Nasibov, A.S. and Shapkin, P.V., (1996) *J. Cryst. Growth*, **161**, 51.
- [28] Tsujimoto, Y., Onodera, Y. and Fukai, M. (1966) *Jpn. J. Appl. Phys.*, **5**, 636.
- [29] Fukuda, T., Umetsu, K., Rudolph, P., Koh, H.J., Iida, S., Uchiki, H. and Tsuboi, N. (1996) *J. Cryst. Growth*, **161**, 45.
- [30] Holton, W.C., Watts, R.K. and Stinedurf, R.D. (1969) *J. Cryst. Growth*, **6**, 97.
- [31] Omino, A. and Suzuki, T. (1992) *J. Cryst. Growth*, **117**, 80.
- [32] Kikuma, I. and Furukoshi, M. (1985) *J. Cryst. Growth*, **71**, 136.
- [33] Rudolph, P., Umetsu, K., Koh, H.J. and Fukuda, T. (1994) *J. Cryst. Growth*, **143**, 359.
- [34] Wang, J.F., Omino, A. and Isshiki, M. (2000) *J. Cryst. Growth*, **214/215**, 875.
- [35] Wang, J.F., Omino, A. and Isshiki, M. (2001) *Mater. Sci. Eng. B*, **83**, 185.
- [36] Wang, J.F., Omino, A. Koo, B.H. and Isshiki, M. (1999) *Bulletin of the Institute for Advanced Materials Processing, Tohoku University*, **55**, 23.
- [37] Byrappa, K. (1991) *Hydrothermal Growth of Crystals*, (ed. Byrappa, K), Pergamon, Oxford.
- [38] Walker, A.C. and Buehler, E. (1949) *Sci. Monthly*, **69**, 148.
- [39] Laudise, R.A. and Ballman, A.A. (1958) *Sci. Monthly* **80**, 2655.
- [40] Klausutis, N., Adamski, J.A., Cillins, C.V. and Hunt, M. (1975) *J. Electron. Mater.*, **4**, 625.
- [41] Hobgood, H.M., Swanson, B.W. and Thomas, R.N. (1987) *J. Cryst. Growth*, **85**, 510.
- [42] Fischer, A.G. (1980) in *Crystal Growth* (2nd Edn.) Ed. Pamplin, B.M. (Pergamon, Oxford) p. 380.
- [43] Asahi, T., Arakawa, A. and Sato, K. (2001) *J. Cryst. Growth*, **229**, 74.
- [44] Triboulet, R. (2003) *Cryst. Res. Technol.*, **38**, 215.
- [45] Allen, E.T. and Crenshaw, J.L. (1912) *Am. J. Sci.*, **34**, 341.
- [46] Trigunyat, G.C. and Chadha, G.K. (1971) *phys. stat. sol. (a)*, **4**, 9.
- [47] Fitzpatrick, B.J. (1998) *J. Cryst. Growth*, **86**, 106.
- [48] Addamiano, A. and Dell, P.A. (1957), *J. Phys. Chem.*, **61**, 1020.
- [49] Addamiano, A. and Aven, M. (1960) *J. Appl. Phys.*, **31**, 36.
- [50] Ebina, A. and Takahashi, T. (1967) *J. Appl. Phys.*, **38**, 3079.
- [51] Washiyama, M., Sato, K. and Aoki, M. (1979) *Jpn. J. Appl. Phys.*, **18**, 869.
- [52] Linares, R.C. (1968) *Trans. Metall. Soc. AIME*, **242**, 441.
- [53] Parker, S.G. and Pinnell, J.E. (1968) *J. Cryst. Growth*, **3/4**, 490.
- [54] Samelson, H. (1962) *J. Appl. Phys.*, **33**, 1779.
- [55] Ujiie, S. and Kotera, Y. (1971) *J. Cryst. Growth*, **10**, 320.
- [56] Lendvay, E. (1971) *J. Cryst. Growth*, **10**, 77.
- [57] Dangel, P.N. and Wuensch, B.J. (1973) *J. Cryst. Growth*, **19**, 1.
- [58] Fujita, S., Mimoto, H., Takebe, H. and Noguchi, T. (1979) *J. Cryst. Growth*, **47**, 326.
- [59] Ohno, T., Kurisu, K. and Taguchi, T. (1990) *J. Cryst. Growth*, **99**, 737.
- [60] Hartmann, H. (1977) *J. Cryst. Growth*, **42**, 144.
- [61] Russell, G.J. and Woods, J. (1979) *J. Cryst. Growth*, **47**, 647.
- [62] Terashima, K., Kawachi, M. and Takena, M. (1990) *J. Cryst. Growth*, **102**, 387.
- [63] Yoneta, M., Uechi, H., Ichino, K., Yoshino, K., Kobayashi, H., Ikari, T., Ohishi, M. and Saito, H. (2000) *phys. stat. sol. (a)*, **180**, 183.
- [64] Lott, K., Anan'eva, G. and Gorokhova, E. (2000) *J. Cryst. Growth*, **214/215**, 894.
- [65] Yoneta, M., Ichino, K., Yoshino, K., Saito, H., Ohishi, M. and Kobayashi, H. (2002) *J. Cryst. Growth*, **237-239**, 1731.

- [66] Blount, B.H., Marlor, G.A. and Bube, R.H. (1967) *J. Appl. Phys.*, **38**, 3795.
- [67] Walker, A.C., J. (1953) *J. Am. Ceram. Soc.*, **36**, 250.
- [68] Laudise, R.A. and Ballman, A.A. (April, 1959) *American Chemical Society Meeting*, Boston, Mass.
- [69] Laudice, R.A., Kolg, E.D. and Caporaso, A.J. (1964) *J. Am. Ceram. Soc.*, **47**, 9.
- [70] Suscavage, M., Harris, M., Bliss, D., Yip, P., Wang, S.-Q., Schwall, D., Bouthillette, L., Bailey, J., Callahan, M., Look, D.C., Reynolds, D.C., Jones, R.L. and Litton, C.W. (1999) in *MRS Internet J. Nitride Semicond. Res.* **4S1**, G3.40.
- [71] Demianets, Lioudmila, N. and Kostomarov, Dmitriy V. (2001) *Ann. Chim. Sci. Mater.*, **26**, 193.
- [72] Sekiguchi, T., Miyashita, S., Obara, K., Shishido, T. and Sakagami, N. (2000) *J. Cryst. Growth*, **214/215**, 72.
- [73] Look, D.C. Reynolds, D.C., Sizelove, J.R., Jones, R.L., Litton, C.W., Gantwell, G. and Harsch, W.C. (1998) *Solid State Commun.*, **105**, 399.
- [74] Park, Y.S. and Reynolds, D.C. (1966) *J. Appl. Phys.*, **38**, 756.
- [75] Shiloh, M. and Gutman, J. (1971) *J. Cryst. Growth*, **11**, 105.
- [76] Piekarczyk, W., Gazda, S. and Niemyski, T. (1972) *J. Cryst. Growth*, **12**, 272.
- [77] Matsumoto, K., Konemura, K. and Shimaoka, G. (1984) *J. Cryst. Growth*, **71**, 99.
- [78] Matsumoto, K. and Noda, K. (1990) *J. Cryst. Growth*, **102**, 137.
- [79] Triboulet, R., N'tep, J.M., Barbe, M., Lemasson, P., Mora-Sero, I. and Munoz, V. (1999) *J. Cryst. Growth*, **198/199**, 968.
- [80] Look, D.C., Reynolds, D.C., Sizelove, J.R., Jones, R.L., Litton, C.W., Cantwell, G. and Harsch, W.C. (1998) *Solid State Commun.*, **105**, 399.
- [81] Eagle-Picher Technologies, News, 1999-9-10.
- [82] Nause, J.E. (2000) SBIR Phase II. Topic 14-Electronic Materials.
- [83] Kulakov, M.P., Kulakovskii, V.D., Savchenko, I.B. and Fadeev, A.V. (1976) *Sov. Phys.-Solid State*, **18**, 526.
- [84] Rudolph, P., Umetsu, K., Koh, H.J. and Fukuda, T. (1994) *Jpn. J. Appl. Phys.*, **33**, 1991.
- [85] Wang, J., Omino, A. and Isshiki, M. (2001) *J. Cryst. Growth*, **229**, 69.
- [86] Rudolph, P., Schäfer, N. and Fukuda, T. (1995) *Mater. Sci. Eng. R*, **15**, 85.
- [87] Tiller, W.A., Jackson, K.A., Rutter, J.W. and Chalmers, B. (1953) *Acta Metall.* **1**, 428.
- [88] Holton, W.C., Watts, R.K. and Stinedurf, R.D. (1969) *J. Cryst. Growth* **6**, 97.
- [89] Kikuma, I. and Furukoshi, M. (1978) *J. Cryst. Growth*, **44**, 467.
- [90] Yoshida, H., Fujii, T., Kamata, A. and Nakata, Y. (1992) *J. Cryst. Growth*, **117**, 75.
- [91] Shone, M., Greenberg, B. and Kaczynski, M. (1988) *J. Cryst. Growth*, **86**, 132.
- [92] Rudolph, P., Schäfer, N. and Fukuda, T. (1995) *Mater. Sci. Eng. R*, **15**, 85.
- [93] Wang, J.F., Omino, A. and Isshiki, M. (2001) *Mater. Sci. Eng. B*, **83**, 185.
- [94] Kikuma, I., Kikuchi, A., Yagata, M., Sekine, M. and Furukoshi, M. (1989) *J. Cryst. Growth*, **98**, 302.
- [95] Kamayama-Yoshida, H., Sasaki, T. and Oguchi, T. (1992) *J. Cryst. Growth*, **117**, 652.
- [96] Robinson, R.J. and Kun, Z.K. (1975) *Appl. Phys. Lett.*, **27**, 74.
- [97] Catano, A. and Kun, Z.K. (1976) *J. Cryst. Growth*, **33**, 324.
- [98] Poindessault, R. (1979) *J. Electron. Mater.*, **8**, 619.
- [99] Koyama, T., Yamashita, K. and Kumata, K. (1989) *J. Cryst. Growth*, **96**, 217.
- [100] O'Hara, S., Halliwell, M.A.G. and Childs, J.B. (1972) *J. Appl. Crystallogr.*, **5**, 401.
- [101] Fujiwara, S., Morishita, H., Kotani, T., Matsumoto, K. and Shirakawa, T. (1998) *J. Cryst. Growth*, **186**, 60.
- [102] Kiyosawa, T., Igaki, K. and Ohsashi, N. (1972) *Trans. J. Jpn. Inst. Met.*, **13**, 248.
- [103] Huang, X.M. and Igaki, K. (1986) *J. Cryst. Growth*, **78**, 24.
- [104] Isshiki, M., Tomizono, T., Yoshita, T., Ohkawa, T. and Igaki, K. (1984) *J. Jpn. Inst. Met.*, **48**, 1176.

- [105] Isshiki, M., Yoshita, T., Tomizono, T., Satoh, S. and Igaki, K. (1985) *J. Cryst. Growth*, **73**, 221.
- [106] Isshiki, M., Yoshita, T., Igaki, K. Uchida, W. and Suto, S. (1985) *J. Cryst. Growth*, **72**, 162.
- [107] Isshiki, M. (1988) *J. Cryst. Growth*, **86**, 615.
- [108] Ohyama, T., Otsuka, E., Yoshita, T., Isshiki, M. and Igaki, K. (1984) *Jpn. J Appl. Phys.*, **23**, L382.
- [109] Ohyama, T., Otsuka, E., Yoshita, T., Isshiki, M. and Igaki, K. (1985) in *Proc. of 17th Int. Conf. Physics of Semiconductors*, San Francisco, 1984 (eds D.J. Chadi and W.A. Harrison), Springer, Berlin, p. 1313.
- [110] Ohyama, T., Sakakibara, K., Otsuka, E., Isshiki, M. and Masumoto, K. (1987) *Jpn. J Appl. Phys.*, **26**, L136.
- [111] Ohyama, T., Sakakibara, K., Otsuka, E., Isshiki, M. and Igaki, K. (1988) *Phys. Rev. B*, **37**, 6153.
- [112] Terashima, K., Kawachi, M. and Takena, M. (1990) *J. Cryst. Growth*, **102**, 387.
- [113] Wright, A.C. (1999) *J. Cryst. Growth*, **102**, 387.
- [114] Triboulet, R., Ndap, J.O., Tromson-Carli, A., Lemasson, P., Morhain, C. and Neu, G. (1996) *J. Cryst. Growth*, **159**, 156.
- [115] Lemasson, P., Ndap, J.O., Fusil, S., Rivière, A., Qu'hen, B., Lusson, A., Neu, G., Tournié, E., Geoffroy, G., Zozime, A. and Triboulet, R. (1998) *Mater. Lett.*, **36**, 162.
- [116] Tournié, E., Morhain, C., Neu, G., Latügt, M., Ongaretto, C., Faurie, J.-P., Triboulet, R. and Ndap, J.O. (1996) *J. Appl. Phys.*, **80**, 2983.
- [117] Tournié, E., Morhain, C., Neu, Faurie, J.-P., Triboulet, R. and Ndap, J.O. (1996) *Appl. Phys. Lett.*, **68**, 1356.
- [118] Lemasson, P., Rivière, A., Didier, G., Tromson-Carli, A. and Triboulet, R. (1999) *J. Cryst. Growth*, **197**, 462.
- [119] Tournié, E., Morhain, C., Ongaretto, C., Bousquet, V., Brunet, P., Neu, G., Faurie, J.-P., Triboulet, R. and Ndap, J.O. (1997) *Mater. Sci. Eng. B*, **43**, 21.
- [120] Tournié, E., Brunet, P., Faurie, J.-P., Triboulet, R. and Ndap, J.O. (1996) *Appl. Phys. Lett.*, **69**, 3221.
- [121] Fischer, A.G., Carides, J.N. and Dresner, J. (1964) *Solid State Commun.*, **2**, 157.
- [122] Lynch, R.T. (1968) *J. Cryst. Growth*, **2**, 106.
- [123] Title, R.S., Mandel, G. and Morehead, F.F. (1964) *Phys. Rev.*, **136**, A300.
- [124] Steininger, J. and England, E.R. (1968) *Trans. Met. Soc. AIME*, **242**, 444.
- [125] Sato, K., Seki, Y., Matsuda, Y. and Oda, O. (1999) *J. Cryst. Growth*, **197**, 413.
- [126] Asahi, T., Arakawa, A. and Sato, K. (2001) *J. Cryst. Growth*, **229**, 74.
- [127] Asahi, T., Yabe, T. and Sato, K. (2003) *The Japan Society of Applied Physics and Related Societies, Extended Abstracts (The 50th Spring Meeting)*, p. 332.
- [128] Kitamura, N., Kakehi, M. and Wada, T. (1978) *Jpn. J Appl. Phys.*, **16**, 1541.
- [129] Taguchi, T., Fujita, S. and Inuishi, Y. (1978) *J. Cryst. Growth*, **45**, 204.
- [130] Korostelin, Yu.V., Kozlovsky, V.I. and Shapkin, P.V. (2000) *J. Cryst. Growth*, **214/215**, 870.

This page intentionally left blank

10 Sapphire Crystal Growth and Applications

V.A. TATARTCHENKO

'Saint-Gobain Crystals', 33 Powers Street, Milford, NH 03055, USA

10.1	Introduction	300
10.2	Sapphire structure	301
10.3	Sapphire crystal growth	302
10.3.1	Verneuil's technique (VT)	302
10.3.2	Floating-zone technique (FZT)	308
10.3.3	Czochralski technique (CzT)	310
10.3.4	Kyropulos technique (KT)	312
10.3.5	Horizontal Bridgman technique (HBT)	313
10.3.6	Heat-exchange method (HEM)	313
10.3.7	Techniques of pulling from shaper (TPS)	314
10.3.8	Flux technique (FT)	318
10.3.9	Hydrothermal technique (HTT)	319
10.3.10	Gas-phase technique (GPT)	319
10.4	Corundum crystal defects	319
10.4.1	Inclusions	319
10.4.2	Dislocations, low-angle grain boundaries, internal stresses	323
10.4.3	Twins	326
10.4.4	Faceting, inhomogeneities of impurity	326
10.4.5	Growth direction	327
10.5	Applications	327
10.5.1	Special windows	327
10.5.2	Domes	328
10.5.3	Substrates	329
10.5.4	Construction material	329
10.6	Brief crystal-growth technique characterization	329
10.6.1	VT	329
10.6.2	FZT	330
10.6.3	CzT	330
10.6.4	KT	330
10.6.5	HBT	330
10.6.6	HEM	330

10.6.7 TPS	330
10.6.8 FT, HTT, GPT	331
10.7 Conclusion	331
References	331
Appendix: sapphire physical properties	334

10.1 INTRODUCTION

Sapphire belongs to the family of corundum crystals. The corundum family of crystals incorporates all crystals of α -aluminum oxide. Pure corundum crystals are colorless and are named "leucosapphire." However, at present, these colorless corundum crystals are most commonly called "sapphire", even though historically the name "sapphire" has been applied to blue corundum.

Different colors of corundum can be obtained by the addition of small amounts of other metallic oxides. Natural and synthetic red ruby contains 1 to 7% chromium oxide. Synthetic alexandrite is produced by the addition of vanadium oxide. 1% titanium and 2% iron oxides give a blue color, while nickel oxide gives a yellow color. An addition of vanadium and cobalt oxides imparts a green color. Green crystals are also produced if the chromium content exceeds 8%.

Sapphire crystal is the main topic of the paper, but sometimes it is difficult to separate the development of sapphire and ruby technologies—there is a large influence of one on the other. Therefore we shall use the term corundum crystals throughout.

The development of many advanced fields in modern engineering is, to a large extent, governed by the success achieved in the techniques of crystal growth. On the other hand, the demand for new crystals for advanced technologies stimulated the improvements in growth techniques of these crystals. Certainly, this concerns only a few very important crystals.

Without any doubt, corundum is one of these because of its unique physical and chemical properties: high melting point, exceptional hardness, transmission over a wide band of wavelengths, radiation and chemical resistance, possibility to grow large crystals, etc.

The history of corundum crystals is a confirmation of the above thesis. It includes some important points:

- 1.1. From antiquity (a collection of genuine rubies was found in Paleolithic excavations) up to the 19th century, sapphire and ruby were known as natural gem crystals.
- 1.2. In 1837, very small artificial corundum crystals were grown by the flux-growth technique.
- 1.3. In 1891, August Verneuil suggested the method of artificial corundum crystal growth [1], which, since 1902, has become the commercial method [2]. The price of crystals had to decrease dramatically. But a solution was found, because of a possibility to discern natural and artificial crystals. Each type of crystal, natural and artificial, occupied its own niche. Natural ones continued to be used as gems. Artificial ones stimulated the development of new domains of corundum usage: cheap jewelry production, watches and some new industrial applications.

- 1.4. In 1960 the laser was invented. In the beginning, ruby was the main laser material. It gave a strong impulse to the development of the Verneuil and Czochralski techniques.
- 1.5. An application of sapphire as substrate material (1970s—silicon on sapphire, 1990s—substrates for laser diodes) stimulated the development of the Kyropulos and horizontal Bridgman techniques.
- 1.6. Shaped sapphire crystal growth (tubes, ribbons) stimulated the widespread application of sapphire as a construction material in microelectronics installations (1980s).
- 1.7. The necessity of large optical windows for aircrafts and spacecrafts in the 1990s stimulated the growth of very large crystals by the heat-exchange technique and gave new impulses for development of shaped-growth and horizontal Bridgman techniques.

10.2 SAPPHIRE STRUCTURE

Specific sapphire physical properties will be discussed below in connection with the particular sapphire application. Here we discuss only the crystallographic structure that we need for crystal growth.

Sapphire crystals belong to the trigonal system (class of symmetry ditrigonal-scalenohedral $-3m$). It has the following elements of symmetry: an axis of mirror rotation symmetry of the sixth order (this is why sapphire sometime is termed a hexagonal system) equal to a triple inversion axis, three axes of the second order, three planes of symmetry, and a center of symmetry [3].

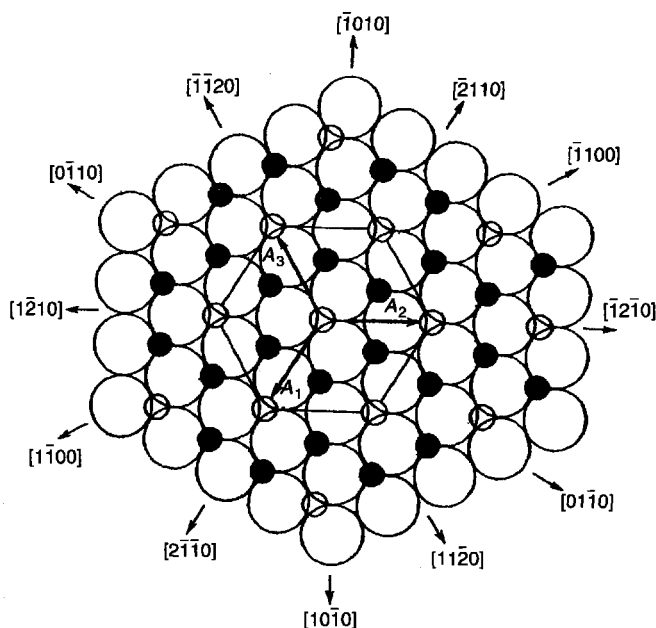


Figure 10.1 Structural diagram of crystal lattice of corundum, showing arrangement of aluminum ions (dots) and octahedral voids (small circles) between two layers of oxygen ions (large circles) in basal $\{0001\}$ plane (upper layer of oxygen ions not shown)

The crystal lattice of corundum is formed by bivalent oxygen ions and trivalent aluminum ions. As for the majority of oxides, the basis of the sapphire structure can be presented as a hexagonal close-packing structure of oxygen ions. The aluminum ions are set in the octahedral voids between the close-packed oxygen ions. They fill two-thirds of these voids, thus forming the so-called corundum motif (Fig. 10.1). The identity period for a hexagonal sapphire lattice determined along the axis of the third order by six layers of oxygen ions and six intermediary layers of aluminum ions.

The parameters of the crystal lattice for hexagonal cells are: $a = 4.748 \pm 0.004 \text{ \AA}$, $c = 12.957 \pm 0.001 \text{ \AA}$,

The main planes and the perpendiculars of these directions are denoted by letters:

$$C\{0001\}, m\{10\bar{1}0\}, a\{11\bar{2}0\}, q\{20\bar{2}5\}, r\{10\bar{1}1\}, t\{40\bar{4}1\}, R\{01\bar{1}2\}, \\ S\{02\bar{2}1\}, P\{11\bar{2}3\}, n\{22\bar{4}3\}, l\{21\bar{3}1\}, w\{11\bar{2}1\}.$$

The fusion temperature of sapphire is 2050°C .

It is important to mention that the *C*-plane has the lowest growth speed in corundum crystals and, as a result, for many techniques the *C*-axis is the most difficult direction of growth.

10.3 SAPPHIRE CRYSTAL GROWTH

Many techniques are now used for sapphire bulk-crystal growth. We propose the following classification of growth techniques:

A. *Melt growth - no-container techniques:*

- 3.1. Verneuil technique (VT).
- 3.2. Floating-zone technique (FZT).

B. *Melt growth - container techniques:*

- 3.3. Czochralski technique (CzT).
- 3.4. Kyropulos technique (KT).
- 3.5. Horizontal Bridgman technique (HBT).
- 3.6. Heat-exchange method (HEM).
- 3.7. Techniques of pulling from shaper (TPS).

C. *Nonmelt growth:*

- 3.8. Flux technique (FT).
- 3.9. Hydrothermal technique (HTT).
- 3.10. Gas phase technique (GPT).

10.3.1 Verneuil's technique (VT)

10.3.1.1 Principal scheme of growth

Figure 10.2 illustrates VT crystal growth. Fine powder of the material from which a crystal is to be grown, is fed into a burner with an oxyhydrogen flame. The powder melts

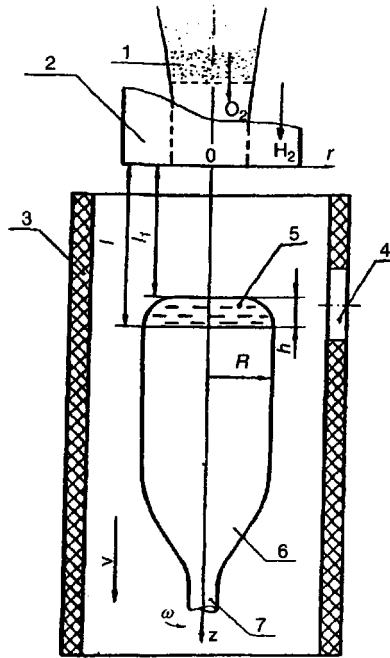


Figure 10.2 Verneuil technique scheme: 1—Stock bin; 2—burner; 3—furnace thermal insulation; 4—view port; 5—melt layer; 6—crystal; 7—seed; R —crystal radius; l_1 —melt surface position relative to the burner; $h = l - l_1$ —melt meniscus height; $z0r$ —coordinate system; V —displacement rate; ω —crystal rotation rate

partially or completely, forming a melted layer on the surface of the seed crystal. The crystal grows in the process of consecutive melt crystallization as a result of sinking the crystal into the colder zone.

Up to the middle of the 20th century this technique was mainly used to grow precious crystals 20 mm in diameter. The equipment, corresponding to the scheme in Fig. 10.2, was very simple because of the absence of special requirements for the crystal quality. But the application of ruby crystals for laser elements changed the situation dramatically.

It is clear why VT was the most widely used technique for laser-element production. The main advantage of VT is the absence of a crucible and, as a result, absence of contamination of a crystal by the crucible material. But it was necessary to increase the crystal dimensions and to improve the crystal quality. This was achieved by modification of the equipment. A modern VT furnace includes: the application of several oxygen and hydrogen channels for more homogeneous burning of hydrogen, preliminary heating of the gases, special heating of the furnace thermal isolation, and automatic growth control.

10.3.1.2 Raw material

Alumina powder is used for corundum crystal growth by VT. The pure aluminum oxide is α -alumina. The different extent of hydration gives γ -alumina, β -alumina, and so on. For instance, γ -alumina is $5Al_2O_3 \cdot H_2O$. Both α - and γ -alumina can be used for crystal growth. The powder has to be extremely fine with sizes of particles from 1 to 20 micrometers. A

widely used scheme of powder fabrication includes:

- Purification of alum by recrystallization.
- Decomposition of alum by heating. The optimal temperature of heating to obtain α -alumina is 1000 °C.

10.3.1.3 Modified VT

We have a need to grow the combination of ruby-sapphire crystals: a ruby crystal with sapphire ends. In this case it is necessary only to change the feeding with either doped or undoped raw material.

Some patents, where significant increases of the dimensions of crystals were achieved, are cited in the review [4]. With respect to the author's statement, the scheme in Fig. 10.3a, using rotation of the seed crystal around the horizontal axis, allowed a single-crystal sapphire disc up to 180 cm² to be obtained; the scheme in Fig. 10.3b with reciprocating motion of the seed crystal in relation to the gas burner allowed plates about 70 cm² in size to be produced; and in the model in Fig. 10.3c a split burner was used to grow crystals in the shape of plates up to 240 cm² in size. Our experience allows us to assert that all the schemes mentioned have problems with cracking of crystals because of internal tension connected with periodic changing of the temperature for each crystal volume and inhomogeneous temperature distribution in the growth zone.

There are VT versions using plasma [5], laser, radiation, Ir resistive heating. However, they do not have a large application.

10.3.1.4 Theoretical investigation of the crystal-growth process by VT (common approach)

Our attention in some experiments was turned to the fact that the growth of corundum crystals of small diameters ~ 5 mm (they are grown especially as seed crystals) was easy. Practically, the growth regime did not need any correction by an operator. The crystals had smooth surfaces and cylindrical shapes. This stimulated our studies on the VT dynamic stability investigation [6–8].

In the technique under consideration the crystal is not restricted by crucible walls, its cross section depends upon the growth parameters. Any deviations of temperature,

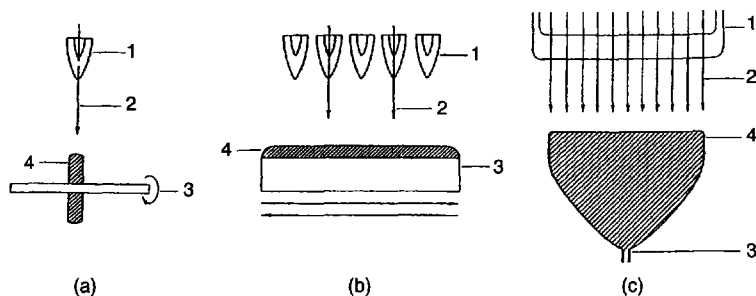


Figure 10.3 Features of the methods for producing corundum crystals of large area: 1—flame; 2—direction of supply of initial powder; 3—crystal nucleus; 4—growing crystal

powder feeding, speed of seed lowering result in crystal cross-sectional changes, in a pinch formation.

It is experimentally found that an increased amount of inclusions, nonuniform impurity distributions, subgrain formation are observed at the pinch locations. The pinches themselves do not seem to cause defect formation, but a change in the crystal dimensions indicates some deviations of the growth conditions (mainly, the crystallization rate) from the optimal ones. From this point of view, constant cross-sectional crystal growth is, to a certain extent, evidence of the dynamic stability of the crystallization process. Therefore, the problem of crystal cross-sectional stabilizations arises. The VT stabilization problem proved to be solvable by a theoretical investigation of the dynamic crystallization-process stability and by selecting on the basis of this analysis such crystallization schemes and conditions that will ensure growth of controlled cross sections of crystals.

10.3.1.5 Dynamic stability of crystallization

For the first time a comparative analysis of dynamic stability of the crystallization process was carried out by this author for CzT and TPS [9]. We strictly recommend using the Lyapunov approach of stability analysis [10] that is now developed in detail for many techniques of growth, VT included. A reader can find the analysis in detail in [6–8]. Here we present the common approach and the main results.

With respect to Lyapunov all the systems under consideration have to be characterized by a finite number, n , of the main variables (degrees of freedom), X_i , that can vary arbitrarily. Thus, for the VT they will include (Fig. 10.2): crystal dimension (for cylindrical round crystal diameter $2R$); the distance between the burner face and the crystallization front l , the liquid/gas interface position l_1 . Consequently, this technique has three degrees of freedom.

In order to grow a crystal of constant cross section, stabilization of the above-mentioned parameters should be provided during the crystallization process. Here stabilization of the crystallization front position means that the crystallization rate should be equal to the crystal lowering rate at any moment, i.e. no random changes of the crystallization rate can be observed.

Naturally, such stabilization can be provided by means of automatic control systems. At the first stage of the analysis our objective is to ensure stabilization of the parameters specified using the internal potentialities of the system and only when such a possibility is not available to find the law of control that can ensure crystallization process stability. It is necessary to mention that growth in the stable regime does not always give a possibility to obtain the crystals with a low level of internal stresses. Sometimes stable growth can be realized only under high temperature gradient conditions. This question has to be specially analyzed.

A set of equations for derivation of each degree of freedom X_i with respect to time t as functions f_i of all others $n - 1$ degrees of freedom X_1, \dots, X_{n-1} and parameters of the process (temperature of melt, velocity of pulling, etc.) has to be obtained for a mathematical analysis of dynamic stability. It can be done on the basis of: a) the Laplace capillary equation and the growth angle ψ_0 (Fig. 10.6) constancy condition; b) the continuity equation (the law of crystallizing substance mass conservation); c) the heat-transfer equations for the liquid and the solid phases with the equations of heat balance at the crystallization front as the boundary conditions (the law of energy conservation).

The limited volume of this chapter does not allow us to give further details about the theoretical model. A reader can find them in [6–8]. Let us note some peculiarities of the problem formulation for VT and the main practical recommendations.

When formulating the heat problem for crystal growth from melts, as a rule, the melt temperature on a fixed point is specified as the boundary condition. This boundary condition for the VT does not correspond to the real situation. Crystal displacement in the furnace muffle results in melt temperature change on its surface. Specificity of the heat conditions of the technique under consideration will be allowed for by specifying the density Q of the heat flow fed from the burner onto the surface of the melted layer.

With the gas flow specified, the density of the heat flow Q depends on the distance between the burner and the level of the melt surface $Q(l)$. The function $Q(l)$ is determined by the burner design and the gas debit.

10.3.1.6 Practical results of the theoretic analysis

Round cylindrical crystals. For the process to be stable the following three conditions have to be fulfilled:

- The diameter of the crystal, $2R$, has to be less than two capillary constants for the sapphire melt. Capillary constant $a = (2\gamma/\rho g)^{1/2}$. Here γ denotes the sapphire melt surface-tension coefficient, ρ denotes melt density, g relates to the gravity acceleration. For sapphire $a = 6$ mm.
- Change in the heat-flow density $Q(l)$ along the furnace muffle in the vicinity of the growth zone at a distance of an order of R should not exceed the crystallization heat.
- The heat-flow density value $Q(l)$ in the vicinity of the growth zone has to be decreased if the distance between the melt surface and the burner is increased.

So, we can see that for the cylindrical round sapphire crystals of large diameters (> 12 mm) stable dynamical growth conditions are impossible. But on the other hand, the theoretical model allows a minimizing of the crystallization process perturbations while growing large-diameter crystals.

For this, the previous two conditions have to be fulfilled (evidently, without the crystal-dimension limitation) and also:

- The temperature of a muffle wall has to be increased.
- Any irregularity of the density distribution of the charge flow falling on the melted layer has to be decreased.

These requirements of the crystallization conditions are in good agreement with our experiments regarding the optimal growth conditions [11, 12]. In the experiments, such hydrogen- and oxygen-flow debits in a three-channel burner meant that a crystal grown closer to the burner had a larger diameter. This condition corresponds to the heat-flow density increasing when approaching the burner. Preheating the gas before feeding it into the burner and increasing the furnace muffle temperature were also used. Crystals grown under these conditions exhibited a smoother surface and improved optical and structural characteristics.

Plate-shaped corundum crystals. The theoretical results are applicable for the growth of plate-shaped crystals: crystal plates of less than two capillary constants thick (12 mm) have to grow stably.

Tube-shaped corundum crystals. The theoretical analysis states: Crystallization of tubes of arbitrary outer diameter is stable if the tube wall thickness is smaller than some critical thickness. This thickness is smaller than the capillary constant (6 mm) and depends both on the heat conditions of the process and on the outer radius of the tube. This crystal thickness of the tube wall increases with the increase in the outer diameter.

10.3.1.7 Crystal growth in the stable regimes

Cylindrical crystals. The result of the theoretical investigation explains why growth of corundum crystals of small diameters (~ 5 mm) is easy, why they have smooth surfaces and cylindrical shapes. They grow in the dynamically stable regime—there are internal mechanisms for dissipation of perturbations.

Tubes. In our experiments (Fig. 10.4) tubes with an outer diameter of 17 to 25 mm, 120 mm long and with walls 3 to 4 mm thick were grown. A crystallization apparatus fitted with a four-channel burner providing charge supply via the central and periphery channels was used. The reader can find all the details of the growth process in [13].

10.3.1.8 Stability-analysis-based automation of VT

As was shown above, when moving to crystals with diameters exceeding the two capillary constants crystallization stability is lost. Practically this means that the crystallization-front position and crystal dimensions are changed. In this case, an operator controls the parameters by changing the gas debit, charge feed and crystal lowering rate using his experience and intuition.

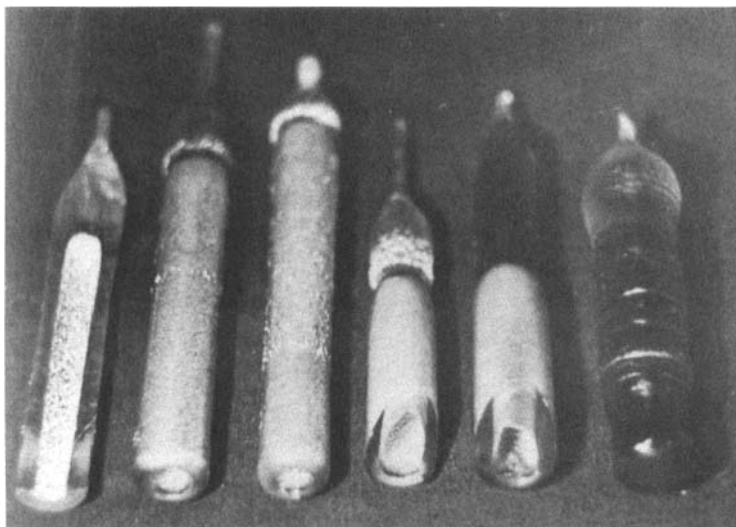


Figure 10.4 Corundum single-crystal tubes grown by author with collaborators from Solid State Physics Institute of Academy of Sciences of Russia by VT in stable regime

An automatic system of control provides better results. When developing systems of growing crystals with automatic diameter control, a problem of the laws of automatic control of the process parameters under some changes in crystal dimensions arises. Up to the publication of our paper [14] the required laws of parameter control were defined from the results of empirical searches.

In [14] it was shown that the theoretical derivation of the laws of process-parameter control ensuring maintenance of the specified crystal cross section can be performed on the basis of the crystal-growth stability analysis. In this instance the controllable parameters side by side with the crystal diameter, the liquid/gas interface position and the melt meniscus height can be treated as the degrees-of-freedom of the crystal-growth process. For VT the density of the heat flow from the burner Q , (this is regulated by changing the gases debit P), the rate of crystal lowering V and the charge flow rate W can be used as control parameters. Usually, P as well as W are used as control parameters at the stage of crystal widening. But after the crystal has already widened from the seed dimension up to the desired diameter, the control is provided by W regulation. In our approach W has to be regarded as an additional (4th) degree-of-freedom. But coefficients of the linear equation for W are unknown. They have to be found from the necessary and sufficient conditions of the set of 4 equations of stability. The problem can have a few solutions. Each solution can be used as the regulation law in the regulation system. In this case our system of crystal growth, including the regulator, has to be stable.

In [14] three different W change laws, which allowed stable growth, were found (Fig. 10.5).

10.3.2 Floating-zone technique (FZT)

The FZ technique (Fig. 10.6) is a second possibility of crystal growth without a crucible. It is widely used for semiconductor and metal crystal growth. RF current direct heating of the melting zone is used in this case. The low electrical conductivity of sapphire even at high temperature requires very high frequency and preliminary heating (see 'cold crucible' below). This is not easy to do. Probably, this is one reason why there are many examples of unusual heat sources being used for corundum FZ growth. Here are some of them.

In [15] preparation of oxide crystals (sapphire included) by the FZ technique has been carried out with heating by a plasma in an oxygen environment (pressure 1 mm Hg). Using a hollow cathode, crystals of 3 mm diameter and 25 mm length have been grown.

In [16] electron-beam heating with a movable tungsten cathode and a stationary crystal in vacuum have been used. Crystals of 4.4 mm diameter and 60 mm length, with a growth speed of 8 cm h^{-1} have been grown.

In [17] resistance heating by an Ir ribbon in an argon–oxygen or a nitrogen–oxygen environment has been used. A ribbon-shaped conductor penetrated the molten zone. In the region of the molten zone, the ribbon was net-like perforated. An additional stability of the molten zone has been fixed because of the ribbon. Crystals of 15 mm diameter and 10 mm length have been grown with the speed of growth $6\text{--}12 \text{ mm h}^{-1}$ and the speed of rotation $10\text{--}12 \text{ rpm}$. In reality, it is not a container-free technique and Ir inclusions have been detected in the crystals.

In [18] radiation heating by a tungsten resistance loop wire in an argon environment has been used. Crystals of 6 mm diameter and 60 mm length have been grown with the growth speed 1.4 cm h^{-1} . It is interesting that crystals of very difficult C -orientation were grown.

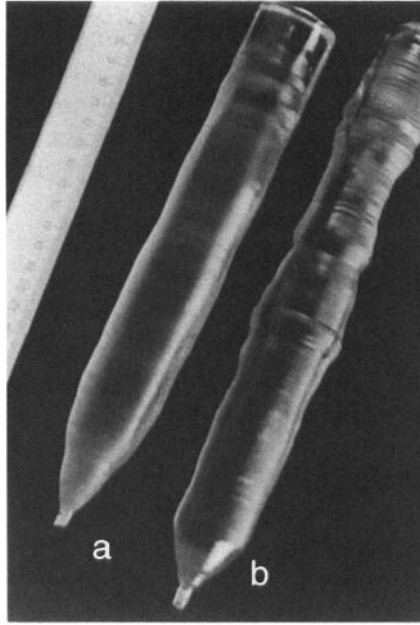


Figure 10.5 Corundum crystals grown by author with collaborators from Solid State Physics Institute of Academy of Sciences of Russia and Institute of Crystallography of Academy of Sciences of Russia in stable (a) and unstable (b) laws of charge control

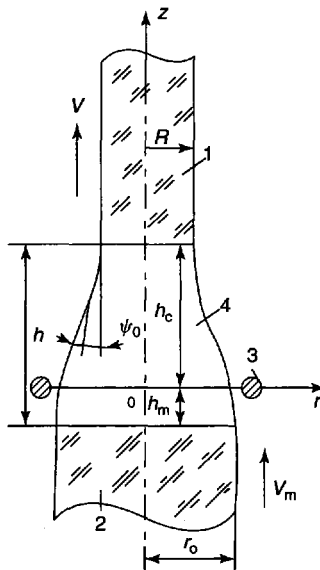


Figure 10.6 Floating-zone technique scheme: 1—growing crystal with radius R ; 2—feeding rod with radius r_0 ; 3—heater; 4—melted zone of volume W ; h_c and h_m —positions of crystallization front and melting front relative to the heater, respectively; ψ_0 —growth angle, V —rate of growing crystal displacement; V_m —the same for melting rod; zOr —coordinate system

In [19] radiation heating by a CO₂ laser in air has been used. The laser of 400 W power allowed crystals of 5 mm diameter and 80 mm length to be grown at a speed of 15 mm h⁻¹ and orientation 0°, 60°, 90° (the angle between the *C*-axis and the growth direction). The crystal quality depended on the application of an additional coaxial heating source, by which the radial and axial temperature gradients were essentially reduced. Under these conditions the crystals were practically free of strain and did not tend to crack, even if unannealed.

In [20] radiation heating by a xenon lamp was used. The lamp of 3.5 kW power has allowed the growth of crystals of 12 mm diameter and 50 mm length at a speed of growth of 0.5–4 cm h⁻¹. Different environments for growth were used: vacuum, air, nitrogen, argon. The growing crystal and the feed rod were rotated with different rates in the same or in opposite directions.

The feed-rod preparation is very important in FZT. The procedure of feed-rod preparation, described in [20], was based on standard ceramic technology. Alumina powder, α -alumina or γ -alumina, with a purity of 99.99% was mixed with dopant if necessary for ruby growth. The well-mixed powder was pressed at 1.0 ton cm⁻³ and sintered for ten hours. The density of sintered rods at 1450°C was about 3.3 g cm⁻³ and that at 1700°C about 3.9 g cm⁻³.

In [6–8] theoretical analysis of FZT dynamic stability was carried out as a system with 4 degrees-of-freedom (Fig. 10.6): $2R$ —growing crystal diameter, h_c and h_m —positions of crystallization front and melting front relative to the heater, respectively, U —the volume of the melting zone.

10.3.3 Czochralski technique (CzT)

CzT is representative of crucible methods (a cold-crucible technique is excluded). Where CzT is used, crystals grow from the melt free surface onto the seed being pulled upwards (Fig. 10.7). The main CzT characteristics are: the crystal rotation and lift; a stationary crucible (in principle, the crucible can be raised but we did not find any information concerning utilization of this possibility for corundum crystals); RF, resistance or plasma heating; large melt volume; moderate temperature gradients; crystal unconfined; large crystals obtained.

This technique has been known since 1918. But it has been used for corundum crystals production only since the 1960s [21–23]. As was mentioned in the Introduction, the application of this technique for corundum and its consequent development was stimulated by the invention of the laser. In particular, from the crystals obtained in [23] laser rods were fabricated. In [17] crystals of good quality 100 mm long by 15 mm diameter were grown at pull rates of 6 to 50 mm h⁻¹.

On the basis of [24] and a few later papers, we estimate the status of the corundum growth by CzT in the middle of the 1970s as the following: iridium or tungsten as crucible material; RF or very rarely resistive heater; sometimes, resistive after-heater using nitrogen, argon or vacuum environment; the speed of growth 1–2.5 cm h⁻¹; the speed of crystal rotation 10–60 rpm; the growth directions *a*, *C*, and *n*; the raw material mass 8 kg; the crystal dimensions 70 mm diameter and 300 mm length or 25 mm diameter and 600 mm length.

The most significant advance made in the CzT of refractory materials has been the application of automatic diameter control. Either crystal- or crucible-weight systems can

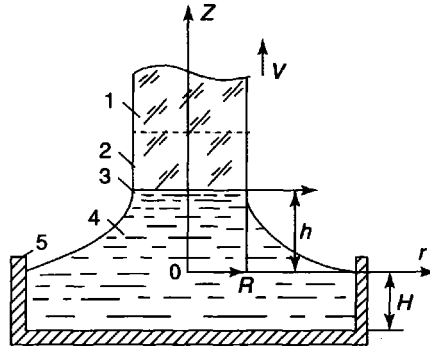


Figure 10.7 Czochralski technique scheme: 1—seed; 2—growing crystal with the radius R ; 3—crystallization front and melting front of height h ; 4—melt; 5—crucible, V —crystal pulling rate; H —melt level in crucible; zOr —coordinate system

be used. Both of them allow programming of crystal diameter increasing from the seed to the required full diameter and then pulling of a controlled-diameter crystal. The first system is preferable because at the stage of crystal widening it is more sensitive.

A distinct achievement has been the successful growth of some oxide single crystals (corundum included) using a cold crucible. According to this technique, material is melted in a large water-cooled container by direct coupling of RF (Fig. 10.8) [25]. The main advantage of the technique is an absence of melt contact with any crucible material. The electrical resistivity of solid sapphire is 22×10^3 ohm cm at 1875°C and that of the melt is 0.1 ohm cm at 2200°C . As a result, the frequency necessary for effective heating of molten alumina is 1 to 10 MHz. The problem is to heat the raw material to the melting temperature. It is possible to use supplementary heating, but the best result is achieved by partial substitution of the cation as metal into the charge. In practice, small pieces of aluminum are placed in the raw material. The RF generator melts the metallic particles and the surrounding powder. The metal is oxidized by the air and does not contaminate the melt. Sapphire crystals up to 35 mm diameter and 160 mm length were grown.

In [6, 7] theoretical analysis of CzT dynamic stability was carried out as a system with 2 degrees-of-freedom (Fig. 10.7): $2R$ —growing crystal diameter, h —position of

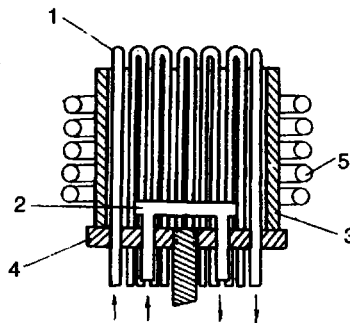


Figure 10.8 A cold-container scheme: 1—water-cooled copper loops; 2—water-cooled bottom; 3—insulating ceramic tube; 4—Teflon or mica support; 5—RF coil

crystallization front. The main conclusion is the following. It is difficult to grow crystals of small (less than 12 mm) diameter because of the absence of capillary stability (remember the situation here is opposite to VT). The dynamically stable growth for the large-diameter crystals can be provided by corresponding heat regimes.

10.3.4 Kyropulos technique (KT)

KT (Fig. 10.9a) was developed thirty years ago [26] and continues to be used as one of the main industrial growth techniques of good optical quality large sapphire crystals. From the point of view of improving crystal quality, KT has the following main advantages: the growth of crystals in vacuum; use of one or a few necking steps to avoid seed defects; use of low temperature gradients in the crystallization zone; using the same zone within the crucible for annealing the crystals. The significant difference in KT, compared with CzT, is the fact that the crystals do not travel in the higher gradient zone above the crucible during growth and annealing.

The simple and inexpensive resistance furnaces with tungsten heaters ‘Omega’ were developed in Russia for KT. The industrial production of more than 300 mm diameter crucibles from an alloy containing 70 % Mo and 30 % W was also developed for KT. Now in industrial production, there are three types of furnaces, for 7, 14 and 25 kg crystals. The duration of the largest crystal growth run is two weeks. From our point of view, the KT is one of the best industrial techniques of sapphire crystal production: The crystals have large dimensions and good optical quality (if good quality raw material is used); growth stations are simple and inexpensive (the weight sensors are not used); crucibles serve for many years.

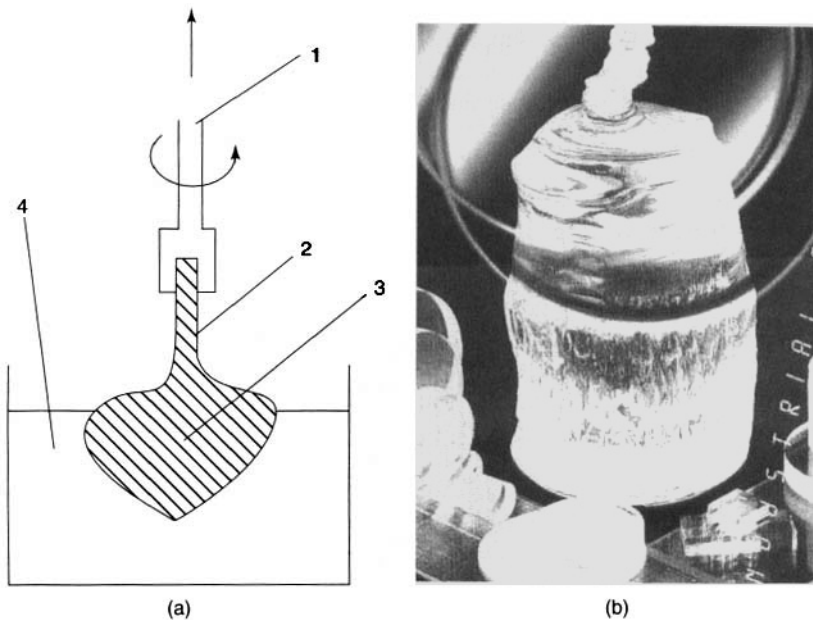


Figure 10.9 (a) Kyropulos technique scheme: 1—rotating and pulling shaft; 2—seed; 3—growing crystal; 4—melt. (b) View of KT crystal

Figure 10.9b from one of the Russian sites on the Internet shows typical crystals grown by KT.

10.3.5 Horizontal Bridgman technique (HBT)

HBT (Fig. 10.10) was developed thirty years ago [27] and continues to be used now in industrial sapphire crystal production. The main idea of HBT is the production of sapphire single crystal plates with a large surface area. This aim was achieved by developing resistance furnaces with molybdenum or tungsten heaters. The crystal growth is realized in flat molybdenum boats. A container filled with aluminum oxide moves at the rate of about 10 mm h^{-1} through the heating zone in a horizontal direction, thus combining the elements of directed crystallization and zone melting. The growth can be realized with or without a seed. In the last case the crucible shape (Fig. 10.10) allows point nucleation. HBT possesses the advantage that the crystallization is carried out under conditions facilitating the evaporation of extraneous impurities. As a result the chemical purity of the crystals is enhanced on average by one order of magnitude compared to the raw material. The plates have a typical size: $170 \times 170 \times 35 \text{ mm}$ (weight about 5 kg). It is easy to obtain plates of *C*-orientation by HBT because in this case *m*, *a*, or an intermediate direction perpendicular to *C*-axis is a direction of growth.

10.3.6 Heat-exchange method (HEM)

HEM is based on directed crystallization by cooling the melt under the conditions of a specific temperature gradient [28]. The crystal is grown in a molybdenum crucible the bottom of which is cooled by blowing gas (Fig. 10.11). The growth is carried out in a graphite resistance furnace in a vacuum 10^{-3} torr. The temperature is reduced during the growth process. The speed of crystal growth is about 10 mm h^{-1} . During the process of HEM growth, the crystal has contact with the crucible—with the bottom at the beginning and with the walls at the end.

The HEM was developed for the production of large sapphire crystals of good optical quality. Here is a progress report in the crystal dimensions grown by HEM: Crystals in the form of discs up to 70 mm in diameter and to 20 mm thick were grown in the first experiments [28, 29]. Crystals up to 200 mm diameter were produced by 1975 [30] and up

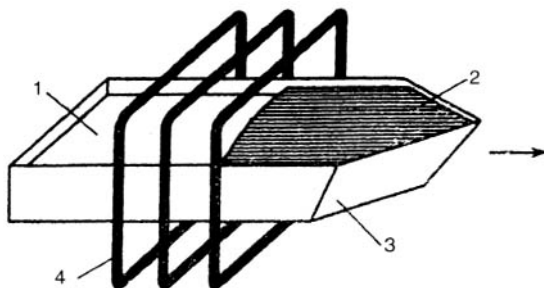


Figure 10.10 Horizontal Bridgman technique scheme: 1—melt; 2—crystal; 3—container; 4—heater

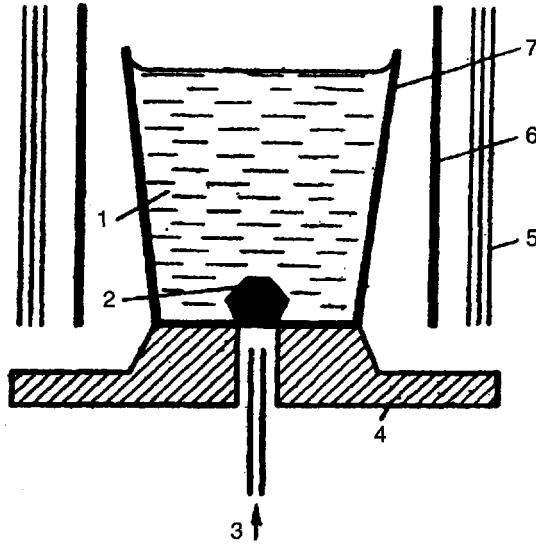


Figure 10.11 Heat-exchange method scheme: 1—melt; 2—crystal; 3—gas inlet; 4—pedestal; 5—radiation shields; 6—heater; 7—crucible

to 340 mm diameter have been available for production since 1996. In 1999 three experimental growth runs demonstrated the feasibility of producing 500-mm diameter sapphire boules. Completely crack-free boules have not been grown, but large-size sapphire pieces up to 400×280 mm have been yielded from these experimental runs [31].

In reality, HEM is a variant of the vertical Bridgman technique VBT. There are some other modifications of VBT—the temperature gradient technique TGT [32] and the gradient solidification method GSM [33]. The last technique was successfully used for dome growth by shaping of the crucibles. We will combine all the techniques mentioned in HEM because of the larger HEM industrial use.

10.3.7 Techniques of pulling from shaper (TPS)

10.3.7.1 Shaped crystal growth

Modern engineering usually uses corundum crystals as plates, rods, tubes or more complicated shapes. There is a loss of expensive material as well as a loss of much time during machining of crystals to obtain a required shape—corundum can be machined only with a diamond tool at very low speed. Therefore, corundum crystals of specified size and shape with controlled defect and impurity structure that allows using them as the final products, with minimal or no additional machining, are preferred.

Now both theoretical and practical aspects of shaped sapphire crystal growth are developed [6, 7]. We have shown above the possibility of growth of shaped corundum crystals by, for instance VT. But the main technique of shaped corundum crystal growth is pulling from the shaper (Fig. 10.12).

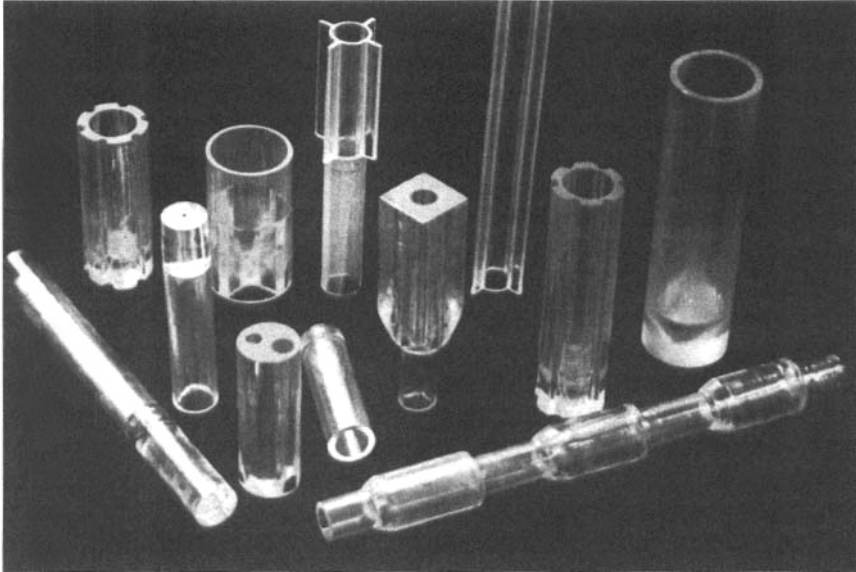


Figure 10.12 Monocrystalline sapphire profiles grown by TPS and VST by the author with collaborators in the Solid State Physics Institute of Academy of Sciences of Russia

10.3.7.2 Technique of pulling from the shaper TPS

The pulling of shaped crystals is carried out by a technique that differs from CzT by the presence of a shaper at the melt surface (Fig. 10.13). The priority in applying holes in plates placed onto the melt surface for shaping melt-pulled crystals belongs to Gomperz [34]. Due to methodical work carried out by Stepanov [35] and his collaborators (the author of this chapter was one of them for some time), the technique was developed for various materials. LaBelle [36] was the first who grew shaped sapphire crystals.

We can find in the literature for shaped crystal growth a technique named the Stepanov technique, EFG—edge-defined film fed growth, CAST—capillary-action shaping technique, and several others. The authors prefer using the different names without serious analyses of the peculiarities of the technique used with respect to others.

In fact, the main idea of all these techniques is to limit the area and the value of liquid-free surface perturbations. As was shown for the first time in [37] only two possibilities can be used for shaping—edges or walls of a shaper. This means that in the theoretical analysis two different boundary conditions have to be used: the fixing of a line on the surface of the meniscus by the edges of the shaper or the fixing of the angle of wetting between the melt and the wall of the shaper. Certainly, each scheme used can be characterized by special design features: 1. Pulling up or down; 2. Using for the shaping only the walls (Fig. 10.13a, f), only the internal edges (Fig. 10.13b, d), only the external edges (Fig. 10.13e, j) or combinations thereof (Fig. 10.13c, g, h, i) with positive (Fig. 10.13b, g) or negative (Fig. 10.13d, e, h, i, j) pressure of the melt; 3. Using a capillary feeding of the zone of growth by the melt (Fig. 10.13d, e, i, j) and so on. We

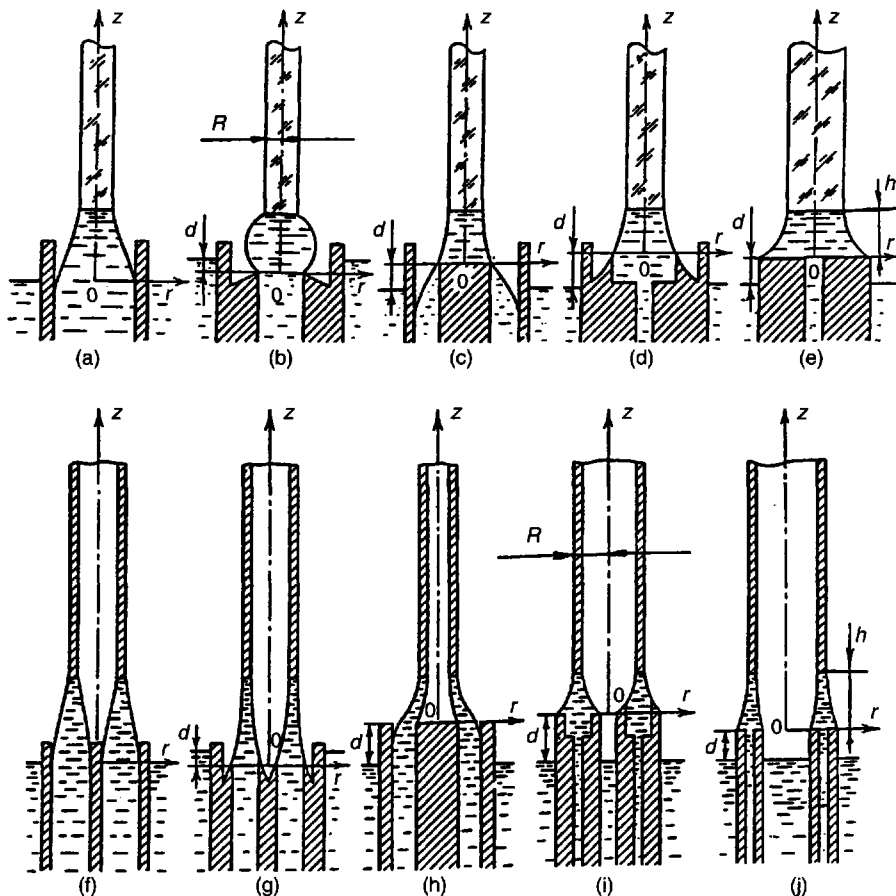


Figure 10.13 Some schemes of pulling from shaper of crystalline rod (a–e) and a tube (f–j) at various melt pressure (d) R —crystal radius, h —crystallization front height

suggested [6, 7] combining all these techniques by using a common title, TPS—techniques of pulling from shaper.

The dimensions and the shape of the specimens being pulled by TPS depend on the following factors: *first*, shaper design; *secondly*, the pressure of feeding the melt to the shaper; *thirdly*, the interface position with respect to the shaper that depends on the rate of pulling and thermal conditions (for this reason, it is not advisable to use the term ‘die’ instead of the term ‘shaper’ as is often done; for the extrusion die strictly determines the profile cross section). A seed shape, as a rule, is not important because it only characterizes the length of the intermediate zone from the seed used to the shape of the crystal characterized by the three above-mentioned factors.

10.3.7.3 Modified TPS

The presence of the shaper in TPS allows realization of some manipulations during the growth process. The variable shaping technique VST [38] allows changing the cross

section of the crystal (periodically if necessary) during pulling. VST is based on controlling the melt mass flow towards the crystallization interface when passing to a new specific cross-sectional shape. In this case, different shaping elements of the same shaper, its free edges or walls, operate by turns. This can be done, for instance, by changing the immersion depth of the shaper in the melt. One of the variants of TPS from [39, 40] is shown in Fig. 10.14. At the beginning, the scheme gives the possibility to change the crystal cross section by changing the feeding as a result of a vacuum formation under the seed. At the same time the scheme from [39] uses periodically different crucibles for feeding that allows changing the doping concentration in the different parts of the crystal.

The scheme of the local shaping technique LST [41] is shown in Fig. 10.15. The horizontal displacement of the seed and shaper with respect to each other in combination with rotation and pulling of the seed allows a variety of shaped crystals (for instance, a dome with thin walls to be obtained).

There is a very interesting modification of TPS used especially for dome growth [42]. There the seed is rotated around a horizontal axis.

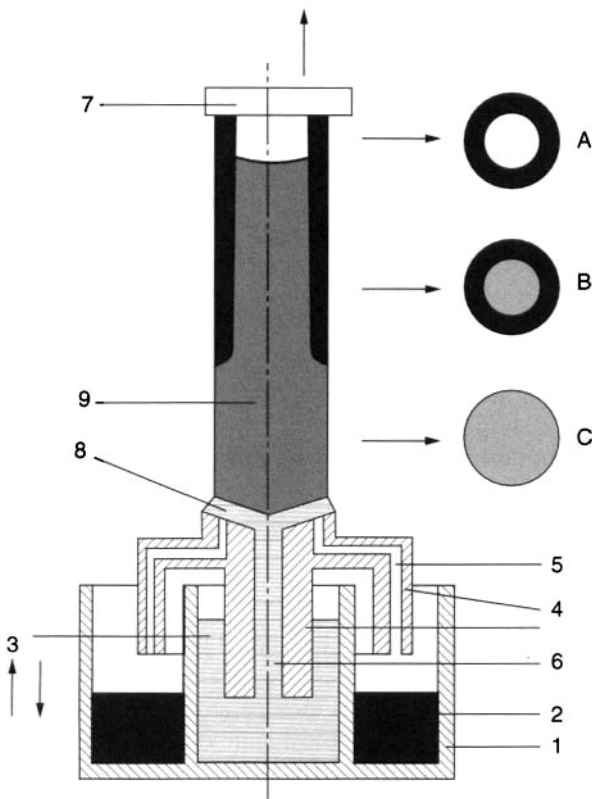


Figure 10.14 Variable composition rod growing scheme: 1—crucible; 2—undoped melt; 3—doped melt; 4—shaper; 5—capillary-feeding channel; 6—noncapillary-feeding channel; 7—seed; 8—meniscus; 9—growing crystal; A, B, C—cross sections of the different parts of the growing crystal

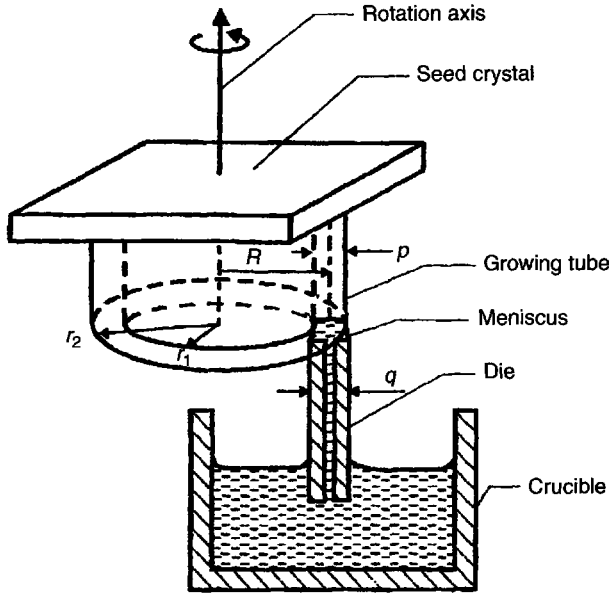


Figure 10.15 Local shaping technique scheme

10.3.7.4 Dynamic stability of TPS

As was mentioned above, for the first time a comparative analysis of dynamic stability of crystallization process was carried out for CzT and TPS [9]. The simplest analysis of CzT and TPS includes crystal dimension $2R$ and crystallization-front position h as degrees-of-freedom, i.e. these techniques have two degrees-of-freedom.

The results of TPS stability analysis show a) *capillary stability* that depends on a scheme of formation of melt meniscus and b) *heat stability* that depends on a temperature distribution at a zone of growth play the main role in providing the dynamic stability. The capillary stability is absent in CzT. The significant advantage in TPS, compared with CzT, is the fact that different designs of the shaper allow the presence of capillary stability as well as that of heat [6, 7].

10.3.7.5 Static stability of the meniscus

Together with the dynamic stability of the crystal-growth process a static stability of the meniscus has to be provided. The presence of a static stability means that the melt meniscus exists for all values of crystallization parameters. An analysis of static stability of the meniscus for TPS together with the dynamic one is carried out in [43].

10.3.8 Flux technique (FT)

The FT is growth of crystals from a nonaqueous solution. As a rule, a mixture of salts is used as a solvent. FT of corundum crystals growth does not have an industrial application.

But for the first time in 1837, Gaudian grew corundum crystals by heating a powdered alumina and potassium sulfide mixture in a crucible covered with charcoal. Only small crystals (probably β - Al_2O_3) were obtained. Another variant of FT is presented in [44]. A mixture of lead, boron, and aluminum oxides and lead fluorine was heated in a platinum crucible to a temperature of about 1350°C until aluminum-oxide dissolution. Crystallization proceeds spontaneously or on a seed during cooling of the mixture to 900°C at the speed of $1^\circ\text{C}/\text{h}^{-1}$. The essential advantage of the process is the relatively low temperature. The disadvantages are a very low growth speed controlled by diffusion (one to two orders lower than from the melt) and the difficulties of obtaining a large crystal (the maximal crystal dimension—plates up to 30 mm).

Single crystals of corundum from cryolite (Na_3AlF_6) flux were grown by spontaneous nucleation, stationary seed, seed-rotation and top-seed-rotation techniques at 1100°C [45]. The maximal dimension of the crystals up to 50 mm was obtained by the seed-rotation method [46].

10.3.9 Hydrothermal technique (HTT)

Corundum crystal are second (after quartz) in terms of size that are grown by HTT. The technique is based on the increased solubility of aluminum oxide in aqueous solutions at elevated temperatures and pressures. Aqueous solutions mainly of Na_2CO_3 , KCO_3 , NaHCO_3 , KHCO_3 , NaOH are used as solvents for aluminum oxide. The growth process is carried out in autoclaves lined with silver or platinum. The temperatures of 400 to 700°C and pressures to 3500 atm are used [47]. Crystals of some kg weight were grown [48]. Industrial application is difficult because of low growth speed (the same order as for FT).

10.3.10 Gas-phase technique (GPT)

Corundum crystal growth from the gas phase was observed for the first time in 1887 during heating of aluminum fluoride in the presence of water. The reaction [49] is:

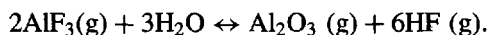
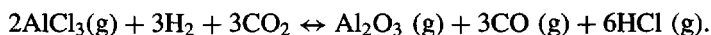


Plate-shape crystals were obtained at a temperature of 800°C .

In [50] the following reaction was used:



The temperature of reaction was 1550 to 1750°C . The crystals were grown on a corundum substrate. The speed of the growth was 0.2 mm h^{-1} . Clearly, the speed is too low for serious industrial production.

10.4 CORUNDUM CRYSTAL DEFECTS

10.4.1 Inclusions

10.4.1.1 Bubbles are the major defects in corundum crystals. Practically, there is no technique to produce corundum crystals bubble free. This is why bubbles are analyzed in

detail. There are two aspects of the problem concerned with bubbles in crystals. The first is an enrichment of the melt by gas and bubble formation in the melt. The second is the capture of the bubbles by the grown crystal.

A vacuum treatment of the melt before the crystal growth reduces the bubble content in the crystals. This is proof that a dilution of gases in the melt is one of the sources of its gas enrichment. But there is a more important gas source for the corundum melt. In spite of the aluminum oxide being stable under normal conditions, its heating is accompanied with thermal dissociation, evaporation of some reaction products and coagulation of others. Mass spectroscopic analysis shows [51] that the products of dissociation of aluminum oxide are O^+ , O_2^+ , Al^+ , AlO^+ , Al_2O^+ , AlO_2^+ , $Al_2O_2^+$. The intensity of thermal dissociation depends greatly on the temperature and environment. It is most intensive if hydrogen is present, less intensive in vacuum and the least intensive in inert atmospheres (argon, nitrogen).

One of the first bubble-formation processes in VT corundum crystals was concerned with the gas adsorption on the surface of feeding-powder particles. But the hypothesis is at variance with the following experimental fact. The γ - Al_2O_3 powder is more friable than α - Al_2O_3 and, therefore, adsorbs more gas on the surface. But corundum crystals grown from γ - Al_2O_3 charge have fewer bubble inclusions. So, the charge dissociation has to be the main reason for bubble formation, and α - Al_2O_3 powder is worse because of sticking of α - Al_2O_3 particles.

The presence of a container complicates the situation. Although the problem is not completely understood at this time, the thermal dissociation of the melt because of the chemical interaction of the melt with the crucible material seems to be a very important cause of the gas appearance in the melt. Here is the list of chemical activity of the main container materials for sapphire crystal growth (from the best to the worst): Ir, W, Mo, Nb, Ta, Zr. As a rule, only the first three materials are used for containers. The reaction of Al_2O_3 with refractory metals is generally believed to involve two stages. For example, with Mo: $Al_2O_3 \rightarrow Al_2O + O_2$; $Mo + O_2 \rightarrow MoO_2$. In reality, the presence of the above-mentioned aluminum-oxide dissociation products greatly complicates the situation. Mass spectroscopic measurements point to the presence of MoO , MoO_2 , and MoO_3 ions.

The diluted gases and the gas products of the above-mentioned reactions are impurities in the melt and assist gas-inclusion formation in the crystals. Here are two possibilities. (a) As a rule, dilution of gases decreases with the temperature. The liberated gases form the bubbles. The crystal catches the bubble that exists in the melt. (b) A nuclear bubble forms on the interface, grows and is caught by the crystal.

The surface-energies estimation [20] deduced that the interface is not an effective heterogeneous site for bubble formation. We agree that this deduction is correct for a flat interface but cavities on the interface can be effective bubble-nucleation sites. In any case, the melt layer near the interface has to be preferable for the bubble formation because of enrichment of the diluted gas rejected by the growing crystal. Direct experiments of the melted-zone quenching [52] improved this mechanism of bubble formation.

As with other impurities, bubbles can form striations, parallel to the interface. The striations are concerned with variations of growth rate and capture of the bubbles situated in the melt layer near the crystallization front. Sometimes it is a result of constitutional supercooling.

Sometimes, long tubes similar to bubbles can be found in corundum crystals. A mechanism of this type of bubble formation is suggested in [53, 54].

In each case, the pits on the interface, formed as a result of loss of morphological stability, initiate bubble capture, especially for high growth rates. In our experiments [6, 7, 55] with ribbons and tubes grown by TPS in the *C*-direction the following results were obtained.

At the crystallization rate of order of 0.2 mm min^{-1} bubbles were absent. In [56] the critical growth rate (0.5 mm min^{-1} for sapphire) has been calculated below which a foreign particle is not trapped by the grown crystal. The interface is planar below this rate.

At crystallization rates of $0.75\text{--}1.5 \text{ mm min}^{-1}$ the bubble distribution is in the shape of a tree-like pile-up with a branch diameter of up to 1 mm (Fig. 10.16). The ends of the ribbon are bubble free, probably because of gas diffusion to the melt surface and loss

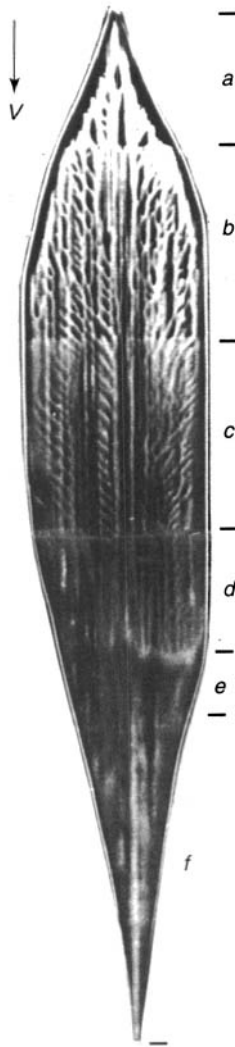
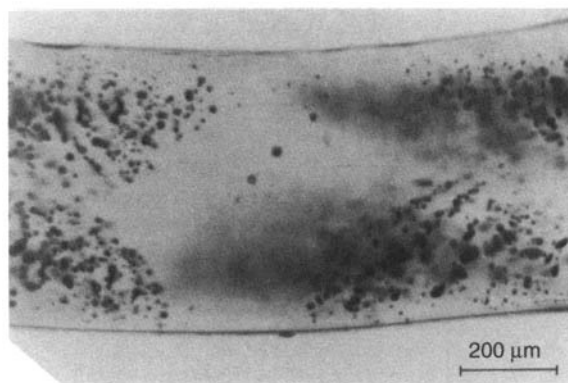


Figure 10.16 Sapphire ribbon pulled with step rate V change: $\rightarrow V$ —growth direction, $V \text{ mm min}^{-1} =$ (a) 0.75; (b) 1.0; (c) 1.25; (d) 1.5; (e) 1.75; (f) 2.0

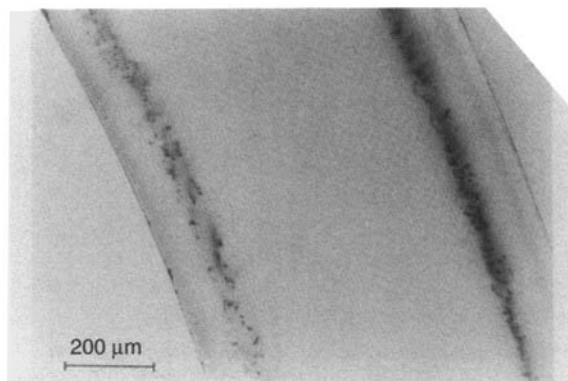
from the melt. The same result was obtained in [20] where small-diameter crystals were bubble free.

The distribution of bubbles over a specimen section normal to the growth direction is shown in Fig. 10.17a,b. The following explanation is proposed for the observed bubble distribution. The plane interface becomes morphologically unstable. Macroscopic concavities, with a diameter up to 1 mm, arise on the crystallization front; these concavities are characterized by an enhanced trapping of bubbles. We suppose that the change of position of the concavities on the crystallization front with time depends on the pattern of the convective flows in the melt that leads to the bubble distribution shown in Figs. 10.16 and 10.17a. This process is in accordance with the Mullins and Sekerka [57] theory for the lowest frequencies [6, 7]. When growing shaped sapphire crystals at rates of 1 to 3 mm min⁻¹ the interface has, as a rule, a convex central part and concave peripheral sections that traps the bubbles (Fig. 10.17b).

As the growth rate is increased further, the entire solid/liquid interface becomes unstable. The crystallization front becomes faceted, with the new interface shape becoming stabilized by the faceting. Figure 10.18 shows the decanted crystallization front of a tube faceted by rhombohedral planes. The bubble distribution in the crystal is a hexagonal



(a)



(b)

Figure 10.17 Cross section of sapphire ribbon pulled with rate V mm min⁻¹ = (a) 0.75; (b) 2.0

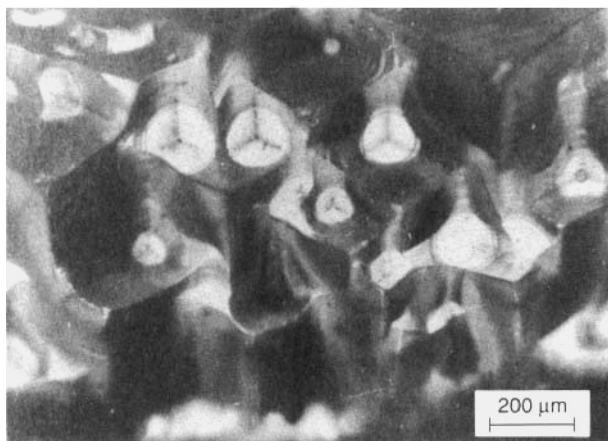


Figure 10.18 Interface of decanted sapphire ribbon grown at a rate of 3 mm min^{-1}

pattern and corresponds to the positions of grooves on the interface. The bubble agglomerations always correspond to cavity positions. The decanted crystallization front of a tube faceted by the $\{11\bar{2}0\}$ and $\{10\bar{1}1\}$ planes is shown in Fig. 10.19a. From geometrical considerations (Fig. 10.19b), it is apparent that the angle γ between the crystal pulling direction and the direction of the band of void pile-up depends on the ratio of the growth rates of the two mentioned faces.

10.4.1.2 Solid inclusions

These are the second type of inclusions. The container material produces metal-particle inclusions, sometimes as a result of the complicated chain of chemical reactions mentioned above—volatile oxide formation, gas transport in the melt and decomposition of oxides with metal-inclusion formation. Experiments show that the small particles of the container metal (Ir, Mo), as a rule, are present in crystals grown from the melt. Small Pt plate-shaped inclusions are found even in flux-grown crystals at temperatures of $1100\text{--}1300^\circ\text{C}$.

Innumerable experimental data demonstrate that the density of small (about $10 \mu\text{m}$) inclusions (bubbles and metal particles) is a few orders of magnitude greater than that of large (about $1000 \mu\text{m}$) ones. The low growth speed and low gradients favor crystal growth with minimum inclusions. KT meets the requirements to a major extent.

Here is an example (American 80/50 standard) of bubbles and solid inclusions requirement for window-grade corundum: maximal allowable size is $500 \mu\text{m}$, and maximal allowable sum of diameters within any 20-mm diameter circle is $1000 \mu\text{m}$. As a rule, KT, CzT, HEM, TPS, HBT material all meet this requirement.

10.4.2 Dislocations, low-angle grain boundaries, internal stresses

Four possible mechanisms of dislocation appearance in corundum crystals can be postulated: 1) intergrowth from seed; 2) formation on rough defects (inclusions, grain boundaries, twins) during growth; 3) condensation of vacancies during growth and cooling; 4) plastic deformation during growth and annealing.

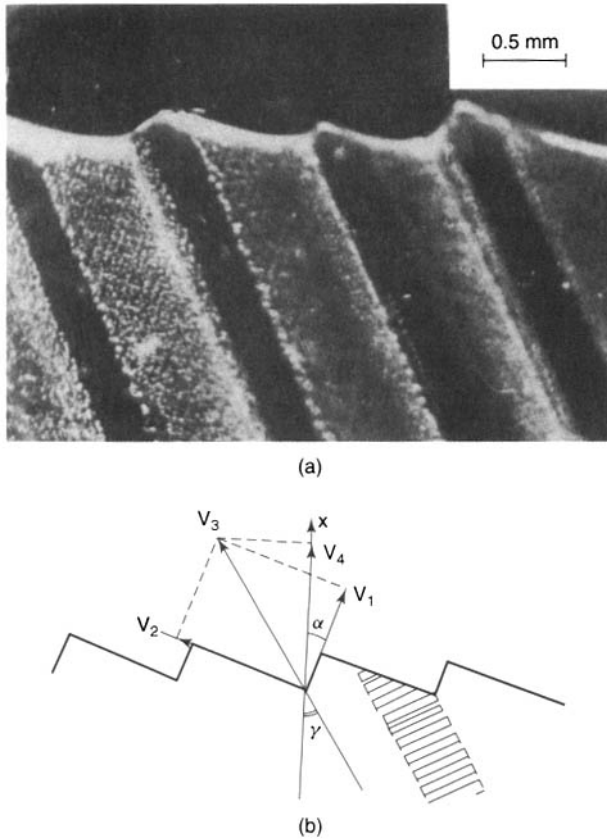


Figure 10.19 (a) View and (b) schematic of the decanted crystallization front of a tube pulled at a rate greater than 5 mm min^{-1}

Theoretically, all dislocations can be identified. The dislocation identification of the first and the second types is obvious. The third type of dislocations, as a rule, have a circular shape because they are a result of collapse of flat round discs obtained by a condensation of nonequilibrium vacancies. The geometry of the last type of dislocations depends on two plastic deformation glissile systems $\{0001\} \langle 11\bar{2}0 \rangle$ and $\{11\bar{2}0\} \langle 10\bar{1}0 \rangle$ in the corundum crystals.

The first source can be eliminated by neck formation, the second one by crystal growth without rough defects. The third mechanism is concerned with a fundamental physical phenomena, but their density is not significant for corundum crystals. As to the plastic deformation, it is a main source of dislocations in corundum crystals [32].

Here is our estimation of the dislocation density in as-grown corundum crystals (on the basis of numerous experimental data): HTT, VT $10^5 - 10^7 \text{ cm}^{-2}$; FZT 10^5 cm^{-2} ; HBT, TPS $10^4 - 10^5 \text{ cm}^{-2}$; HEM 10^4 cm^{-2} , CzT 10^4 cm^{-2} in the center of crystals and 10^2 cm^{-2} at the periphery; FT $10^3 - 10^2 \text{ cm}^{-2}$; KT $10^3 - 10 \text{ cm}^{-2}$.

Certainly, the dislocation density is a relative characteristic of crystals because the crystal quality can be characterized only taking into account, as a minimum, six dependent parameters: (a) The dislocation density; (b) The density of low-angle boundaries; (c) The

degree of subgrain disorientation; (d) Residual stresses value; (e) Twins; (f) Impurity inhomogeneities. Here is an example, confirming this thesis. The main source of dislocations and internal stresses in HTT crystals is the inclusions, deforming the crystal lattice. As a rule, in HTT and VT crystals the density of dislocations is comparable but residual stresses in HTT crystals ($\sim 20 \text{ kg mm}^{-2}$) are higher than in VT crystals ($\sim 10 \text{ kg mm}^{-2}$) because of the difficulty of the stress relaxation in HTT crystals at the low ($\sim 550^\circ\text{C}$) temperature of growth in comparison with the plasticity range ($> 1000^\circ\text{C}$). During annealing, at the beginning, the dislocation density of both crystals is increased because of deformation (yield point for 1850°C is $\sim 4 \text{ kg mm}^{-2}$). But the resulting quality of HTT crystals, as a rule, is worse.

The defect structure of crystals grown from the melt, flux and gas phase is formed as a result of complex interactions of growth, in situ annealing and cooling. Let us examine two examples—VT and TPS.

A large fraction of our investigations by the polarization-optical method of subgrain and deformation structure of long VT corundum crystals denote three zones of quality. It is better at the beginning and the end of crystals and it is worse for the central part. This trend has the following explanation. For the beginning, the crystal is located inside a muffle and grows under conditions of a relative low temperature gradient and internal stresses. The plastic deformation of this part of the crystal, the dislocation appearance and low-angle boundary formation, as a result of polygonization of dislocations, mainly take place during crystal cooling in the cold zone. The central part of the crystal grows and is cooled under conditions of a higher temperature gradient. The end of the crystal is cooled at low speed within the muffle. So, the first and the last crystal parts have only one factor assisting the defect formation: the rigid conditions of cooling for the beginning of the crystal growth and the rigid conditions of growth for the end of the crystal. As for the central part, both factors are present.

The defect structure of TPS-grown sapphire crystals was studied both by the optical polarization method and by the technique of widely diverging X-ray beams [6, 7, 55]. The tube samples with diameters of 4 to 40 mm and wall thickness in the range 0.5 to 3 mm were investigated.

It has been established that, in the absence of low-angle grain boundaries propagating from the seed, the initial part of the crystal does not contain subgrain (or low-angle grain) boundaries. Then, as the crystal grows the dislocation density increases and subgrain boundaries are formed. The misorientation of adjacent subgrains increases with distance from the seed, reaches a certain limit, and then decreases slightly with further growth. The decrease is probably associated with a rearrangement of the subgrain structure; i.e. subgrains with large misorientations branch into a series of subgrain boundaries with smaller misorientations. In addition, there is a decrease in the density of subgrain boundaries that are at large angles to the growth direction. The subgrain boundaries that remain are approximately parallel to the growth direction; the density of these boundaries (with misorientations as high as 5° to 10°) stays constant.

It should be noted that, at high crystallization rates, crystals that are free of low-angle grain boundaries can sometimes be grown. This is probably explained by the fact that the time spent by the growing crystal in the plastic zone is not long enough for polygonization processes to occur.

The presence of bubbles is a source of additional stresses that gives rise to dislocation generation and boundary formation. Subgrain boundaries are frequently observed to form along planes of piled-up bubbles.

So, we can conclude that in both analyzed examples (VT and TPS) the quality of crystals at the beginning, at a lower temperature gradient, was better.

Our experience of sapphire crystal growth by different techniques allows a statement to be made that only temperature gradients less than 2°C mm^{-1} give the possibility to grow crystals without low-angle boundaries and dislocation density of the order $\leq 10^3 \text{ cm}^{-2}$.

10.4.3 Twins

At temperatures lower than 800°C single-crystal sapphire is essentially brittle and is not deformed by the usual dislocation mechanism. Twinning is the only mode of deformation. The following rhombohedral twin systems in sapphire were identified:

$\{0\bar{1}\bar{1}2\}$ $\{0\bar{1}11\}$, $\{0\bar{1}14\}$ $\{02\bar{2}1\}$.

The twinning process consists of two distinct stages: the twin nucleation and the twin growth. The nucleation stress is higher than the growth stress. In [58] the nucleation stress at 600°C was determined experimentally. It is high and strictly depends on surface treatment. It was found to be $13\text{--}18 \text{ kg mm}^{-2}$ for polished specimens and $36\text{--}41 \text{ kg mm}^{-2}$ for polished and heat-treated ones. During growth the stress of twin formation has to be averaged. It corresponds to the residual stress in HTT crystals $\sim 20 \text{ kg mm}^{-2}$, where the twins can be found more often.

10.4.4 Faceting, inhomogeneities of impurity

Faceted growth is a normal mode of HTT, GPT, FT growth. The singular faces appearance on the interface in CzT, KT is not very important for sapphire growth but increases non-homogeneity in ruby growth because the distribution coefficient of chromium is different for faceted and nonfaceted interfaces. But for TPS and VT faceting may be a serious source of defects.

The geometrical form of TPS tubes can differ slightly from ideal for reasons of a crystallographic nature. According to the Curie theorem, in the process of growth, there is an interaction between the crystal symmetry and that of the medium (i.e. the thermal environment in which the crystal grows). In the grown crystal, only those elements of symmetry are exhibited that are common both for the crystal and for the medium. This is why grown crystals are faceted, depending on the orientation. If a sapphire tube is pulled in the directions $\langle 10\bar{1}0 \rangle$, $\langle 11\bar{2}0 \rangle$ or intermediate ones with $\rho = 90^\circ$ (ρ is the angle between the *C*-axis and the pulling direction), the close-packed basal plane (0001) becomes parallel to the growth direction and facets the tube [6, 7, 55]. If ρ differs slightly from 90° , a step-like faceting by the basal plane appears on the lateral surface of the tube. Tubes grown in the [0001] direction are faceted on the outside by $\{11\bar{2}0\}$ planes and on the inside by $\{10\bar{1}0\}$ planes. Faceting is reduced if the temperature gradient at the interface increases.

In VT-grown crystals [59] faceting with the (0001) plane appeared when the temperature gradient was reduced by a special muffle design and preliminary gas heating. Low gradients improved crystal quality but faceting deformed the crystal shape.

The faceting in both the above-mentioned cases can be explained because of supercooling, i.e. the singular face needs to grow with the same speed as an isothermal part of the interface.

Impurity inhomogeneities are important for ruby crystals. There are macroscopic and microscopic periodic inhomogeneities (striations) along the axes of growth. Macroscopic ones concerned with the impurity concentration changing during the growth because of the distribution coefficient that is not equal to one. TPS allows the growth of crystals with a macroscopically homogeneous distribution of impurity. Microscopic inhomogeneity is concerned with the periodic changing of growth parameters or constitutional supercooling.

10.4.5 Growth direction

Corundum crystal growth in the *C*-axis direction is very difficult for all techniques of melt growth, except TPS. TPS allows growth of all profile crystals in the *C*-direction without any problems. Furthermore, if we grow corundum filaments without seeds, the spontaneous orientation of the filament coincides with the *C*-axis. What is the reason for this? For many melt-growth techniques the growth in the *C*-direction requires an appearance of the singular *C*-plane on the interface. The *C*-plane has the lowest growth speed. TPS crystals, the filaments especially, grow with a high speed. The interface loses morphological stability and is faceted by the rhombohedral faces, as is shown in Fig. 10.18. So, the *C*-plane does not participate in the growth. As for filament orientation, the orientation of *C*-axes is the most preferred orientation for its growth with respect to the Curie principle. On the other hand, the filament interface is also faceted by the rhombohedral faces.

10.5 APPLICATIONS

10.5.1 Special windows

Application for modern airborne optical reconnaissance systems is one of the most impressive fields of sapphire usage. Practically speaking sapphire does not have any competitors in this field. Below are the requirements for the windows and evidence that sapphire meets all these requirements.

- *High optical transmission.* Sapphire has good optical properties in the 3–5 μm wavelength atmospheric transmission window (Fig. 10.20).
- *High abrasion resistance.* Sapphire has a hardness of 9 on the Mohs scale (the hardness of diamond is 10). It is the most durable commercially available infrared window material. It has the best resistance to erosion by rain and sand of any available window material.
- *Shock resistance.* Sapphire also has excellent thermal-shock resistance. But its thermal-shock resistance is limited by loss of mechanical strength at high temperature from 70 kg mm^{-2} at room temperature to 20 kg mm^{-2} at 600 °C. Doping or ion implantation with Mg, Ti can double the compressive strength at 600 °C [60]. Heat treatment at 1450 °C in an air atmosphere enriched with oxygen increases the compressive strength by 1.5 times. Neutron irradiation with 1×10^{22} neutrons increases the *C*-axes compressive strength by a factor of 3 at 600 °C [61].
- *Minimal optical scatter.* Sapphire is available routinely with minimal optical scatter.

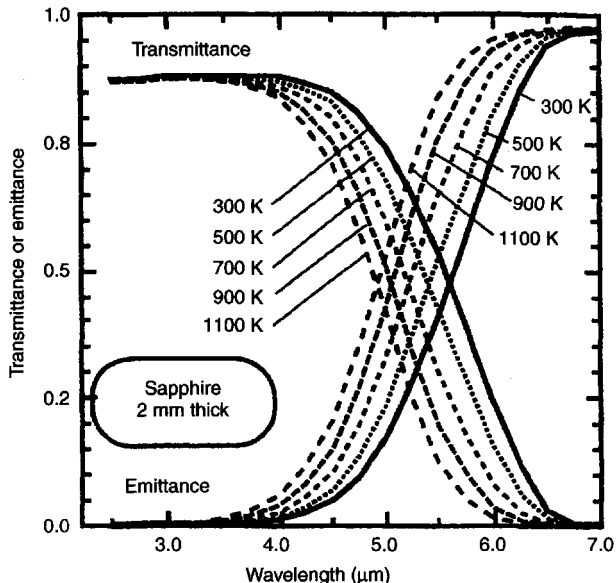


Figure 10.20 Reproduced from D.C. Harris (1999) Overview of progress in strengthening sapphire at elevated temperature, *Proceedings SPIE*, 3705, 2–11, with permission from SPIE.

- *High refractive-index uniformity.* Its simple oxide composition and its availability in single-crystal form are advantages of sapphire. For stringent optical applications, *C*-axes optics are preferred as this is the zero-birefringence orientation. It is difficult to grow high-quality *C*-boules by HEM. Therefore, this orientation can be cored orthogonal to the growth axis of *a*- or *m*-boules. Larger windows of *a*- or *m*-orientations are fabricated from current production. The *m*-orientation boules are preferable, as the polished pieces have shown more symmetry than the *a*-windows [62]. The HBT has an advantage because it is simple to obtain plates of *C*-orientation. A current polishing technique for *a*-plane nonhomogeneities of sapphire crystals, allows production of a 330-mm diameter window having a transmitted wave-front error of 0.059 wave rms. But in [63] it is suggested to use computer-controlled optical finishing to meet the challenging emerging requirements of transmitted wavefront errors for 500-mm diameter windows.
- *Large size.* The requirement is up to 750 mm diameter. The maximal dimensions achieved are 280 × 400 mm (HEM) and 315 × 480 mm (TPS).

10.5.2 Domes

The requirements for rocket nose cones correspond to those mentioned above. The traditional technique of dome production is a mechanical treatment of HEM and KT crystals. The effort of production is concerned with minimization of the treatment by growth of crystals having a shape close to a dome. There are some successful examples of this kind: GSM diameter to 150 mm [33], noncapillary feeding diameter to 80 mm [40], local shaping technique [41], modified EFG diameter to 40 mm [42].

10.5.3 Substrates

An application of sapphire in electronics as substrate for silicon-on-sapphire devices was rather large in the 1970s. In that case the {1102} face was used [64]. The requirements were not very rigid. But since the 1990s sapphire is becoming the main substrate material for blue and white laser diodes. The {0001} face is used for the epitaxy. The requirements on the wafer quality are very high both from the point of view of crystal structure and orientation and polishing quality. Sometimes special misorientation of the wafer is used to get better quality of deposited layer [65]. The analysis of crystal quality carried out above allows us to give the following recommendations concerning existing technique application for substrate production: KT is the best, then CzT, HEM, HBT, TPS.

10.5.4 Construction material

Sapphire is increasingly becoming the material of choice for engineers faced with the design challenges of extreme conditions, such as those found in high-temperature, high-pressure or aggressive chemical environments. There are many examples of this sapphire product in the former Saphikon (now Saint-Gobain Crystals) catalog. The industrial technique of welding of sapphire pieces is also developed there.

Sapphire tubes, plates and more complicated assemblies are used as superior alternatives to quartz, alumina, and silicon carbide: in semiconductor processing applications (plasma-containment tubes, process-gas injectors, thermocouple protectors); in spectroscopy and chemical and biological analysis; lamps and lamp envelopes (high-intensity lamps, flash-lamps, ultraviolet sterilizations); GaAs backer/carriers; mail-sorting optical windows, etc.

10.6 BRIEF CRYSTAL-GROWTH TECHNIQUE CHARACTERIZATION

Let us briefly characterize, from different points of view, the industrial crystal-growth techniques mentioned above.

10.6.1 VT uses modern furnaces that make possible the preparation of relatively large corundum crystals up to 60 mm diameter. Crystals of 30–35 mm diameter can have lengths up to 500 mm. However their optical quality is not sufficient. The main reasons for this are the following:

- High temperature gradient ($10\text{--}50^\circ\text{C mm}^{-1}$) is realized.
- Distribution of temperature in the burner flame is not stable and homogeneous.
- The melt layer on the surface of the grown crystal is thin. Falls of agglomerated powder particles are systematic perturbations of the melt layer.
- As a result, there are systematic perturbations of the growth speed.

- All this develops: high internal stresses ($8\text{--}12\text{ kg mm}^{-2}$); bubble formation; subgrain formation with misorientation of the order of some degrees; inhomogeneous impurity distribution.

But this technique is the least expensive, it has its own niches of application: artificial jewelry, watch windows, jeweled bearings, and so on.

10.6.2 FZT does not have industrial application. Maximal-sized crystals of 12 mm diameter and 60 mm length have been grown. It is interesting that the very difficult to grow *C*-orientation has been obtained.

10.6.3 CzT is widely used for ruby and sapphire crystal production. We could not find the latest publications concerning corundum growth by CzT. But we can estimate its current status by using the Union Carbide (now Saint-Gobain Crystals) catalog: The dimension of crystals is 150 mm diameter and 600 mm length; the pulling directions are *r*, *a*, *m*, *C*, and *n*. The crystals are recommended for ultraviolet uses up to 250 nm. The optical quality is evaluated by using a Twyman–Green-type double-pass interferometer. A typical value of the double wavefront distortion is less than 0.03 of a wavelength per inch of crystal length.

10.6.4 KT is a widely used industrial technique. It allows growth of crystals with temperature gradients of $0.05\text{--}1.0\text{ }^{\circ}\text{C mm}^{-1}$ and annealing in the same growth volume. As a result, crystals do not have any subgrains, residual stresses are $0.1\text{--}0.3\text{ kg mm}^{-2}$ and, as a result, a low dislocation density. The maximal diameter and weight of crystals achieved is consequently 300 mm and 30 kg.

10.6.5 HBT is one of the most widely used industrial techniques. The main advantage is the possibility to grow *C*-orientation plates of large surface area (available: $220 \times 220 \times 30\text{ mm}$). It is very important for window production (because of the absence of crystallographic birefringence) and for LED substrates. The crystals have a moderate quality.

10.6.6 HEM as mentioned above, is used for large and good optical quality window production. The crystals have large dimensions (340 mm current production and $280 \times 400\text{ mm}$ maximal) and rather good optical quality.

10.6.7 TPS is used for the growth of different shapes of material. But the most impressive result, including industrial production, is achieved in sapphire growth. TPS has the following advantages with respect to other growth techniques:

- (a) The crystals have the shape needed for the most rational practical use.
- (b) The range of crystal dimensions is large: filaments of 0.02 mm diameter; tubes of 0.9 mm to 85 mm diameter; plates $480 \times 315 \times 10\text{ mm}$ in size.

- (c) Crystals, as a rule, have more perfect structure. As was explained above, the constant cross section crystal growth is, to a certain extent, evidence of the absence of defects caused by changing of the crystallization rate. It is necessary to mention that it does not concern the structural quality depending on temperature gradients and high growth speed often used in TPS.
- (d) The separation of the growth zone from the melt in the crucible allows realization of continuous feeding by the raw material during the growth process. As a result, we can have a short time of the melt presence before the growth, if necessary. Periodical changes of the doping are also possible.
- (e) The distribution of impurities along the axis of crystals is more uniform; If the distribution coefficient of impurities is not equal to one during crystal growth the concentration of impurities changes along the axis of crystals. A solution to this problem can be found by localization of the melt at the zone of growth without stirring it with other melt volume. This situation we have, for instance, when using a floating crucible of small volume for CzT. The more effective result gives the capillary feeding in TPS.
- (f) The distribution of impurities in the cross section of a crystal can be controlled. At the same time the use of special systems of capillaries for feeding allows control of the distribution of impurities along the cross section of crystals.
- (g) A combination of doped and undoped parts is achieved in the same crystal. As for crystal quality, there is no data on crystals with low growth rate. Crystals grown at a high speed have a moderate quality.

10.6.8 FT, HTT, GPT are interesting from the point of view of the peculiarities of sapphire crystallization, especially at relatively low temperature. GPT has an industrial application for sapphire whisker growth.

10.7 CONCLUSION

In conclusion, it is important to mention the monograph [66]. It is rather old (the Russian original was published in 1974) but it contains much interesting information concerning sapphire.

REFERENCES

1. A. Verneuil, (1910) Sur un nouveau procédé de fusion et d'affinage de l'alumine chromée et la production d'une matière possédant la composition, la dureté et la densité du rubis, *Plis Cachettes* #4752, 23 décembre 1891 et #4849, 19 décembre 1892, ouverts 11 juillet 1910: *Paris Acad. Sci., Comptes Rendus*, **151**, 131–132.
2. A. Verneuil, (1902) Production artificielle du rubis par fusion, *Paris Acad. Sci., Comptes Rendus*, **135**, 791–794.
3. N.V. Belov, (1947) *Structure of Ionic Crystals and Metallic Phases* [*Struktura Ionnykh Kristallov I Metallicheskih Faz into Russian*], Academy of the Sciences of the USSR, Moscow.

4. Ch. Barta, (1968) Corundum monocrystals of large area, in *Crystal Growth (Rost Kristallov, Russian)*, N.N. Sheftal (Ed.), **6A**, 178–181, Consultants Bureau, New York.
5. W.J. Alford and W.H. Bauer, (1967) Radiofrequency plasma growth and crystalline perfection of single crystal alumina, *J. Phys. Chem. Solids Suppl.*, **1**, 71–74.
6. V.A. Tatartchenko, (1993) *Shaped Crystal Growth*, Kluwer Academic Publishers, Dordrecht, Boston, London.
7. V.A. Tatartchenko, (1994) Shaped Crystal Growth, in *Handbook of Crystal Growth*, D.T.J. Hurle (Ed.), **2b**, North-Holland, Amsterdam, London, New York, Tokyo.
8. V.A. Borodin, E.A. Brener, and V.A. Tatartchenko, (1982) Investigation of the crystallization process in the Verneuil technique, *Cryst. Res. Technol.* **17**, 1187–1197.
9. V.A. Tatartchenko, (1973) Influence of capillary phenomena on the stability of the crystallization process during the pulling of shaped specimens from the melt, *Fiz. Khim. Obrabotki Mater. [Sov. Phys. Chem. Mater. Treatment]* #6, 47–50.
10. G.A. Korn A and T.M. Korn, (1962) *Mathematical Handbook for Scientists and Engineers*, p. 282, McGraw-Hill Book Company, New York, San Francisco, Toronto, London, Sydney.
11. V.A. Tatartchenko and G.I. Romanova, (1973) Stability of crystallization by Verneuil technique, *Monokristalli I Technika [Sov. Single Crystals Tech.]*, #2, 48–53 Charkov.
12. G.I. Romanova, V.A. Tatartchenko and N.P. Tichonova, (1976) Stability of crystallization at the crystal growth by the gas flame technique, *Trudi Goi*, **54**, #188, pp. 10–13 [*Sov. Proc. State Optical Institute*], Leningrad.
13. V.A. Borodin, E.A. Brener, T.A. Steriopo, V.A. Tatartchenko and L.I. Chernishova, (1982) Growing single crystal corundum tubes by Verneuil technique in stable conditions, *Cryst. Res. Technol.*, **17**, 1199–1207.
14. V.A. Borodin, E.A. Brener, V.A. Tatartchenko, V.I. Gusev and I.N. Tsigler, (1981) Automation of the Verneuil technique on the basis of stability analysis, *J. Cryst. Growth*, **52**, 505–508.
15. W. Class, H.R. Nesor, and G.T. Murray, (1967) Preparation of oxide crystals by a plasma float-zone technique, in *Crystal Growth*, H.S. Peiser (Ed), pp. 75–80, Pergamon, Oxford.
16. A.I. Somov, A.I. Svinarenko, and A.G. Tiutiunnik, (1966) Growth of corundum crystals by electron beam floating zone, *Proc. Acad. Sci. USSR, Inorg Mater. (Russ.)*, **2**, 1892–1894.
17. B. Cockayne, M. Chesswas, and D.B. Gasson, (1967) Single crystal growth of sapphire, *J. Mater. Science*, **2**, 7–11.
18. G. Petit-Le Du and J. Aubree, (1967) Cristallogenèse du rubis par zone flottante dans un four a résistance, *Rev. Phys. Appl.*, **2**, 264–270.
19. K. Eickhoff and K. Gürs, (1969) Tiegelfreies zonenschmelzen von rubinkristallen durch ayfheizen der schmelzzone mittels laser, *J. Cryst. Growth*, **6**, 21–25.
20. M. Saito, (1985) Gas-bubble formation of ruby single crystals by floating zone melt growth with an infrared radiation convergence type heater, *J. Cryst. Growth*, **71**, 664–672.
21. A.E. Paladino and B.D. Roiter, (1964) Czochralski growth of sapphire, *J. Am. Ceram. Soc.*, **47**, 465–468.
22. T.B. Reed and R.E. Fahey, (1964) Czochralski growth of sapphire crystals in a resistance furnace, *Solid State Res. Lincoln Lab. Mass. Inst. Technol.*, #4, 23–33.
23. F.R. Charvat, J.C. Smith and O.H. Nestor, (1967) *Crystal Growth*, Pergamon Press, 45.
24. Sapphire single crystals, (1966) *Rev. Sci. Instrum.*, **37**, 817–821.
25. V.V. Osiko, (1982) High-temperature Non-metallic Crystalline Materials, in: Krishnan Lal (ed), *Synthesis, Crystal Growth and Characterization*, North-Holland Publishing Company, Amsterdam, New York, Oxford.
26. M.I. Musatov, (1975) Optimizing the method of growing high-quality large corundum crystals, *Sov. J. Opt. Technol.*, **42**, 461–464.
27. Ch.S. Bagdasarov, (1977) Problems of synthesis of refractory optic crystals, in *Russian Rost Kristallov*, E.I. Givargizov (Ed.), **11**, pp 179–195, Erevan State University, Erevan, [*Transl. Growth of Crystals*, Consultants Bureau, New York, 1978].

28. F. Schmid and Viechnicki, (1970) Growth of sapphire discs from the melt by a gradient furnace technique, *J. Am. Ceram. Soc.*, **53**, 528–529.
29. D. Viechnicki and F. Schmid, (1974) Crystal growth using the heat exchanger method (HEM), *J. Cryst. Growth*, **26**, 162–164.
30. C.P. Khattak and F. Schmid, (1984) Growth of large-diameter crystals by HEM for optical and laser applications, *Proc. SPIE*, **505**, 4–8.
31. F. Schmid, C.P. Khattak, H.H. Rogers, D.M. Felt, J. Askinazi and R.V. Wientzen, (1999) Current status of very large sapphire crystal growth for optical applications, *Proc. SPIE*, **3705**, 70–77.
32. Zhang Quiang, Deng Peizhen and Gan Fuxi, (1991) X-ray topographic observation of dislocation structure in sapphire single crystal grown by temperature gradient technique, *J. Cryst. Growth*, **108**, 377–384.
33. A. Horowitz, S. Biderman, D. Gazit, *et al.*, (1993) The growth of dome-shaped sapphire crystals by the gradient solidification method (GSM), *J. Cryst. Growth*, **128**, 824–828.
34. E.V. Gomperz, (1922) Untersuchungen an einkristalldrähten, *Z. Phys.*, **8**, 184–190.
35. A.V. Stepanov, (1959) A new technique of production of sheets, of tubes, of rods with different cross section from a melt, *Zhurnal Tekhnicheskoi Fiziki.*, **39**, 1302–1307 (Transl. in: *Sov. Phys.-Tech. Phys.*).
36. H.E. LaBelle, (1980) EFG, the invention and application to sapphire growth, *J. Cryst. Growth.*, **50**, 8–17.
37. V.A. Tatartchenko, A.I. Saet and A.V. Stepanov, (1969) Boundary conditions of capillary shaping at crystallization from melts, *Izvestiya Akademii Nauk SSSR, Seriya Fizicheskaya*, **33**, 1954–1959 (Transl. In: *Bulletin of the Academy of Sciences of the USSR, Physical Series*).
38. V.A. Borodin, V.V. Sidorov, T.A. Steriopol and V.A. Tatartchenko, (1986) Variable shaping growth of refractory oxide shaped crystals, *J. Cryst. Growth*, **82**, 89–94.
39. V.N. Kurlov and S.V. Belenko, (1998) The growth of sapphire shaped crystals with continuously modulated dopants, *J. Cryst. Growth*, **191**, 779–782.
40. V.N. Kurlov and B.M. Epelbaum, (1997) Fabrication of near-net-shaped sapphire domes by noncapillary shaping method, *J. Cryst. Growth*, **177**, 175–180.
41. V.A. Borodin, V.V. Sidorov, S.N. Rassolenko, T.A. Steriopol, V.A. Tatartchenko and T.N. Yalovets, (1990) Local shaping technique and new growth apparatus for complex sapphire products, *J. Cryst. Growth*, **104**, 69–76.
42. J.W. Locher, H.E. Bennet, P.C. Archibald and C.T. Newmyer, (1990) Large diameter sapphire dome: fabrication and characterization. *Proc. SPIE*, **1326**, 2–10.
43. V.A. Tatartchenko, V.S. Uspenski, E.V. Tatarchenko and B. Roux, (2000) Theoretical investigation of crystal growth shaping process with the wetting boundary condition, *J. Cryst. Growth*, **220**, 301–307.
44. V.A. Timofeeva and R.A. Voskarian, (1963) Corundum crystal growth from lead fluorine flux, *Crystallography [Sov. Kristallographia]*, **8**, #2, 293–296.
45. K. Watanabe and I. Sunagawa, (1982) Surface micro-topography of corundum crystals grown from cryolite flux, *J. Cryst. Growth*, **57**, 367–378.
46. K. Watanabe, A. Iida and Y. Sumioshi, (1981) Growth of corundum single crystals by seed rotation method, *J. Cryst. Growth*, **54**, 381–393.
47. R.A. Laudise and A.A. Ballman, (1958) Hydrothermal synthesis of sapphire, *J. Am. Chem. Soc.*, **80** #11, 2655–2657.
48. K.F. Kashkurov, P.I. Nikitichev, V.V. Osipov, L.D. Sizova and A.V. Simonov, (1967) Growth of big corundum crystals by hydrothermal method, *Crystallography [Sov. Kristallographia]*, **12**, #5, 956–957.
49. A.A. Shternberg and V.A. Kuznetsov, (1964) Corundum crystallization on seed from gas phase, *Crystallography [Sov. Kristallographia]*, **9**, #1, 121–123.
50. P.S. Schaffer, (1965) Vapor-phase growth of alpha alumina single crystals, *J. Am. Ceram. Soc.*, **48**, #10, 508–511.

51. Kh.S. Bagdasarov, (1980) Synthesis of large single crystals of corundum, in *Ruby and Sapphire (Translated from Russian)*, L.M. Belyaev (Ed.), National Bureau of Standards, Washington, D.C.
52. M. Saito, (1986) Growth process of gas-bubble in ruby single crystals by floating zone method, *J. Cryst. Growth*, **74**, 385–390.
53. A.V. Zhdanov, G.A. Satunkin, V.A. Tatartchenko and N.N. Talyanskaya, (1980) Cylindrical pores in a growing crystal, *J. Cryst. Growth*, **49**, 659–664.
54. V.A. Tatartchenko, (1994) Cylindrical pores in a growing crystal, *J. Cryst. Growth*, **143**, 294–300.
55. V.A. Tatartchenko, T.N. Yalovets, G.A. Satunkin, L.M. Zatulovsky, L.P. Egorov and D.Ya. Kravetsky, (1980) Defects in shaped sapphire crystals, *J. Cryst. Growth*, **50**, 335–340.
56. A.A. Chernov, D.T. Temkin and A.M. Melnikova, (1976) Theory of inclusion capture at the melt crystal growth, *Kristallographia (Sov. Crystallography)*, **21**, #4, 652–660.
57. W.W. Mullins and R.F. Sekerka, (1964) Stability of flat interface at crystallization of dilute binary alloy, *J. Appl. Phys*, **35**, 444–453.
58. E. Savrun, C. Toy, W.D. Scott and D.C. Harris, (1999) Is sapphire inherently weak in compression at high temperature? *Proc. SPIE*, **3705**, 12–16.
59. V.A. Borodin, V.A. Tatartchenko, L.I. Chernishova and T.N. Yalovets, (1980) Influence of thermal conditions on faceting of corundum crystals grown by Verneuil technique, *Crystallography [Sov. Kristallographia]* **25**, #3, 590–594.
60. D.C. Harris, (1999) Overview of progress in strengthening sapphire at elevated temperature, *Proc. SPIE*, **3705**, 2–11.
61. T.M. Regan, D.C. Harris, R.M. Stroud *et al.*, (2001) Compressive strengthening of sapphire by neutron irradiation, *Proc. SPIE*, **4375**, 31–40.
62. M. Smith, K. Schmid, F. Schmid and C.P. Khattak, (1999) Correlation of crystallographic orientation with processing of sapphire optics, *Proc. SPIE*, **3705**, 85–92.
63. J. Askinazi, R.V. Wientzen and C.P. Khattak, (2001) Development of large aperture, monolithic sapphire optical windows, *Proc. SPIE*, **4375**, 1–11.
64. Zhang Shou-Qing, Tang Liang-An, Wang Wen, and Le Shou-Hong, (1980) The relationship between growth orientation and grain boundary generation in sapphire plate crystals grown by the EFG technique, *J. Cryst. Growth*, **50**, 659–662.
65. T. Yuasa, Y. Ueta, Y. Tsuda, *et al.*, (1999) Effect of slight misorientation of sapphire substrate on metalorganic chemical vapor deposition growth of GaN, *Jpn. J. Appl. Phys*, **38**, 703–705.
66. L.M. Belyaev (1980) (Ed.), *Ruby and Sapphire*, National Bureau of Standards, Washington, D.C., (Translation from Russian original, published in 1974).

APPENDIX: SAPPHIRE PHYSICAL PROPERTIES

As a rule, the data are averaged from different sources. Sometimes the sources are indicated.

Melt

- Melting point 2050 °C
- Density 3.05 g cm⁻³
- Specific heat 1.26 J g⁻¹K⁻¹
- Thermal conductivity 0.1 W cm⁻¹K⁻¹ (25 K)
- Latent heat 1046 J g⁻¹

- Emissivity 0.9
- Melt/gas surface tension 700 dyn cm^{-1}
- Electric resistivity 0.1 ohm cm (2200°C)

Crystal

Thermal

- Specific heat vs temperature:

$$0.76 \text{ J g}^{-1} \text{ K}^{-1} \text{ (} 25^\circ\text{C)}$$

$$1.26 \text{ J g}^{-1} \text{ K}^{-1} \text{ (} 1000^\circ\text{C)}$$

- Thermal expansion coefficient vs temperature and orientation:

$$6.5 \times 10^{-6} \text{ }^\circ\text{C}^{-1} \text{ parallel to } C\text{-axis (} 100^\circ\text{C)}$$

$$9.1 \times 10^{-6} \text{ }^\circ\text{C}^{-1} \text{ parallel to } C\text{-axis (} 1200^\circ\text{C)}$$

$$5.5 \times 10^{-6} \text{ }^\circ\text{C}^{-1} \text{ perpendicular to } C\text{-axis (} 100^\circ\text{C)}$$

$$8.2 \times 10^{-6} \text{ }^\circ\text{C}^{-1} \text{ perpendicular to } C\text{-axis (} 1200^\circ\text{C)}$$

- Thermal conductivity vs temperature:

$$110 \text{ W cm}^{-1} \text{ K}^{-1} \text{ (} 25 \text{ K)}$$

$$1.0 \text{ W cm}^{-1} \text{ K}^{-1} \text{ (} 175 \text{ K)}$$

$$0.4 \text{ W cm}^{-1} \text{ K}^{-1} \text{ (} 300 \text{ K)}$$

$$0.1 \text{ W cm}^{-1} \text{ K}^{-1} \text{ (} 1800 \text{ K)}$$

- Emissivity 0.9

Physical/mechanical

- Density 3.98 g cm^{-3} (25°C)
- Cleavage: none, however, well-developed parting on basal and rhombohedral planes is common.
- Fracture: conchoidal, brittle.
- Young's modulus vs temperature:

$$435 \text{ GPa parallel to } C\text{-axis (} 25^\circ\text{C)}$$

$$386 \text{ GPa parallel to } C\text{-axis (} 1000^\circ\text{C)}$$

- Shear modulus 175 GPa
- Modulus of compression 250 GPa

- Poisson's ratio 0.27–0.30 orientation dependent
- Tensile strength vs orientation and temperature [60]:
 - 450 MPa parallel to *C*-axis (25 °C)
 - 300 MPa parallel to *C*-axis (800 °C)
 - 300 MPa perpendicular to *C*-axis (25–800 °C)
- Compressive strength vs orientation and temperature [60]:
 - 2.0 GPa uniform (25 °C)
 - 2.4 GPa parallel to *C*-axis (25 °C)
 - 500 MPa parallel to *C*-axis (400 °C)
 - 200 MPa parallel to *C*-axis (700 °C)
 - 2.0 GPa perpendicular to *C*-axis (25 °C)
 - 1.5 GPa perpendicular to *C*-axis (800 °C)
- Flexural strength vs orientation and temperature [60]:
 - (500–800)MPa parallel to *C*-axis (25 °C)
 - (700–950)MPa parallel to *C*-axis (500 °C)
 - (500–800)MPa parallel to *C*-axis (1000 °C)
 - 1000 MPa perpendicular to *C*-axis (25 °C)
 - 600 MPa perpendicular to *C*-axis (500 °C)
 - 200 MPa perpendicular to *C*-axis (1000 °C)
- Twin-formation strength vs surface treatment [58]:
 - (140–180)MPa compression parallel to *C*-axis (600 °C polished)
 - (360–410)MPa compression parallel to *C*-axis (600 °C polished and heat treated)
- Yield point
 - 40 MPa (1850 °C)
- Hardness vs orientation:
 - 9(Mohs scale)
 - (1500–1900)Knoop parallel to *C*-axis
 - (2000–2200)Knoop perpendicular to *C*-axis

Optical

- Transmission vs wavelength (0.8 mm thickness)

67 % (0.2 μm)

80 % (0.3 μm)

87 % (1.0 μm)

87 % (2.0 μm)

79 % (5.0 μm)

- Refractive index vs wavelength (ordinary ray)

1.85(0.27 μm)

1.80(0.48 μm)

1.75(3.2 μm)

1.70(4.3 μm)

1.65(5.1 μm)

- Birefringence: weak, 0.007–0.010
- Temperature coefficient of refractive index:

$$13 \times 10^{-6} \text{ } ^\circ\text{C}^{-1} \text{ (visible range)}$$

Electrical

- Electric resistivity vs temperature:

10^{16} ohm cm (25 $^\circ\text{C}$)

10^{11} ohm cm (500 $^\circ\text{C}$)

10^6 ohm cm (1000 $^\circ\text{C}$)

2.2×10^4 ohm cm (1875 $^\circ\text{C}$)

- Dielectric strength 480 kV cm⁻¹
- Dielectric constant vs orientation:

11.6(10^3 – 10^9 Hz, 25 $^\circ\text{C}$) parallel to *C*-axis.

9.4(10^3 – 10^9 Hz, 25 $^\circ\text{C}$) perpendicular to *C*-axis.

- Loss tangent vs orientation:

8.6×10^{-5} (10^{10} Hz, 25 $^\circ\text{C}$) parallel to *C*-axis.

3.0×10^{-5} (10^{10} Hz, 25 $^\circ\text{C}$) perpendicular to *C*-axis.

- Magnetic susceptibility vs orientation:

0.21×10^{-6} parallel to *C*-axis.

0.25×10^{-6} perpendicular to *C*-axis.

Other Properties

- Weathering resistance: Unaffected by atmospheric exposure
- Sea-water resistance: Unaffected by marine exposure
- Biological resistance:

Unaffected by in-vivo exposure

Nonthrombogenic

Nonreactive with body fluids

11 Crystal Growth of Fluorides

P.P. FEDOROV, V.V. OSIKO

Laser Materials and Technology Research Center GPI, Vavilov str., 38, Moscow
119991, Russia

11.1 Introduction	339
11.2 Polymorphism and crystal growth	340
11.3 Solid solutions: decomposition and ordering	342
11.4 Type of compound melting: congruent/incongruent	347
11.5 Phases that are not in equilibrium with melt	347
11.6 Dopant segregation coefficients	348
11.7 Morphological stability	348
11.8 Hydrolysis and melt fluoride growth	350
Acknowledgments	352
References	352

11.1 INTRODUCTION

Inorganic fluoride single crystals feature large bandgaps, very wide optical transmittance ranges from vacuum-ultraviolet (VUV) to mid-IR wavelength regions, lower refractive indices than those of oxides, and typically lower phonon energies (which drastically reduce multiphonon relaxation rates of rare-earth ions). Both ordered and disordered (due to heterovalent isomorphism) crystalline media may be created in fluoride systems. This makes fluoride crystals attractive media for several photonics fields and for use in medicine, semiconductor processing, optical communications, etc. The above refers to lasers for the visible, UV and IR regions, including media for upconversion processes, long-wavelength lasers, optical amplifiers, diode-pumped lasers, tunable solid-state lasers based both on color centers and on media doped with active ions (Co^{2+} , Nd^{3+} , Ce^{3+} , Cr^{3+} , Dy^{2+} , Sm^{2+} , etc) [1–5, 61]. Recent research activities cover the development of technology and crystal growth for solid-state laser media such as RF_3 (R —rare-earth element) [6], LiRF_4 ($R = \text{Gd-Lu, Y}$) [5, 7–10], Colquirite-type crystals (LiCaAlF_6 - LiCAF , LiSrAlF_6 - LiSAF) [5, 7, 11], BaR_2F_8 [12], fluorite-type solid solutions $\text{M}_{1-x}\text{R}_x\text{F}_{2+x}$ and $\text{Na}_{0.5-x}\text{R}_{0.5+x}\text{F}_{2+2x}$ [13, 14], LiKRF_5 ($R = \text{Gd-Lu, Y}$) [15, 16], $\text{K}_5\text{Li}_2\text{RF}_{10}$ ($R = \text{La-Gd}$), [17], KMgF_3 [5], etc.

Single crystals of ultra-high-quality CaF_2 have been noted as lens materials in photolithography for 157-nm-based systems in the next generation of semiconductor manufacturing. Ultra-high-quality BaF_2 [18], LiCAF or BaLiF_3 (BLF) [19] are considered as useful materials for the compensation of chromatic aberration.

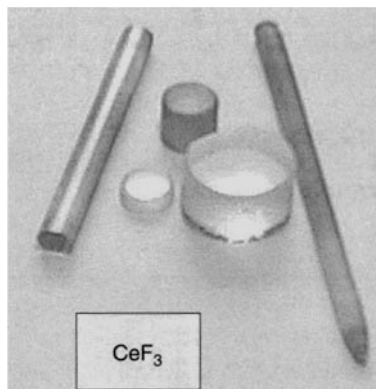


Figure 11.1 Single crystals of fast radiation-hard scintillator CeF_3 grown by Bridgman technique at Laser Materials and Technology Research Center

Table 11.1 Properties of CeF_3 scintillating crystals

Melting temperature, ($^{\circ}\text{C}$)	1443
Unit-cell parameters, (\AA)	a 7.112, c 7.279
Density, (g cm^{-3})	6.157
Radiation length (cm)	1.7
Light yield (in ratio with NaI, %)	4.5
Decay time (ns)	5; 28
Emission peak, (nm)	285; 305; 340
Radiation hardness, (rad)	10^7 – 10^8
Transmittance range, (μm)	0.3–9.5
Hygroscopicity	None

Other fields of interest are fast scintillators (KMgF_3 , CeF_3 , BaF_2 , etc.) [20], see Fig.11.1, thermoluminescent dosimeters [21], holographic materials (semiconductor $\text{CdF}_2:\text{Ga}$ [22]), transparent magnetic systems, etc., see Table 11.1.

Fluoride crystal growth is reviewed in [3, 23]. Previous studies are compiled in [24].

One aim of our survey is to show relations of phase diagrams with features of fluoride crystal growth. Successive transformations of phase equilibria in a series of similar systems, especially with rare-earth fluorides, allow the most convenient (beneficial) system to be chosen for the growth process. The other aim is to consider growth problems arising from the chemical properties of fluorides. The list of references cited is limited by the size of the chapter.

11.2 POLYMORPHISM AND CRYSTAL GROWTH

Polymorphism of compounds is an important factor complicating the melt growth of single crystals. The pattern of phase transitions in rare-earth trifluorides RF_3 is presented in Fig.11.2a [25, 26]. La–Nd fluorides and high-temperature polymorphs of Sm–Gd fluorides crystallize in the trigonal tysonite (LaF_3) structural type ($P3c1$, $Z = 6$, cation

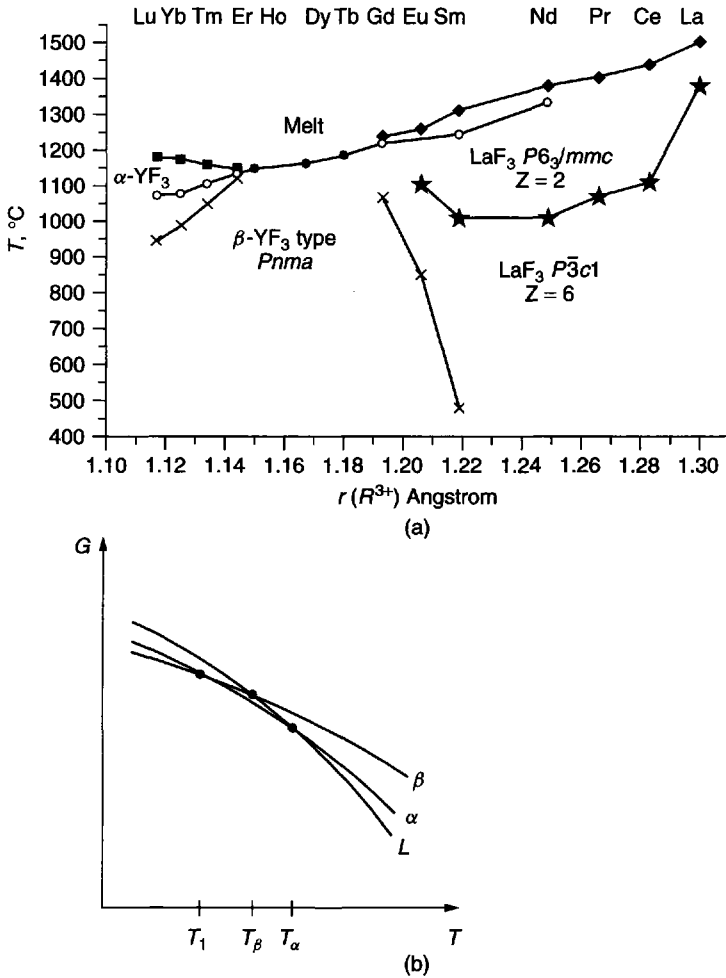


Figure 11.2 (a) Pattern of polymorphism and morphotropy in RF_3 series according to data [25, 26]; o—metastable melting temperature of low-temperature β - YF_3 polymorph, ξ —peak temperature of diffuse DTA effect. 'Fluorine' ionic radii for c.n. 8 after [40]; (b) Temperature dependence of the Gibbs free energy G of the melt L , and of the α - and β -polymorph. T_1 is the temperature of polymorphic transformation, T_α is the equilibrium melting temperature, and T_β is the temperature of metastable melting of low-temperature polymorph

coordination number is 11). Sm–Lu, Y fluorides crystallize in a related orthorhombic structural type β - YF_3 ($Pnma$, $Z = 4$, c.n. is 9). High-temperature RF_3 polymorphs for $R = Er$ –Lu, Y belong to structural type of α - YF_3 , which is similar to α - UO_3 and anti- Li_3N [25]. Tb, Dy, Ho fluorides have no solid-state phase transitions. The earlier communication about polymorphism in Tb, Dy, Ho trifluorides [27] was actually associated with oxygen contamination [28]. Previous communications about polymorphism in ZnF_2 , MnF_2 , ZrF_4 , UF_4 , and $PbCl_2$ also dealt with oxygen impurities.

In spite of the fact that Gd, Er, and Y fluorides have constructive phase transitions, their crystals can be grown by direct melt crystallization (see, e.g., ref. [29]). The

prerequisite for crystal growth is the melt undercooling down at least to the metastable melting temperature of the low-temperature polymorph, see Fig. 11.2b. The undercooling values $\Delta T = T_\alpha - T_\beta$, obtained from thermodynamic calculations or by extrapolation of low-temperature liquidus curves in binary phase diagrams, are approximately 20, 16, and 40 °C for GdF_3 , ErF_3 , and YF_3 , respectively [25]. There is no need to quench the grown crystal. Essentially, grown single crystals undergo phase transition intrinsic to them when heated.

Polymorphism is characteristic of monoclinic BaR_2F_8 compounds ($C2/m$, $Z = 2$). BaYb_2F_8 and BaLu_2F_8 have high-temperature orthorhombic polymorphs ($Pnma$, $Z = 8$) [30]. As in $\beta\text{-YF}_3$, strong undercooling of the melt in graphite crucibles (about 100 °C) enables one to grow crystals of monoclinic BaYb_2F_8 by direct melt crystallization or by using a seed crystal of the same structure. On the other hand, the $\alpha \leftrightarrow \beta$ BaLu_2F_8 phase transition is retarded. This allowed growth of single crystals of high-temperature orthorhombic α -phase [12, 31]. A high temperature gradient G and rapid cooling of the crystal are required. According to our data, and contrary to the opinion of [12, 23], single crystals of monoclinic BaY_2F_8 have no solid-state phase transition.

Phase transitions, close to second-order ones, are quite different phenomena. In such a case it is not possible to quench high-temperature polymorphs. Such transitions are typical of fluoroperovskites AMF_3 ($A = \text{Na, K, Rb}$; $M = \text{Mg, Ni, Co, Zn, Fe, Mn, Cd, Ca}$) and elpasolite A_2BRF_6 . In these compounds small M or B and R cations occupy the positions in fluorine octahedrons, and large monovalent A cations are 12-coordinate. Phase transitions are caused by various rotations of octahedrons. Slow and gradual cooling of grown crystals is essential, i.e. small G values and low pulling rates. Phase transitions during cooling lead to twinning of crystals [32, 33]. It should be mentioned that important crystals KMgF_3 (perovskite) and BaLiF_3 (antiperovskite) crystals are cubic ($Pm\bar{3}m$) and have no phase transitions.

Order-disorder phase transitions, similar to second-order ones, are apparently characteristic of tysonite-type compounds RF_3 ($R = \text{La-Gd}$). With increasing temperatures, in such crystals the low-temperature phases with $P3c1$ symmetry, $Z = 6$, gradually transform to high-temperature high symmetry ones ($P6_3/mmc$, $Z = 2$) [26], see Fig. 11.1a. Reverse transition on cooling leads to twinning [34]. Anionic vacancies, which are introduced together with heterovalent impurities, stabilize high-temperature phases. Probably, these phase transitions are first-order ones, but are diffuse because of impurities, above all, oxygen. Typical oxygen concentration in tysonite crystals, grown under fluorinating atmosphere is about 0.05 wt % [28]. Actual melt-grown crystals contain domains of different high- and low-temperature form structure [30].

11.3 SOLID SOLUTIONS: DECOMPOSITION AND ORDERING

According to the 3rd thermodynamic law, decomposition and (or) ordering processes must take place during cooling in all crystals of high-temperature phases with variable composition.

In the LiF-MF_2 systems, the solid solutions $\text{Li}_{1-2x}\text{M}_x\text{F}_2$ with $x \leq 0.22$ exist, see Fig. 11.3. For most of their concentration region, these solid solutions decompose on cooling. The limiting concentration of MgF_2 or NiF_2 in optically transparent LiF crystals is about 1 mol %. MgF_2 doping is used for control of the generation of color centers in LiF [2].

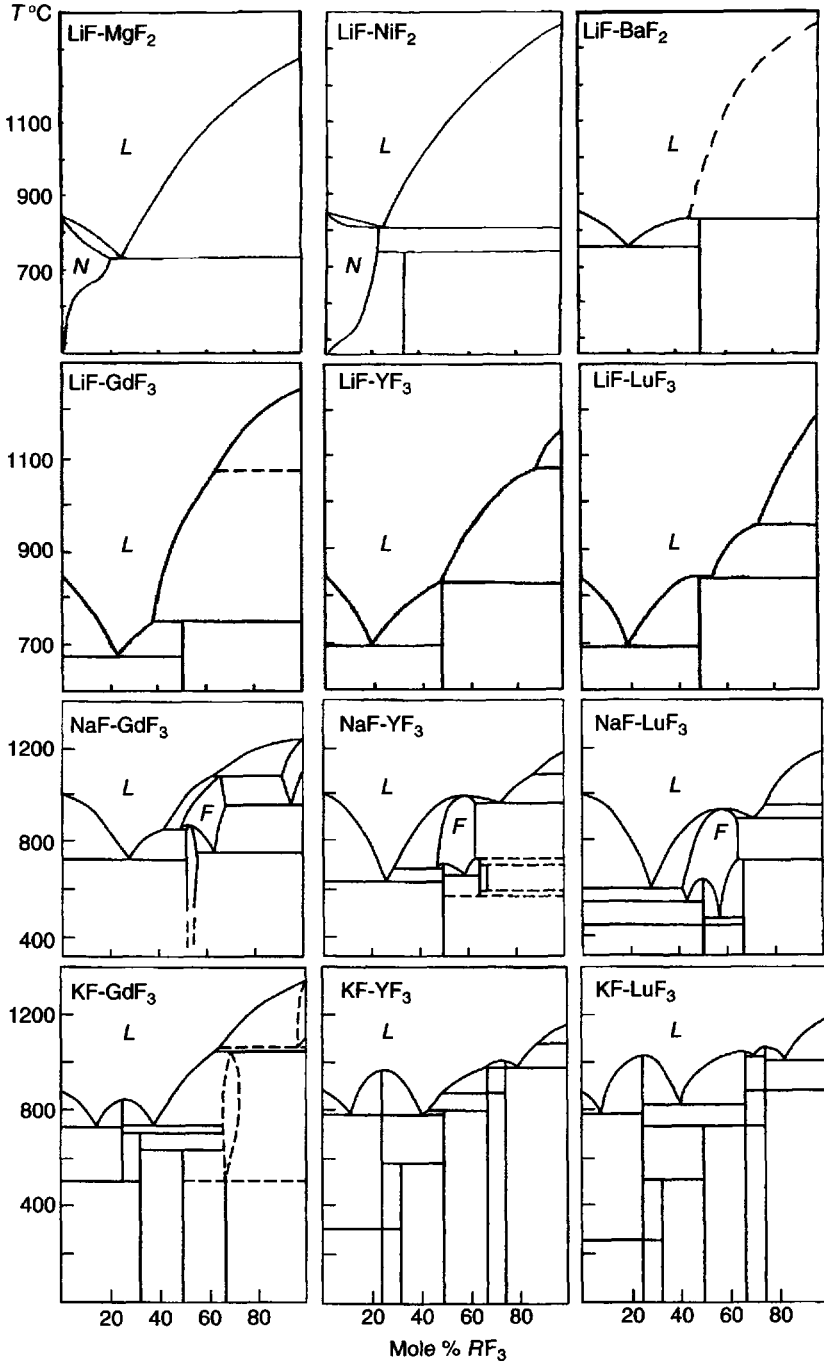


Figure 11.3 Phase diagrams of the systems LiF-MF_2 ($M = \text{Mg, Ni, Ba}$) and MF-RF_3 ($M = \text{Li, Na, K}$; $R = \text{Gd, Y, Lu}$), adapted from [35, 36]. L —melt, N —solid solutions with NaCl-type structure, F —fluorite-type nonstoichiometric phases

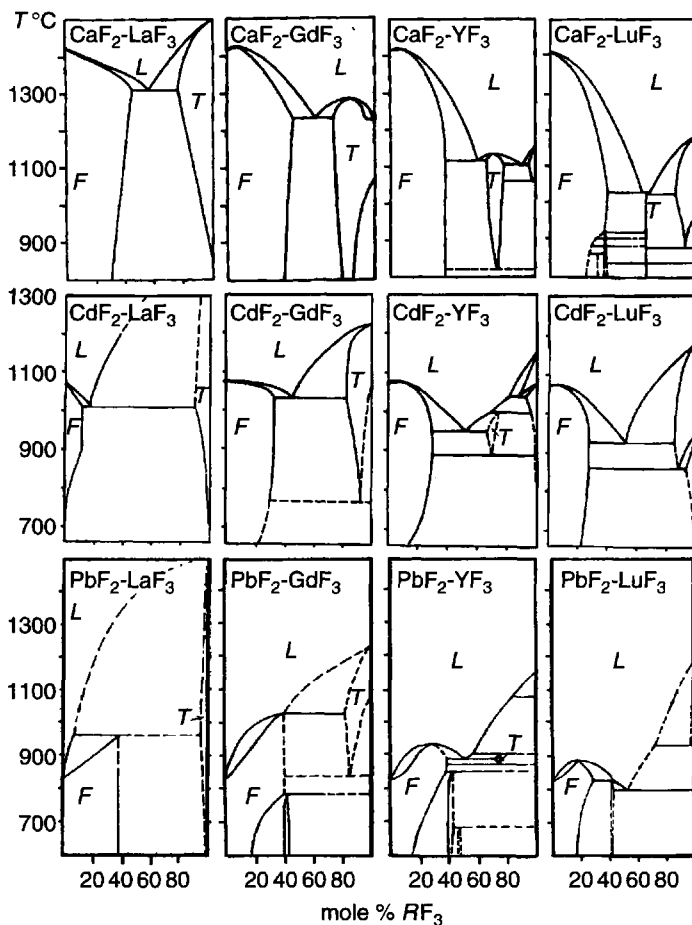


Figure 11.4 Phase diagrams of the systems MF_2-RF_3 ($M = Ca, Cd, Pb$; $R = La, Gd, Y, Lu$), adapted from [35] L —melt, F —fluorite-type solid solutions, T —tysonite-type solid solutions and nonstoichiometric phases

The systems with retarded decomposition of solid solutions are important for practical use. One can find good examples in the systems of MF_2 fluorite-type fluorides ($M = Ca, Sr, Ba, Pb, Cd$) with RF_3 rare-earth trifluorides ($R = La-Lu, Y$). Heterovalent isomorphism in these systems is extensive, see Fig. 11.4. The phase diagrams of MF_2-RF_3 (systems $M = Sr, Ba$) can be found in [23]. Wide regions of solid solutions $M_{1-x}R_xF_{2+x}$ ($x \leq 0.52$) on the base of MF_2 are formed in these systems [23, 35]. Maxima on melting curves of these solid solutions exist in many systems, which is the result of stabilization of crystal structure by isomorphic substitution and by processes of point-defect association [23, 37, 38]. With decreasing temperature, these solid solutions became thermodynamically unstable with respect to decomposition to the components (systems with $R = La-Nd$, and all systems with CdF_2 , see Fig. 11.5) or different type ordering [30]. However, in spite of thermodynamic instability, melt-grown single crystals of solid solutions maintain optical transparency for tens of years (probably due to very low values of cation diffusivity) [39].

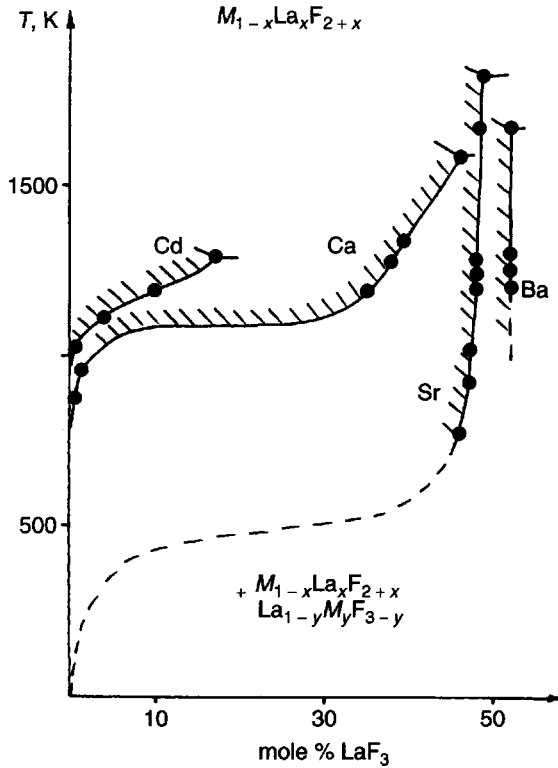


Figure 11.5 Temperature dependencies of solubility of LaF_3 in MF_2 (decomposition of $M_{1-x}\text{La}_x\text{F}_{2+x}$ solid solutions). Points—limiting concentrations of solid solutions. Adapted from [35]

Complicated processes of defect-cluster formation and transformation, which lead to micro- (nano-) heterogeneity, take place in these crystals [23, 30, 38]. With decreasing R^{3+} ionic radius stability of ordered phases, which have compositions $M_2\text{RF}_7$, $M_5\text{R}_8\text{F}_{31}$, $M_4\text{R}_3\text{F}_{17}$, etc., increases, and consequently, the stability of disordered phases decreases.

Anion-deficient tysonite-type $R_{1-y}M_y\text{F}_{3-y}$ phases on the base of RF_3 ($R = \text{La-Nd}$) or high-temperature RF_3 polymorphs ($R = \text{Sm-Gd}$) are the second important type of heterovalent solid solutions in these systems. Introduction of anion vacancies during formation of solid solutions stabilizes the tysonite crystal structure. Increasing the area of temperature stability of $\alpha\text{-GdF}_3$ due to formation of $\text{Gd}_{1-y}M_y\text{F}_{3-y}$ with different MF_2 solutions is presented in Fig. 11.6. In the case of CaF_2 and SrF_2 retarding of solid-solution eutectoid decomposition gives the possibility to stabilize high-temperature $\alpha\text{-GdF}_3$ polymorph in the single-crystal form [41]. Morphotropic transitions in the RF_3 series (disappearing of tysonite-type structure) lead to transformation of tysonite RF_3 -based solid solution to individual nonstoichiometric phases (berthollides). Berthollides melt congruently in the systems with CaF_2 and SrF_2 , and melt-grown tysonite crystals are practically (not thermodynamically) stable in these systems. The concentration ranges of these phases are close to the composition MR_2F_8 with decreasing R^{3+} ionic radius. Phases $R_{1-y}\text{Ca}_y\text{F}_{3-y}$ ($R = \text{Tb-Lu}$) undergo low-temperature monoclinic ordering. Berthollides with tysonite-type structure in the systems with BaF_2 , CdF_2 , PbF_2 are not so stable.

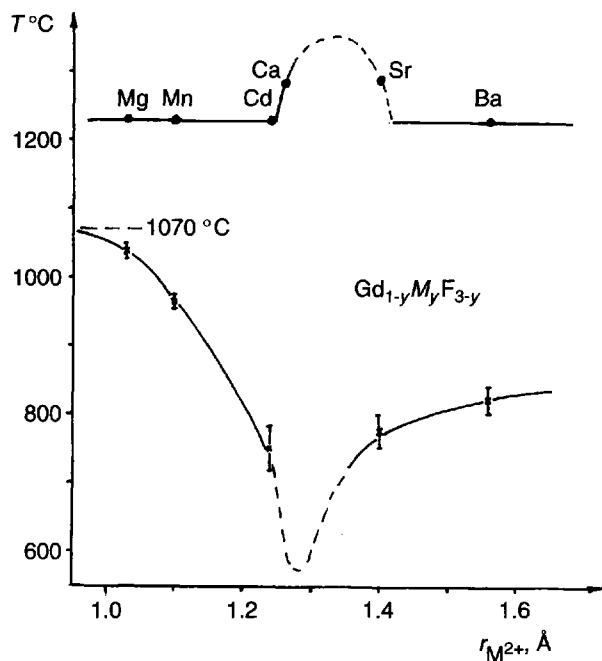


Figure 11.6 Interval of thermal stability of $\alpha\text{-Gd}_{1-y}\text{M}_y\text{F}_{3-y}$ solid solutions versus M^{2+} ionic radii [35]. 'Fluorine' ionic radii for c.n. 8 after [40]

In the NaF-RF_3 ($R = \text{Pr-Lu, Y}$) systems high-temperature nonstoichiometric fluorite-type phases $\text{Na}_{0.5-x}\text{R}_{0.5+x}\text{F}_{2+2x}$ exist also, but only as individual intermediate phases (berthollides) [36]. All of them are thermodynamically unstable at room temperature. Practical stability of these phases varies dramatically in systems with different RF_3 , increasing with decreasing R^{3+} ionic radius. Single crystals can be prepared by the usual method of crystallization starting from Tb. In the concentration range of these phases the most stable composition corresponds to the point of the eutectoid decomposition. Composition arrangement of maxima on melting curves is not fixed, as was stated in [42]. This is gradually shifted in the rare-earth series, and is equal to 60 ± 1 mol % YF_3 for NYF ($\text{Na}_{0.4}\text{Y}_{0.6}\text{F}_{2.2}$) and 57.5 ± 1 mol % LuF_3 for NLF ($\text{Na}_{0.425}\text{Lu}_{0.575}\text{F}_{2.15}$). Besides the eutectoid decomposition, processes of ordering of high-temperatures solid solution take place on cooling. Fluorite-related ordered phases form, such as NaR_2F_7 ($R = \text{Ho, Er, Y, Yb}$), $\text{Na}_7\text{R}_{13}\text{F}_{46}$ ($R = \text{Y, Tm-Lu}$), etc. The NaRF_4 compounds crystallised in special hexagonal gagarinite structural type, related to UCl_3 (less of mid-temperature polymorph of NaLuF_4 , which is fluorite related). The fluorite-gagarinite transformation has the features of a not retarding polymorphic transition. Low-temperature annealing of grown crystals of fluorite solid solutions requires care.

In the KF-RF_3 systems, compared with NaF-RF_3 systems, the stability of disordered fluorite-like phases decreases (so they are not interesting for crystal growth), ordered fluorite-related compounds (KRF_4 for $R = \text{Tb-Lu, Y}$, KR_2F_7 , KR_3F_{10}) became more stable, achieving an equilibrium with the melt in some cases. This gives a possibility of melt crystal growth compounds, such as congruent-melting cubic KY_3F_{10} [4, 62].

11.4 TYPE OF COMPOUND MELTING: CONGRUENT/INCONGRUENT

Crystal growth of compounds that melt incongruently is usually performed from a nonstoichiometric starting melt composition, which corresponds to primary melt crystallisation of the desired compound. Actual crystal growth is carried out from the solution (flux), which may belong to the same (binary or ternary) system as the compound under growth (self-flux), or differ in chemical composition. As a rule, the Czochralski or the top-seeded solution growth (TSSG) technique is used. Single crystals of incongruently melting compounds, such as BaLiF_3 (BLF), KYF_4 [43], $\text{Ba}_4\text{Y}_3\text{F}_{17}$ were prepared. Single crystals of BLF, for example, were grown from a starting melt with 43–40 mol % BaF_2 [19]. For ternary incongruently melting compound KLiYF_5 , binary eutectic $\text{KF} + \text{LiF}$ was used as a flux [16].

Very interesting phenomena take place in the LiF-RF_3 systems [36, 44]. Compounds LiRF_4 ($R = \text{Sm-Lu}$, Y) crystallize in sheelite-related structural type (tetragonal system, $I4_1/a$). Single-crystal LiYF_4 (YLF), LiGdF_4 (GLF), LiLuF_4 (LLF) and solid solutions on the basis of these compounds are very popular laser hosts. The compounds formed in the systems with $R = \text{Gd-Ho}$ clearly melt incongruently, while those formed with $R = \text{Tm-Lu}$ melt congruently. The problem of the phase equilibrium type in the LiF-YF_3 system was the topic of discussion (see history of the problem in [23]). Actually, the melting character of the compounds formed by LiF with ErF_3 and YF_3 is close to the transition between congruent and incongruent melting (bifurcation point). The relevant equilibrium transformations are described by the following phase reactions:



(eutectic, congruently solidifying LiRF_4), and



(peritectic, incongruent solidifying LiRF_4). The difference between the compositions of the liquid phase corresponding to the opposite patterns falls within a concentration interval of 1 mol %. On the background of a strong and irregular undercooling of the melt with respect to crystallization of both LiYF_4 and YF_3 (e.g., in graphite crucibles), fluctuations develop in the solidification character of LiYF_4 : patterns (1) and (2) become alternating. Crystallization processes are sensitive to impurities. In order to stabilize the crystal growth it is better to use starting compositions with an excess of 1–3 % LiF [7, 10].

The type of melting in LiCAF and LiSAF compounds was discussed in Ref. [45]. It is known that crystal growth of high-quality incongruently melting LiCAF is more difficult than congruently melting LiSAF [3].

11.5 PHASES THAT ARE NOT IN EQUILIBRIUM WITH MELT

Crystal growth of such phases requires use of a solvent. For example, low-temperature compounds K_2RF_5 ($R = \text{Lu}$, Y) have been crystallized by a hydrothermal technique using a reaction of concentrated aqueous solutions of KF with lanthanide oxides under hydrothermal conditions [46, 47].

11.6 DOPANT SEGREGATION COEFFICIENTS

Uniform distribution of dopant ions is an important condition for preparing laser-quality single crystals. Small differences between ionic radii of rare earths provides, in many cases, the existence of continuous solid solutions between isostructural phases (LiRF_4 , BaR_2F_8 , etc.), convenient for crystal growth. However, increasing differences in ionic sizes deteriorates, in general, the conditions for isomorphous substitution.

To evaluate the influence of the size factor on the distribution coefficient, the following Gaussian-type semiempirical relation [38] can be used

$$k = k^0 \exp[-b(r - r_0)^2] \quad (11.3)$$

where k^0 , b , r_0 are parameters, r_0 being the optimal ionic radius for isomorphous substitution. For the isovalent isomorphism only, r_0 coincides with the ionic radius of the substituted cation. For fluorite-type matrices, values of k^0 linearly decrease with the melting entropy (this means that the k^0 depends upon the surface roughness). In actual processes of crystal growth impurity distributions along the crystals are described by the effective distribution coefficients k_{eff} . As a rule, $k < k_{\text{eff}} < 1$ or $1 < k_{\text{eff}} < k$.

The method of codoping with charge compensation is used for improving the conditions of dopant incorporation into crystals. For example, Na^+ was codoped with Ce^{3+} in order to maintain the charge neutrality at the substitution divalent actions in BaLiF_3 and LiCAF/LiSAF crystals [5]. If the differences in the size of the substituting cations are large, codoping with the intermediate size cation is used (see, e.g., Ref. [22]).

11.7 MORPHOLOGICAL STABILITY

Melt crystallization of fluoride- or tysonite-type solid solution systematically leads to formation of a cellular structure (see Fig. 11.7a) as a result of loss of flat-interface stability. The reason for this morphological instability is the well-known concentration or constitutional undercooling phenomenon. The simplest stability criterion of a flat interface during directional solidification of a two-component melt, which takes into account only mass transport, is as follows:

$$GR/D > m\Delta x = F(x) \quad (11.4)$$

where G is the temperature gradient, R is the solidification rate, D is the interdiffusion coefficient, m is the slope of the liquidus curve, Δx is the concentration jump at the solidification interface [48, 49]. The right-hand part of Equation (11.4), $F(x)$, was named the 'stability function'. It can be calculated from a phase diagram, see Fig. 11.8. Comparison of calculated stability functions with the results of crystal growth of fluorite solid solutions allowed us to evaluate the values of cation diffusivities in melts for a number of $\text{MF}_2\text{-RF}_3$ systems ($D \sim 5 \times 10^{-5}$ and 5×10^{-6} $\text{cm}^2 \text{s}^{-1}$ for $M = \text{Ca}$ and Ba , respectively; SrF_2 -based melts are characterized by intermediate D values). This gives the possibility to calculate the values of G and R necessary for preparing homogeneous cell-free crystals.

At small concentrations of the second component, $F(x)$ is a straight line, starting from the origin of (T, x) coordinates, which corresponds to the well-known Tiller's approximation. Another important case is the vicinity of extrema points in melting curves—minima

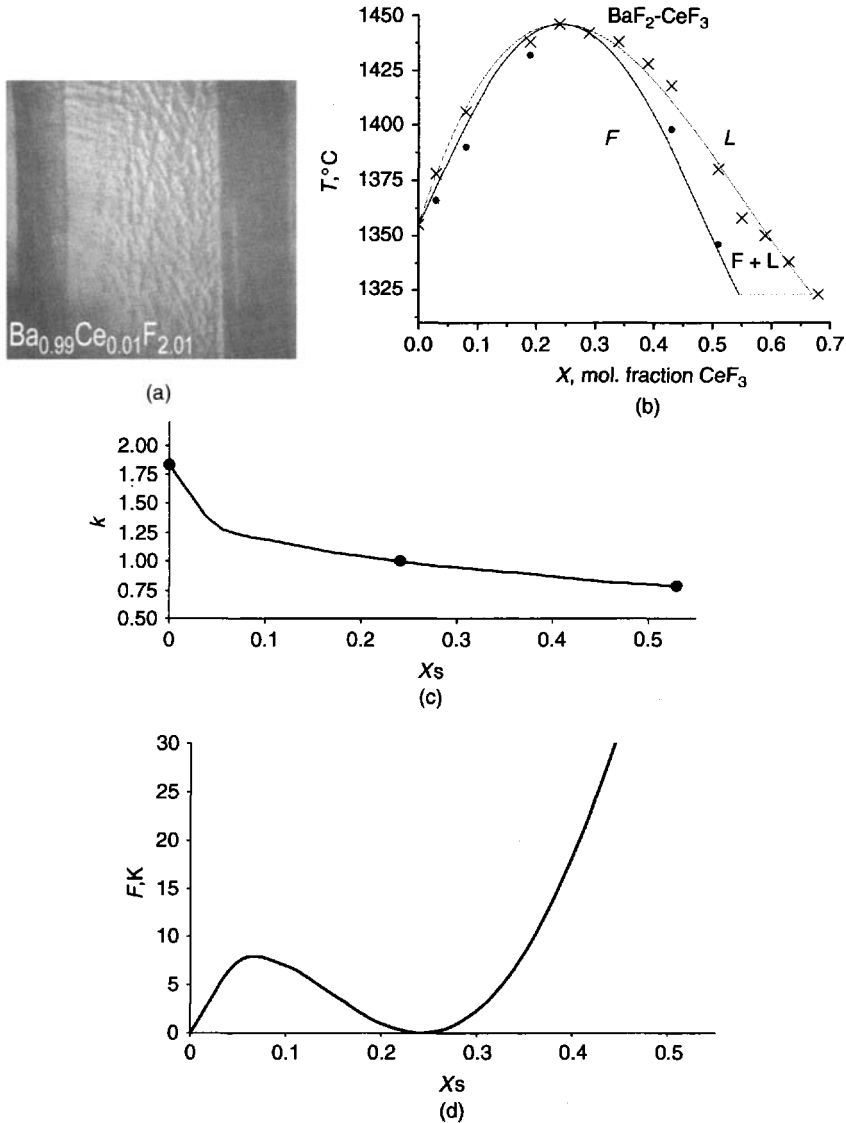


Figure 11.7 Photograph of cellular structure in $\text{Ba}_{0.99}\text{Ce}_{0.01}\text{F}_{2.01}$ crystal (diameter 7 mm), grown by Bridgman technique (a), part of phase equilibria for $\text{BaF}_2\text{-CeF}_3$ system (b), distribution coefficient (c) and stability function for $\text{Ba}_{1-x}\text{Ce}_x\text{F}_{2+x}$ solid solution (d)

and maxima. At such points $F(x) = 0$, $F'(x) = 0$, so the vicinity of such points is very convenient for preparing high-quality crystals.

On the basis of thermodynamical-topological analysis of directional solidification of multicomponent systems the existence of special congruently melting compositions in ternary $\text{MF}_2\text{-M}'\text{F}_2\text{-RF}_3$ systems—saddle points—was predicted [50]. Some of them were studied [51, 52]. The concentration near to such points are also very beneficial for growth of cell-free single crystals, see Fig. 11.8.

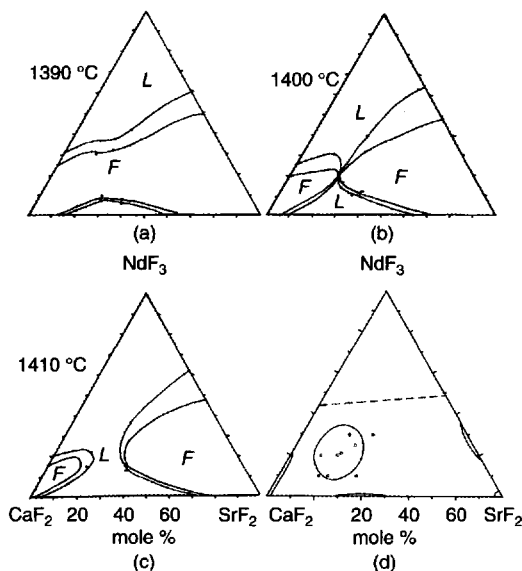
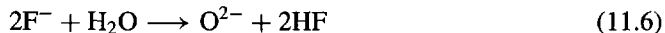


Figure 11.8 Saddle point on the melting surfaces of $\text{Ca}_{1-y}\text{Sr}_y\text{Nd}_y\text{F}_{2+x}$ fluorite-type solid solution in the CaF_2 - SrF_2 - NdF_3 system: liquid–solid phase equilibria at 1390 °C (a), 1400 °C (b) and 1410 °C (c), area of cell-free crystal growth at $R = 5 \text{ mm h}^{-1}$, $G = 30 \text{ K cm}^{-1}$ (o—cell-free crystals, ●—crystals with cells), dashed line—limiting concentration of fluorite-type solid solution (d). Composition of saddle point: $21 \pm 2 \text{ mol } \% \text{ NdF}_3$, $21 \pm 2 \text{ mol } \% \text{ SrF}_2$

11.8 HYDROLYSIS AND MELT FLUORIDE GROWTH

Fluorides are known to be sensitive to oxygen contamination. This property is very important for crystal growth. Thermodynamic calculations indicate that the most frequent source of oxygen is water vapor. Other sources, such as carbon dioxide or nitrate impurities in the initial reagents for RF_3 synthesis may also be important. The process of hydrolysis, which takes place under heating (pyrohydrolysis), includes several stages: adsorption of H_2O molecules on the surface, substitution of fluorine ions with hydroxyl and oxide ions according to the reactions



The next stage is the formation of second phase (hydroxyfluoride, oxyfluoride, oxide) after accumulation of a critical oxygen concentration. This process, which may take place during the cooling of crystals, leads to formation of inclusions and ‘milkiness’ in crystals. The final products of pyrohydrolysis are oxides.

The stability of compounds to pyrohydrolysis decreases in the following sequence: $\text{NaF} > \text{SrF}_2 > \text{BaF}_2 > \text{LiF} > \text{CaF}_2 > \text{BeF}_2 > \text{MgF}_2 > \text{RF}_3 > \text{AlF}_3 > \text{BiF}_3 > \text{ZnF}_2 > \text{ThF}_4 > \text{UF}_4$ [53]. The stability of the rare-earth fluorides RF_3 differs substantially, LaF_3 is the most stable, LuF_3 and ScF_3 are the least stable. CeF_3 is anomalously sensitive to H_2O [54]; the complicated role of oxygen impurity during thermal treatment of CeF_3 powder was described in Ref. [55].

Oxygen impurities in fluoride single crystals manifest themselves in additional absorption both in the UV (0.2–0.3 μm) and IR (about 10 μm) ranges.

OH^- radicals present absorption bands at 3 μm [5, 56]. Absorption bands in the range 3.3–3.6 μm were attributed to HCO^- [9]. The presence of oxygen changes the sensitivity of the materials to ionizing radiation [21].

The first stage of fluoride crystal growth is the processing of the feed materials. It may include a combination of some operations, such as drying chemicals under vacuum with slight heating (e.g., about 200 $^\circ\text{C}$) to remove water; sublimation; fluorination of solid reagents with such agents as HF, KHF_2 , NH_4F , NH_4HF_2 ; melting of feed materials under fluorinating atmosphere; zone melting. An argon-filled glove box should be used for operation with hygroscopic, for example, KF-containing, materials. Previously sintered or melted reagents are preferable to powders.

Only LiF and NaF single crystals are possible to grow under air. As a result, they contain noticeable amounts of OH^- group. Such crystals are used for fabrication of color-center lasers (after γ - or electron irradiation). Normally, fluoride crystal growth has to be carried out under a controlled atmosphere. Vacuum chambers have advantages in comparison with flowing systems [57]. High-purity inert gas (argon, helium) is often insufficient for preparing high-quality crystals [5]. A reactive fluorinating atmosphere should be used. The first fluorinating agent was HF [58]. HF is a highly corrosive gas and reacts readily at high temperatures with metals, such as stainless steel. Application of the Teflon decomposition process to crystal growth was discovered in Ref. [59]. Such decomposition gives gaseous CF_4 and C_2F_4 . According to [56], the efficiency of fluorinating agents decreases in the sequence $\text{C}_2\text{F}_4(\text{g}) > \text{NF}_3(\text{g}) > \text{CF}_4(\text{g}) > \text{COF}_2(\text{g}) > \text{SF}_6(\text{g})$. NF_3 reacts readily with graphite, the usual heater and crucible material. An argon/ CF_4 atmosphere is widely used [5, 7]. A combination of different agents (for example, argon/ CF_4 /HF [6]) may be effective. Different schemes of fluorinating-atmosphere realization in crystal growth chambers are presented on Fig. 11.9.

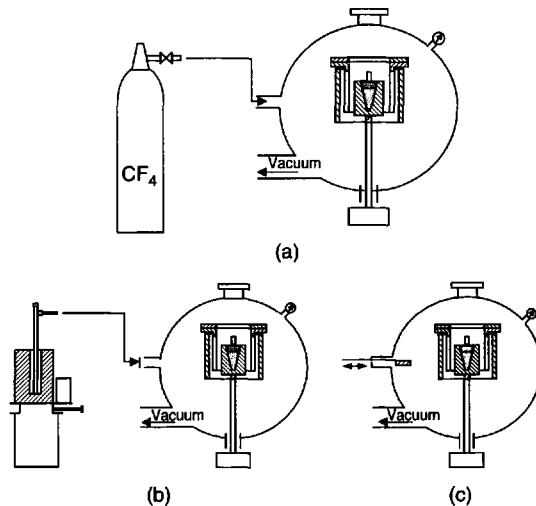
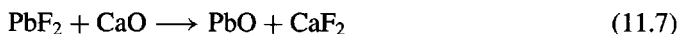


Figure 11.9 Schemes of creation of reactive fluorination atmosphere with use of gas (HF , CF_4 , etc) (a) and by Teflon pyrolysis process (b, c)

Another means of purification of fluorides melts and crystals is the scavenger principle [57, 60]. 0.3–5 wt% PbF₂ is mixed with raw fluoride (e.g., CaF₂ or BaF₂) powder in order to remove oxide impurity according to the reactions:



According to data [18, 57, 60], lead is practically fully removed from CaF₂ or BaF₂ single crystals. According to our data, however, RF₃ single crystals, grown by the scavenger process, contain noticeable amounts (~ 0.035 wt%) of lead.

Some useful descriptions of apparatus and crucibles for Bridgman and Czochralski techniques are described in Refs. [63–67].

ACKNOWLEDGMENTS

The authors greatly appreciate the technical assistance of A.M. Samartsev and S.V. Kuznetsov.

REFERENCES

1. A.A. Kaminskii, (1996) *Crystalline Lasers: Physical Properties and Operating Schemes*, CRC Press, Boca Raton, NY, p. 561.
2. T.T. Basiev, S.B. Mirov, and V.V. Osiko, (1988) Room temperatures color center lasers, *IEEE J. Quantum Electron.*, **24**, 1052–1069.
3. R. Burkhalter, I. Dohnke, and J. Hulliger. (2001) Growing of bulk crystals and structuring waveguides of fluoride materials for laser applications, *Prog. Cryst. Growth Charac.*, **42**, 1–64.
4. M. Laroche, S. Girard, R. Moncorge, M. Bettinelli, R. Abdulsabirov, and V. Semashko, (2003) Beneficial effect of Lu³⁺ and Yb³⁺ ions in UV laser materials, *Opt. Mater.*, **22**, 147–154.
5. K. Shimamura, H. Sato, A. Bensalah, V. Sudesh, H. Machida, N. Sarukura, and T. Fukuda. (2001) Crystal growth of fluorides for optical applications, *Cryst. Res. Technol.*, **36**, 801–813.
6. J.M. Breteau, and J.Y. Gesland, (1996) Spectroscopic and lasing properties of a diode pumpable Nd:GdF₃ crystal, *Opt. Mater.*, **5**, 267–271.
7. H. Sato, A. Bensalah, H. Machida, M. Nikl, and T. Fukuda, (2003) Growth and characterization of 3-in size Tm, Ho-codoped LiYF₄ and LiLuF₄ single crystals by the Czochralski method, *J. Cryst. Growth*, **253**, 221–239.
8. B. Chai, J. Lefaucher, and A. Pham, (1993) Growth of Nd:GdLiF₄ single crystals, *Proc. SPIE*, **1863**, 9–12.
9. S.L. Baldochi, K. Shimamura, K. Nakano, N. Mujilatu, and T. Fukuda, (1999) Ce-doped LiYF₄ growth under CF₄ atmosphere, *J. Cryst. Growth*, **205**, 537–542.
10. H. Chen, S. Fan, H. Xia, and J. Xu, (2002) Bridgman growth of fluoride laser crystal Ce³⁺: LiYF₄, *J. Mater. Sci. Lett.*, **21**, 457–459.
11. Y. Wang, C. Huang, L. Chen, and Z. Fang, (1996) Crystal growth of Cr³⁺: LiCaAlF₆ by Bridgman technique, *J. Cryst. Growth*, **167**, 176–179.
12. A.A. Kaminskii, A.V. Butashin, J. Hulliger, Ph. Egger, S.N. Bagayev, H.J. Eichler, J. Findeisen, B. Liu, U. Tauber, P. Peuser, and S.N. Sulyanov, (1998) New anisotropic rare earth fluorides BaR₂F₈ (R = Y, Dy–Lu): growth and characterization, *J. Alloys Compd.*, **275–277**, 442–446.

13. M.Yu. Sharonov, A.L. Bratus, B.K. Sevastyanov, Z.I. Zhmurova, A.A. Bystrova, E.A. Krivandina, L.N. Demianets, and B.P. Sobolev, (1994) The amplification and excited state absorption of Nd-doped nonstoichiometric crystals with fluorite structure in the 1.3 μm region, *Opt. Commun.*, **111**, 245–252.
14. V.V. Apollonov and T.V. Ouarova, (1999) Single crystal lasers for UV and VUV regions, *Proc. Int. Conf. "Laser 98"*, STS Press, McLean, VA, USA, 720–724.
15. P.P. Fedorov, N.M. Khaidukov, M.D. Val'kovskii, L.V. Medvedeva, O.S. Bondareva, and B.P. Sobolev, (1993) Synthesis of the compounds LiKRF_5 ($R = \text{Gd to Lu}$), *Russ. J. Inorg. Chem.*, **38**, 405–407.
16. B. Chai, A. Pham, and G. Lutts, (1993) Growth of high quality single crystal of KLiYF_5 by TSSG method, *Proc. SPIE*, **1863**, 160–163.
17. P. Solarz, I. Soko'ska, and W. Ryba-Romanowski, (2002) Photoluminescence of $\text{K}_5\text{Li}_2\text{LaF}_{10}:\text{Ho}^{3+}$ and $\text{K}_5\text{Li}_2\text{LaF}_{10}:\text{Ho}^{3+}, \text{Yb}^{3+}$, *J. Molec. Struct.*, **614**, 325–331.
18. T. Yonezawa, K. Matsuo, J. Nakayama, and Y. Kawamoto, (2003) Behaviors of metal-oxide impurities in CaF_2 and BaF_2 single-crystals grown with PbF_2 scavenger by Stockbarger's method, *J. Cryst. Growth*, **258**, 385–393.
19. A. Bensalah, K. Shimamura, T. Fujita, H. Sato, M. Nikl, and T. Fukuda, (2003) Growth and characterization of BaLiF_3 single crystal as a new optical material in the VUV region, *J. Alloys Compd.*, **348**, 258–262.
20. P.A. Rodnyi, (2001) Progress in fast scintillators, *Radiat. Meas.*, **33**, 605–614.
21. A.V. Gektin, (2000) Scintillators and storage phosphors based on ABX_3 crystals, *J. Lumin.*, **87–89**, 1283–1285.
22. P.P. Fedorov, I.I. Buchinskaya, S.P. Ivanov, B.P. Sobolev, A.S. Shcheulin, and A.I. Ryskin, (2002) A new class of holographic materials based on semiconductor CdF_2 crystals with bistable centers, Part II, Growth of optically perfect crystals, *Opt. Spectrosc.*, **92**, 125–132.
23. B.P. Sobolev, (2001) *The rare earth trifluorides. V. 1. The high temperature chemistry of the rare earth trifluorides. V.2. Introduction to materials science of multicomponent metal fluoride crystals*. Institut d'Estudis Catalans, Barcelona, p. 520 (2000); p. 459.
24. K.-Th. Wilke, (1973) *Kristallzuchtung*, VEB Deutscher Verlag der Wissenschaften, Berlin.
25. P.P. Fedorov and B.P. Sobolev, (1995) Morphotropic transitions in the rare-earth trifluoride series, *Crystallogr. Rep.*, **40**, 284–290.
26. O. Greis and M.S.R. Cader, (1985) Polymorphism of high purity rare earth trifluorides, *Thermochim. Acta*, **87**, 145–150.
27. R.E. Thoma and G.D. Brunton, (1966) Equilibrium dimorphism of the lanthanide trifluorides, *Inorg. Chem.*, **5**, 1937–1939.
28. B.P. Sobolev, P.P. Fedorov, D.B. Steynberg, B.V. Sinitsyn and G.S. Shakhkalianian, (1976) On the problem of polymorphism and fusion of lanthanide trifluorides. I. Influence of oxygen on phase transition temperatures, *J. Solid State Chem.*, **17**, 191–199.
29. L.G. Van Uitert, H.M. O'Bryan, H.J. Guggenheim, R.L. Barns and G. Zyzdik, (1977) Correlation of the thermal expansion coefficients of rare earth and transition metal oxides and fluorides, *Mater. Res. Bull.*, **12**, 307–314.
30. O. Greis and J.M. Haschke, (1982) Rare earth fluorides, *Handbook on the Physics and Chemistry of Rare Earths*. Eds. K.A. Gscheidner and L. Eyring. North-Holland, Amsterdam, New York, Oxford. **5**, 387–460.
31. V. Tmoucova, P.P. Fedorov, A.A. Bystrova, T. Sramkova, and B.P. Sobolev, (1998) Electric and dielectric properties of monoclinic BaR_2F_8 ($R = \text{rare earth elements}$) single crystals, *Solid State Ion.*, **106**, 301–307.
32. A. Ocafrain, J.P. Chaminade, O. Viraphong, R. Cavagnat, M. Couzi and M. Pouchard, (1996) Growth by the heat exchanger method and characterization of neighborite, NaMgF_3 , *J. Cryst. Growth*, **166**, 414–418.
33. K.S. Aleksandrov, I.N. Flerov, A.F. Bovina, and V.N. Voronov, (1984) The study of phase transitions in single crystals with elpasolite structure, *Ferroelectrics*, **54**, 237–240.

34. B. Maximov, H. Schultz, (1985) Space group, crystal structure, and twinning of LaF_3 , *Acta Cryst.*, **B41**, 88–91.
35. P.P. Fedorov, 1991 High temperature chemistry of rare earth fluorides: basis for preparing of new materials, *Doctoral Thesis*, Moscow Institute of Fine Chemical Technology, 608 p. (in Russian).
36. P.P. Fedorov, (1999) Systems of alkali and rare-earth metal fluorides, *Russ. J. Inorg. Chem.*, **44**, 1703–1727.
37. V.V. Osiko, (1965) Thermodynamics of optical centers in crystals of $\text{CaF}_2\text{-R}^{3+}$, *Solid State Phys.*, **7**, 1294–1302, in Russian.
38. P.P. Fedorov, (2000) Heterovalent isomorphism and solid solutions with a variable number of ions in the unit cell, *Russ. J. Inorg. Chem.*, **45**, Suppl. 3, S268–S291.
39. D.J. Chermak, X.Y. Zhang, N.K. Wayne and E.B. Watson, (2001) Sr, Y, and REE diffusion in fluorite, *Chem. Geol.* **181**, 99–111.
40. R.D. Shannon, (1976) Revised effective ionic radii and systematic studies of interatomic distances in halides and chalcogenides, *Acta Cryst.*, **A32**, 751–767.
41. A.A. Kaminskii, N.R. Agamalyan, G.A. Denisenko, S.E. Sarkisov, and P.P. Fedorov, (1982) Spectroscopy and laser emission of disordered $\text{GdF}_3\text{-CaF}_2\text{:Nd}^{3+}$ trigonal crystals, *phys. stat. sol. (a)*, **70**, 397–406
42. R.E. Thoma, H. Insley, and G.M. Hebert, (1966) The sodium fluoride—lanthanide trifluoride systems, *Inorg. Chem.*, **5**, 1222–1229.
43. B. Chai, J. Lefacher, A. Pham, G. Lutts, and J. Nicholls, (1993) Growth of high quality single crystals of KYF_4 by TSSG method, *Proc. SPIE*, **1863**, 131–135.
44. P.P. Fedorov, L.V. Medvedeva, B.P. Sobolev, and V.M. Reiterov, (2002) Revision of LiF-RF_3 phase diagrams, *Growth of Crystals*, **21**, eds. E.I. Givargizov and A.M. Melnicova, Consultants Bureau, N.Y., London. 141–153.
45. D. Klimm and P. Reiche, (2002) Comments on ‘Phase equilibria in the pseudo-binary systems LiF-CaAlF_5 and LiF-SrAlF_5 ’ [*J. Cryst. Growth* **235** (2002) 596], *J. Cryst. Growth*, **249**, 388–390.
46. N.M. Khaidukov and P.P. Fedorov, (1990) K_2LnF_5 compounds, *Russ. J. Inorg. Chem.*, **35**, 383–384.
47. N.A. Dybinskii, N.M. Khaidukov, I.G. Garipov, L.N. Demianets, A.K. Naumov, V.V. Semashko, and V.A. Malyusov, (1990) Spectral-kinetic and lasing characteristics of new Nd^{3+} -activated laser hosts of the KF-RF_3 system, *J. Mod. Opt.*, **37**, 1355–1360.
48. P.P. Fedorov, T.M. Turkina, V.A. Meleshina and B.P. Sobolev, (1991) Cellular substructure in single crystalline solid solutions of inorganic fluorides having the fluorite structure, *Growth of Crystals*, **17**, eds. E.I. Givargizov and S.A. Grinberg, Consultants Bureau, N.Y., London. 165–176.
49. P.P. Fedorov, (2001) Morphological stability of the solidification front near minima and maxima in the liquidus line in binary solid-solution systems, *Inorg. Mater.*, **37**, 84–92.
50. P.P. Fedorov, (1996) Compositions of congruently melting three-component solid solutions determined by finding acnodes on ternary system fusion surfaces, *Growth of Crystals*, **20**. Eds. E.I. Givargizov, A.M. Melnicova. Consultants Bureau, N.Y., London. 103–116.
51. V.A. Stasyuk, I.I. Buchinskaya, N.A. Ust’yantseva, and P.P. Fedorov, (1998) Phase diagram of the $\text{CaF}_2\text{-SrF}_2\text{-NdF}_3$ system, *Russ. J. Inorg. Chem.*, **43**, 766–770.
52. P.P. Fedorov, V.A. Stasyuk, N.A. Ivanovskaya, I.I. Buchinskaya, S.V. Isaev, and A.G. Papashvili, (1999) Crystallization of the fluorite solid solution in the $\text{CaF}_2\text{-SrF}_2\text{-NdF}_3$ system in the vicinity of a saddle point on the liquidus surface, *Doklady Phys. Chem.*, **369**, 217–219.
53. J.C. Warf, W.D. Cline, and R.D. Tevebaugh, (1954) Pyrohydrolysis in the determination of fluoride and other halides, *Analyt. Chem.*, **26**, 342–346.
54. C.V. Banks, K.E. Burke, and J.W. O’Laughin, (1958) The determination of fluorine in rare-earth fluorides by high temperature hydrolysis, *Analyt. Chim. Acta*, **19**, 239–243.

55. T. Inagaki, Y. Yoshimura, Y. Kanda, Y. Matsumoto, K. Minami, (2000) Development of CeF_3 crystal for high-energy electromagnetic calorimetry, *Nucl. Instrum. Methods Phys. Res.*, A **443**, 126–135.
56. R.C. Pastor, (1999) Crystal growth of metal fluorides for CO_2 laser operation II. Optimization of the reactive atmosphere process (RAP) choice, *J. Cryst. Growth*, **203**, 421–424.
57. I.V. Stepanov, P.P. Feofilov, (1957) Artificial fluorite, *Growth of Crystals*, **1**, Eds. A.V. Shubnikov and N.N. Sheftal, Acad. Sci. of USSR, Moscow, 229–241, in Russian.
58. H.J. Guggenheim, (1961) Growth of single crystals calcium fluoride with rare earth impurities, *J. Appl. Phys.*, **32**, 1337–1338.
59. Yu.K. Voron'ko, V.V. Osiko, V.T. Udovenchik, and M.M. Fursikov, (1965) Optical properties of $\text{CaF}_2\text{-Dy}^{3+}$ crystals, *Solid State Phys.*, **7**, 267–273, in Russian.
60. D.C. Stockbarger, (1949) Artificial fluorite, *J. Opt. Soc. Am.*, **39**, 31–40.
61. S. Kuck, (2001) Laser-related spectroscopy of ion-doped crystals for tunable solid-state lasers, *Appl. Phys. B* **72**, 515–562.
62. J.-P.R. Wells, A. Sugiyama, T.P.J. Han, and H.G. Gallagher, (1999) Laser site selective excitation of K_3YF_{10} -doped with samarium, *J. Lumin.*, **85**, 91–102.
63. M. Robinson and D.M. Cripe, (1966) Growth of laser-quality rare-earth fluoride single crystals in a dynamic hydrogen fluoride atmosphere, *J. Appl. Phys.*, **37**, N5, 2072–2074.
64. P. Selgert, N.R. Whippley and W. Assmus, (1984) A low cost puller for crystal growth in fluorinating atmospheres, *J. Cryst. Growth*, **69**, 198–200.
65. A. Linz and D. Gabbe, (1984) Growth of fluoride laser host crystals, *Proc. 1st Int. Conf. Tunable Solid State Lasers*, La Jolla, Calif., 115–121.
66. K. Recker, F. Wallrafen, R. Büscher and G. Lehmann, (1981) Crystal growth, EPR, and luminescence of $\text{BaZnF}_4\text{:Mn}$, *phys. stat. sol. (b)*, **107**, 699–706.
67. D.A. Jones, B. Cockayne, R.A. Clay, and P.A. Forrester, (1975) Stockbarger crystal growth, optical assessments and laser performance of holmium-doped yttrium erbium lithium fluorides, *J. Cryst. Growth*, **30**, 21–26.

This page intentionally left blank

12 Scintillators: Crystal Growth and Scintillator Performance

A. GEKTIN

Institute for Scintillation Materials, 60 Lenin Ave., 61001, Kharkov, Ukraine

12.1 Introduction	357
12.2 Scintillator applications	358
12.2.1 High-energy physics	359
12.2.2 Medical imaging	361
12.3 Scintillation-material efficiency estimation	361
12.4 Halide scintillator growth	364
12.5 Activator distribution in scintillation single crystals	374
12.6 Oxide scintillation crystal growth	376
12.7 Influence of single-crystal perfection on scintillation characteristics	378
12.8 New scintillation crystals	381
12.9 Conclusion	382
List of definitions and abbreviations	383
References	383

12.1 INTRODUCTION

Nowadays, scintillation materials and detectors form the basis for many radiation-detection devices. The ability to convert different ionizing radiations into visible light provided an activity that could be conditionally called ‘scintillation material science’ (when it is a question of scintillation-materials production) and ‘detection systems engineering’ (when, in fact, a detection device is developed using one or another material). Scintillation properties are typical for many materials (organic, plastic, liquid, ceramic scintillators). But in this review we focus on the principal trend—scintillation single crystals.

The first application of the scintillation technique and CaWO_4 crystals as scintillators date from the period of Roentgen’s discovery of X-rays and Rutherford’s study of alpha-particle scattering [1].

Rapid evolution of this activity dates back to the early 1950s when the first high-performance $\text{NaI}(\text{Tl})$ scintillator material was grown [2]. During the last five decades thousands of different dielectric media have been investigated for the purpose of more efficient scintillation-material production, but only a few of them are reported to be practically

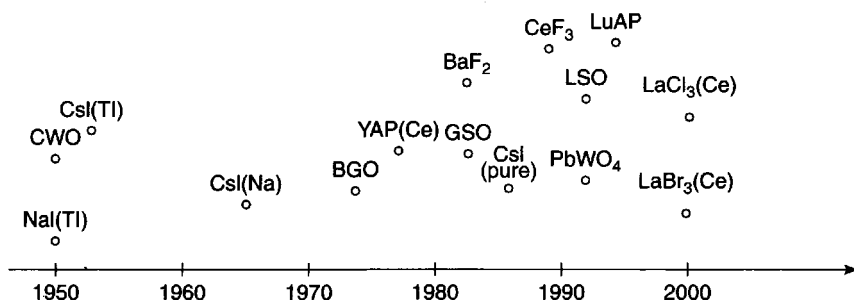


Figure 12.1 Commercially available scintillator history

applied and form, so far, a number of commercially available scintillation materials. The main scintillators and their transition from R&D to practical application are shown in Fig. 12.1. Thus, a number of scintillators instead of one kind of material appeared and today as we stand on the verge of real mass practical application there are still several new types of materials, like LuAP [3], LaBr and LaCl doped with Ce^{3+} [4], LYSO [5], etc. But why have we failed to manufacture a 'perfect' scintillator up to now?

There are some principal scintillation-crystal requirements:

First, is high density and high atomic number of the material. These parameters determine the efficiency of radiation absorption. In addition scintillator compactness and the ability to produce reasonable-sized single crystals are required.

The second requirement is the high light emission (luminescence) efficiency, i.e. the capability to convert absorbed energy into visible-light photons as efficiently as possible. The matter concerns visible light—since the wavelength of emitted irradiation defines the possibility to use a scintillator together with a light receiver.

The third critical parameter is the scintillation pulse decay time, which determines the operation speed of the detector as a whole.

The scintillator must be highly transparent at the wavelength of emitted irradiation to ensure the output of the scintillated light in a crystal with minimum intrinsic loss.

Radiation hardness is the ability to preserve properties under continuous irradiation fields.

When practically applied, the crystal is required to possess other specific properties like low afterglow, low background, chemical and mechanical stability, etc. These practical tasks require optimization of physical scintillator parameters as well as pragmatic requirements, namely—to produce quite cheap, large-sized scintillators in volume.

Thus, the above requirements are found to be far from simple. Moreover, scientific development and the principles of the search for new materials rather prevent the approach to 'perfect scintillator' production. Different fields of scintillator applications mainly claim requirements to one of the listed parameters that strongly prohibits the possibility of meeting the rest of the requirements within reasonable limits.

12.2 SCINTILLATOR APPLICATIONS

At present scintillators are widely used in nuclear medicine, high-energy physics and astrophysics, security systems, geophysics, environmental control, and industrial applications.

Applications Properties	Tomography CT, PET	Nuclear medicine SPECT	High-energy physics	Industry	Security	Environment
High density and atomic number	++	+	+++	++	+	++
High light yield	+++	++	+++	+	-	++
Fast response	+	-	++	-	-	-
High transparency	+	-	+++	+	-	-
Convenient emission range	+	-	++	+	++	++
Radiation stability	-	-	+++	-	-	+
Large size of single crystal	+++	-	+++	-	-	-
Low cost	+++	+++	+++	++	++	+

Figure 12.2 Correspondence between scintillator parameters and applications

The most important scintillator parameters required by one or another application are shown in Fig. 12.2. Despite the convention of such an analysis, it is obvious that the most rigid requirements are connected with high-energy physics and medical imaging.

12.2.1 High-energy physics

Inorganic scintillation crystals possessing a wide cross section for gamma-photon photoabsorption, an effective value of density, atomic number, and sufficient speed of operation are used in experimental high-energy physics as scintillators for electromagnetic calorimeters.

If we analyze the history of scintillator development for this use [6] (Table 12.1), we see that NaI(Tl) (despite its high hygroscopicity) dominated in the 1960s. Then the period of BGO began. Towards the end of the 20th century two large projects, namely, BELLE (KEK, Japan) [7] and BaBar (SLAC, USA) [8] based on CsI(Tl) scintillators were carried out. In the middle of the 1990s from the beginning of the CMS and ALICE (LHC, CERN, Switzerland) projects [9] a new epoch was marked by PbWO₄. Huge-sized electromagnetic calorimeters (up to 3–5 m in diameter) required a very large number of crystals. For example, the BELLE and BaBar projects required in total about 38 tons of CsI(Tl) scintillation crystals. The CMS project will need in 16 tons of PbWO₄ crystals.

In all cases the main problems and needs in long-term R&D were connected with technology and single-crystal perfection problems. First, long (300 mm) single crystals were needed. Secondly, light-output-uniformity requirements dictated the necessity of high stability and uniformity of single crystals on the whole. Thirdly, the beam intensity rise required increased crystal radiation hardness, i.e. R&D of radiation-damage suppression [10, 11].

At the same time BaF₂ and CeF₃—two other halide scintillators—were considered to be alternatives. Despite numerous developments [12] these scintillators had never been widely adopted, whereas pure CsI had been applied to the PiBeta and KTeV [13] experiments.

PbWO₄-based scintillators give an example of the most dynamic development of a new scintillator starting with the first literature reports [14] until a prototype was successfully

Table 12.1 Main crystal calorimeters in the world (For more details see ref. [6])

	Crystal Ball	CLEO II	L3	BaBar	Belle	L^* LoI	GEM EoI	GMS EoI	$L3P$ EoI	ALICE	CMS	
Where	SPEAR	CESR	LEP	SLAC	KEK	SSC	SSC	LHC	LHC	LHC	LHC	
When	1972	Late	1980s	1999						2005		
Beam	$e^+ e^-$	$e^+ e^-$	$e^+ e^-$	$e^+ e^-$	$e^+ e^-$	pp	pp	pp	pp	ion ion	pp	
Beam energy	4	6	100	9 + 3,1	8 + 3.5	20	20	20	20	5,5-A	7	
	GeV					TeV						
Crystal	NaI(Tl)		CsI(Tl)	BGO	CsI(Tl)	CsI(Tl)	BaF ₂	BaF ₂	CeF ₃	CeF ₃	PbWO ₄	PbWO ₄
Number [k]	0.7		7.8	11.4	6.8	8.8	26	15	45	100	36	82
Length [X_0]	16		16	21.5	16	16	24.5	24.5	25	25	22	25
Photodetector	PMT		Si PD	Si PD	Si PD	Si PD	V4T	V4T	SiPD	VPD	Si PD	APD/V3T

developed and tested that allowed appropriate crystals to be chosen for the biggest project (CMS—82 000 full-size single crystals and ALICE—36 000 crystals) and to start their mass production during 2001.

12.2.2 Medical imaging

In spite of the large scintillator production volume for high-energy physics applications, the main market of the detectors is connected with medical imaging, in particular with X-ray CT (computer tomography—1501 per year), SPECT (single-photon emission tomography—gamma cameras—60001 per year), PET (positron emission tomography—5001 per year), X-ray diagnostic machines (50 0001 per year) [15]. The biggest scintillation single-crystal market is connected with their application as gamma camera (SPECT) detectors. Detector size should allow full-body screening, therefore crystal dimensions reach 600×500 mm, which is a driving force for large-size single-crystal growth. Modern medical-equipment modifications lead to the production of curved detectors [16] as well as cylindrical ones for brain SPECT [17]. NaI(Tl) single crystals serve as a basis for this research.

X-ray computer tomograph allows the spatial density arrangement of the considered object to be restored. One of the most important requirements concerning scintillators is a short decay time and low afterglow level because at least 100 projections per second are accomplished in a CT machine. CT (X-ray computer tomography) diagnostics is mainly based on CdWO_4 single crystals and is in great need of alternative materials to replace Cd-containing materials.

PET allows measurement of the arrangement of special isotopes injected and distributed in the human body that emit positrons with further annihilation with electrons. This is achieved due to the detection of annihilation of gamma-quanta (511 keV energy) registration. As a rule, the annihilation radiation is detected by special scintillation detectors or a matrix matched to the position-sensitive photomultiplier tube (PMT). PET systems require the development of heavy, fast and highly efficient materials. Initially all prototypes and commercially available PET systems were based on BGO scintillators, but continuous search for more efficient materials led to new scintillators production, namely, LSO ($\text{Lu}_2\text{SiO}_5:\text{Ce}^{3+}$) [18], GSO $\text{Gd}_2\text{SiO}_5:\text{Ce}^{3+}$ [19] as well as LYSO ($(\text{Lu} - \text{Y})_2\text{SiO}_5:\text{Ce}^{3+}$) [5], i.e. it is impossible to find a unique scintillation material even in the framework of similar applications.

12.3 SCINTILLATION-MATERIAL EFFICIENCY ESTIMATION

The classic method of scintillation-material efficiency (η) estimation is based on a phenomenological approach dividing the process into three stages [20, 21]. First, this is absorption of the incident ionizing particle by the crystal host and energy conversion into thermalized electrons and holes. The conversion efficiency of this stage (β) depends on the crystal-host type and the search for a scintillation matrix has to start from the estimation of the β efficiency. The second stage is migration, i.e. transfer of electron and hole excitations to the luminescence center (S —energy-transfer efficiency). This stage is partly structure sensitive due to capturing of some carriers by deep and shallow traps, color-center formation, radiation-induced transformation of some impurity states, etc. In

this stage, the role of structural perfection and the possibility of more efficient scintillators production will be determined. The last stage relates to the radiative efficiency of luminescence centers (Q) and the optimal concentration of these centers. Total efficiency could be defined as:

$$\eta = \beta S Q \quad (12.1)$$

Conditionally, scintillators could be divided into groups according to the initial luminescence mechanisms [21] (Table 12.2). These mechanisms exactly define the specific character of the scintillator and the potential limitation of its efficiency.

Intrinsic luminescence-based scintillators possess fast response (short decay time), but have relatively low light yield as a result of luminescence quenching with increasing temperature. The problem of low luminescence efficiency is peculiar to crystals possessing cross-luminescence. In this case a low light yield is compensated for a short scintillation pulse decay time (a few nanoseconds or even less).

First, extrinsic luminescence is associated with doped crystals. In the role of activator, a dopant ion may be either a direct luminescence center or may promote luminescence as in the case of impurity-bound exciton emission (e.g. for CsI(Tl) or CsI(Na) scintillators).

All the stages and corresponding processes are described in [21, 22] in greater detail. It is noteworthy that such relative division into types allows the substance class to be defined as well as the possibility to use one or another scintillator material being specifically applied. Scintillator efficiency is evaluated by the quantity of photons emitted at 1-MeV energy absorption. Table 12.3 presents the most efficient scintillators and current fields of their application. As a whole the overwhelming majority of contemporary scintillators are dielectric crystals. Nevertheless, scintillation characteristics availability is also typical for a series of wide-bandgap semiconductors. As early as the 1960s the possibilities of doping ZnO with Ga and In were studied [23]. The obtained fast detectors with a decay time of about 1 ns remained useless, however. Later, ZnSe(Te) crystals were pulled [24]. In and Te doping of CdS is yet another example of scintillator development by isoelectronic donors and acceptors structure [25].

It follows from Table 12.3 that practically all known scintillators belong to two material types. These are either halide crystals or oxides, i.e. wide-bandgap materials. In most cases the issue concerns the matrix used for other applications. For example, laser materials, optical materials (from UV to IR regions) as well as crystals for applied lithography. A

Table 12.2 Types of inorganic scintillators and examples of representative materials (For more details see ref. [21])

Intrinsic

Excitonic: CsI, BaF₂

Self-activated: Bi₄Ge₃O₁₂, CeF₃, CdWO₄, LuTaO₄

Semiconductors: CuI, HgI₂, PbI₂.

Extrinsic

Activated: NaI:Tl⁺, CsI:Tl⁺, CaF₂:Eu²⁺

Cerium activated: Lu₂SiO₅:Ce³⁺, LaAlO₃:Ce³⁺, glass:Ce³⁺

Semiconductors: CdS:Te²⁻, ZnO:Ga, CdS:In

Core-valence luminescence

BaF₂, CsF, RbF, KMgF₃, BaLu₂F₈

Table 12.3 The most efficient and usable scintillators

	NaI(Tl)	CsI(Na)	CsI(Tl)	CsI undoped	⁶ LiI(Eu)	CaF ₂ (Eu)	BaF ₂	GSO(Ce)	CdWO ₄	BGO	LSO	LuAP:Ce
Density [g cm ⁻³]	3.67	4.51	4.51	4.51	4.08	3.18	4.88	6.71	7.9	7.13	7.4	8.34
Melting point [K]	924	894	894	894	719	1691	1627	2173	1598	1323	2150	2233
Hygroscopic	yes	Yes	slightly	slightly	very	no	no	no	no	no	no	no
Wavelength of emission maximum [nm]	415	420	550	310	470	435	310 220(195)	440	470/450	480	420	365
Refractive index at emission maximum	1.85	1.84	1.79	1.95	1.96	1.47	1.50(310 nm) 1.54(220 nm)	1.85	2.2–2.3	2.15	1.82	1.97
Light output [% of NaI(Tl)] (for gamma-rays)	100	85	45	5–6	30–35	50	16(slow) 5(fast)	20	25–30	15–20	75	≈ 60
Primary decay time [μs]	0.23	0.63	1	0.01	1.4	0.94	0.63(slow) 0.0006–0.0008 (fast)	0.06	20/5	0.3	0.04	0.018
Afterglow (after 6 ms) [%]	0.3–5	0.5–5	0.1			< 0.3			0.1 after 3 ms	0.005 after 3 ms		
Lower wavelength cutoff [nm]	300	300	320	260	425	395	135	395	330	320	320	320

distinctive feature is the specially required doping, principally with Tl ions for halides and Ce, Tb, Pr for oxides (when maintaining high-transparency requirements, structural purity and perfection are also necessary).

Conventional SPECT, coincidence counting systems, matrix (pixilated) detector advanced scanners are based on NaI(Tl) or CsI(Tl) crystals. Long single crystals (300 mm) being highly uniform both inside the crystal and from crystal to crystal are used for high-energy physics. Large size of crystals, volume production and low-price requirements made this material indispensable during recent decades. The main efforts were directed not to the search for new dopants and host crystals but to growth-process advancement.

The situation in the case of oxide single crystals is somewhat different. The need for large-size crystal growth, except PbWO₄ single crystals for high-energy physics applications, is defined by the productive cost efficiency as a whole. (A considerable quantity of mid- and small-sized scintillators is used for PET, CT scanners for medical imaging.) Economic expediency of innovative activity directed towards increased yield and corresponding price cutting is of importance here.

Thus, it should be readily noted that high-energy physics and medical applications are two principal driving forces promoting the search for and the growth of scintillation materials.

12.4 HALIDE SCINTILLATOR GROWTH

Practically all currently known growth techniques were applied for halide scintillator growth developments. Namely, the Bridgman–Stockbarger method [26], the Kyropulos method [27] and the Czochralski technique [28]. The main crystal-perfection requirements were maximum possible transparency and optimal activator content.

From the beginning of the 1950s alkali-halide single crystals were manufactured either by Bridgman–Stockbarger or Kyropulos techniques. The Stockbarger method utilized a heater chamber with two sections divided by a baffle into upper and lower heated chambers. The upper section is heated to a temperature above the melting point and the bottom section is heated to a temperature below the melting point of the crystal. Crystallization begins at the lower section and process upwards through the melt as the crystal is lowered from the upper part of the furnace chamber to the bottom part. Usually an inert gas is used during filling of the quartz crucible. A slight overpressure of inert gas reduces impurities by prevention of outside contaminants from leaking into the furnace. Occasionally, small amounts of certain gases, called scavengers, are introduced into the crystallization chamber in order to react with and draw out harmful impurities that are known to exist in the melt (raw material).

In actual practice, the main problem relates to nonuniform distribution of the activator along the alkali-halide single crystals. This is because all dopants have segregation coefficients that are not equal to unity. Thus, if the crucible with a melt and crystal is lowered the crystal has a lower activator concentration than the melt and this difference will increase continuously. This means that the activator concentration can vary drastically to the bottom of the crystal. For example, typical distributions of Tl ions in NaI and CsI crystals may vary by more than 50 times and lead to activator segregation and luminescence quenching.

Modern trends of growth-method development gave impetus to the critical need for gamma-camera detectors. The necessity of growing large-size single crystals with high

uniformity of transparency as well as luminescent parameters occurred along with the above-mentioned requirements. From this point onwards a new line of activity, namely, large-size halide scintillation single-crystal growth emerged.

On the one hand, this could be provided by proportionally increasing the crystallization furnace size. On the other hand, this aim could be achieved by means of fulfilling continuous crystal-growth principles [29]. Even in the case of crystals growing by small temperature gradients the first approach is connected with the necessity of interface-shape maintenance during the crystal-growth process. The second group of methods allows the crystal/melt interface position to be fixed, but this uses a more complicated hardware implementation and also the logical design of melt feeding in the course of growth.

Continuous-growth developments were applied to a method using both an ampoule and pulling on the seed method.

In the first case, the principle of Stockbarger's method modification bears the following character (see Fig. 12.3 [30]). The ampoule in which the crystal is grown is coupled to the melt-feeding system. In the course of single-crystal growth (i.e. positioning the ampoule with a growing crystal at the bottom of the growth chamber) the melt is fed from the upper feeder. In this case the crystal size is limited by the ampoule diameter and the growth chamber height. A general objective of this technique is to provide a continuous process for the growth of ultrapure halide crystals in a Bridgman–Stockbarger furnace [26]. It was a goal to develop technology that allows the crucible to be occupied fully by causing additional charging of material to the crucible. Another specific objective of this technique is to provide a process by which the residual activator concentration in the crystal is essentially uniform, despite segregation coefficients that may be much greater or less than unity. The surplus of activator impurity accumulated when the crystal is grown in height has to allow feeding by the host material only.

There is also a method of horizontal continuous crystal growth for plates of any dimensions (Fig. 12.4) [31]. A traveling crucible or crystal slab can be used if the heaters are stationary. Activator impurity concentration control can be achieved by adding activator in solid form. This invention related to both the growth and purifying of crystal material, but this invention did not find commercial realization.

In general, the idea of a continuous-growth process originated from metallurgy with many different casting techniques. But direct transfer of such methods was not successful due to the necessity to provide at least:

- (i) conditions for the single-crystal growth,
- (ii) additional purification ability,
- (iii) uniform activator impurity distribution.

These developments were started in the 1970s and 1980s for semiconductors (Si, first of all) [32–34] and halide crystal growth [35]. Some of these developments solved the problem of continuous growth of columnar structure rods [33], some allowed not only to sustain permanent feeding, but produced an extra purification effect [32], but only two of them found practical application for scintillator growth [34, 35]. Both techniques were based on the Kyropoulos method with feeding by solid raw material (granules or powder) or previously melted raw materials.

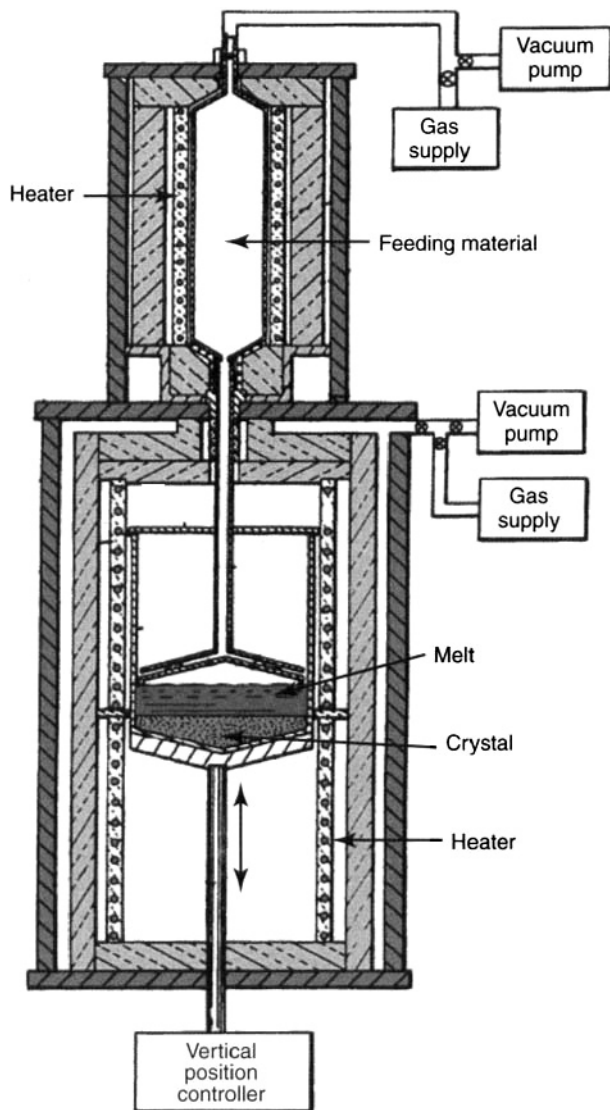


Figure 12.3 Stockbarger technique with raw-material feeding system [30]

Because of the seeming external simplicity of this continuous-growth method, methods of pulling the crystal on the seed by way of raw-material feeding were widely adopted in practice [29, 35–39].

Figure 12.5 presents the principle of automated crystal-growth technology with a powder-feeding system [29, 35, 36]. In this case the crystal size is limited by the crucible diameter and the crystallization chamber height. Crystal-diameter control was applied as the main principle of this design. The solution of mass-balance equations describing the relationship between crystallizing as a single crystal: melt weight and constant raw-material feeding assures crystal-diameter stability (and crystal/melt interface position,

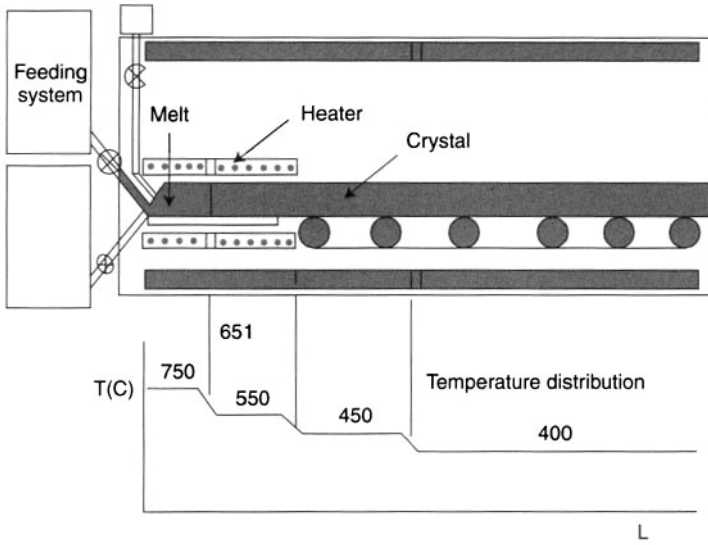


Figure 12.4 Horizontal continuous crystal growth for plate growth technique with powder-feeding system [31]

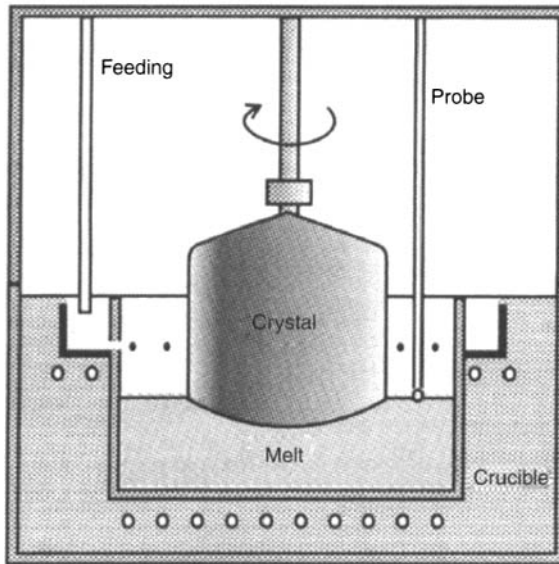


Figure 12.5 Principle of continuous-growth technique with powder-feeding system

respectively) and to carry out continuous growth. Actually, the material-balance equation turns out to be rather simple:

$$\frac{dm_1}{dt} = \frac{dm_s}{dt} \tag{12.2}$$

where m_s, m_1 —masses of crystal and melt, respectively.

These values are connected with the main pulling parameters—axial pulling rate (V) and single-crystal cross-sectional area (s):

$$\frac{d^2 m_s}{dt^2} = \rho_s \left(s \frac{dV}{dt} + V \frac{ds}{dt} \right) = \frac{d^2 m_1}{dt^2} \quad (12.3)$$

where ρ_s —crystal density.

To pull the crystal with $V, s = \text{const}$ it is necessary to use one of following means:

$V = \text{const}$ —crystal-length gauge, melt-level control,

$s = \text{const}$ —crystal-diameter control,

$\frac{dm_1}{dt} = \text{const}$ —melt-weight control, melt-level control,

$\frac{dm_s}{dt} = \text{const}$ —crystal-weight control.

Among these automated crystal-growth principles only the first is used to produce large-sized alkali-halide single crystals.

As a first approximation (steady-state process) the crystal diameter is described by the following expression:

$$d = 2 \left(\frac{m}{\pi \rho_s V_p} \right)^{\frac{1}{2}} \quad (12.4)$$

where ρ_s —crystal density; m —feeding rate; V_p —pulling rate.

As a second approximation [29], complementary factors should be taken into account, for example, undermelted single-crystal appearance and evolution, material loss due to evaporation from the free-surface area of the melt, etc. Taking into account these factors the simple Equation (12.4) moves to the much more intricate, but practically realizable equation:

$$d = 2 \left\{ \frac{m + \left(\frac{\pi D^2 h}{4} - W_s \right) \rho_1 \alpha T^* - (\rho_s - \rho_l) W_s - \frac{\pi D^2}{4} (\rho_l h^* - \gamma)}{\pi \rho_s V_p \left[1 - \left(\frac{h^*}{V_p} + \frac{\gamma}{\rho_s V_p} \right) \right]} \right\} \quad (12.5)$$

where W_s —single-crystal volume below melt level, γ —evaporation rate.

Taking into account that $h^* \ll V_p$ and $\gamma \ll \rho_s V_p$ one can obtain:

$$d \approx d_s \left\{ 1 + \frac{1}{2m} \left[\left(\frac{\pi D^2}{4} h - W_s \right) \rho_1 \alpha T^* - (\rho_s - \rho_l) W_s - \frac{\pi}{4} (D^2 \rho_l - d^2 \rho_s) h - \frac{\pi}{4} (D^2 - d_s^2) \gamma \right] \right\} \quad (12.6)$$

Practical control of the mass balance between the growing crystal and the raw-material feeding can be described by the following expression derived from the balance equation:

$$\frac{\pi d^2}{4} V \rho_s = m_1 \quad (12.7)$$

where d —crystal diameter.

For $\dot{m}_s = \dot{m}_1$:

$$2 \frac{\Delta d}{d} + \frac{\Delta V}{V} = \frac{\Delta m_1 \Delta m_s}{m_1 m_s} \quad (12.8)$$

In practice, the crystals are grown using sensors.

1. Crystal-diameter control

$$\frac{\Delta V}{V} = \frac{\Delta m_1}{m_1} - 2 \frac{\Delta d}{d} = \frac{2 \frac{\Delta d}{d}}{\left(\frac{\rho_1 D^2}{\rho_s d^2} \right) - 1}; \quad D \text{—crucible diameter}$$

2. Crystal-weight control

$$\frac{\Delta V}{V} = \frac{\rho_s d^2 \Delta m_s}{\rho_1 D^2 m_s} \Rightarrow \frac{\Delta d}{d} = \frac{1}{2} \left(1 - \frac{\rho_s d^2}{\rho_1 D^2} \right) \frac{\Delta m_s}{m_s}$$

3. Melt-weight control

$$\frac{\Delta V}{V} = \frac{\rho_s d^2 \Delta m_1}{\rho_1 D^2 m_1} \Rightarrow \frac{\Delta d}{d} = \frac{1}{2} \left(1 - \frac{\rho_s d^2}{\rho_1 D^2} \right) \frac{\Delta m_1}{m_1}$$

4. Crystal-length control

$$\frac{\Delta d}{d} = \frac{1}{2} \left(\frac{\rho_1 D^2}{\rho_s d^2} - 1 \right) \frac{\Delta l}{V}; \quad V = \frac{dl}{dt}; \quad l \text{—crystal length.}$$

For growing crystals more than 400–500 mm in diameter the method of growth-process control by melt-level elevation was widespread. The principle of this method is shown in Fig. 12.6. The melt level in the crucible is measured by an electrocontacting probe. Essentially the melt-level elevation accuracy is determined by the height of the meniscus formed during melt-level lowering. Contact breaking is evidence of melt-level lowering as a result of crystal pulling. Via the sensor signal the melt is fed until contact generation is re-established. It should be noted that practical crystal pulling is based on heater-temperature control also.

For automated heater-temperature control a signal has to be proportional to the melt-level displacement 'h'. At the beginning of the process (axial stage of the growth) the melt-level displacement rises slowly. Later, this change is significant for the process stability. Since the melt-level gauge possesses high sensitivity (about 10–30 μm) the system as a whole must be protected from separate local perturbations potentially leading to crystal-growth jumps. These are crucible vibrations, pulling-speed jumps, strong oscillations on the melt surface area due to feeding raw material ingress, etc. Another peculiar feature of the growth control relates to the sensitivity of the system to the average temperature of the melt. This leads to a corresponding change in the melt-level height. This feature is advantageous and disadvantageous at the same time. It was shown that the random fast perturbations of the melt temperature are automatically smoothed without substantially

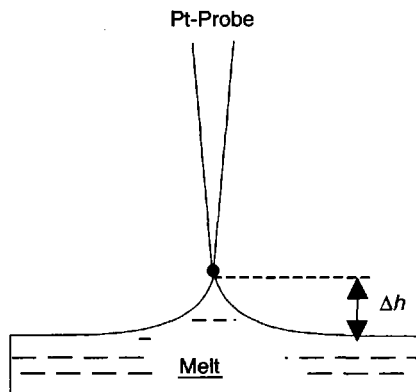


Figure 12.6 Electrocontacting probe and melt

affecting the crystal growth, because the level probe immediately responds with a signal compensating the perturbation. But on the other hand, the gradual change of the melt temperature in the course of growth results in the gradual deviation of the crystal diameter from that required. Fortunately, this deviation is not large. For crystals with diameter 300 mm and 750 mm length the relative deviation of crystal diameter did not exceed 1.5%.

The temperature distribution in the large melt volume defining convective flows depends primarily on the melt and crucible sizes (diameters). This factor is significant for the crystal/melt interface curvature and appearance of local nonflatness. At d/D (d —diameter of crystal, D —diameter of crucible) about 0.8 the interface shape is convex, while it is substantially flat at $d/D = 0.5$. This criteria-limited crystal size for the fixed crucible diameter is one of the peculiarities of the technology.

The equipment used and the alkali-halide single-crystal growth technique are described in [29, 34] in detail. Essentially, the method and the equipment are commercially applied. At present NaI(Tl), CsI(Na), CsI(Tl), CsI(pure) with diameter up to 600 mm and 750 mm in height are grown using them. The total weight of the ingot reaches 400–500 kg.

Thus, the authors succeeded in combining a number of important advantages in one method. Namely,

1. Continuous growth for large and long single crystals.
2. Fixed 'crystal/melt' interface, i.e. constant growth conditions on the solidifying interface.
3. The possibility of raw-material and activator feeding.
4. Large crucible volume assures good melt convection (and homogenization).
5. Simple control method based on electrocontacting-probe application.
6. Growth-furnace construction provides for rotating of both crystal holder and crucible with melt, i.e. the possibility of melt homogenization and thermal-field symmetrization in the growing crystal.

Often, some of the advantages of this method are fraught with hidden disadvantages. For example, large crystal volume and large melt free surface area result in significant

losses due to substance evaporation (especially activator evaporation in the case of high volatility) and the impossibility of additional raw-material purification. These factors are important from the practical point of view since they define the cost efficiency of the growth process due to the primary raw-material cost.

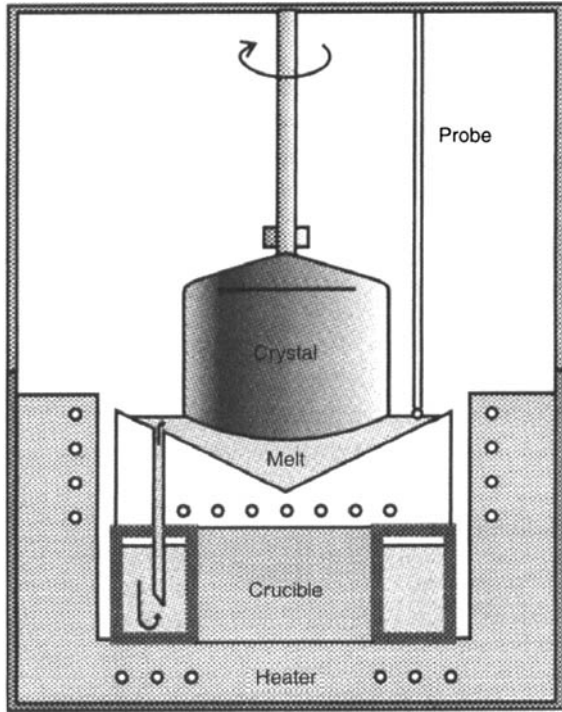


Figure 12.7 Principle of continuous-growth technique with melt-feeding system

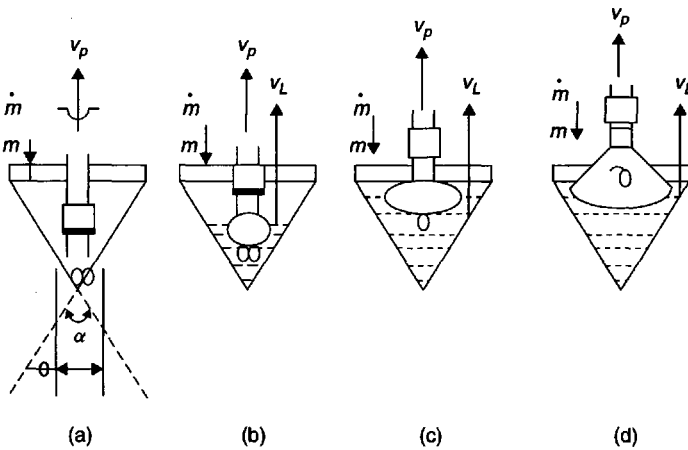


Figure 12.8 Stages of crystal growth: (a)—starting stage; (b–d)—radial growth

The method of automated crystal growth with a melt-feeding system is also well known [29, 37, 39]. This method is based on the same crystal and raw-material weight balance equations (12.5) and (12.6), but possesses a number of specific features. The essence of this method is the process of pulling the crystal from the small conical crucible (i.e. initial substance and activator evaporation is negligible), but melted raw material is fed from the special toroidal crucible (Fig. 12.7). The method concept is presented at Fig. 12.8. The initial stage of radial growth is started in the lowest part of the conical crucible where the melt-surface diameter is comparable to the seed-crystal diameter (Fig. 12.8). At the radial growth stage the crystal is pulled up at a rate, V_p . Simultaneously, the melt level is elevated at a rate, V_l , by means of feeding the raw material at the mass rate \dot{m}^* , such that $V_p > V_l$. Such elevations of seed crystal and melt sustain the permanent diameter increase and stable radial growth of single crystal (stages b–d, at Fig. 12.8). The melt temperature being adjusted so that the linear speed of the radial growth is essentially equal to that of the melt-surface diameter increase. Thus the radial growth from the seed diameter to the determined value of the single-crystal ingot is performed at a minimum free surface of the melt.

When the radial growth feeding rate has to compensate both the crystal-growth rate and the increase of the melt volume in the crucible:

$$\dot{m}^* = \dot{m}_s^* + \dot{m}_l^* \quad (12.9)$$

For a conical crucible this equation is transferred to

$$\pi [d_s(t)]^2 (V_p - V_l) \rho_s + \pi [d_l(t)]^2 V_l \rho_l = 4\dot{m}^* \quad (12.10)$$

where d_l depends on the vertex angle (ξ) as

$$d_l(t) = 2t V_l \tan \xi / 2 + d_0 \quad (12.11)$$

(d_0 is the melt-surface diameter at the initial moment of the growth).

When the radial growth is completed, the electrocontact-probe lifting is stopped and the melt-level position is fixed ($V_l = 0$). The axial growth stage is started from this moment.

Axial and radial temperature gradients in the ingot and melt temperature are of critical importance for the ingot diameter and crystal mass rate. Since the melt and crystal temperature are independent parameters defining the mass rate, the automated control of crystal diameter even at the steady-state stage of axial growth can be done by means of feedback, provided that certain parameters indicate how the growth rate affects the melt temperature. This note has to be made in the growth-technology manuals.

Such crystal-growth technology allows combination of all known advantages of the powder-feeding method (continuous growth for large and long single crystals; fixed 'crystal/melt' interface, i.e. constant growth conditions on solidifying interface; simple control method based on electrocontact probe application) possessing additional abilities:

1. An extra raw-material purification (like reactive atmosphere protective process (RAP))
2. Melt feeding, i.e. doping with activated melt.

One of the most important aspects of the raw-material feeding method is the quasicontinuity maintenance of the growth process. Any crystallization speed jump (regardless of the initiating cause—temperature jump, melt-level jump, etc.) leads to an instantaneous crystallization speed change. Depending on the perturbation magnitude intrinsic crystal structural defects appear as well as activator distribution nonuniformity in the crystal, foreign impurities and capture of gases dissolved in the melt. Therefore one of the main elements of a stable scintillation single-crystal growth technique is one-time feeding-value optimization and feeding frequency. It is evident that the feeding dose should be minimal, but the frequency should be maximal. Only in this way can the quasicontinuity process be ensured. This procedure is described in [39]. Since the feeding is done only when the electrocontacting probe is out of contact with the melt, i.e. when the limiting meniscus becomes broken, it is performed in a discrete regime. The melt mass, Δm_0 required to resume the probe contact with the melt surface in the crucible is defined by the Δh value and the free melt surface area (area of ring enclosed between the crucible wall and the crystal):

$$\Delta m_0 = \pi \{ [d_1(t)]^2 - [d_s(t)]^2 \} \Delta h \rho_l / 4 \quad (12.12)$$

Since the crystal pulling and the probe displacement are done in a continuous manner, the meniscus becomes broken in certain time intervals, when its height attains its limiting value so that the surface tension becomes unable to maintain it. When the meniscus is broken, an ordinary melt dose Δm_0 is added to the crucible, the contact is renewed to be broken again after the time period $\Delta \tau$, and so on.

The feeding mass rate can be presented as

$$m = \Delta m_0 / \Delta \tau = \pi \{ [d_1(t)]^2 - [d_s(t)]^2 \} \Delta h \rho_l / 4 \Delta \tau \quad (12.13)$$

It follows from Equation (12.13) that the constancy of $\Delta \tau$ shows that the free melt surface $[d_1(t)]^2 - [d_s(t)]^2$ is constant or the crystal diameter $d_s(t) = \text{const.}$, (in the case when the melt level is stable, $d_1(t) = \text{const.}$). If the melt level in a conical crucible rises linearly in time (this is equivalent to a linear increase of $[d_1(t)]^2$ then the constancy of $\Delta \tau$ points to a linear increase of the growing-crystal cross section. Thus, $\Delta \tau$ (time intervals between the feeding operations) is an exact parameter bearing information on the growing-crystal diameter that is useful in governing an automated pulling system. An increase in $\Delta \tau$ reveals a diminution of the crystal diameter while, in contrast, its decrease shows that the diameter is increasing.

From Equations (12.10) and (12.13), the relationship between the crystal diameter and the control parameter is obtained

$$[d_s(t)]^2 = [d_1(t)]^2 (\Delta h \rho_l - V_1 \rho_l \Delta \tau) / \Delta h \rho_l + (V_p - V_1) \rho_s \Delta \tau \quad (12.14)$$

Realizing feedback between $\Delta \tau$ and the melt temperature allows control of the crystal growth mass rate or its diameter to be established. Note that no additional sensor is necessary to measure $\Delta \tau$. The information is obtained from the electrocontact probe that governs the feeding. The time intervals are therefore measured from the cessation of feeding (restoring the probe contact with the melt) to the start of the next feeding (the contact break). Since $\Delta \tau$ is measured between each two feedings, the process information and, consequently, the control efficiency increases by several orders when a conical crucible

is used. Assuming, for simplicity sake, $V_1 = 0$, we obtain from Equation (12.14) that the process information is determined as

$$1/\Delta\tau = [d_s(t)]^2 V_p \rho_s / \{ [d_1(t)]^2 - [d_s(t)]^2 \} \Delta h \rho_l \quad (12.15)$$

It follows from Equation (12.15) that, at constant V_p , the feeding frequency $1/\Delta\tau$ depends on the ratio of the crystal cross-sectional area to that of the melt free surface. So, for example, when a crystal is grown-out radially in a 500-mm diameter, cylindrical crucible to a 100-mm diameter, that ratio amounts to 0.04, while it is 1.25 in the case of a conical crucible where the initial melt surface diameter $d_0 = 150$ mm. That is, in the initial radial growth stage, at a usual pulling speed, e.g., 5 mm h^{-1} , and a real limiting meniscus height amounting to 0.2 mm, the information on the current crystal diameter will arrive at the control system every 2400 s in the first case and every 125 s in the second one.

12.5 ACTIVATOR DISTRIBUTION IN SCINTILLATION SINGLE CRYSTALS

The overwhelming majority of halide scintillators are doped crystals (see Table 12.3). In these, maximum scintillator efficiency is achieved by optimal activator concentration. At smaller concentrations the light output does not reach the maximum value and the concentration quenching occurs at too high activator concentrations that results in scintillator light output reduction again.

Therefore the technology of uniform activator distribution along the ingot provides a stimulus for classical single-crystal growth technique development. In terms of activator distribution in the growing crystals all conventional methods are similar to zone melting [40]. (The melt in the crucible playing the role of the melted zone.)

The impurity distribution along the crystal height by equilibrium crystallization is described by the expression:

$$C_s = \frac{k_0 C_0}{1 - (1 - k_0)g} \quad (12.16)$$

where g —the fraction of frozen ingot; C_s —concentration at height g ; C_0 —starting concentration; k_0 —segregation coefficient.

This means that if crystallization conditions change, a scintillation single crystal will possess nonuniform scintillation characteristics and only certain crystal sections will meet the practical requirements.

Continuous growth allows control of the impurity content in the melt, thereby giving an opportunity to obtain scintillators with uniform activator distribution along the whole single-crystal ingot. In this case the impurity evaporation (TI, for instance) from the melt surface is a sink, and the feeding system is an additional input that has to balance the TI content in the melt [39].

It is easy to sustain the balance for the concentration in the melt and crystal:

From the activator and melt balance:

$$\frac{dC_1}{dm_1} + \frac{C_1}{m_1} \left(1 + \frac{dm_s}{dm_1} \right) - \frac{C_f}{m_1} \left(1 + \frac{dm_s}{dm_1} \right) = 0 \quad (12.17)$$

where m_s , m_1 —crystal and melt weights; C_1 , C_f —activator concentration in melt and feeding.

For automated pulling, as described above:

At $\frac{dm_s}{dm_1} = p = \text{const.}$ for activator concentration in crystal (C_s):

$$C_s = kC_{l_0} \left(\frac{m_1}{m_{l_0}} \right)^{\frac{k}{p}-1} + kC_f \frac{1-p}{k-p} \left[1 - \left(\frac{m_1}{m_{l_0}} \right)^{\frac{k}{p}-1} \right] \quad (12.18)$$

Index "0" marks the initial stage.

At the stationary stage of the crystal growth the activator concentration in the crystal is not too complicated:

$$C_s = C_f + (kC_{l_0} - C_f) \exp \left\{ -k \frac{\Delta m_s}{m_{l_0}} \right\} \quad (12.19)$$

Generally it is possible to split all scintillation growth techniques and materials into two groups. First, materials and activator with low efficiency of activator evaporation (low-volatility impurities). A typical example of such a scintillator is CsI(Na). The second case relates to the high efficiency of activator evaporation. The most popular NaI(Tl) scintillator belongs to this group.

In practice, due to the high rate of thallium iodide evaporation the ingot is grown from the undoped melt in the radial growth stage. When the finite crystal diameter size is reached and the melt free surface area is minimized, melt feeding is performed in such a way that the Tl content reaches the set value.

Activator feeding after radial growth to sustain the balance is:

$$pC_f - kC_1(t)m - \gamma C_1(t) - \frac{dC_1(t)}{dt} m_1 = 0 \quad (12.20)$$

or the activator concentration in the crystal will be:

$$C_s = kC_1 = \frac{kpmC_f}{km + \gamma} \left(1 - e^{-\frac{km+\gamma}{m_1}t} \right) \quad (12.21)$$

At small times corresponding to the real growth procedure this value is:

$$C_s = kC_1 \approx \frac{kpm}{m_1} C_f t \quad (12.22)$$

After that the appropriate thallium content level in the raw material feed could be chosen so that the impurity distribution in the grown crystal is uniform.

For a low-volatility activator it is possible to pull from an initially doped melt.

At the radial growth stage at $p = \text{const.}$ and $C_f = 0$

$$C_s = kC_{l_0} \left(\frac{m_1}{m_{l_0}} \right)^{\frac{k}{p}-1} \quad (12.23)$$

Feeding with C_s/k raw material provides the uniform activator concentration (C_s) along the growth axis.

These examples demonstrate a possibility to determine experimentally all the process parameters and to achieve uniform activator distribution in the whole ingot. First, the selected thallium iodide feeding concentration value determines the raw material amount to reach a given activator concentration. Secondly, the thallium concentration value is determined during continuous feeding providing uniform activator distribution along the whole crystal. The Tl distribution uniformity in grown CsI(Tl) crystals does not exceed $\pm 6\%$ [39].

The importance of the continuous-growth process with feeding capability to obtain not only large-sized single crystals, but also physically uniform scintillators, is a critical advantage of continuous-growth methods.

Numerous algorithms of large-sized crystal production and technical modifications of their realization systems are given in [29].

12.6 OXIDE SCINTILLATION CRYSTAL GROWTH

The main oxide scintillator production techniques are based on the Czochralski or Bridgman methods. In spite of the fact that the number of oxide scintillators is steadily growing, scientists and engineers fix their attention on known growth methods adapted to perfect-crystal production peculiarities. Unlike halide scintillators, oxide materials are used for radiation registration both as undoped crystals (i.e. based on intrinsic luminescence)—BGO ($\text{Bi}_4\text{Ge}_3\text{O}_{12}$), CWO (CdWO_4), PWO (PbWO_4), BSO ($\text{Bi}_4\text{Si}_3\text{O}_{12}$), and doped mostly with trivalent cerium (i.e. activated luminescence)—LSO:Ce ($\text{Lu}_2\text{SiO}_5:\text{Ce}^{3+}$), GSO:Ce ($\text{Gd}_2\text{SiO}_5:\text{Ce}^{3+}$), YAP:Ce ($\text{YAlO}_3:\text{Ce}^{3+}$), LuAP:Ce ($\text{LuAlO}_3:\text{Ce}^{3+}$). It is worth noting that if the first group of crystals has intermediate melting temperatures, the second group will belong to materials with melting temperatures higher than 2000°C .

Historically, industrial production of oxide scintillators began with tungstate and germanate growth. In particular, every effort was made to develop methods of BGO production proposed as a scintillator for the first time in 1973 [41]. Thus let us consider the main aspects determining single-crystal growth process stability, single-crystal quality (first of all the scintillation characteristics is uniformity along the crystal length) and production efficiency as a whole.

To achieve the above goals the crystallization-speed constancy, the external manifestation of which is the crystal-diameter constancy, is of critical importance. Crystal-diameter constancy may be reached either by varying the crystal pulling speed or changing the heater capacity. Structural uniformity and optical-performance requirements limit the pulling speed value, therefore the main control parameter (at fixed pulling and crystal rotation speed) is the heater power, as a rule. By crystal growth without feeding, the melt-level change in a crucible results in a continuous 'crystal/melt' interface movement deep into the crucible. In this case, to assure the crystal-diameter constancy it is necessary to provide a melt-temperature decrease that is limited by the temperature stability of the crystalline system. Thus, crystal-growth techniques with melt feeding are dominant, allowing us (as in the above cases) to maintain heat and mass balance in the growth process.

In these cases the algorithm of crystal-growth control is based on the heat balance:

$$\frac{d(C_m m T_1)}{dt} = W(t) - W_c(t) - W_f(t) - W_b(t) - W_w(t) \quad (12.24)$$

where $\frac{d(C_m m T_1)}{dt}$ — melt heat-content change per time unit

W — power transferred from the heaters to the melt

W_c — power loss through the crystal

W_f — power loss from the melt free surface area

W_b, W_w — power loss due to heat abstraction from crucible surface

C_m — specific heat

m — melt mass

Stable algorithms of system control and empirical parameter-selection principles for the system of crystal-pulling control equations are described in [42] in detail.

The peculiarity of oxide scintillator growth is based on initial raw-material polymorphism, for instance, Bi_3O_3 and GeO_2 for BGO scintillators. Except for the main phase ($\text{Bi}_4\text{Ge}_3\text{O}_{12}$) there are a series of other compounds that are stable within the temperature range from 913 °C to 1304 °C. Namely, these are $\text{Bi}_4\text{Ge}_3\text{O}_{12}$; $\text{Bi}_{12}\text{GeO}_{20}$; $\text{Bi}_2\text{Ge}_3\text{O}_5$; $\alpha\text{-Bi}_2\text{O}_3$; GeO_2 ; $\text{Bi}_4\text{Ge}_3\text{O}_{12}$; $\text{Bi}_{12}\text{GeO}_{20}$; $\text{Bi}_2\text{Ge}_3\text{O}_9$; $\text{Bi}_4\text{Ge}_3\text{O}_{12}$; $\text{Bi}_2\text{Ge}_3\text{O}_9$; $\text{Bi}_4\text{Ge}_3\text{O}_{12}$. Inclusion of these phases in the crystal is undesirable even if they do not influence material optical transparency. First, it is conditioned on scintillation characteristics loss. Secondly, this leads to light scattering and an absorption-level increase in the crystals. From this point of view three phases are the most dangerous ones: stable phases $\text{Bi}_{12}\text{GeO}_{20}$ and $\text{Bi}_2\text{Ge}_3\text{O}_9$; and the metastable phase Bi_2GeO_5 . Monophase raw-material production solves only part of the problem. Metastable phase Bi_2GeO_5 may crystallize from the metastable melt on temperature lowering in the course of single-crystal growth. Thus, monophase-system development requirements impose additional restrictions upon the crystal-growth process as a rule.

Similar problems as with germanates occur in the case of growing silicates. For example, there are three intermediate stable and metastable phases for bismuth silicate ($\text{Bi}_4\text{Si}_3\text{O}_{12}$). Correspondingly, melt homogenization involves additional crystal-growth temperature requirements.

Many scintillators are tungstates— AWO_4 where A is Ca, Cd, Zn or Pb. The Czochralski technique is the dominant crystal-growth method for these crystals. The main conditions allowing the manufacture of crystals with good scintillation characteristics are stated in [42]. These are:

1. vacuum melting of raw material,
2. low pulling speed at high crystal rotation speed,
3. seed orientation [100] to prevent intensive twinning,
4. high axial temperature gradient,
5. careful raw-material synthesis to achieve maximum single-crystal stoichiometry.

It is worth noting that there is also a low-efficiency scintillator—PWO—along with relatively high-aperture materials in this group of scintillators. The first mention of this

scintillator as a particle-detecting material was made in 1992 [14], when a suggestion that due to the unique high density it may be applied in high-energy physics was put forward. In fact, high ionizing particle energy considerably mitigates the light-output requirements. At the same time if the radiation hardness of this material is high enough, it may be both a technically and commercially effective scintillator for large electromagnetic calorimeters. This scintillator development progress is one of the most striking examples during the last decade. The first long crystals (230 mm) were grown in 1994, a year later they successfully passed tests in CERN and were put in the forefront as scintillation detectors for CMS and ALICE [9]. It took several years to develop a radiation-hard PWO crystal-growth technique [11, 43], before the production of these scintillators started [44]. Simultaneous investigations [45] showed that it is possible to grow such crystals using the Bridgman method as well, however, industrial application requires additional updating of this method in comparison with the Czochralski technique.

Another example of industrial application technology progress and implementation are connected with the development of cerium-doped lutetium orthosilicates (LSO— $\text{Lu}_2\text{SiO}_5(\text{Ce})$). Several years passed from the moment of taking out a patent for this material (1990) [46], until scintillator prototypes for PET scanners were developed. However, LSO scintillation single-crystal growth technique advancement took almost 10 years. As a result positron emission tomography, a new line of investigation, was developed and widely adopted in nuclear-medicine diagnostics.

12.7 INFLUENCE OF SINGLE-CRYSTAL PERFECTION ON SCINTILLATION CHARACTERISTICS

As stated above (see Equation (12.1)), parameters Q and S depend on scintillation single-crystal structural perfection. The Q value determines the maximum light-output parameters. It strongly depends on the luminescence-center concentration and distribution uniformity, i.e. it is determined by the possibility of activator-distribution control in a crystal (discussed in Section 12.5). The energy transfer efficiency (S) depends directly on energy-loss minimization. The main sources of scintillation efficiency loss may be divided into several groups, Fig. 12.9 [10].

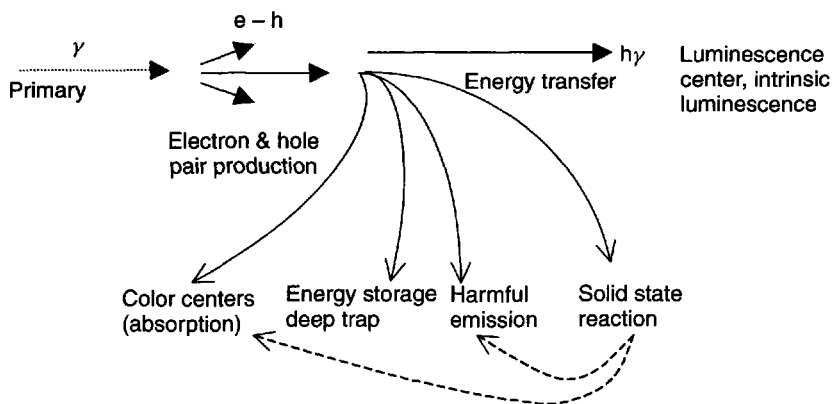


Figure 12.9 Crystal imperfections and energy losses on irradiation

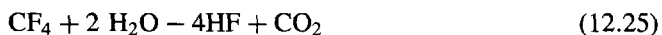
First, this is energy storage. The issue concerns charge-carrier trapping by their own point (vacancy, for example) and impurity defects. Secondly, these are radiation-induced solid-state transformations, for instance, different color-center formation. Thirdly, these are radiochemical transformations connected with the presence of foreign impurities. Finally, these are charge-carrier traps with the further relaxation accompanied by a slow afterglow (phosphorescence). All these factors are present in scintillators to a greater or lesser extent and their elimination requires special efforts at the stage of single-crystal growth. In some cases, for example, CsI(Tl) scintillators initially used for medical X-ray CT diagnostic devices were gradually replaced by CdWO₄ single crystals with a lower afterglow level. This example is quite representative since CsI(Tl) possesses 3–4 times higher light output, but these advantages are not enough to exceed present disadvantages.

Crystal perfection is of critical importance for undoped scintillators with intrinsic luminescence. Relatively low light output makes them sensitive even to small energy-transfer loss (*S* parameter). The most typical example is CsI (pure) or CsI—CsBr scintillator [47, 48]. This material has a short decay time and is suitable for HEP (high-energy physics) applications taking into account its low cost [13]. However, such applications require a minimal level of slow components along with fast scintillations in the UV range of 300 nm. Its applicability criterion is the fast/total ratio, i.e. the relationship between the fast emission component and the total emitted radiation. Usually this ratio is 0.75–0.8., i.e. a minimum 20% of scintillations do not correspond to the main fast emission. The investigations showed [49] that there are components connected with the presence of traces of sodium ions (emission at 410 nm), oxygen-containing ions CO₃ (410 nm), O²⁻ and O₂²⁻ (430 and 530 nm).

It is noteworthy that almost all halide materials possess a low yield point and are liable to plastic deformation in the course of single-crystal growth. As different investigations show [10], this deformation value and residual stress level are so high, and the reasons for plastic deformation are so significant, that this effect cannot be neglected. Internal stresses and plastic deformation consequences result in band formation in the region of 460–480 nm. Consequently, continuous afterglow with the typical time from 2 to 30 ms may be observed in a crystal. Undoubtedly, the influence of these factors may be reduced due to crystal aging (and corresponding stress recovery) or its thermal annealing, but it is a question of additional procedures influencing scintillator production and application specificity.

Oxygen-containing impurity is the main reason for low halide scintillator radiation hardness. In the mid-1990s this reason served as a basis for the R&D of superpure BaF₂ crystal production methods for the SSC project [50, 51]. Then the same problem emerged during the development of special raw-material processing methods and long CsI(Tl) single-crystal growth atmosphere. During recent years this problem touched on the advancement of complex fluoride compound growth (LiBaF₃:Ce, LiCaAlF₆:Ce, LiYF₄:Ce). Common contaminants of different fluorides relate to water and air components. These components caused special problems as they are present not only in the initial raw material, but are also absorbed on powder and content in growth atmosphere. The oxygen content commonly originated from OH⁻ impurity [52]. When such impurities are present they can be accompanied by complexes like Me(OH)₂ [53]. A practical recommendation to eliminate or at least minimize these impurities is for a raw-material treatment for several hours under a CF₄ atmosphere. CF₄ is often useful like a reactive

atmosphere (RAP) agent to fast-acting HF [54]:



A CF_4 atmosphere yields a double effect of purification. First, this leads to moisture elimination even in trace quantities. Secondly, slight HF atmosphere formation allows reaction with $\text{M}(\text{OH}^-)$ and (MO^{2-}) complexes formed in the melt.

Crystal growing in a RAP atmosphere requires a graphite crucible and furnace growth-chamber vacuumization. In these cases the crucible is isolated from the growth chamber due to placing it into a special ampoule [55]. In the case of a large-sized crystal growing reactive-atmosphere treatment is possible (see Fig. 12.10) only at the stage of preliminary melt preparation. Then the melt is placed into a conical crucible positioned directly in the growth chamber where the ingress of oxygen-containing components into the growing crystal is minimized due to gas-atmosphere selection. In some particular cases application of scavengers shows high efficiency also [56].

Another group of structural imperfections radically influencing single-crystal scintillation characteristics is connected with the presence of nonstoichiometric defects in the crystal. This is typical for halide and oxide multicomponent scintillators.

The difference in various component volatility leads to the loss of stoichiometry of single crystal appearing at the very beginning of the crystal-growth process. Therefore, the selection of components with a surplus of the more volatile substance at the beginning is typical for such crystals. For instance, for $\text{LiYF}_4:\text{Ce}$ the initial ratio is 50.5 % LiF: 49.5 % YF_3 [57], for $\text{LiBaF}_3:\text{Ce}$ this ratio is 57 % LiF: 43 % BaF_2 [58]. In typical oxide scintillators, $\text{Bi}_4\text{Si}_3\text{O}_{12}$, for example, an extra Bi_2O_3 content exceeds 1–5 % [42].

Such technological procedures allow a reasonable single-crystal ingot uniformity level to be reached (and later the scintillator itself), however, it is obvious a priori that every crystal is physically not perfectly uniform. This means that some special engineering

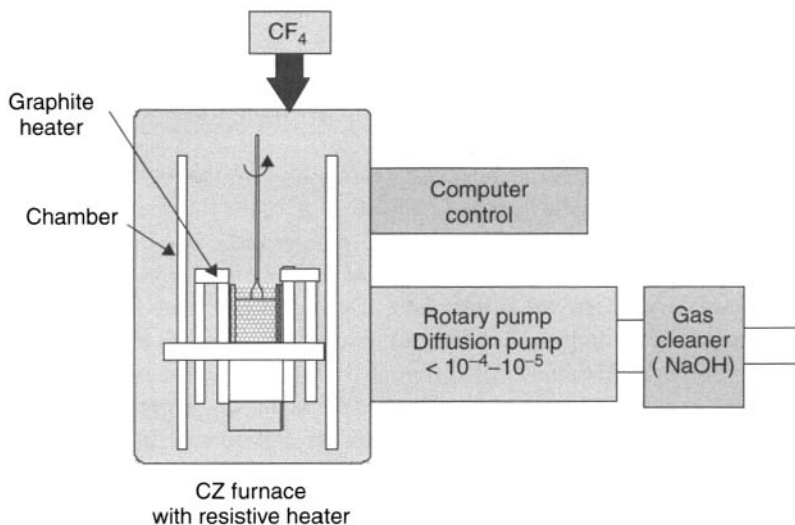


Figure 12.10 Czochralski system for fluoride growth in special atmosphere

efforts are needed for large-sized scintillators and special applications, since they will 'mask' this nonuniformity by means of special crystal treatment, light-reflective coating selection (light-collection tuning), 'scintillator-photoreceiver' assembly optimization, special measures increasing material radiation hardness. The latter activity is directly connected with the single-crystal growth technology.

Methods of radiation-hard scintillation single-crystal production are connected with maximum-purity crystal growth (see above). In fact, pragmatic methods include searching for dopants to decrease the radiation-damage level. The history of the last decade has two examples of such a methodology. Both of them are connected with detecting-system development for high-energy physics, where radiation load during operational life of the assembly may reach 1–10 Mrad.

The physical idea of 'stabilizing dopants' is connected with radiation-defect accumulation quenching forming under the influence of high-energy quanta. In the perfect scintillator all electron-hole pairs have to relax in luminescence centers or annihilate nonradiatively. In a real crystal a fraction of these excitations is localized resulting in radiation-defect formation, which then reduce scintillation efficiency either by luminescence quenching or material-transparency degradation not allowing the output of all scintillation flashes. Additional impurities have to 'bind' their own structural defects thereby preventing charge-carrier trapping. Often such investigations are of 'random-search' character. Thus, to increase the radiation hardness of BaF_2 for the SSC calorimeter various impurities were introduced into the crystals. It was shown that some of them reduced radiation hardness, some of them are of 'neutral character', i.e. do not change material radiation hardness and only a small fraction of them promoted a radiation-hardness increase [59]. A wide range of experiments was carried out with PWO scintillator radiation-damage suppression for LHC (CERN). In this case, several approaches and groups of impurities were approved [5].

12.8 NEW SCINTILLATION CRYSTALS

Many years of scintillator applications have shown that despite the long-term search a perfect scintillator has not been found. Moreover, the scintillation material range widened showing that the different applications specificity only classifies materials according to the most important parameters, i.e. the period of scintillator 'specialization' for different applications began. This tendency to domination resulted in a search for special and new scintillators and corresponding growth-technique development.

The history of PWO scintillation crystal development we were discussing is the proof of this.

New $\text{LaCl}_3:\text{Ce}$ and $\text{LaBr}_3:\text{Ce}$ scintillation single crystals are the most important discoveries during the past few years [60, 61]. Two years passed from the beginning of their discovery to the first detector prototype development [16]. The distinctive feature determining the advantage of these materials is the record high light output and high energy resolution improving spectroscopic characteristics of the detection systems. High hygroscopicity (typical for the majority of halide scintillators) is the main disadvantage of these crystals. Essentially, taking into account radiation registration efficiency of these scintillators, it should be noted that they are better than $\text{NaI}(\text{Tl})$. Due to the relative simplicity of the crystal lattice, two-component composition and low melting temperature these crystals were considered to be alternatives for medical and industrial application.

Another actively developing trend is connected with new fast scintillators for medical-diagnostic systems (PET systems, first of all). The LSO scintillator discovery promoted a new intensive materials search. Thus, the first scintillators based on LuAP:Ce (lutetium aluminate) were grown in 1995. This material possesses still higher density than LSO, however, it is much more difficult to manufacture. Aluminate and garnet phases result in system breakdown and the presence of multiple-phase impurities reduces the LuAP scintillation efficiency [3]. It took 7 years to develop commercially available material [62]. It should be noted that one of the most efficient crystal-growth conditions stabilization methods is the introduction of impurities forming a continuous series of solid solutions with anion or cation, for instance, CsI host was replaced by CsI-CsBr [48, 63]. In the past few years it was used for oxide scintillators growth. First, LuAP due to high yttrium content is actually Lu(Y)AP [64]. Another similar example is lutetium yttrium orthosilicate doped with Ce [5]. 20% yttrium introduction not only stabilizes the crystal-growth conditions, but also allows material with higher light output to be obtained. Consequently, this material possesses three times higher light output in comparison with BGO, six times shorter decay time and almost twice as good an energy resolution.

On the whole (see Table.12.4 [65]) series of lutetium compounds (borates, aluminates, silicates, etc.) suitable for scintillation applications were obtained during the last few years. In the future the question of one or another material domination will be connected with the possibility and simplicity of single-crystal growth.

12.9 CONCLUSION

Several dozen useful scintillators have been developed during the last decades and each of them have found application. High-energy physics and medical imaging are the main driving forces for the search and development of new more advanced materials for scintillators. At the same time each new step in this development moves us farther from the dream of an ideal scintillator. The examples presented in this review were chosen to demonstrate a wide list of materials and problems for each type of scintillator (halogenide and oxide single crystals). Potential benefits of each new scintillator stimulate the crystal-growth technology and new engineering of dielectric media.

High-energy physics (E-calorimeters) and medical imaging (PET and SPECT systems) are expected to need multiton production of extremely uniform and efficient materials that

Table 12.4 Scintillation materials prospective for PET application (For more details see ref. [65])

Material	Density g cm^{-3}	$Z_{\text{eff.}}/\text{Ph. Abs. coeff}$ at 511 keV, $\text{cm}^{-1}/X_0, \text{cm}$	LY Ph/MeV	τ ns	λ nm
$\text{Lu}_2\text{S}_3:\text{Ce}$	6.2	66.7/0.241/1.25	28 000	32	592
$\text{LuAlO}_3:\text{Ce}$	8.34	64.9/0.29/1.1	11 400	17	365
$\text{Lu}_2\text{SiO}_5:\text{Ce}$	7.4	66/0.28/1.1	27 000	40	420
$\text{Lu}_2\text{SiO}_7:\text{Ce}$	6.23	64.4/0.21/1.39	30 000	30	380
$\text{LuF}_3:\text{Ce}$	8.3	61.1/0.31/1	8000	23 + slow	310
$\text{LuBO}_3:\text{Ce}$	7.4	64.5/0.28/1.32	26 000	39	410

claim a well-established technology base. New crystal-growth technologies have to follow the modern trend—large-size single-crystal growth to provide full-body scanning, long scintillators and extremely uniform matrixes and multiscintillator registration devices.

The future is expected to bring continuous crystal-growth technologies with the ability to purify a crystal during the growth process and maintenance of a uniform activator distribution along the crystal length. Successful examples of continuous scintillator growth technologies were described to show the ability to increase the efficiency of the growth technique by automated melt-level control. Relatively simple mass-balance algorithms were adopted to large cross section alkali-halide scintillator growth with feeding by the host and activator powder and melt. It is shown that this approach allows crystallization conditions to be fixed (crystal/melt interface position in the temperature field) and further increases scintillator efficiency.

The main trend for the oxide-scintillator technology is shifted to the development of high melting point crystal growth (above 2000 °C). Crystal-growth technology and know-how are of great importance to sustain the stoichiometry and uniform Ce activator distribution along ingots. For over forty years numerous efforts have been dedicated to the growth of optical, laser and scintillator oxides. The achieved scintillator crystal performance demonstrates many resources that should be extracted to reach the best yield of efficient scintillators and reasonable price/performance ratio.

In conclusion, one could say that the modern tendency in scintillator search and development needs crystal-growth technique upgrades both for commercially availability and new scintillators.

LIST OF DEFINITIONS AND ABBREVIATIONS

m_s - mass of crystal

m_1 - mass of melt

V - pulling rate

s - crystal cross-sectional area

ρ_1, ρ_s - density of melt and crystal, respectively

m - feeding rate

D - crucible diameter

h - melt height

W_s - crystal growth rate

α - thermal expansion coefficient

d - crystal diameter

C - activator concentration

k - segregation coefficient

$p = \frac{dm_s}{dm_1} = \text{const}$ - continuous growth criteria

REFERENCES

1. E. Rutherford, J. Chadwick, and C. Ellis, (1930) *Radiation from Radioactive Substances*, Cambridge University Press, Cambridge.
2. R. Hofstadter, (1949) *Phys. Rev.*, **75**, 796.

3. S. Derenzo, W. Mosses, A. Fedorov, and A. Gektin, *IEEE Trans. Nucl. Sci.*, **42**(4), 275–279.
4. E.V.D van Loef, P. Dorenbos, and C.W.E van Eijk *et al.*, (2001) *Proc. 6th Int. Conf. Inorganic Scintillators and Their Applications*, Chamonix, Eds. E. Auffray, R. Chipaux, P. Lecoq, C. Pedrini, M. Schneegans, 254–258.
5. M. Korzhik, (2003) *Physics of Oxide Scintillators*, Minsk.
6. P. Lecoq, (2000) How high energy physics is driving the development of new scintillators, *Proc. 5th Int. Conf. Inorganic Scintillators and Their Applications*, Moscow, 1999. Ed. V. Mikhailin, Moscow State University, 3.
7. BELLE Collaboration, (1995) Technical Design Report, KEK Report 95-1.
8. BaBar Technical Design Report (1995), SLAC-R-95-457.
9. CMS Technical proposal (1994), CERN/LHCC 34–38.
10. A. Gektin, and N. Shiran, (1997) Scintillation losses in irradiated CsI-based scintillators, *Proc. of Int. Conf. on Inorganic Scintillators and their Applications*, Yin Zhvien (Eds), Shanghai, 115–121.
11. Tungstate crystals. (1998) *Proc. Of the Int. Workshop on Tungstate Crystals*, S. Baccaro, B. Borgia, I. Dafinei, E. Longo (Eds), Roma.
12. L. Halliburton, and G. Edwards, (1994) in *Scintillator and Phosphor Materials MRS Symposium Proceedings*, **348**, 423–433.
13. K. Arisaka *et al.*, (1992) *KTeV Design Report*, FN-580.
14. (a) V. Selivanov, L. Nagornaya, and Y. Vostretsov *et al.*, 437–441.
(b) V. Kachanov, V. Vasilenko and L. Nagornaya, *et al.*, 381–382.
(c) M. Kobayash, M. Ishii, Y. Usiki, and H. Yahagi, 357–379.
(1992) In *Heavy Scintillators for Scientific and Industrial Applications*, P. Lecog, F. De Notaristefani, M. Schneegans (Eds), Frontlines.
15. W.W. Moses, (1999) How high energy physics is driving the development of new scintillators, *Proc. 5th Int. Conf. Inorganic Scintillators and Their Applications*, Moscow, 11–12.
16. www.Bicron.com
17. S. Genna, (1988) *IEEE Trans. Nucl. Sci.*, **NS-35**, 654–658.
18. C. Melcher, and I. Schweitzer, (1992) *IEEE Trans. Nucl. Sci.*, **5–39**, 502–505.
19. T. Fukazava, and K. Takagi, (1983) *Appl. Phys. Lett.*, **42**(1), 43–45.
20. A. Lempicky, (1995) *J. Appl. Spectrosc.*, **62**(4), 209–231.
21. M. Weber, (2002) *J. Lumin.*, **100**(1–4), 35–45.
22. S. Derenzo, and M. Weber, (2003) *Nucl. Instrum. Methods Phys. Res.*, **A505**, 111.
23. W. Lehmann, (1966) *Solid-State Electron.*, **9**, 1107.
24. V. Ryzhikov, V. Silin, and N. Starzhinsky, (1993) *Nucl. Tracks Radiat. Meas.*, **21**, 53.
25. P. Schotanus, P. Dorenbos, and V. Ryzhikov, (1992) *IEEE Trans. Nucl. Sci.* **NS-39**, 546.
26. D. Stockbarger, (1936) *Rev. Sci. Instrum.*, **7**(3), 133–137.
27. S. Kyropoulos, (1926) *Z. Anorg. Allgem. Chem.* 308–313.
28. I. Czochralski, (1918) *Z. Phys. Chem.*, **92**, 219.
29. (2002) *Crystal growth (Halide crystals)*, V. Goriletsky, B. Gryniov, and B. Zaslavsky *et al.* (Eds), ‘Acta’, Kharkov.
30. U.S. Patent 5,178,719. Continuous refill crystal growth method.
31. U.S. Patent 5,993,540. Continuous crystal plate growth process and apparatus.
32. U.S. Patent 4,547,258. Deposition of silicon at temperatures above its melting point.
33. U.S. Patent 4,834,832. Process and apparatus for the manufacture of silicon rods.
34. U.S. Patent 4,036,595. Continuous crystal growing furnace.
35. V. Goriletsky, V. Nemenov, and L. Eidelman, *et al.*, (1981) *J. Cryst. Growth*, **52**, 509–513.
36. L. Eidelman, V. Goriletsky, and V. Nemenov, (1985) *Cryst. Res. Technol.*, **20**(2), 167–172.
37. B. Zaslavsky, (1999) *J. Cryst. Growth*, **200**, 476–482.
38. W. Bardsley, G. Green, C. Holliday, and D. Hurlle, (1972) *J. Cryst. Growth*, **26**(3), 277–279.

39. A. Gektin, and B. Zaslavsky, (2003) *Halogenide scintillators. Crystal growth and performance in Crystal Growth Technology*, H. Scheel and T. Fukuda (Eds), John Wiley & Sons Ltd., Chichester, UK. 511–528.
40. V. Pfann, (1990) *Zone Melting*, Mir, Moscow.
41. M. Weber, and R. Monchamp, (1973) *Appl. Phys.*, **44**, 5495–5498.
42. L. Atroshenko, S. Burachas, L. Galchinetsky, and B. Grynyov (1998) *Scintillation Crystals and Radiation Detectors on its Base*, Naukova Dumka Kiev, pp: 310.
43. M. Kobayshi, Y. Usiki, and M. Ishii *et al.*, (1999) How high energy physics is driving the development of new scintillators, *Proc. 5th Int. Conf. Inorganic Scintillators and their Applications*, Moscow, 137–146.
44. E. Auffray, F. Cavallari, and P. Lecoq *et al.*, (2001) *Proc. 6th Int. Conf. Inorganic Scintillators and their Applications*, Chamonix, 111–115.
45. K. Tanji, M. Ishii, and Y. Usiki *et al.*, (1999) *J. Cryst. Growth*, **204**, 505–511.
46. (1990) U.S. Patent 4,958,080.
47. S. Kubota, S. Sakuragi, and S. Hashimoto *et al.*, (1988) *Nucl. Instrum. Methods*, **A268**(1), 275–277.
48. A. Gektin, A. Gorelov, and V. Rykalin *et al.*, (1990) *Nucl. Instrum. Methods*, **A294**(3), 591–594.
49. A. Gektin, N. Shiran, and T. Charkina *et al.*, (1992) in *Heavy Scintillators for Scientific and Industrial Applications*, P. Lecog, F. De Notaristefani, M. Schneegans (Eds), Frontieres, 493–498.
50. GEM Letter of intent (1991), SSCL SR-1184.
51. H. Newman, G. Graffa, and Ren-yuan Zhu, (1994) in ‘Scintillator and Phosphor Materials’ *Mater. Res. Soc. Symp. Proc.*, **348**, 3–27.
52. A. Pastor, (1975) *Mater. Res. Bull.*, **10**, 493–497.
53. S. Morato, L. Courrol, and L. Gomes *et al.*, (1991) *phys. stat. sol. (b)*, **163**, K61–K63.
54. R. Belt, and R. Uhrin, (1991) *J. Cryst. Growth*, **109**, 340.
55. E. Villora, K. Shimamura, and N. Ichinose, (2003) in *7th Int. Conf. Inorganic Scintillators and their Applications*, Valencia, (poster presentation)
56. J. Allain, M. Couchaud, and B. Ferrand *et al.*, (1994) in ‘Scintillator and Phosphor Materials’ *Mater. Res. Soc. Symp. Proc.*, **348**, 105–110.
57. I. Raineri, S. Baldochi, and A. Santo, (1996) *J. Cryst. Growth*, **166**, 423–428.
58. S. Baldochi, K. Shimamura, K. Nakano, and T. Fukuda, (1999) *J. Cryst. Growth*, **200**, 521–526.
59. SHAOXIA Ren, Gang Chen, and Fengyin Zhang *et al.*, (1994) in ‘Scintillator and Phosphor Materials’ *Mater. Res. Soc. Symp. Proc.*, **348**, 435–440.
60. E. Van Loef, P. Dorenbos, and C. Van Eijk, (2001) *Appl. Phys. Lett.*, **79**, 1573–1575.
61. O. Guillot-Noel, J. de Haas, and P. Dorenbos *et al.*, (1999) *J. Lumin.*, **85**, 21–26.
62. A. Fedorov, A. Ananenkov, and M. Korzhik *et al.*, (2003) *7th Int. Conf. Inorganic Scintillators and their Applications*, Valencia.
63. K. Shachova, A. Panova, and V. Goriletsky *et al.*, (2001) *Radiat. Meas.*, **33**, 769–771.
64. A. Petrosyan, K. Ovanesyan, and G. Shiran *et al.*, (2000). *J. Cryst. Growth*, **211**, 252–254.
65. M. Korzhik, and P. Lecoq, (2001) *IEEE Trans. Nucl. Sci.*, **48**(3), 628–631.

This page intentionally left blank

13 Growth of Quartz Crystals

K. BYRAPPA

University of Mysore P.B. No.21, Manasagangotri Mysore 570 006, India

13.1 Introduction	387
13.2 History of quartz crystal growth	388
13.3 Physical chemistry of the growth of quartz	391
13.4 Solubility	392
13.5 Apparatus	396
13.6 Crystal growth	396
13.7 Growth of high-quality (and dislocation-free) quartz crystals	398
13.7.1 Growth rate	399
13.7.2 Seed effect	400
13.7.3 Nutrient effect	400
13.8 Defects observed in synthetic α -quartz single crystals	401
13.9 Processing of α -quartz for high-frequency devices	402
13.10 Conclusions	404
References	404

13.1 INTRODUCTION

Quartz is one of the most abundant minerals and occurs both as a primary and a secondary constituent of rocks in nature. References to quartz are known from 1505 onwards. It may have been derived from the Saxon word '*Querkluffertz*', or cross-vein-ore, which could easily have become condensed to 'querertz' and then to quartz [1].

Quartz, SiO_2 , exists both in crystalline and amorphous forms in nature. The crystalline form of quartz has over 22 polymorphic modifications. The principal crystalline forms of SiO_2 are α -quartz, β -quartz, tridymite and cristobalite, with each possessing a well-defined field of stability under equilibrium conditions. The α -quartz transforms to β -quartz at temperature $> 573^\circ\text{C}$ and vice versa.

α -quartz has trigonal symmetry, belongs to the enantiomorphous crystal class 32, and its space group is $P3_121$ or $P3_221$ according to its right- or left-handedness. Its structure was among the first to be investigated by X-ray techniques as early as 1914 by Bragg [2]. The structure of quartz is made up of SiO_4 tetrahedra, which are linked by sharing each of their corners with another tetrahedron. In the 3-dimensional framework thus formed every Si^{4+} has four oxygens and every oxygen has two silicons as nearest neighbors.

Table 13.1 Applications for α -quartz

Industrial equipment	Precision oscillators, optical fibers, dielectric materials, radio communication, cable communication, electronic applications, measurement equipment, pager, security system (alarm), etc.
Consumer equipment	Electronic hand calculator, watch, clock, timer, cable TV, color TV, video recorder, RF converter, transceiver, radio equipment, electronic appliance, microcomputer and computer terminal, TV-game machine, telephone, copying machine, etc.

There are several studies on the hydrothermal synthesis of other varieties of silica like coesite, β -quartz, stishovite, cristobalite and tridymite [3–6]. However, the scope of this chapter has been restricted to the growth of large-size single crystals of quartz by the hydrothermal technique. In this respect it is only the α -quartz that is an important electronic material and it can be grown as large bulk single crystals, whereas the other varieties of silica have been obtained so far only as fine crystalline products, or tiny crystallites.

Quartz, as a piezoelectric crystal, has the ability to convert electric waves into mechanical waves and to reverse the process. Because of this property quartz is widely used in filters, timing and frequency-control applications, optical fibers and dielectric applications and so on. In recent years, quartz '*tuning forks*' have become essential for timing functions in electronic watches and in timing circuits for computers and telecommunications. Quartz crystal is one of the most transparent materials over a wide range of optical frequency from the UV to the IR region, and it exhibits double refraction (birefringence) and optical rotatory power. Because of these properties, quartz crystal is utilized as optical devices in a large scale. Typical applications are to an optical low-pass filter (OLPF) for video cameras and a waveplate for optical pickup. Table 13.1 gives a wide range of applications for α -quartz.

The principal source of electronic grade natural quartz is Brazil. Today, the electronics industries are largely inclined to use synthetic quartz, because natural quartz crystals are generally irregular in shape, automatic cutting is cumbersome and the yield is low. Over 3000 tons of quartz is produced annually for a variety of applications. The cost involved in the production of quartz is as follows:

End users ~ US\$1,000,000,000,000
 Equipment ~ US\$5,000,000,000
 Components ~ US\$1,00,000,000

Thus quartz takes the first place in value and quantity of single-crystal piezoelectric materials produced by man.

13.2 HISTORY OF QUARTZ CRYSTAL GROWTH

Schafthual (1845) obtained quartz crystals upon transformation of freshly precipitated silicic acid in Papin's digester [7]. The history of quartz growth has been discussed in

detail in the studies [8, 9]. When Brazil imposed an embargo on the supply of high-purity quartz that was a strategic material for telecommunication purposes during the Second World War, hydrothermal researchers began to think seriously about the bulk crystal growth of quartz. At that time, Brazil was the only country in the world that was a source of electronic-grade natural quartz, and even today the situation is the same. Many countries like USA, UK, Germany, the former Soviet Union entered the field and the success achieved was immense.

The author feels that it is highly appropriate to discuss briefly the historical contribution made by the German hydrothermal researchers with reference to the increased growth rate and growth of large-size single crystals of quartz. In contrast to the slow rate of growth achieved by the earliest workers, like De Senarmont and Spezia, the captured German reports have shown that Nacken, using natural alpha-quartz as seed crystals and vitreous silica as the nutrient, had grown quartz crystals in an isothermal system and had succeeded in obtaining large single crystals of quartz from a small seed [10]. Professor Richard Nacken (1884 to 1971) worked on the synthesis of various minerals from 1916 onwards. From 1927 or 1928, he started working only on the hydrothermal growth of quartz crystals. On Nacken's work, Sawyer writes (cited by Bertaut and Pauthenet, 1957) that '... Nacken made quartz crystals of 1-inch diameter using hydrothermal method and the conditions are given as...' followed by some biographical data. Similarly, Nacken's emphasis on quartz growth has also been written about by Sawyer. However, much of the work carried out by Nacken during the late 1930s and 1940s remained as intelligence reports as he could not publish much [11]. During 1950, Nacken published his work on quartz that remains a classic even today [12]. Figure 13.1 shows a photograph of the quartz crystals obtained by Nacken [10]. As mentioned earlier, Doetler was the first to use closed nickeled gun-barrel autoclaves, way back in 1890. It attained its prominence during World War II when several laboratories in many countries began working on the growth of large-size crystals of quartz. This is also partly connected to the availability of alloys, containing Mo, and other important metals that provided better strength to the alloys. Many countries attempted to grow large single crystals of quartz using old cannon barrels with closed

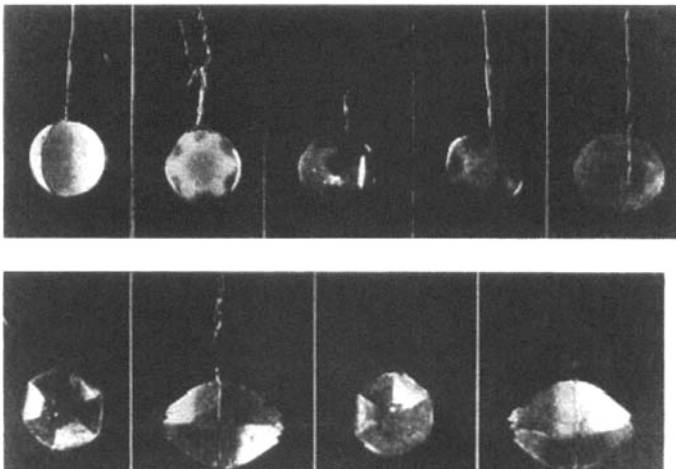


Figure 13.1 Photograph of the quartz crystals obtained by Nacken [10]

ends during the early 1940s. In this regard the contributions of Lobachev and Shtenberg are important. By the mid-1940s, many laboratories particularly in the USA, Germany, Russia, and the UK, were actively engaged in the growth of large quartz crystals.

In this regard the contributions of Kennedy [13] Morey and Hesselgesser [14], Tuttle and England [15], Roy and Roy [16] are very important. The $\text{SiO}_2\text{-H}_2\text{O}$ system was studied in great detail. Following this, many other laboratories in Europe, North America, the former Soviet Union, and Japan took up the study of phase equilibria in several simple and complicated systems [16]. These studies laid a firm foundation for the crystal growers. At this time Professors Yamasaki, Kumitomi, Ohara, and Dr Akitsu were doing excellent work in hydrothermal research in Japan. Some of them were closely associated

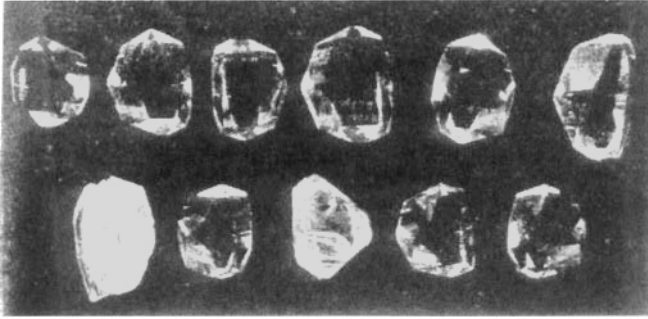


Figure 13.2 Quartz crystals obtained by Walker [18]



Figure 13.3 Quartz crystals obtained at AT & T Bell Labs during the 1970s



Figure 13.4 Growth of quartz crystals in the world's largest autoclave at Toyo Communications Ltd., Japan

with industry, like Toyo Communication Co Ltd., Nippon Dempa Co. Ltd., which resulted in the successful growth of large-size quartz single crystals. Though they started in a very small way during the post-war period, Japan is now the largest producer of commercial quartz in the world. Japan alone produces > 50 % of the world's annual production, it has the largest autoclaves in the world [17]. Figure 13.2 shows the quartz crystals obtained by Walker during the 1950s [18]. Figure 13.3 shows the commercial production of quartz at AT & T Bell Labs. during the 1970s [19].

Presently, in Japan, in one experimental run, about 4000 to 4500 kg of quartz is produced. The early success in producing commercial quartz crystals in Japan during the post-war period, paved the way for the entry of several others into the field. Some of the prominent ones are Professors Noda, Doimon, Kiyooora, and Dr. Itoh. When the North American laboratories were concentrating mainly on the development of new designs of autoclaves, the study of phase equilibria, and the commercial production of quartz, Japan concentrated essentially on the growth of quartz crystals, and achieved its goal in becoming the world's largest producer. Figure 13.4 shows the world's largest autoclave at Toyo Communication Co. Ltd. Japan producing over 5000 kg of quartz in one experimental run.

13.3 PHYSICAL CHEMISTRY OF THE GROWTH OF QUARTZ

No one book on crystal growth gives a complete picture of the theoretical aspects of hydrothermal growth. Similarly, no author has followed a definite approach to discuss the physical chemistry of hydrothermal growth of crystals covering aspects of physicochemical and hydrodynamic principles, solutions, solubility, phase equilibria, thermodynamics, kinetics, modeling or intelligent engineering of the hydrothermal reactions, and so on [9].

The hydrothermal physical chemistry today has enriched our knowledge greatly through a proper understanding of hydrothermal solution chemistry. There are several groups all over the world working on various aspects of physical chemistry under hydrothermal conditions.

The growth of a single crystal into the seed can be carried out in two ways:

- (a) Recrystallization of the solid substance, including its dissolution in the liquid phase, convective mass transfer of the dissolved part of the substance to the growth zone or seed.
- (b) Dissolution of the mixture of the nutrient components with the help of their convective mass transport into the growth zone and interaction of the dissolved components on the seed surface.

The methodology of the growth of single crystals on a seed is the establishment of growth conditions in which the process is represented by the sum of macro- and micro-processes occurring between the interface boundary of the solution and the crystal. The composition and concentration of the solution, temperature and pressure, hydrodynamic conditions and surface contact of the phases are some of the basic physical and chemical parameters that determine the regime and rate of dissolution of the nutrient, mass transport and possibility of the formation of new phases.

The following conditions are adopted in selecting the most suitable mineralizers [9]:

- i. Congruence of the dissolution of the test compounds.
- ii. A fairly sharp change in the solubility of the compounds with changing temperature or pressure.
- iii. A specific quantitative value of the absolute solubility of the compound being crystallized.
- iv. The formation of readily soluble mobile complexes in the solution.
- v. A specific redox potential of the medium ensuring the existence of ions of the required valence.

Additionally, the solvent should have the desired viscosity, insignificant toxicity and very weak corrosion activity with respect to the apparatus.

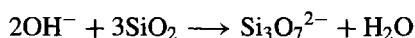
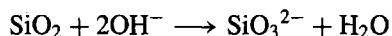
Thermodynamic principles enable one to determine how to design a reaction to yield phase-pure phases. Without knowledge of how to do this, it is impossible to distinguish a process that is being controlled by thermodynamics versus kinetics. A large number of publications have appeared on this aspect based on both theoretical and experimental data. Thermodynamic studies yield rich information on the behavior of solutions with varying pressure-temperature conditions. Some of the commonly studied aspects are solubility, stability, yield, dissolution-precipitation reactions and so on, under hydrothermal conditions.

13.4 SOLUBILITY

Solubility is one of the most important aspects in hydrothermal crystal growth. The early literature survey clearly shows that the very slow growth rate achieved until the works

of Spezia [20] Nacken [12] and Wooster and Wooster [21] were published, was mainly attributed to the lack of knowledge on the solubility of quartz. The same applies to other compounds also. Spezia [20] carried out a systematic study of the solubility of quartz. Since then much progress has been achieved in the understanding of the solubility in general for various inorganic compounds. During the 1960s, new methods of investigating the solubility and the new experimental set up for the determination of solubility under hydrothermal conditions were proposed [22, 23].

The solubility of quartz in pure water was found to be too low for crystal growth (0.1–0.3 wt %), but the solubility could be markedly increased by the addition of OH^- , Cl^- , F^- , Br^- , I^- , and acid media, which act as mineralizers. For example, the reactions



show the formation of various complexes or species during the hydrothermal crystallization of quartz. Hosaka and Taki [24] have used Raman spectra to identify and quantify such species.

In pure aqueous solutions (even at 400°C and 25 000 psi), the solubility of quartz is too low to allow growth to take place in any reasonable time. Alkaline additions, such as NaOH, Na_2CO_3 , KOH and K_2CO_3 are all effective as mineralizers in this pressure and temperature range. A small increase in molarity results in only a slight increase in the growth rate, whereas a large increase begins to produce an additional phase along with quartz. The minimum molarity for a good growth rate is about 0.25 M for NaOH. Concentrations of about 4.0 M for NaOH and 2.0 M for KOH form sodium or potassium silicates along with α -quartz. Laudise and Ballman [25] have measured the solubility of quartz in 0.5 M NaOH as a function of % fill and temperature. The quartz solubility dependences on % fill and temperature are shown in Figs. 13.5 and 13.6.

In recent years mixed solvents are being used even in the growth of quartz. High-quality large quartz crystals have been obtained in NaCl and KCl solutions, NaOH and Na_2CO_3 solutions, (10%) [26, 27]. Most of the literature data available on the solubility of α -quartz deal with the data in various solutions at elevated temperatures and pressures. It was recently observed that in the growth of quartz crystals under hydrothermal conditions, the evaluation of pressure generation and its effect on the dissolution in different aqueous solutions are the important steps. Hence the authors have studied the solubility of α -quartz in NaOH (1 M) + Na_2CO_3 (1 M) using high-pressure conditions from 200 MPa to 350 MPa at temperatures of 400°C [25]. The impetus for this work was provided by the fact that the high-frequency applications of α -quartz require sheets with small thickness, of the same order of size as the defects (such as inclusions, etch pits and dislocations). Thus the pressure can promote new solvents for hydrothermal growth, especially for reducing their concentration. Figures 13.7 and 13.8 show the solubility-limit comparison between NaOH (1 M) and Na_2CO_3 (1 M) versus pressure at 400°C; and log solubility (S_1) in NaOH (1 M) and in Na_2CO_3 (1 M) versus $1/P$. These experimental results show that Na_2CO_3 appears to be a better solvent than sodium hydroxide in the high-pressure domain for a temperature close to 400°C. From Fig. 13.7 the enthalpy values have been calculated and are as follows.

$$\Delta H_T = 2395 \pm 5 \text{ cal mole}^{-1} \text{ for NaOH(1 M); } 200 \leq P \leq 350 \text{ MPa}$$

$$\Delta H_T = 4001 \pm 2 \text{ cal mole}^{-1} \text{ for Na}_2\text{CO}_3(1 \text{ M}); 150 \leq P \leq 350 \text{ MPa}$$

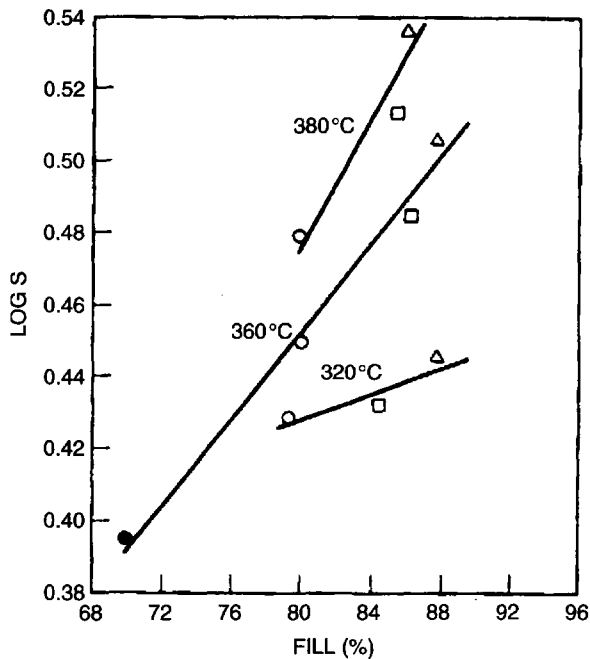


Figure 13.5 Quartz solubility dependence on % fill

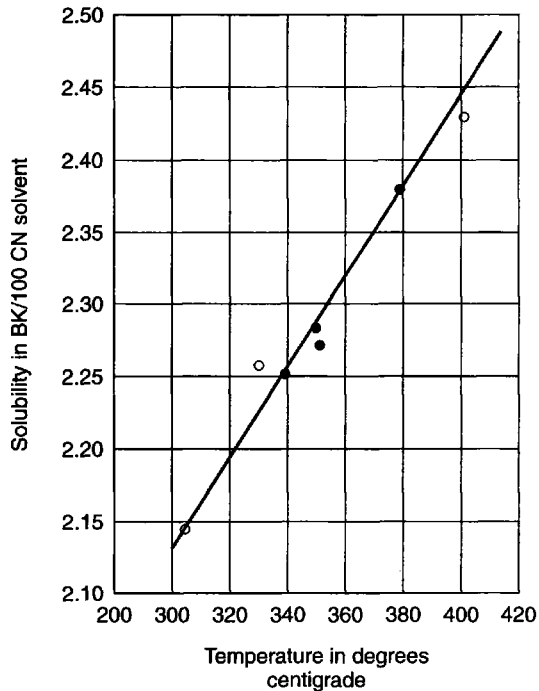


Figure 13.6 Solubility of quartz versus temperature

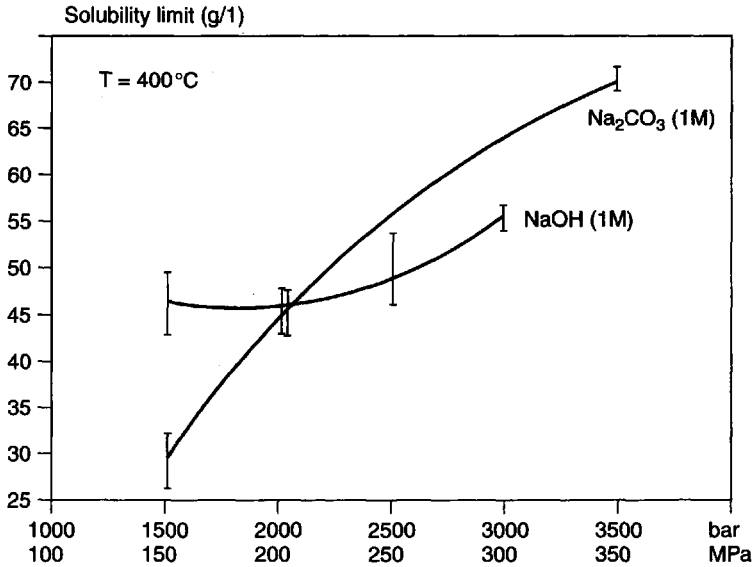


Figure 13.7 Solubility-limit comparison between NaOH (1 M) and Na₂CO₃ (1 M) versus pressure at 400°C

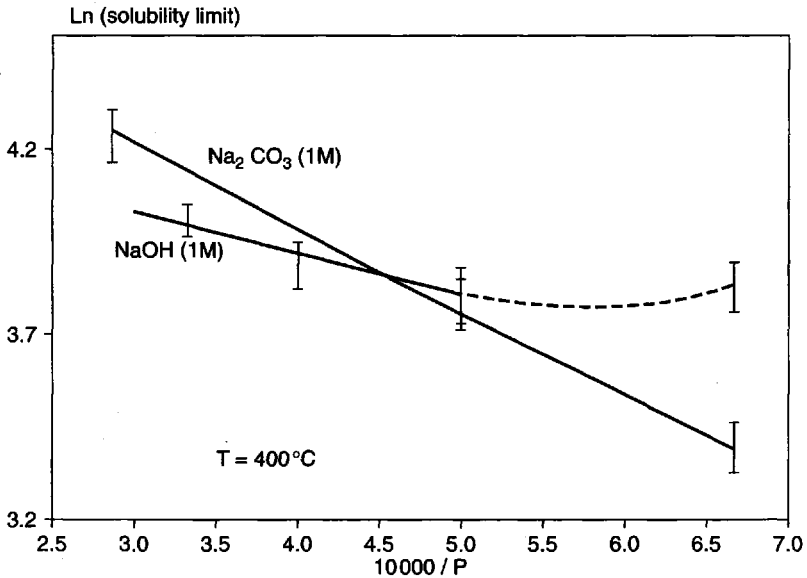


Figure 13.8 Log solubility (S_1) in NaOH (1 M) and in Na₂CO₃ (1 M) versus $1/P$

An important result of solubility determinations is the delineation of the pressure, temperature and composition regions, where the temperature coefficient of solubility is negative. These regions are to be avoided in the growth of quartz, since it requires a different setup; otherwise, it will result in the loss of seed crystals.

13.5 APPARATUS

Advances in any scientific field of research depend largely on the equipment available. Crystal growth or material processing under hydrothermal conditions requires a pressure vessel capable of containing highly corrosive solvent at high temperature and pressure. The experimental investigations under hydrothermal conditions require facilities that must operate routinely and reliably under extreme pressure-temperature conditions. Thus the experimenter has to face a variety of difficulties, and often, peculiar problems pertaining to the design, procedure and analysis.

Designing a suitable or ideal hydrothermal apparatus, popularly known as an autoclave, is the most difficult task and perhaps impossible to define, because each project has different objectives and tolerances.

An ideal hydrothermal autoclave should have the following characteristics [9]:

- a) Inertness to acids, bases and oxidizing agents.
- b) Easy to assemble and disassemble.
- c) A sufficient length to obtain a desired temperature gradient.
- d) Leak-proof with unlimited capabilities at the required temperature and pressure.
- e) Rugged enough to bear high-pressure and high-temperature experiments for long durations, so that no machining or treatment is needed after each experimental run.

These problems can be overcome through a careful selection of the alloy containing small additives such as Ti, Mo, V, heating in a H₂-free atmosphere and alloys with low thermodynamic activity. Some crystals can be grown readily within the autoclave without any lining or liners or cans. For example, the growth of quartz can be carried out in low-carbon steel autoclaves. The low-carbon steel is corrosion resistant in systems containing silica and NaOH, because the relatively insoluble NaFe-silicate forms and protectively coats the ground vessel. In contrast, the growth of berlinite crystals requires a teflon lining or beakers because phosphorus is highly corrosive; it can even corrode platinum if used for a long time.

In the growth of quartz crystals the liner has an assembly shown in Fig. 13.9. [28]. The lower portion of the liner is filled with the required nutrient material and, in the upper portion, a seed holder is placed and this is the growth zone (cooler zone). In between the growth zone and nutrient zone a baffle having a definite per cent of opening is placed. The baffle is placed at an appropriate position.

13.6 CRYSTAL GROWTH

In the growth of α -quartz by the conventional method the autoclaves used by most workers were modified Bridgman-type autoclaves. The typical laboratory size autoclave is 1 diameter \times 1 ft length. The pressure autoclave used in Europe and USA is the '13 inches' diameter and > 10 ft length autoclave with 350 l internal volume, which gives some 150 kg of quartz per cycle. But an evolution concerning vessel dimensions has to be noted, especially in Japan, where autoclaves with 1000 l to 5000 l of internal volume are in operation producing 500 to 2000 kg quartz per cycle.

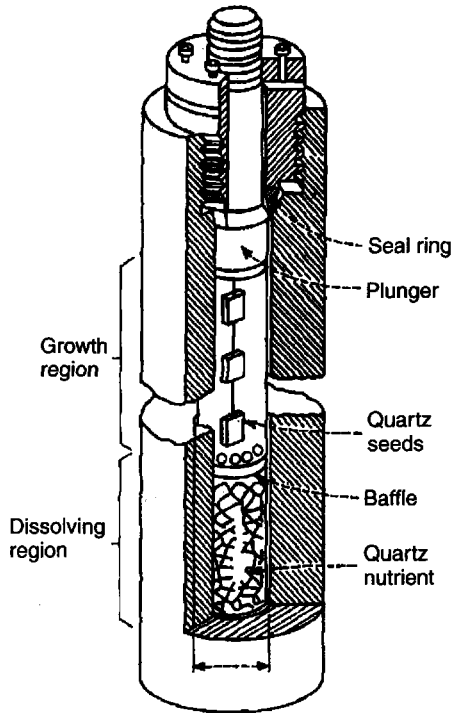


Figure 13.9 Growth of quartz crystals using a liner

In the growth of α -quartz, the available nutrient material such as small particle size α -quartz, silica glass, high-quality silica sand or silica gel is placed in a liner made up of iron or silver with a suitable baffle and a frame holding the seed plates. A mineralizer solution with a definite molarity is poured into the liner to make the required per cent fill. The increased solubility in the presence of mineralizer increases the supersaturation without spontaneous nucleation and consequently allows more rapid growth rates on the seeds. Figure 13.9 shows the cross section of the modified Bridgman autoclave used in the growth of quartz crystals. The commercial autoclaves used have 10-inch inner diameter, and are 10 ft long unlined. These autoclaves can work at conditions up to 30 000 psi and 400°C. Most of these experiments are carried out for 25 to 90 days to obtain full size (4 cm) in the Z-direction and 12.5 to 15 cm in Y-direction crystals. The temperature gradient is varied according to the nutrient used. About 1 N NaOH or Na₂CO₃ is the most commonly used mineralizer. The solubility change with temperature is smaller in NaOH and slightly larger in Na₂CO₃. The temperature of the autoclave at the nutrient zone is usually kept at 355–369°C and, in the growth zone, it is kept at 350°C. The addition of lithium improves the growth rate and small amount of Li salts are routinely added to the solution [29]. The solubility is also, to some extent, a function of increasing pressure. The per cent fill in the autoclave controls the pressure, and it is usually about 80% for hydroxyl mineralizer (20 000 psi internal pressure). In most of the experiments the per cent opening of the baffle is 20%, even lower per cents are used by several workers. However, commercial growers especially do not disclose the actual per cent open of the baffle area and their geometry.

The optimum growth conditions for synthesis of quartz based on the work in Bell Laboratories are [30, 31]:

Dissolution temperature	- 425 °C
Growth temperature	- 375 °C
Pressure	- 15 000–25 000 psi
Mineralizer concentration	- 0.5–1.0 M NaOH
Temperature gradient (ΔT)	- 50 °C
% fill	- 78–85 %
Growth rate in (0001)	- 1.0–1.25 mm day ⁻¹

The quality of the grown crystals is also a function of the seed orientation and its quality. Strained seeds generally produce strained growth regions [32]. The seeds are polished to a very fine finish before use. Most high-quality crystals are grown using seeds, the surface of which is perpendicular to the *Z*-direction since the *Z*-growth region is the lowest in aluminum concentration. Though the main part of quartz production consists of 'Y bar' crystals, that is, small crystals (*Z* = 20 to 25 mm, 64 mm seed) capable of producing several *Y* bars per crystal, the 'pure *Z*' bars are also produced representing 10 to 20 % of this production. But in medium- and high-quality grades we notice a rise in demand for crystals of very large dimensions and upper-medium quality, especially in the USA, for manufacturing wafers used in surface-wave applications [33]. Earlier, most of the seeds used were natural quartz cut into a definite orientation, but in recent years this practice is only used when a high-quality crystal is desired.

The growth of quartz crystals has been understood precisely with reference to the growth temperature, temperature gradient, per cent of fill, solubility, per cent of baffle as a function of per cent of fill.

The type of crystal to be grown depends on the application, as different properties are required in each case. For optical use, high uniformity, low strain and low inclusion counts are needed since all of these can affect the transparency. For surface acoustic-wave devices, large pieces are needed that can take a very high quality surface finish. The quality of the material required for resonators used in time and frequency devices varies with the application. The more precise the need, the more stringent are the requirements. For most applications, a truly high-quality material is not needed. For high-precision uses, such as in navigational devices and satellites, a very high quality material must be used. Most of the recent research on quartz growth is for improved resonator performance, which requires the growth of high-quality and low-dislocation quartz. Figure 13.10 shows the fabrication of resonators from a single crystal.

13.7 GROWTH OF HIGH-QUALITY (AND DISLOCATION-FREE) QUARTZ CRYSTALS

It is well known that the hydrothermal growth of quartz in the industrial sector is at least 45 years old. Though many improvements have been brought about, it is still more of an art than a truly reproducible industrial and scientific process. The growth of high-quality quartz crystals depends on many parameters, like phase relationships, the nutrient's solubility, thermodynamics (state equations, kinetics of reaction, impurity repartition), crystal

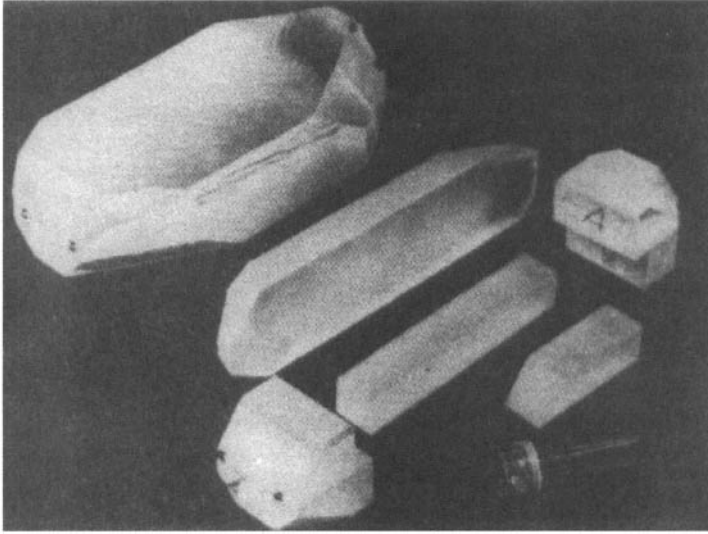


Figure 13.10 Fabrication of resonators from a single crystal

defect characterization, and so on. The other aspect is that the needs for cheaper material in a wide range of applications like clocks, microprocessors, etc., result in medium-quality product being satisfactory, and the low profitability of financing long and expensive studies. Though much of the recent publications on quartz is on the possibility of obtaining/growing high-quality quartz crystals for stringent electronic applications, this group is still in the minority. Except for quartz, no other material coming from hydrothermal synthesis has a sizable industrial use; even though AlPO_4 , GaPO_4 , $\text{Li}_2\text{B}_4\text{O}_7$ or microcrystallites show interesting promise, industry does not seem ready to make an important R & D effort concerning these products [9].

Several criteria are used to evaluate the quality of quartz crystals. The most commonly used criterion is the Q value or quality factor, and is a measure of the acoustic loss of the material.

The quality factor, Q can be considered as the inverse of the fraction of the energy lost per cycle. The highest values of Q are required in order to prevent loss of energy into coherent phonons. The acoustic Q for natural α -quartz crystal varies in the range 1 to 3×10^6 , while for synthetic quartz crystals, the value drops to 2.105 to 1.106. Thus in the last two decades, the main objective among quartz crystal growers is to improve Q , which in turn leads to the production of a low concentration of physicochemical and structural defects.

13.7.1 Growth rate

Growth rate is determined by the ratio of increase in thickness of the seed and duration of the run. The growth rate along the main crystallographic axes, R_c , is determined by dividing the thickness of the layer grown on the seed, $(h_1 - h_0)/2$, by the run duration t , and is expressed in mm per day. It has also been known for some time that qualitatively acoustic Q is inversely proportional to growth rate and directly related to chemical

impurities, which will be discussed separately. The internal friction (inverse of mechanical Q) is dependent on the growth rate of synthetic quartz crystals.

13.7.2 Seed effect

The seed plays a predominant role in the quality of the resulting crystal. For higher-frequency applications a smaller X -axis dimension is needed. Z -growth material is desired for resonators as it has been shown that this material is about an order of magnitude lower in aluminum concentration [34]. The thickness of the seed is usually between 1 to 2 mm. Until recently, it was necessary to use natural seeds for the preparation of low-dislocation crystals. This is an extremely tedious process since only a small portion of natural crystals is of sufficient quality for seed use, resulting in a complicated selection process. The seeds must also be of sufficient size for useful crystal growth.

13.7.3 Nutrient effect

The quality of the nutrient has a profound effect on the purity of the grown crystal. It appears that most of the impurities incorporated into the crystal come from the nutrient and not from the autoclave walls. The search for new sources of nutrient is not a new field of research. In the previous century, earlier workers tried several varieties of nutrient materials to obtain α -quartz under hydrothermal conditions. However, the results were not satisfactory owing to the lack of knowledge on the solubility data for quartz, which resulted in a very low growth rate.

There are several laboratories throughout the world still working to find a suitable nutrient for high-quality quartz growth. Hosaka and Miyata [35] have obtained high-quality α -quartz crystals using cristobalite as the nutrient. The authors used high-purity α -cristobalite powder compacted into grains of 0.5–1.00 mm or into lumps of approximately 1 cm in diameter, for the hydrothermal synthesis of α -quartz.

α -cristobalite is a polymorphic form of silica, as are quartz and tridymite, and has a higher solubility than quartz [36]. α -cristobalite powder [37] has the following advantages: it can be obtained in a high-purity state with low contents of Al and alkaline metallic ions, and can be prepared with relative ease as particles of uniform size. As compared with the conventional growth of synthetic quartz crystals using Brazilian lascas, the use of α -cristobalite powder may be expected to allow:

- (i) Synthesis of high-purity large quartz crystals.
- (ii) Synthesis of microquartz crystals having uniform grain size.

Hosaka [38] attempted to crystallize microquartz crystals by a hydrothermal hot-pressing method using α -cristobalite powder as a source material. Figure 13.11 shows α -quartz crystals grown at high (left) and low (right) fillings using α -cristobalite as the nutrient. The % fills and pressure greatly influences the growth rate. However, a considerable amount of work has to be carried out for the industrial production of α -quartz using cristobalite as the nutrient.

The study of solubility of quartz in the presence of mixed solvents has shown that the solvent separates into two silicate phases: light and heavy phases. In fact, the light phase

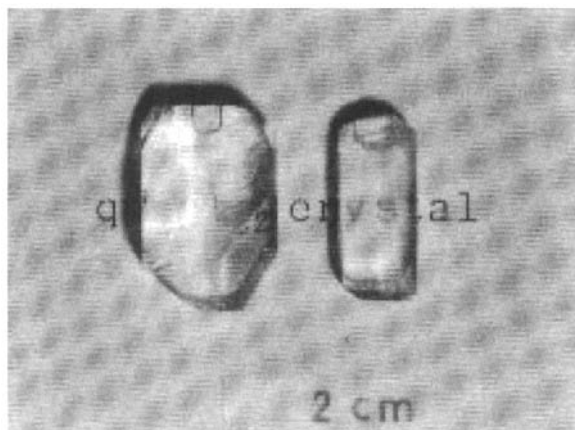


Figure 13.11 α -quartz crystals obtained using cristobalite as nutrient

is the true solution and the silica concentration in this solution reflects the real solubility of quartz. The heavy phase is a silicate glass from a semiliquid colloid under the run conditions to solid state after cooling. The silica concentration in the heavy phase does not show the real quartz solubility and always exceeds it. The presence of such a heavy phase greatly affects the quality of the grown quartz crystals by introducing numerous solid inclusions, often generating dislocation or twins [39]. Thus for the growth of low-dislocation quartz it is necessary to understand the solubility of quartz in a given solvent in order to minimize the heavy-phase formation.

13.8 DEFECTS OBSERVED IN SYNTHETIC α -QUARTZ SINGLE CRYSTALS

The defects present in the synthetic α -quartz crystals play an important role in determining its quality and in turn applications. Much of the recent studies on quartz are essentially focused on defect studies. All the defects present in quartz can be classified into 2 types:

- Physicochemical defects
- Structural defects

Physicochemical defects are mainly induced by the nature of the nutrient of the solvent and also by the chemical contamination of the solution by the metal constituting the reaction vessel. Quite often, solid or liquid inclusions, like $\text{NaFe}^{3+}\text{Si}_2\text{O}_6$ (acmite), are inserted in the α -quartz. The most important impurity in quartz is H^+ , which easily fits interstitially in the large (1 \AA) channels that lie parallel to the c -axis to charge compensate for Al^{3+} , which goes to a Si^{4+} site. It enters the lattice from the growth solutions as OH^- , the O^{2-} being incorporated in the SiO_2 lattice. Similarly, Laudise [28] has studied the dependence of the effective partition coefficient for OH^- impurity in quartz on growth rate (Fig. 13.12). Lithium salt is added to the solvent to check the aluminum concentration in the grown crystal. The entry of Al occurs in the use of (OH^-) - and (CO_3) -based

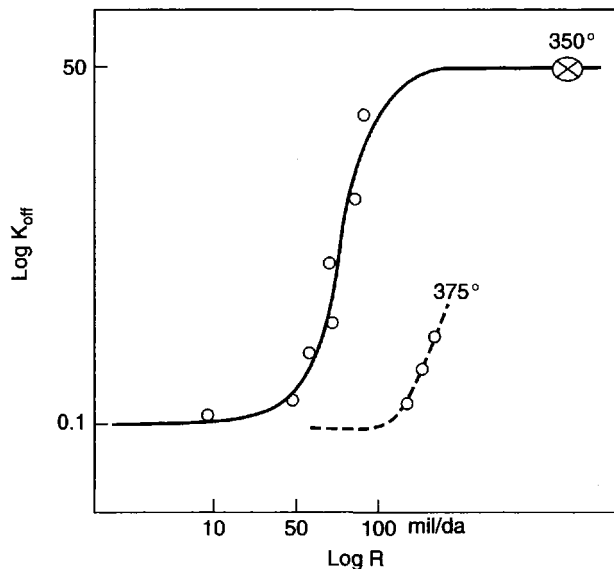


Figure 13.12 Effective partition coefficient for OH^- impurity in quartz versus growth rate

Table 13.2 Impurities in different sectors in synthetic quartz

Sector	Al	Na	Li
Z	5	1	0.5
+X	31	9	5
-X	122	40	5
S	85	26	16

mineralizers. Table 13.2 gives the distribution of impurities in different sectors of synthetic quartz that has been studied by Yoshimura *et al.* [40], and Iwasaki and Kurashige [41].

13.9 PROCESSING OF α -QUARTZ FOR HIGH-FREQUENCY DEVICES

The study of the type of defects present on silica surfaces would be of great importance for a better understanding of electrical or piezoelectric properties. The development of high-frequency devices (24 MHz \rightarrow 100 MHz or more), induce some strong constraints concerning the shaping of the α - SiO_2 material. Low-defect, high-purity synthetic quartz should have the characteristics shown in Table 13.3 [42].

The existence of defects, either physicochemical or structural, in synthetic quartz crystals leads to the critical modifications of devices. There are three different parameters on which the quality of quartz depends [43]:

Table 13.3 Desirable and achieved parameters in synthetic quartz

Parameter	Desirable	So far achieved
Etch channel density	$< 10 \text{ cm}^{-2}$	< 86
Inclusion density	$< 10 \text{ bar}^{-1}$	
Impurity concentrations (ppb)		
Al	< 200	700
Li	< 300	300
Na	< 500	1640
K	< 40	300
Fe	< 100	1800
Q (3500/3800 cm^{-1})	$< 2.5 \times 10^6$	$> 2.5 \times 10^6$
Strain	none	variable
Fringe distortion	$< 0.05 \text{ RMS}$	variable

- i. Chemical impurities, e.g. $(\text{OH})^-$ distribution—induce a large decrease of the acoustic ‘ Q ’. The substitution $\text{O}^{2-} \rightarrow (\text{OH})^-$ being coupled with the cationic one ($\text{Si}^{4+} \rightarrow \text{M}^{3+}$), the M^{3+} impurities can play an important role concerning the chemical aging of resonators and its behavior versus ionizing radiations.
- ii. Crystal defects like dislocations, etching channels, fractures, etc., which influence the acoustic distribution.
- iii. Inclusions (iron, sodium, acmite, aluminum, etc.).

As the application of quartz goes to higher and higher frequency devices, the thickness of the quartz plate drops. For example:

24-MHz range applications	—	$\sim 70 \mu\text{m}$ thickness
100-MHz range applications	—	$\sim 6\text{--}7 \mu\text{m}$ thickness

The thinning of the quartz plate depends upon the frequency measurements and can be expressed as,

$$F(\text{MHz}) = \frac{K(\text{MHz } \mu\text{m}^{-1})}{e(\mu\text{m})}$$

where ‘ e ’ is the plate thickness and K a constant characteristic of the material and of its orientation, F = resonance frequency.

Sweeping is one of the most popularly used techniques in recent years to enhance the performance of quartz resonators. Sweeping or solid-state electrolysis or electrodiffusion is generally performed under vacuum or air or hydrogen or other desired atmosphere [44–46]. During sweeping, the crystal is placed in an electric field and heated.

There are several other techniques employed for the fabrication of piezoelectric high- to ultrahigh-frequency devices based on quartz resonators. The important ones are: chemical polishing, and ion beam etching (IBE). The reverse thermodynamic relations are employed for the refinement of chemical polishing. Several solvents, like HF and NH_4HF_2 , NaOH, KOH, $x\text{H}_2\text{O}$, NaOH, $x\text{H}_2\text{O}$, etc., are used [47].

Similarly, the industrial chemical etching process is especially dedicated for large thickness removals without damaging the blank surface texture. This is most useful for frequency applications of quartz, because the mechanical grinding and lapping introduce surface stresses. Fluoride media is the most popularly used one for this type of chemical polishing [48]. Recently, Cambon *et al.* [49] have tried industrial chemical etching successfully in the temperature range 150 to 180 °C using concentrated NaOH solvents. During the chemical-etching process, several factors influence the process: kinetics, etching temperature, etching time, plate orientation, SiO₂ concentration, solvent concentration, wafer carrier geometry, and so on. By this process about 3200 quartz plates can be processed. The resonators manufactured by this process have demonstrated a high level of performance, even higher than those obtained by mechanical means.

In recent years there is a growing interest in morphological variations, growth-rate monitoring using various seed orientations and also computer simulation in the precise calculation of growth rates of various faces [50–53]. These studies greatly help in understanding the growth technology for the commercial production of defect-free and the most economic quartz crystals.

13.10 CONCLUSIONS

The growth of bulk single crystals of quartz is still an attractive field of research, especially the growth of defect-free quartz crystals for space-grade applications. An understanding of solubility and the growth mechanism is still incomplete although laser Raman spectroscopy and other advanced techniques like computer simulation are yielding rich amounts of information to intelligently engineer the growth processes, thereby minimizing the growth defects.

REFERENCES

1. Tomkeieff, S.I., (1942) On the origin of the name "Quartz", *Min. Mag.*, **26**: 172.
2. Bragg, W.H., (1914) The X-ray spectra given by crystals of sulphur and quartz. *Proc. Roy. Soc.* **89**: 575.
3. Hosaka, M., Miyata, T. and Sunagawa, I., (1995) Growth and morphology of quartz crystals synthesized above the transition temperature. *J. Cryst. Growth*, **152**: 300–306.
4. Arndt, J. and Rombach, N., (1976) Synthesis of coesite from aqueous solutions, *J. Cryst. Growth*, **35**: 28–32.
5. Dyuzheva, T.I., Lityagina, L.M., Bendeliani, N.A., Nikolaev, N.A. and Dorokhova, G.I., (1998) Hydrothermal synthesis of coesite (SiO₂), *Crystallogr. Rep.* **43**: 511–513.
6. Barth, T.F.W., (1932) The cristobalite structure : I High-cristobalite. II-Low-cristobalite., *Am. J. Sci.*, **Ser. 5**, **23**: 350; **24**: 97.
7. Schaffthual, K.F.E., (1845) *Gelehrte Anzeigen Bayer. Akad.* **20**: 557, 569, 575, 592.
8. Iwasaki, F. and Iwasaki, H., (2002) Historical review of quartz crystal growth, *J. Cryst. Growth* **237–239**: 820–827.
9. Byrappa, K and Yoshimura, M., (2001) *Handbook of Hydrothermal Technology*, Noyes Publications, N.J., USA, 01–896.
10. Nacken, R., (1946) *Artificial quartz crystals, etc.*, U.S. Office of Technical Services Report PB-6948.

11. Nacken, R., (1946) *Artificial quartz crystals, etc.*, U.S. Office of Technical Services Report, PB-18-748, and 28,897.
12. Nacken, R., (1950) Hydrothermal synthese als grundlage fur zuchtung von quarz-kristallen, *Chem. Z.*, **74**: 745–749.
13. Kennedy, G.C., (1950) A portion of the system silica-water, *Econ. Geol.* **45**: 629–623.
14. Morey, G.W., and Hesselgesser, J.M., (1951) The solubility of some minerals in superheated steam at high pressure. *Econ. Geol.* **46**: 821–835.
15. Tuttle, O.F. and England, J.L., (1955) A preliminary report on the system $\text{SiO}_2\text{-H}_2\text{O}$, *Bull. Geol. Soc. Am.* **66**: 149–152.
16. Roy, D.M., and Roy, R., (1955) Synthesis and stability of minerals in the system $\text{MgO-Al}_2\text{O}_3\text{-SiO}_2\text{-H}_2\text{O}$, *Am. Min.* **40**: 147–178.
17. Taki, S., (1991) Improvement of growth process and characterization of quartz crystals, *Prog. Cryst. Growth Charact.*, **23**: 313–339.
18. Walker, A.C., (1953) Hydrothermal synthesis of quartz crystals, *Ind. Eng. Chem.*, **36**: 250–256.
19. Laudise, R.A., (1992) *personal communication*.
20. Spezia, J.G., (1905) La pressione e chimicament inattiva nella solubilita e ricostituzione del quarzo, *Atti Accad. Sci. Torino Contrib. Geol. Chim.*, **40**: 254–262.
21. Wooster, N. and Wooster, W.A., (1946) Preparation of synthetic quartz, *Nature*, **157**: 297.
22. Shternberg, A.A., (1973) Controlling the growth of crystals in autoclaves in *Crystallization Processes under Hydrothermal Conditions* (Lobachev, A.N. (ed.)) Consultants Bureau, New York, p. 225–240.
23. Demianets, L.N., Emelyanova, E.N. and MelnikoV, O.K., (1973) Solubility of sodalite in aqueous solutions of NaOH under hydrothermal conditions in *Crystallization Processes under Hydrothermal Conditions*. (Lobachev, A.N. (ed.)), Consultants Bureau, New York, p. 125–150.
24. Hosaka, M. and Taki, S., (1990) Hydrothermal growth of quartz crystals in NaCl solution, *J. Cryst. Growth* **100**: 343–346.
25. Laudise, R.A. and Ballman, A.A., (1961) The solubility of quartz under hydrothermal conditions, *J. Phys. Chem.* **65**: 1396–1400.
26. Hosaka, M. and Taki, S., (1981) Hydrothermal growth of quartz crystals in NaCl solution. *J. Cryst. Growth*, **52**: 837.
27. Lafon, F. and Demazeau, G., (1994) Pressure effects on the solubility and crystal growth of α -quartz. *J. Phys. IV*, **4** [C₂]: 177–182.
28. Laudise, R.A., (1991) What is materials chemistry? In: *Materials for Nonlinear Optics Chemical Perspectives* (Marder, S.R., Sohn, J.E., and Stucky, G.D., eds) pp. 410–433, Am. Chem. Soc., Washington DC.
29. Laudise, R.A., Ballman, A.A., and King, J.C., (1965) Impurity content of synthetic quartz and its effect upon mechanical Q. *J. Phys. Chem. Solids.* **26**: 1305–1308.
30. Laudise, R.A., (1987) Hydrothermal crystal growth—some recent results, in *Advanced Crystal Growth*, Dryburgh, P.M., Cockayne, B and Barraclough, K.G. (eds.), Prentice Hall, New York, 267–288.
31. Laudise, R.A. and Sullivan, R.A., (1959) Pilot plant production of synthetic quartz. *Chem. Eng. Prog.*, **55**: 55–59.
32. Barns, R.L., Kolb, E.D., Laudise, R.A., Simpson, E.E., and Kroupa, K.M., (1976) Production and perfection of ‘Z-face’ quartz, *J. Cryst. Growth*, **34**: 189–197.
33. Buisson, X. and Arnaud, R., (1994) Hydrothermal growth of quartz crystals in industry. Present status and evolution, *J. Phys. IV*, **4** [C₂]: 25–32.
34. Lipson, H.G. and Armington, A.F., (1987) Aluminum and hydroxide distribution in cultured quartz grown from ⁺x seeds, *J. Cryst. Growth*, **80**: 51–59.
35. Hosaka, M. and Miyata, T., (1993) Hydrothermal growth of α -quartz using high-purity α -cristobalite as feed material, *Mater. Res. Bull.*, **28**: 1201–1208.
36. Avakov, V.A. and Vinogradov, B.N., (1972) Solubility of SiO_2 polymorphs. *Izv. Vyssh. Ucheb. Zaved., Khim. Teknol.*, **17**: 879–882.

37. U.S. Patent—No. 4853198, August 1, 1989
38. Hosaka, M., (1991) Synthesis of micro α -quartz crystals by hydrothermal hot-press method, *J. Cryst. Growth*, **112**: 291.
39. Balitsky, V.S., Kurashige, M., Balitskaya, L.V., Iwasaki, H. and Iwasaki, F., (2000) Study of quartz solubility and heavy phase formation under industrial synthetic quartz growth conditions, Yanagisawa, K. and Feng, Qi (eds) *Proc. Joint ISHR & ICSTR*, Nishimura Tosha-Do Ltd. Japan, 318–321.
40. Yoshimura, J., Miyazaki, T., Wada, T., Kohra, K., Ogawa, T. and Taki, S., (1979) *J. Cryst. Growth* **46**: 691.
41. Iwasaki, F. and Kurashige, M., (1978) *J. Appl. Phys.* **17**: 817.
42. Johnson, G.R., Irvine, R.A. and Foise, J.W., (1990) A parametric study of the variables involved in quartz growth, *IEEE Proc. 44th Annual Symposium on Frequency Control*, p. 216–221.
43. Demazeau, G. and Lafon, F., (1994) Hydrothermal crystal growth of α -quartz: new specificities correlated to applications, *J. Phys. IV*, **4** [C₂]: 13–18.
44. Lipson, H.G., Kahan, A. and O' Connor, J., (1983) Aluminium and hydrogen defect centers in vacuum swept quartz, *IEEE Proc. 37th Annual Symposium on Frequency Control*, 169–173.
45. Gualtieri, J.G., (1985) The influence of temperature and electric field on the etch-channel density in swept cultured quartz, *IEEE Proc. 39th Annual Symposium on Frequency Control*, p. 247–254.
46. Martin, J., (1987) Electro diffusion or sweeping of ions in quartz *IEEE Proc. 41st Annual Symposium on Frequency Control*, p. 167–174.
47. Deleuze, M., Cambon, O., Goiffon, A., Ibanez, A. and Philippot, E., (1994) Controlled dissolution of quartz material part I. Controlled dissolution of quartz plates in potassium and sodium hydroxides: Chemical thinning down of SC cuts, *J. Phys. IV*, **4** [C₂]: 79–84.
48. Brauer, K. and Muller, E., (1984) Correlation between parameters of plastic deformation in doped NaCl crystals. *Cryst. Res. Technol.* **19**: K101–109.
49. Cambon, O., Deleuze, M., Michel, J.P., Aubry, J.P., Goiffon, A. and Philippot, E., (1994) Controlled dissolution of quartz material part II, quartz chemical etching applied to blanks industrial manufacturing, *J. Phys. IV*, **4** [C₂]: 85–91.
50. Iwasaki, H., Iwasaki, F., Marina, E.A. and Balitsky, V.S., (1989) Influence of the degree of supersaturation on growth rates of hydrothermally grown quartz. U.S. Patent—No. 4853198, August 1, 329–332.
51. Balitsky, V.S., Marina, E.A., Balitskaya, L.V., Belimenko, L. and Bondarenko, G.V., (1989) Growing and investigation of the wedge-like quartz crystals, U.S. Patent—No. 4853198, August 1, 333–335.
52. Iwasaki, H., Iwasaki, F., Balitsky, V.S., Balitskaya, L.V. and Makhina, I.B., (1998) Growth rates anisotropy of synthetic quartz crystals grown on Z-cut hexagonal seeds and computer simulations of growth process, *J. Cryst. Growth* **187**: 481–489.
53. Iwasaki, H., Iwasaki, F., Yokokawa, H., Kurashige, M. and Oba, K., (2002) Computer simulation of growth process in synthetic quartz crystals grown from X-bar, Y-bar and rectangular Z-plate seeds, *J. Cryst. Growth* **234**: 711–720.

14 Crystal Growth of Diamond

HISAO KANDA

*National Institute for Materials Science, 1-1 Namiki, Tsukuba, Ibaraki
305-0044, Japan*

14.1	Introduction	407
14.2	Diamond synthesis	408
14.2.1	Phase diagram of carbon	408
14.2.2	Direct transformation	408
14.2.3	Agents for diamond formation	409
14.2.4	Carbon source	411
14.2.5	High-pressure apparatus	412
14.2.6	Diamond growth methods	412
14.3	Properties of diamond single crystals made with high-pressure methods	417
14.3.1	Morphology	417
14.3.2	Surface morphology	419
14.3.3	Inclusions	421
14.3.4	Atomic impurities, color and luminescence	422
14.3.5	Color control	423
14.4	Summary	428
	References	428

14.1 INTRODUCTION

Diamond is one of the most attractive materials because of its superior properties such as hardness, thermal conductivity, optical transparency and wide bandgap, etc. Interests in diamond industries may be in three fields, i.e. jewelry, mechanical engineering, and electronics. Gemmologists are interested in the size of a single crystal, colors and the origin of natural diamonds. Hardness and toughness may be important in the mechanical engineering industry. Semiconducting properties and thermal properties are important for electronic applications.

Attempts to make diamond have a long history, more than 100 years, but reproducible success was only achieved in 1955 [1], with lift-off diamond science and technology. Today, two methods for diamond synthesis have been established, which are the high-pressure method and the chemical vapor deposition (CVD) method, and a variety of

diamonds are being made in laboratories and factories across the world; large crystals, fine powder, polycrystalline aggregates, thin films and colored crystals as well as colorless ones.

In this chapter, I focus on the high-pressure method to make bulk, single-crystal diamonds and the characteristics of the synthetic diamonds. Research on CVD diamond has been active since the 1980s [2], but this field is not included in this chapter, because the CVD methods is suitable for growth of thin films but not bulk crystals.

In the following methods are described to grow diamond under high pressure and the characteristics of synthetic diamond single crystals are discussed.

14.2 DIAMOND SYNTHESIS

14.2.1 Phase diagram of carbon

When a crystal grows, it must normally be thermodynamically stable, although growth can occur even in metastable conditions, and, therefore, information of the phase stability of material is important. It is well known that diamond is a high-pressure phase of carbon, while graphite is stable at one atmosphere. The equilibrium line between diamond and graphite is the most important for diamond synthesis. The line is expressed by the following equation [3]:

$$P(\text{kbar}) = 19.4 + T(\text{C})/40$$

This equation was determined by thermodynamic calculation [4] and experiments of the phase transition between diamond and graphite [3]. However, there are still ambiguities in the equation because of difficulties in measurement of the stability of diamond and graphite. We do not know suitable pressure or temperature scales to determine pressure and temperature. Pressure in a high-pressure cell can be calibrated by measuring the phase change of materials such as Bi, Tl and Ba at room temperature, but the calibration is not applied at elevated temperatures strictly speaking. Temperature is measured using thermocouples, but the emf of the thermocouple depends on pressure. It is necessary to modify the emf under high-pressure conditions, but this is difficult. In spite of the ambiguity of the measurements, the measurements of pressure and temperature help to roughly estimate the temperature and pressure inside the high-pressure cell, when we start experiments using a new high-pressure cell.

14.2.2 Direct transformation

Even in a diamond-stable region, graphite does not necessarily transform to diamond because of kinetics. Much excess pressure is required for diamond formation from graphite. An early attempt was carried out at pressures above 10 GPa [5]. On heating graphite by passing electric current through the graphite, the graphite is converted to diamond.

Visible evidence of the transformation has been obtained using a diamond anvil cell (DAC) [6]. Graphite compressed in the DAC is changed to transparent diamond upon heating by a laser. Transparent material has been obtained from graphite single crystal even at room temperature with compression in a DAC, although it is reversed to opaque

when the pressure is released [7]. The transparent diamond formed at room temperature is identified to be hexagonal diamond instead of cubic diamond by using an in-situ X-ray diffraction technique [8]. Recently, transparent polycrystalline diamond with 1 mm diameter has been made from graphite at a very high pressure of 12–25 GPa and temperatures of 2300–2500 °C [9]. Carbon nanotubes are useful as the carbon source [10]. There is a report that shearing stress has a positive effect on transformation of graphite to diamond [11].

The methods to make diamond with direct transformations have disadvantages from the technical point of view. The diamond made by the direct conversion has a polycrystalline form consisting of tiny crystallites, and it is difficult to produce large-size diamond crystals because a large-volume, high-pressure space is not realized. If diamond is made at lower pressure and temperature, it would be easier to make large crystals, because a large-volume, high-pressure vessel is more easily constructed. Agents that reduce minimum temperature and pressure for the transformation from graphite to diamond are important for the production of diamond.

14.2.3 Agents for diamond formation

Discovery of the agents was one of the most important breakthroughs in the first successful work on synthetic diamond [1, 12]. The diamond crystals were made at pressures as low as 5 GPa and 1500 °C of temperature with the help of the agents.

The GE researchers surveyed a variety of materials, and found suitable materials working as agents [12]. They are transition metals such as Cr, Mn, Fe, Co, Ni, Ru, Rh, Pd, Os, Ir and Pt. Their alloys are also effective. The metals melt at the HPHT condition and dissolve carbon, followed by precipitation of diamond in the molten metals. They essentially act as a solvent for carbon, but the agents are called catalyst-solvent, solvent/catalyst or catalysts in papers on diamond synthesis, because early work noted that all substances that dissolve carbon do not act as agents for conversion of graphite to diamond [13]. In this chapter, the agents are called solvent/catalysts. In these solvent/catalysts, Fe, Co and Ni are major components of the agents and are used most popularly in production of high-quality diamond crystals currently. I will mainly describe synthesis of diamond using the 'solvent/catalysts'.

We can simply understand the process of diamond formation as a category of solution growth, when the 'solvent/catalyst' metal is used, namely, diamond crystals grow in molten metal solution supersaturated with carbon. The growth cell must be heated so that the metal melts in the metal-carbon system, because the metal is solid at room temperature.

As a typical case, a phase diagram of Ni-C system at a high pressure of 5.4 GPa is presented in Fig. 14.1 [14], showing that Ni and C have a eutectic correlation, and that the solubility of carbon increases with an increase of temperature above the eutectic temperature. Diamond grows at temperatures higher than the eutectic temperature, where liquid phase appears. However, there is an upper temperature limit for growth of diamond. As shown in Fig. 14.1, the temperature is indicated by a horizontal line at 1728 K, at which diamond and graphite are in thermodynamic equilibrium. Graphite becomes stable above the temperature, and graphite crystals grow from the molten metal. The equilibrium temperature increases with increasing pressure, whereas the eutectic temperature does not

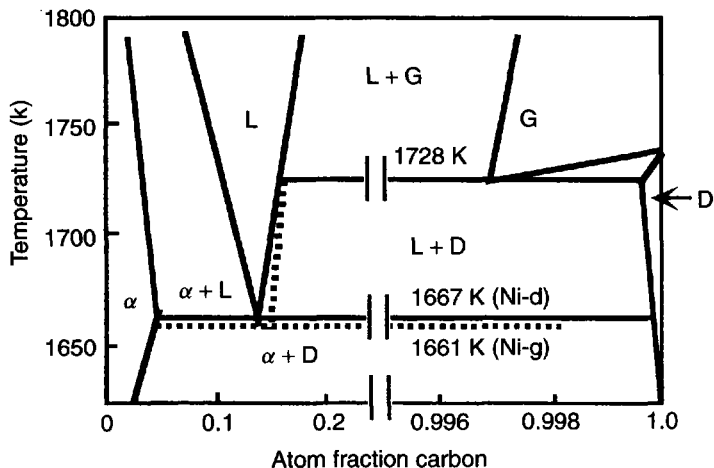


Figure 14.1 Ni-C phase diagram at 5.4 GPa (Redrawn from [14])

change much. The pressure of the growth cell must be high enough that the equilibrium temperature is higher than the eutectic temperature.

When the 'solvent/catalysts' are carbide-forming metals such as iron (Fe), the minimum temperature for diamond formation is different. The temperature is a peritectic temperature, at which carbides decompose, rather than the eutectic temperature.

After the discovery of the 'solvent/catalysts' by GE researchers, other materials have been established to act as agents for diamond growth.

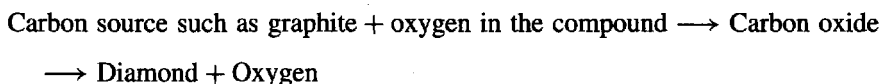
Wakatsuki [15] has reported that some alloys that do not contain the metal elements used as the 'solvent/catalysts' play the role of agents. The alloys consist of two types of metal elements: one is carbide-forming metals such as Ti and Nb, and the other are metals that have a weak interaction with carbon, such as Cu.

It has been found that Mg assists conversion of graphite to diamond [16]. Mg is a carbide-forming element, but diamond forms at high temperatures above 1800°C where magnesium carbide decomposes. Mg and carbon have a peritectic relation.

Later, it has been confirmed that diamond grows from other metals such as Cu, Zn and Sn [17]. Phosphorus and sulfur have also been found to play the role of agent [18–20]. These elements have a weak interaction with carbon, and the solubility of carbon has not been definitely determined. When these elements are used as agents, diamond does not grow even if liquid phase is formed at elevated temperatures, in contrast diamond forms immediately after liquid phase appears in the case of a carbon-'solvent/catalysts' (such as Ni and Fe) system. Temperatures are required to be much higher than their melting temperatures. In the case of Cu, diamond grows at temperatures above 1500°C, in spite of the melting temperature of Cu being 1300°C. The minimum temperature at which diamond starts growing is not clearly defined as the melting temperature. When concentrations of carbon in the metal exceed a threshold, diamond may start to grow, even if the solubility of carbon is negligibly small.

Nonmetallic compounds such as carbonates and sulfates have become evident as aids to diamond synthesis [21, 22]. The compounds are carbonates such as CaCO_3 , sulfates such as Na_2SO_4 , phosphates, borates, hydroxides, etc. Some of them are components in

natural rocks, suggesting that natural diamond has grown from these compounds in the deep earth interior. It has been confirmed that diamond forms from H_2O as well [23]. The growth mechanism of diamond from these nonmetallic compounds may be interpreted in the carbon–oxygen system with the following chemical reaction:



This is because all compounds containing oxygen can be agents for diamond formation.

Temperatures as high as 2000°C are required for rapid formation of diamond, when these nonmetallic agents are used [21, 22]. However, it has been reported that diamond crystallizes from carbonate-, oxalate-C systems at pressures and temperatures as low as 5.7 GPa and 1200°C , which is similar to the growth conditions of natural diamond [24].

There is a report that hydrogen is also an aid to convert graphite to diamond [25]. In this case, reaction other than that in the carbon–oxygen system must be considered.

As summarized in Table 14.1, a variety of materials have been confirmed to play the role of agents for diamond synthesis. However, Fe, Co and Ni maintain the position of the most powerful agents currently. Diamond grids and large crystals are being made using these metals in laboratories and factories. As an exception, diamond sintering has been carried out using the nonmetallic catalysts, producing polycrystalline diamond with high thermal stability [26].

14.2.4 Carbon source

Graphite is usually used as the carbon source. Qualities such as purity and crystallinity of the graphite may be considered. According to Tsuzuki *et al.* [27, 28] the degree of

Table 14.1 Solvent/catalysts for synthesis of diamond

Solvent/catalyst	Description	References
Transition metals	Cr, Mn, Fe, Co, Ni, Ru, Rh, Pt, Ta, Os, Ir, Pt and alloys containing them. Fe, Co and Ni are the most conventional.	[12]
Cooperative catalysts	Alloys of a group (Ti, Zr, Hf, V, Nb, Mo, W) and the other group (Cu, Ag, Au)	[15]
Mg	Carbide-forming elements	[16]
P, S	Nonmetallic elements	[18, 19]
Cu, Zn, Sn	Metals that dissolve carbon negligibly	[17]
Oxyacid salts	Salts of alkali and alkali earth metals with oxyacid ions such as CO_3 , SO_4 and OH	[21, 22]
H_2O		[23]
Hydrides	LiH and CaH_2	[25]

crystallinity of graphite is not an important factor for diamond synthesis, but adsorbed gases on the starting carbon and atmospheric gases in the high-pressure cell deteriorate the conversion to diamond in the metal solvent/catalyst system. In particular, hydrogen and hydrogen-containing materials have the most harmful effect for diamond synthesis.

Carbon-containing compounds such as SiC [29], carbonates [30, 31], hydrocarbons [32] and carbides [33] have been used as carbon sources, and diamond has been grown successfully.

Isotopically modified graphite can be used to synthesize ^{13}C -enriched or isotopically pure diamond. The natural abundance of ^{13}C in carbon is 1.2%, but several types of diamond with different contents of ^{13}C have been made in order to study defect structures. Isotopically pure ^{12}C and ^{13}C carbon powder is commercially available, and if we use a mixture of the carbons, diamond with required contents of ^{13}C can be made [34]. It has been found that isotopically pure diamond exhibits a thermal conductivity 50% higher than normal diamond [35].

14.2.5 High-pressure apparatus

As described above, we need pressure and temperature conditions higher than 5 GPa and 1400 °C to grow diamond, and special apparatus to generate such pressures must be used. High-pressure techniques are the most important for high-pressure diamond synthesis. Several types of apparatus have been invented. The so-called belt-type apparatus is well known, because the GE group announced the first success in diamond synthesis using this type of apparatus in 1955 [1, 36], and the apparatus has been very popular for diamond production worldwide. Figure 14.2 shows a belt-type apparatus installed in the National Institute for Materials Science, Tsukuba, Japan. The size and details of apparatus in laboratories and factories are variable, and they are not disclosed in the literature. Figure 14.3 shows a schematic drawing of a belt-type high-pressure vessel, which consists of two punches and a die made of sintered tungsten carbide. The punch, sometimes called the 'anvil', compresses an assembly filled in the die. The assembly consists of a number of parts including a heater as well as the carbon source and the agents. A graphite tube is usually used as the heater, which does not change to diamond even under diamond-stable conditions of 5 GPa and 1400 °C. Force is loaded to the high-pressure vessel with oil pressure in a large and strong frame.

Other types of high-pressure apparatus are being used for diamond growth. Multianvil-type apparatus compress tetrahedral-, cubic- and octahedral-shaped materials containing sample and heater with four, six and eight anvils, respectively. 'BARS' or the split-sphere-type of apparatus is one of the multianvil types [37]. There is an opposed anvil-type apparatus consisting of two punches with concave surfaces, called a toroidal apparatus [38].

14.2.6 Diamond growth methods

In the following part, I describe diamonds grown from Fe, Co, Ni and their alloys, so-called conventional 'solvent/catalysts'. As described above, diamond grows from molten metal supersaturated with carbon. There are two methods to produce a solution supersaturated with carbon. Figure 14.4 shows a schematic diagram of a metal-carbon system with



Figure 14.2 1500-ton belt-type high-pressure apparatus (National Institute of Advanced Industrial Science and Technology, Japan)

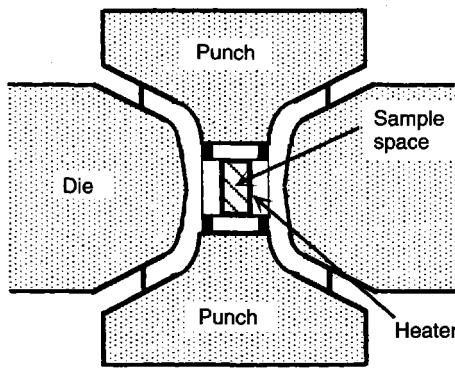


Figure 14.3 Schematic of cross section of a belt-type high-pressure apparatus

eutectic correlation at a high-pressure condition. In addition to the stable phase relation shown in solid lines, dotted lines are presented, which are of a metastable graphite-carbon system. δC_2 indicates the solubility difference between graphite and diamond. More graphite dissolves in the molten metal than diamond, and the metal solution saturated with graphite results in a supersaturated solution with respect to diamond. δC_1 is the solubility difference due to the temperature dependence of the solubility of diamond. If a temperature gradient is present in the metal solution, the cooler region becomes supersaturated with carbon.

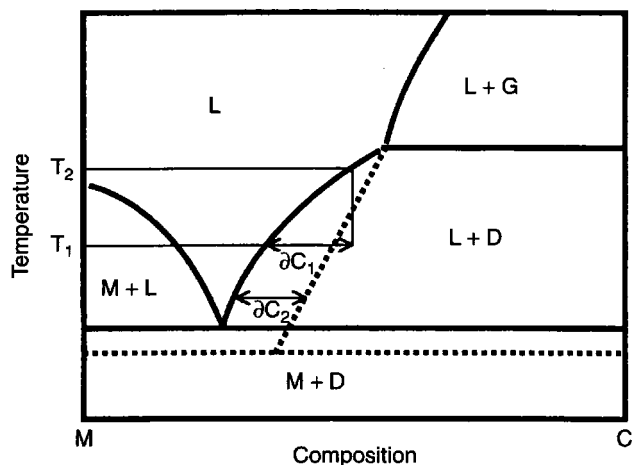


Figure 14.4 Schematic representation of the solubility curves of carbon. Solid lines and dotted lines are metal–diamond system and metal–graphite system, respectively. δC_2 : solubility difference between diamond and graphite, δC_1 : Difference between solubility at T_2 and that at T_1

The driving force of the former method is the chemical-potential difference between diamond and graphite, and that of the latter method is the temperature gradient inside the molten metal. The two methods are described in the following.

14.2.6.1 Chemical-potential-difference method

An example of a sample assembly for growth with this method is shown in Fig. 14.5. A metal disc is sandwiched by two graphite discs in an NaCl pressure medium filled in a graphite heater. When the assembly is compressed above 5 GPa in a high-pressure apparatus, then heated to around 1500 °C, the metal disc melts and diamond crystals nucleate and grow at the interfaces between the metal and the graphite as shown in Fig. 14.5. A thin film of the metal is present between the grown diamond and the graphite. Figure 14.6 shows the diamond crystals covered with metal film. The picture was taken after removing the graphite with an acid treatment. The presence of the metal film indicates that carbon atoms of the graphite dissolve into the thin metal film, and diffuse to precipitate on the growing diamond. The film moves into the graphite disc, as the graphite is consumed and diamond grows.

If the pressure is high enough, the solubility difference is large, and the supersaturation in the molten metal becomes high, resulting in high growth rates. All of the graphite disc is consumed in a few minutes, and a diamond aggregate is formed. The aggregate is so fragile that it is broken into small pieces with irregular shapes.

In order to grow regular-shaped crystals, the pressure must be controlled precisely within a range of 0.2 GPa near the equilibrium condition between diamond and graphite [39]. Nucleation density is suppressed at the condition so that diamond crystals grow without contacting each other. Figure 14.7 shows crystals with a regular shape. They are commercially available for application as cutting tools. Such crystals have dimensions ranging from 0.1 to 1 mm. It is difficult to grow crystals larger than 1 mm.

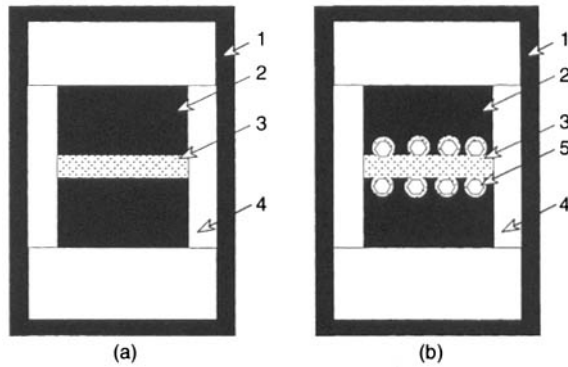


Figure 14.5 Schematic drawing of diamond growth with a motivation of chemical-potential difference between diamond and graphite. (a) before and (b) after. 1: Graphite heater, 2: Graphite disk, 3: Metal solvent/catalyst, 4: NaCl capsule, 5: Grown diamond crystal

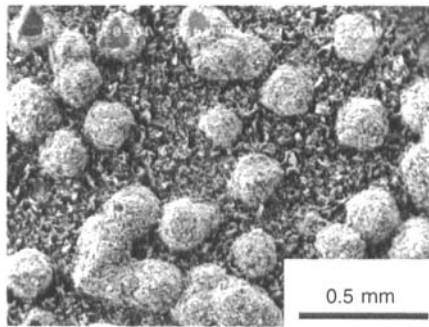


Figure 14.6 Diamond particles grown from graphite in metal solvent/catalyst. The spherical particles are diamonds covered with metal thin film

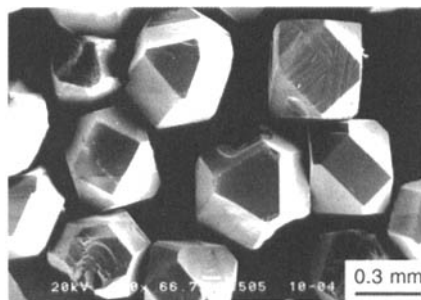


Figure 14.7 Commercial diamond grit grown as shown in Fig. 14.5 (ELEMENTSIX SDA 100S)

Spontaneous nucleation is not observed at pressures very close to the equilibrium boundary between diamond and graphite, but diamond is able to grow if a nucleus is present [14]. Wakatsuki *et al.* [40] have succeeded in the growth of 2-mm crystals on a seed crystal under the condition where no nucleation occurs.

14.2.6.2 Temperature-gradient method

The GE research group succeeded in the growth of large crystals by this method for the first time [41, 42].

In this method, a relatively thick metal ‘solvent/catalyst’ disc is used so that a temperature gradient is present inside the disc. Figure 14.8 shows a sample assembly for the growth by this method. A graphite disk or diamond powder as the carbon source and a synthetic diamond grit as a seed crystal is placed at the top and bottom of a metal disk, respectively. In the assembly, the top side of the metal is higher in temperature than the bottom side, because the top part of the metal is located at the center of the graphite heater. More carbon atoms are dissolved from the carbon source located at the hotter region, and are transported to the cooler region, and then precipitate on the seed crystal to form a new crystal.

When the assembly, placed in a high-pressure vessel, is compressed, and then heated, a crystal starts growing on the seed crystal. The crystal becomes larger continuously until the heating power is turned off, although the space of the growth cell limits the size of the grown crystal. Figure 14.9 shows an example of a crystal grown on a seed crystal. Usually the seed crystal is removed from the grown crystal when it is recovered from the high-pressure vessel. A trace of the seed crystal is seen on the bottom surface of the grown crystal.

Growth rate depends on supersaturation, which is equivalent to the temperature gradient. A large gradient gives high growth rates, but metal inclusions are readily incorporated. On the other hand, a small gradient gives low growth rates, although incorporation of inclusions can be avoided. There is an optimum gradient to grow inclusion-free crystals with reasonable rates. The temperature gradient is controlled by changing the assembly of the high-pressure cell; i.e. the shape and size of the graphite heater and the thermal conductivity of the pressure media.

The growth temperature has also been considered to optimize growth conditions for high-quality diamond. Sumiya *et al.* [43] have determined growth temperatures under

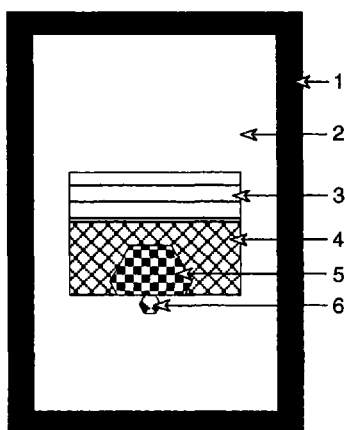


Figure 14.8 Schematic drawing of a cell assembly for diamond growth with the temperature-gradient method. 1: Graphite heater, 2: NaCl capsule, 3: Diamond particles as carbon source, 4: Metal solvent/catalyst, 5: Grown diamond, 6: Seed crystal

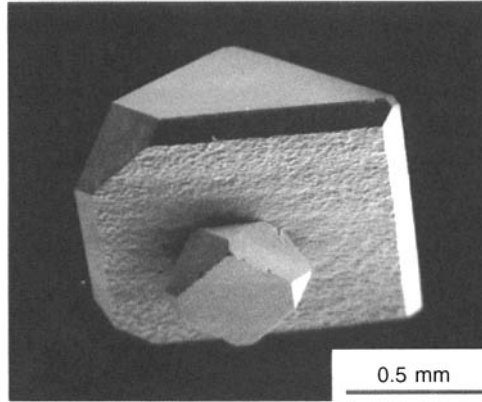


Figure 14.9 A diamond crystal made by the temperature-gradient method. The small rectangular crystal is the seed crystal

which inclusion-free crystals grow. Temperature control within 40°C and 10°C around 1350°C is required for growth of yellow crystals and colorless crystals, respectively. The colors are described in a later section.

A large seed crystal has an advantage to increase the growth rate of the high-quality diamond particularly in the beginning of growth [43, 44]. A crystal with 5 mm dimension has been employed as the seed crystal. Considering the factors, Sumiya *et al.* have succeeded in growth of 10-mm sized high-quality crystals with rates as high as 15 mg h^{-1} for yellow crystals and $6\text{--}7\text{ mg h}^{-1}$ for colorless ones. The growth rates are much higher than reports published previously [41, 45]. There is still a problem to be overcome; why are high-quality colorless diamonds more difficult to grow than yellow ones?

An attempt has been made to suppress incorporation of metallic inclusions [46]. Based on calculation of diffusion of carbon atoms in the molten metal a cell assembly has been designed in which the diameter of the metal solvent is small near the seed crystal. The small diameter reduces the supply of carbon atoms to the seed crystal in the early stages of growth, causing suppression of incorporation of metal inclusions.

The dimension of the metal 'solvent/catalyst' is another parameter that limits the size of the grown crystal. The world record for a large synthetic diamond is 34.80 cts made by ELEMENTSIX (formerly DeBeers) in 1992 (Fig. 14.10). Commercially available ones are in the range from 1 to 10 mm, and are used for cutting tools, wire-drawing dies and heat sinks.

14.3 PROPERTIES OF DIAMOND SINGLE CRYSTALS MADE WITH HIGH-PRESSURE METHODS

14.3.1 Morphology

The diamond grown from the solvent/catalysts shows a variety of morphologies.

A single crystal grown in isolation is polyhedral. An octahedron is the most typical shape of natural diamond, but a cubo-octahedron shape is commonly observed for the high-pressure synthetic diamond as shown in Fig. 14.11, namely, $\{100\}$ surfaces develop



Figure 14.10 The world's largest synthetic diamond crystal grown by the temperature-gradient method (ELEMENTSIX, formerly DeBeers)

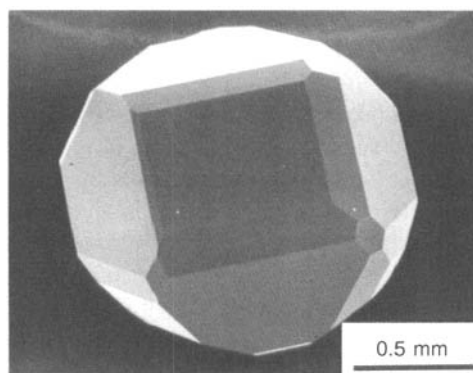


Figure 14.11 A typical grown diamond, which exhibits dominant $\{111\}$ and $\{001\}$ surfaces accompanying small $\{011\}$ and $\{113\}$ surfaces

as do $\{111\}$ surfaces. There are reports that $\{100\}$ are more dominantly grown at a lower-temperature condition, while $\{111\}$ are dominant at high temperatures [47].

Minor surfaces such as $\{113\}$ and $\{011\}$ commonly appear in addition to $\{111\}$ and $\{001\}$. $\{115\}$ surfaces have also been reported to appear, although they are much less common [41, 48, 49]. An early paper reports that $\{117\}$ appear [42], but $\{115\}$ indexing may be correct. The appearance depends on the composition of the solvent/catalysts. When metals other than Ni are used, $\{113\}$ and $\{011\}$ are commonly observed in addition to $\{111\}$. $\{115\}$ surfaces are reproducibly observed on diamond grown at lower temperatures, when Co-Ti alloy is used, according to our experience.

Recently, other minor surfaces have been found on diamond grown from a phosphorus melt [20], which are {013} and {119}. The appearance of the {013} surfaces is curious, because (011) directions, so-called periodic bond chains, are not included on the surface.

Twinned crystals also grow. They have {111} faces as the twin boundary. When twin boundaries are frequently formed, the overall morphology shows a complex form like an aggregate (Fig. 14.12). There is a tendency for twinned crystals to grow when pure nickel is used as the solvent/catalyst or the growth temperature is relatively low [43, 50].

When materials containing H₂O such as hydroxides and pyrophyllite are present in the growth cell, the grown diamond exhibits a very different morphology. Spiral patterns with high step heights or needle-like crystals, Fig. 14.13, are formed [51].

14.3.2 Surface morphology

Surface morphology also shows a large difference between natural and synthetic diamonds [52–54]. Dendritic patterns are almost always observed on synthetic diamonds, as shown in Fig. 14.14. The patterns vary from irregular to regular ones. The regular patterns are related to the symmetry of the diamond lattice. Patterns with six-fold symmetry are seen

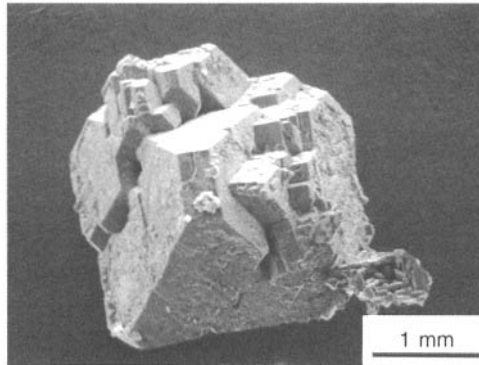


Figure 14.12 An aggregate diamond grown from a single crystal with successive formation of twinning during growth

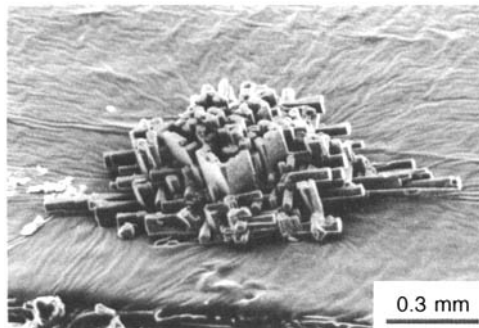


Figure 14.13 ‘Diamond dendrite’

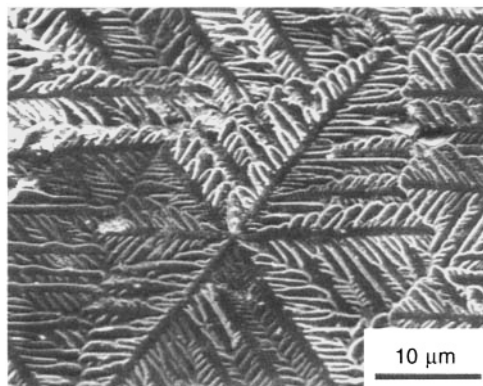


Figure 14.14 Dendritic patterns observed on synthetic diamond surfaces grown from molten metal solvent/catalysts

on $\{111\}$ surfaces, and four-fold symmetry on $\{001\}$ surfaces. These patterns are fixed by overgrowth when solvent/catalysts are frozen by turning off the electric power. When the metal is frozen, carbon atoms in the molten metal are segregated to precipitates on the growing crystal. The dendritic patterns make observation of as-grown surfaces difficult. However, as-grown surfaces have been observed on some diamonds, from which very low growth steps are detectable.

Growing surfaces are not covered with the dendritic pattern, if the growing diamond has left the molten-metal bath before the metal is frozen. It is not easy to intentionally take off the growing crystal from the molten-metal bath in a high-pressure vessel, but it sometimes happens accidentally [48]. Figure 14.15 shows an example of an as-grown surface. It is found that the as-grown surface is highly smooth, although 3 nm of growth steps are detected under a differential interference contrast microscope.

When diamond crystals grow from nonmetallic solutions such as carbonates and phosphates, no dendritic pattern is formed, because the carbon solubility is probably extremely low. Very beautiful growth patterns are observed on diamonds grown from sodium carbonate (Fig. 14.16) [55].

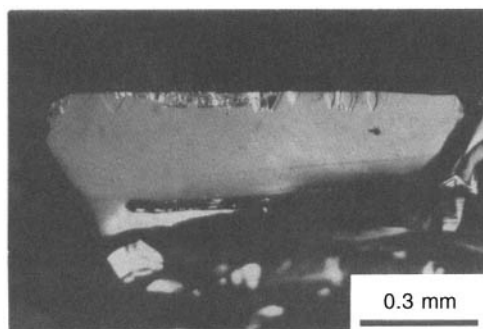


Figure 14.15 Smooth as-grown surface of a synthetic diamond, on which no dendritic pattern is formed

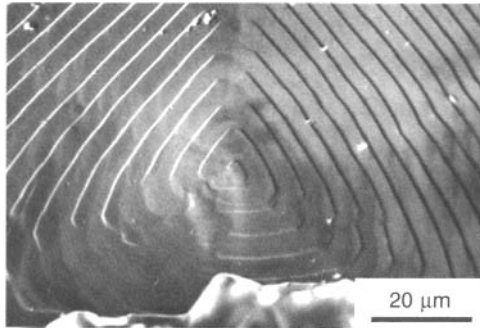
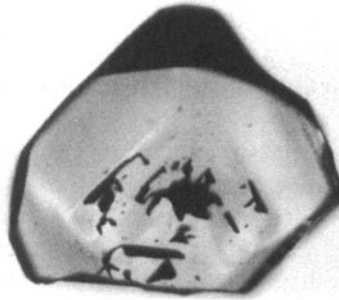
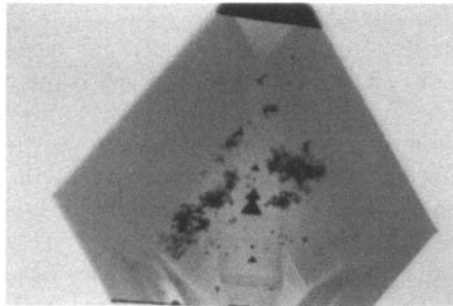


Figure 14.16 Spiral growth pattern observed on a synthetic diamond surface grown from molten Na_2CO_3



(a)



(b)

Figure 14.17 Two types of inclusions observed in synthetic diamond (2 mm wide) grown from molten Co metal. (a) bulky metallic inclusion and (b) fine-grained inclusions are seen

14.3.3 Inclusions

Grown diamonds frequently contain a variety of inclusions. Most readily visible inclusions are metallic solvent/catalysts. They have the shape of rods or sheets with round edges. Large ones have an irregular shape as shown in Fig. 14.17a. They are formed when a depression formed on the growing surface is covered with subsequent growth layer. The

inclusions tend to be formed at high growth rates. In order to avoid formation of inclusions, the growth rate must be controlled not to exceed a threshold. The threshold limits the maximum growth rate. The threshold depends on the composition of the solvent/catalyst. When a solvent/catalyst that produces a colorless crystal is used, inclusions are readily entrapped. In order to grow inclusion-free colorless crystals, the growth rate must be kept lower than that for nitrogen-containing yellow crystals. In commercial production, therefore, the yellow crystals are made with high growth rates, i.e. lower cost.

Fine inclusions are also observed, as shown in Fig. 14.17b. The size of each particle is of the order of micrometers, and they are present as isolated particles or aggregates. Their chemical composition has not been identified. When a Ti-containing alloy is used to make nitrogen-free diamond, TiC is formed in the solvent/catalyst. The TiC particles are entrapped in a growing diamond as inclusions. In order to suppress formation of the TiC particles, Cu is alloyed into the solvent/catalyst [43].

Other types of inclusions have been observed. Needles, spiral coils, like springs, have been demonstrated in previous papers [56, 57].

14.3.4 Atomic impurities, color and luminescence

Foreign atoms can be incorporated into the diamond lattice during growth to form point defects and modify physical properties such as optical, electrical and thermal ones, but a limited number of elements have been reported to be used as dopants, i.e. hydrogen, boron, nitrogen, silicon, phosphorus, cobalt and nickel. The impurities have been studied by means of spectroscopic methods; optical absorption, luminescence and ESR. The optical data have been summarized in publications [58, 59]. ESR spectroscopy provides information on the impurities more directly, and detailed investigation has been carried out for various types of diamond [2, 60].

Nitrogen and boron are quite readily incorporated and have been well studied [61, 62]. Based on concentrations and forms of nitrogen and boron impurities, diamonds are classified into several types, Type Ia, Ib, IIa and IIb [58].

Types Ia and Ib contain nitrogen, while type II is nitrogen free. The type II are separated into types IIa and IIb. Impurities are negligible in type IIa, while type IIb contains boron atoms. Type Ia contains nitrogen in aggregated forms, and type Ib has nitrogen in an isolated form. Type Ia is further divided into two types, IaA and IaB. Nitrogen atoms are in paired form in type IaA, and an aggregate of four nitrogens and a vacancy is contained in type IaB. The types are readily identified by infrared absorption spectroscopy, because they exhibit their own characteristic absorption spectra between 1400 and 1000 cm^{-1} .

Type IIa, i.e. pure diamond, is transparent in a wide spectral range from the ultraviolet to the infrared. Light is absorbed at wavelengths lower than 220 nm because of its bandgap. On the other hand, type Ib has strong absorption for energies above 1.7 eV, giving rise to a yellow color. Type IaA and IaB are colorless, but have strong absorption in the UV region. Type IIb that contains boron gives a blue coloration, and exhibits characteristic absorption bands in the infrared region.

Hydrogen impurities are not considered in high-pressure synthetic diamond, although they are very important for CVD diamond, because CVD diamond grows in a hydrogen-rich atmosphere. As for natural diamond, hydrogen-related absorption peaks are observed

at 3107 and 1450 cm^{-1} in an infrared absorption spectrum [63]. There is only one paper concerning hydrogen. Kiflawi *et al.* [64] found that the 3107 cm^{-1} peak appears when some types of high-pressure synthetic diamond are heated above 2000 °C.

Silicon impurities are also important in CVD diamond rather than high-pressure diamond. This impurity was found in CVD diamond first, because silica glass is commonly used as a chamber in which source gases decompose to form diamond in a plasma. Si impurities can be doped in high-pressure diamond if Si-containing alloys are used as the solvent/catalysts. The Si impurity produces luminescence and an absorption peak at 1.68 eV, which is outside the visible region. Absorption spectra taken at high resolution showed splitting of the band into several peaks, whose intensities correspond to isotope abundances [65]. The spectrum has unambiguously confirmed that the peak is of the silicon impurity.

Phosphorus impurities have recently been established in CVD diamond to act as donors to give rise to n-type semiconducting character [66]. In high-pressure diamond, the presence of phosphorus impurities was detected by an EPR technique [67]. The diamond was grown from molten phosphorus. However, the phosphorus accompanies a nitrogen atom at a next-nearest position, and it is not expected to act as a donor.

Nickel and cobalt impurities are found in diamond grown from nickel and cobalt melts, respectively. They are uniquely found in high-pressure synthetic diamond, although nickel has been detected occasionally in natural diamond [68]. The impurities have been detected by ESR and EPMA techniques [46, 68, 69] with concentrations up to 70 ppm. The ESR analysis has concluded that the nickel atoms sit on substitutional and interstitial sites [69, 70], and that they are present as complexes, labeled NE1, NE2, etc, of nickel, nitrogen and vacancies [71, 72]. A number of absorption and luminescence bands related to nickel impurities have been recorded [73–75]. An attractive green color and green luminescence are observed.

The influence of cobalt impurities on optical properties is weaker than that of Ni. The cobalt impurities contribute very little absorption, although strong luminescence is observed [76]. ESR measurements have given evidence of incorporation of cobalt impurities [77].

Incorporation of the impurities depends on growth conditions. Factors that influence the incorporation are the composition of the solvent/catalysts, growth temperature, growth rates and purity of the carbon source. Atomic arrangement of the impurities can be changed with heat treatment at high-pressure conditions.

In the following section, changes of optical properties due to the impurities are described with respect to experimental factors for growth.

14.3.5 Color control

14.3.5.1 Effect of the metal solvent/catalysts

Components of the metallic catalyst/solvents are expected to be readily incorporated into grown crystals. However, Ni and Co are the only elements incorporated as optically active centers [73, 76]. More than twenty of the Ni-related absorption and luminescence bands have been reported [59, 73–75]. There have been no reports on incorporation of Fe, in spite of it being a major component of the metallic solvent/catalyst. Attempts at doping

with impurities have been made by adding other elements as a component of the alloy used as the solvent/catalysts, but silicon is the only element that has been established to be incorporated as an optical center [65].

Concentrations of nitrogen are influenced by the composition of the solvent/catalysts. A considerable amount of nitrogen is incorporated into crystals if no effort is made to avoid the incorporation. The source of the nitrogen impurity has not been confirmed. It may be supplied from the carbon source, the metallic catalyst/solvent or materials used as the sample capsule. However, the concentrations are controlled by changing the composition of the metallic catalyst/solvents [41, 78]. 100 to 400 ppm of nitrogen is present in a grown crystal, when typical metallic solvent/catalysts such as Ni, Co and Fe are used. In order to grow a type IIa crystal in which the nitrogen concentration is negligible, elements called a 'nitrogen getter' such as Ti, Zr and Al are added to the metals [41, 42]. These elements have a strong affinity for nitrogen, and it is reasonably expected that nitrogen in the reaction cell preferentially stays in the molten metals that contain the nitrogen getters. Addition of a few per cent of Ti to Ni or Co is sufficient to grow type IIa crystals.

Ti and Zr have the strongest gettering effect, but other elements such as V and Cr also have the gettering effect, although their effect is weaker. When weaker getters are employed, more getter must be added to the metal solvents/catalyst. If the gettering effect is not sufficient, grown crystals exhibit a pale yellow color.

The Ni-related optical centers are influenced by concentrations of nitrogen. A brownish-yellow crystal (Fig. 14.18a) grows from pure Ni without the nitrogen getters, but a green color is induced with alloying the getters to Ni metal (Fig. 14.18b). Addition of a higher content of the getters produces a brown color (Fig. 14.18c).

The depths of the colors described above are not uniform in a crystal. As shown in Fig. 14.18, a growth-sector dependence is clearly seen. Usually, the depth of the yellow color caused by nitrogen is in the order of $\{111\} > \{001\} > \{011\} = \{113\}$ [79], although the order is the reverse in crystals grown at the lowest temperatures, namely, $\{001\} > \{111\}$ [47]. The Ni-related colors are seen only in $\{111\}$ sectors [80].

Even within a sector, incorporation of impurities is not uniform. Time-dependent fluctuations of growth conditions, such as growth temperature, produces inhomogeneity. The effect of an intentional change of growth temperature is described in the following section. Even on a growth surface impurities are not uniform. It has been observed that incorporation depends on orientation of vicinal surfaces of growth hillocks [81, 82]. Figure 14.19 shows an example in which radial patterns are seen in a cathodoluminescence image. The radial patterns have a one-to-one correlation with the vicinal surfaces.

When phosphorus is used as the agent, phosphorus-containing diamond can be made, but a detailed study has not been done, although it is a very interesting impurity with respect to semiconducting technology.

14.3.5.2 Doping with impurities

Alloying is not necessary to dope impurities. If boron powder is present in any region of the reaction cell, it is easily incorporated into a grown crystal [83]. We put the boron powder between the graphite disk and the metal disk in the cell assembly shown in Fig. 14.8 to grow a boron-doped crystal.

The boron-doped diamond crystal exhibits a blue color and is an electrically conductive p-type semiconductor. The depth of the blue color and electrical conductivity increases

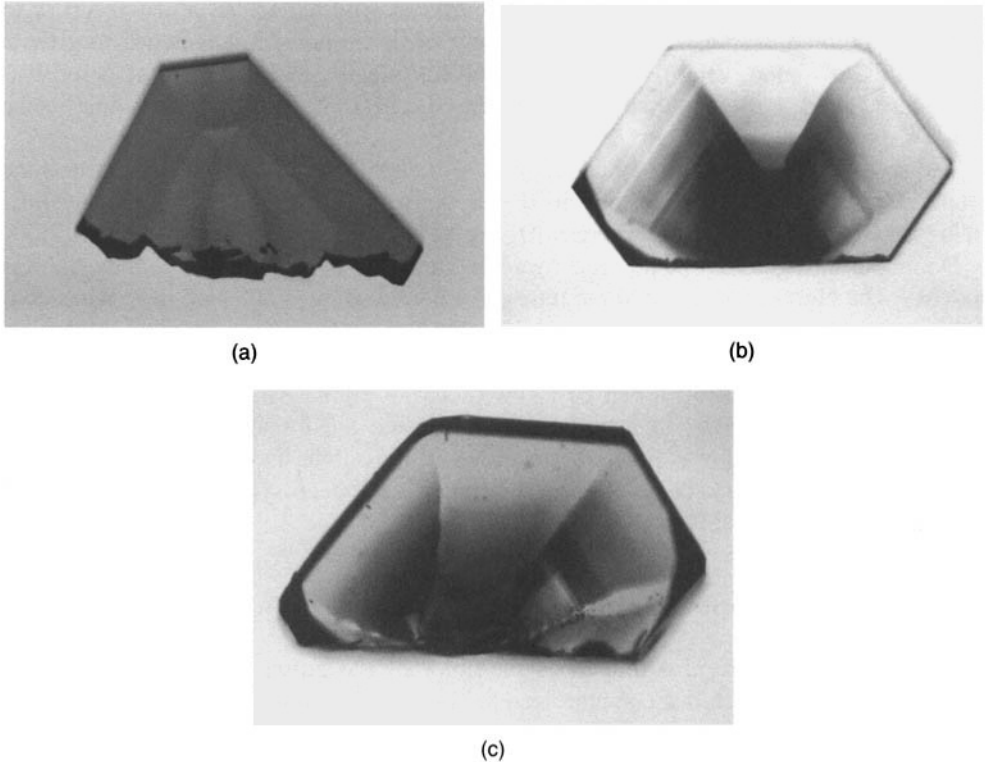


Figure 14.18 (Plate 4) Cross section of three colored diamonds (2 mm wide) grown from nickel-containing alloys. (a) Yellow, (b) green and (c) brown crystals were grown from pure Ni, Ni-2% Ti and Ni-3% Ti, respectively

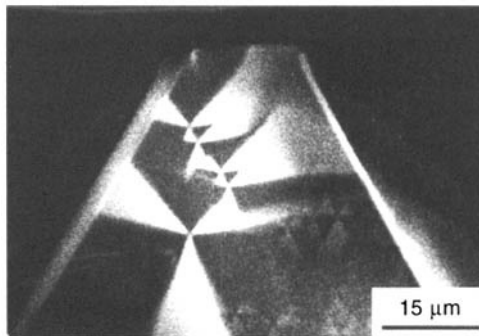


Figure 14.19 Cathodoluminescence image observed on a (111) growth surface of synthetic diamond. The contrast corresponds to vicinal faces of growth hillocks

with an increase of the amount of boron powder. However, the depth of the blue coloration is not proportional to the concentration of boron, but is proportional to a concentration of uncompensated acceptor centers, i.e. $N_{\text{boron}} - N_{\text{nitrogen}}$, where N_{boron} and N_{nitrogen} are concentrations of boron and nitrogen, respectively [62]. When the solvent/catalyst

does not contain the nitrogen getter, more boron is required to be added in order to grow blue-colored crystals. For example, 10 mg of boron powder was added to grow a blue-colored diamond using pure Ni as the solvent/catalyst, whereas 1 mg of boron was sufficient to grow a blue-colored crystal, when Ni-2%Ti alloy is used, according to the author's experience.

The sector dependence of the blue color is also clearly seen. {111} sectors exhibit the deepest blue color, when boron is heavily doped, but with light doping of boron, the yellow color persists in {111} sectors, whereas {011} and {113} sectors give a blue color [79].

Doping of nitrogen may be possible by adding nitrogen-containing compounds, but it is not easy. The highest concentration of nitrogen reported so far is 800 ppm [84], when conventional metal solvent/catalysts are used, in contrast it is not unusual for natural diamond containing 2000–3000 ppm of nitrogen to be found. Under nonconventional conditions, the concentrations of nitrogen can be a few thousand ppm. Diamond grown from non-metallic solvents, Na_2SO_4 , in a boron nitride capsule are found to contain 1700 ppm of nitrogen [85]. Borzdov *et al.* [86] succeeded in the synthesis of diamond containing 3300 ppm using FeN as agent. ^{15}N -enriched diamond has been synthesized with addition of ^{15}N nitrides [87] or aniline [88].

14.3.5.3 Effect of growth temperature

The growth temperature also influences the color of the grown crystals. Early papers noted that colorless crystals are synthesized at higher temperature, whereas lower growth temperatures give a yellow color [53]. Precise control of the growth temperature confirmed the nitrogen concentration gradually decreases with increasing growth temperature [47].

We have investigated the temperature effect on color systematically. When the growth temperature is changed intentionally during a growth run, the grown crystal exhibits a color change in the crystal at a position where the temperature was changed [89]. Figure 14.20 shows an example of the color change. This is a (110) cross section of a crystal grown from Co with boron doping. An inner region that was grown in the first half of a growth period gives a yellow color, and an outer region grown in the second



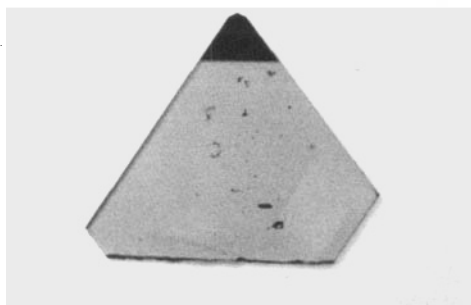
Figure 14.20 (Plate 5) Cross section of a boron-doped synthetic diamond (2 mm wide), which was polished parallel to the growth direction. The crystal was grown by changing the temperature during growth. The yellow region was grown at a lower temperature, while the blue region was grown at a higher temperature

half gives a dark blue color. The crystal was grown at a lower temperature in the first half, then grown at a higher temperature in the second half, indicating that a blue color is formed at higher temperatures, and a yellow color at lower temperatures. The color change from yellow to blue is due to a decrease of the nitrogen concentrations with an increase of temperature.

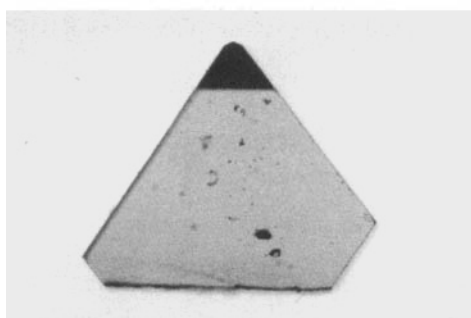
Nitrogen impurities are found to be in paired form, i.e. type IaA, instead of an isolated form, type Ib, when the growth temperature is higher than 1500 °C [90]. We expect that the pairs are formed with aggregation of isolated nitrogen during growth, because nitrogen atoms are mobile at such high growth temperatures. The effect of heat treatment on the impurities is described in the following section.

14.3.5.4 Color change with heat treatment

Diffusion of the nitrogen impurities caused by heating under high-pressure conditions has been studied in detail [91, 92]. The isolated nitrogen atoms diffuse to form aggregates such as pairs and four atoms with heat treatment, although structural models of the latter two have not been established. The yellow color due to isolated nitrogen atoms is faded to colorless by the aggregation as shown in Fig. 14.21(a, b). The colorless crystal contains nitrogens in the paired form, which is commonly present in natural diamonds.



(a)



(b)

Figure 14.21 (Plate 6) Color change with heat treatment at 1800 °C and 6 GPa. (a) Yellow color before the treatment has faded to (b) colorless after the treatment. Cross section of a 2-mm crystal grown from Co

The aggregation rates from isolated atoms to pairs are determined quantitatively by infrared absorption spectroscopy, assuming that the rate obeys the second-order kinetics; $dn/dt = -kn^2$, where n , t and k are concentration of the isolated nitrogen, annealing time and kinetic coefficient, respectively. The rate constant, k , is $1.9 \times 10^{-5} \text{ min}^{-1} \text{ ppm}^{-1}$, which gives 50 % conversion of 500 ppm of isolated nitrogens to the pairs by 2 h heating at 1600°C [91], although Evans and Qi [92] gave a one order lower value of the constant. Other reports suggest the aggregation rate may depend on radiation damage and growth conditions of a crystal and location in a crystal [47, 93, 94].

Evans and Qi [92] carried out annealing at temperatures higher than 2500°C for further aggregation to larger clusters of nitrogen atoms such as four nitrogens surrounding a vacancy, which are classified as type IaB. On the other hand, it has been noted that the heat treatment causes some dissociation of the aggregated forms of nitrogen [95]. Colorless diamond containing nitrogen aggregates becomes brilliant yellow because of partial dissociation of the nitrogen. Kinetics taking account of both aggregation and dissociation of nitrogen have been studied recently [96].

Crystals containing Ni have different behaviors of color change with heat treatment. The yellow color of the crystals grown from pure Ni is changed to brown, and the green color is also changed to brown, respectively. Both of the treated crystals are brown in color, but the former exhibits a number of absorption bands in the visible region, whereas the latter has a simple increase of absorption towards short wavelengths [74]. The color change may be due to aggregation of nickel and nitrogen impurities. ESR measurements have proposed a complex structural model consisting of a nickel atom, nitrogen atoms and vacancies [71, 72].

14.4 SUMMARY

Fifty years have passed since the first success in artificial diamond synthesis was reported. Synthesis technology has progressed remarkably. The largest crystal made is 34.8 carats (7 g) in weight. Ideally pure crystals have also been made. Some synthetic diamonds are distributed in the gem market. The technology may have reached a goal, however, we realize that the technology has not reached that of nature, when compared with natural diamond. The Callinan diamond, the largest natural diamond, is as large as 3106 carats. We have also not succeeded in making pink diamonds similar to those found in diamond mines.

REFERENCES

- 1 F.P. Bundy, H.T. Hall, H.M. Strong and R.H. Wentorf, Jr., (1955) Man-made diamond, *Nature*, **176**, 51–55
- 2 G. Davies, (1994) *Properties and Growth of Diamond*, INSPEC, IEE, London
- 3 C.S. Kennedy and G.C. Kennedy, (1976) The equilibrium boundary between graphite and diamond, *J. Geophys. Res.*, **81**, 2467–2470
- 4 R. Berman and F. Simon, (1955) On the graphite—diamond equilibrium, *Z. Elektrochem.*, **59**, 333–338
- 5 F.P. Bundy, (1963) Direct conversion of graphite to diamond in static pressure apparatus, *J. Chem. Phys.*, **38**, 631–43

- 6 S. Yusa and K. Takemura, (1995) Development of diamond anvil cell for laser heating and experiments of transformation of graphite to diamond, *New Diam.* No.39, 2–7 in Japanese
- 7 W. Utsumi and T. Yagi, (1991) Light-transparent phase formed by room-temperature compression of graphite, *Science*, **252**, 1542–1544
- 8 T. Yagi, W. Utsumi, M. Yamanaka, T. Kikegawa and O. Shimomura, (1992) High-pressure in situ X-ray-diffraction study of the phase transformation from graphite to hexagonal diamond at room temperature, *Phys. Rev. B*, **46**, 6031–6039
- 9 T. Irifune, A. Kurino, S. Sakamoto, T. Inoue and H. Sumiya, (2003) Ultrahard polycrystalline diamond from graphite *Nature*, **421**, 599–600
- 10 H. Yusa, (2002) Nano crystalline diamond directly transformed from carbon nanotubes under high pressure, *Diam. Relat. Mater.*, **11**, 87–91
- 11 V.V. Aksenenkov, V.D. Blank, N.F. Borovikov, V.G. Danilov and K.I. Kozorezov, (1994) Production of diamond single crystals in graphite under plastic deformation, *Sov. Phys.-Dokl.*, **39**, 700–703
- 12 H.P. Bovenkerk, F.P. Bundy, H.T. Hall, H.M. Strong and R.H. Wentorf, Jr., (1959) Preparation of diamond, *Nature*, **184**, 1094–1098
- 13 H.M. Strong, (1963) Catalytic effects in the transformation of graphite to diamond, *J. Chem. Phys.*, **39**, 2057–2062
- 14 H.M. Strong and R.E. Hanneman, (1967) Crystallization of diamond and graphite, *J. Chem. Phys.*, **46**, 3668–76
- 15 M. Wakatsuki, (1966) New catalysts for synthesis of diamond, *Jpn. J. Appl. Phys.*, **5**, 337
- 16 N.V. Novikov and A.A. Shulzhenko, (1990) The increase of synthetic diamond growth rate, in *Science and Technology of New Diamond*, S. Saito, O. Fukunaga and M. Yoshikawa (Eds), KTK Sci. Pub, Tokyo, pp. 217–9
- 17 H. Kanda, M. Akaishi and S. Yamaoka, (1994) New catalysts for diamond growth under high pressure and high temperature, *Appl. Phys. Lett.*, **65**, 784–786
- 18 M. Akaishi, H. Kanda and S. Yamaoka, (1993) Phosphorus: an elemental catalyst for diamond synthesis and growth *Science*, **259**, 1592–1594
- 19 K. Sato and T. Katsura, (2001) Sulfur: a new solvent-catalyst for diamond synthesis under high-pressure and high-temperature conditions, *J. Cryst. Growth*, **223**, 189–194
- 20 Yu. Pal'yanov, I. Kupriyanov, A. Khokhryakov, Yu. Borzdov, V. Gusev and J. Van Royen, (2003) Crystal growth and characterization of HPHT diamond from a phosphorus-carbon system, *Diam. Relat. Mater.*, **12**, 1510–1516
- 21 M. Akaishi, H. Kanda and S. Yamaoka, (1990) Synthesis of diamond from graphite-carbonate systems under very high temperature and pressure, *J. Cryst. Growth*, **104**, 578–581
- 22 M. Akaishi, H. Kanda and S. Yamaoka, (1990) High pressure synthesis of diamond in the systems of graphite-sulfate and graphite hydroxide, *Jpn. J. Appl. Phys.*, **29**, L1172–L1174
- 23 S. Yamaoka, M. Akaishi, H. Kanda and T. Ohsawa, (1992) Crystal growth of diamond in the system of carbon and water under very high pressure and temperature, *J. Cryst. Growth*, **125**, 375–377
- 24 Yu.N. Palyaov, A.G. Sokol, Yu.M. Borzdov, A.E. Khokhryakov and N.V. Sobolev, (1999) Diamond formation from mantle carbonate fluids, *Nature*, **400**, 417–418
- 25 L.F. Kulikova M.D. Shalimov, V.N. Slesaren and E.N. Yakovlev, (1988) Synthesis of diamonds in graphite—metal hydride systems, *Sov. J. Superhard Mater.*, **10**, 1–3
- 26 M. Akaishi, Y. Hosokawa, K. Kawamura and Y. Noguchi, (2001) Synthesis of fine-grained polycrystalline diamond and its properties, *Proc. 8th NIRIM International Symposium on Advanced Materials*, 33–34
- 27 A. Tsuzuki, S. Hirano and S. Naka, (1984) Effect of crystallinity of starting carbons on diamond formation in presence of nickel under high pressure and high temperature condition, *J. Mater. Sci.*, **19**, 1153–1158
- 28 A. Tsuzuki, S. Hirano and S. Naka, (1985) Influencing factors for diamond formation from several starting carbons, *J. Mater. Sci.*, **20**, 2260–2264

- 29 S.M. Hong and M. Wakatsuki, (1993) Diamond formation from the SiC-Co system under high pressure and high temperature, *J. Mater. Sci. Lett.*, **12**, 283–285
- 30 M. Arima, Y. Kozai and M. Akaishi, (2002) Diamond nucleation and growth by reduction of carbonate melts under high-pressure and high-temperature conditions, *Geology*, **30**, 691–694
- 31 S. Yamaoka, M.D. Shaji Kumar, H. Kanda and M. Akaishi, (2002) Formation of diamond from CaCO₃ in a reduced C-O-H fluid at HP-HT, *Diam. Relat. Mater.*, **11**, 1496–1504
- 32 S. Yamaoka, M.D. Shaji Kumar, H. Kanda and M. Akaishi, (2002) Thermal decomposition of glucose and diamond formation under diamond-stable high pressure-high temperature conditions, *Diam. Relat. Mater.* **11**, 118–124
- 33 L.-W. Yin, M.-S. Li, J.-J. Cui, Z.-D. Zou, P. Liu and Z.-Y. Hao, (2002) Diamond formation using Fe₃C as a carbon source at high temperature and high pressure, *J. Cryst. Growth*, **234**, 1–4
- 34 A.T. Collins, G. Davies, H. Kanda and G.S. Woods, (1989) Spectroscopic studies of carbon-13 synthetic diamond, *J. Phys. C: Solid State Phys.*, **21**, 1363–1376
- 35 T.R. Anthony, W.F. Banholzer, J.F. Fleischer, L. Wei, P.K. Kuo, R.L. Thomas and R.W. Peyoe, (1990) Thermal diffusivity of isotopically enriched ¹²C diamond, *Phys. Rev. B*, **42**, 1104–1111
- 36 H.T. Hall, (1960) Ultra-high-pressure, high-temperature apparatus: the 'Belt', *Rev. Sci. Instrum.*, **31**, 125–131
- 37 J.E. Shigley, E. Fritsch, J.I. Koivula, N.V. Sobolev, I.Y. Malinovsky and Y.N. Pal'yanov, (1993) The gemological properties of Russian gem-quality synthetic yellow diamonds, *Gem Gemol.*, **29**, 228–248
- 38 G.S. Oleinik, I.A. Petrusha, N.V. Danilenko, A.V. Kotko and S.A. Shevchenko, (1998) Crystal-oriented mechanism of dynamic recrystallization nucleation in cubic boron nitride, *Diam. Relat. Mater.*, **7**, 1684–1692
- 39 M. Wakatsuki, (1984) Synthesis researches of diamond, in *Materials Science of the Earth's Interior*, I. Sunagawa (Ed.) Terra Sci. Pub. Co., Tokyo, pp. 351–74
- 40 M. Wakatsuki and K. Takano, (1987) Suppression of spontaneous nucleation and seeded growth of diamond, in *High Pressure Research in Mineral Physics*, H. Manghnani and Y. Shono (Eds), TERRAPUB, Tokyo/AGU, Washington, pp. 203–207
- 41 R.H. Wentorf, Jr., (1971) Some studies of diamond growth rates, *J. Phys. Chem.*, **75**, 1833–1837
- 42 H.M. Strong and R.M. Chrenko, (1971) Further studies on diamond growth rates and physical properties of laboratory-made diamond, *J. Phys. Chem.*, **75**, 1838–1843
- 43 H. Sumiya, N. Toda and S. Satoh, (2002) Growth rate of high-quality large diamond crystals, *J. Cryst. Growth*, **237–239**, 1281–1285
- 44 H. Sumiya, S. Sato, K. Tsuji and S. Yazu, (1990) Synthesis of 1-cm large size diamond single crystals, *Proceedings of the 31st High Press. Conf. Japan*, pp. 48–49 in Japanese.
- 45 S. Vagarali, M. Lee and R.C. DeVries, (1990) Progress of large diamond growth technology and future prospects, *J. Hard Mater.*, **1**, 233–245
- 46 W. Li, H. Kagi and M. Wakatsuki, (1996) A two-stage method for growing large single crystals of diamond with high quality, *J. Cryst. Growth*, **160**, 78–86
- 47 S. Satoh, H. Sumiya, K. Tsuji and S. Yazu, (1990) Difference in nitrogen concentration and aggregation among [111] & {100} growth sectors of large synthetic diamonds, in *Science and Technology of New Diamond* S. Saito, O. Fukunaga and M. Yoshikawa (Eds), KTK Sci. Pub. Tokyo, pp. 351–355
- 48 H. Kanda, T. Ohsawa, O. Fukunaga and I. Sunagawa, (1989) Effect of solvent metals upon the morphology of synthetic diamonds, *J. Cryst. Growth*, **94**, 115–124
- 49 M.-L.T. Rooney, (1992) [115] Growth in boron-doped synthetic diamonds, *J. Cryst. Growth*, **116**, 15–21
- 50 H. Kanda, T. Ohsawa and S. Yamaoka, (1990) Differences in morphology and impurity content of synthetic diamond grown from molten nickel, *J. Cryst. Growth*, **99**, 1183–1187
- 51 H. Kanda, T. Ohsawa, O. Fukunaga and I. Sunagawa, (1989) Effect of H₂O upon the morphology of diamonds grown from nickel at high temperature and pressure, in *Morphology and Growth Unit of Crystals*, I. Sunagawa (Ed.), Terra Sci. Pub. Co., Tokyo, pp. 531–542

- 52 S. Tolansky and I. Sunagawa, (1959) Interferometric studies on synthetic diamonds, *Nature*, **184**, 1526–1527
- 53 H.P. Bovenkerk, (1961) Some observations on the morphology and physical characteristics of synthetic diamond, *Am. Mineral.*, **46**, 952–963
- 54 H. Kanda, M. Akaishi, N. Setaka, S. Yamaoka and O. Fukunaga, (1980) Surface structures of synthetic diamond, *J. Mater. Sci.*, **15**, 2743–2748
- 55 H. Kanda, M. Akaishi and S. Yamaoka, (1990) Morphology of synthetic diamonds grown from Na₂CO₃ solvent-catalyst, *J. Cryst. Growth*, **106**, 471–475
- 56 H. Kanda, (1990) Patterns observed in cross-sections of high pressure synthetic diamond, in *New Diamond*, New diamond forum (ed.) Ohmsha Ltd, Tokyo, pp. 58–62
- 57 Yu.N. Pal'yanov, A.F. Khokhryakov, Yu.M. Borzdov, A.G. Sokol, V.A. Gusev, G.M. Rylov and N.V. Sobolev, (1997) Growth conditions and real structure of synthetic diamond crystals, *Russ. Geol. Geophys.*, **38**, 920–945
- 58 G. Davies., (1977) The optical properties of diamond, in *Chemistry and Physics of Carbon*, Vol.13, P.L. Walker and P.A. Thrower (Eds), Dekker, New York, pp 1–143
- 59 A.M. Zaitsev, (2001) *Optical Properties of Diamond: A Data Handbook*, Springer-Verlag, Berlin
- 60 M.H. Nazare and A.J. Neves, (2001) *Properties, Growth and Applications of Diamond*, INSPEC, IEE, London
- 61 W. Kaiser and W.L. Bond, (1959) Nitrogen, A major impurity in common type I diamond, *Phys. Rev.* **115**, 857–863
- 62 A.T. Collins and A.W.S. Williams, (1971) The nature of the acceptor centre in semiconducting diamond, *J. Phys. C: Solid State Phys.*, **4**, 1789–1800
- 63 G.S. Woods and A.T. Collins, (1983) Infrared absorption spectra of hydrogen complexes in type I diamonds, *J. Phys. Chem. Solids*, **44**, 471–475
- 64 I. Kiflawi, D. Fisher, H. Kana and G. Sittas, (1996) The creation of the 3107 cm⁻¹ hydrogen absorption peak in synthetic diamond single crystals, *Diam. Relat. Mater.*, **5**, 1516–1518
- 65 C.D. Clark, H. Kanda, I. Kiflawi and G. Sittas, (1995) Silicon defects in diamond, *Phys. Rev. B*, **51**, 16681–16688
- 66 S. Koizumi, M. Kamo, Y. Sato, H. Ozaki and T. Inuzuka, (1997) Growth and characterization of phosphorus doped {111} homoepitaxial diamond thin films, *Appl. Phys. Lett.*, **71**, 1065–1067
- 67 J. Isoya, H. Kanda, M. Akaishi, Y. Morita and T. Ohshima, (1997) ESR studies of incorporation of phosphorus into high-pressure synthetic diamond, *Diam. Relat. Mater.*, **6**, 356–360
- 68 J.H.N. Loubser, W.P. Reyneveld, (1966) Electron spin resonance of nickel in synthetic diamonds, *Nature*, **211**, 517
- 69 J. Isoya, H. Kanda, J.R. Norris, J. Tang and M.K. Bowman, (1990) Fourier-transform and continuous-wave EPR studies of nickel in synthetic diamonds; site and spin multiplicity, *Phys. Rev. B*, **41**, 3905–3913
- 70 J. Isoya, H. Kanda and Y. Uchida, (1990) EPR studies of interstitial Ni centers in synthetic diamond crystals, *Phys. Rev. B*, **42**, 9843–9852
- 71 V.A. Nadolinny and A.P. Yelisseyev, (1994) Structure and creation conditions of complex nitrogen nickel defects in synthetic diamonds, *Diam. Relat. Mater.*, **3**, 1196–1200
- 72 V.A. Nadolinny, A.P. Yelisseyev, J.M. Baker, M.E. Newton, D. Twitchen, S.C. Lawson, O.P. Yuryeva and B.N. Feigelson, (1999) A study of C-13 hyperfine structure in the EPR of nickel-nitrogen-containing centres in diamond and correlation with their optical properties, *J. Phys.: Condens. Matter*, **11**, 7357–7376
- 73 A.T. Collins and P.M. Spear, (1982) Optically active nickel in synthetic diamond, *J. Phys. D*, **15**, L183–187
- 74 S.C. Lawson and H. Kanda, (1993) An annealing study of nickel point defects in high-pressure synthetic diamond, *J. Appl. Phys.*, **73**, 3967–3973
- 75 A. Yelisseyev, S. Lawson, I. Sildos, A. Osvet, V. Nadolinny, B. Feigelson, J.M. Baker, N. Newton and O. Yuryeva, (2003) Effect of HPHT annealing on the photoluminescence of synthetic diamonds grown in the Fe–Ni–C system, *Diam. Relat. Mater.*, **12**, 2147–2168

- 76 S.C. Lawson, H. Kanda, K. Watanabe, I. Kiflawi, Y. Sato and A.T. Collins, (1996) Spectroscopic study of cobalt-related optical centers in synthetic diamond, *J. Appl. Phys.*, **79**, 4348–4357
- 77 D.J. Twitchen, J.M. Baker, M.E. Newton and K. Johnston, (2000) Identification of cobalt on a lattice site in diamond, *Phys. Rev. B*, **61**, 9–11
- 78 H. Kanda, Y. Sato, N. Setaka, T. Ohsawa and O. Fukunaga, (1981) Growth of diamond at high temperatures and pressures, *J. Chem. Soc. Jpn.*, no. 9, 1349–1356 in Japanese.
- 79 R.C. Burns, V. Cvetkovic, C.N. Dodge, D.J.F. Evans, M.-L.T. Rooney, P.M. Spear and C.M. Welbourn, (1990) Growth-sector dependence of optical features in large synthetic diamonds. *J. Cryst. Growth*, **104**, 257–279
- 80 A.T. Collins, H. Kanda and R.C. Burns, (1990) The segregation of nickel-related optical centres in the octahedral growth sectors of synthetic diamond, *Philos. Mag. B*, **61**, 797–810
- 81 F.C. Frank, A.R. Lang, D.J.F. Evans, M.-L.T. Rooney, P.M. Spear and C.M. Welbourn, (1990). Orientation-dependent nitrogen incorporation on vicinals on synthetic diamond cube growth surfaces, *J. Cryst. Growth*, **100**, 354–376
- 82 H. Kanda, M. Akaishi and S. Yamaoka, (1991) Impurity distribution among vicinal slopes of growth spirals developing on the {111} faces of synthetic diamonds, *J. Cryst. Growth*, **108**, 421–424
- 83 R.H. Wentorf, Jr. and H.P. Bovenkerk, (1962) Preparation of semiconducting diamonds, *J. Chem. Phys.*, **36**, 1987–1990
- 84 A.T. Collins and S.C. Lawson, (1989) Spectroscopic studies of a thermochromic centre in synthetic diamond grown by the temperature gradient method, *Philos. Mag. Lett.*, **60**, 117–122
- 85 H. Kanda, M. Akaishi and S. Yamaoka, (1999) Synthesis of diamond with the highest nitrogen concentration, *Diam. Relat. Mater.*, **8**, 1441–1443
- 86 Yu. Borzdov, Yu. Pal'yanov, I. Kupriyanov, V. Gusev, A. Khokhryakov, A. Sokol and A. Efremov, (2002) HPHT synthesis of diamond with high nitrogen content from an Fe₃N-C system, *Diam. Relat. Mater.*, **11**, 1863–1870
- 87 M.I. Samoilovich, G.N. Bezrukov, V.P. Butuzov and L.D. Podol'skikh, (1975) Peculiarities in electron paramagnetic resonance and infrared spectra of diamonds alloyed with the isotope N¹⁵, *Sov. Phys. Dokl.*, **19**, 409–10
- 88 A.T. Collins and G.S. Woods, (1982) An anomaly in the infrared absorption spectrum of synthetic diamond, *Philos. Mag.*, **B46**, 77–83
- 89 H. Kanda and S.C. Lawson, (1995) Growth temperature dependence of incorporation of impurities in high pressure synthetic diamond, *Indust. Diam. Rev.*, **55**, 56–61
- 90 Yu.A. Kluev, Yu.A. Dudenkov and B.I. Nepsha, (1973) The peculiarities of diamond genesis in connection with the growth forms and the distribution in them of impurity optical active centres, *Geokhimiya*, 1029–1036 in Russian.
- 91 R.M. Chrenko, R.E. Tuft and H.M. Strong, (1977) Transformation of the state of nitrogen in diamond, *Nature*, **270**, 141–144
- 92 T. Evans and Z. Qi, (1982) The kinetics of the aggregation of nitrogen atoms in diamond, *Proc. R. Soc. Lond. A*, **381**, 159–178
- 93 A.T. Collins, (1980) Vacancy enhanced aggregation of nitrogen in diamond, *J. Phys. C*, **13**, 2641–2650
- 94 H. Kanda and S. Yamaoka, (1993) Inhomogeneous distribution of nitrogen impurities in {111} growth sectors of high pressure synthetic diamond, *Diam. Relat. Mater.*, **2**, 1420–1423
- 95 M.R. Brozel, T. Evans and R.F. Stephenson, (1978) Partial dissociation of nitrogen aggregates in diamond by high temperature-high pressure treatment, *Proc. R. Soc. Lond. A*, **361**, 109–127
- 96 F. De Weerd and A.T. Collins, (2003) The influence of pressure on high-pressure, high-temperature annealing of type Ia diamond, *Diam. Relat. Mater.*, **12**, 507–510

15 Growth of Silicon Carbide

T.S. SUDARSHAN¹, D. CHEREDNICHENKO¹, AND R. YAKIMOVA²

¹*Department of Electrical Engineering, University of South Carolina, 301 S. Main St. Rm 3A71, Columbia, SC 29208 USA*

²*Linköping University, Dept of Physics and Measurement Technology, S-581 83 Linköping, Sweden*

15.1 Introduction	433
15.2 Historical development	434
15.3 Industrial production of SiC wafers	435
15.3.1 Growth along the conventional <i>c</i> - or [0001] direction	435
15.3.2 Bulk SiC growth along alternate orientations	436
15.3.3 Bulk growth of semi-insulating SiC	436
15.3.4 Bulk-crystal doping	437
15.4 Essentials of the bulk growth process and thermal-stress-generation mechanisms	437
15.4.1 Basics of the bulk growth process	437
15.4.2 Thermal-stress-generation mechanisms	443
15.5 Growth-related defects	444
15.6 Outlook	447
Acknowledgements	447
References	447

15.1 INTRODUCTION

To date, silicon carbide (SiC) is the most advanced candidate to replace conventional semiconductors in high-power electronics technology, e.g. motor controllers and power distribution in electric vehicles. Because of its unique properties: wide bandgap, excellent thermal conductivity, high breakdown field strength, chemical stability, etc., silicon carbide is an attractive semiconductor for high-temperature, power-control, and high-speed communication devices. It is expected that GaN-based devices grown on SiC substrates will meet the demand of satellite communications for small-size devices operating at higher powers than current Si- or GaAs-based devices.

The availability of substrates allowing homoepitaxial growth of layers and structures needed for fabrication of different devices is the main advantage of SiC compared to

other WBG semiconductors. Recently, much progress has been made in the industrial production of SiC substrates, but the high growth temperature and the lack of congruent melting of SiC set limitations on the crystal-growth method. SiC boules are commonly grown by physical vapor transport (PVT) implemented with seeded sublimation techniques. Since the invention of the sublimation-based bulk growth technique for SiC, considerable progress has been made in the improvement of SiC crystal quality by understanding the relation between growth conditions and defect formation and improving control over the growth process.

This chapter will review bulk growth of SiC substrate material by sublimation and by high-temperature chemical vapor deposition (HTCVD) and the mechanisms of generation of growth-related structural defects that are detrimental in power devices.

15.2 HISTORICAL DEVELOPMENT

The importance of SiC as a hard abrasive material was realized in 1892 by Acheson [1]. He developed an industrial process to produce SiC for the purposes of grinding and cutting. Even though the viability of SiC as an electronic material was shown in 1907 by the demonstration of a light emitting diode [2], it was not until 1955 that Lely developed a method to produce single-crystal SiC [3]. The primary limitation of the Lely process was that using this process, only platelets 5 to 10 mm in diameter and 2 mm thickness were produced. Even though the availability of Lely platelets spurred the demonstration of a variety of SiC-based electronic devices, the absence of a bulk-growth process, primarily due to the absence of SiC in liquid phase under conditions suitable for crystal growth, was the primary barrier for further development as an electronic and optoelectronic material. The above difficulties were overcome by Tairov and Tsvetkov [4], by using a single-crystal SiC seed, placed in a graphite crystallization cylinder, to which vapor was delivered by a sublimating SiC source. The approach for producing the ingots (boules) was based on the principle of supersaturated vapor condensing on a single-crystal seed in a quasiclosed crucible volume.

The seminal work of Tairov and Tsvetkov utilized a single-crystal SiC Lely platelet with the {0001} face as the seed surface. Polycrystalline SiC grains synthesized from high-purity Si and C were used as the vapor source or charge placed in a graphite crucible. The boule growth process was investigated in the 1800 to 2600 °C range at partial argon pressures from 0.1 mTorr to 760 Torr. The growth rate of the boules was controlled by the growth temperature, axial temperature gradient, and the pressure of the inert gas. The boule diameter depended on the starting seed diameter and its length was determined by the volume of the SiC starting material and its complete decomposition. The primary impurities in the grown material were nitrogen (donor) and boron (acceptor), the source for both of the above was primarily the graphite used in the furnace for the crucible and thermal insulation. The authors suggested that the purity of the grown crystal could be improved by lowering the crystal-growth temperature (to reduce boron) and to carry out growth in vacuum conditions (to reduce nitrogen). Growth of boules 8 mm in diameter and 8 mm long, grown at a rate of $\sim 2 \text{ mm h}^{-1}$, were demonstrated. The grown boules were of a single polytype 4H or 6H, using the respective type seeds to initiate growth. Hence, the breakthrough in bulk SiC ingot growth came with the seeded sublimation growth process that laid the foundation for modern SiC wafer fabrication for the SiC-based semiconductor industry. The above process is also referred to as the 'physical vapor

transport (PVT)' process. The boules produced by this process are generally sliced into wafers using an ID or multiple-wire diamond saw and polished using diamond particle abrasives. It is to be noted that SiC exists in many polytypes (over 200) each representing a different stacking sequence of the atomic planes along the [0001] direction [5]. For power electronic and optoelectronic applications, 4H- and 6H-SiC represent the most common polytypes.

15.3 INDUSTRIAL PRODUCTION OF SIC WAFERS

15.3.1 Growth along the conventional *c*- or [0001] direction

Silicon carbide bulk growth has been pursued in both university and industry laboratories addressing both fundamental growth mechanism and practical production issues [6–27]. The historical development of the work related to SiC bulk growth is presented in [28]. The latest achievements in the bulk growth of large size SiC crystals by Cree Research and Nippon Steel Corp. are reviewed in Refs. [17, 29]. In order to describe the essential features of SiC bulk crystal growth using seeded sublimation, the description of the growth furnace provided by Ohtani *et al.* [29] is highlighted below with the aid of the schematic diagram of the growth system shown in Fig. 14.1 [30].

The crucible assembly consisted of a graphite lid to which the seed was attached and a graphite cylinder containing the source powder that was industrial-grade abrasive SiC powder. Mirror-polished SiC wafers were used as seeds. The crucible assembly was covered with thermal insulation made of graphite felt, and placed in a quartz chamber, equipped with an RF induction heating system [30]. During growth, typical seed temperatures of 2200 to 2300 °C and source temperatures of 2300 to 2400 °C were used. By appropriate positioning of the crucible and the thermal-insulation materials, the required thermal gradient was created between the source powder and the seed crystal.

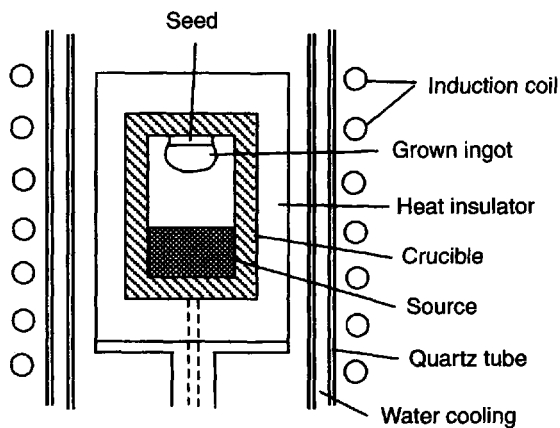


Figure 15.1 Schematic drawing of a cross-sectional view of a PVT SiC growth system (Reprinted from Takahashi and Ohtani, *phys. stat. sol. (b)* **202** (1997) 163, copyright (1997) with permission from Wiley-VCH)

During heating, an argon overpressure of ~ 600 Torr was maintained to avoid crystal-growth initiation on the seed surface at lower temperatures, which would lead to undesired polytype formation. After reaching the growth temperature of $2200\text{--}2400^\circ\text{C}$, the argon pressure was lowered to $10\text{--}20$ Torr to initiate crystal growth, at the typical thermal gradients between the source and seed of $10\text{--}20^\circ\text{C cm}^{-1}$, resulting in growth rates of $0.2\text{--}2\text{ mm h}^{-1}$. The above approach led to the fabrication of 50-mm 6H wafers with a low micropipe density of below 10 cm^{-2} and enlargement to 75-mm crystals [29].

Generally, the quality of the grown crystal, in terms of defect density, improves if the impurities in the growth reactor are decreased. Hence, selection of the graphite components is of great importance in order to reduce impurities in the growing boules. The graphite components can be purified to below the parts per million weight (ppm wt) range; but this process is expensive and adds to the cost of the resulting wafers. Reduction of B and S is especially difficult. The level of any background impurity in the commercial undoped wafers is reported to be less than ~ 0.1 ppm, including nitrogen [16].

15.3.2 Bulk SiC growth along alternate orientations

A new degree of freedom in SiC MOS technology exists using $(11\bar{2}0)$ plane wafers for MOSFET fabrication [29]. The epitaxial film grown on the $(11\bar{2}0)$ surface exhibits enhanced mobility. Furthermore, growth on the $(11\bar{2}0)$ surface, i.e., growth perpendicular to the c -axis exhibits full suppression of micropipes that are so pernicious in crystals grown along the c -axis. The above attractive features have spurred great interest among crystal growers in the $[11\bar{2}0]$ growth direction, also sometimes called a -face SiC crystal growth. Bulk growth in the $[11\bar{2}0]$ or a -direction rather than producing the a -face wafers by slicing a c -direction grown crystal is essential in order to produce large-diameter wafers having uniform doping concentration, for device applications. A further advantage of a -direction growth is the possibility of growing a single polytype material, which is normally a challenge in c -direction grown crystals. In spite of the above advantages, a primary problem is an increase in the density of stacking faults in the a -face grown material. For example, the stacking fault density in 6H $[11\bar{2}0]$ grown crystal is ~ 10 times higher than that of the 6H $[0001]$ grown crystal [29]. Hence, crystal growth in directions perpendicular to the c -direction is inherently susceptible to stacking-fault generation.

15.3.3 Bulk growth of semi-insulating SiC

Semi-insulating SiC (SI-SiC) substrates are essential for the fabrication of high-frequency and microwave power devices including SiC MESFETs and GaN/AlGaN high electron mobility transistors (HEMTs). There are two distinct methods available to achieve SI properties in SiC: (i) by incorporating specific impurities into the material that introduces deep energy levels within the bandgap; this method is called extrinsic doping and (ii) by incorporating intrinsic defects into high-purity SiC boules to introduce deep levels. In both cases, the deep levels compensate the shallow dopants (nitrogen and boron) to pin the Fermi level near the middle of the bandgap. In the first-generation commercial SI-SiC, vanadium (V) was used for compensating the shallow dopants [31, 32]. Degradation in the performance of RF power devices is attributed to the presence of vanadium [32].

Two distinct types of vanadium-free high-purity SI-SiC substrates, one grown by the conventional sublimation (PVT) method referred to as HPSI, and the second by high-temperature chemical vapor deposition (HTCVD), are now commercially available. In both cases, intrinsic defects are believed to be responsible for the SI properties. Two- and three-inch (50 mm and 75 mm) 4H-SI-SiC wafers produced using a high-purity PVT process are commercially available, exhibiting uniform resistivities greater than $2 \times 10^9 \Omega \text{ cm}$.

In the HTCVD technique, purified silane and ethylene are used as gas precursors (source material) [33]. Diluted in a carrier gas, the above precursors are continuously fed into an open heating zone, at $> 2000^\circ\text{C}$, where nucleation of Si- and C-containing clusters takes place in the gas phase. Above this hot zone where nucleation of Si and C clusters takes place, the axial temperature distribution is similar to that in a PVT system. In this region, further sublimation (dissociation) of the clusters into vapor species occurs that are then crystallized onto a 50-mm diameter 4H-SiC seed surface that is maintained at a lower temperature. The above growth process can be seen as gas-fed sublimation. A lower concentration of shallow impurities introduced by the growth system (compared to PVT) will require a smaller concentration of deep levels needed for compensation to produce the SI material. Finally, it is to be noted that the HTCVD bulk growth process can also be used for the growth of n-doped SiC.

15.3.4 Bulk-crystal doping

Silicon carbide boules can be doped either n- or p-type during growth with nitrogen or aluminum being the main n- and p-type dopants, respectively. SiC wafers are currently used for the commercial production of gallium nitride (GaN)-based blue light emitting diodes (LEDs) and Schottky diodes. For both the above applications, n-type doped SiC substrates are used. The n-type doping is achieved by controlling the amount of nitrogen added to the inert gas (argon) in the growth reactor. P-type doped SiC wafers are required for the manufacture of a variety of high-power electronic devices. A description of p-doped crystal growth can be found in Refs. [28, 34].

15.4 ESSENTIALS OF THE BULK GROWTH PROCESS AND THERMAL-STRESS-GENERATION MECHANISMS

15.4.1 Basics of the bulk growth process

The primary stages of bulk SiC growth are: dissociative sublimation of the source charge, mass transfer of the evaporated Si and C species in the gas phase, crystallization of the species onto the SiC seed, and removal of the heat of crystallization. Correspondingly, there are three main regions of the crucible, as shown in Fig. 15.2. The processes taking place in these regions determine the growth rate and crystal quality, and hence, identification and control of the important parameters in these regions is essential for producing low defect density bulk crystals.

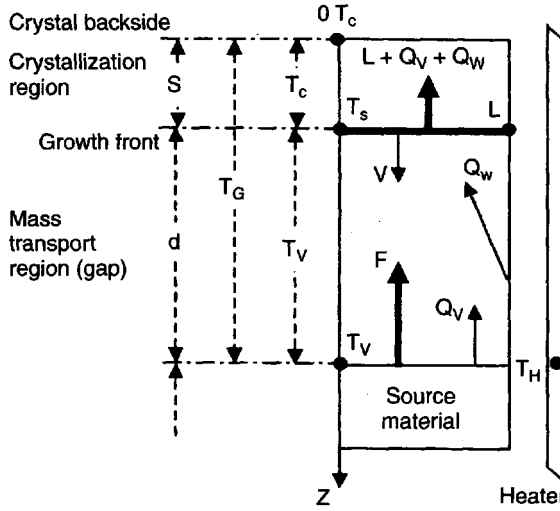


Figure 15.2 Schematic of the model domain of the growth crucible (Reprinted from Cherednichenko *et al. J. Cryst. Growth*, **262** (2004) 175, with permission from the author)

15.4.1.1 SiC source region

The driving force for bulk SiC growth is provided by applying a temperature gradient such that the SiC source is at a higher temperature relative to the seed, both placed inside the crucible. The main species in the sublimed vapor present in the gas phase are: Si, SiC₂, Si₂C, and SiC. The composition of the sublimed vapor and the vapor stoichiometry (the Si/C ratio) in the mass-transport region depends on the source temperature, source polytype composition, and the preparation conditions of the source charge, especially the source-charge grain size [6].

The sublimation temperature determines the maximum vapor pressure of the chemical species and composition (stoichiometry) of the vapor. At low sublimation temperatures, the vapor nonstoichiometry is high, resulting in an excess of free silicon in the vapor and a large amount of solid residual carbon in the source volume, called source graphitization. Furthermore, if the excess silicon reaches supersaturation at the crystallization surface it leads to silicon liquid-phase formation (at the growth surface), resulting in the generation of various defects in the crystal volume. The high volatility of the residual carbon species at high temperatures will also stimulate the formation of carbon second-phase inclusions as defects in the crystal volume. The vapor stoichiometry $\eta(T)$ approaches the optimum value of unity as the source temperature is increased to approximately 2700 K. Using Van't Hoff's equation, the partial pressure of the chemical species in the vapor could be expressed in terms of the thermodynamic parameters of the sublimation process:

$$\log p_i = A_i/T_V + B_i \quad (15.1)$$

where p_i is the partial pressure of a given chemical species; T_V is the sublimation temperature; A_i and B_i are the tabulated thermodynamic parameters of sublimation [35]. The sum of partial pressures gives the total vapor pressure, $p(T)$. The expression for $p_i(T_V)$ above

allows us to find the temperature dependence of the SiC vapor stoichiometry coefficient $\eta(T_V)$ [35]:

$$\eta(T_V) = \frac{p_{\text{Si}} + p_{\text{SiC}_2} + 2 \cdot p_{\text{Si}_2\text{C}} + p_{\text{SiC}}}{p_{\text{Si}} + 2 \cdot p_{\text{SiC}_2} + p_{\text{Si}_2\text{C}} + p_{\text{SiC}}} \quad (15.2)$$

where $p_{\text{Si}_x\text{C}_y}$ stands for the partial pressure of each major component of SiC evaporation.

The size of the SiC source grains influences the thermal conductivity of the source, the diffusivity of vapor through the source volume, and the effective surface area of sublimation. Each of the above factors affect the secondary processes (specifically the source-volume recrystallization) which influences the growth rate and, as a result, the crystal quality. Low thermal conductivity of the source ($\lambda_C/\lambda_P \gg 100$ at 2500 K [36, 37], where λ_C and λ_P are the thermal conductivities of the SiC seed and the SiC source material, respectively) causes a significant difference in the heating rate of the source-material region compared with that of the seeding substrate. Hence, the seeding substrate is overheated during the long temperature ramp-up period (~ 1 to 2 h after the furnace heating power is turned on). As a result, the seed-surface sublimation leading to its graphitization can take place at the initial stage of bulk growth.

Furthermore, intense source recrystallization (preferential evaporation from the SiC source-grain asperities), governed by the essential capillarity of the source grains, is also initiated at the high sublimation temperature. As a result of these self-congruent recrystallization processes, a new, thermodynamically more stable, polycrystalline structure of the source material is formed. Rapid formation of a uniform polycrystalline structure is the ideal situation. However, since the above process is a slow one that proceeds during the entire period of growth, the source volume is not in a stable condition.

The effective surface area of sublimation depends on the size of the source grains, increasing with a decrease of grain size. At a fixed temperature, the effective rate of sublimation is high for a large surface area, leading to intense source graphitization. Using the pellet-source seed model, the amount of residual carbon M_C , accumulated in the source, can be expressed as a function of pellet radius, temperature, and time of sublimation [Cherednichenko, unpublished]:

$$M_C = M_0 \cdot (1 - 1/\eta(T)) \cdot [1 - (1 - \beta(T) \cdot t/R_0)^3] \quad (15.3)$$

where M_C is the mass of residual carbon and M_0 is the initial mass of the SiC source; R_0 is the initial pellet radius. The effective rate of sublimation, i.e., the flux of sublimated atoms $\beta(T)$, expressed in number of atoms $\text{cm}^{-2} \text{s}^{-1}$, can be expressed based on Knudsen's formula:

$$\beta(T) = \frac{p \cdot \Omega}{\sqrt{2\pi} \cdot M \cdot kT} \quad (15.4)$$

where Ω is the average volume of the sublimated molecular species; M is the molecular weight; k is the Boltzmann constant; and p is the equilibrium pressure of the vapor at temperature T . It is clear from Equation (15.3) that for a given period of sublimation, the level of source graphitization for small radius grains is much higher than for large grains. The maximum level of graphitization is very sensitive to the temperature of sublimation: $M_C = M_0 \cdot [1 - 1/\eta(T)]$. At temperatures where the stoichiometry coefficient

$\eta(T)$ is unity, the source graphitization can be fully eliminated, which is the ideal source sublimation condition.

Based on the above discussion it is clear that due to sintering and graphitization of the source volume, the physical properties of the source grains continuously change during the entire growth period including the total volume of the source material, effective surface area of sublimation, thermal conductivity, density, and vapor diffusivity. Consequently, the relative vapor pressures of the gas species, and hence Si/C ratio, varies during the growth period. The temperature distribution in the source volume is an important parameter of bulk crystal growth since, during the long duration of growth, it is important to maintain uniformity of vapor over the entire area of the evaporating source. Furthermore, both the vapor composition and evaporation rate must be maintained constant and uniform over the duration of the growth period.

15.4.1.2 Mass-transfer region

Bulk growth of SiC via physical vapor transport (PVT) is generally conducted in the presence of an inert gas (argon). Hence, the sublimated vapor (Si, SiC₂, Si₂C, and SiC) and argon gas mixture is considered as the medium where Si- and C-containing species are transported from the source to the seed surface. Analysis based on heat- and mass-transport phenomena in the gas mixture indicates that the mass transport is primarily driven by diffusion rather than convection [17–20, 28]. The key expressions that describe the diffusion process are indicated below. The diffusive mass flux F of the SiC vapor across the mass-transport gap is

$$F = \Delta p_S \cdot D/kT \cdot d = \theta \cdot \Delta T_S \quad (15.5)$$

where $\Delta p_S = (p_V - p_S)$; $\theta = p_V \cdot \Delta H/RT^2 \cdot R_D$; $R_D = k \cdot T \cdot d/D$ stands for the diffusion resistance of the mass-transport region; d is the source-to-seed distance; p_V represents the equilibrium pressure of the SiC vapor at the top surface of the SiC source at temperature T_V ; p_S is the equilibrium pressure at the surface of crystallization at temperature T_S ; ΔH is the enthalpy of sublimation; $\Delta T_S = T_V - T_S$; $T = \sqrt{T_V \cdot T_S}$ is the absolute average temperature in the growth cell; R is the gas constant; and D is the diffusion coefficient. The source-to-seed distance and, as a result, the diffusion resistance of the mass-transport region depend on the instantaneous value of crystal thickness: $d = (d_0 - S)$ (where S is the crystal thickness and d_0 is the initial source-to-seed distance). For the SiC vapor and argon system, the diffusion-coefficient approximation is given by [19, 38]

$$D(p_{Ar}, T) = D_0 \cdot \left(\frac{T}{T_0}\right)^n \cdot \frac{p_0}{p_{Ar} + p_V(T)} \quad (15.6)$$

p_{Ar} is the argon partial pressure and $p_V(T)$ is the total pressure of SiC vapor, parameters n , D_0 , T_0 and p_0 are equal to 1.8, $1 \times 10^{-1} \text{ cm}^2 \text{ s}^{-1}$, 273 K and 1 atm (760 Torr), respectively (D_0 is a function of the size and mass of diffused atoms).

From the above expressions, we can surmise that the vapor flux in the mass-transport gap can be controlled by R_D the resistance for diffusion and ΔT_S the source-to-growth front temperature difference. A large R_D leads to the essential reduction of crystal growth

rate and can even practically stop growth, when the source-to-seed distance is large. However, too low a value of R_D can lead to high growth velocity, including 3D growth and formation of high thermal stress in the growing boule as a result of increasing latent heat that must be dissipated, leading to high defect generation. The resistance for diffusion R_D primarily depends on ' T and d ' and D , which in turn can be controlled by P_{Ar} , the argon pressure. Growth control is less practical to accomplish by controlling ' T and d ' during growth. Achieving control of growth via the ambient gas pressure is easier to implement and hence, an inert gas such as argon is commonly used for SiC bulk growth using PVT.

In Equation (15.5), another important factor that influences growth is the temperature difference between source and seed $\Delta T_S = T_V - T_S$. The temperature difference ΔT_S determines the vapor supersaturation at the crystallization surface:

$$\varepsilon(\Delta T_S) = \frac{\Delta H}{R \cdot T^2} \cdot \Delta T_S \quad (15.7)$$

where $\varepsilon(\Delta T_S)$ is the coefficient of vapor supersaturation determined by the average temperature in the growth reactor and the source-crystal temperature difference ΔT_S .

As follows from Equations (15.5) and (15.7), the vapor flux and supersaturation are proportional to the temperature difference ΔT_S . The value ΔT_S must be optimized since a high rate of growth ($\gg 1.0 \text{ mm h}^{-1}$) leads to defect generation due to the formation of essential thermal stress. Moreover, when the temperature difference $\Delta T_S \geq 100 \text{ K}$ the supersaturation becomes large enough to initiate silicon second-phase condensation [39] and planar-defect formation [40].

15.4.1.3 Crystallization

As noted earlier, crystal growth arises by the Si and C species from the sublimated vapor arriving at the SiC seed surface. The primary factors that determine crystal growth from the vapor at the earliest stage of crystallization include the rate of nucleation and the critical radius of nucleation centers. When the size of nucleation centers begins to exceed the critical radius R_C , the nucleation and, as a result, the growth process will begin to develop spontaneously. By minimization of the Gibbs potential, it can be shown that supersaturation primarily determines the critical radius, which for the SiC 2-D nucleation center is equal to:

$$R_C = \frac{4 \cdot \gamma_2}{3 \cdot k \cdot T} \cdot \frac{\Omega}{\varepsilon(\Delta T_S)} \quad (15.8)$$

and the critical volume of the nucleation site is:

$$V_R = \frac{6}{\sqrt{3}} \cdot \frac{\gamma_1}{\gamma_2} \cdot R_C^3 \quad (15.9)$$

here γ_1 is the specific surface energy of the crystal c - (or 0001) face and γ_2 that of the p -face (prism or $\bar{1}\bar{1}00$ face).

For the specific surface energy of $\gamma_1 = 2.22 \text{ J m}^{-2}$, $\gamma_2 = 5.57 \text{ J m}^{-2}$ [41], $\varepsilon \cong 0.2$ and $T = 2500 \text{ K}$, Equation (15.8) yields the critical characteristic size of the nucleation center

equal to $R_C \cong 10^{-8}$ m. The nucleation-center volume corresponding to this radius is equal to $V_R \cong 2 \times 10^{-24}$ m³. To create a nucleation center of this size, the number of atoms that must agglomerate at a site for spontaneous nucleation is $N = V_R/\Omega \cong 10^5$ ($\Omega = M/N_A \cdot \rho \cong 2 \times 10^{-29}$ m³; N_A is Avogadro's number; $M = 40.1$; the molecular weight; and $\rho = 3200$ kg m⁻³; the density of SiC). In practice, it is not possible to establish a nucleus of such large critical radius by the fluctuating surface concentration of adsorbed chemical species under typical growth conditions ($\varepsilon \leq 0.2$).

Experiments, however, indicate that SiC crystals practically begin to grow from very small supersaturation values. Burton *et al.* [42] proposed that an imperfection present at the surface of a real crystal could serve as a nucleation center to initiate growth at a small supersaturation. It was shown that the steps formed at intersections of screw dislocations with the crystal surface are especially effective nucleation centers. At present there is clear experimental evidence of the existence of growth spirals at the SiC crystal growth front that indicate the significant influence of screw dislocations on the SiC growth process as seen in Fig. 15.3 [43]. The normal rate of advance of any portion of the rotating spiral, as a function of spiral radius is [42]:

$$V(\rho) = V_S \cdot (1 - \rho_C/\rho) \quad (15.10)$$

where

$$V_S = 2 \cdot \varepsilon(\Delta T_S) \cdot D_S \cdot \tau_S \cdot \nu \cdot \exp(-\Delta H/R \cdot T_S) \quad (15.11)$$

is the maximum velocity of step propagation in the spiral process of growth; D_S is the surface diffusivity of an adsorbed molecule); τ_S is the mean lifetime of molecules in the adsorbed position; ν is the atomic vibration frequency; and ρ_C is the radius of a critical nucleus at the spiral step. When $\rho \leq \rho_C$ (close to the dislocation core), $V(\rho)$ changes sign, indicating that in this area the growth is negative (or sublimation). The large capillarity of the dislocation core significantly increases the equilibrium vapor pressure at the surface of crystallization and the vapor supersaturation reached at temperature difference ΔT_S is not sufficient to maintain growth at this location. This is one of the reasons why screw dislocations can serve as a source of micropipe formation.

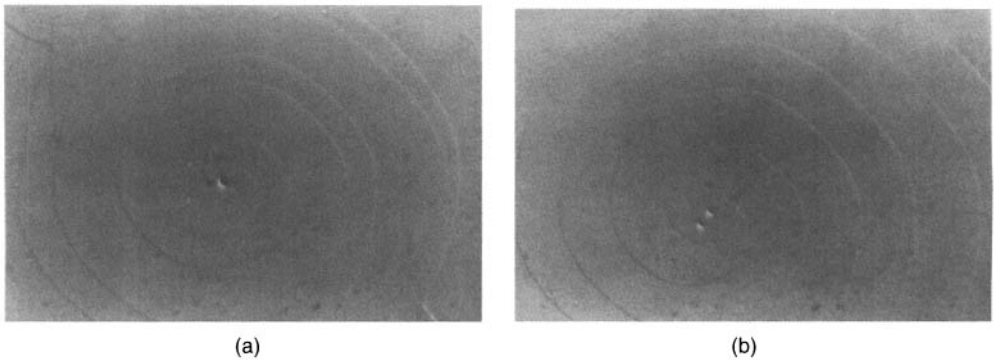


Figure 15.3 Two noninteracting growth spirals emerging from neighboring screw dislocations. (Reprinted from Syväjärvi, PhD Dissertation (1999) Linköping University, Sweden, copyright (1999) with permission from the author)

15.4.2 Thermal-stress-generation mechanisms

It is important to note that the processes responsible for defect generation in the crystal are due to those that take place inside the growing boule. Defects in SiC can be broadly categorized into two types (1) large structural defects including micropipes, planar defects, and polytype inclusions and (2) crystallographic defects (dislocations). The velocity of crystal growth determines the amount of heat released as a result of the chemical reaction of the growth front (also called the latent heat of crystallization). According to Equation (15.5), the flux F in the diffusive mass-transport region is strongly dependent on the supersaturation ε (Equation 15.7), the total vapor pressure of the SiC species p_V , the diffusive resistance R_D , and the average temperature T in the reactor. The velocity of growth dS/dt is proportional to the diffusive flux intensity F (law of mass conservation):

$$V = dS/dt = F \cdot \Omega \quad (15.12)$$

Another primary factor that influences growth velocity is the heat dissipation through the growing crystal volume, expressed by the heat-balance equation:

$$\lambda \cdot \nabla T|_{z=S} = \Delta H_1 \cdot \gamma \cdot dS/dt + Q \quad (15.13)$$

where ΔH_1 is the specific energy of chemical reaction [J kg^{-1}]; λ is the thermal conductivity of SiC; $\nabla T|_{z=S}$ denotes the axial temperature gradient in the crystal and $Q = Q_V + Q_W$ is the amount of heat adopted by the crystal surface from the furnace ($Q_V = \eta_V \cdot (T_V - T_S)$), $Q_W = \eta_W \cdot (T_W - T_S)$, $\eta_V(T_V)$ is the coefficient of heat emissivity of the top source surface [$\text{J cm}^{-2} \text{s}^{-1} \text{K}^{-1}$], whereas $\eta_W(T_W)$ represents the amount of heat energy radiated from the chamber wall [$\text{J cm}^{-2} \text{s}^{-1} \text{K}^{-1}$] (see Fig. 15.2). The right-hand side of the equation represents the total amount of heat absorbed from the surface of crystallization and the left-hand side represents the heat flux conducted through the crystal volume [$\text{J cm}^{-2} \text{s}^{-1}$].

Both of the above factors, mass transport (described by F) and heat dissipation through the surface of crystallization, which are mutually dependent (i.e., a self-congruent process) influence the growth velocity. Solving Equations (15.12) and (15.13), we can obtain an analytical expression for growth rate in the self-congruent condition of growth [44]:

$$dS/dt = \Omega \cdot \theta \cdot \Delta T_G \cdot G(S) \quad (15.14)$$

where

$$G(S) = \frac{(1 - \sqrt{\pi} \cdot \eta_W \cdot S/2\lambda)}{[1 + \sqrt{\pi} \cdot (\eta_V + \eta_W + \Delta H_1 \cdot \gamma \cdot \Omega \cdot \theta/S_1) \cdot S/2\lambda]} \quad (15.15)$$

is the dimensionless growth-dynamics function. Here $\Delta T_G = (T_V - T_C)$, T_C is the temperature of the crystal back side; λ is the thermal conductivity of SiC; $S_1 = (1 - S/d_0)$ is the dimensionless instantaneous source-crystal distance (d_0 is the initial source-crystal distance).

Substitution of Equation (15.14) into Equation (15.12) results in the expression for the self-congruent variation of the crystallization temperature during the growth process:

$$T_S(S) = T_V - \Delta T_G \cdot G(S) \cdot S_1 \quad (15.16)$$

From the above analysis (Equation 15.14), it is clear that growth rate is maximum at the initial stage when growth is limited only by the intensity of mass transport of the species. As the crystal thickness develops to $S > 1.0$ mm, the influence of heat dissipation becomes dominant. The crystal growth rate will be limited and the growth can stop if the heat released as a result of phase transformation is not removed through the crystal causing the temperature of the growth front to approach that of the evaporating source. Hence, it is important to control heat dissipation through the crystal volume from the very early stages of growth. Although mass transport can be controlled, by controlling the Ar pressure, to produce the optimum velocity of growth (< 1 mm h⁻¹), the maximum crystal thickness that can be reached, under given conditions of mass transport, is determined by the intensity of heat dissipation and the parasitic heat Q_w , which depends on the heating-element geometry and crucible design.

The axial temperature difference ΔT_C across the growing crystal is given by:

$$\Delta T_C(S) = \Delta T_G \cdot [1 - G(S)] \quad (15.17)$$

where $\Delta T_C(S) = T_S(S) - T_C$. It is important to note that ΔT_C is a function of instantaneous crystal thickness S and it depends on supersaturation and all the parameters contained in the expression for $G(S)$ in Equation (15.15) (e.g., η_V , η_W), and it determines the thermal stress σ produced in the growing crystal and final crystal quality:

$$\sigma(S) = \frac{\alpha \cdot E}{(1 - \nu)} \cdot \Delta T_C(S) \quad (15.18)$$

where E is Young's modulus, α is the coefficient of thermal expansion, and ν is Poisson's parameter. Equation (15.18) indicates that the thermal stresses, as well as the growth velocity, depend on the same parameters contained in the expression for $G(S)$. This correlation clearly follows from Equation (15.13). According to this heat-balance equation (Equation (15.13)), increasing the growth rate increases the amount of heat released as a result of the phase transformation at the surface of crystallization. Therefore, the crystal growth rate will be limited and the growth can stop if the generated heat is not removed through the crystal causing the temperature of the growth front to approach that of the evaporating source. Furthermore, a nonuniform temperature distribution in the crystal, as a result of heat dissipation, will induce thermal stress, and as a consequence, defect generation in the crystal volume. Defect generation becomes significant when the induced thermal stress $\tau(r, \theta, z)$ exceeds the value of critically resolved shear stress τ_C (1.0 MPa) at the high SiC growth temperature [16, 45].

15.5 GROWTH-RELATED DEFECTS

During growth of single polytype bulk crystals, defects may be formed by four possible mechanisms: (a) inherited from the seed, (b) misoriented nuclei, (c) plastic deformation, and (d) second-phase Si or carbon inclusions. SiC is extremely hard at room temperature, but becomes rather plastic at growth temperatures (> 2200 °C). Thus, basal-plane slip may occur resulting in the formation of so-called basal-plane dislocations, predominantly of

edge character. As noted in Section 15.4.2, if the thermal stress generated during crystal growth exceeds the critically resolved shear stress by a factor of two, intense plastic flow occurs, resulting in high-density dislocation generation. Since solid deformation at high temperatures is tightly entwined with the phenomena of self-diffusion, the movement of dislocations is essentially nonconservative and results in the formation of very complicated defect structures [45].

Most undesired extended defects are those propagating along the growth direction and intersecting the growth surface, since SiC substrates are fabricated by slicing wafers nearly parallel to the growth surface. Screw-dislocation generation requires higher energy than basal-plane edge dislocations and they are usually produced by imperfect nucleation and particularly during growth on singular (atomically flat) surfaces. In this case, mosaicity and even polytype inclusions may occur. Screw dislocations in the boules originate mainly from SiC seeds and they are preferred nucleation and growth-promoting centers. Threading dislocations can also be generated by plane misalignment during growth, as a consequence of the overgrowth of inclusions on the growth surface [47], or at the boundaries of slightly misoriented grains [48]. Any nonuniformity in temperature in the region of a spiral growth step will result in a change in the speed of advance of the spiral step. The step region with a lower temperature, and higher supersaturation, will advance faster than a region with a higher temperature. The faster moving front will overcome the slower moving part of the spiral, resulting in secondary nucleation of a new spiral. The presence of any obstacles at the growth front will intensify the above process, leading to the generation of additional screw dislocations. Nonuniformity of thermal stress at the growth surface can also generate additional screw- and edge-dislocation nucleation sites. Threading edge dislocations have been suggested to originate from postgrowth-induced glide and slip [50].

Persistent sources of dislocations are the low-angle grain boundaries between misoriented domains, the latter being a subject of several investigations concerning the domain origin [51–53]. The majority of results have supported the assumption that SiC crystals grow with the aid of screw dislocations (spiral growth mechanism) providing numerous independent growth centers. Due to temperature nonuniformity at the growth surface, initial misorientation between nuclei may occur and further develop into domain boundaries. It has also been proposed that misoriented domain boundaries can be formed by polygonization of threading edge dislocations, the latter being introduced into SiC crystals by prismatic slip during postgrowth cooling [54].

Micropipes primarily follow the growth direction (*c*-axis) in SiC boules and substrates, and easily propagate into subsequently deposited epitaxial layers. After Frank's theory [55, 56], micropipes are generally considered as an empty-core of screw dislocations that forms when the energy in the highly strained region around a dislocation line is released, creating a cylindrical-shaped free surface. Micropipes can be observed in the middle of such spirals where growth dislocations intersect the surface (Fig. 15.4). Several mechanisms of micropipe formation have been proposed [10, 45, 57, 58]. Micropipes are generally considered to be empty-core screw dislocations with a large strain energy (large Burger's vector). However, it is to be noted that the diameter of a micropipe ($\sim 1 \mu\text{m}$) is too large to be considered as a super screw dislocation as per the discussion below. Estimation shows that the value of specific energy in the dislocation core is practically equal to the evaporation energy of SiC, $U_0 \cong 531.4 \text{ kJ mol}^{-1}$ [59]. Using this specific energy value and Burger's vector $b_0 \cong 15.2 \text{ \AA}$, it is shown that the size of the stable open core produced by the above process is $\cong 1 \text{ nm}$ and a thermodynamically stable visible

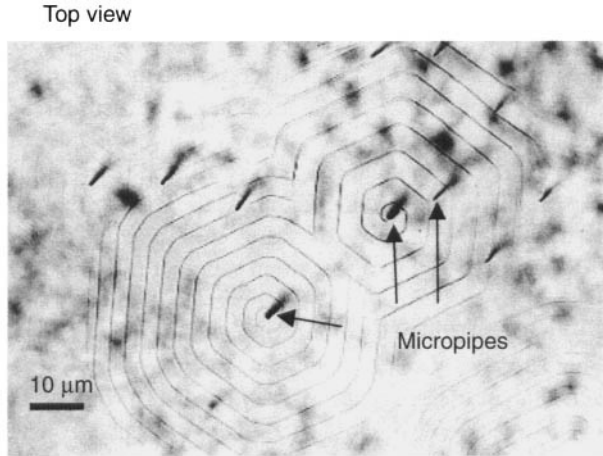


Figure 15.4 Spiral growth pattern and micropipes (black holes) in the middle of the spirals

open core (diameter $\geq 1 \mu\text{m}$) cannot be formed. On the other hand, for $b = 9 \cdot b_0$, the equilibrium radius of the hollow core of a dislocation r_P is $\cong 40 \text{ nm}$ ($\cong 26 \cdot b_0$). Consequently, dislocations with a Burger's vector of b_0 initially present in the substrate, can propagate into the SiC bulk during the growth process as a single dislocation. Thus it can be stated that only superdislocations can produce hollow pipes. But even for superdislocations, the equilibrium radius of the hollow core is actually much smaller than that of any observed micropipes [60]. Hence a thermodynamically stable hollow core of a dislocation can be considered only as an initial stage of micropipe formation. Additional factors in the growth process would be involved in the formation of micropipes, as observed in bulk crystals.

There is yet another kind of structural defect that is quite prevalent in SiC bulk crystals, called a planar or hexagonal defect. It is a flat, often hexagonal, platelet-shaped cavity with lateral dimensions significantly larger than its thickness [58]. The planars lie parallel to the basal plane, typically a few micrometers in thickness, with trench-like depressions at the edges, and often associated with the formation of dislocations and micropipes. It was shown that the nonstoichiometry of the vapor, the large supersaturation, and high volatility of residual carbon species are the primary factors that determine the formation of planar defects and second-phase inclusions [39, 40, 61].

Structural defects in SiC substrates and epitaxial layers have been studied extensively during the last decade resulting in considerable progress in material quality. This is reflected in the attainment of micropipe densities as low as 0.9 cm^{-2} for a 2-inch 4H (N-doped) wafer and 22 cm^{-2} for a 3-inch 4H (N-doped) wafer [62]. The density of the threading dislocations is commonly determined by using hot KOH etching and is in the range of 10^3 – 10^4 cm^{-2} [63]. These defects are either formed during growth or during the postgrowth cooling stage and consequently, they can be minimized by further optimization of the growth process.

Material-evaluation and defect-characterization tools are essential to determine the quality of wafers produced in order to provide feedback to the crystal growers and for further wafer processing leading to the fabrication of devices. Techniques employed for material evaluation and defect characterization can be found in Ref. [28].

15.6 OUTLOOK

The primary challenge in the commercialization of SiC-based power electronic devices is the high density of micropipes in wafers with diameters greater than 75 mm. Although significant progress has been made in the reduction of micropipe density, the cost of low micropipe density wafers ($< 10 \text{ cm}^{-2}$ in 75-mm diameter wafers) is still very high. The forward-voltage degradation of pin diodes is attributed to the presence of basal-plane dislocations. Hence, in addition to reducing the densities of micropipes and screw dislocations, the thrust of current research is to reduce basal-plane dislocations. Production of low defect density, large-diameter, semi-insulating wafers and wafers with high p-type doping are also at the forefront of the technological challenge of bulk crystal growth. Although alternate orientation wafers, especially those in the (1120) plane or *a*-face, offer many advantages, especially zero micropipe density, the main challenge is in the production of large-diameter wafers ($> 50 \text{ mm}$) with low density of stacking faults. Finally, production of large-diameter SiC wafers of good quality at low cost is the key for the commercial success of SiC technology.

ACKNOWLEDGEMENTS

This work was supported by ONR, Grant No. N0000140210667. The authors are grateful to Okmetic AB, Sweden and especially to Dr Alexandre Ellison for providing materials on HTCVD growth. The authors thank Ms Julie Morris for her invaluable assistance in the preparation of this manuscript.

REFERENCES

1. E.G. Acheson, (1893) *J. Franklin Institute*, **194**.
2. H.J. Round, (1907) *Electrical World*, **19**, 309.
3. J.A. Lely, (1955) *Ber. Dtsch. Keram. Ges.* **32**, 229.
4. Y.M. Tairov, and V.F. Tsvetkov, (1978) *J. Cryst. Growth* **43**, 209.
5. A.R. Verma, and P. Krishna, (1966) *Polymorphism and Polytypism in Crystals*, John Wiley & Sons, Inc., New York.
6. Y.M. Tairov, (1995) *Mater. Sci. Eng. B* **29**, 83–89.
7. S. Nishino, T. Higashino, T. Tanaka, and J. Saraie, (1995) *J. Cryst Growth* **147**, 339.
8. R. Yakimova, M. Syväjärvi, T. Iakimov, H. Jacobsson, A. Kakanakova-Georgieva, P. Råback, and E. Janzén, (2001) *Appl. Surf. Sci.* **184**, 27–36.
9. V.D. Heydemann, G.S. Rohrer, E.K. Sanchez, and M. Skowronski, (1998) *Mater. Sci. Forum* **264–268**, 37.
10. D. Hofmann, E. Schmitt, M. Bickermann, M. Kölbl, P.J. Wellmann, and A. Winnacker, (1999) *Mater. Sci. Eng. B* **61–62**, 48–53.
11. R. Madar, M. Anikin, K. Chourou, M. Labeau, M. Pons, E. Blanquet, J.M. Dedulle, C. Bernard, S. Milita, and J. Baruchel, (1997) *Diam. Relat. Mater.* **6**, 1249.
12. R. Yakimova, T. Iakimov, M. Syväjärvi, H. Jacobsson, P. Råback, A. Vehanen, and E. Janzén, (1999) *Proc. MRS Spring Meeting*, April 5–9, San Francisco.
13. R. Stein and P. Lanig, (1993) *J. Cryst. Growth*, **131**, 71.
14. V.D. Heydemann, N. Schulze, D.L. Barrett, and G. Pensl, (1996) *Appl. Phys. Lett.* **69**, 3728.

15. G. Augustine, McD. Hobgood, V. Balakrishna, G. Dunne, and R.H. Hopkins, (1997) *phys. stat. sol. (b)* **202**, 137.
16. St.G. Müller, R.C. Glass, H.M. Hobgood, V.F. Tsvetkov, M. Brady, D. Henshall, J.R. Jenny, D. Malta, and C.H. Carter Jr., (2000) *J. Cryst. Growth* **211**, 325–332.
17. St.G. Müller, R.C. Glass, H.M. Hobgood, V.F. Tsvetkov, M. Brady, D. Henshall, D. Malta, R. Singh, J. Palmour, and C.H. Carter Jr., (2001) *Mater. Sci. Eng. B* **80**, 327–331.
18. M. Pons, E. Blanquet, J.M. Dedulle, I. Garcon, R. Madar and C. Bernard, (1996) *J. Electrochem. Soc.* **143**(11) 3727.
19. Q.S. Chen, H. Zhang, and V. Prasad, (2001) *J. Cryst. Growth* **230**, 239.
20. H.J. Rost, D. Siche, J. Dolle, W. Eiserbeck, T. Muller, D. Schultz, G. Wagner, J. Woolweber, (1999) *Mater. Sci. Eng. B* **61–62**, 68.
21. R. Yakimova and E. Janzén, (2000) *Diam. Relat. Mater.* **9**, 432–438.
22. D.L. Barrett, J.P. McHugh, H.M. Hobgood, R.H. Hopkins, P.G. McMullin, R.C. Clarke, and W.J. Choyke, (1993) *J. Cryst. Growth* **128**, 358–362.
23. R.C. Glass, D. Henshall, V.F. Tsvetkov, and C.H. Carter Jr., (1997) *phys. stat. sol. (b)* **202**, 149.
24. Y.M. Tairov and V.F. Tsvetkov, (1976) in: *First European Conference on Crystal Growth*, Abstract Book, p. 188.
25. Y.M. Tairov and V.F. Tsvetkov, (1981) *J. Cryst. Growth* **52**, 146–150.
26. S. Nishino, (1995) in: *Properties of Silicon Carbide*, ed. G. Harris, INSPEC, the Institution of Electrical Engineers, United Kingdom.
27. D.L. Barrett, R.G. Seidensticker, W. Gaida, R.H. Hopkins, and W.J. Choyke, (1991) *J. Cryst. Growth* **109**, 17–23.
28. T.S. Sudarshan, (2004) in: *SiC Power Materials and Devices*, ed. Zhe Chuan Feng, Springer-Verlag.
29. N. Ohtani, T. Fujimoto, M. Katsuno, T. Aigo, and H. Yashiro, (2002) *J. Cryst. Growth* **237–239**, 1180–1186.
30. J. Takahashi and N. Ohtani, (1997) *phys. stat. sol. (b)* **202**, 163.
31. N.T. Son, B. Magnusson, Z. Zolnai, A. Ellison, and E. Janzén, (2003) *Mater. Sci. Forum* **433–436**, 45–50.
32. St.G. Müller, M.F. Brady, W.H. Brixius, R.C. Glass, H.McD. Hobgood, J.R. Jenny, R.T. Leonard, D.P. Malta, A.R. Powell, V.F. Tsvetkov, S.T. Allen, J.W. Palmour, and C.H. Carter, Jr., (2003) *Mater. Sci. Forum* **433–436**, 39–44.
33. A. Ellison, B. Magnusson, N.T. Son, L. Storasta and E. Janzén, (2003) *Mater. Sci. Forum* **433–436**, 33–38.
34. T.L. Straubinger, M. Bickermann, R. Weingärtner, P.J. Wellmann, and A. Winnacker, (2002) *J. Cryst. Growth* **240**, 117–123.
35. S.K. Lilov, (1993) *Mater. Sci. Eng. B* **21** 65.
36. I.I. Parfenova, Yu.M. Tairov, and V.F. Tsvetkov, (1990) *Sov. Phys.-Semicond.* **24**(2) 158.
37. St.G. Müller, J. Fricke, D. Hofmann, R. Horn, O. Nilsson, and B. Rexer, (2000) *Mater. Sci. Forum*, **338–342**, 43.
38. E.L. Cussler, (1984) in: *Mass Transfer in Fluid Systems* University Press, Cambridge, 1984.
39. R.V. Drachev, G.D. Straty, D.I. Cherednichenko, I.I. Khlebnikov, and T.S. Sudarshan, (2001) *J. Cryst. Growth* **233**, 541.
40. Y. Khlebnikov, R. Drachev, C. Rhodes, D. Cherednichenko, I. Khlebnikov, and T.S. Sudarshan, (2001) *Mater. Res. Soc. Symp.* **640**, H5.1.2–H5.1.6.
41. E. Pearson, T. Takai, T. Halicioglu, and W.A. Tiller, (1984) *J. Cryst. Growth* **70**, 33.
42. W.K. Burton, N Cabrera, and F.C. Frank, (1951) *Philos. Trans. Roy. Soc. London*, **A243**, 299–358.
43. M. Syväjärvi, (1999) *PhD Dissertation* Linköping University, Linköping, Sweden.
44. D.I. Cherednichenko, R.V. Drachev, and T.S. Sudarshan, (2004) *J. Cryst. Growth*, **262**(1–4) 175.

45. D.I. Cherednichenko, R.V. Drachev, I.I. Khlebnikov, X. Deng, and T.S. Sudarshan, (2003) *Mater. Res. Soc. Symp. Proc.* **742**, K2.18.1.
46. R. Yakimova, M. Syväjärvi, T. Iakimov, H. Jacobsson, P. Råback, A. Vehanen, and E. Janzén, (2000) *J. Cryst. Growth* **217** 255–262.
47. E.K. Sanchez, J.Q. Liu, M. de Graef, M. Skowronski, W.M. Wetter, and M. Dudley, (2002) *J. Appl. Phys.* **91**, 1143–1148.
48. M. Tuominen, R. Yakimova, R.C. Glass, T. Tuomi, and E. Janzén, (1994) *Mater. Res. Soc. Symp. Proc.* **339**, 729–734.
49. M. Selder, L. Kadinski, F. Durst, T.L. Straubinger, P.L. Wellmann, and D. Hofmann, (2001) *Mater. Sci. Forum* **353–356**, 65.
50. S. Ha, N.T. Nuhfer, M. De Graef, G.S. Rohrer, and M. Skowronski, (2000) *Mater. Sci. Forum*, **338–342**, 447–480.
51. R.C. Glass, L.O. Kjellbeg, V.F. Tsvetkov, J.E. Sundgren, and E. Janzén, (1993) *J. Cryst. Growth* **132**, 504–510.
52. M. Tuominen, R. Yakimova, R.C. Glass, T. Tuomi, and E. Janzén, (1994) *J. Cryst. Growth* **144**, 267–272.
53. P. Pirouz, (1998) *Philos. Mag. A* **78**(3), 727.
54. S. Ha, N.T. Nuhfer, G.S. Rohrer, M. De Graef, and M. Skowronski, (2000) *J. Cryst. Growth* **220**, 308–315.
55. F.C. Frank, (1951) *Acta Cryst.*, **4**, 497–501.
56. B. Van Der Hoek, J.P. Van Der Eerden, and P. Bennema, (1982) *J. Cryst. Growth* **56**, 621.
57. J.W. Yang, (1993) PhD Thesis, Case Western Reserve University.
58. T.A. Khur, E.K. Sanchez, M. Skowronski, W.M. Vetter, and M. Dudley, (2001) *J. Appl. Phys.* **89**, 4625.
59. D.I. Cherednichenko, Y.I. Khlebnikov, I.I. Khlebnikov, R.V. Drachev, and T.S. Sudarshan, (2001) *J. Appl. Phys.* **89**(7), 4139–4141.
60. J. Heindl, W. Dorsch, H.P. Strunk, St.G. Müller, R. Eckstein, D. Hofmann, and A. Winnacker, (1998) *Phys. Rev. Lett.* **80**(4), 740.
61. R.V. Drachev, D.I. Cherednichenko, I.I. Khlebnikov Y.I., Khlebnikov, and T.S. Sudarshan, (2003) *Mater. Sci. Forum* **433–436**, 99–102.
62. S.G. Müller, M. Brady, B. Brixius, G. Fechko, R.C. Glass, D. Henshall, H.McD. Hobgood, J.R. Jenny, R. Leonard, D. Malta, A. Powell, V.F. Tsvetkov, S.T. Allen, J. Palmour, and C.H. Carter Jr, (2002) *Mater. Sci. Forum* **389–393**, 23–28.
63. D. Hobgood, M Brady, W Brixius, G. Fechko, R. Glass, D. Henshall, J Jenny, R. Leonard, D. Malta, S.G. Müller, V. Tsvetkov, and C. Carter, Jr., (2000) *Mater. Sci. Forum*, **338–342**, 3–8.

This page intentionally left blank

16 Photovoltaic Silicon Crystal Growth

T.F. CISZEK

Siliconsultant, P.O. Box 1453, Evergreen, CO 80437, USA

16.1	Introduction	451
16.2	Traditional silicon growth methods applied to PV	452
16.2.1	Czochralski growth	452
16.2.2	FZ growth	455
16.2.3	Comparisons between CZ and FZ growth for PV	456
16.3	Multicrystalline ingot growth methods for PV	459
16.3.1	Casting and directional solidification	459
16.3.2	Semicontinuous electromagnetic casting	461
16.4	Ribbon or sheet growth methods for PV	463
16.4.1	Small-area solid/liquid interface growth methods	463
16.4.2	Large-area solid/liquid interface growth methods	468
16.5	Thin-layer growth on substrates for PV	472
16.6	Comparison of growth methods	473
	References	475

16.1 INTRODUCTION

For a number of reasons, the photovoltaic (PV) or solar-cell application of semiconductor silicon has spawned an unusually large array of diverse approaches to its material growth. Of course, the traditional growth approaches developed in the silicon electronics industry are used. These are Czochralski (CZ) growth and float zoning (FZ). But more than a dozen alternative growth approaches have been explored over the years. The factors driving the search for alternative growth methods involve tradeoffs between crystal quality (the higher the quality, the higher the attainable solar-cell light-conversion efficiency η) and crystal substrate cost (low costs per watt of electricity generated by the solar cell are essential if the PV technology is to be commercially viable). Unlike silicon crystals used in the electronics industry, crystal perfection, purity, and uniformity are not necessarily the most desirable attributes for crystalline Si incorporated into commercial PV modules. Tradeoffs are routinely made, weighing these attributes against cost, throughput, energy consumption, and other economic factors. Such tradeoffs for PV use have led to far

more alternative growth methods for silicon than the many decades of semiconductor technology development have. Of course, the highest cell efficiencies are obtained on very pure, defect-free, crystalline silicon with high minority charge-carrier lifetime τ . A solar cell is more sensitive to carrier lifetime than many other electronic devices.

In this chapter, we will describe the application of traditional CZ and FZ Si growth methods to PV material and look at alternative ingot, ribbon, sheet and thin-layer growth techniques that have been developed specifically for PV material. We will describe some characteristics of the growth processes and resultant materials, and make comparisons between the methods. Only a handful of alternative methods that have been explored over the years have stood the test of time and are still actually in current use for PV production.

16.2 TRADITIONAL SILICON GROWTH METHODS APPLIED TO PV

16.2.1 Czochralski growth

The workhorse growth method of the semiconductor silicon industry is Czochralski growth named after Jan Czochralski who introduced an early version of the present-day process in 1916, and published it as a method for studying the crystallization rate of metals [1]. Further modifications by Teal and Little [2] brought the technique closer to the process known today as the Czochralski or CZ method shown schematically in Fig. 16.1 as it is applied to silicon. CZ growth is used by several Si PV manufacturers and produces $\langle 100 \rangle$ dislocation-free single crystals amenable to surface texturing.

A concise description of PV Si CZ growth is as follows: Purified solid silicon feed-stock is loaded in a quartz crucible sitting within a cylindrical graphite holder or susceptor mounted on a rotatable, translatable pedestal shaft. A picket-fence graphite heater surrounds the susceptor. A small-diameter $\langle 100 \rangle$ dislocation-free seed crystal is mounted axially above the crucible and is also capable of rotation and vertical translation (by a wire or a shaft). A water-cooled chamber with copious graphite felt or similar insulation decoupling it from the heater area encloses the hot zone and allows evacuation of the chamber and/or purging with high-purity argon inert gas.

Three-phase electrical power is applied to the heater and melts the silicon in the rotating crucible. The counter-rotating seed is brought to thermal equilibrium with the melt, attached and withdrawn upward to grow new silicon material first in a thin neck geometry (by using relatively high power and/or pulling speed) during which process any dislocations formed during the initial seed/melt contact grow to the periphery and are eliminated. Then power is reduced and pulling is slowed to transition the growth diameter to the desired final one. When full diameter is reached, power and pulling speed are increased to the new required/desired equilibrium growth levels and automatically controlled based on sensor input of the optical/thermal position of the crystal periphery near the solid/liquid interface. During this phase, the rotating crucible is moved upward as needed to maintain the solid/liquid interface at an optimum position in the heater, compensating for the falling crucible melt level due to consumption by the growing crystal. When the melt is nearly consumed, pull speed and power are increased to taper the crystal to a smaller size for separation from the melt, so that the dislocations slipping back into the crystal upon thermal shock of separation will not propagate into the cooler,

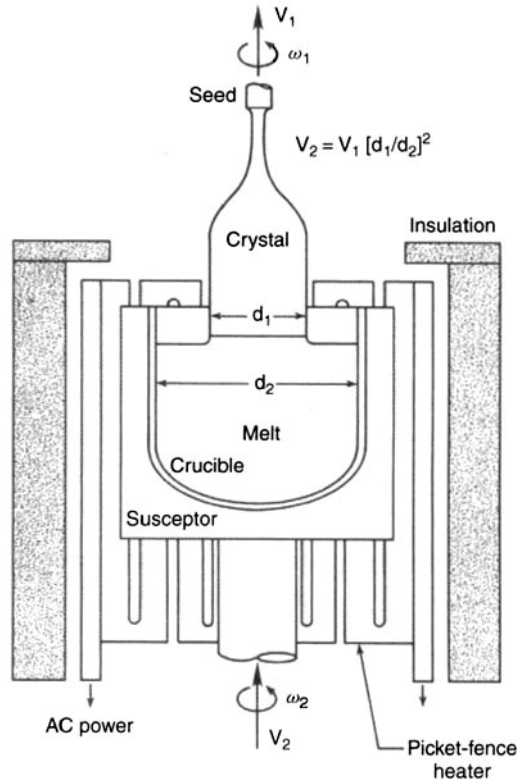


Figure 16.1 Schematic diagram of the silicon CZ crystal-growth method. Reproduced from Scheel (2003) *Crystal Growth Technology*, with permission from John Wiley & Sons, Ltd

full-diameter portion of the crystal. See Zulehner and Huber [3] for a more detailed description of the modern CZ process.

The upper limit for growth rate or pulling rate v_m that can be expected from the CZ process and other directional solidification techniques for silicon ingots is

$$v_m = \frac{1}{L\rho_m} \left(2 \frac{\sigma \varepsilon K_m T_m^5}{d} \right)^{1/2} \quad (16.1)$$

where L is latent heat of fusion, ρ_m is density at the melting temperature, σ is the Stefan–Boltzmann constant, ε is emissivity, K_m is the thermal conductivity at the melting temperature T_m , and d is the crystal diameter [4]. Maximum silicon growth rate v_m is shown as a function of crystal diameter in Fig. 16.2. Realistically, $v \sim 0.25v_m$ can be practically achieved.

The focus of CZ technology development specific to Si PV has largely been on efforts to reduce the cost of the crystalline product. One way to do this is by pushing v higher through improvements in insulation, hot-zone geometry design, thermal-gradient control, and gas-purging strategies. Electrical power requirements for CZ growth are on the order of 60 kWh kg^{-1} in the IC industry. The more cost-conscious PV industry has been achieving $35\text{--}40 \text{ kWh kg}^{-1}$ for CZ growth, and some recent experiments [5] indicate

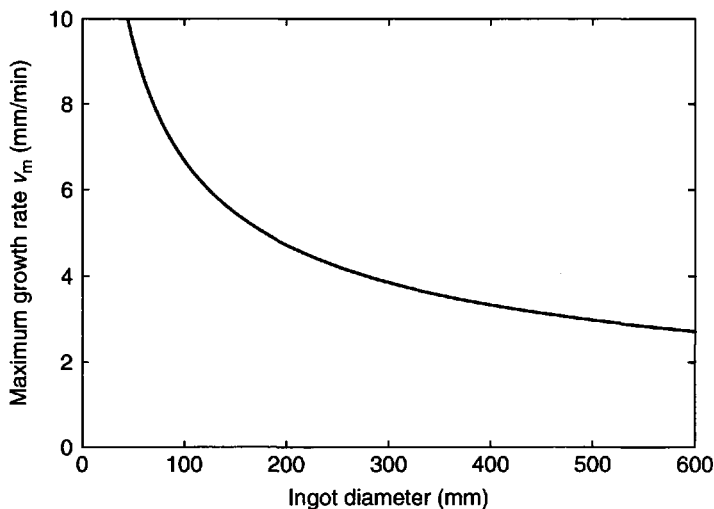


Figure 16.2 Maximum growth rate vs. ingot diameter

that levels on the order of 18 kWh kg^{-1} may be achieved for 150-mm diameter crystals by using improved insulation materials and lower argon gas-flow rates. Not only were energy requirements reduced, but also argon consumption was reduced from $3 \text{ m}^3 \text{ kg}^{-1}$ of Si to $1 \text{ m}^3 \text{ kg}^{-1}$ of Si. Also, the oxygen content in the crystals was reduced by 20%, crystal growth rate was increased from 1.28 kg h^{-1} to 1.56 kg h^{-1} , and relative solar-cell efficiency increased by 5%.

Approximately 30% of the costs in CZ Si PV technology are in the crystal ingot, 20% in wafering, 20% in cell fabrication, and 30% in module fabrication. High-speed wire saws that can wafer several entire ingots in one operation have greatly improved the throughput of the wafering process. A wire saw can produce about $500 \text{ wafers h}^{-1}$ compared to about 25 wafers h^{-1} for older inside-diameter (ID) saw technology. Furthermore, it creates shallower surface damage ($10 \mu\text{m}$) than the ID saws ($30 \mu\text{m}$), and allows thinner wafers to be cut, thus increasing the number of wafers per ingot. Currently, about 20 wafers are obtained from 1 cm of ingot. Efforts are underway to obtain $35 \text{ wafers cm}^{-1}$. Problems with increased breakage are seen with the thinner wafers—especially in the sawing process. At $20 \text{ wafers cm}^{-1}$ and a wafer thickness $> 300 \mu\text{m}$, breakage is on the order of 15%. This can rise to on the order of 40% when the wafer thickness is decreased to $200 \mu\text{m}$. It is clear that wafer handling will be an important issue as wafers become thinner.

Maximizing crystal yield/cost of the feedstock has been carried out through development of feedstock-recharging or melt-replenishment systems, and reclaiming cut ends of crystals and residual Si left in the crucible after growth. There are also a number of efforts underway to find alternative processes for manufacturing silicon feedstock with slightly relaxed physical property specifications at lower costs. However, since the Si solar cell is a minority charge-carrier device, there are limits to how many impurities can be tolerated without dramatically reducing performance. A summary of impurity tolerances was published by Davis *et al.* [6].

16.2.2 FZ growth

Float-zoned (FZ) silicon produces the highest PV performance, and the best recorded silicon solar-cell efficiency (ratio of cell-output electrical power to solar power incident on the cell), 24 %, has been achieved for devices fabricated on FZ wafers [7]. But the device-processing procedures needed to achieve the high efficiencies are expensive and time consuming. So, as in the semiconductor industry, more CZ wafers than FZ wafers are used for PV. Recently, simplification of the processing procedures for high efficiency has been achieved, and substantial resource investment in FZ for PV has come about to take advantage of the better performance.

Float zoning of Si was introduced by Keck and Golay [8] in 1952 and has been extensively developed through to the present time, with primary applications in silicon power devices and detector materials. A schematic of the FZ process is shown in Fig. 16.3. The crystal is grown downward from the bottom of the cylindrical Si feed rod. The apparatus must provide a closed inert-gas environment of argon through which sliding and rotating shafts pass vertically to provide the crystal growth and feed-rod translation and rotation motion. Induction heating at frequencies of about 2–3 MHz forms the melt by inducing AC current to flow in the silicon, resulting in heating and melting. The induction coil is water cooled and no hot objects other than silicon itself are touching or

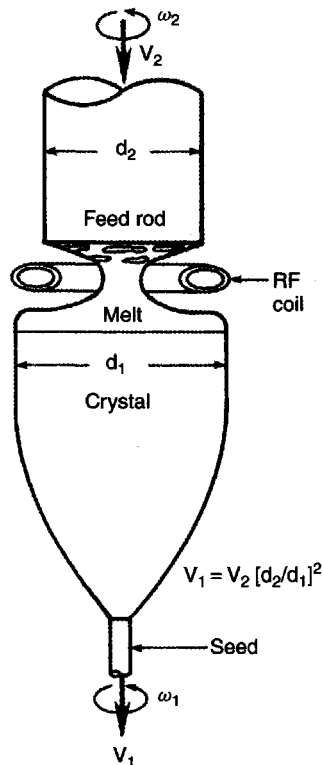


Figure 16.3 Schematic diagram of the silicon FZ crystal-growth method. Reproduced from Scheel (2003) *Crystal Growth Technology*, with permission from John Wiley & Sons, Ltd

in close proximity to the silicon. Hence the purity of the method is high. Note though that silicon does not couple to the induction-heating coil when cold, so a graphite preheater is first coupled to the induction coil, radiates heat to the silicon feed rod, and then is withdrawn when the rod becomes warm. So this preheater must be of high purity. A pendant drop of silicon is then melted on the bottom of the rotating feed rod and the seed, approximately 5 mm in diameter, is touched to the melt drop.

As in CZ growth, a long thin neck is first grown by increasing RF power and downward pulling speed. When dislocations have been eliminated, the seed travel speed is reduced to about 3–4 mm min⁻¹ and RF power is adjusted to increase the crystal size to the desired diameter. While there is a limit to the molten-zone height imposed by surface tension, the crystal diameter has no fundamental limit, and diameters have progressed over the years, as have CZ diameters, albeit at a slower rate of progress. Diameters over 150 mm have been realized. Keller and Muhlbauer [9] describe the FZ process in more detail. Power requirements for FZ growth are on the order of 30 kWh kg⁻¹.

16.2.3 Comparisons between CZ and FZ growth for PV

There are two principal technological advantages of the FZ method for PV Si growth. The first is that large τ values are obtained due to higher purity and better microdefect control, resulting in 10% to 20% higher solar-cell efficiencies. The second is that faster growth rates and heat-up/cool-down times, along with absences of a crucible and consumable hot-zone parts, provide a substantial economic advantage. Table 16.1 compares the characteristics of the FZ and CZ methods. The main technological disadvantage of the FZ method is the requirement for a uniform, crack-free cylindrical feed rod. A cost premium (100% or more) is associated with such poly rods.

Because of the lower purity of 'Solar Grade' silicon and because of some efforts to use nonconventional dopants like Ga to reduce light-degradation effects in PV silicon, it is important to understand impurity redistribution during crystal growth. The way impurities

Table 16.1 Comparison of the CZ and FZ growth methods

Characteristic	CZ	FZ
Growth Speed (mm min ⁻¹)	1 to 2	3 to 5
Dislocation-free?	Yes	Yes
Crucible?	Yes	No
Consumable material cost	High	Low
Heat-up/cool-down times	Long	Short
Axial-resistivity uniformity	Poor	Good
Oxygen content (atoms cm ⁻³)	> 1 × 10 ¹⁸	< 1 × 10 ¹⁶
Carbon content (atoms cm ⁻³)	> 1 × 10 ¹⁷	< 1 × 10 ¹⁶
Metallic impurity content	Higher	Lower
Bulk minority charge-carrier lifetime (μs)	5–100	1000–20 000
Mechanical strengthening	10 ¹⁸ oxygen	10 ¹⁶ nitrogen
Production diameter (mm)	150–200	100–150
Operator skill	Less	More
Polycrystalline Si feed form	Any	Crack-free rod

redistribute during FZ growth differs substantially from CZ growth. In the general case, impurity redistribution is affected both by segregation and evaporation. The evaporation effect is only pronounced when growth is conducted in a vacuum ambient. In FZ growth, we consider a long silicon feed ingot with initial uniform concentration C_0 of any given impurity. One end of the ingot is melted, and a molten zone is moved along the rod at a travel rate v . Impurity evaporation increases as v decreases, because the molten zone is then exposed to vacuum for a longer time. Evaporation also increases as the ratio of free-surface area to volume of the molten zone increases. Longer molten zones experience greater evaporation. Thus, the effective evaporation coefficient g is a function of specific growth conditions, as is the effective segregation coefficient k . Segregation increases as k decreases, but evaporation increases as g increases. Peizulaev [10] has derived an expression for the impurity distribution in an ingot after n zone passes, when both evaporation and segregation are operative:

$$C_n(x)/C_0 = [k/(k+g)]^n [1 - (1-k-g)Z_n e^{-(k+g)x}] \quad (16.2)$$

where

$$Z_n = n - \sum_{s=1}^{n-1} (n-s)(k+g)^{s-1} e^{-s(k+g)} [(s+x)^{s-2}/s!] \{(s-1)x + (s+x) [1 - (k+g)x]\} \quad (16.3)$$

and n is the number of times the ingot is zone melted, k is the effective segregation coefficient, g is the effective evaporation coefficient, and $C_n(x)$ is the impurity concentration at position x along the ingot (x is in units of melt-zone length) after n solidification passes.

In the last melt zone to freeze of an ingot, that is N melt zones long (i.e., for $N-1 < x < N$), the impurity concentration profile is expressed by

$$C_n(x) = C_n (N-1)(N-x)^{(k-1)} e^{-g[x-(N-1)]} \quad (16.4)$$

Equations (16.2)–(16.4) together describe the impurity profiles resulting from FZ growth, and they are also applicable to any method where source material is continuously fed into a molten zone at the same rate as the product silicon is withdrawn. These include continuous Czochralski growth, and some of the nontraditional growth methods that have been developed for PV that will be discussed in a later section (electromagnetic continuous casting, continuous dendritic web growth, continuous edge-defined, film-fed growth (EFG), etc.). Of course, the effective segregation and evaporation coefficients and the size and geometry of the molten zone may be very different for various growth methods.

Equation (16.4), taken by itself, is essentially the normal-freezing equation. It thus describes the impurity-concentration profile for techniques such as normal CZ growth, as well as any growth method with a fixed, initial charge that is completely melted before the growth process is started (batch casting, batch directional solidification, ribbon growth from a nonreplenished melt, etc.). Of course, again, the effective segregation and evaporation coefficients can be quite different for different growth methods.

In the case of a nearly cylindrical melt geometry with evaporative impurity loss from the cylindrical surface, g is a function of zone length l , ingot radius r , and solidification rate v . In addition to the variable parameters, g also depends on fixed parameters such as the molar volume V of the host material (Si), the molar evaporation time s of the impurity

(the time required for one mole of the 'pure' impurity to evaporate from 1 cm² surface area at a temperature equal to the zone-melting temperature), the activity coefficient γ of the impurity, in the molten silicon host, and the Langmuir coefficient α for the impurity. The expression for g is then given by [10]

$$g = 2V\alpha\gamma/srv \quad (16.5)$$

The effective evaporation coefficient can also be experimentally obtained.

Using Equations (16.2)–(16.4) and the effective segregation coefficients and effective evaporation coefficients from Table 16.2 for selected impurities in silicon, and assuming $v = 3 \text{ mm min}^{-1}$, a cylindrical ingot, and a melt height equal to the ingot diameter, the calculated concentration profiles for the selected impurities after a single FZ ingot solidification in argon ($g = 0$) and in a vacuum are shown in Figs. 16.4a and b. Additional solidification passes further reduce the impurity concentrations. With appropriate values of k and g , these equations are applicable to most melt-replenished, semicontinuous Si growth methods. A vacuum ambient is, in general, more effective for impurity reduction. However, growth of FZ single crystals in vacuum is problematic because Si also evaporates from the floating zone, lodges on hot-zone components, and can later dislodge and disrupt single-crystal growth if Si particles land in the molten zone. So even if prepasses are carried out in a vacuum, the final crystal-growth pass must be done in an inert gas. Dopants with $k_e > \sim 0.1$ (e.g. B, P) must be supplied continuously during FZ growth to obtain an approximately uniform doping along the length of the crystal. However, if k_e is

Table 16.2 Effective segregation coefficients and evaporation coefficients for selected impurities in silicon

Impurity	Effective segregation coefficient	Effective evaporation coefficient
Al	0.003 ^{a)}	0.2 ^{e)}
Sb	0.07 ^{a)}	100 ^{e)}
As	0.5 ^{a)}	7 ^{e)}
B	0.9 ^{a)}	0.007 ^{e)}
Cu	0.04 ^{b)}	0.035 ^{b)}
Ga	0.014 ^{a)}	1.7 ^{e)}
Au	0.004 ^{b)}	0.012 ^{b)}
In	0.007 ^{a)}	7 ^{e)}
Fe	0.00001 ^{c)}	0.035 ^{e)}
Mn	0.00005 ^{c)}	0.35 ^{e)}
P	0.45 ^{d)}	0.71 ^{d)}

^{a)} Calculated from equilibrium values (see, e.g., Keller and Muhlbauer [9])

^{b)} From Hadamovsky [11]

^{c)} Equilibrium (not effective) value

^{d)} From Ziegler [12]

^{e)} Theoretical value calculated from Bradshaw and Mlavsky [13] by Crossman [14], under the same assumptions used here for melt height and growth rate.

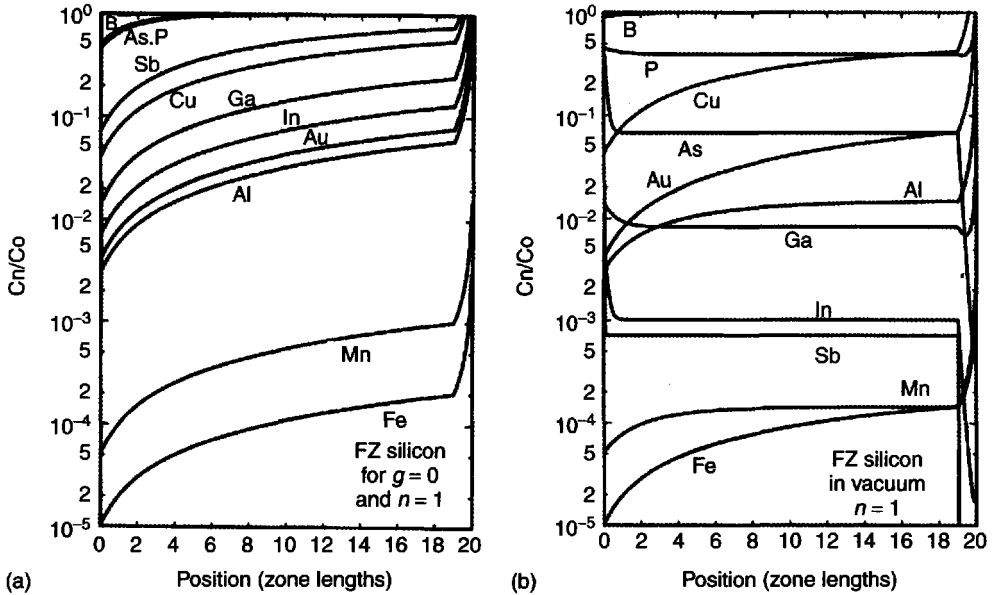


Figure 16.4 Concentration profiles for selected impurities after a single FZ ingot solidification (a) in argon ($g = 0$, left) and (b) in vacuum (right)

$< \sim 0.1$ (e.g. Ga, In), uniform doping can better be obtained using the pill-doping method, where an excess of the dopant is placed at the starting end of the feed rod and most is swept along with the floating zone except for the small fraction k_e that is incorporated in the crystal.

In addition to describing the last zone to freeze in a zone-refining process, Equation (16.4) also applies to CZ growth and the directional solidification of batch melts. In Fig. 16.5, Equation (16.4) is plotted for the same impurities listed in Table 16.2, for growth in > 1 -bar argon ($g \sim 0$, Fig. 16.5a) and in vacuum (Fig. 16.5b). With appropriate determination of the effective segregation and evaporation coefficients, Equation (16.4) is relevant to most batch growth processes for silicon (CZ, EFG, dendritic web, batch casting, etc.). Note that use of a vacuum or a partial vacuum can be useful in processes like CZ growth or casting/directional solidification to obtain more uniform doping with dopants such as P or Ga.

16.3 MULTICRYSTALLINE INGOT GROWTH METHODS FOR PV

16.3.1 Casting and directional solidification

If we relax the requirement for a crystallographic structure that is single crystalline and dislocation free, simpler multicrystalline growth methods can be used. They have the advantage of reduced operator skill, reduced manpower for growth, simpler equipment, and large ingot batch sizes. The drawback is somewhat reduced PV-cell performance due to grain-boundary effects. However, the performance reduction is not too severe if

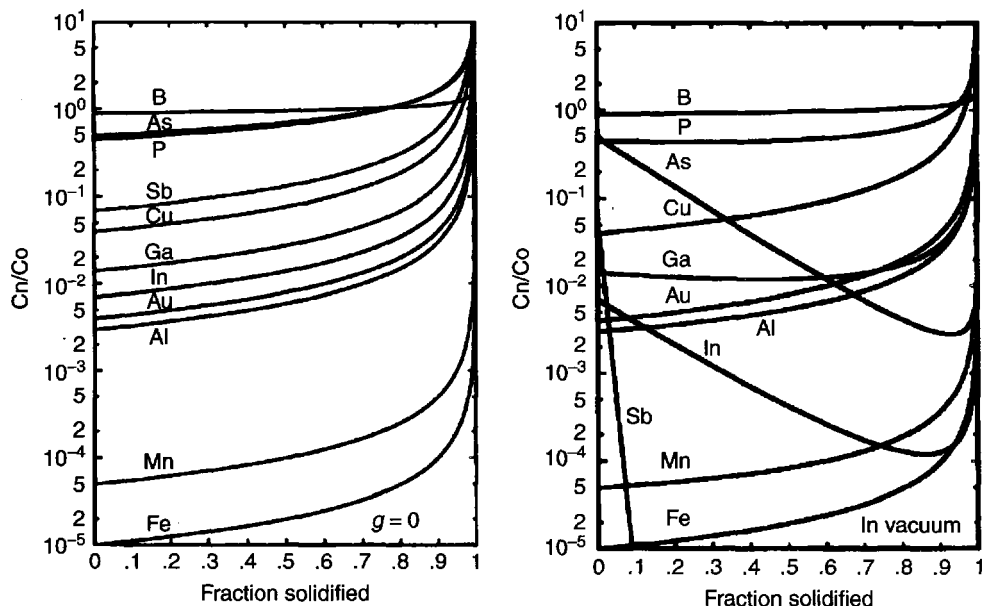


Figure 16.5 Concentration profiles for selected impurities after directional solidification (e.g. CZ growth) (a) in >1 -bar argon ($g \sim 0$, left) and (b) in vacuum (right)

the multicrystalline structure has grains on the order of mm to cm in width that are approximately columnar along the solidification direction. Casting of multigrain silicon has been in use for more than 80 years. Runyan [15] compiled a summary of early silicon-casting approaches in 1965. Si casting into graphite molds as an alternative to CZ growth for PV applications was reported in 1976 by Fischer and Pschunder [16].

Directional solidification can be carried out in a crucible after (or as) silicon is poured into it from a second melting crucible, as shown in Fig. 16.6. This process is usually referred to as silicon casting. Alternatively, the silicon can be melted and directionally solidified in a single crucible (i.e. the bottom crucible in Fig. 16.6). This technique is referred to as directional solidification. Because melting and solidification are decoupled in casting, higher throughputs are possible. But the process and equipment are more complex. Directional solidification is simpler than casting, because no melt pouring is involved, but there are longer reaction times at high temperature between the melt and the crucible, and longer turnaround times. Most multicrystalline-Si ingots for PV consumption use the single-crucible directional-solidification method. Proprietary methods have been developed to minimize sticking between the crucible and the solidified silicon, and ingot cracking.

Multicrystalline ingots $690 \text{ mm} \times 690 \text{ mm}$ in cross section and weighing 240 kg are grown in total cycle times of 56 h. The resultant throughput is 4.3 kg h^{-1} . The larger solid/liquid interface area, compared to CZ crystals, more than offsets the somewhat lower linear growth rates leading to higher throughputs for directional solidification by a factor of ~ 3 . Either resistance heating or induction heating, as shown in Fig. 16.6, can be used. Energy consumption is in the range of $8\text{--}15 \text{ kWh kg}^{-1}$. The solid/liquid interface

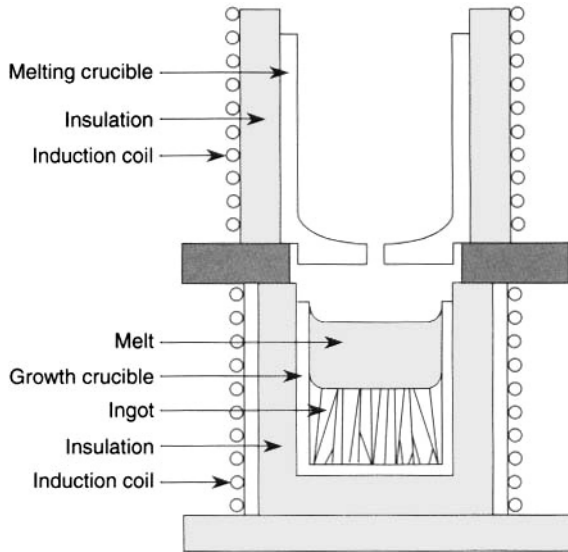


Figure 16.6 Schematic diagram for directional solidification of multicrystalline silicon. Reproduced from Scheel (2003) *Crystal Growth Technology*, with permission from John Wiley & Sons, Ltd

is submerged and precipitates or slag at the melt surface do not disrupt growth. Directional solidification is a simpler process requiring less skill, manpower, and equipment sophistication than CZ, which can make it a lower-cost process.

Impurity redistribution during solidification is similar to that shown for CZ growth in Fig. 16.5. Impurity contents can be higher in multicrystalline ingots than in CZ ingots, depending on the crucibles and feedstock used. Portions of the bottom, sides, and top surface of the ingot are discarded because of low minority-carrier lifetime from impurities or the previously mentioned grain-boundary effects. Multicrystalline solar cells are about 85 % as efficient as CZ cells. The best efficiency of small cells, with sophisticated processing, is 18.6 %. Typical large production cell efficiencies are 13–14 %, with good consistency.

16.3.2 Semicontinuous electromagnetic casting

Electromagnetic casting (EMC) was first applied to semicontinuous silicon ingot growth by Ciszek [17, 18] in 1985. EMC is based on induction-heated cold-crucible melt confinement, but with no crucible bottom. A parallel, vertical array of close-spaced, but not touching, water-cooled, conducting fingers is attached at one end to a water-cooling manifold. The other end of each finger is closed. An internal distribution system carries cooling water to the tip of each finger and back again. The shape of the region enclosed by the close-spaced fingers determines the cross section of the cast ingot, and a wide variety of shapes are possible (circular, hexagonal, square, rectangular, etc.). Silicon is melted on a vertically movable platform (typically graphite or previously grown silicon) located within the finger array. The melting is accomplished by induction heating after suitable preheating. The induction coil, placed outside the finger array (Fig. 16.7), induces

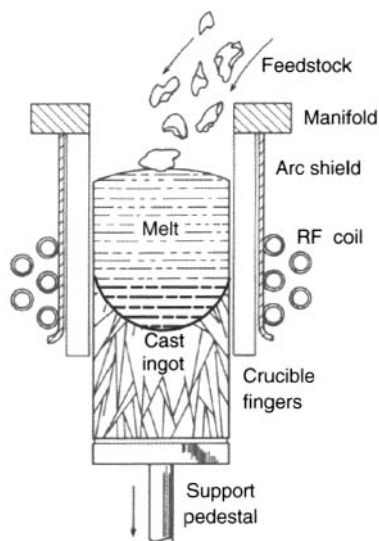


Figure 16.7 Schematic diagram for semicontinuous electromagnetic casting of silicon. Reproduced from Scheel (2003) *Crystal Growth Technology*, with permission from John Wiley & Sons, Ltd

a current to flow in the periphery of each finger, around the finger's vertical axis. Like a high-frequency transformer, each finger in turn induces a current to flow in the periphery of the silicon charge, about its vertical axis. The silicon is heated by its resistance to the current flow. There is a Biot–Savart-law repulsion between the current flowing in the periphery of the silicon melt and the currents flowing in the fingers, because they are induced to flow in opposite directions at any particular instant in the RF cycle. Thus, the melt is repulsed from the water-cooled fingers. The open-bottom arrangement allows the platform to be withdrawn downward, solidifying the molten silicon, while new melt is formed by introducing feed material from the top. In this way, semicontinuous casting can be conducted.

Feed perturbances or slag at the melt surface do not affect the solidification front because the solid/liquid interface is submerged. A variety of feed-silicon geometries can be used (melts, rods, pellets, chunks, etc.). The cross section of the ingots has evolved over years of development and is currently about 350 mm × 350 mm. Ingot lengths > 3 m have been demonstrated. The cold fingers allow steep thermal gradients and consequently fast growth speeds ($\sim 2 \text{ mm min}^{-1}$), even in ingots with large cross sections. But they also cause a steeply curved interface that is concave toward the melt, and a grain structure that is neither as columnar nor as large as in conventional directional solidification. The average grain size is on the order of 1.5–2 mm in large ingots. The effect of smaller grain sizes decreasing τ is largely offset by the relatively high purity and freedom from oxygen and carbon impurities ($O < 6 \times 10^{15}$; $C < 8 \times 10^{16} \text{ cm}^{-3}$) which increase τ , so that solar-cell efficiencies of about 14–15% are obtained on 15 cm × 15 cm cells. The throughput of EMC is the highest of any ingot growth technique—up to approximately 30 kg h⁻¹. A recent installation of EMC ingot growth in France expects the capacity of a single furnace to be 15 MW y⁻¹ of PV modules. EMC power consumption can be as low as 12 kWh kg⁻¹.

16.4 RIBBON OR SHEET GROWTH METHODS FOR PV

The expense and material loss (kerf loss) of ingot wafering has been the motivation for innovating a plethora of silicon ribbon or sheet growth methods. These will be briefly discussed in the approximate chronological order they were reported, but will be presented in two categories: growth from a solid/liquid interface approximately equal in area to the ribbon cross section (small-area solid/liquid interface), and growth from a solid/liquid interface area substantially greater than the area of the ribbon cross section (large-area solid/liquid interface). One major difference between these two interface types is the potential linear growth rate. For small-area solid/liquid interfaces, the calculated maximum growth rate v_{SA} is given [4] by

$$v_{SA} = \frac{1}{L\rho_m} \left(\frac{\sigma\epsilon(W+t)K_m T_m^5}{Wt} \right)^{1/2} \quad (16.6)$$

where W is ribbon width, t is ribbon thickness, and the other symbols are the same as used in Equation (16.1). If $t \ll W$, then $(W+t)/W$ approaches 1 and the growth-rate dependence on geometry is approximately proportional to $(1/t)^{1/2}$. Achieved linear growth rates for the small-area solid/liquid interface methods are typically on the order of a few cm min^{-1} . For large-area solid/liquid interface methods, the growth rate v_{LA} is given by

$$v_{LA} = \frac{4\alpha K_m b}{(2K_m - \alpha t)tL\rho_m} \Delta T \quad (16.7)$$

where α is the effective coefficient of heat transfer, b is the length of the solid/liquid interface (in the pulling direction), and ΔT is the temperature gradient between melt and substrate (or free surface, if no substrate is used) [19]. Equation (16.7) predicts a 6-m min^{-1} growth rate at $\Delta T = 160^\circ\text{C}$, and experimental pulling speeds near that value have been realized. The indication is that v_{LA} can be hundreds of times faster than v_{SA} , especially if b and ΔT are maximized.

16.4.1 Small-area solid/liquid interface growth methods

The earliest two ribbon methods were devised before PV applications were significant. Silicon dendritic web growth (Fig. 16.8) was reported by Dermatis and Faust [20] in 1963; Stepanov growth through a nonwetting shaper slot (Fig. 16.9) was reported by Boatman and Goundry [21] in 1967. These two techniques can produce single or twinned silicon ribbons. Stepanov growth of single-crystal ribbon was difficult to develop over about 12 mm wide. Dendritic web growth continued to be developed for PV until quite recently. It reached 80 mm widths, 120 mm thickness, and semicontinuous lengths, but has the drawback of low areal growth rate or throughput.

Edge-defined, film-fed growth (EFG) was the first silicon growth method targeted for PV applications. We grew the first EFG Si ribbons in 1972 (Ciszek [22]) and the first EFG Si tubes in 1975 (Ciszek [23]), applying technology that had been reported for growth of shaped sapphire in 1971 [24]. High-density graphite was used for the capillary die. Over the years, these two technologies have been developed and merged into the

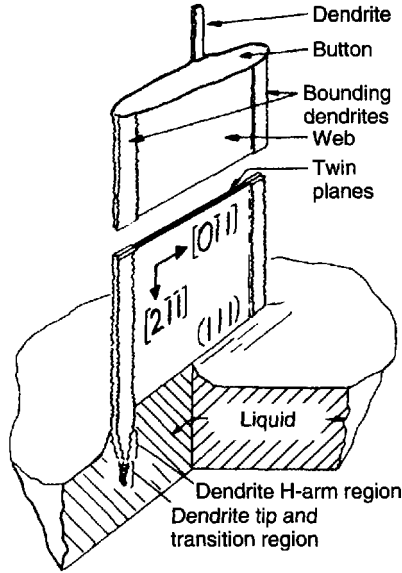


Figure 16.8 Silicon dendritic web ribbon growth. Reproduced from Scheel (2003) *Crystal Growth Technology*, with permission from John Wiley & Sons, Ltd

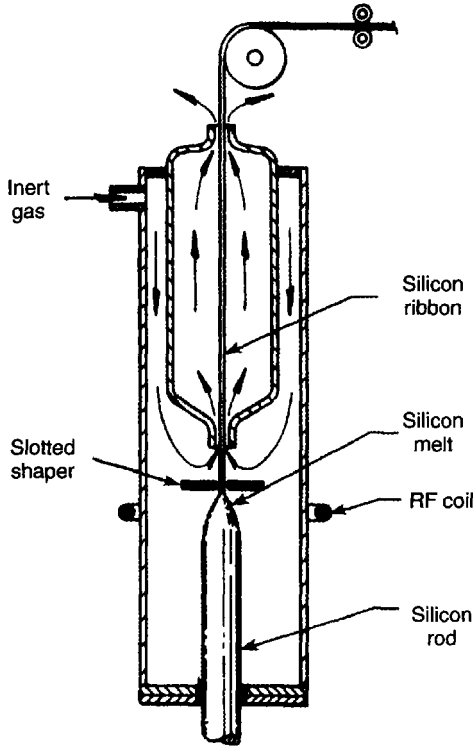


Figure 16.9 Silicon Stepanov ribbon growth. Reproduced from Ciszek (1984) *Journal of Crystal Growth*, with permission from Elsevier Science, Ltd

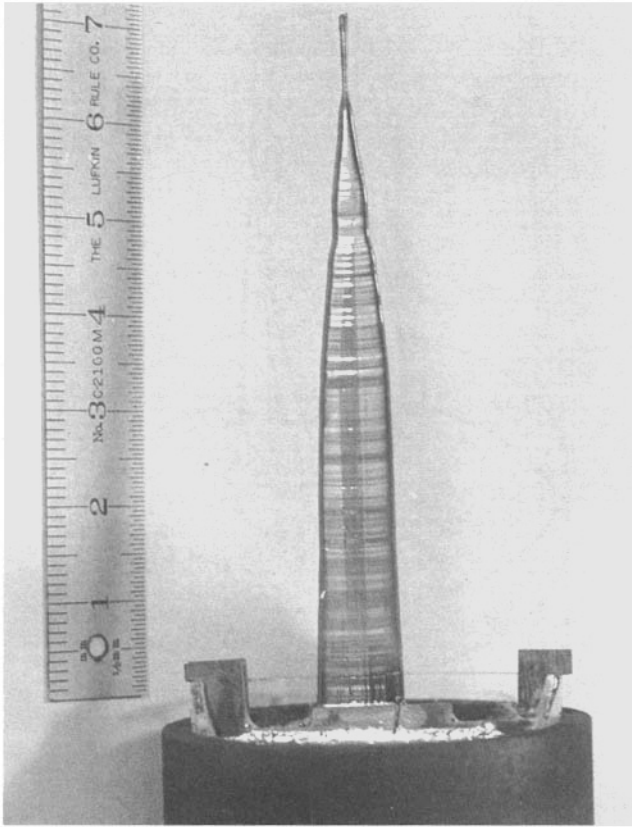


Figure 16.10 First Si ribbon grown by the EFG method

process RWE Schott Solar currently uses for its PV sheet production. Long octagonal tubes are now grown 200–300 μm thick, with 100–150 mm wide faces. PV cell blanks are laser-cut from the flat tube walls. The first EFG Si ribbon is shown in Fig. 16.10, and a schematic of the EFG growth process is shown in Fig. 16.11. The silicon melt rises up capillary channels in the die and spreads over the die top surface. The die top edges pin the base of the meniscus from which the growing object solidifies. Growth is generally multicrystalline, with long multiple twin boundaries being favored.

The late 1970s saw an explosion of novel growth techniques for silicon ribbons fueled in large part by the US PV program during that period. One of these was called ribbon-to-ribbon float zoning or RTR and was reported in 1976 [25]. It achieved a width of 75 mm with a $\sim 2\text{-mm}$ grain size, a thickness of 100 μm , and a 3–9-cm min^{-1} growth rate. Laser heating was used to form the floating zone (Fig. 16.12) using polycrystalline Si ribbon feedstock that was vapor deposited onto a Mo substrate and then separated from the substrate. There were some difficulties with zone stability that were partially solved by melting the central region but not the edges of the feed ribbon.

The silicon-on-ceramic SOC growth technique [26] was also published in 1976. This was a simple dip-coating method wherein a flat mullite ($2\text{SiO}_2:3\text{Al}_2\text{O}_3$) substrate was immersed in liquid silicon and withdrawn at a controlled rate to obtain a desired thickness.

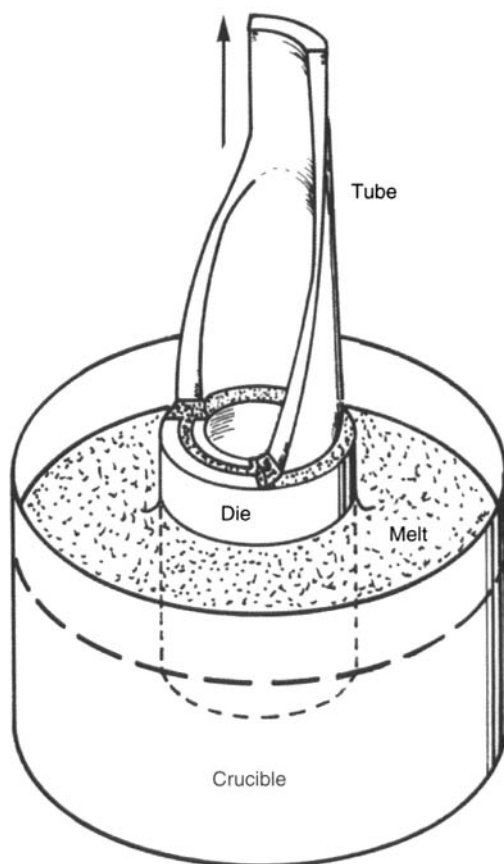


Figure 16.11 Schematic diagram of the EFG growth method. Reproduced from Scheel (2003) *Crystal Growth Technology*, with permission from John Wiley & Sons, Ltd

Marginal wetting of the mullite by liquid Si dictated the need for applying a thin film of carbon on the substrate to enhance wetting. Silicon thickness was found to vary inversely as the square of the pulling speed (as would be expected from Equation (16.6)). Relatively low throughput rates and low PV-cell efficiencies (from the small grain size) discouraged further work with the method. A somewhat similar approach, but using thin carbon substrates passed continuously through a melt was published in 1977 [27]. This is the ribbon-against-drop or RAD method shown schematically in Fig. 16.13. A reel-to-reel process was developed based on RAD. Both of these processes feature easy thermal and mechanical control, but tend to nucleate numerous grains that limit PV-cell performance. Also in 1977, an inverted Stepanov technique was worked on briefly [28]. It achieved 2-cm wide multicrystalline ribbons 0.5 mm thick at a growth rate of 1 cm min^{-1} .

In 1980, we introduced the edge-supported pulling (ESP) technique (Ciszek and Hurd [29, 30]). This passes two filaments upward through small holes in the crucible bottom and bridges them with a seed or plate where they emerge at the top melt surface. Subsequent Si solidification continuously converts the top of the liquid silicon meniscus into a growing ribbon, filling the space between the filaments and the seed (Fig. 16.14a). The technique is like dendritic web growth except that foreign filaments are used (typically

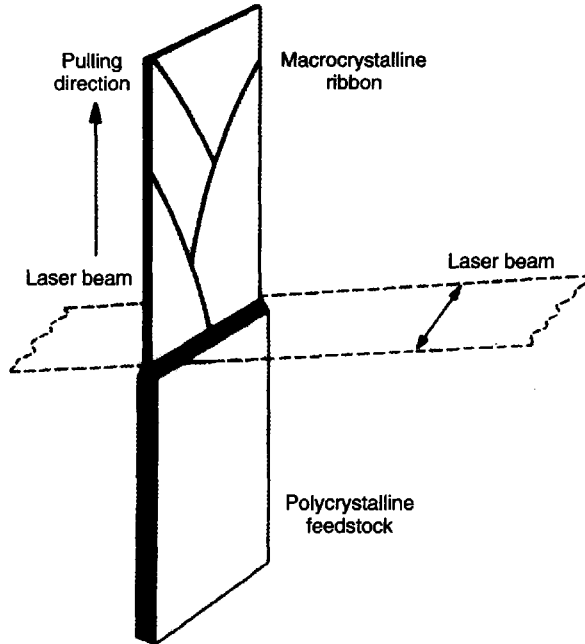


Figure 16.12 Schematic diagram of the RTR growth method. Reproduced from Ciszek (1984) *Journal of Crystal Growth*, with permission from Elsevier Science, Ltd

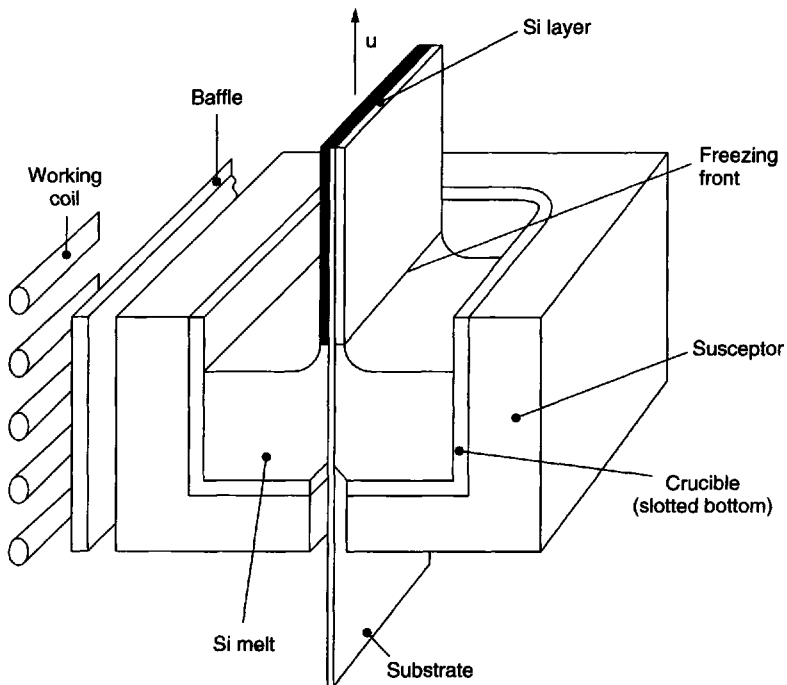


Figure 16.13 Schematic diagram of the RAD growth method. Reproduced from Ciszek (1984) *Journal of Crystal Growth*, with permission from Elsevier Science, Ltd

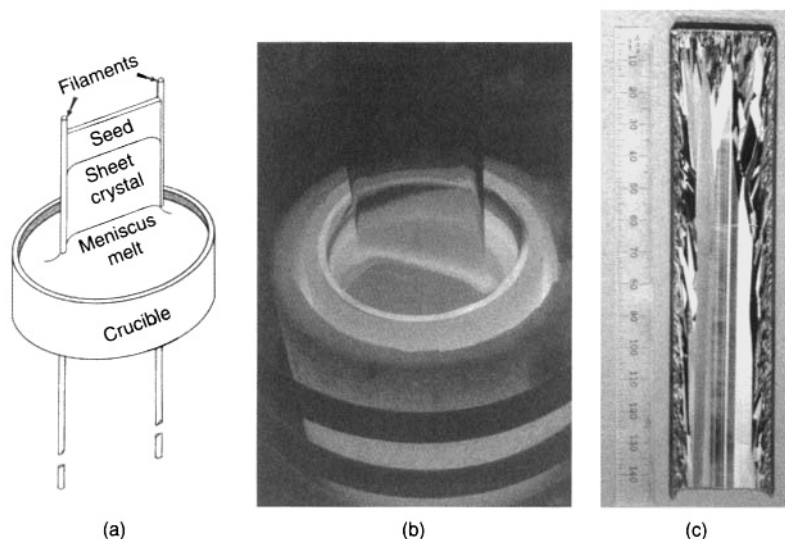


Figure 16.14 (a) Schematic diagram of the ESP/string ribbon growth method. Reproduced from Scheel (2003) *Crystal Growth Technology*, with permission from John Wiley & Sons, Ltd, (b) Growth of a semicontinuous 3-cm wide ESP ribbon, (c) Evolution of equilibrium grain structure in an ESP ribbon. Reproduced from Cizek (1984) *Journal of Crystal Growth*, with permission from Elsevier Science, Ltd

carbon based). Thus the stringent temperature-control requirements for controlled dendrite growth are eliminated, making the technique more industrially friendly and easier to scale up. Figure 16.14b shows semicontinuous ESP ribbon growth in progress using carbon-based filaments, a quartz crucible, a graphite susceptor, and RF heating. While grains are continually nucleated at the filament boundaries, the central region of the ribbon is large-grained multicrystalline material, typically dominated by longitudinal twin boundaries. The evolution of the equilibrium grain structure is shown in Fig. 16.14c, where an etched ESP ribbon grown with a graphite ‘seed’ is depicted. After a period of dormancy, the technique was revived by Evergreen Solar for their current commercial solar-cell production and renamed ‘String Ribbon’. The width has been increased to 100 mm and multiple ribbons are grown from one furnace.

In 1987, a technique was reported for the growth of large-grained multicrystalline silicon sheets from powder-feed stock (SSP) [31]. SSP is a multistage process using optical heating. First, the silicon powder is dispersed to a uniform thickness on a long, flat quartz plate and partially melted from the top surface to form a free-standing feed ribbon. The feed ribbon is moved on quartz rails through an optical heating lamp that zone melts the mid-region (but not the cooler edges at the rails) to form a large-grained multicrystalline structure except for the edges. The process is shown schematically in Fig. 16.15. It is somewhat like the RTR method, but uses more practical optical heating and is run horizontally.

16.4.2 Large-area solid/liquid interface growth methods

The lure of high throughputs or areal growth rates resulting from high linear pulling speeds dictated by Equation (16.7) has motivated a number of large-area solid/liquid interface growth methods. The concept was first experimentally demonstrated for ice and

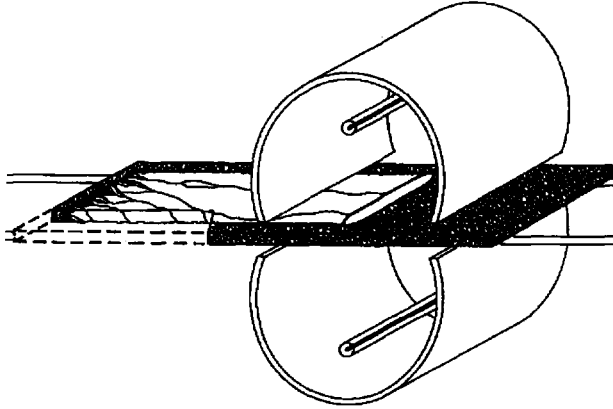


Figure 16.15 Schematic diagram of the SSP growth method. Reproduced from A. Eyer *et al.*, *Crystal Structure and Electrical Properties of Silicon Sheets grown from Powder (SSP Method)* [31], with permission from IEEE. © 1987 IEEE

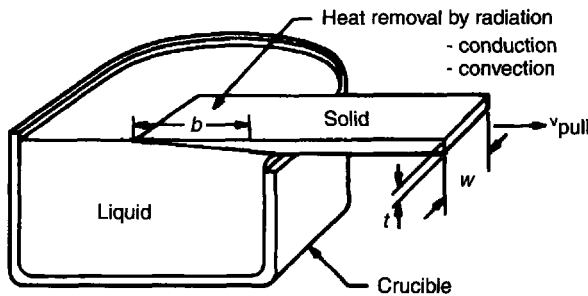


Figure 16.16 Schematic diagram of horizontal ribbon growth HRG. Reproduced from Cizek (1984) *Journal of Crystal Growth*, with permission from Elsevier Science, Ltd

germanium crystals, which were pulled laterally off the free melt surface in a brim-full crucible by Bleil [32] in 1969. A schematic of horizontal ribbon growth (HRG) is shown in Fig. 16.16. The heat of fusion generated by solidification is removed vertically through the ribbon and its opposite surface by the usual processes of conduction, radiation, and convection, while the ribbon itself is being pulled perpendicular to this direction. The large area $b \times W$ available for heat removal (compared to $t \times W$ for vertically pulled ribbons) allows faster pulling speeds. Two approaches have been explored—one using a free surface opposite the solid/liquid interface, similar to the case shown in Fig. 16.16, and the other utilizing a temporary or permanent substrate opposite the solid/liquid interface.

We will first look at the large-area solid/liquid interface approaches attempting to utilize a free silicon surface. In 1976, Koyanagi attempted to use the HRG approach for silicon with limited success [33]. In 1980, Kudo [34] added convective cooling and active thermal control to the process as shown schematically in Fig. 16.17. He achieved growth rates of $100\text{--}900\text{ mm min}^{-1}$ at a width of 50 mm and a minimum thickness of $200\text{ }\mu\text{m}$. Ribbons over 200 cm long were grown. The surface morphology was irregular, and there was a tendency to dendritic growth. These problems would have to be resolved for successful application of the method. Bates and Jewett [35] reported their version of free-surface HRG, called low-angle silicon sheet (LASS) in 1981. It used radiative cooling and passive

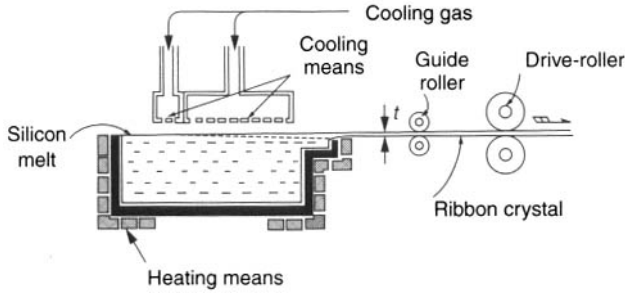


Figure 16.17 The HRG method with convective cooling and active thermal control. Reproduced from Cizek (1984) *Journal of Crystal Growth*, with permission from Elsevier Science, Ltd

thermal modifiers. Somewhat wider (up to 150 mm) and longer (900 cm) ribbons were grown, slightly thicker ($300\ \mu\text{m}$), and at comparable speeds of $90\text{--}700\ \text{mm min}^{-1}$. Once again, a dendritic structure and irregular surface morphology were problematic. Maintaining a single-crystal leading edge in the face of the high pulling speeds appears to be quite difficult with the free-surface HRG methods.

The large-area solid/liquid interface approaches that utilize a temporary or permanent substrate allow nucleation to be heavily influenced by the substrate, and in general, small-grained multicrystalline crystallography results. An early technique reported by Cizek and Schwuttke [36] in 1977 used a mesh-like or perforated carbon substrate pulled vertically through the melt. The technique was called contiguous capillary coating (CCC) because the melt could permeate the open carbon structure and provide a solidified silicon sheet with the front and rear surfaces contiguously connected (Fig. 16.18). Furthermore, the structure could carry the melt some distance from the level in the crucible before solidification, providing an extended-area solid/liquid interface and thus high pulling speeds. The CCC technique was later developed in a horizontal mode by Grabmaier *et al.* [37] who called it the S-web method. Pulling speeds in the range $40\text{--}2000\ \text{mm min}^{-1}$ have been used in the CCC/S-Web method.

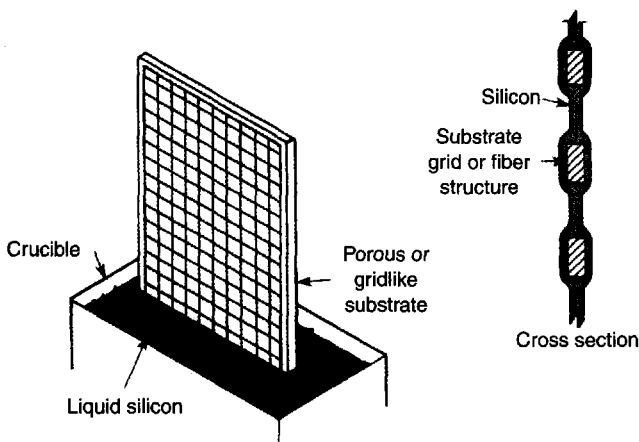


Figure 16.18 Schematic diagram of the CCC growth method. Reproduced from Cizek (1984) *Journal of Crystal Growth*, with permission from Elsevier Science, Ltd

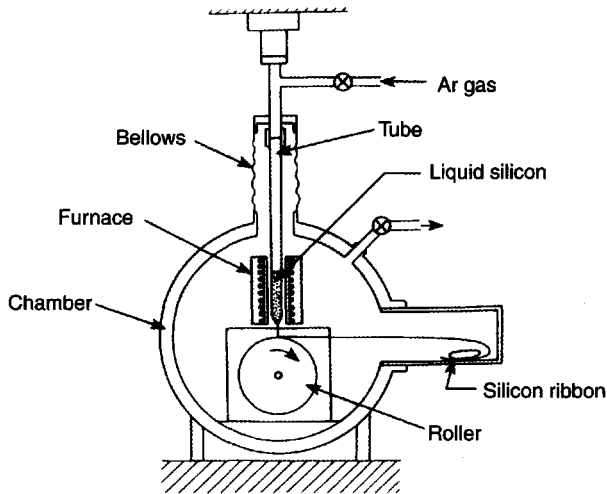


Figure 16.19 Schematic diagram of the RQ/melt spinning method. Reproduced from Ciszek (1984) *Journal of Crystal Growth*, with permission from Elsevier Science, Ltd

Roller quenching (RQ) or melt spinning solidifies a ribbon from a stream of liquid silicon fed onto a cooled, rapidly rotating metal cylinder. The solid silicon is immediately removed or thrown off the cylinder that serves as a temporary substrate. In 1980, Tsuya, *et al.* [38] reported growing 50-mm wide Si ribbons at phenomenally fast rates of up to $2 \times 10^6 \text{ mm min}^{-1}$, and at a thickness of $20 \mu\text{m}$. A schematic diagram of his method is shown in Fig. 16.19. Some concerns with the RQ method are the very small grain size (the work referenced above achieved 10–30- μm columnar grains) and stresses in the ribbon. Quite low cell efficiencies were obtained, on the order of 5%, even when a CVD epitaxial coating was grown on the ribbons. In addition to published work, there have been some proprietary, unpublished efforts that have achieved geometrically uniform ribbons, but still with low PV-cell efficiencies.

In 1981, an inverted, extended-meniscus version of the SOC process was reported [39]. It is called the SCIM (silicon coating from an inverted meniscus) technique and is shown in Fig. 16.20. The substrate again was mullite ceramic sheet material, 125 mm wide by

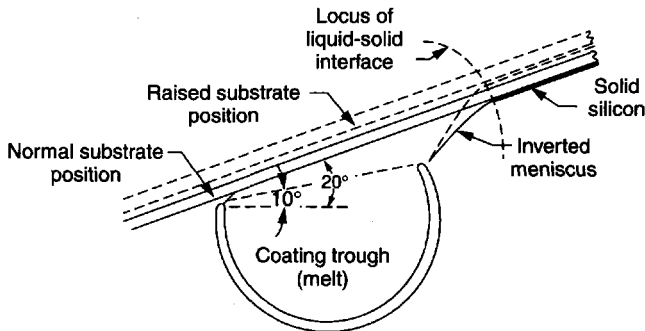


Figure 16.20 Schematic diagram of the SCIM method. Reproduced from Ciszek (1984) *Journal of Crystal Growth*, with permission from Elsevier Science, Ltd

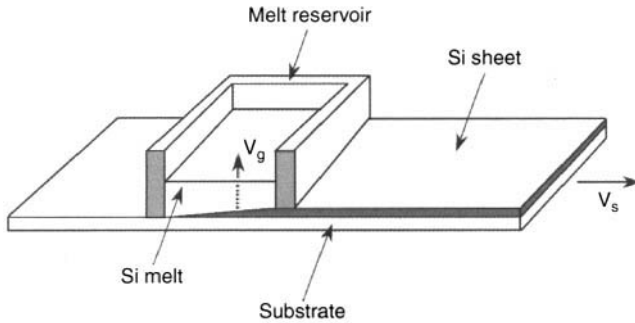


Figure 16.21 Schematic diagram of the RGS method. Reproduced from Scheel (2003) *Crystal Growth Technology*, with permission from John Wiley & Sons, Ltd

1000 mm long. Disappointingly slow growth speeds were attained, up to 20 mm min^{-1} , indicating that full advantage was not made of the potential for a large-area solid/liquid interface.

Techniques that were more successful in attaining a large-area solid/liquid interface include forms of sheet casting [40, 41], and techniques in which the substrate served as a wall or bottom of the crucible, either static or transitory. These include interface-controlled crystallization (ICC) and its follow-up, the ramp-assisted foil-casting technique (RAFT) [42], and especially the 'ribbon growth on substrate' (RGS) technique [19] shown in Fig. 16.21. In these methods, a substrate such as graphite or a mullite-type ceramic are rapidly passed, for example, under the bottom of a melt reservoir, serving temporarily as the crucible bottom. The ribbon or sheet nucleates and solidifies on the moving substrate and, in some cases, can be subsequently removed from the substrate leaving a free-standing Si sheet and a reusable substrate. Nucleation is at the substrate surface, and grain growth is columnar but small (typically under 2 mm grain width at the upper sheet surface). The larger the length of the melt reservoir, the larger is b in Equation (16.7), and the faster is the pull speed. One company, using a conceptually similar process, but with a proprietary method of supplying the silicon feed material has attained sheet widths over 150 mm and throughputs over $1500 \text{ m}^2 \text{ day}^{-1}$ from a single growth furnace. This compares favorably with the throughput of the fastest ingot-growth methods. The main challenge is to obtain higher cell and module efficiencies in the face of small grain sizes and use of solar-grade feedstock.

16.5 THIN-LAYER GROWTH ON SUBSTRATES FOR PV

Thin-layer silicon is considered to be $< 50\text{-}\mu\text{m}$ thick polycrystalline silicon deposited on a foreign substrate. While a few per cent of PV module sales utilize amorphous silicon thin-film technology, there have not been many successes so far in using thin-layer silicon growth methods for PV, and over 95 % of module sales utilize ingot or sheet growth technology. Potential advantages of thin-layer approaches include less Si usage, lower deposition temperatures relative to melt growth, monolithic module construction possibilities, and relaxed requirements for lifetime and diffusion length. Disadvantages include incomplete light absorption and the probable need for light trapping, a likelihood

that grain sizes will be small, attainment of a low-cost substrate, and difficulty in making rear contacts if the substrate is an insulating material.

The R&D challenge for successful thin-layer Si is to produce a 10–50- μm silicon layer of sufficient electronic quality with a diffusion length greater than the layer thickness and a grain size comparable to the thickness. A fast deposition rate of $> 1 \mu\text{m min}^{-1}$ on a low-cost substrate such as glass is needed. There is not yet any significant quantity of thin-layer crystalline Si in commercial production for PV because only partial successes have been achieved in meeting the challenge. Fast chemical vapor deposition (CVD) of $> 1\text{-}\mu\text{m}$ grain-size layers on foreign substrates has been accomplished, *but* at high T ($\sim 1200^\circ\text{C}$) and with contamination. Fast CVD has been carried out at intermediate T on foreign substrates, *but* with submicrometer grain size. Low- T ($< 600^\circ\text{C}$) epitaxial growth of high-quality Si layers on Si substrates has been done by CVD, *but* at low growth rates ($< 0.05 \mu\text{m min}^{-1}$). Fast epitaxy ($1 \mu\text{m min}^{-1}$) of high-quality Si layers was carried out at intermediate temperatures ($700\text{--}900^\circ\text{C}$), e.g., by liquid phase epitaxy (LPE) *but* on Si substrates. Solid-state crystallization can produce smooth Si at intermediate T , *but* at slow rates, from slowly grown a-Si layers, and the growth is highly stressed. Low- T poly/microcrystalline growth has made 10% cells, *but* at slow growth rates. Similarly, low- T micro/amorphous direct-gap 13% cells have been grown, *but* again at slow growth rates.

A new approach to atmospheric-pressure iodine vapor transport (APIVT) growth [43] shows considerable promise, and has achieved 5–20- μm thick Si layers with 5–10- μm grain size at $1\text{--}10 \mu\text{m min}^{-1}$ growth rate directly on hi- T glass at $850\text{--}950^\circ\text{C}$. A scanning electron microscopy (SEM) photomicrograph of a layer is shown in Fig. 16.22. Effective grain-boundary passivation will be needed even with these relatively large grains [44].

16.6 COMPARISON OF GROWTH METHODS

Technological characteristics of some of the methods used to grow silicon crystals for photovoltaic applications are summarized in Table 16.3. The methods shown are the ones

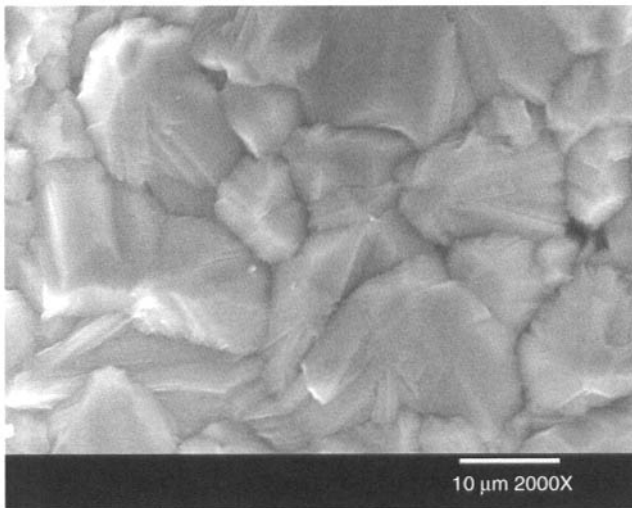


Figure 16.22 Grain structure in a APIVT thin layer grown on glass

Table 16.3 Comparison of some PV silicon crystal-growth techniques

Method	Width (cm)	Weight (kg)	Growth rate (mm min ⁻¹)	Growth rate (kg h ⁻¹)	Throughput (m ² day ⁻¹)*	Energy use (kWh kg ⁻¹)	Energy use (kWh m ⁻²)**	Efficiency (typical %, best %)
Czochralski	15	50	0.6–1.2	1.5	30	18–40	21–48	< 15, 20
Float-zone	15	50	2–4	4	80	30	36	< 18, 24
Directional solidification/casting	69	240	0.1–0.6	3.5	70	8–15	9–17	< 14, 18
Electromagnetic casting	35	400	1.5–2	30	600	12–20	14–24	< 13, 16
Dendritic web	8	—	12–20	—	1.6	—	200	< 15, 17
Capillary die growth	80	—	15–20	—	20	—	20	14, 16
Edge-supported pulling	16	—	12–20	—	3.4	—	55	< 13, 16
Large-area solid/liquid interface	20	—	1000–6000	—	> 1000	—	—	< 12, 16
Thin-layer Si	2	—	10 ⁻³ ‡	—	—	—	—	—, 13

*Areal throughput for ingots assumes 20 wafers cm⁻¹

**Only the energy for growth is included

— indicates data are not available or not appropriate

‡ deposition rate perpendicular to the substrate

that either are still being pursued for PV or have been until recently. Many of the approaches that have been tried over the years are no longer under exploration. A variety of approaches have viability for further development, which is a strong point for Si PV commercial growth. As mentioned in the introduction, cost-driven tradeoffs are made in Si PV crystal-growth technology. This is evident in both the ingot and sheet-growth approaches. For example, the highest throughput ingot method, electromagnetic casting, yields slightly lower cell efficiencies because although the purity level is higher, the grain sizes are smaller. A similar situation is seen in ribbons and sheets, where substrate melt shaping has tremendous throughput potential, but with smaller grain sizes (and lower PV-cell efficiencies). The diversity and redundancy in approaches is healthy for the industry and increases the probability that further reductions in PV module cost will be achieved.

REFERENCES

- [1] J. Czochralski, (1917) A new method for the measurement of crystallization rate of metals, *Zeitschrift des Vereines Deutscher Ingenieure* **61**, 245–351.
- [2] G.K. Teal and J.B. Little, (1950) Growth of germanium crystals, *Phys. Rev.* **78**, 647.
- [3] W. Zulehner and D. Huber, (1982) 'Czochralski-Grown Silicon,' in: *Crystals - Growth, Properties, and Applications* **8**, Ed: J. Grabmaier, Springer-Verlag, Berlin pp. 1–143.
- [4] T.F. Ciszek, (1976) *J. Appl. Phys.* **47**, 440.
- [5] G. Mihalik, B. Fickett, R. Stevenson, and P. Sabhapathy, *Presentation at the 11th American Conference on Crystal Growth & Epitaxy*, Tucson, AZ, August 1–6, 1999.
- [6] J.R. Davis, Jr., A. Rohatgi, R.H. Hopkins, P.D. Blais, P. Rai-Choudhury, J.R. McCormick, and H.C. Mollenkopf, (1980) *IEEE Trans. Electron. Devices* **ED-27**, 677.
- [7] J. Zhao, A. Wang, P. Altermatt and M.A. Green, (1995) *Appl. Phys. Lett.* **66**, 3636.
- [8] P.H. Keck and M.J.E. Golay, (1953) *Phys. Rev.* **89**, 1297.
- [9] W. Keller and A. Muhlbauer, (1981) *Floating-Zone Silicon*, Dekker, New York.
- [10] S. Peizulaev, (1967) *Inorg. Mater.* **3**, 1329.
- [11] H.F. Hadamovsky, (1967) *Kristall Tech.* **2**, 415.
- [12] G. Ziegler, (1958) *Z. Met.* **49**, 491.
- [13] S.E. Bradshaw and A.I. Mlavsky, (1956) *J. Electron.* **2**, 134.
- [14] L. Crossman, private communication.
- [15] W.R. Runyan, (1965) *Silicon Semiconductor Technology*, McGraw-Hill Book Company, New York.
- [16] H. Fischer and W. Pschunder, (1976) *IEEE 12th Photovoltaic Specialists Conf. Record*, IEEE, New York 86.
- [17] T.F. Ciszek, (1985) *J. Electrochemical Soc.* **132**, 963.
- [18] T.F. Ciszek, (1986) U.S. Patent 4,572,812.
- [19] H. Lange and I.A. Schwirtlich, (1990) *J. Cryst. Growth* **104**, 108–112.
- [20] S.N. Dermatis and J.W. Faust, Jr., (1963) *IEEE Trans. Commun. Electron.* **82**, 94.
- [21] J. Boatman and P. Goundry, (1967) *Electrochem. Technol.* **5**, 98.
- [22] T.F. Ciszek, (1972) *Mater. Res. Bull.* **7**, 731.
- [23] T.F. Ciszek, (1975) *phys. stat. sol. (a)* **32**, 521.
- [24] H.E. LaBelle, A.I. Mlavsky and B. Chalmers, (1971) *Mater. Res. Bull.* **6**, 571, 581, 681.
- [25] I.A. Lesk, A. Baghdadadi, R.W. Gurtler, R.J. Ellis, J.A. Wise and M.G. Coleman, in: *12th IEEE Photovoltaic Specialists Conf. Record*, Baton Rouge, LA, 1976 (IEEE, New York, 1976) 173.
- [26] J.D. Heaps, R.B. Maciolek, J.D. Zook and M.W. Scott, in: *12th IEEE Photovoltaic Specialists Conf. Record*, Baton Rouge, LA, 1976 (IEEE, New York, 1976) 147.

- [27] C. Belouet, J.J. Brissot, R. Martres and Ngo Tich-Phuoc, in: *Proc. Photovoltaic Solar Energy Conf.*, Luxembourg, 1977, 164–175.
- [28] K.M. Kim, S. Berkman, M.T. Duffy, A.E. Bell, H.E. Temple and G.W. Cullen, *Silicon Sheet Growth by the Inverted Stepanov Technique*, DOE/JPL-954465 (Final Report, June, 1977).
- [29] T.F. Ciszek and J.L. Hurd, 'Melt growth of silicon sheets by edge-supported pulling,' in: *Proceedings of the Symposia on Electronic and Optical Properties of Polycrystalline or Impure Semiconductors and Novel Silicon Growth Methods*, Eds. K.V. Ravi and B. O'Mara. St. Louis, MO; 11–16 May, 1980 (The Electrochemical Soc., Pennington, NJ, 1980, Proceedings Volume 80–5) pp. 213–222.
- [30] T.F. Ciszek and J.L. Hurd, (1986) *Apparatus for melt growth of crystalline semiconductor sheets*, US Patent 4,594,229.
- [31] A. Eyer, R. Schindler, I. Reis, N. Schillinger and J.G. Grabmaier, in: *19th IEEE Photovoltaic Specialists Conf. Record*, New Orleans, LA, 1987 (IEEE, New York, 1987) 951.
- [32] C.E. Bleil, (1969) *J. Cryst. Growth* **5**, 99.
- [33] T. Koyanagi, in: *12th IEEE Photovoltaic Specialists Conf. Record*, Baton Rouge, LA, 1976 (IEEE, New York, 1976) 627.
- [34] B. Kudo, (1980) *J. Cryst. Growth* **50**, 247.
- [35] H.E. Bates and D.M. Jewett, in: *15th IEEE Photovoltaic Specialists Conf. Record*, Kissimmee, FL, 1981 (IEEE, New York, 1981) 255.
- [36] T.F. Ciszek and G.H. Schwuttke, (1977) *NASA Tech Briefs*, Winter, 432.
- [37] J.G. Grabmaier, H. Foll, H.A. Aulich and B. Freienstein, in: *Proceedings of the Symposia on Materials and New Processing Technologies for Photovoltaics*, 161st Electrochemical Society Meeting, Montreal, Canada (1982).
- [38] N. Tsuya, K.I. Arai, T. Takeuchi, K. Ohmor, T. Ojima and A. Kuroiwa, (1980) *J. Electron Mater.* **9**, 111.
- [39] S.B. Schuldt, J.D. Heaps, F.M. Schmidt, J.D. Zook and B.L. Grung, in: *15th IEEE Photovoltaic Specialists Conf. Record*, Kissimmee, FL, 1981 (IEEE, New York, 1981) 934.
- [40] Y. Maeda and T. Yokoyama, in: *16th IEEE Photovoltaic Specialists Conf. Record*, San Diego, CA, 1982 (IEEE, New York, 1982).
- [41] M. Suzuki, I. Hide, T. Matsuyama, H. Yamashita, T. Suzuki, T. Moritani and Y. Maeda, (1990) *J. Cryst. Growth* **104**, 102.
- [42] A. Beck, J. Geissler and D. Helmreich, (1990) *J. Cryst. Growth* **104**, 113.
- [43] T.H. Wang and T.F. Ciszek, (2000) 'Growth of large-grain silicon layers by atmospheric iodine vapor transport,' *J. Electrochem. Soc.*, **147**(5) 1945–1949.
- [44] T.H. Wang, M.R. Page, R.E. Bauer, T.F. Ciszek, M.D. Landry and Qi Wang, 'Passivation and compatible device processing of APIVT-Si thin layers,' in: *30th IEEE Photovoltaic Specialists Conf. Record*, (IEEE, New York, 2003).

17 Bulk Crystal Growth Under Microgravity Conditions

THIERRY DUFFAR

Institut National Polytechnique de Grenoble, EPM/ENSHMG, BP 95, 38402, Saint Martin D'Herès, France

17.1	Introduction	477
17.2	Experimental and technological environment	502
17.2.1	Technical limitations: time, size, power and space management	502
17.2.2	Environmental limitations: the gravity level	504
17.3	Scientific achievements	505
17.3.1	Segregation studies in Bridgman configuration	505
17.3.2	Experiments of crystal growth from a molten zone or molten drop	508
17.3.3	Sample–crucible interactions and structural aspects	510
17.3.4	Growth from solutions	514
17.3.5	Growth from the vapor phase	515
17.4	Conclusion and future directions	516
17.4.1	Summary of major breakthroughs	516
17.4.2	Problems still to be investigated and perspectives	517
	References	517

17.1 INTRODUCTION

Space exploration has offered physicists the opportunity to perform experiments under a totally new environment characterized by the absence of gravity forces, therefore impeding physical phenomena such as natural convection, hydrostatic pressure or sedimentation. In the framework of crystal growth, the effect of natural convection on the chemical segregation was known since the 1950s and it was expected that, in the absence of convection in the melt, crystals with a constant chemical composition could be obtained. In the case of growth from the vapor phase, convection was also known to have an accelerating effect on the growth rate. Therefore the first space experimenters have been essentially trying to produce homogeneous crystals and to check the validity of the existing theories.

The very first experiments were performed during the 3rd and 4th Skylab missions operated by the NASA in 1973 and 1974. Grown from the liquid phase, an InSb:Te

crystal presented the expected homogeneous dopant distribution, however, Ge:Ga crystals gave contrasting results. GeTe and GeSe crystals grown from the vapor phase showed growth rates much higher than expected from pure diffusion. A GaSb boule grown from a molten sphere showed unexpected striations.

The Soviets joined the Americans in 1975 during the Apollo–Soyouz Test Project (ASTP), not only to shake hands in space but also to perform crystal-growth experiments on both sides, also with somewhat unexpected results. After a mixture of enthusiastic and disappointing experimental results, it finally appeared that limitations associated with the spacecraft environment (residual-gravity forces, power, time or size contingency, safety matters, etc.) had made things much more complicated than initially thought. Simultaneously, the general enhancement of crystal quality, associated with unexpected sample/crucible interactions, focused some researcher attention toward new problems such as structural quality and wetting. The overall result has been an increase of space crystal-growth experiments and of the associated theoretical effort during the intervening years.

The next experiments were performed onboard the NASA space shuttle on the US side, in the European Spacelab integrated in the cargo bay (FSLP, SL3, D1, D2, Spacelab-J, USML1/2, IML1/2, LMS), in the Spacelab rack or in dedicated automatic payloads (USMP-1/2, Get Away canisters). On the Russian side, the orbiting stations Salyut and MIR permitted a large number of experiments, on the occasion of long-term manned missions. The European Space Agency developed programs based on unmanned short (Maser, Texus and Maxus sounding rockets series) or long (the EURECA automatic satellite that remained in orbit for one year) duration flights, in parallel with collaborations with the American and Russian agencies. The technology of retrievable satellites was also developed by the Russians (Foton satellites), the People's Republic of China and, recently, Japan.

The present survey aims to address all the space crystal-growth experiments performed so far, provided that they deal with bulk crystal growth. Some fifteen experiments devoted to mass crystallization of various substances and about one hundred experiments investigating the growth of protein and biological crystals are not considered here. In addition, a number of experiments have been performed on the solidification of metallic alloys, which are much more related to metallurgy and not included here, in spite of the fact that some of them were directly related to matters concerning crystal growth, like chemical segregation or solid/liquid interface stability.

About one hundred and fifty bulk crystal-growth experiments have been performed under microgravity conditions so far. Some of them have been announced in official documents, or in international conferences, but they never led to significant publications and information about the results is lacking. On the other hand, this statistic does not include the major part of the large number of crystals grown under Soviet Union control onboard the Salyut and MIR space stations (see Regel, 1983, Markov *et al.*, 1997). For example, the Tass Agency claimed that 3 kg of semiconductor crystals were grown on board MIR between its operational start and mid-1990 and that 23 crystals were grown onboard in a single mission (Soyouz TM9, landed August 1990). However, data on these experiments and their results are very scarce, so that only well-documented experiments have been taken into account.

Tables 17.1 to 17.4 list all these experiments, following the different growth processes used. Some experiments concerned several samples and sometimes two or more flights were necessary:

Table 17.1 Microgravity crystal-growth experiments by the Bridgman method. 'Ge:Ga' means gallium-doped germanium

Ref.	Flight	Material	Diam. (mm)	Growth rate ($\mu\text{m s}^{-1}$)	Thermal gradient (K cm^{-1})	Pe	GrSc	Results
Ang and Lacy, 1979	ASTP, 1975	AlSb	10					Better homogeneity obtained in space (on ground: sedimentation is suspected).
Averyanov <i>et al.</i> , 1999	Salyut-6, 1979–80	HgCdTe	8	0.19				Crystals are more homogeneous and have better electrical properties when grown in space. Dewetting occurred.
Bollong and Proux, 1989	Maser-1, 1987	$\text{Cd}_{0.21}\text{Hg}_{0.79}\text{Te}$	15	Quench				Space sample is homogeneous in the axial and radial directions.
Buhrig <i>et al.</i> , 2000	MIR, 1997	Ge:Zn	6	1.9	15	1.6	2.4	The Zn was incorporated from the vapor phase and showed unexpected equilibrium incorporation. Finally explained by Ma convection due to composite wetting (Pätzold <i>et al.</i> , 2002).
Calzadilla <i>et al.</i> , 1991	Salyut, 1980	Ge:In	7.8	3.2	100	0.5		Axial segregation is close to diffusive conditions, but has been perturbed by a bubble.
Chen <i>et al.</i> , 2000 and 2001 Lin <i>et al.</i> , 1998 and 1999	Chinese satellites, 1987–1996	SI-GaAs	20					EPD is decreased by a factor 3 in μg and is more homogeneous. Stoichiometry is controlled at $0.50007 \pm 6 \times 10^{-6}$. FET made on μg GaAs show improvement of all electrical characteristics (Chen <i>et al.</i> , 2001)

(continued overleaf)

Table 17.1 (continued)

Ref.	Flight	Material	Diam. (mm)	Growth rate ($\mu\text{m s}^{-1}$)	Thermal gradient (K cm^{-1})	Pe	GrSc	Results
Chernov <i>et al.</i> , 1984 Golovin <i>et al.</i> , 1984	Soviet sounding rocket	Ge:Zn:Sb Ge:Zn:Sb	8	100–300				Dewetting. The immediate lower level of dislocations, compared to the seed, is attributed to dewetting and to a growth rate higher than the dislocation velocity. Diffusive transport in the melt.
Crouch <i>et al.</i> , 1987	STS 61-A, 1985	$\text{Pb}_{0.8}\text{Sn}_{0.2}\text{Te}$	16	1	20	1.6	3200	Axial and radial segregation are typical of strong mixing in the melt. Due to technical problem in the cooling unit, the growth rate is not ascertained. Dewetting occurred.
Derebail <i>et al.</i> , 1992	KC-135 parabolic flight	InSb	5 9					Video observation of the S/L interface through the transparent silica crucible. No dewetting was observed. Bubbles were attracted by the advancing S/L interface.
Duffar <i>et al.</i> , 1988	Spacelab D1, 1985	InSb:Sn	10 and 14	4	10	4.4	30	Axial segregation shows diffusive conditions in regions far from an unexpected bubble. Radial segregation is strongly influenced by the bubble.

Duffar <i>et al.</i> , 1998	EURECA, 1992	GaSb:In	10	0.1	20–30	0.06	3.4	Axial segregation fits with purely diffusive behaviour. Radial segregation shows slight differences between sides of the sample.
Duffar <i>et al.</i> , 1999	Spacelab D2, 1993	GaSb:Te Ga _{0.9} In _{0.1} Sb	14	1.5 0.9	20–40	1 0.6		Axial and radial segregation are typical of full mixing owing to Ma convection due to a groove running all along the crucible inner wall. Dewetting on the rough crucible.
Duhanian <i>et al.</i> , 1997	Spacelab LMS, 1996	Ga _{0.8} In _{0.2} Sb:Te	12	1.1	35	0.66	100	Axial and radial segregation show strong mixing. $k_{\text{eff}} = 0.3$ (Duhanian, 1998). Dewetting on the BN crucible but not on the SiO ₂ part.
Fiederle <i>et al.</i> , 2004	STS-95, 1998	CdTe:Zn,V	14	0.27 166	40			Dewetting occurred and was shown not to depend on growth rate or pressure difference. Better quality, stoichiometry and electrical properties obtained in μg , including the sample solidified at very high velocity.
Fujiwara <i>et al.</i> , 1994	Spacelab J, 1992	Ga _{0.03} In _{0.97} As	12	1.1	60	1.3	1400	Axial segregation shows mixing in the melt. $k_{\text{eff}} = 2.6$ (3.2 on the earth).

(continued overleaf)

Table 17.1 (continued)

Ref.	Flight	Material	Diam. (mm)	Growth rate ($\mu\text{m s}^{-1}$)	Thermal gradient (K cm^{-1})	Pe	GrSc	Results
Galazka <i>et al.</i> , 1981	Salyut 6, 1978	$\text{Hg}_{0.78}\text{Cd}_{0.22}\text{Te}$	8	1	30	1.3	90	Diffusive conditions, homogeneous samples are obtained for low growth rates. At high growth rate destabilisation of the interface is obtained. Dewetting is observed.
Gillies <i>et al.</i> , 1997	USMP-2, 1994	$\text{Hg}_{0.8}\text{Cd}_{0.2}\text{Te}$	7	0.27	35	0.3	60	Axial segregation shows some mixing in the melt. Mixing is enhanced during periods of higher residual gravity level (shuttle attitude change). Clear correlation between the amplitude and orientation of the gravity vector and radial segregation.
Hildmann <i>et al.</i> , 1994	Texas 28	Ge:Ga	10	17	100	9	39	Segregation during the microgravity period corresponds to Tiller's curve.
Kashimov, 1979	Salyut 6	InSb:Te	8	3.1	75	3.1	120	The electrical resistivity is constant along the sample axis. Striations disappeared in space. Dewetting occurred.
Kinoshita and Yamada, 1995	Spacelab J, 1992	$\text{Pb}_{0.8}\text{Sn}_{0.2}\text{Te}$	1.5	1.5	40	2.2	5000	Axial segregation is between diffusive and convective conditions. A numerical simulation shows that the gravity level was between 10^{-4} and $10^{-5}g_0$.

Larson <i>et al.</i> , 1994	USML1, 1992 USML2	CdZnTe	13	0.44	33			Dewetting occurred. The crystal quality is dramatically improved compared to earth: no twins nor grains, EPD 100 times lower, lower residual stresses.
Lendvay <i>et al.</i> , 1985	Salyut 6	GaSb	8	3.1	60			Dewetting occurred all along sample. Structural properties and hole mobility are improved.
Markov, 1979	Salyut 6	Ge:Ga	8	3.1	100	1.3	58	Axial segregation is controlled by diffusion. Radial segregation is influenced by interface shape and microsegregation is decreased.
Matthiesen <i>et al.</i> , 1999	USML1, 1992 USML2 1995	GaAs:Se	15	0.5 1.5	7	6 12	258	Bubbles in USML1 samples due to fractioned initial sample (Kaforey <i>et al.</i> , 1997). Segregation corresponding to full mixing.
Moskowitz <i>et al.</i> , 1997	USML-1, 1992	GaAs:Se	15	2.5 to 5	7	12.5 25	680	Beginning of growth was dominated by diffusion, but suddenly changed to full mixing. Order-of-magnitude analysis shows that this cannot be explained by the measured microgravity-level fluctuations.

(continued overleaf)

Table 17.1 (continued)

Ref.	Flight	Material	Diam. (mm)	Growth rate ($\mu\text{m s}^{-1}$)	Thermal gradient (K cm^{-1})	Pe	GrSc	Results
Nishinaga <i>et al.</i> , 1997	Chinese Satellite 14, 1992	GaSb:Te	6					Axial segregation is diffusion-like. No striations, in spite of a large free surface on the sample. The free surface is attributed to dewetting and low EPD is associated with it.
Parfeniev <i>et al.</i> , 2000	MIR	Te	5.6	11	40			Dewetting leading to better structural quality and hole mobility.
Popov <i>et al.</i> , 1990	MIR	RbAg ₄ I ₅		1.38	10			Phase proportions are different in space and on earth.
Regel <i>et al.</i> , 1990	MIR, 1987	GaSb:Te	7	2.8	25	2.45		Presence of free surfaces. However, resistivity distribution is more homogeneous in space. Striations are suppressed under microgravity conditions.
Rodot and Tottereau 1984	FSLP, 1983	PbTe:Ag	17	2.8	30			Segregation corresponds to Tiller's curve.
Schilz <i>et al.</i> , 1994	Texus 30	Ge _{0.85} Si _{0.15}	10	17				
Su <i>et al.</i> , 2002	USML1 1992	Hg _{0.84} Zn _{0.16} Te	8	0.04	65	0.4	110	Dewetting occurred. Structural quality is somewhat better. The radial segregation is in correlation with interface shape, which was asymmetric and fluctuating. Convection is highly suspected, in spite of the very low gravity level (0.4 μg).

Walter, 1985	Texus 6	Ge:Ga		55						The microhomogeneity is excellent compared to ground material and to the portion solidified under high gravity.
Wei <i>et al.</i> , 2000	Chinese satellite	HgCdTe								Defect concentration is lower and more homogeneous in the μg crystals.
Wilcox <i>et al.</i> , 1975	Skylab 3, 1973	GaInSb	8	2.22		80				Destabilization occurred earlier than on the ground. Dewetting observed. 70% less twinning and 18% fewer grains were observed.
Witt <i>et al.</i> , 1975	Skylab 3, 1973	InSb:Te	14	3-5		40	7	330		No microsegregation observed. The axial distribution is a plateau, showing a diffusive transport in the melt. Dewetting occurred.
Witt <i>et al.</i> , 1978	ASTP, 1975	Ge:Ga	10	8-10		50	4.7	190		Some microsegregation is observed at the beginning and on external facets. Axial segregation is diffusive when a transient growth rate is taken into account (Favier <i>et al.</i> , 1979). Fluctuations in the radial and axial distribution are attributed to interface deformation. On earth, $k_{\text{eff}} = 0.099$. Dewetting occurred.

(continued overleaf)

Table 17.1 (continued)

Ref.	Flight	Material	Diam. (mm)	Growth rate ($\mu\text{m s}^{-1}$)	Thermal gradient (K cm^{-1})	Pe	GrSc	Results
Yee <i>et al.</i> , 1975	Skylab 4, 1974	$\text{In}_x\text{Ga}_{1-x}\text{Sb}$ $x = 0.1 \text{ to } 0.5$	8	2.2	80	0.88		Destabilization occurs earlier than in the sample processed on the ground. The associated chemical heterogeneity make any conclusion about the transport regime difficult.
Yue and Voltmer, 1975	Skylab III, 1973	Ge:Ga	7.5	5	20	2	25	Experiment essentially devoted to microsegregation: fluctuations are 15 to 20 % on the earth and reduced to 3 % in space. Axial macrosegregation gives $k_{\text{eff}} = 0.2$, to be compared to 0.12 on ground. Some convection existed in space. Radial segregation is sensitive to interface shape. Necking at the beginning of growth.
Zemskov <i>et al.</i> , 1977	ASTP 1975	$\text{Ge}_{0.99}\text{Si}_{0.01}:\text{Sb}$	9.5		20			Si and Sb axial and radial distribution is heterogeneous (200 % for radial segregation), probably because of destabilization. However, resistivity is homogeneous.

Zemskov <i>et al.</i> , 1983	Salyut 6	InSb:Te	13	3	10	4.8	110	Presence of free surfaces, depending on gravity level. Transport of Te is diffusive, but perturbed when close to the free surface. In one sample, radial distribution is homogeneous (3–5 %), related to interface curvature, but in the other one it is heterogeneous (25 %).
Zemskov <i>et al.</i> , 1991	Kosmos, 1986 Foton-3 1989	InSb:Te	13	3	10–15	4.8		Presence of free surfaces. No impurity striations. Mass transport essentially diffusive. Free surface (necking) sensitive to gravity perturbations (Zemskov <i>et al.</i> , 2001)

Table 17.2 Microgravity crystal-growth experiments from a floating zone or a molten drop ('Ma' is for both 'Marangoni convection' and 'Marangoni number'. 'Ge:Ga' means gallium-doped germanium)

Ref.	Flight	Material	Diam. (mm)	Zone length (mm)	Growth rate ($\mu\text{m s}^{-1}$)	Thermal gradient (K cm^{-1})	Ma	Results
Abbaschian <i>et al.</i> , 1996	STS-57	InBi	7	33	0.56–5.6		Encaps.	Liquid encapsulated by silicone oil. Encapsulation allowed more stable zone. EPD lower than on earth and than in unencapsulated sample.
Averyanov <i>et al.</i> , 1999	Salyut-6, 1981–82	HgCdTe	10		0.28		Coated	Crystals are more homogeneous and have better electrical properties when grown in space. Dewetting occurred.
Barmin <i>et al.</i> , 1992	Photon, MIR, 1985–1991	Ge:Ga, Ge:Sb InSb:Te GaSb:Te	15 20		1.1 1.4 1.9			Total stirring in the melt (Ma). Growth striations, but less than in earth-grown Cz. Striations are decreased (3.5% to 2.1%) when a magnetic field is applied (0.03 T). Ma > critical value (but no figure given)
Camel and Tison, 1990	MASER-2	Ge:Ga	6	7	100	35	350	Ma is strong but less than convection on ground and than expected theoretically. Radial segregation is sharp, in qualitative agreement with Ma flow. Oxide layer should have damped convection. $k_{\text{eff}} = 0.34$.

Camel <i>et al.</i> , 1994	D2, 1993	Ge:Ga	10	19 to 30	12	24	2800	Axial segregation shows convectodiffusive regime ($k_{\text{eff}} = 0.64$). Radial segregation is nonsymmetric, with variations during pulling. Seebeck measurement was implemented to see oscillations, but no oscillations appeared, in spite of a Ma higher than critical value. Conclusion is that Ma was partially damped by oxide layers not fully covering the melt.
Carlberg, 1984, 1986	Texus 10 Texus 12 Texus 14b	Ge:Ga	5		50 to 80			Convection in the melt ($k_{\text{eff}} = 0.2$ to 0.4) but no striations. Radial segregation is related to interface shape. When the melt surface is covered, the axial segregation is diffusive but radial segregation is disturbed (by bubbles?).
Cröll <i>et al.</i> , 1986	TEXUS 12, 1985	Si:P	7.6	23			Coated	Surface-coated. Purely diffusive conditions in space. On earth, gravity-driven convection led to segregation.

(continued overleaf)

Table 17.2 (continued)

Ref.	Flight	Material	Diam. (mm)	Zone length (mm)	Growth rate ($\mu\text{m s}^{-1}$)	Thermal gradient (K cm^{-1})	Ma	Results
Cröll <i>et al.</i> , 1987	D1, 1985	Si:P	10	20	80	50	10 000	Surface partially coated. The uncoated ground and flight portions show Ma aperiodic striations, but the striation contrast is stronger on earth. No microstriations in the coated part of the space sample. 0.2–0.5 mm striations on the coated earth sample, attributed to nonstationary gravity-driven convection.
Cröll <i>et al.</i> , 1991	TEXUS 22, 1989	Si:Sb	7.6	Variab.	80	35	Variab.	Alternative coated and noncoated surfaces. This permitted measurement of the critical Ma for onset of striations: 100, in agreement with numerical simulations (Rupp, 1990). Experiment on earth gave 100–150. Striation amplitude is 27% in space and 37% on the earth. The contribution of gravity on the flow is significant on earth. Ma has a strong effect on radial segregation, involving the bulk volume of the melt.

Cröll <i>et al.</i> , 1994	TEXUS 29, 1992	Si:P Si:Sb	8	8–12	1.4	25	1300	<p>The intensity of striations is lower in space. The interface is more curved, maybe due to the absence of buoyancy convection. Striations are related to Ma convection. Their spatial period is independent of growth rate, suggesting a broad spectrum of frequency turbulence. Amplitude increases with growth rate. No significant radial segregation. By decreasing the zone length, the critical Ma for instability is evaluated: 375 ± 125. The frequency range is 0.034–0.055 Hz. Good agreement of both values with numerical simulation. Below the critical Ma, there are no striations.</p> <p>A combination of floating-zone and solution growth: the melt was Bi as a solvent for GaSb. The crystal quality is good. The radial segregation is high, showing Ma. Due to the very low growth rate, possible striations are undetectable.</p>
Cröll <i>et al.</i> , 1996	D2, 1993	GaAs GaAs:Te	20	20	1, 2 and 33			
Cröll <i>et al.</i> , 1998	STS-77, 1996	GaSb:Te	16		1.7 and 17			
Cröll <i>et al.</i> , 1998	STS-77, 1996	GaSb in Bi	15	6	0.017	20	70	

(continued overleaf)

Table 17.2 (continued)

Ref.	Flight	Material	Diam. (mm)	Zone length (mm)	Growth rate ($\mu\text{m s}^{-1}$)	Thermal gradient (K cm^{-1})	Ma	Results
Eyer <i>et al.</i> , 1984	FSLP, 1983	Si:P	10		80			Difficulty in stabilizing the zone. Striations due to turbulent Ma, similar to striations obtained on earth. Striation amplitude is 5% in space and 10% on earth. Earth crystals with an oxide layer did not show striations.
Eyer <i>et al.</i> , 1985	TEXUS, 1983	Si:P	8	12	80			Time-dependent thermocapillary flows are the predominant cause for dopant heterogeneity in space and on earth.
Hayakawa <i>et al.</i> , 2000	Chinese satellite	GaSb-InSb	10	4 to 20				In a first step, GaSb is dissolved into the InSb molten zone, then the zone is solidified. Convection is shown to have a large effect on S/L interface shape.
Herrmann and Müller, 1995	D2, 1993	GaAs GaAs:Si	20	12 to 36	1.6 to 2.2			5 samples grown, with and without magnetic field. Striations at 0.1 Hz: segregation < 10% with field, = 17% without. Striations at 0.008 Hz only without field: segregation = 40%.
Iwai and Segawa, 1993	Spacelab-J, 1992	PbSnTe	10	16	0.56		Coated	Enclosed in a tube. The homogeneity and crystal perfection is better than in the ground reference sample. This is qualitatively attributed to less convection in space.

Kartavykh <i>et al.</i> , 1999	Foton	Ge:Ga	15	12–30	1.39–1.9	3	264 (thermal) 13 000 (solutal)	k_{eff} varies with dopant concentration. Later attributed to solutal Marangoni effect (Artemyev <i>et al.</i> , 2001).
Kimura and Miyazaki, 2002	Parabolic flight	$\text{Ba}(\text{B}_{0.9}\text{Al}_{0.1})_2\text{O}_4$	3	5	300			Crystallization profiles are similar in space and on the earth.
Kölker, 1984	FSLP, 1983	Si	11	11	About 1			Solidification from a sphere. Evidence of Ma, but difficult to quantify because of simultaneous sample rotation.
Kölker, 1987	D1, 1985	Si	11	11	0.3			Solidification from a sphere. No rotation, chemical striations due to Ma.
König, 1998	MIR, 1994	$\text{Bi}_{0.5}\text{Sb}_{1.5}\text{Te}_3$	8	20.5 16.5	3.3 1.7	40 35	Coated	The zone was enclosed in a silica tube. Very small bubbles did not lead to Ma convection. No striations, but segregation of Te is dominated by convection: $k_{\text{eff}} = 0.2$ (0.17 on earth). Bi/Sb segregation is rather dominated by diffusion ($k_{\text{eff}} = 0.88$). Radial segregation is 10 % (20 % on ground), in agreement with numerical simulation (Kaddeche <i>et al.</i> , 1996)

(continued overleaf)

Table 17.2 (continued)

Ref.	Flight	Material	Diam. (mm)	Zone length (mm)	Growth rate ($\mu\text{m s}^{-1}$)	Thermal gradient (K cm^{-1})	Ma	Results
Lopez <i>et al.</i> , 1999	STS-77 1996	GaSb GaSb:Te	16		0.28–1.7		Encaps.	Encapsulated in NaCl–KCl. Encapsulation stabilized the zone and no striations were observed. EPD is 20 times lower than in the seed.
Maffei <i>et al.</i> , 1997a and b	STS-77, 1996	$\text{Bi}_{12}\text{GeO}_{20}$	10	10	1.4 0.7			Lower EPD and better optical absorption spectra
Müller and Rupp, 1991	TEXUS 20 and 24	GaAs:Si	10	14	> 25	30	2000	Some dopant striations.
Nakamura <i>et al.</i> , 1998, 1999	TR-IA-4 TR-IA-6	Si	10	10			1300 to 14 000	No pulling but interesting temperature fluctuations (up to 5 K) and X-ray measurements of fluid velocity (25 to 55 mm s^{-1}). The critical Marangoni number between one unsteady and two flow cells is about 1500. Azimuthal fluctuations of T° generate azimuthal Ma flow.
Nakata <i>et al.</i> , 1998	Drop tube	Ge:Sb, GaSb	0.7					Single crystals are obtained in spite of the very high growth rate. Under 1g, in crucibles, polycrystals occurred.
Saghir <i>et al.</i> , 2000	STS-77 (1996)	CdGeAs_2	9	10	0.55		Encaps.	Sample surrounded by LiCl–KCl eutectic to prevent evaporation. CdGeAs_2 was obtained, one sample with large grains and another single crystal. Due to technical problems, the quality could even be enhanced.

Schweizer <i>et al.</i> , 1999	Texus 36 (1998)	Si:Sb	10		17	10–20	1700–3500	Measurement of temperature and huge growth-rate fluctuations. All correlated well with chemical striations.
Sleptsova <i>et al.</i> , 1997	Foton-9 (1994)	Ge:Ga	15	25				No oscillation is observed. A thermocouple in the melt shows a frequency of 0.05 Hz, but the theoretical Ma oscillations are at 0.25–0.43 Hz. The sample center was not molten.
Tillberg and Carlberg, 1990	MASER-2	Ge:Ga	6	6		130 90	660	Partially covered zones, various thermal gradients. $k_{\text{eff}} = 0.75$, showing Ma convection lower than expected: could be explained by partial oxide layers. Radial segregation is related to interface curvature but is very sensitive to the convective level.
Walter, 1977	Skylab, 1974	InSb InSb:Se	8	15	3 to 7	15 to 35	615	Solidification from a sphere. Striations are observed close to the seed, but not attributed to convection. An oxide layer prevented Ma (Bourgeois and Spradley, 1976)

(continued overleaf)

Table 17.2 (continued)

Ref.	Flight	Material	Diam. (mm)	Zone length (mm)	Growth rate ($\mu\text{m s}^{-1}$)	Thermal gradient (K cm^{-1})	Ma	Results
Wang <i>et al.</i> , 1990	Chinese satellites, 1987–88	GaAs GaAs:Te GaAs:Si	9					Striations due to nonstationary Ma at the beginning; disappeared at the end, maybe because zone length decreased as well.
Zemskov <i>et al.</i> , 1991	Foton 3, 1987	InSb:Te	10	10	1.4	12	200	Total stirring in the melt (Ma). Striations are not suppressed by a magnetic field (0.038 T). Solutal Ma is dominant and the critical value for nonstationary flow is: $5 \times 10^5 < \text{Ma}^* < 10^7$. Microsegregation on the facets is sensitive to g-jitters (Zemskov <i>et al.</i> , 1997), especially to orbital period (Zemskov <i>et al.</i> , 2001)

Table 17.3 Microgravity crystal-growth experiments from solution. 'InP:S/In' means S-doped InP from a solution in In

Ref.	Flight	Material	Size (mm)	Growth rate ($\mu\text{m s}^{-1}$)	Results
Chen <i>et al.</i> , 1990, 2003	Chinese satellite, 1988, 1992, 1994	α -LiIO ₃ /H ₂ O	7	0.012	Better quality in space. Crystal habit does not change. [0001] growth rate in μg higher than on the earth. The critical pH also depends on gravity. Later explained by boundary-layer visualisation showing absence of convective perturbation in μg .
Danilewsky <i>et al.</i> , 1989, 1990	Spacelab D1 1985	InP:S/In	3.7	0.023	Striations are less pronounced than on the ground. Type II striations (macrostep related) have been studied.
Danilewsky <i>et al.</i> , 1994	Spacelab D2, 1993	GaAs:Te/Ga	1.3	0.02	Growth rate was identical in μg and on ground. Dopant distribution more homogeneous in space.
Danilewsky <i>et al.</i> , 1996(I)	EURECA, 1992	AlGaSb/Ga	4 and 4.2	0.01	Growth rate 20 % lower in μg and less heterogeneity occurred. No type II striations.
Danilewsky <i>et al.</i> , 1996(II)	EURECA, 1992	InP:S/In	5.9 and 6.8	0.015	Destabilisation occurred as the growth rate was higher than on the ground. Diffusive axial segregation. Radial segregation is related to interface shape. Striations are related to the orbital period (Boschert <i>et al.</i> , 1999)
Eiche <i>et al.</i> , 1996	EURECA, 1992	CdTe:Cl/Te	10	0.022 and 0.05	Destabilisation of the interface in μg , prevented on the ground by convective mixing.
Haar <i>et al.</i> , 1987	Spacelab D1, 1985	PbSnTe/PbSn	2.8	0.043	With rotation. Less striations. Perturbed by a bubble, then better. Electrical carrier mobility 6 times higher in μg .

(continued overleaf)

Table 17.3 (continued)

Ref.	Flight	Material	Size (mm)	Growth rate ($\mu\text{m s}^{-1}$)	Results
Inatomi <i>et al.</i> , 1999	Parabolic flight and drop tube	GaP/Ga			Observation of the interface morphology through the substrate by IR interferometry. Facets are seen and growth rate is decreased compared to on the ground.
Kodama <i>et al.</i> , 1990, 1994, 1998 Suzuki <i>et al.</i> , 1995	TEXUS 19, Spacelab D2, STS-40, Jap. Satellite	GaAs:Sn/Ga GaAlAs/GaAl	0.2		Cubic Ga or Ga-Al solvent surrounded by 6 substrates. Only Type II striations (interface morphology) are observed in space. The dissolving and growing interfaces remain flat and smooth in space. Diffusion growth with constant diffusive flux and thermodynamical equilibrium. Higher growth rate in space.
Lockowandt <i>et al.</i> , 2001	Maxus 7 1996	SiC/Si-Sc	0.01	0.05	LPE growth from a Si-Sc solvent. Growth rate 1.5 times lower than on ground, showing that convection is not as negligible as generally believed. Better structural quality. The Sc incorporation is 100 times lower in μg .
Nagel and Benz, 1984	Spacelab FSLP, 1983	GaSb/Ga	0.15–0.2	0.052	Microsegregations are decreased in μg . Striations are limited to defected regions. On earth, strong rotational striations everywhere.
Regel and Nguyen Thanh Nghi, 1984	Salyut 6	GaP/Ga GaP:Zn,O/Ga			Diffusive transport and lower growth rate. Destabilized interface due to lower convection in space. Permitted computation of diffusion coeff. of P in Ga.

Rodot <i>et al.</i> , 1983	Salyut 6, 1979	GaAs/Ga	8	0.018	Higher growth rate and crystal quality in space. Striations.
Salk <i>et al.</i> , 1994	Foton 7-8	GaAs:Te/Ga CdTe and CdTeSe:Cl/Te	10	0.074	Partial growth under rotating magnetic field 400 Hz, 2 mT. The RMF generates a stable fluid flow improving the radial and axial distribution of electrical properties. Fewer deep levels gave good detector properties (Fiederle <i>et al.</i> , 1996)
Schönholz <i>et al.</i> , 1984	Spacelab FSLP, 1983	CdTe/Te	1, 5	0.07	Quality similar to on the ground.
Senchenkov <i>et al.</i> , 1999	Foton-11	InP:S/In	7.2, 8.3, 8.5	0.042	Under rotating magnetic field, 400 Hz, 2-1 mT. The RMF has an effect on the growth rate in μg , but not on the earth (already convective transport).

Table 17.4 Microgravity crystal-growth experiments from the vapor

Ref.	Flight	Material	Size (mm)	Growth rate ($\mu\text{m s}^{-1}$)	Results
Bruder <i>et al.</i> , 1986 Cadoret <i>et al.</i> , 1989	Spacelab D1, 1985 Spacelab SL1, SL3	CdTe HgI ₂	2, 4	0.07	Decrease of defect density with grown length. At quasiequilibrium, nucleation is sensitive to gravity condition. On earth, convection affects growth.
Coupat <i>et al.</i> , 1994	IML1	HgI ₂	2	0.005	Direct interaction between surface kinetics and vapor-phase transport. Better quality in space.
Eiche <i>et al.</i> , 1995	EURECA, 1992	CdTe:Cl	11.3	0.027	Axial symmetric resistivity due to segregation of chlorine and compensation.
Kimura <i>et al.</i> , 1994	Spacelab D2, 1993	InP	Layer		Thickness and shape are influenced by gravity on ground. Flat interfaces in space, transport governed by diffusion.
Launay <i>et al.</i> , 1988	Spacelab D1, 1985	Ge	Layer		Experiment on transport rates. The transport in space is purely diffusive. This permitted computation of the kinetic reaction parameters.
Piechotka <i>et al.</i> , 1998	STS-77, 1996	HgI ₂	5	0.001 to 0.03	Microgravity decreases mass transport by 17 %, showing that convection has an effect at 1g, in low-pressure ampoules.
Siche <i>et al.</i> , 2002	MIR, 1997 Foton 11	ZnSe			Transport rate much higher than expected from pure diffusion. Better quality of μg crystals.
Steiner <i>et al.</i> , 1999 Van den Berg, 1993	IML1	HgI ₂			Duplicate results obtained by Van den Berg in SL3. The 6 times increase of electronic transport properties is attributed to the absence, under μg , of impurity or I ₂ precipitates.

Van den Berg and Schneppe, 1989	SL3	HgI ₂	12	6g/96 h	Crystal-surface stability is much higher without convection, permitting an increase in the diffusive flow rate. Structural quality and electronic transport properties are improved.
Wiedemeyer <i>et al.</i> , 1975	Skylab 3-4, 1973-74	GeSe GeTe	millimetric		Considerable improvement of the μg crystals in terms of chemical and structural homogeneity. Transport much higher than expected from pure diffusion.
Wiedemeyer <i>et al.</i> , 1977, 1986	ASTP 1975	GeSeTe GeSSe, GeS	millimetric		Considerable improvement of the μg crystals in terms of chemical and structural homogeneity. Transport much higher than expected from pure diffusion.

- Bridgman growth. In Table 17.1, 42 experiments related to gradient freeze as well as Bridgman techniques are listed. Of course, the classical distinction between horizontal and vertical growth is not relevant in space.
- Floating-zone. Table 17.2 also includes growth from molten spheres and attached or levitated drops, giving a total of 35 experiments.
- Growth from solution, Table 17.3 with 15 experiments.
- Growth from the vapor phase. The 12 experiments in Table 17.4 include physical transport (evaporation/condensation of a specimen) and chemical vapor growth (a chemically active substance is used for the material transport in the vapor phase).

Ninety per cent of the experiments concerned classical semiconductors, the other ten per cent being essentially for detectors (HgI_2 , BGO). This is related to their interest for applications, to the technical industrial problem of crystal micro- and macrohomogeneity, likely to be significantly improved in space, and to the large amount of characterization methods available for these materials. One half of the experiments dealt with model materials, such as Ge or the antimonides, because of their low melting point and toxicity, with the aim to focus on specific physical or theoretical aspects. The others experiments were focusing on application-oriented crystals such as GaAs, InP or II-VIs. Si is a special case because most of the related experiments focused on capillary convection.

17.2 EXPERIMENTAL AND TECHNOLOGICAL ENVIRONMENT

17.2.1 Technical limitations: time, size, power and space management

There are several ways to perform experiments under microgravity conditions. One classical classification concerns the duration of weightlessness provided.

Drop towers and free-fall tubes offer experimental times of a few seconds, planes following parabolic trajectories offer tens of seconds and sounding rockets minutes. Only very specific experiments can be performed, either on very small samples or with very high growth rates. Indeed some physical problems related to crystal growth (microsegregation, wetting, etc.) have been successfully investigated by these means.

The space shuttle offers experiment durations of some hours and this has been an important source of microgravity experiments on crystal growth because, with such durations, crystals with useful dimensions, for characterization purposes for example, can be grown at classical growth rates.

Finally, space stations and automatic satellites permit the growth of large crystals even at very low growth rates, with experiment duration longer than one week.

From a technical point of view, space crystal-growth facilities are generally designed to provide the experimenter with (Fig. 17.1):

- A vacuum-tight metallic cartridge or fused-silica ampoule in which the investigator should integrate all the pieces necessary to perform the experiment: sample, single-crystal seed, crucible, getters (for atmosphere quality), thermal insulation, thermocouples, electrodes, etc. Typical dimensions are internal diameters from 8 to 25 mm and useful length from 50 to 300 mm.
- A furnace able to reach predetermined temperatures (generally up to 1200°C) and thermal gradients. Some facilities provide a pulling mechanism of the cartridge or

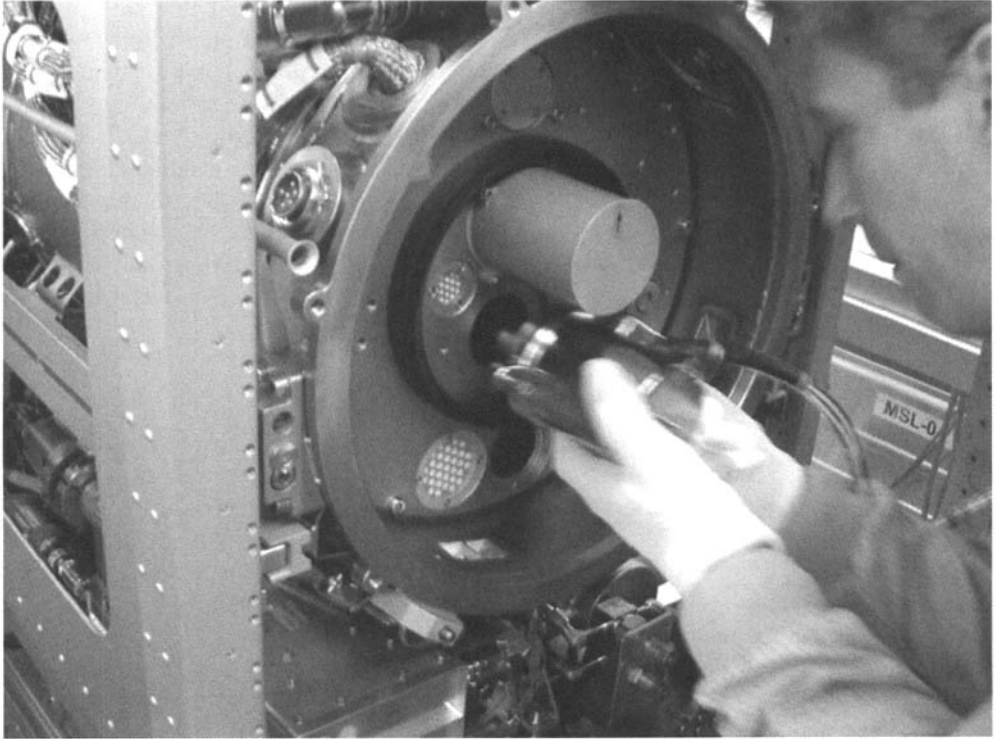


Figure 17.1 European astronaut Thomas Reiter, during International Space Station crew ground training, is inserting an experimental cartridge in a furnace of the Microgravity Science Laboratory. Courtesy: European Space Agency

of the furnace. Technologies are based on multizone resistance heating in the case of metallic cartridges, generally devoted to Bridgman or vapor-phase growth, and on mirror furnaces for fused-silica ampoules, generally devoted to experiments involving a molten zone.

—Electronics designed to apply a predetermined thermal and pulling program to the facility and to interface the thermocouple or electrode readings coming from the cartridge. Some facilities offer the opportunity of real-time modification of the thermal profile, via radio operation. Some are equipped with diagnostic capabilities, such as Peltier pulse marking, thermoelectric (Seebeck) or resistivity measurements.

In space, energy is scarce. Sounding rockets and the space shuttle take the energy from batteries, whose weight is a critical aspect of the mission-payload definition. Space stations and retrievable satellites are energized through photovoltaic panels, generally limited in terms of instantaneous power. Therefore the furnaces are designed to reach the required temperatures with overall power limited to 500 W or 1 kW, including the energy necessary to operate the electronics, motor and vacuum pumps.

The scientist has to deal with another constraint concerning the overall timetable of microgravity experiments. Generally, the experiments are submitted in the framework of a call for proposals issued by the space agencies. Once the experiment is selected, it is

necessary to wait for a flight opportunity, then to develop the specific flight hardware with a number of preliminary, qualification and engineering tests. The samples, sometimes the entire set of data, are often delivered several months after the flight. Finally, owing to the unique character of the specimens, characterization procedures are performed step by step and it is often necessary to wait for characterization results before going through the next steps, especially in the case of destructive techniques. Just to give an example, the author submitted the LMS-AGHF-ESA8 experiment in 1988, it flew in 1996, so that 9 years passed between the experiment submission and the publication of the first results (Duhanian *et al.*, 1997). The situation may be even worse: when the shuttle program experienced the dramatic Challenger accident, all scientific experiments suffered a 5-year delay.

17.2.2 Environmental limitations: the gravity level

The 'microgravity' term is the source of a common error. In fact, the absolute gravity level is quite high in a spacecraft, some 8.4 ms^{-2} in the space shuttle orbiting at an altitude of 500 km. The gravity forces are counterbalanced by the centrifugal forces due to the orbiter rotation around the earth, so that all equipments onboard are in a situation similar to free-fall under vacuum. The correct term should normally be 'weightlessness' or, more precisely, 'microweightlessness'. However, microgravity is the generally accepted term, due to the fact that the feeling, especially experienced by the astronauts, is as if there was no gravity at all.

The most important parameter, the basis of all these crystal-growth experiments, is obviously the actual acceleration experienced by the liquid sample. The initially rather naïve expectation that all gravity-related effects vanish in space quickly gave way to a more realistic view. In practice, the residual acceleration vector acting on the sample is not negligible at all. It can be divided into a quasisteady part and another part fluctuating in both amplitude and direction (Hamacher *et al.*, 1987).

Stationary residual acceleration is due to the drag of the residual atmosphere on the spacecraft, to the gravity gradient along the sample, related to the attraction exerted on it by the spacecraft center of mass and to any rotation of the spacecraft around its center of mass. Typical values are 10^{-6} times the terrestrial gravity g_0 , depending on the mass and size of the spacecraft and the distance of the experiment to the center of mass.

Fluctuating accelerations (also referred as g -jitters) are related to mechanical systems (pumps, motors, typical frequency 10–100 Hz), to crew activity (0.1 to 10 Hz), to structure vibrations (10^{-2} Hz) and, more generally, to any activity leading to a redistribution of the mass locations inside the orbiter. They can reach $10^{-2}g_0$, but due to their random, high-frequency and compensating nature, they are not expected to cause large motions in the melt. Some fluctuations, including solar or terrestrial gravity fields, are also related to the orbital period ($10^{-5}g_0$, 10^{-3} to 10^{-4} Hz) and their effect has been observed in some samples (Boschert *et al.*, 1999; Zemskov *et al.*, 2001).

Crystals are generally grown at low growth rates, and the quantity solidified in one second is of the order of, or less than, one micrometer. Therefore fluctuations with frequencies higher than 1 Hz cannot be experimentally observed in the samples. Furthermore, in practice, the viscosity of melts and diffusion coefficients of solutes are such that momentum, mass and solutal transfers at frequencies higher than 10^{-1} or 10^{-2} Hz are filtered. Then crystal growth is essentially sensitive to low frequencies. Unfortunately, accelerometers rarely have the capability to measure residual accelerations below 10^{-3} Hz and the

knowledge of the effective acceleration level acting on an experiment is mainly based on mathematical computations of the mechanical state of the spacecraft.

17.3 SCIENTIFIC ACHIEVEMENTS

17.3.1 Segregation studies in Bridgman configuration

Chemical segregation, of the constituents or of the dopant, is a key problem during crystal growth, both from the theoretical and applied points of view. It has been proved that, under purely diffusive transport conditions in the liquid phase, axially homogeneous crystals are obtained, after an initial transient (Tiller *et al.*, 1953). On the contrary, when strong natural or forced convection homogenizes the liquid, the chemical concentration in the crystal evolves continuously. For intermediate situations, generally encountered during classical growth on the ground, the behavior is more complicated and it is only recently that a full understanding has been obtained, but for diluted materials only. A rule of thumb is that axial segregation is perturbed by convection when the convective liquid velocity, in the vicinity of the solid/liquid interface, is close to, or higher than, the growth rate.

The radial segregation (i.e. segregation along the radius of a crystal or wafer) obeys more complicated laws and is related to the curvature of the solid/liquid interface and to the level of convection. For a very low (respectively, high) convective level, the liquid is homogenized by diffusion (respectively, convection) and radial segregation is low. For intermediate convective levels, it can be very high, with a maximum when the liquid velocity is of the order of the growth rate.

Microsegregation is a generic term for a random or periodic chemical concentration fluctuation along the crystal axis or radius. It can be caused by growth-rate fluctuations, due to technical problems or to heat-transfer variations (possibly related to convection in the melt). Nonstationary convection influences the amount of solute reaching the solid/liquid interface and is the other cause of microsegregation.

Natural convection was thus recognized as the key source in the problem of segregation in crystal growth from the melt. Due to the unavoidable thermal gradients in the liquid phase during any crystal-growth process, and the associated buoyancy convection, it is impossible to get purely diffusive transport conditions on earth. Therefore experimentation under microgravity conditions has been extensively used with the aim of reaching convection-free growth conditions.

The results of the pioneering experiments by Witt *et al.* (1975), clearly showing the ability to obtain the theoretical plateau under a diffusive regime, gave rise to a strong optimism in the future of growing homogeneous semiconductors in space, including industrial production. However, subsequent attempts to obtain the same results with larger or concentrated samples gave less enthusiastic conclusions and it became obvious that residual gravity accelerations were acting in the system, in a rather complicated manner.

From the point of view of axial segregation, both diffusive (see Fig. 17.2) and convective (see Fig. 17.3) transport regimes were obtained under microgravity conditions. Figure 17.4 is a plot in nondimensional numbers of the regions where diffusive or convective segregation curves are expected to be obtained. The Grashof-Schmidt number is a measure of the natural convection in the experiment and of its effect on solute transport:

$$\text{GrSc} = \beta g \nabla T L^4 / \nu D$$

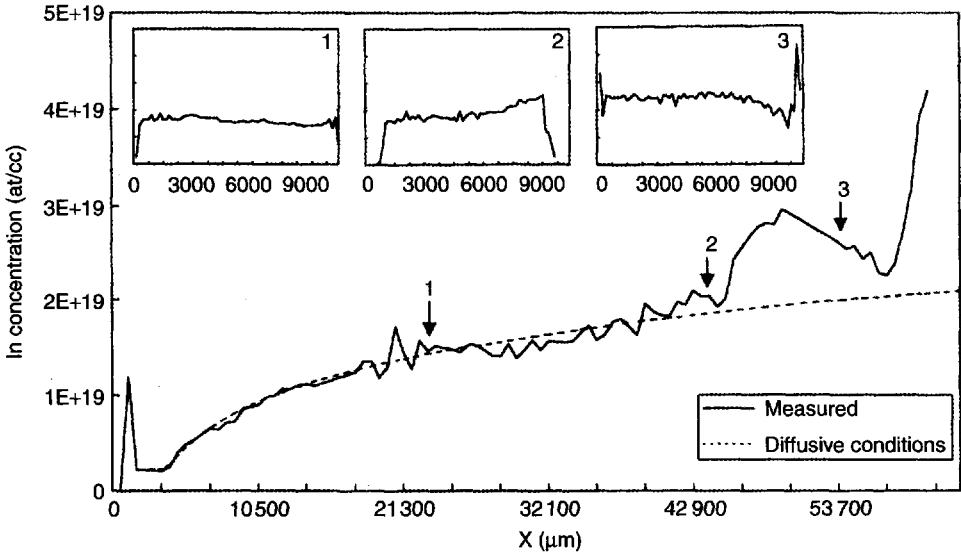


Figure 17.2 The axial chemical segregation of In in a $Ga_{0.99}In_{0.01}Sb$ crystal grown by the Bridgman method onboard the EURECA automatic satellite. Due to the very low value of the residual gravity during this flight, the experimental data fit well with the theoretical prediction in the case of diffusive transport in the melt. The bump after 43 mm of growth is attributed to trapping of the solutal boundary layer by a sudden increase of growth rate. Insets are radial-segregation curves showing the effect of residual convection. (Duffar *et al.*, 1998)

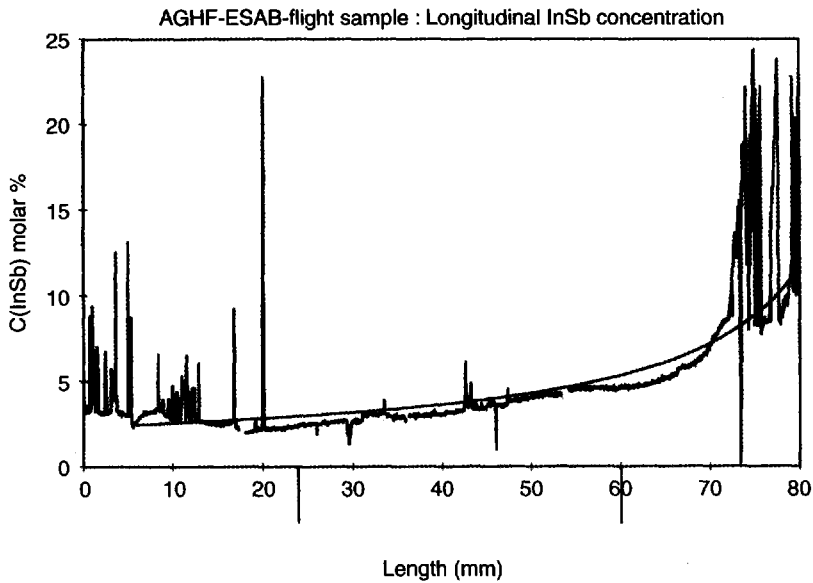


Figure 17.3 Segregation of In during the Bridgman growth of $Ga_{0.8}In_{0.2}Sb$ during the LMS space-lab mission. The line is the theoretical segregation curve in the case of full mixing in the melt. (Duhanian *et al.*, 1997)

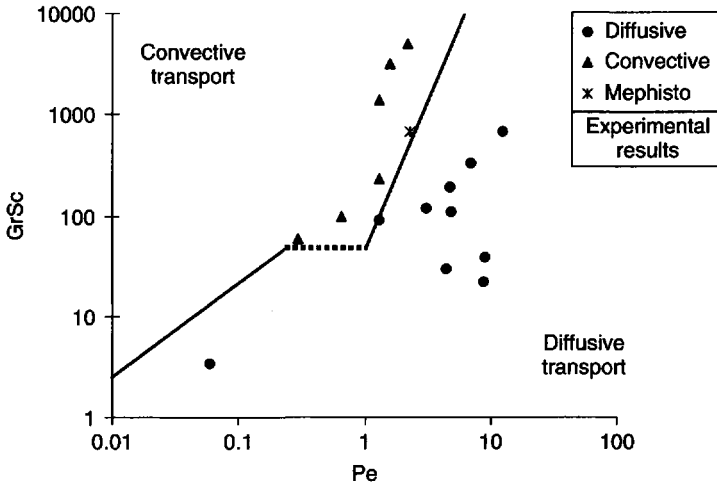


Figure 17.4 This GrSc/Pe diagram can be understood as a convection/growth rate diagram. The two straight lines are the theoretical predictions for the transition between diffusion-dominated transport in the melt (lower right side) and convection-dominated transport (upper left side). The points correspond to all the experiments performed in space for which diffusive (dots) or convective (triangles) transport has been experimentally and unambiguously identified. The Mephisto point corresponds to the experimental transition obtained by varying the growth rate (Pe) at constant convective level

where β is the coefficient of thermal expansion of the liquid, g the actual gravity acceleration, ∇T the thermal gradient acting on the liquid, L a typical dimension of the experiment (for example the diameter), ν the liquid viscosity and D the diffusion coefficient of the solute in the melt.

A major problem is concerned with the value of the residual gravity level, g , effectively acting on the fluid and consequently on the segregation. For example, in the case of the Skylab experiments, authors give values ranging from $10^{-4}g_0$ (Walter, 1977) to $10^{-6}g_0$ (Yue and Vottmer 1975). For Salyut, it is estimated to change between $5 \times 10^{-5}g_0$ and $9 \times 10^{-7}g_0$, depending on the station attitude (Kashimov, 1979). A careful analysis of the Bridgman space experiments evidencing convective mixing has been performed (Duffar *et al.*, 1999a, b): order-of-magnitude arguments led to the conclusion that the effective gravity level acting on the segregation in the shuttle experiments is $10^{-5}g_0$. This conclusion is confirmed by numerical simulations trying to compare the experimental segregation results with the melt hydrodynamics (Kinoshita *et al.*, 1997, Bune *et al.*, 1997).

The Peclet number is a measure of the growth rate R , normalized by the experiment dimension and the diffusion coefficient:

$$Pe = RL/D$$

The straight lines in Fig. 17.4 correspond to the theoretical prediction of the limit between diffusion dominated and convection dominated solute transport regimes in the melt (see Garandet and Duffar 2001 for a complete analysis of the segregation problem in microgravity).

The points represent the results of all the space experiments that gave useful and unambiguous axial segregation data. They are the experiments in Table 17.1 for which a Pe and a GrSc number have been calculated and for which a clear conclusion on the diffusive or convective transport has been drawn. It can be seen that all the experimental results for which the chemical segregation is typical of a diffusive (respectively, convective) transport are in the diffusive (respectively, convective) area of the diagram.

The situation regarding the axial segregation is clear but it is not the same for the radial-segregation problem. Theoretically, radial segregation is supposed to be maximum for the experiments close to the straight lines in Fig. 17.4. As ground-based experiments are performed under rather strong convective motion, theoreticians agree on the fact that radial segregation must generally be higher under microgravity conditions than on earth. However, experimenters paid little attention to the radial-segregation phenomena up to now and very few experimental results are available (see Fig. 17.2 for an example). Some results suggest this behavior but are insufficient to fully support this prediction. Some experimenters looked at the effect of a modification of the direction of the gravity vector with respect to the sample axis. It was shown that the radial segregation is enhanced when the gravity vector is offaxis and the results agreed qualitatively with the theoretical models of the phenomena (Gillies *et al.*, 1997).

Regarding microsegregation, there are very few quantitative data, but most of the authors recognized that striations are decreased when the experiment is performed in space with respect to similar experiments on the earth. Only the MEPHISTO experiment, on Sn:Bi metal, owing to its diagnostic capabilities, permitted correlation of the effect of a calibrated transient gravity perturbation with the numerical simulation of heat, momentum and solute transfer in the experiment (Alexander *et al.*, 1997).

17.3.2 Experiments of crystal growth from a molten zone or molten drop

Table 17.2 gives an overview of the space crystals grown from a floating zone. Three experiments involving a molten drop are also included. It can be seen that these experiments are a German specialty, probably because Germany has industrial interest in float zoning of silicon. Marangoni numbers (Ma), which characterize the intensity of the thermocapillary flow, are computed following the expression:

$$\text{Ma} = -\frac{\partial\sigma}{\partial T} \frac{\nabla T z^2}{\nu\rho\kappa}$$

where $\partial\sigma/\partial T$ is the variation of surface tension with temperature, ρ the density and κ the thermal diffusivity. For the sake of comparison z is always taken as half of the zone length given in the table, because generally the zone is heated from the middle and therefore the temperature gradient causing the thermocapillary convection, ∇T , acts only on the half-zone length. However, depending on the growth configuration, the thermal gradient may act on a larger length, sometimes the full zone.

The trigger for this research was the paper from Chang and Wilcox (1975) who speculated on the predominant effect of unstable Marangoni convection on the existence of dopant segregations and striations in floating-zone silicon single crystals. Due to the

unavoidable buoyancy-driven convection, it was difficult to demonstrate this effect on earth: attempts to grow crystals with a coated surface led to decreased striations, but it was difficult to draw a clear conclusion. Obviously, space experiments could clarify the situation and the pioneering work was performed by Eyer in the First Spacelab Flight and also in sounding rockets, demonstrating unambiguously the predominance of Marangoni convection, even on the earth. Cröll continued this work and, with a sequence of well-designed experiments, including coated and partially coated melts and magnetic fields, he totally clarified the situation by evaluating the critical Marangoni number for the onset of unsteady convection and, consequently, of striations.

Attempts to apply this kind of experiment to germanium led to the general conclusion that germanium melts are covered with an oxide layer preventing the capillary convection from reaching the critical value. However, Marangoni convection did exist in germanium, but at a lower level than expected theoretically, so that authors generally concluded that the oxide layer would only partially cover the melt and therefore the capillary convection would not be totally blocked. The effect of the dopant on the solutally induced capillary convection has also been clarified.

Experiments by Müller and by Cröll, during the D2 Spacelab mission, dramatically demonstrated the capability to grow GaAs up to 20 mm in diameter in space, with a greatly enhanced structural quality (Fig. 17.5). On earth, only crystals up to 6 mm in diameter can be grown, because the density of the melt is too large, making it impossible to maintain the stability of larger liquid zones. Similarly, InSb and GaSb crystals up to 16 mm in diameter were obtained. In the case of GaSb, Cröll *et al.* (1986) obtained the critical Marangoni number in space, something that is impossible on earth because the allowed liquid zones are too small. This permitted experimental verification of the variation of the critical Marangoni number with the Prandtl number, as predicted by numerical simulations (Fig. 17.6):

$$\text{Ma}_{\text{Cr}} = 2.2 \times 10^4 \text{Pr}^{1.32}$$

The agreement between the calculated and measured hydrodynamic frequencies is also good. On this point, one experiment clearly showed that a wide spectrum of frequencies can be obtained in some cases. Recent experiments have shown that temperature and growth-rate oscillations, with a frequency of 0.5 to 1 Hz, are perfectly correlated to striations in the crystal. These experiments permitted evaluation of the critical Ma number between one unsteady loop to several loops: 1500 for Si. Azimuthal temperature differences also generate azimuthal thermocapillary movements.

For all the materials, striations are less pronounced in space, suggesting that buoyancy-driven convection on earth, even when stable, enhances the effect of the unsteady capillary convection. Attempts to block the thermocapillary flow in space by magnetic fields, either in Si, Ge, InSb or GaAs, were not successful, in spite of a significant damping. This was due to field magnitudes being too low, as calculated by Müller and Rupp (1991). Experiments of floating zones encapsulated in viscous liquids have shown that Ma convection can be blocked and generally led to good-quality crystals.

It is worth noting that an experiment was devoted to BGO, Fig. 17.7. In spite of numerous microcracks, due to rapid cooling, the quality of the crystal was found to be better than typical earth-grown crystals.

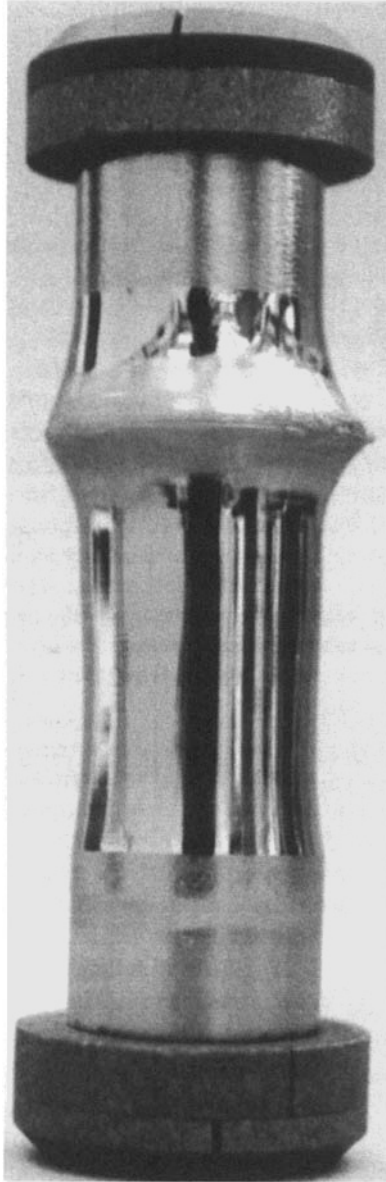


Figure 17.5 GaAs crystal obtained during the D2 Spacelab mission by the floating-zone method. The crystal is 20 mm in diameter. By comparison, crystals up to only 6 mm in diameter can be grown by this technique on earth. (Herrmann and Müller, 1995)

17.3.3 Sample–crucible interactions and structural aspects

The majority of experimenters have reported about the detachment of samples from the crucibles during Bridgman crystal growth in space. This so-called detached growth can take several aspects, including bubbles at the interface between sample and crucible,

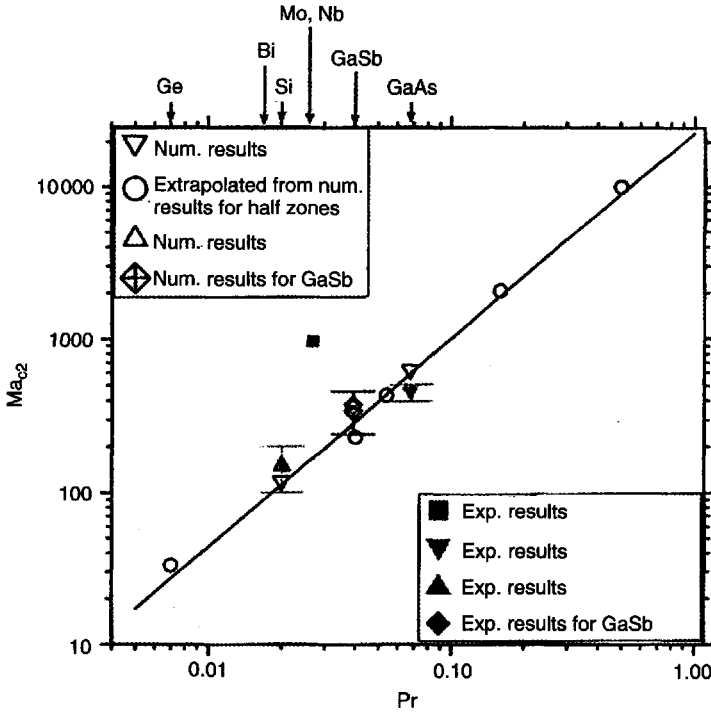


Figure 17.6 The critical Marangoni number between steady and oscillatory thermocapillary convection, Ma_{cr2} is shown to depend on the material Prandtl number, Pr . Experimental results obtained in space for Si, GaSb and GaAs agree well with the numerical predictions

a large decrease of the sample diameter (often called necking), and a constant small gap between the crystal and the crucible (Regel and Wilcox 1998, give a review of the observations).

If explanations for the two first cases are rather obvious and related to gas bubbles or differential wetting phenomena, it took a long time to get a satisfactory explanation for the third case, which has been given the name of 'dewetting' (Duffar *et al.*, 1997). The gap, in the solid state at the melting temperature, has been measured to be in the range 1 to 70 μm , depending on the configuration, and very uniform all along the sample. This is the sign of a very stable growth process. The crystal surface is generally shiny and wavy ridges are sometimes present (see right side of Fig. 17.8). Further space experiments have shown that the dewetting phenomenon is sensitive to the crucible material, to its roughness and to the cartridge-atmosphere purity, but not to the crystal growth rate. The explanation of the phenomenon, obviously correlated to the absence of hydrostatic pressure pushing the melt into strong contact with the crucible wall, involves the wetting behavior of the molten sample on the material, influenced by atmospheric purity and crucible roughness. In some cases, the existence of pressure differences between the hot and cold sides of the sample, possibly due to gas rejection at the solid/liquid interface, can have an effect, but it has been shown experimentally that this is not mandatory. The general configurations of dewetting are shown in Fig. 17.9. Theoretical predictions of the gap thickness are in good agreement with the measured values.

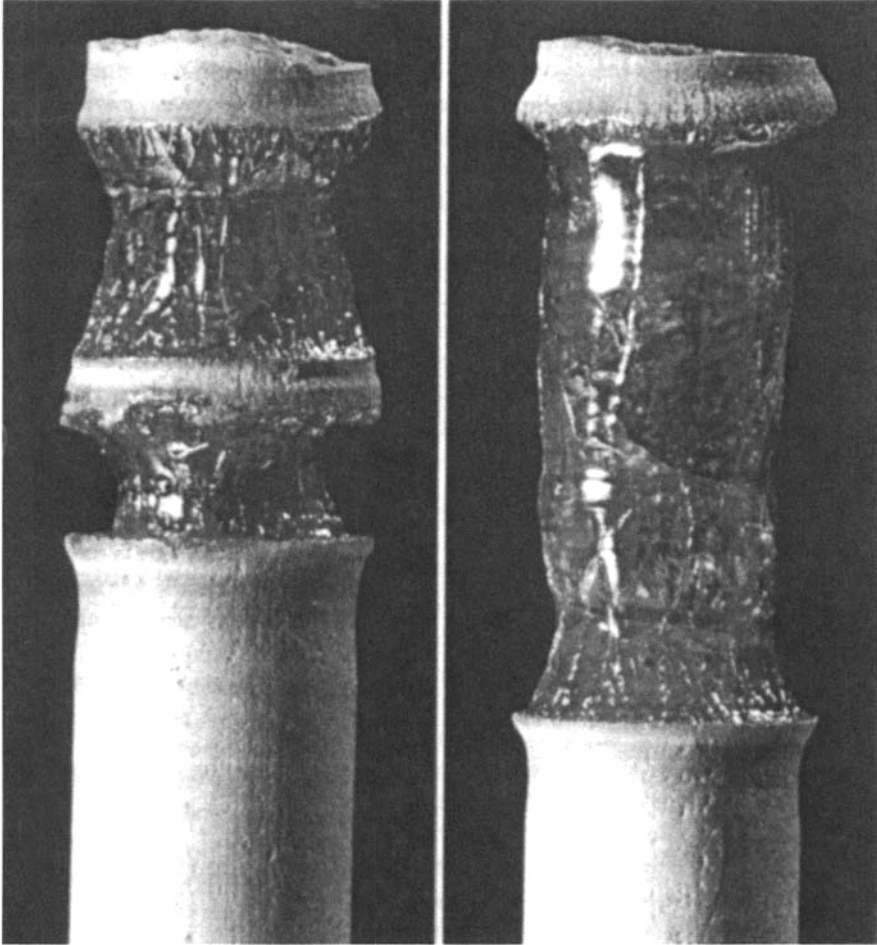


Figure 17.7 $\text{Bi}_{12}\text{GeO}_{20}$ crystals obtained by the floating-zone onboard the STS-77 flight of the shuttle (10 mm diameter). In spite of numerous microcracks, the optical and structural properties were improved compared to on the earth (Maffei *et al.*, 1997)

When no detachment was observed, the structural quality of space-grown crystals was very similar to that of crystals obtained on the earth. On the contrary, the structural quality was generally dramatically enhanced when detachment, and especially the dewetting phenomenon, occurred. It was also generally observed that, in samples with partial contact with the crucible, twins or grains appeared in the contact areas, but not on the detached ones. Furthermore, the transition from a fully polycrystalline material to a full single crystal has been obtained in a dewetted sample (Duffar *et al.*, 1998). The dislocation density in the grown ingots is also dramatically decreased, sometimes by two orders of magnitude, when there is no contact.

It can be concluded that microgravity by itself has no direct appreciable effects on the crystal quality but indirectly, through the absence of hydrostatic pressure and owing to the wetting phenomena, it may induce an improvement of crystal quality. Probably the

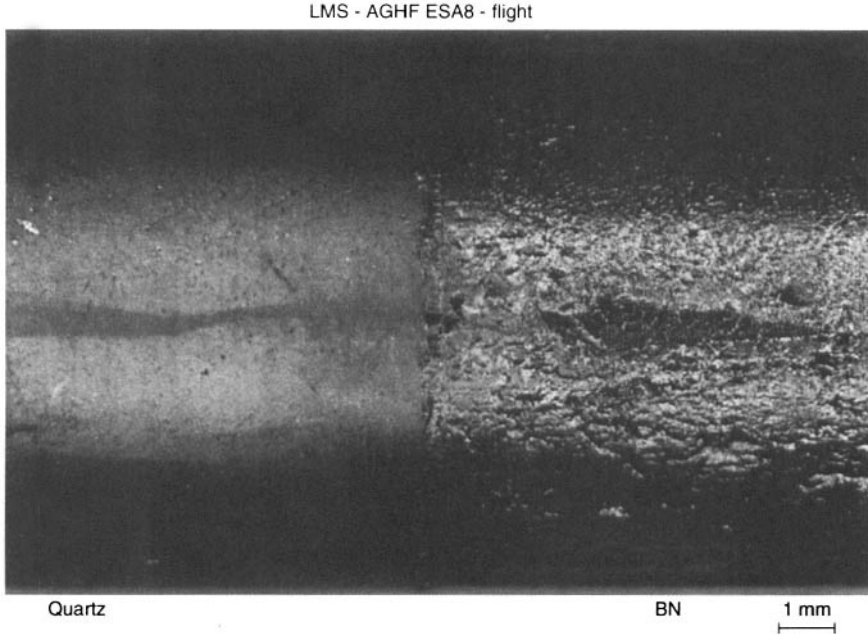


Figure 17.8 The external surface of a $\text{Ga}_{0.8}\text{In}_{0.2}\text{Sb}$ sample, 12 mm in diameter. On the right, grown in a BN crucible during the LMS Spacelab mission. Such a shiny and somewhat corrugated surface is typical of the occurrence of the dewetting phenomenon during the growth, associated with an increase of crystal quality. The gap between the sample and the crucible, taking into account the differential dilatation, was $30\ \mu\text{m}$ all along the 5 cm grown in BN ($\theta_{\text{GaSb}/\text{BN}} = 134^\circ$). On the left side, the crucible material changed to machined fused silica and no dewetting was observed ($\theta_{\text{GaSb}/\text{SiO}_2} = 112^\circ$)

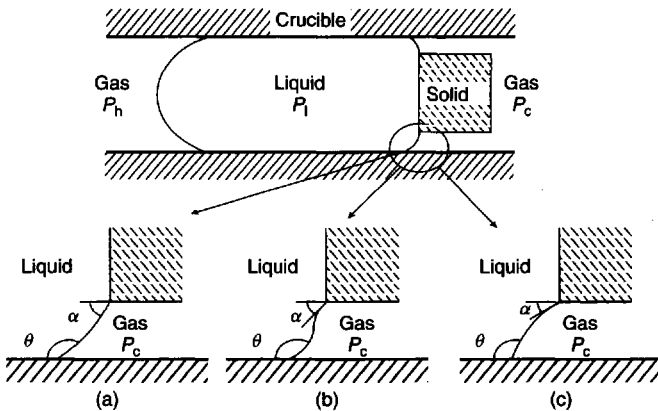


Figure 17.9 Classical dewetting configurations for a smooth crucible. θ is the wetting angle of the melt on the crucible and α the growing angle of the material. P_h and P_c are gas-pressure differences acting on the hot and cold sides of the sample. (a) No or low gas-pressure difference. The dewetting criterion is $\theta + \alpha \geq 180^\circ$. (b) Intermediate gas-pressure difference. (c) High pressure difference. Configurations (b) and (c) have also been obtained on the earth by applying a gas pressure on the crystal side of the sample

most significant and spectacular improvement has been obtained in CdTe crystals grown dewetted from carbon-coated silica crucibles (Larson *et al.*, 1994): compared to the best-known earth-processed samples, the dislocation density has been decreased by two orders of magnitude and neither grains nor twins appeared, while the residual mechanical stresses were also decreased. On earth, it is simply impossible to grow such CdTe single crystals from the melt and twins or grains always appear.

17.3.4 Growth from solutions

The saga of the THM solution growth under microgravity conditions has been written by the Kristallographisches Institut der Universität Freiburg, Germany. This travelling heater method is a combination of molten zone and of solution growth. In this case, the sample seed and feed and the molten solvent are enclosed in a tube and no Marangoni convection is supposed to occur (except in the case of unexpected bubbles). Because the material is dissolved at the advancing interface and deposited at the receding one, the crystal growth rate is influenced by the transport mechanism in the solvent (see Elwell and Scheel 1975, for general considerations in the field). However, it is generally measured by dividing the thickness of the grown layer by the deposition time, so that only a mean value is obtained. Segregation phenomena can occur if the sample is doped and here also the main interest has been focused on striations. A kind of striations, called 'type II striations' is related to the kinetics of the solution-growth process and is very difficult to study on the earth because of the masking effect of the convection-related striations.

GaSb:Te/Ga were grown in FSLP and D1 and InP:S/In in D1. Samples showed much less dopant striations, generally localised close to crystal defects (Benz *et al.*, 1987). There were very few rotational striations. Kinetic (type II) striations are also decreased but are much easier to observe. The macroscopic (axial) distribution of the dopant is also more homogeneous and all of this is attributed to the decrease of buoyancy convection in space. It is from these experiments that the Freigurger team constructed a theoretical explanation of the mechanism of formation of the kinetic striations (Danilewsky *et al.*, 1990), showing that a critical growth rate exists, below which there are no striations. This conclusion has been confirmed during the growth of GaAs:Te/Ga in D2 where type II striations were only found in the sample zones solidified at a high rate.

One remaining problem concerned the macroscopic chemical homogeneity because, due to the very low growth rate, of the order of mm day^{-1} , segregation is very sensitive to residual convection. CdTe:Cl/Te and CdTeSe:Cl/Te were grown onboard Russian Foton satellites, in 1991 and 1992. The novelty was the use of a rotating magnetic field. The result, as confirmed by careful numerical simulation of the hydrodynamics in the experiment, is that the well-defined and stationary convective motion, created by the magnetic field, improved the axial and radial homogeneity of the samples.

Three experiments were performed onboard the long-duration retrievable satellite EURECA. This permitted long crystals to be grown even with very low growth rate, and under particularly low microgravity values. AlGaSb/Ga and InP:S/In have shown a very good homogeneity, without any kind of striation. This has been the occasion to show that, in the THM process of compound materials, the axial segregation is mainly controlled by the dissolution at the advancing interface (GaSb and AlSb have different dissolution rates). For InP, the sulfur axial segregation is in perfect agreement with Tiller's law and radial segregation is related to the interface shape.

A few other space experiments have been devoted to semiconductor solution growth. In Salyut, GaAs/Ga showed type-II striations and interface destabilisation. The four times higher growth rate measured in space, compared to an earth sample, is still unexplained. GaP/Ga samples showed interface destabilisation and the growth rate versus deposition temperature plot evidenced diffusive transport in the melt and this permitted measurement of the diffusion coefficient and computation of the growth rate as a function of the Rayleigh number, for ground applications. Japanese researchers have grown AlGaAs/Ga and GaAs/Ga from hermetic Ga cubes. They found diffusive conditions and type-II striations. They explain a rather higher growth rate under microgravity by a constant diffusive flux associated to interface equilibrium. An important experiment focused on LPE growth of SiC from a Si/Sc solution. It was shown that, contrarily to the general assumption, convection is actually acting on the growth process.

17.3.5 Growth from the vapor phase

Two different methods can be used to grow crystals from the vapor phase; however, both are sensitive to convection in the gas, so that, under purely diffusive transport, the crystal growth rate should dramatically decrease.

The sublimation method involves direct transport of the material by evaporation from a hot reservoir and deposition at a colder site. Experiments on the growth of CdTe by this technique have clearly shown a diffusion-limited transport in the vapor phase. In this regard, it is important to know whether convection, in the case of systems with low vapor pressure, at the mbar level, still exists on the earth. A number of experiments have been performed with HgI₂ in order to try to answer this question, but they generally gave contradictory results. Sometimes, evidence of an effect of convection was found while in other cases no such effect was observed. In any case, all authors generally concluded that the physical phenomena involved in physical vapor sublimation, transport, nucleation and condensation are very complex and interactive and that possibly not all the relevant parameters had been totally controlled in these experiments. ZnSe has been grown in MIR and also showed better quality, with a growth rate similar to that on the earth.

As for the other method, called chemical vapor transport, a chemical reactant can be used to transport the material from a feed zone, at high temperature, to the growth zone, at a rather lower temperature. GeSe and GeTe have been grown by this technique onboard Skylab, using gaseous iodine as transport agent and GeSeTe and GeSSe by using chlorine during the ASTP program. In any case, the quality and size of the crystals were improved when grown in space. However, the growth rate was much higher than expected under purely diffuse transport in the vapor phase and the first hypothesis was a chemically driven gravitational convection. The problem was finally attributed to much more complex chemical-reaction systems than initially taken into account. This was proven during the STS-7 and D1 shuttle flights where simpler systems were used to grow Ge and GeSe: growth rates were within the error limits of theoretical predictions for diffusive transport. Launay *et al.* (1988) also used iodine for the transport of Ge during the D1 mission and diffusive transport was clearly evidenced. It has then been possible to compute the kinetic factors of the heterogeneous reaction governing the vapor-phase transport. During the D2 mission, InP was grown with chlorine transport and this experiment also demonstrated the better homogeneity of the space crystals and the diffusion-limited transport.

17.4 CONCLUSION AND FUTURE DIRECTIONS

Crystal growth under microgravity conditions is a 30-year-old discipline. Through some hundred experiments, it helped to investigate, and in several cases to solve, physical questions involved in the crystal-growth processes. Furthermore, a close look at the result columns in Tables 17.1–17.4 demonstrates that the quality of the crystals is generally improved in microgravity conditions, compared to on the earth. Crystals are more homogeneous, present fewer striations and better structural quality. The attempts to prepare electronic devices on substrates cut from space crystals have almost systematically shown a clear improvement and a better stability of the electronic or optical properties.

From the first encouraging results, it was foreseen that a truly industrial crystal-growth production would be valuable in space. However, further results have shown that, due to size, energy, time and, above all, unavoidable residual-gravity contingencies, this cannot be expected in the mid-term. However, microgravity research permitted elucidation of a number of scientific problems.

17.4.1 Summary of major breakthroughs

The effect of natural convection on axial chemical segregation in crystals has been clarified in the case of diluted alloys. Considering radial or microsegregation, some insights have been obtained, but further experimental efforts are needed to validate the existing theory. This is also the case for concentrated semiconductor alloys where the coupling between chemical field, hydrodynamics and the melting temperature makes things much more complicated.

The role of thermocapillary convection on the striations obtained in crystals grown from a floating zone has been identified and it has been shown that, even on earth, it is dominant over the buoyancy convection. Critical parameters for the onset of convective instability have been determined. The occurrence of striations in the THM solution growth method was also understood with the help of space experiments.

Owing to the dewetting of the crystals from the crucibles, it has been possible to investigate and quantify the effect of crucible adhesion on the generation of twins, grains and dislocations. CdTe single crystals grown in space exhibit a dramatically better quality than those obtained on earth.

Crystal-growth experiments from the vapor phase have shown the usefulness of the microgravity environment to get a better understanding of the chemical reactions and kinetics. In this respect, it is strange that only a small number of experiments have been performed on this topic.

The better understanding of crystal-growth processes gained from experiments performed under microgravity permitted the development of new technologies on the ground, including the use of magnetic fields or baffles in order to decrease the convective level in Bridgman, Czochralski or floating-zone techniques.

The use of gas-pressure differences in order to counterbalance the hydrostatic pressure and avoid crystal–crucible contact allowed the achievement of dewetting conditions also on earth, and consequently provided improved GaSb (Duffar *et al.*, 2001) and CdTe (Chevalier *et al.*, 2004) crystals. This is a unique example of a terrestrial technical process directly arising from a microgravity discovery.

17.4.2 Problems still to be investigated and perspectives

On the chemical-segregation problem, very few papers give quantitative information about the radial segregation in the samples and it is not possible to know if the experiments close to the theoretical lines in Fig. 17.4 show a higher segregation compared to the experiments far from this boundary. It can be seen in the table that authors often conclude that radial segregation is due to interface curvature, even in the case where they do not characterize this curvature by intentional mechanical or electrical marking. This point deserves more careful attention in the future because it can a priori be expected that radial segregation is, on the contrary, rather attributed to residual convection.

A general remark is that the process parameters required in order to draw conclusions on the segregation behavior are either missing or of poor quality. The shape and curvature of the solid/liquid interface is also of interest and fluctuation or evolution of these parameters should also be given. Comparison with the thermal field in the cartridge as computed by numerical simulation of the heat fluxes can also be very useful. From the sample-evaluation point of view, chemical segregation should be measured axially and radially and fluctuations, if any, must be characterised by amplitude and frequency. Clearly there is a need for further experiments using in situ measurements in order to quantify precisely the crystallization parameters.

A few experiments, performed under extremely high growth rates, have given single crystals with good structural quality. There is a need to clarify such behavior. The dewetting phenomenon by itself has never been directly observed and various theoretical descriptions of the phenomenon are still under study. Video recording of the advancing interface is expected to clarify the situation.

In the field of vapour growth, there is a need for carefully designed experiments. A critical point is the fact that a number of experiments have shown growth rates of the same order as those observed on the ground, in contradiction with theoretical prediction. Similarly, unexpectedly high growth rates have been measured during solution growth in space. The growing technological importance of the PVT growth process for SiC should boost interest in complementary microgravity experiments.

During the past 30 years, the science of growing crystals has gained benefit from the experiments performed under microgravity conditions. Meanwhile, the experimental techniques evolved and the new generation of space growth facilities, especially designed in view of the International Space Station, are equipped with in situ diagnostic equipments, aiming to investigate, in better conditions, the remaining microgravity-relevant problems.

REFERENCES

Comments and additions to the list of references, if any experiment or important publication in the field is missing, would be very much appreciated.

Abbaschian R., Lopez C., Gokhale A., Jensen E., and Raman R. (1996) 'Liquid encapsulated float-zone of InBi in microgravity' *Solid. Sci. Process.* I. Ohnaka and D.M. Stefanescu (Eds). The Minerals, Metals and Materials Soc., 319–329

Alexander J.I., Garandet J.P., Favier J.J., and Lizee A. (1997) 'G-jitter effects on segregation during directional solidification of tin-bismuth in the Mephisto furnace facility' *J. Cryst. Growth* **178** 657–661

- Ang C.Y., and Lacy L. (1979) 'Gravitational influence on the liquid state homogenization and solidification of aluminum antimonide' *Met. Trans. A* **10A** 519–528
- Artemyev V.K., Folomeev V.I., Ginkin V.P., Kartavykh A.V., Mil'vidskii M.G., and Rakov V.V. (2001) 'The mechanism of Marangoni convection influence on dopant distribution in Ge space grown single crystals' *J. Cryst. Growth* **233** 29–37
- Averyanov I.S., Nesmelova I.M., Baryshev N.S., and Belozherov A.F. (1999) 'Cadmium mercury telluride grown in space' *J. Opt. Technol.* **66** 342–343
- Barmin I.V., Egorov A.V., and Senchenkov A.S. (1992) 'Results of crystal growth experiments by FZM on Zona facilities in microgravity' *Proc. VIIIth Europ. Symp. Materials and Fluid Sciences in Microgravity*, Brussels, 12–16 April 1992, ESA SP-333, 591–596
- Benz K.W., Danilewsky A., Notheisen B., and Nagel G. 'Growth of III-V semiconductors by the travelling heater method under microgravity' *Proc. 6th Europ. Symp. Material Sciences under Microgravity Conditions*, Bordeaux, 2–5 December 1986 (ESA SP-256, 1987) 345–347
- Bollong A.B., and Proux G.T. (1989) 'Analysis of Cd_{0.21}Hg_{0.79}Te quenched in 10⁻⁴g' *J. Cryst. Growth* **94** 475–480
- Bourgeois S.V., and Spradley L.W. (1976) 'Thermocapillary convection in microgravity crystal growth melts of InSb' *Lett. Heat Mass Transfer* **3** 193–204
- Boschert S., Danilewsky A.N., and Benz K.W. (1999) 'Numerical simulation of the influence of the orbiters attitude on the μ g growth of InP:S crystals from an In solution during the EURECA-1 flight' *J. Cryst. Growth* **205** 92–96
- Bruder M., Dian R., and Nitsche R. 'Vapour zone crystallization of cadmium telluride' *Scientific Results of the D1 Mission*, Norderney, 27–29 August 1986, 288–292
- Buhrig E., Schwichtenberg G., and Patold O. (2000) 'Growth of Zn-doped germanium under microgravity' *Cryst. Res. Technol.* **35** 911–919
- Bune A.V., Gillies D.C., and Lehoczky S.L. 'Numerical modeling of HgCdTe solidification: effects of phase-diagram, double-diffusion convection and microgravity level' *Proc. Xth Europ. and VIth Russ. Symp. Physical Sciences in Microgravity*, St Petersburg, 15–21 June 1997, 26–33
- Cadoret R., Brisson P., and Magnan A. (1989) 'HgI₂ nucleation experiments performed in the SL1 and SL3 flights' *Nucl. Instrum. Methods Phys. Res. A* **283** 339–347
- Calzadilla A.O., Mosina G.N., Ratnikov V.V., Sorokin L.M., Tregubova A.S., Fuentes J., Shulpina I.L., and Scheglov M.P. (1991) 'Specific features of crystallization of In-doped Ge under Microgravity' *Microgravity Sci. Technol.* **IV/3** 172–178
- Camel D., and Tison P. 'Semi-confined Bridgman growth of Ge:Ga in Maser-2' *Proc. VIIth Europ. Symp. Materials and Fluid Sciences in Microgravity*, Oxford, 10–15 September 1989, ESA SP 295 (1990) 63–68
- Camel D., Tison P., and Carlberg T. 'Floating zone crystal growth of Ge' *Proc. Scientific Results of the D2 Mission*, Norderney, (1994) 494–501
- Carlberg T. 'A preliminary report on floating-zone experiments with Ge crystals in a sounding rocket' *Proc. 5th Europ. Symp. Material Sciences under Microgravity*, Schloss Elmau 5–7 November 1984, ESA SP- 222, 367–373
- Carlberg T. (1986) 'Lateral solute segregation during floating zone crystal growth under different gravity conditions' *J. Cryst. Growth* **79** 71–76
- Chang C.E., and Wilcox W.R., (1975) 'Inhomogeneities due to thermocapillary flow in floating zone melting' *J. Cryst. Growth* **28** 8–12
- Chen N.F., Zhong X., Lin L., Xie X., and Zhang M. (2000) 'SI-GaAs grown in outer space' *Mater. Sci. Eng. B* **75** 134–138
- Chen N.F., Zhong X., Lin L., Zhang M., Wang Y., Bai X., and Zhao J. (2001) 'Comparison of FET characteristics between space grown and earth grown GaAs single crystal substrates' *Appl. Phys. Lett.* **78** 478–479
- Chen W.C., Mai Z.H., Ma W.Y., Jia S.Q., and Xu, L. (1990) 'Growth of α -LiIO₃ crystal under microgravity conditions' *J. Cryst. Growth* **99** 1273–1275

- Chen W.C., Li C.R., and Liu D.D. (2003) 'Post research on α -LiIO₃ crystal growth in space' *J. Cryst. Growth* **254** 169–175
- Chernov A.A., Maksimovskii S.N., Vlasenko L.A., Kholina E.N., Martovitskii V.P., and Lev-tov V.L. (1984) 'Growth of germanium crystals with low dislocation density in a condition of weightlessness' *Sov. Phys.-Crystallogr.* **29** 222–225
- Chevalier N., Dusserre P., Garandet J.P., and Duffar T. (2004) 'CdTe single crystal growth on earth by the dewetting process' *J. Cryst. Growth* **261** 590–594.
- Coupat B., Badaud J.P., Fournier J.P., Er-Raji S., Cadoret R., and Magnan A. (1994) 'Interactions between growth kinetics and physical vapour transport of HgI₂ in microgravity' *J. Cryst. Growth* **141** 465–472
- Cröll A., Müller W., and Nitsche R. (1986) 'Floating-zone growth of surface coated silicon under microgravity' *J. Cryst. Growth* **79** 65–70
- Cröll A., Müller W., Nitsche R. and Kölker H. 'Floating zone crystallization of silicon' *Proc. Norderney Symposium on the Results of the D1 German Mission*, 27–29 August 1987, DFVLR Ed. 1987, 260–264
- Cröll A., Muller-Sebert W., Benz K.W., and Nitsche R. (1991) 'Natural and thermocapillary convection in partially confined silicon melt zones' *Microgravity Sci. Technol.* **III** 204–215
- Cröll A., Dold P., and Benz K.W. (1994) 'Segregation in silicon floating-zone crystals grown under microgravity and in magnetic field' *J. Cryst. Growth* **137** 95–101
- Cröll A., Schweizer M., Tegetmeier A., and Benz K.W. (1996) 'Floating-zone growth of GaAs' *J. Cryst. Growth* **166** 239–244
- Cröll A., Kaiser Th., Schweizer M., Danilewsky A.N., Lauer S., Tegetmeier A., and Benz K.W. (1998) 'Floating-zone and floating-solution-zone growth of GaSb under microgravity' *J. Cryst. Growth* **191** 365–376
- Crouch R.K., Fripp A.L., Debman W.J., Woodell G.A., Clark I.O., Carlson F.M., and Sim-chick R.T. 'Results from a compound semiconductor crystal growth experiment in a low gravity environment' *1st Int. SAMPE Electronics Conf.*, 23–25 June 1987, 330–336
- Danilewsky A.N., and Benz K.W. (1989) 'InP growth from In solutions under reduced gravity' *J. Cryst. Growth* **97** 571–577
- Danilewsky A.N., Benz K.W., and Nishinaga T., (1990) 'Growth kinetics in space and earth grown InP and GaSb crystals' *J. Cryst. Growth* **99** 1281–1286
- Danilewsky A.N., Nagel G., and Benz K.W. (1994) 'Growth of GaAs from Ga solution under reduced gravity during the D2 mission' *Cryst. Res. Technol.* **29** 171–178
- Danilewsky A.N., Lauer S., Bischofink G., and Benz K.W. (1996) 'Long term crystal growth under microgravity during the EURECA-1 mission (I): THM growth of Al_xGa_{1-x}Sb' *Cryst. Res. Technol.* **31** 11–18
- Danilewsky A.N., Meinhardt J., and Benz K.W. (1996) 'Long term crystal growth under microgravity during the EURECA-1 mission (II): THM growth of sulphur-doped InP' *Cryst. Res. Technol.* **31** 139–149
- Derebail R., Hoekstra B., and Wilcox W.R. 'The influence of gravity on the directional solidification of InSb' 30th *Aerospace Science Meeting and Exhibit*, 6–9 January 1992, Reno, NV, paper n° AIAA 92–0841
- Duffar T., Potard C., and Dusserre P. (1988) 'Growth analysis of the InSb compound by a calorimetric method in microgravity' *J. Cryst. Growth* **92** 467–478
- Duffar T., Boiton P., Dusserre P., and Abadie J. (1997) 'Crucible dewetting during Bridgman growth in microgravity. Part two: smooth crucibles' *J. Cryst. Growth*, **179** 397–409
- Duffar T., Serrano M.D., Moore C.D., Camassel J., Contreras S., Dusserre P., Rivoallant A., and Tanner B.K. (1998) 'Bridgman solidification of GaSb in space' *J. Cryst. Growth* **192** 63–72
- Duffar T., Serrano M.D., Lerin L., and Santailier J.L. (1999a) 'Marangoni convective effect during crystal growth in space' *Cryst. Res. Technol.* **34** 457–465
- Duffar T., and Garandet J.P. (1999b) 'Effect of microgravity level on the chemical segregation in mixed semiconductor crystals' *Microgravity Sci. Technol.* **XII/1** 69–73

- Duffar T., Dusserre P., and Giacometti N. (2001) 'Growth of GaSb single crystals by an improved dewetting process' *J. Cryst. Growth* **223** 69–72
- Duhanian N., Marin C., Abadie J., Chaudet M., Dieguez E., and Duffar T. (1997) 'Chemical segregation and crystal crucible interaction during the growth of $\text{Ga}_{0.8}\text{In}_{0.2}\text{Sb}$ in space' *Microgravity Sci. Technol.* **XI/4** 187–193
- Duhanian N. 'Etude des ségrégations solutales à l'intérieur de l'alliage GaInSb en cours de solidification directionnelle en front plan suivant la méthode bridgman' PhD Thesis, Univ. Paris-VII (1998)
- Eiche C., Joerger W., Fiederle M., Ebling D., Schwarz R., and Benz K.W. (1995) 'Investigation of CdTe:Cl grown from the vapour phase under microgravity conditions with time dependent charge measurement and photoinduced current transient spectroscopy' *J. Cryst. Growth* **146** 98–103
- Eiche C., Joerger W., Fiederle M., Ebling D., Salk M., Schwarz R., and Benz K.W. (1996) 'Characterization of CdTe:Cl crystals grown under microgravity conditions by time dependent charge measurement' *J. Cryst. Growth* **166** 245–250
- Elwell D., and H.I. Scheel (1975) 'Crystal Growth from High Temperature Solutions', Academic Press, London
- Eyer A., Leiste H., and Nitsche R. 'Crystal growth of silicon in spacelab 1: experiment ES321' *Proc. 5th Europ. Symp. Material Sciences under Microgravity*, Schloss Elmau 5–7 November 1984, ESA SP- 222, 173–181
- Eyer A., Leiste H., and Nitsche R. (1985) 'Floating zone of silicon under microgravity in a sounding rocket' *J. Cryst. Growth* **71** 173–182
- Favier J.J., Arragon P., Martin E.P., and Witt A.F. 'Analyse non-stationnaire de la macroségrégation pendant la solidification dans l'espace du système Ge-Ga' *Proc. 3rd Europ. Symp. Material Sciences in Space*, Grenoble, 24–27 April 1979, 306–308
- Fiederle M., Eiche C., Joerger W., Salk M., Senchenkov A.S., Egorov A.V., Ebling D.G., and Benz K.W. (1996) 'Radiation detector properties of CdTeSe:Cl crystals grown under microgravity in a rotating magnetic field' *J. Cryst. Growth*, **166** 256–260
- Fiederle M., Duffar T., Babentsov V., Benz K.W., Dusserre P., Corregidor V., Dieguez E., Roosen G., Launay J.C., and Chevrier V. (2004) 'Dewetted growth of CdTe. Part 1: Growth in microgravity (STS95)' *Cryst. Res. Technol.* **39** 481–490
- Fujiwara S., Irikura M., Araki T., Tatsumi M., Murai S., and Shirakawa T. (1994) 'Crystal growth of InGaAs in microgravity' *Sumitomo Tech. Rev.* **38** 63–67
- Galazka R.R., Warminski T., Bak J., Auleytner J., Dietl T., Okhotin A.S., Borovikova R.P., and Zubritskij I.A. (1981) 'Directional crystallization of CdHgTe in microgravity conditions' *J. Cryst. Growth* **53** 397–408
- Garandet J.P., and Duffar T. (2001) 'Fluid Flow and segregation in crystal growth from the melt', Chapter 13 in 'Physics of Fluids in Microgravity', R. Monti (Ed.), Taylor & Francis, London, ISBN 0-415-27581-4, pp. 433–488
- Gillies D.C., Lehoczy S.L., Szofran F.R., Watring D.A. Alexander H.A., and Jerman G.A. (1997) 'Effect of residual accelerations during microgravity directional solidification of HgCdTe on the USMP-2 mission' *J. Cryst. Growth* **174** 101–107
- Golovin B.I., Khazieva R.A., Kholina E.N., Yurushin B.I., Maksimovskii S.N., and Vlasenko L.A. (1984) 'Nature of the impurity distribution in germanium during zero-gravity crystallization' *Izv. Akad. Nauk SSSR, Neorg. Mater.* **20** 5–8
- Haar M., Dornhaus R., and Brötz G. 'Growth of PbSnTe by the travelling heater method' *Proc. Norderney Symp. on Scientific Results of the German Spacelab Mission D1*, 27–29 August 1986 (DFVLR 1987) 283–288
- Hamacher H., Fitton B., and Kingdon J. (1987) 'The environment of earth orbiting systems', Chapter I of 'Fluid Sciences and Materials Science in Space', H.U. Walter (Ed.), Springer Verlag, ISBN 3-540-17862-7
- Hayakawa Y., Okano Y., Hirata A., Imaishi N., Kumagiri Y., Zhong X., Xie X., Yuan B., Wu F., Liu H., Yamaguchi T., and Kumagawa M. (2000) 'Experimental and numerical investigations on

- dissolution and recrystallization processes of GaSb/InSb:GaSb under μg and terrestrial conditions' *J. Cryst. Growth* **213** 40–50
- Herrmann F.M., and Müller G. (1995) 'Growth of 20 mm diameter GaAs crystals by the floating-zone technique with controlled As-vapour pressure under microgravity' *J. Cryst. Growth* **156** 350–360
- Hildmann B.O., Möller U., and Bähr G. 'Convection and crystal growth of Ge:Ga' *Final Reports of Sounding Rocket Experiments in Fluid Sciences and Material Sciences* (ESA SP-1132, vol 4, 1994) 130–136
- Inatomi Y., Kaiser T., Dold P., Benz K.W., and Kuribayashi K., 'Semiconductor growth interface from solution in short duration low gravity environment', *SPIE Conf. on Materials Research in Low Gravity II*, Denver, Colorado, July 1999, SPIE Vol. 3792, 139–146
- Iwai S., and Segawa Y. 'Growth of PbSnTe single crystal by traveling zone method' *NASDA Summary Report on the Science Results of Fuwatto 1992 Space Experiment* (ref. N96-16385 04–29, 1993)
- Kaddeche S., Garandet J.P., Barat C., Ben Hadid H., and Henry D. (1996) 'Interface curvature and convection related macrosegregation in the vertical Bridgman configuration' *J. Cryst. Growth* **158** 144–152
- Kaforey M.L., Bly J.M., and Matthiesen D.H. (1997) 'Void formation in GaAs crystals grown in microgravity' *J. Cryst. Growth* **174** 112–119
- Kartavykh A.V., Kopeliovich E.S., Mil'vidskii M.G., and Rakov V.V. (1999) 'Anomalous effect of dopant distribution in Ge crystals grown by FZ technique aboard spacecrafts' *J. Cryst. Growth* **205** 497–502
- Kashimov F.R. 'Structural and physical characteristics of InSb single crystals grown under near-zero gravity conditions' *Proc. 3rd Europ. Symp. Material Sci. in Space*, Grenoble 24–27 April 1979, ESA SP-142 (1979) 9–15
- Kimura H., and Miyazaki A., (2002) 'Crystallization from a molten zone and pendant drop under supercooling conditions' *J. Cryst. Growth* **237–239** 1835–1839
- Kimura T., Nishimura T., Ono, H., and Takamiya S. 'Vapor phase epitaxy of InP with halide transport', *Proc. Scientific Results of the D2 Mission*, Norderney, 1993, DLR-WPF, 1994, 509–513
- Kinoshita K., and Yamada T. (1995) ' $\text{Pb}_{1-x}\text{Sn}_x\text{Te}$ crystal growth in space' *J. Cryst. Growth* **147** 91–98
- Kinoshita K., Kato H., and Yoda S.I. 'Growth of compound semiconductor crystals in microgravity' *Proc. Xth Europ. and VIth Russ. Symp. Physical Sciences in Microgravity*, St Petersburg, 15–1 June 1997, 21–25
- Kodama S., Suzuki Y., Ueda O., and Ohtsuki O. (1990) 'GaAs solution growth experiment in microgravity' *J. Cryst. Growth* **99** 1287–1290
- Kodama S., Ueda O., Ohtsuki O., and Suzuki Y. (1994) 'GaAs solution growth experiment in μg using Get Away Special Program' *Advanced Materials '93*, III-A; *Trans. Mater. Res. Soc. Jpn.*, **16A** 695–698
- Kodama S., Nakajima K., Suzuki Y., Ohtsuki O., and Sakai H. (1998) 'Compositional variation in AlGaAs crystals grown by LPE under microgravity and terrestrial conditions' *J. Cryst. Growth* **194** 166–172
- Kölker H. 'Crystallization of a silicon sphere' *Proc. 5th Europ. Symp. Material Sciences under Microgravity*, Schloss Elmau 5–7 November 1984, ESA SP- 222, 169–172
- Kölker H. 'Crystallization of a silicon sphere' *Proc. Norderney Symposium on the Results of the D1 German Mission*, 27–29 August 1987, DFVLR Ed. 1987, 264–267
- König F. (1998) 'Zone melting of $\text{Bi}_{0.5}\text{Sb}_{1.5}\text{Te}_3$ crystals under microgravity' *Cryst. Res. Technol.*, **33** 219–232
- Larson D.J., Alexander J.I., and Gillies D. 'Orbital processing of high-quality CdTe compound semiconductors' *NASA Conf. Publication*, **3272**, Vol. 1 (1994) 129–138
- Launay J.C., Debegnac H., Zappoli B., and Mignon C. (1988) 'Germanium epitaxial growth in closed ampoules' *J. Cryst. Growth* **92** 323–331

- Lendvai E., Harsy M., Görög T., Gyuro I., Pozgai I., Kolkai F., Gyulai J., Lohner T., Mezey G., Kotai E., Paszti F., Hrpajov V.T., Kultchisky N.A., and Regel L.L. (1985) 'The growth of GaSb under microgravity conditions' *J. Cryst. Growth* **71** 538–550
- Lin L., Zhong X., and Chen N. (1998) 'Improvement of stoichiometry in semi-insulating GaAs grown under μg ' *J. Cryst. Growth* **191** 586–588
- Lin L., Zhang M., Zhong X., Yamada M., and Chen N. (1999) 'Outer space grown semi-insulating GaAs and its applications' *Science in China E-42* 456–461
- Lockowandt C., Yakimova R., Syvajarvi M., and Janzen E. 'High temperature furnace for LPE of SiC in microgravity'; <http://www.ssc.se/ssd/papers/lpe/lpe.html>, 2001
- Lopez C.R., Mileham J.R., and Abbaschian R. (1999) 'Microgravity growth of GaSb single crystals by the liquid encapsulated melt zone (LEMZ) technique' *J. Cryst. Growth* **200** 1–12
- Maffei N., Quon D.H.H., Aota J., Kuriakose A.K., and Saghir M.Z. (1997a) 'Float zone crystal growth of $\text{Bi}_{12}\text{GeO}_{20}$ in a microgravity environment' *J. Cryst. Growth* **180** 105–112
- Maffei N., Quon D.H.H., Aota J., Chen T.T., McCaffrey J., and Saghir M. (1997b) 'Characterization of $\text{Bi}_{12}\text{GeO}_{20}$ processed in a microgravity environment' *J. Cryst. Growth* **181** 382–389
- Matthiesen D.H., Kaforey M.L., and Bly J. 'The study of dopant segregation behaviour during the growth of GaAs in microgravity' *NASA Conf. Publ. N° 209092* (1999) 451–456
- Markov E.V. 'The influence of space conditions on directional crystallization of Ge and its properties' *Proc. 3rd Europ. Symp. Material Sci. in Space*, Grenoble 24–27 April 1979, ESA SP-142 (1979) 17–23
- Markov E.V., Antropov V.Y., Biryukov V.M., Goncharov V.A., Dyakov Y.N., Pilgoon A., Pekisov V.A., Chegrov V.P., Ivanov A.I., and Nikitsky V.P. 'Space materials for microelectronics' *Proc. Xth Europ. and VIth Russ. Symp. Physical Sciences in Microgravity*, St Petersburg, 15–21 June 1997, 11–20
- Moskowitz M.E., Bly J.M., and Matthiesen D.H. (1997) 'Comparison of OARE accelerometer data with dopant distribution in Se-doped GaAs crystals grown during USML-1' *J. Cryst. Growth* **174** 108–111
- Müller G., and Rupp R., (1991) 'The role of Marangoni convection in the growth of GaAs crystals by the floating zone technique under microgravity' *Crystal Prop. Prep.* **35** 138–154
- Nagel G., and Benz K.W. (1984) 'Travelling heater growth of GaSb under reduced gravity during the first Spacelab mission' *Adv. Space Res.* **4** 23–26
- Nakamura S., Hibiya T., Kakimoto K., Imaishi N., Nishizawa S.I., Hirata A., Mukai K., Yoda S.I., and Morita T.S. (1998) 'Temperature fluctuations of the Marangoni flow in a liquid bridge of molten silicon under microgravity on board the TR-IA-4 rocket' *J. Cryst. Growth* **186** 84–94
- Nakamura S., Hibiya T., Imaishi N., Yoda S.I., Nakamura T., Koyama M., Dold P., and Benz K.W. (1999) 'Observation of periodic Ma convection in a molten bridge on board the TR-IA-6 rocket' *J. Jpn. Microgravity Appl.*, **16** 99–103
- Nakata J., Kuratani N., Tomozawa H., Nishimura Y., Yokogawa N., and Inagawa I. (1998) 'Seedless crystallization of levitated Ge and GaSb spherical melts under microgravity' *Jpn. J. Appl. Phys.* **37** L1396–L1399
- Nishinaga T., Ge P., Huo C., He J., and Nakamura T. (1997) 'Melt growth of striation and etch pit free GaSb under microgravity' *J. Cryst. Growth* **174** 96–100
- Parfeniev R.V., Farbshtein I.I., Shulpina I.L., Yakimov S.V., Shalimov V.P., Turchaninov A.M., Ivanov A.I., and Savin S.F. (2000) 'Tellurium recrystallization under microgravity conditions and the resulting properties of samples' *Phys. Solid State* **42** 244–252
- Pätzold O., Fischer B., and Cröll A. (2002) 'Melt flow and species transport in μg gradient freeze growth of germanium' *Cryst. Res. Technol.* **37** 1058–1065
- Piechotka M., Kaldis E., Wetzel G., and Flisch A. (1998) 'Kinetics of physical vapour transport at low pressure under microgravity conditions' (in 2 parts) *J. Cryst. Growth* **193** 80–89 and 90–100
- Popov A.S., Kostandinov I.Z., Mateev M.D., Alexandrov A.P., Regel L.L., and Baturin N.A. (1990) 'Phase analysis of RbAg_4I_5 grown in microgravity' *Microgravity Sci. Technol.* **III** 41–43

- Regel L.L. 'The main results of the space material science experiments within the framework of the Intercosmos programme' *Proc 4th Europ. Symp. Material Sciences under Microgravity*, Madrid, 5–8 April 1983 (ESA SP-191) 409–415
- Regel L.L., and Nguyen Thanh Nghi, (1984) 'On basic results of the joint Soviet-Vietnamese programme 'Halong' on space semiconductor technology' *Acta Astronautica* **11** 155–162
- Regel L.L., Shumaev O.V., Vidsensky I.V., Safonova I.M., Vederkinov A.A., Melikhov I.V., Komarov V.F., Ivanov A.I., and Suleiman S. (1990) 'Experiments on crystallization of semiconductor materials, eutectic alloys and crystal growth from water solution in microgravity' *Acta Astronautica* **21** 331–348
- Regel L.L., and Wilcox W.R. (1998) 'Detached solidification in microgravity—a review' *Microgravity Sci. Technol.*, **XI/4** 152–166
- Rodot H., Guillaume J.C., Chevallier J., Boulou M., Kriapov V.T., Kashimov F.R., Markova T.I., and Zoubirski I.A. (1983) 'Defects in GaAs grown from solution under microgravity conditions' *Physica B* **116** 168–176
- Rodot H., and Tottereau O. 'Cristaux de PbTe élaborés en microgravité' *Proc. 5th Europ. Symp. Material Sciences under Microgravity*, Schloss Elmau 5–7 November 1984, ESA SP-222, 135–139
- Rupp R. 'Über die Herstellung von Galliumarsenid mit dem tiegelfreien Zonenschmelzverfahren unter besonder Berücksichtigung der thermokapillaren Konvektion' PhD Thesis, Erlangen (1990)
- Saghir M.Z., Labrie D., Ginovker A., Paton B.E., George A.E., Olson K., and Simpson A.M., (2000) 'Float zone crystal growth of CdGeAs₂ in microgravity: numerical simulation and experiment' *J. Cryst. Growth*, **208** 370–378 and 379–388 (in 2 parts)
- Salk M., Fiederle M., Benz K.W., Senchenkov A.S., Egorov A.V., and Matioukhin D.G. (1994) 'CdTe and CdTe_{0.9}Se_{0.1} crystals grown by the travelling heater method using a rotating magnetic field' *J. Cryst. Growth* **138** 161–167
- Schilz J., Möller U., and Bähr G. 'Gravity related effects on segregation during directional solidification of Ge–Si' *Final Reports of Sounding Rocket Experiments in Fluid Sciences and Material Sciences* (ESA SP-1132, vol 4, 1994) 137–140
- Schönholz R., Dian R., and Nitsche R., 'Solution growth of CdTe' *Proc. 5th Europ. Symp. of Material Sciences under Microgravity*, Schloss Elmau, 5–7 Nov. 1984 (ESA SP 222, pp 163–167)
- Schweizer, M., Cröll A., Dold P., Kaiser Th., Lichtensteiger M., and Benz K.W., (1999) 'Measurement of temperature fluctuations and microscopic growth rates in a silicon floating zone under microgravity' *J. Cryst. Growth* **203** 500–510
- Senchenkov A.S., Barmin I.V., Danilewsky A.N., Meinhardt J., and Benz K.W., Presented at the *Int. Academy Astronautics Congress Amsterdam*, 1999, paper n° IAA-99-IAA.12.1.04
- Siche D., Böttcher K., Rinas U., and Hartmann H. (2002) 'Crystal growth of zinc selenide under μg conditions', *J. Cryst. Growth* **244** 249–256
- Sleptsova I.V., Senchenkov A.S., Egorov A.V., Barmin I.V., Prokorhov I.A., Tison P., Camel D., and Hieu G. 'GeZon experiment: an attempt to explore Marangoni convection during floating zone melting in space' *Proc. Xth Europ. Symp and VIth Russian Symp. on Phys. Sci. in Microgravity*, St Petersburg, 15–21 June 1997, 68–71
- Steiner B., Van den Berg L., and Laor U. (1999) 'Enhancement of mercuric iodide detector performance through increases in wafer uniformity by purification and crystal growth in microgravity' *J. Appl. Phys.*, **86** 4677–4687
- Su C.H., Sha Y.G., Lehoczky S.L., Szofran F.R., Gillies D.C., Scripa R.N., Cobb S.D., and Wang J.C. (2002) 'Crystal growth of HgZnTe alloy by directional solidification in low gravity environment' *J. Cryst. Growth* **234** 487–497
- Suzuki Y., Kodama S., Ueda O., and Ohtsuki O. (1995) 'GaAs crystal growth from metallic solution under microgravity' *Adv. Space Res.* **16–7** 195–198
- Tillberg E., and Carlberg T (1990) 'Semi-confined Bridgman growth of germanium crystals in microgravity' *J. Cryst. Growth* **99** 1265–1272

- Tiller W.A., Jackson K.A., Rutter J.W., and Chalmers B. (1953) 'The redistribution of solute atoms during the solidification of metals' *Acta Met.* **1** 428–437
- Van den Berg L., and Schnepfle W.F. (1989) 'Mercuric iodide crystal growth in space' *Nucl. Instrum. Methods Phys. Res. A* **283** 335–338
- Van den Berg L. (1993) 'Growth of single crystals of mercuric iodide on the ground and in space' *Mater. Res. Soc. Symp. Proc.* **302** 73–78
- Walter H.U. (1977) 'Generation and propagation of defects in InSb' *J. Electrochem. Soc.* **124** 250–258
- Walter H.U. (1985) 'Striations in germanium' *Sounding Rockets ESA SP-1132* 168
- Wang Z.G., Li C.J., Cao F.N., Shi Z.W., Zhou B.J., Zhong X.R., Wan S.K., Xu S.D., and Lin L.Y. (1990) 'Electrical characteristics of GaAs grown from the melt in a reduced gravity environment' *J. Appl. Phys.* **67** 1521–1524
- Wei L., Wang W., Wang B., Ju X., Wu Z., Kurash I., Li Y., Tan X., and Ma M. (2000) 'Study of defects in HgCdTe grown under μg ' *Nucl. Technol.* **23** 381–383
- Wiedemeyer H., Klaessig F.C., Irene E.A., and Wey S.J. (1975) 'Crystal growth and transport rates of GeSe and GeTe in microgravity environment' *J. Cryst. Growth* **31** 36
- Wiedemeyer H., Sadeek H., Klaessig F.C., Norek M., and Santandrea R. (1977) 'Morphology and transport rate of mixed IV-VI compounds in micro-gravity' *J. Electrochem. Soc.* **124** 1095–1102
- Wiedemeyer H. 'Vapor transport and crystal growth of IV-VI compounds under normal and reduced gravity conditions' *Proc. Vith Symp on Material Sciences under Microgravity Conditions*, Bordeaux, 2–5 December 1986, 29
- Wilcox W.R., Yee J.F., Lin M.C., Sarma K., and Sen S. (1975) 'Directional solidification of InSb–GaSb Alloys', *Skylab Science Experiments*, Vol. 38 of *Science and Technology*, edited by the American Astronautical Soc. 27–41
- Witt A., Gatos H.C., Lichtensteiger M., Lavine M.C., and Herman C.J. (1975) 'Crystal growth and steady state segregation under zero gravity: InSb' *J. Electrochem. Soc.* **122** 276–283
- Witt A., Gatos H.C., Lichtensteiger M., and Herman C.J. (1978) 'Crystal growth and segregation under zero gravity: Ge' *J. Electrochem. Soc.* **125** 1832–1840
- Yee J.F., Lin M.C., Sarma K., and Wilcox W.R. (1975) 'The influence of gravity on crystal defect formation in InSb–GaSb alloys' *J. Cryst. Growth* **30** 185–192
- Yue J.T., and Voltmer F.W. (1975) 'Influence of gravity-free solidification on solute microsegregation' *J. Cryst. Growth* **29** 329–341
- Zemskov V.S., Raukhan M.R., Barmin I.V., Senchenkov A.S., Shulpina I.L., and Sorokin L.M. (1983) 'Special features of solidification of alloyed single crystal of InSb in zero gravity conditions' *Fiz. Khim. Obrabotki Mater.* **17** 56–65
- Zemskov V.S., Kubasov V.N., Belokurova I.N., Titkov A.N., Shulpina I.L., Safarov V.I., and Guseva N.B. 'Ge–Si solid solutions' *Apollo-Soyuz Test Project*, NASA TM X-77360, MSFC (1977) IX/1-IX/36
- Zemskov V.S., Raukhan, M.R., Kozitsina E.A., Baikov A.A., Barmin I.V., and Senchenkov A.S. 'Experiments on directional crystallization of InSb on Foton Automatic satellites' *Proc. AIAA/IKI Microgravity Sci. Symp.*, Moscow, 13–17 May 1991, 124–129
- Zemskov V.S., Raukhan, M.R., Shalimov V.P., Senchenkov A.S., and Kiryanov A.I. 'Gravity sensitivity of the facet effect during InSb:Te crystals grown by FZM in space flight' *Proc. Xth Europ. Symp and Vith Russian Symp. on Physical Sci. in Microgravity*, St Petersburg, 15–21 June 1997, 95–104
- Zemskov V.S., Raukhan, M.R., and Shalimov V.P. (2001) 'Gravitational sensitivity of melts at the growth of InSb:Te crystals by the Bridgman and floating zone methods under the conditions of microgravity' *Cosmic Res.* **39** 351–358 (*Kosmicheskie Issledovaniya* **39** (2001) 375–383)

Index

Note: Page references in *italics* indicate figures and those in **bold** represent tables.

- Abbreviations, 383
- Absorption bands, fluoride crystals, 351
- Accelerated crucible rotation technique (ACRT), 102–103, 168, 222, 228
 - axial composition profiles of high- x crystals, 230
 - bidirectional rotation, 230
 - cadmium mercury telluride, 225–234
 - interface depth versus rotation rate plot, 226, 228
 - LSMS crystal purity survey, 234
 - meridional flow streamlines, 103
 - radial x variations, 228, 229
 - use at BAE SYSTEMS, 238
- Acceleration, effect on space experiments, 504–505
- Acceptors, 45, 46, 66, 142
- Acmite, 401
- Aggregate diamonds, 419
- AlGaAs/Ga, 515
- AlGaSb/Ga, 514
- Algebraic grid generation, 93
- ALICE, 359, 378
- Alkali-halide single crystals, nonuniform distribution of activators, 364
- Alumina powder, 303
- Ammonothermal method, 175
- Ampoule rotation, 105, 106, 107
- Antiperovskite (BaLiF₃), 342
- Atmospheric-pressure iodine vapor transport (APIVT) growth, 473
- Autoclaves, 396
- Automated crystal growth
 - melt-feeding system, 371, 372
 - powder-feeding system, 366, 367
- Automated heater-temperature control, 369
- Autoradiographs, InSb[Te] wafers, 159, 160
- Axial heat flux (AHP) growth system, 96
- Axial segregation, 505, 508
 - convective, 505, 506
 - diffusive, 505, 506
- Axisymmetric melt growth systems, results of small perturbations, 105, 112
- BaBar CsI(Tl) scintillator project, 359
- BaCeF crystals
 - cellular structure, 348, 349
 - distribution coefficient, 349
 - stability function, 349
- Backward Euler method, 90
- BaF₂, 359, **363**
- BaF₂–CeF₃, phase equilibria, 349
- BaLiF₃ (antiperovskite), 342
- BaLu₂F₈, 342
- Baroclinic instability flow, 20, 21, 22
- Basal plane dislocations, 444
- BaYb₂F₈, 342
- BELLE CsI(Tl) scintillator project, 359
- Belt-type high-pressure apparatus, 412, 413
 - cross-section, 413
 - photograph, 413
- Berlinite crystals, 396
- Berthollides, 345, 346
- BGO (bismuth germanium oxide), 359, **363**, 509, 512
- Bismuth silicate (Bi₄Si₃O₁₂), growth phases, 377
- Blue-violet laser diodes, 203
- Boric oxide, 50, 53
- Boron, as contaminant of GaAs, 50
- Boron-doped diamond crystals, 424
- Boundary conditions, **82**, 83–84
- Boussinesq approximation, 82

- Brain SPECT, curved and cylindrical detectors, 361
- Bridgman crystal growth technique, 167, 269
 cadmium mercury telluride (CMT), 223–224
 closed, 277
 free boundary, 84
 high-pressure, 236, 237, 277
 II-VI compound semiconductors, 276–277
 InSb, 164–165
 modified, 235
 tilted, 106, 107
- Bridgman–Stockbarger crystal growth technique, 276, 364
- Bromine-methanol, 263
- Bubbles, in corundum crystals, 319–323, 325
- Bulk crystal growth processes, 77–78
- Bulk solution growth, growth velocity modelling, 85
- Bulk-flow model, 22
- Cadmium, purity, 242
- Cadmium mercury telluride (CMT), 209–240, 234
 ACRT growth, 225–234
 ACRT solid/liquid interfaces in quenched high-*x*, 231, 233
 annealing, 215
 as-quenched microstructure, 214
 axial composition profile, 218, 219
 Bridgman growth, 223–224
 bulk growth techniques, 209
 CdTe seed crystals, 221
 compounding, 213–214
 conductivity types, 221
 crystal diameters, 236
 crystal growth, 211–238
 device results, 221
 diameter limit, 214
 dislocation densities, 215
 doping, 216, 220
 electrical properties, 221, 234
 impurities from Bridgman growth, 224
 IR images of ACRT slices, 232, 233
 LSMS purity survey of Bridgman crystals, 234
 mercury and tellurium elemental purification, 222–223
 n-type material, 223
 p to n type conversion, 224
 p–n junction formation, 236
 p-type material, 221
 phase equilibria, 210–211
 pressure–temperature phase diagram, 211, 212, 230
 production, 209
 quenching, 214
 residual impurities, 216
 rocking furnace, 213
 secondary recrystallization, 214–215
 solid state recrystallization, 212–217
 structural properties and seeding, 221
 tellurium precipitation, 214
 THM purification, 219–220
 uses in IR devices, 234–235
 wavelength variations in ACRT, 231, 232
- Cadmium telluride
 contamination sources of polycrystals, 245
 crystal growth, 243–260
 dewetted growth from crucibles, 514, 516
 growth by sublimation method, 515
 p-type, 246, 248
 polycrystal carrier concentrations, 243, 244
 polycrystals grown by pBN boats, 243, 246
 polycrystals grown by quartz boats, 243, 245
 VGF single-crystal growth, 244–260
- Cadmium zinc telluride (CZT), 241–267
 3D analysis of Bridgman growth, 104–106, 112
 5-inch crystal, 244, 247
 axisymmetric analysis of Bridgman growth, 102–104
 carrier concentration, 248, 249
 carrier concentration as a function of Li and Na concentrations, 245, 248
 carrier concentration grown by VGF technique, 244, 247
 characteristics of wafers, 264–265
 correlation between IR transmittance and carrier concentration, 254, 255
 correlation between Li and Na concentrations, 249
 crystallographic misorientation, 264
 dicing, 263
 dislocation density (EPD), 256
 effect of wafer annealing of precipitates, 254
 etching, 262
 growth furnace, 260
 high-quality substrates, 261
 infrared detector arrays, 241
 inspection of wafers, 263
 IR transmittance, 255, 256
 lapping, 263
 large diameter crystals, 241

- large-sized substrates, 266
- p-type carrier concentration, 246, 248
- polishing, 263
- postgrowth ingot annealing, 251, 252
- postgrowth ingot annealing temperature of Cd reservoir and, 251, 252
- precipitates, 250–254
- process flow, 261–263
- quality substrates, 266
- slicing process, 262
- surface roughness, 265, 266
- surface void defects, 250
- Te precipitates reduction, 250
- thickness variation and warp, 264–265
- uses, 241
- Zn concentration mapping, 257
- Zn concentration maps of 4-inch, 260, 261
- CaF₂, 339, 363
- Callinan diamond, 428
- Calorimeters, scintillation crystal requirements, 359, 360
- Capillary effects, 85
- Capillary-action shaping technique (CAST), 315
- Carbide-forming metals, 410
- Carbon, phase diagram, 408
- Carl Zeiss Si diode array spectrometer, 257
- CaSrNdF, saddle point on melting surfaces, 349, 350
- Cast recrystallize anneal (CRA), 212, 222
- Cathodoluminescence, 66
- Cats2D, 91, 92, 101, 103
- CaWO₄ crystals, as scintillators, 357
- CdS, In and Te doping, 362
- CdTe:Cl/Te, growth on satellites, 514
- CdTeSe:Cl/Te, growth on satellites, 514
- CdWO₄, 361, 363
- CeF₃, 359
 - properties, 340
 - single crystals, 340
- Cell-free single crystals, 349, 350
- CERN, 378
- CF₄, 379–380
- Charge-carrier trapping, 379
- Chemical polishing, 403
- Chemical segregation, 505, 517
- Chemical vapor deposition (CVD), 284, 407, 408, 473
- Chemical vapor transport (CVT), 270, 272–274, 281, 283, 288, 515
- Chips, improvement in performance, 2
- Chlorine, as transport agent, 515
- Chromium, 45, 46, 49
- Cleavage, indium antimonide, 153
- CMS project, 359, 378
- CMT *see* Cadmium mercury telluride
- Cobalt, impurities in synthetic diamonds, 423
- Codes, crystal-growth modelling, 87, 89
- Codoping, 348
- Cold-crucible technique, corundum crystal growth, 311
- Compound melting, types, 347
- Computer modelling, 73–119
 - difficulties, 74
 - modelling examples, 98–111
 - present state, 75–77
 - transport modelling, 75, 79–89
- Computer-aided analysis, 89–97
- Confined bulk crystal growth methods, 77
- Congruent melting, 347
- Conical etch pits, 161
- Conservation equations, for bulk crystal growth from liquids, 79, 81, 112
- Contiguous capillary coating (CCC), 470
- Continuous crystal growth, 365
- Continuum interface representation, 84–86
- Continuum transport modelling, 76, 79, 112
- Convection, effect on growth rate, 477, 505, 507
- Convective axial segregation, 505, 506
- COP (crystal-originated particles) defect, 36, 37
- Copper, 45, 46
- Corundum crystals, 300, 309
 - automatic diameter control, 310
 - bubble distribution, 321
 - bubbles, 319–323
 - crystallization dynamic stability, 305–306
 - Czocharlski growth technique (CzT), 310–312
 - defects, 319–327
 - diameters, 306
 - dislocation density in as-grown, 324
 - flux growth technique (FT), 318–319
 - gas-phase growth technique (GPT), 319
 - growth C-axis direction, 327
 - growth in stable regimes, 307
 - Horizontal Bridgman growth technique (HBT), 313
 - Hydrothermal growth technique (HTT), 319
 - inclusions, 319–323
 - Kyropulos growth technique (KT), 312–313
 - lattice, 301
 - plate-shaped, 306

- Corundum crystals, (*continued*)
practical results of theoretic analysis,
306–307
pulling from shaper growth techniques,
314–318
round cylindrical, 306, 307
shaped growth, 314
solid inclusions, 323
theoretical investigation of VT crystal
growth, 304–305
tube-shaped, 307
Verneuil's sapphire growth technique,
329–330
- Cristobalite, 387, 400
 α -Cristobalite, 400
- Critical Marangoni number, and Prandtl
number, 509, 511
- Critical resolved shear stress (CRSS), 152, 162
- Critical Reynolds number, and critical rotation
rates, 226, 227
- Crystal-growth modelling, 139–141
examples, 98–111
- Crystal-pulling control equations, 377
- CrysVUn⁺⁺, 139
- CrysVUN, 87, 89, 91, 105
- CsI (pure), 363, 379
- CSI–CsBr, 379
- CsI(Na), 363, 370, 375
- CsI(pure), 370
- CsI(Tl), 363, 364, 370
replacement by CdWO₄, 379
Tl distribution uniformity, 376
- Cusp magnetic field, 27–30
CZ-Si growth system, 28
growth conditions, 28
oxygen concentration as function of
solidified fraction, 29
radial distribution of oxygen concentration,
29
- CVD *see* Chemical vapor deposition
- CVT *see* Chemical vapor transport
- CZ-Si crystal growth, 11–13
basic process, 11–12
IT as driving force, 39
oxygen concentration in silicon melt, 26
oxygen transportation mechanism, 25, 27
schematic diagrams with cusp magnetic
field, 28
- CZ-Si crystal growth apparatus, 6–9
hot-zone, 9, 10
photograph, 7
recharge system, 8–9
reducing Ar pressure, 7–8
schematic diagram, 6
- Czochralski, Jan, 452
- Czochralski modelling, 99
- Czochralski technique, 7, 19, 49, 77, 78, 300,
364
corundum crystal growth, 310–312, 330
dynamic stability analysis, 311
fluoride crystal growth, 347
InSb, 155–164, 169
InSb common defects, 161
photovoltaic silicon crystals, 452–454
photovoltaic silicon growth, 451
schematic diagram of silicon crystal growth
method, 453
silicon, 89
- CZT *see* Cadmium zinc telluride
- Damköhler number, 110
- Decanted sapphire ribbon, interface, 322, 323
- Deep level transient spectroscopy (DLTS),
64–65
- Defect-cluster formation and transformation,
345
- Defect-selective etching, 175
- Defects
indium antimonide, 153, 161
microscopic, 113
- Definitions, 383
- Deforming grids, and ALE methods, 92–94
- Deforming-grid methods, 90, 91, 95, 112
failure situations, 91, 92
in time-dependent problems, 94
- Dendrites, 214
- Detached growth, in space, 510–511
- Dewetting, 480, 481, 482, 483, 484, 511–512,
513, 516, 517
- Dewetting configurations, 511, 513
- Diamond, phase transition between graphite
and, 408
- Diamond anvil cell (DAC), 408
- Diamond crystals, 407–432
agents for formation, 409–411
agents for synthesis, 411
annealing, 428
as-grown surfaces, 420
blue, 424–425
boron-doped synthetic, 426
brown, 424, 425
carbon source, 411–412

- chemical-potential-difference growth
 - method, 414–415
 - classification, 422
 - color change with heat treatment, 427–428
 - color control, 423–428
 - colorless, 417
 - covered in metal film, 414, 415
 - dendritic patterns, 419, 420
 - doping with impurities, 424–426
 - effect of growth temperature on color of, 426–427
 - green, 424, 425
 - growing regular-shaped crystals, 414
 - grown on a seed crystal, 416, 417
 - growth, 407–432
 - growth methods, 412–417
 - growth patterns from sodium carbonate, 420, 421
 - high-pressure synthesis apparatus, 412
 - high-pressure synthetic, 417, 418
 - hydrogen impurities, 422–423
 - impurities, 422–423
 - inclusions, 421–422
 - largest synthetic, 417, 418
 - morphology of single crystals from solvent/catalysts, 417–419
 - nonmetallic compounds as synthesis aids, 410
 - properties of single crystals from high-pressure method, 417–428
 - size limit parameters, 417
 - spiral patterns dendrite, 419
 - surface morphology of single crystals from solvent/catalysts, 419–420
 - synthesis, 407, 408–417
 - temperature-gradient growth method, 416–417
 - tetrahedrally arranged facets, 157
 - transparent polycrystalline, 409
 - twinned crystals, 419
 - types, 422
 - yellow, 417, 425
- Diamond grit, 414, 415
- Differential-algebraic equations (DAEs), 89–90
- Diffuse-interface models, 84, 86, 112
- Diffusion, indium antimonide, 153
- Diffusive axial segregation, 505, 506
- Direct melt crystallization, 341, 342
- Discretization, 89–90
 - interface, 112
- Discretized transport models, phase interfaces representation, 90
- Dislocation reduction, 135–136
- Dislocation-free Czochralski silicon crystals, 33
- Dislocation-reduction anneal (DRA) process, 215
- Dislocations
 - corundum crystals, 323–326
 - density, 134
 - GaAs, 55
 - InP, 133–134
- DLTS *see* Deep level transient spectroscopy
- DNS (direct numerical simulation), 22
- Donors, 45, 46, 46, 143
 - segregation coefficients, 46, 47
- Dopants, 43, 141–145
 - choice of, 45
 - dislocation density reduction, 135
 - in FZ Si crystal growth, 15
 - influence on distribution coefficient, 348
 - n-type InP, 141–142
 - p-type InP, 142
 - segregation coefficients, 348
- Doping, 423–424
 - of nitrogen in diamond synthesis, 426
- Double crystal X-ray diffraction (DXD), 67
- Drop towers, 502
- DZIG (denuded-zone intrinsic gettering), 32
- Edge-defined film-fed growth (EFG), 315, 463, 465, 466
- Edge-supported pulling (ESP) technique, 466, 468
- Effective evaporation coefficients, 458
- Effective segregation coefficients, 458
- Ekman flow, 226, 227
- Ekman layer thickness, 226
- Ekman pumping, 104
- EL2, 52–53, 58–59, 65
 - luminescence, 66
- Electrocontacting probe, 369, 370, 373
- Electrodifusion, 403
- Electromagnetic calorimeters, 359
- Electromagnetic casting, 461
- Element-edge-interface method (EEIM), 95, 96
 - comparison to deforming-grid method, 95
- Elliptic grid generation, 93
- ELOG (epitaxial lateral overgrowth), 174
- Elpasolite (A_2BRF_6), 342
- EMCZ (electromagnetic Czochralski), 38, 39
- Energy, in space, 503
- Enthalpy method, 90, 112

- Equations, macroscopic transport phenomena, 112
- ErF₃, 342
- Etch pits
densities, 161
star arrays, 161
- EURECA, 514
- European Space Agency, 478
- European Spacelab, 478
- Experimental cartridge, 502, 503
- Extrinsic doping, 436
- Faceting, 85, 113, 157–158
- Facets, segregation to, 159–161
- Fast scintillators, 340
- Feed materials, processing, 351
- Feed-rod preparation, FZT, 310
- FEMAG, 87, 89
- Fiber-optic telecommunication detectors, 221
- Finite-difference discretization method, 90
- Finite-element discretization method, 90
- Finite-volume discretization method, 90
- Fixed-domain methods, 112
- Fixed-grid methods, 90, 91, 112
simple, 94–96
- Float-zone technique (FZT), 77, 451
feed-rod preparation, 310
preliminary heating, 308
refinement of silicon sheets, 98–102
sapphire crystal growth, 308–310, 330
silicon growth, 455–456
- Floating crucible, 167
- Fluoride crystals, 339–355, 379–380
cellular structure, 348, 349
hydrolysis and melt fluoride growth, 350–352
morphological stability, 348–350
oxygen impurities of single, 351
purification, 352
uses, 339
- Fluoride-type solid solution, melt
crystallization, 348
- Fluorinating agents, efficiency, 351
- Fluorination atmospheres, schemes, 351
- Fluoroperovskites (AMF₃), 342
- Flux technique (FT), 300
corundum crystal growth, 318–319
sapphire crystal growth, 331
- Fourier transform infrared (FTIR) map, 230, 231
- FPD (flow-pattern defects), 36, 37
- Free-boundary problems, solving, 84
- Free-fall tubes, 502
- Front-track methods, 91, 112
- Full-wafer mapping, 141
- FZT *see* Float-zone technique
- g-jitter effects, modelling, 88
- Ga-N₂ isobars, 192, 193
- GaAs/Ga, 515
- (Ga,In)Sb, 166–167
- GaInSb crystals
axial chemical segregation of In, 505, 506
segregation of In during Bridgman growth
of, 505, 506
- Galerkin finite-element method, 90
- Galerkin-least Squares method, 90, 105
- Gallium antisite defect, 44
- Gallium arsenide (GaAs), 43–71, 509, 510
comparison of growth by fixed-grid and
deforming-grid methods, 92
conducting, 64–65
contamination of HB and horizontal GF, 49
crystalline defects, 54–59
deep level defects, 63–65
dopants, 45–48
electrical analysis of defects, 61–65
growth in quartz crucible with/without boric
oxide, 55
growth rate control, 51
growth of SI LEC, 52–53
growth techniques, 48–54
identification of shallow impurities in n-type,
63
identification of shallow impurities in p-type,
62
impurity and defect analysis, 59–61
introduction of boron, 56
mapping of surface properties, 67
melt formation, 48
n-type crystals, 50
optical analysis of defects, 65–67
oxygen in, 61
p-type, 52, 62
p-type doping in melt-grown, 47
phase diagram, 44
photoluminescence spectra, 66
rocking curves, 67, 68
segregation coefficients for impurities, 45
shallow donors and acceptors, 45, 46
shape control, 51
Si doping, 55

- solidus, 44, 45
- Te doping, 56
- Gallium nitride (GaN), 173–207
 - 2D-nuclei, 190
 - 100- μm thick, 201
 - 150- μm thick, 199, 201
 - applications of pressure-grown bulk substrates, 201–203
 - asymmetry of plate-like crystals, 185, 186
 - beryllium doping, 185
 - blue LEDs, 437
 - bonding, 176
 - crystallization, 176
 - crystallization experiments, 182
 - crystallization on the free gallium surface, 192–193
 - crystallization from atomic nitrogen solutions, 175
 - crystallization from solution, 179–182
 - crystallization in a temperature gradient, 188–192
 - decomposition in supersat. Ga:N soln, 179, 180
 - defect-selective etching, 187–188, 189
 - dependence of growth rate on GaN/Al₂O₃ substrates, 198, 199, 200
 - deposited on GaN/Al₂O₃ and single-crystalline GaN, 198, 199
 - deposited on GaN/Al₂O₃ substrates, 199, 201
 - development of optoelectronic devices, 174
 - directional crystallization and foreign substrates, 194–201
 - directional growth, 205
 - epitaxial layers growth rates, 174
 - free-electron concentration distribution, 186, 187
 - grown at different supercoolings, 192, 193
 - growth on Ga-polar surface, 196, 197
 - growth instabilities, 184
 - growth on N-polar surface, 196
 - growth of quality crystals, 175
 - high-pressure crystallization results, 193, 194
 - increasing lateral size of crystals, 191
 - laser diode characteristics, 203, 204
 - melting temperature, 175
 - Mg doping, 184, 187
 - morphology, 183–185
 - morphology of as-grown surfaces of 40- μm GaN, 199, 200
 - n-type, 184, 185, 196
 - native point defects, 185
 - near-dislocation-free crystals, 194
 - nucleation dependence on supersaturation, 189
 - nucleation rate, 190, 191
 - nucleation theory, 181
 - optical properties, 201, 202
 - oxygen doping, 185
 - phase diagrams and growth methods, 175–182
 - physical properties of pressure-grown, 185–188
 - polarity, 184
 - problems growing crystals, 194
 - role of high pressure in synthesis, 178–179
 - seeded growth from solutions in gallium on GaN substrates, 195–197
 - seeded growth from solutions in gallium on GaN/sapphire substrates, 197–201
 - semi-insulating, 184
 - solution growth, 175
 - study of structure of pressure-grown, 186
 - substrates grown under pressure, 173–207
 - surface crystals grown at different supercoolings, 192
 - synthesis from liquid Ga and N₂ plasma, 178, 179
 - TEM scans, 187, 188
 - uses, 173
- Gallium–gallium nitride system, liquidus line, 178, 182
- Gamma camera detectors, 361, 364
- GaN-Ga-N₂ system, thermodynamic properties, 175–182
- GaP/Ga, 515
- Gas-phase technique (GPT), corundum crystal growth, 319
- Gas-pressure differences, 516
- GaSb, 478, 509
- GaSb:Te/Ga, 514
- GdF₃, 342
- α -GdF₃, temperature stability, 345, 346
- Ge:Ga crystals, 478
- Geostrophic turbulence flow, 22
- Germanium, Marangoni convection, 509
- GeSe, 478, 515
- GeSeTe, 515
- GeSSe, 515
- GeTe, 478, 515
- Gettering effect, 32
- Gibbs free energy
 - gallium nitride (GaN), 176, 177

- Gibbs free energy (*continued*)
temperature dependence, 341
- Global heat analysis, 22
- Global model, 23
- Global two-dimensional solution, 87
- Glow-discharge mass spectrometry (GDMS), 59, 60, 125
- GOI (gate-oxide integrity) defects, 36
- Gradient freeze method, 277, 292
- Gradient solidification method (GSM), 314
- Grain boundaries, 325
- Graphite, 411
direct transformation to diamond, 408–409
isotopically modified, 412
phase transition between diamond and, 408
- Grashof number, 22
- Grid-generation methods, 93
- Growth morphology, predicting, 113
- Growth rate, quartz crystals, 399–400
- H₂O, diamonds formed from, 411
- Halide scintillators, 359, 362, 374
crystal-diameter, 373
crystal-diameter control, 369
crystal-growth stages, 371, 372
crystal-length control, 369
crystal-weight control, 369
growth, 364–374
growth of large-size single crystals, 365
low radiation hardness, 379
plastic deformation, 379
required doping, 364
- Hall-effect analysis, 61–62
- Hall-effect measurements, 215
- Hazards, in InP synthesis, 123–124, 128
- Heat- and mass-transfer processes, analysis, 18–24
- Heat-exchange method (HEM), 300
sapphire crystal growth, 313–314, 330
- Hemispheric pits, CZ InSb, 161
- Heterojunction bipolar transistor (HBT), 122
- HF, 351
- HgTe–CdTe system
liquidus and solidus lines in pseudobinary, 211
pseudobinary phase diagram, 229
- High electron mobility transistors (HEMTs), 436
- High-energy physics, 381, 382
use of scintillators, 359
- High-pressure growth, 216
- High-pressure method, diamond synthesis, 407, 408
- High-temperature chemical vapor deposition (HTCVD), 437
- Horizontal Bridgman technique (HBT), 48, 77, 277, 300
corundum crystals, 313, 330
InSb small crystals, 165
- Horizontal casting, 216
- Horizontal continuous crystal growth, 365, 367
- Horizontal gradient freeze (GF) method, 49
- Horizontal ribbon growth (HRG), 469, 470
- Hot-zone, CZ-Si apparatus, 9, 10
- HPSI, 437
- Hydride vapor phase deposition (HVPE), 174
- Hydrogen
as aid for graphite to diamond conversion, 411
in heat treatment of semi-insulating InP, 144
in InSb crystal growth, 154
- Hydrolysis, and melt fluoride growth, 350–352
- Hydrothermal autoclaves, characteristics for ideal, 396
- Hydrothermal technique (HTT), 269, 270
corundum crystal growth, 319, 331
K₂RF₅, 347
quartz growth, 388
wide-bandgap II-VI semiconductors, 277–279
ZnO growth, 282
- Hydrothermal technique (HTT) internal stresses of sapphire crystals, 325
- ICP (inductively coupled plasma) method, 257
- II-VI compound semiconductors
applications, 269
Bridgman method, 276–277
controlling growth, 277
crystal-growth methods, 270–280
CVT growth parameters, 274
growth from liquid phase, 276–280
growth from vapor phase, 272–276
growth of single crystals, 277
physical and chemical properties, 270, 271–272
wide-bandgap, 269–297
see also Wide-bandgap II-VI compounds
- Imperfections, 105
- Impurities, concentration profiles in PV Si crystals, 457, 458, 459, 460
- Impurity-bound exciton emission, 362

- (In, Tl)Sb, 168
In(As, Sb), 168
In(Bi, Sb), 168–169
Inclusions
 α -quartz crystals, 401
 diamond crystal metallic, 417
 diamonds, 421–422
 fine, 421, 422
 irregular shaped, 421
 solid, 323
Incongruent melting, 347
Incremental quenching, 216
Indium, raw material for InP, 125
Indium antimonide (InSb), 509
 {111} planes, 151, 152
 anomalous segregation of impurities, 159
 applications, 150
 bandgap, 149, 150
 Bridgman growth, 164–165
 characteristics, 150
 cleavage on {110} planes, 153
 conical etch pit patterns, 153–154
 crystallography, 151–154
 Czochralski growth, 155–164
 defects, 153, 161–162
 diffusion, 153
 dopants, 154–155
 evolution, 169
 growth axis choice and implications, 162–163
 growth conditions, 154
 history, 149–150
 impurities, 154–155
 infrared detectors, 150
 lattice, 151, 152
 melting point, 154
 polarity, 151–152
 production challenges, 156–162
 properties, 151–155
 related pseudobinary (ternary) alloys, 165–169
 significant growth parameters, 154, 155
 size evolution and drivers, 163–164
 slip, 152, 161–162, 164
 Tl-substituted, 168
 twinning, 152, 156–157
 VGF growth, 164–165
 X-radiation interaction, 151
Indium phosphide (InP), 121–147, 515
 chemical bonding, 124
 control of crystal shape, 130
 controlled crystallization, 126
 crystal seed cone cross-section, 133
 crystal structure, 124–125
 defects, 132–135
 diameter control, 131–132
 hazards in synthesis, 123–124, 128
 material properties, 122–123
 polycrystalline synthesis system, 126, 127
 seed-end carrier concentration, 128
 single-crystal growth, 129–132
 single-crystal yield, 137
 synthesis, 125–129
 synthesis hazards, 128
 temperature dependence of saturated vapor pressure, 123
 uses, 122
Industrial chemical etching process, 404
Infrared detector arrays, 241
Infrared devices, uses of CMT
 Bridgman/ACRT material, 234–235
Infrared transmittance, 254–256
Inorganic fluoride single crystals, 339
Inorganic scintillators, 362
InP:S/In, 514
InSb:Te crystals, 477–478
InSb *see* Indium antimonide
Interface motion, bulk-crystal-growth systems, 96
Interface-controlled crystallization (ICC), 472
Interfacial boundary conditions, 95
International Technology Roadmap for Semiconductors (ITRS), 2
Inverted Stepanov technique, 466
Iodine, as transport agent, 515
Iodine transport method, 281, 288
Ion beam etching (IBE), 403
Iron
 acceptor in InP, 142
 in diamond formation, 410
 doping, 142, 143
Iterative solvers, 76

K₂RF₅, 347
KF-RF₃ systems, stability, 346
KMgF₃ (perovskite), 342
KTP *see* Potassium titanyl phosphate
KY₃F₁₀, 346
Kyropulos technique (KT), 293, 300, 364, 365
 corundum crystals, 312–313, 330
 furnace types, 312

- LaBr₃:Ce, 381
LaCl₃:Ce, 381
LaF₃, temperature dependencies of solubility in MF₂, 344, 345
Laminar flow, 89
Laplace-transform DLTS, 65
Large-area solid/liquid interface growth methods, 468–472
Large-eddy simulation (LES), 22, 23, 89
Laser diodes
 II-VI compound semiconductors, 269
 low-power blue, 174
 structure of GaN, 203, 204
Laser-scattering tomography (LST), 253, 254
Lely process of SiC single-crystal production, 434
Level-set method, 90, 91
LiCAF, 347
LiF-MF₂ systems, decomposition, 342, 343
LiF-YF₃ system, 347
Light-emitting diodes (LEDs)
 high-brightness blue and green, 174
 II-VI compound semiconductors, 269
Liner assembly, quartz crystal growth, 396, 397
Liquid boric-oxide glass, 128
Liquid encapsulated Czochralski (LEC) growth
 GaAs, 49–52
 InP, 129
 pullers, 50, 129, 130
 wide-bandgap II-VI materials, 279–280
Liquid inclusions, 106
Liquid phase epitaxy (LPE), 209, 473
LiSAF, 347
Local shaping technique (LST), 317, 318, 347
Localized vibrational modes (LVM), 59–61, 65
Low-angle silicon sheets (LASS), 469
Low-carbon steel autoclaves, 396
Low-dislocation crystals, 400
Low-temperature luminescence, from point defects, 66
LSI (large-scale integration) chips, 1–2
 fabrication, 24
 void defects, 37
LST (laser-scattering tomography) defects, 36
LuAP:Ce (lutetium aluminate), 363, 382
Luminescence, 362
 room-temperature measurements, 67
 in semiconductors, 66
Lutetium orthosilicates (LSO), 363, 382
 cerium-doped (LSO–Lu₂SiO₅(Ce)), 378
Lutetium yttrium orthosilicate, 382
Lyapunov approach of stability analysis, 305
Macroscopic modelling, microscopic phenomena integration, 75
Macroscopic transport phenomena, 74
Magnesium, in conversion of graphite to diamond, 410
Magnesium carbide, 410
Magnetic fields, 516
 application to a conducting liquid, 82
 manipulating convection, 88
Mapping, 62
Marangoni effect, 84
 CZ-Si growth system, 39
Marangoni flow, 23
Marangoni numbers (Ma), 508–509
Mass balance, 109, 110
Mass transport, 109
Medical imaging, 361, 382
Melt feeding, 372
Melt growth, species mass conservation, 97
Melt volume, 100
Melt-grown GaAs, donors, 46
Melt-grown semi-insulating GaAs
 defects in, 54–59
 native defects, 57–58
 point defects, 57–59
 structural defects, 54–56
Melt-growth methods, 77
Melt-growth models, 112
 sharp-interface, 84
Melt-growth systems, growth kinetics, 85
Melt-level elevation, 369, 370
Melt-weight control, 369
Meniscus, static stability, 318
Meniscus-defined growth, 77, 98
Mercury cadmium telluride, Zn concentration and uniformity, 256–260
Mercury purification, 222–223
Metal organic chemical vapor deposition (MOCVD), 174
Metal solvent/catalysts, effect on diamond color, 423–424
Metal–carbon system, schematic diagram, 412, 414
Metal-insulator-semiconductor (MIS) detectors, 213
Metal-organic vapor phase epitaxy (MOVPE), 209
Metallurgical-grade silicon (MG-Si), 4

- Method of spines, 93
 MF_2 fluorite-type fluorides, 344
 $MF_2 - RF_3$, phase diagrams, 344
 MgF_2 doping, 342
Microgravity, 504
Microgravity conditions, bulk crystal growth under, 477–524
Microgravity crystal-growth experiments
 by Bridgman method, 479–487, 502
 classification, 502
 crystal quality, 516
 float zone or molten drop, 488–496, 502, 508–510
 from solution, 479–499, 502, 514–515
 from vapor, 500–501, 502, 515, 516, 517
 timetable, 503–504
Micropipes, 445, 446, 447
Microsegregation, 505, 508
Mineral silica, 4
Minority traps, 64
MIR orbiting station, 478
Misfit dislocations, 214
Modelling *see* Computer modelling
Modelling examples, crystal-growth, 98–111
Modelling techniques, 39
Modified Bridgman autoclaves, 396, 397
Modified techniques of pulling from the shaper (TPS), 316–317
Modified Verneuil's sapphire growth technique, 304
Modified-Lely method, 276
Molecular beam epitaxy (MBE), 209
Monoclinic BaR_2F_8 compounds, 342
Multicrystalline silicon
 directional solidification, 460–461
 impurities, 461
- Nacken, Richard, 389
 $NaF-RF_3$, 346
 $NaFe^{3+}Si_2O_6$, 401
 $NaI(Tl)$, 359, 361, 363, 364, 370, 375
Nakagawa etchant, 256
'Nanotopography', 16
 $NaRF_4$, gagarinite crystals, 346
NASA, 477
Natural convection, effect on axial chemical segregation, 516
Navier–Stokes equations, 100
'Needle-eye technique', 15
Newton's method, 90
Ni–C system, phase diagram, 409, 410
- Nickel
 effect on color of diamond crystals, 428
 impurities in synthetic diamonds, 423
NIR mapping system, 257, 258
NIR measurement, temperature dependence, 259, 259
NIR transmission spectra, 257, 258
Nitrides, structural defects, 174
Nitrogen
 in diamond synthesis, 424
 impurities in diamonds, 427
 solubility in liquid gallium, 192, 193
Nitrogen getters, 424
No-penetration conditions, 82, 83
No-slip conditions, 82, 83
Noninertial reference frames, 82, 88
Normal freeze segregation, 158
Nucleation
 InSb (111) growth plane, 162
 InSb[Te], 160
 rate of, 181
Nucleation theory, 181
Numerical interface representation, 90–92
Numerical modelling, 39
- Optical low-pass filters (OLPF), 388
Optical transparency, single crystals of solid solutions, 344
Optoelectronics, short-wavelength, 173
Order–disorder phase transitions, 342
Oxidation-induced stacking faults (OSF), 33–35
Oxide scintillators, 362, 363
 crystal growth, 376–378
 crystal-diameter constancy, 376
 crystal-growth control, 377
 doping, 364
 high melting point crystal growth, 383
 single crystals, 364
 uses, 376
Oxygen
 precipitation and gettering, 30–33
 in Si crystals, 27–30, 35, 36
- Parallel-computing development, 76
Partial-differential-equation-based grid generation, 93
pBN-polycrystal boats, 243, 246
 $PbWO_4$, 359
Peclet number, 507
Pellet source seed model, 439

- Penetration conditions, 83
Perovskite (KMgF_3), 342
PET (positron emission tomography), 361
Phase diagrams, 348, 350
 pressure-temperature phase diagram, 230
 wide-bandgap II-VI compounds, 270, 273
Phase transitions, 342
Phase-field method, 90, 112
Phosphorus, raw material for InP, 125
Phosphorus impurities, in CVD diamond, 423
Photo-induced current transient spectroscopy (PICTS), 63
Photo-thermal ionization spectroscopy (PTIS), 63
Photoluminescence, 66
Photovoltaic silicon crystals, 451-476
 casting and directional solidification, 459-461
 comparison of growth methods, 473-475
 comparisons between CZ and FZ growth, 456-459
 concentration profiles for selected impurities, 458, 459
 Czochralski growth, 452-454
 dendritic web growth, 463, 464
 feedstock, 454
 FZ growth in a vacuum, 458
 growth rate as function of crystal diameter, 453, 454
 large-area solid/liquid interface growth methods, 468-472
 multicrystalline ingot growth methods, 459-462
 ribbon or sheet growth methods, 463-472
 small-area solid/liquid interface growth methods, 463-468
 Stepanov growth, 463, 464
 thin-layer growth on substrates, 472-473
 see also Silicon
Physical vapor transport (PVT), 272, 274-276, 281, 434, 435, 517
 SiC growth system schematic diagram, 435
 ZnSe single crystal growth, 288
Pill-doping method, 459
Piper-Polich method, 274
Point defects, SI GaAs low-temperature luminescence, 66
Polycrystalline GaAs, 53
Polycrystalline InP, GDMS impurity analysis, 129
Polycrystalline silicon, manufacture, 3-6
Polymorphism, 340, 342
Position-sensitive photomultiplier tube (PMT), 361
Post-growth annealing method, 251
Potassium titanyl phosphate (KTP)
 particle pathlines around rotating crystals, 108
 solution growth morphological stability, 106-111
Powder-feeding method, 372
Preconditioned generalized minimal residual (GMRES) method, 90
Preconditioners, 77
Pressure autoclaves, 396
Pressure-controlled-LEC (PC-LEC), 136
Pseudosolid-domain mapping, 93
Pulling from the shaper techniques *see* Techniques of pulling from shaper (TPS)
Pulling parameters, 368
PWO, 377-378
Pyrohydrolysis, 350
Pyrolytic boron nitride (pBN), 126, 243, 246
Quality factor, quartz crystals, 399
Quantitative furnace modelling, 112
Quantum wells, 122
 β -Quartz, 387
Quartz, fabrication from a single crystal, 398, 399
Quartz boats, 243
Quartz crucibles, 53
Quartz crystals, 387-406
 aluminum concentration check, 401
 apparatus for hydrothermal growth, 396
 applications, 388
 characteristics of low-defect, high-purity, 402, 403
 chemical impurities, 403
 commercial production at AT & T Bell Labs, 390, 391
 conditions for selecting most suitable mineralizer, 392
 crystal defects, 403
 crystalline forms, 387
 dependence of effective partition coefficient OH^- impurity on growth rate, 401, 402
 distribution of impurities in synthetic, 402
 effect of nutrient materials on quality, 400
 effect of seed on quality, 400
 grown by Nacken, 389
 growth rate, 399-400
 growth of a single crystal into the seed, 392

- history of growth, 388–391
- Hydrothermal growth, 388, 390, 396
- inclusions, 403
- log solubility in NaOH and Na₂CO₃, 393, 395
- obtained by Walker, 390, 391
- optimum growth conditions for synthesis, 398
- physical chemistry of growth, 391–392
- principal source, 388
- production costs, 388
- quality factor Q , 399
- quality of grown crystals, 398
- quality parameters, 402–403
- solubility, 392–395
- solubility in mixed solvents, 400–401
- structure, 387
- type of crystals to be grown, 398
- α -Quartz crystals, 387
 - applications, 388
 - defects in synthetic crystals, 401–402
 - growth, 396–398
 - obtained using α -cristobalite, 400, 401
 - physicochemical defects, 401
 - processing for high-frequency devices, 402–404
- Quartz resonators, 403
- Quasi-steady-state models, 96–97
- Quench anneal, 212
- Quenching studies, CMT, 228–229

- Radial segregation, 505, 508
- Radial x variations, 223, 228, 229
- Radiation heat-transfer modelling, 86–87
- Radiation-detection devices, 357
- Radiation-hard scintillation single-crystal production, 381
- Radiochemical transformations, 379
- Ramp-assisted foil-casting technique (RAFT), 472
- RANS (Reynolds-averaged Navier–Stokes), 22
- Rare-earth trifluorides (RF₃), 339, 344
 - high-temperature polymorphs, 341
 - pattern of polymorphism and morphotropy, 340, 341
 - phase transitions, 340, 341
- Raw-material feeding method, halide scintillators, 373
- Raw-material feeding system, 365, 366
- Raw-material purification, 372
- Reactive ion etching, 236

- Red phosphorus, 126
- Reference frames, 82, 88, 99
- Residual gravity level, 507
- Resistivity maps
 - Fe doped wafers, 143, 144
 - SI GaAs wafer, 62
- Resonators
 - fabrication from single quartz crystal, 398, 399
 - produced by chemical etching processing, 404
- Reverse contrast (RC) defect, 59
- Reynolds-averaged Navier–Stokes (RANS), 89
- RFe, transformation to berthollides, 345
- Ribbon growth on substrate (RGS) technique, 472
- Ribbon or sheet growth methods, photovoltaic silicon crystals, 463–472
- Ribbon-against-drop (RAD) method, 466, 467
- Ribbon-to-ribbon float zoning (RTR), 465, 467
- Ribbon-to-ribbon (RTR) process, 98
 - reference frame, 99
 - results, 101
- Rocket nose cones, requirements, 328
- Rocking curves, GaAs wafer, 67, 68
- Roller quenching (RQ) method, 471
- Rotary Bridgman technique, 168
- Rotating magnetic fields, 39
- Rubies, 300
 - impurity inhomogeneities, 327
- Ruby-sapphire crystals, 304

- S doping, InP, 141
- S-web method, 470
- Saddle points, 349, 350
- Salyut, 478
- Sapphire crystals, 194, 302–319
 - applications, 327–329
 - crystallographic structure, 301–302
 - data, 335–338
 - dome production, 328
 - electrical data, 337–338
 - facetted growth, 326
 - growth by floating-zone technique (FZT), 308–310
 - growth by horizontal Bridgman technique, 313
 - melt data, 334–335
 - optical data, 337
 - physical properties, 334–338
 - physical/mechanical data, 335–336

- Sapphire crystals, (*continued*)
 principal growth scheme, 302–303
 pulling from shaper growth techniques,
 315–316
 raw material, 303
 resistance properties, 338
 shaped growth, 314
 single crystal production, 313
 as substrates in electronics, 329
 thermal data, 335
 TPS-grown defect structure, 325
 twinning process, 326
 Verneuil's growth technique, 302–308
 windows requirements, 327–328
- Sapphire substrates, 197–201
 as seed material for ZnTe, 292
- Satellites, automatic, 502
- Scavenger principle, 352
- Scavengers, 364
- Schottky-barrier method, 64
- SCIM (silicon coating from an inverted
 meniscus) technique, 471
- Scintillation pulse decay time, 358
- Scintillation-material efficiency estimation,
 361–364
 stages, 361–362
- Scintillator crystals, 357–385
 activator distribution of single, 374–376
 activator evaporation, 375
 applications, 357, 358–361
 conditions for manufacture of crystals with
 good characteristics, 377
 Czochralski system for fluoride growth,
 380
 development history, 357–358, 359, 360
 extrinsic luminescence, 362
 future of, 383
 groups, 362
 growth in a RAP atmosphere, 380
 growth techniques and materials, 375
 impurity distribution, 374
 influence of single-crystal perfection on
 characteristics, 378–381
 initial luminescence mechanisms, 362
 low luminescence efficiency, 362
 lutetium compound, 382
 material types, 362, 363
 medical imaging, 361
 melt-level elevation, 369, 370
 new, 381–382
 radiation hardness, 358
 requirements, 358
 sources of efficiency loss, 378
 use in experimental high-energy physics,
 359–361, 364
- Screw dislocations
 CZ InSb, 161
 SiC, 445
- Second-order trapezoid rule, 90
- Secondary ion mass spectrometry (SIMS), 59
- Seebeck coefficient, 236
- Seed-end wafers, dislocation patterns, 135
- Seeded chemical vapor transport (SCVT), 276,
 281, 283
- Seeded growth
 GaN from solutions in Ga on GaN
 substrates, 195–197
 GaN from solutions in Ga on GaN/sapphire
 substrates, 197–201
- Seeded physical vapor transport (SPVT), 269,
 270, 276
- Segregation coefficients, of dopants in
 melt-grown GaAs, 46, 47
- Selenium, purification, 289
- Semi-infinite melt scheme, 167
- Semi-insulating GaAs, deep level defects,
 63–64
- Semi-insulating InP, 142–145
- Semi-insulating LEC GaAs, 52–53
- Semi-insulating SiC (SI-SiC) substrates, bulk
 growth, 436–437
- Semiconductor-grade silicon (SG-Si), 5
- Semiconductors
 melting conditions, 175, 176
 roadmap, 2–3
- Semicontinuous edge-supported pulling (ESP)
 ribbon growth, 468
- Semicontinuous electromagnetic casting,
 461–462
- Semicontinuous silicon ingot growth, 461
- Shallow acceptors, low-temperature
 luminescence, 66
- Shallow donors, 143
- Sharp-interface methods, 84, 86, 91, 112
- Siemens method, 5
- Silica, 4, 400
- Silica crucible, 9–11
- Silicon, 1–42
 behavior of oxygen and vacancies in
 crystals, 35, 36
 crystal-growth method and technology, 3–18
 defect and wafer quality, 30–39
 diameter growth control of crystals, 8
 dislocation-free crystal growth, 12–13, 14

- float-zone (FZ) crystal growth, 13–16
- grown-in defects of crystals, 33–39
- high-purity polycrystalline silicon, 3–6
- improvement in chip performance, 2
- impurities in CVD diamond, 423
- intrinsic point defects, 35
- melt process, 18–30
- in SI GaAs, 57
- slicing crystals, 17
- vacancies in crystals, 35
- void defects of wafers, 39
- wafer processing, 16–18
- wafer size, 3
- wafers polishing process, 18
- see also* CZ-Si; Photovoltaic silicon crystals
- Silicon carbide (SiC)
 - advantages, 433
 - boule growth process, 434
 - bulk growth process, 437–442
 - commercialization challenge, 447
 - crystal growth rate, 444
 - crystallization, 441–442
 - defect types, 443
 - doping of boules, 437
 - factors affecting crystal growth, 441
 - growth, 433–449
 - growth in argon gas mixture, 440
 - growth by sublimation, 434
 - growth crucible, 437, 438
 - growth direction, 435–436
 - growth-related defects, 444–446
 - historical development, 434–435
 - industrial production, 435–437
 - LPE growth from Si/Sc solution, 515
 - mass transfer region, 440–441
 - n-type doping, 437
 - nucleation centers, 441–442
 - p-type doping, 437
 - planar or hexagonal defects, 446
 - properties, 433
 - screw dislocations, 442
 - seeded sublimation, 435
 - source region, 438–440
 - sublimation temperature, 438
 - substrates and homoepitaxial growth, 433
 - temperature dependence of vapor stoichiometry coefficient, 439
- Silicon melt
 - measuring silica (or oxygen) dissolution rate, 25
 - visualization of flow field, 19
- Silicon sheet from powder (SSP), 468, 469
- Silicon-on-ceramic (SOC) growth technique, 465
- Silicon-oxygen binary system, phase diagram, 30, 31
- Simple fixed-grid method, 94–96
- SiO₂ *see* Quartz
- Skylab missions, 477
- 'Slush' growth, 216
- Small-area solid/liquid interface growth
 - methods, photovoltaic silicon, 463–468
- Sn doping, 141
- Solar-cell silicon *see* Photovoltaic silicon crystal growth
- Solid inclusions, corundum crystals, 323
- Solid phase recrystallization (SPR), 280, 281
- Solid solutions, decomposition and ordering, 342–346
- Solid state electrolysis, 403
- Solid state laser media, 339
- Solid state recrystallization (SSR), 209, 212–217, 222, 280, 281
- Solid state transformations, radiation-induced, 379
- Solute-feeding, 167
- Solution crystal growth, coupled surface and bulk transport model, 108
- Solution growth with agitation, 77, 78
- Solution-growth bulk crystal growth methods, 77
- Solution-growth model, 113
- Solution-growth system, behavior of steps, 110, 111
- Solvent/catalysts, for diamond formation, 409
- Space crystal-growth experiments, 478
- Space shuttle, 502
- Space stations, 502
- SPECT (single-photon emission tomography), 361
- Spectral discretization method, 90
- Spiral shearing flow, 225
- SSP (Silicon sheet from powder), 468, 469
- SSR *see* solid state recrystallization
- Stability functions, 348
- Step bunches, 106, 110
- Step motion, 108
- Step spacing, 110
- Stepanov technique, 315
- Stockbarger method, 364
 - modified, 365, 366
- Streamline-upwind Petrov–Galerkin method, 105

- Striations
 segregation in InSb, 158–159
 type II, 514
 Structural defects, heteroepitaxial nitrides, 174
 Sublimation method, 434, 515
 Sublimation THM, ZnTe single crystal growth, 293
 Sulfur, in SI GaAs, 57
 Supercooling, 195
 Supersaturation, 86
 Surface light scattering observation (S-LS), 253
 Surface quality, GaAs substrates, 67
 Sweeping, enhancing quartz resonators performance, 403

 Taylor–Görtler-type flow instability, 103, 104
 Teardrop-shaped pits, 161
 Techniques of pulling from shaper (TPS), 315–316, 318, 330–331
 Teflon decomposition process, 351
 Tellurium
 inclusions in CZT, 102
 purification, 223
 purity, 242, 243
 Temperature gradient reduction, 135
 Temperature gradient technique, 314
 diamond growth, 416–417
 Ternary antimonides, 165
 Ternary phase diagram, In(As, Sb), 168
 Thallium iodide feeding concentration, 376
 Thermal-stress-generation mechanisms, 443–444
 Thermally stimulated currents (TSC)
 spectroscopy, 63, 64
 Thermocapillary convection, role on striations, 516
 Thermophysical property data, 23
 Thin-layer silicon, 472
 Threading edge dislocations, 445
 Three-dimensional phenomena, modelling difficulties, 76
 Three-dimensional transport phenomena, 76
 Tiller's approximation, 348
 Time scales, bulk crystal growth, 74
 Time-dependent transport models, 76
 Time-domain charge measurement (TDCM), 62
 Top-seeded solution growth (TSSG) technique, 347
 Toroidal apparatus, 412
 TPS *see* Techniques of pulling from shaper
 Tracer particles, 19–20

 Tracking, interface, 112
 Transient Couette flow, 225
 Transition metals and alloys, diamond formation agents, 409
 Transport equations, 97
 Transport modelling, 75, 76, 79–89, 112
 governing equations, 79–83
 nomenclature, 80–81
 Traps, 63, 64
 Traveling heater method (THM), 77, 167, 209, 217–222, 514
 ACRT and, 220
 CdTe and HgTe feed materials, 218, 219
 CMT growth, 217–222
 experimental arrangement, 218
 furnace arrangement, 218
 mass and heat transport, 220–221
 principle, 217
 segregation of impurities, 218–219
 temperature profile, 218
 wide-bandgap II–VI materials, 279
 Tridymite, 387, 400
 Tube crystals, float-zone growth modelling, 99
 Turbulence flow models, 22, 89
 Twinning, 342
 at 'edge' facets, 156
 InP, 132–133
 InSb, 152
 Tysonite-type compounds (RF_3), 342
 Tysonite-type solid solution, melt crystallization, 348

 Vacuum processing, indium antimonide, 154
 Vapor-controlled Czochralski (VCZ), 53, 136
 Variable shaping technique, 316–317
 Verneuil sapphire growth technique, 300, 302–308
 characterization, 329–330
 crystal quality, 325
 principal scheme of growth, 302–303
 raw material, 303
 stability analysis-based automation, 307–308
 theoretical investigation, 304–305
 Vertical Bridgman technique (VBT), 77, 78, 277, 278, 314, 331
 CZT growth, 102
 ZnSe growth, 284
 Vertical gradient freeze (VGF) technique, 53–54, 77, 91, 92, 136–138
 advantages, 137
 CdTe single-crystal growth, 244–260

- diameter control of GaAs, 53
- dislocation density of GaAs, 54
- furnace, 137
- growth sequence of InP, 137
- InSb, 164–165
- S-doped InP ingot, 138
- temperature distribution in furnace, 260
- ZnTe single crystal growth, 292
- Void defects, 37, 39, 254
 - LSI chip fabrication, 37
 - octahedral, 37
 - Si crystals, 35, 36
 - Si wafers, 39
 - sketch, 37
- Volume-of-fluid method, 91
- von Mises stresses, calculation, 140
- Voronkov's model, 38
- Wafer processing
 - CdZnTe, 260–265
 - silicon, 16–18
- Wafer size, InSb evolution, 163
- Wetting procedure, 197–198
- Wetting-line locations, 100
- Wide-bandgap II-VI compounds, 269–297
 - growth from solid phase, 280
 - liquid encapsulation Czochralski (LEC), 279–280
 - phase diagrams, 270
 - see also* II-VI compound semiconductors
- X-ray CT (computer tomography), 361
- X-ray diagnostic machines, 361
- X-ray diffraction, 67
- YF₃, 342
- Zinc
 - concentration correlation between ICP and wavelength analysis in CZT, 257, 258
 - p-type dopant, 142
 - purification, 289
- Zinc oxide (ZnO), 269, 282–284
 - growth from liquid phase, 282–283
 - growth from vapor phase, 283–284
 - hydrothermal growth of single crystals, 277, 278
- Zinc selenide (ZnSe), 269, 284–291
 - band-edge emission grown by PVT method, 290
 - band-edge emissions, 286, 287
 - crystal grown by Bridgman method, 285, 286
 - CVD growth method, 284
 - CVT single crystal growth method, 288
 - experimental values summary, 286, **287**
 - growth from liquid phase, 284–288
 - growth from solid phase, 290–291
 - growth from vapor phase, 288–290
 - growth velocity and temperature gradient at growth interfaces, 284, 285
 - purification of selenium, 289
 - purification of zinc, 289
 - SSR growth mechanism, 291
- Zinc sulfide (ZnS), 269, 280–282
 - dependence of grain size on annealing atmosphere and temperature, 282
 - faceting geometry of lattice, 157, **158**
 - growth from liquid phase, 280–281
 - growth from solid phase, 281–282
 - growth from vapor phase, 281
 - lattice, 151
 - SSR/SPR growth, 281
- Zinc telluride (ZnTe), 269, 291–294
 - grown by KT and GF combination, 292–293
 - grown by LEC technique, 280
 - growth from liquid phase, 291–293
 - growth from vapor phase, 293–294
 - twin-free single crystals, 293
 - X-ray rocking curve FWHM, 294
- Zincblende structure, 124, 125